NASA Technical Memorandum 87563

Reports of Planetary Geology and Geophysics Program—1984

APRIL 1985

NASA

NASA Technical Memorandum 87563

Reports of Planetary Geology and Geophysics Program—1984

Compiled by
Henry E. Holt and T. R. Watters
NASA Office of Space Science and Applications
Washington, D.C.

National Aeronautics
and Space Administration

**Scientific and Technical
Information Branch**

1985

Foreword

This is a compilation of abstracts of reports from Principal Investigators of NASA's Office of Space Science and Applications, Solar System Exploration Division, Planetary Geology and Geophysics Program.

The purpose is to provide a document which succinctly summarizes work conducted in this program. Each report reflects significant accomplishments within the area of the author's funded grant or contract.

No attempt has been made to introduce editorial or stylistic uniformity; on the contrary, the style of each report is that of the Principal Investigator and may best portray his research.

Joseph M. Boyce
Discipline Scientist
Planetary Geology and Geophysics Program

Page intentionally left blank

TABLE OF CONTENTS

CHAPTER 15 - GEOLOGICAL MAPPING, CARTOGRAPHY AND GEODESY

CHAPTER 16 - SPECIAL PROGRAMS

ADDITIONAL ABSTRACTS

CHAPTER 1

OUTER PLANETS AND SATELLITES

Page intentionally left blank

HOT SPOTS ON IO: CORRELATION OF INFRARED EMISSION AND VISIBLE REFLECTANCE

A.S. McEWEN
U.S. Geological Survey, Flagstaff, AZ, 86001
Dept. of Geology, Arizona State University, Tempe, Arizona, 85287
L.A. SODERBLOM
U.S. Geological Survey, Flagstaff, AZ, 86001,
D.L. MATSON and T.V. JOHNSON
Jet Propulsion Laboratory, Pasadena, CA, 91109

Hot spots detected by the Voyager 1 infrared spectrometer (IRIS) seem to correspond to relatively dark albedo features seen in the Voyager 1 imaging data (1). The inverse correlation, however, that all dark albedo features may be hot spots, has been rejected due to published statements which suggest that about 5% of Io's surface is covered by "black" features (2,3,4), whereas only 1-2% of Io is covered by hot spots (5). However, the 5% estimate is too high; only about 1% of the surface is covered by features with reflectivities ≤ 0.3 in all visible wavelengths. Within the region covered by IRIS, all of the largest dark features were identified as hot spots. Therefore, the relationship between albedo and volcanic hot spots may be much more direct and exact than generally believed.

This paper presents a correlative study of IRIS data and two recently compiled data sets: Voyager imaging mosaics and measurements of Io's thermal emission from the NASA Infrared Telescope Facility (IRTF). These data were used to refine the correlation between dark spot optical properties (albedo and color) and thermal emission, to examine this correspondence on a satellite-wide scale, and to identify additional hot spots not included in the IRIS inventory. The first new data set consists of global multispectral mosaics in four bandpasses (0.35 through 0.60 μm) compiled from Voyager 1 and 2 images (6). The second new data set is the disk-integrated radiance of Io measured as a function of rotational position and at wavelengths including 8.7, 10, and 20 μm (7). The 8.7 and 10 μm channels are the most useful for determining the global flux and its variation with longitude for three reasons: 1) the majority of the hot spot flux is emitted at these wavelengths due to the typical hot spot temperatures of 200 to 450 K; 2) this flux is far in excess of reflected solar radiation so it can be measured when Io is illuminated; 3) this flux is also significantly greater than the passive background component, even when Io is illuminated. In addition, 4.8 μm eclipse observations (8,9) were used to constrain very hot sources (>300 K) that occur within about 70° from the sub-Jupiter point.

The orange filter (0.59 ± 0.03 μm) global mosaic is the best discriminator of the dark albedo features because the great majority of the surface is bright (albedo >0.5) at this wavelength. Discreet dark albedo features, covering ~1% of the surface, can be identified by orange filter albedo ≤ 0.3, so this is how we chose to define "dark" spots. The total disk-integrated area of dark spots, as a function of central longitude, was convolved from the global mosaics. This curve is strikingly similar to Io's 8.7 and 10 μm radiance. Two maxima are evident: one centered near 300°W, the hemisphere that includes Loki and other hot spots detected by IRIS, and a broad maxima from 90° to 180°W. Examination of the global mosaics reveals that the source of this second maxima is a large annular structure ~1000 km in diameter, ~100 km in width, and concentric about a point near 140°W and 75°S (herein referred to as the "ring"). About 200 arc degrees of the ring has a dark albedo, centered on 120°W and 70°S. As the dark portion of the ring seems to dominate the excess thermal flux in this hemisphere, its temperature can be modelled directly from the IRTF data; the resultant model temperature is 280 K.

In order to test the hypothesis of a simple temperature-albedo relationship, one can first compare the temperature and area models by Pearl and Sinton (1) for the IRIS features, and for the ring quoted above, with the orange filter albedos. Pearl and Sinton solved for both temperatures and areas as unknowns, finding one or two anomalously hot temperatures and areas for each feature. They point out that these are the simplest models that fit the data within significant residuals, and that large lateral temperature gradients can be present. In order to model temperature versus albedo, we used the modality of the orange filter histograms of each feature to define the areas, then solved for the temperatures. Our results show an inverse correlation between albedo and temperature. Two trends are apparent in the temperature-albedo plot: features associated with active volcanic plumes (Loki, Pele, and Amirani/Maui) are hotter as a function of albedo than spots at which no active plume was detected.

Next, we modelled temperatures for the dark features based on the 8.7 and 10 μm IRTF data and the 4.8 μm eclipse observations. With the ring fixed at 280 K, all other dark features were grouped into two albedo bins: ≤0.2 and 0.2-0.3, to define the areas and locations, and the best-fit temperatures are 350 K and 250 K respectively. This inversion was also run with the IRIS fluxes fixed, resulting in model temperatures of 340 K and 275 K for the two albedo bins. These temperature-albedo relations fall in about the middle of the points modelled on the IRIS spectra. Several more complicated models were tested, but these gave about the same results, within significant residuals, so they were discarded.

The results of our modelling include the identification of hot spots outside the region covered by IRIS and below the resolution of IRIS. In addition to the ring, these include Amaterasu Patera at 307°W, 37°N, and approximately 50 smaller features (areas <1000 km^2). The estimated total global heat flow from our model is 1.9 W m^{-2}.

Our interpretation of these results is that the hot spots are liquid sulfur lava lakes, for the following reasons: 1) The melting point of sulfur is 390 K, and the model hot spot temperatures range from ~200 to 450 K. Although small spots may have higher temperatures, such as Pele, these may be short-lived (10) and contribute only a small percentage of the total flux. Temperatures lower than 390 K are not inconsistent with the sulfur lake model as lower (conductive) temperatures may occur around the feature and through surface crusts. 2) The albedos and colors of the dark spots, measured from the global mosaics, are consistent with the laboratory measurements of Nelson et al. (4) for liquid sulfur. 3) High-resolution images of the dark features, especially Loki and Creidne Paterae, show morphologies suggestive of lava lakes, such as crusts, floating debris, melting, and convection. 4) Finally, and most importantly, this hypothesis provides a simple and direct explanation for why dark spots are hot on Io.

REFERENCES

1. Pearl, J.C. and W. Sinton, 1982, Hot spots of Io, The Satellites of Jupiter, 724-755.
2. Masursky, H., G.G. Schaber, L.A. Soderblom, and R.G. Strom, 1979, Preliminary geologic mapping of Io, Nature, 280, 725-728.
3. Carr, M.H., H. Masursky, R.G. Strom, and R.J. Terrile, 1979, Volcanic features of Io, Nature, 280, 729-732.
4. Nelson, R.M., D.C. Pieri, S.M. Baloga, D.B. Nash, and C. Sagan, 1983, The reflection spectrum of liquid sulfur: Implications for Io, Icarus, 56, 409-413.

5. Matson, D.L., G.A. Ransford, and T.V. Johnson, 1981, Heat flow from Io, J. Geophys. Res., 86, 1664-1672.
6. Soderblom, L.A., T.V. Johnson, J. Mosher, and A.S. McEwen, 1984, Global multispectral mosaics of Io, in preparation.
7. Johnson, T.V., D. Morrison, D.L. Matson, G.J. Veeder, R.H. Brown, and R.M. Nelson, 1984, Io volcanic hot spots: Stability and longitudinal distribution, Science, in press.
8. Sinton, W.M., 1981, The thermal emission spectrum of Io and a determination of the heat flux from its hot spots, J. Geophys. Res., 86, 3122-3128.
9. Morrison, D. and C.M. Telesco, 1980, Io: Observationsl constraints on internal energy and thermophysics of the surface, Icarus, 44, 226-233.
10. McEwen, A.S. and L.A. Soderblom, 1983, Two classes of volcanic plumes on Io, Icarus, 55, 191-217.

IO: GENERATION OF SILICATE MAGMA BY SHEAR MELTING AT THE BASE OF A BASALTIC LITHOSPHERE.

Michael H. Carr. U.S. Geological Survey, Menlo Park, CA 94025

Tidal theory and observational evidence indicate that about 1 W m^{-2} of energy is released at the surface of Io. If all this tidal energy were released uniformly throughout a rigid lithosphere then the lithosphere would be only about 10 km thick. Furthermore, this form of tidal dissipation would result in no melting of silicates for the heat would all be generated within the rigid lithosphere, above the zone of melting, and conducted to the surface. This 'thin skin' model appears improbable on two grounds. First, 10-km high mountains cannot be supported by such a thin lithosphere, they probably require that the lithosphere be at least 30 km thick (Yoder pers. comm.). Second, 2-3 km deep calderas and 2-3 km high escarpments require that the landscape be composed largely of materials with strength and thermal properties comparable to silicates (Clow and Carr, 1980). Sulfur is unlikely to dominate in the upper few kilometers because it behaves ductilely at too low a temperature to support the observed relief. If the landscape is dominantly silicate then high rates of silicate volcanism are implied, which is contrary to the thin skin model. These problems are resolved if the lithosphere is considerably thicker than 10 km, but, as demonstrated below, such a thick lithosphere implies that most of the tidal energy is dissipated by viscous deformation at the base of the lithosphere not by flexure of the rigid lithosphere as originally proposed by Peale et al. (1979)

In order to place limits on how much tidal energy can be dissipated within a rigid lithosphere, depth-temperature profiles were calculated for different lithosphere thicknesses assuming that the tidal energy was dissipated uniformly throughout the lithosphere. At maximum energy dissipation for a given lithosphere thickness, solidus temperatures are just reached at the base of the lithosphere and no heat is conducted into the lithosphere from below; if more energy were dissipated in, or conducted into the lithosphere, it would become thinner. As an example, solidus temperatures are reached at the base of a 30 km basalt lithosphere with a conductivity of 4.5 W m^{-1} $°K^{-1}$ when the dissipation rate is 1.2 x 10^{-5} W m^{-3}, giving a total heat flux at the surface of 0.36 W m^{-2}. This latter figure falls far short of the 1 W m^{-2} that must be dissipated. The temperature profile would be changed if the effective conductivity of the near surface materials were enhanced, such as by upward movement of sulfur magmas, or decreased, such as by the presence of sulfur rich materials, but such affects are small. For thicker lithospheres the problem is even more severe. For example, no more than 0.18 W m^{-2} can be dissipated in a 60-km thick lithosphere without causing it to thin.

Thus a thick lithosphere implies that a significant fraction of the tidal energy is dissipated below the depth where solidus temperatures are reached. One possibility is that Io has a crust consisting of a low melting temperature fraction such as basalt, overlying a mantle of a high

melting temperature fraction such as peridotite. At the base of the crust basalt would be at its melting temperature but underlain by rigid peridotite at a temperature above the basalt solidus but below the peridotite solidus. The rigid peridotite could then flex like the basalt crust thereby generating tidal heat. The maximum amount of heat that can be so generated can be calculated on the assumption that the Q and the rigidity of the basalt and peridotite are identical and that the amplitude of flexure of the peridotite is the same the basalt. If all these conditions hold then the rate of heat generation per unit volume will be the same in both peridotite and basalt, thereby enabling a temperature profile within the rigid peridotite to ba calculated together with the thickness of rigid peridotite and the total heat generated within it. The heat generated within the peridotite so calculated is almost certainly an upper limit and the thickness a lower limit since the amplitude of flexure of the peridotite is likely to be less than that in the basalt, and the rate of heat generation correspondingly smaller, because of the higher confining pressures. Even the maximum value for heat generation falls short of that needed to account for all the tidal energy. With a 30 km thick basaltic lithosphere a maximum of 0.15 W m^{-2} can be tidally dissipated within the rigid peridotite, which, on the above assumptions, would be 15 km thick. This, together with the maximum of 0.36 W m^{-2} generated in the basaltic lithosphere, gives a total dissipation of 0.51 W m^{-2}. For a 60 km lithosphere the equivalent figure is 0.27 W m^{-2}, far short of the required 1 W m^{-2}. Thus if the lithosphere of Io is thicker than about 10-15 km, as appears probable, then a significant fraction of the tidal energy must be dissipated by some mechanism other than tidal flexure.

A plausible possibility is that some of the tidal energy is dissipated by viscous deformation in a zone of partial melting at the base of the basaltic lithosphere. The viscosity of basalt falls rapidly from about 10^{21} poises at the solidus to about 10^{7} poises at a temperature 100°C above the solidus (Shaw, 1969), a drop of an order of magnitude every 7°C increase in temperature. Thus, once partial melting starts shear stresses will tend to be relieved in the melt zone, thereby raising temperatures, lowering the viscosity further, and causing the basaltic lithosphere to become decoupled from the underlying peridotite. The mechanism is similar to that proposed by Shaw (1970) for Earth tides. The minimum energy dissipated in this way is simply the difference between the total tidal energy (1 W m^{-2}) and the maximum amounts calculated above for the energy dissipated by rigid flexure. With maximum tidal energy dissipated within the lithosphere no heat can be conducted upward out of the melt zone without thinning the lithosphere; heat from in or below the melt zone must be transported upward as silicate magma. Thus for any thickness of lithosphere the rate of magma generation can be calculated, as well as the rate of resurfacing on the assumption that all the magma reaches the surface. For a 30 km thick lithosphere, the resurfacing rate thus calculated is 0.36 cm yr^{-1}, for a 60 km thick lithosphere the rate is 0.46 cm yr^{-1}. At the other extreme where no heat is generated in the rigid lithosphere and the maximum amout of of heat is conducted upward out

of the melt zone, the equivalent rates are 0.46 and 0.51 cm yr^{-1} respectively. These rates are for transport of magma to the near-surface. Some indeterminate fraction will be injected as sills and dikes, the rest erupted onto the surface.

A question arises as to whether the basaltic magma will be bouyant enough to reach the surface. On Earth the density contrast between basaltic lava and peridotote provides the hydrostatic head which drives the magma to the surface (Eaton and Murata, 1960). In the model just described we have only the density contrast between molten basalt and solid basalt to create the pressure differential at the source. Taking plausible values for the change in volume on melting (0.0132 cm^3 gm^{-1}) and the coefficient of volume expansion (9.6×10^{-5} $°K^{-1}$) for basalts suggest that with a 30 km lithosphere the height limit for volcanoes is 1.8 km. For a 60 km thick lithosphere the height limit is 3.6 km. These relatively small heights are consistent with the general lack of large volcanic edifices despite high rates of volcanism.

Thus if the lithosphere of Io is thicker than 30 km, as appears probable, then high rates of silicate volcanism are implied and a significant fraction of the tidal energy must be dissipated by viscous deformation rather than rigid flexure.

References

Clow, G. D., and Carr, M. H., 1980, Stability of sulfur slopes on Io: Icarus, v. 44, p. 268-279

Eaton, J. P., and Murata, K. J., 1960, How volcanoes grow. Science, v. 132, p. 925-926

Shaw, H. R., 1969, Rheology of basalt in the melting range. J. Petrology, v. 10, p. 510-535.

Shaw, H. R., 1970, Earth tides, global heat flow and tectonics. Science, v. 168, p. 1084-1087.

STABILITY OF THE GALILEAN SATELLITES IN DEEP ORBITAL RESONANCE

Richard Greenberg, Planetary Science Institute, Tucson, Az 85719

The Galilean satellites are locked in the Laplace resonance, which is responsible for forcing their significant orbital eccentricities (Greenberg, 1976). The eccentricities in turn result in tidal energy dissipation within the satellites that is responsible for the great thermal activity on Io, including both volcanism observed by Voyager and heat flux measured from Earth (Peale et al., 1979). Tidal heating probably played a dominant role in shaping Europa as well.

The resonance results from the nearly 2:1 commensurability of orbital periods (or equivalently of mean motions) taken by pairs. The mean motions of Io and Europa obey the relation $n_1 - 2n_2 = \nu$, where ν is a small constant much smaller than either n_1 or n_2. Current values are $n_1 \approx 200^\circ$/day, $n_2 \approx 100^\circ$/day, and $\nu \approx 0.8^\circ$/day. Geometrically, this relationship implies that the longitude of conjunction of Io and Europa is nearly fixed, moving only at the slow rate ν. The pair Europa and Ganymede are also near a 2:1 commensurability with $n_2 - 2n_3$ equal to the same small value ν. Thus conjunction of Europa and Ganymede also migrates at the same slow rate ν.

These geometrical relations enhance the mutual gravitational effects with two important results. First, the angle between these two conjunction longitudes, ϕ, is stabilized at the constant value 180°. Second, orbital eccentricities are enhanced, promoting tidal heating with the important geological consequences.

Tidal energy dissipation has other important effects as well. It affects the long-term orbital evolution of the satellites. Ultimately, any tidal heat dissipated within a satellite must come from the satellite's orbital energy. Long-term evolution may also be affected by tides raised on Jupiter by the satellites. This process may add energy to the satellites' orbits at the expense of Jupiter's rotation. Because tidal effects are strongly dependent on distance between planet and satellite, tides raised on or by Io, rather than other satellites, dominate the evolution.

Yoder (1979) pointed out that tides raised on Io tend to drive the system out of resonance (toward greater ν and correspondingly smaller eccentricities) while tides raised on Jupiter tend to drive the system towards "deeper" resonance (smaller ν and larger forced eccentricities). Yoder proposed that the system began out of resonance ($\nu >> 0$) but evolved into resonance due to tides on Jupiter. As the eccentricity increased, tides on Io became increasingly important, until the decrease in ν was halted by the contrary tendency of the tides on Io. Thus Yoder interpreted the present value of ν as representing an equilibrium between the competing effects. The only difficulty with that elegant theory is that the high measured and inferred heat loss from Io would require a correspondingly high tidal dissipation in Jupiter (Greenberg, 1982). The required rate is higher than has yet been explained by Jovian interior models.

In attempting to solve that problem, I proposed two alternative scenarios (Greenberg, 1982). The first had Io's bulk alternately melting and refreez-

ing, with corresponding shifts in the equilibrium value of ν. This scenario was highly speculative, particularly in its geophysical assumptions, but recent modeling by Ojakangas and Stevenson (1984) suggests episodic heating may be reasonable. My other suggestion was that tides on Io have always dominated, so the system has simply evolved outward from deep resonance (possibly having started on the other side of exact commensurability with $\nu < 0$) and is on its way out of resonance toward $\nu >> 0$.

Yoder and Peale (1981) objected to the latter hypothesis on very convincing grounds. They showed that the equilibrium configuration of the Laplace relation, with $\phi = 180^\circ$, would be unstable for values of $\nu < \nu_{crit}$, where $\nu_{crit} = 0.14^\circ$/day, so evolution from deep resonance seemed implausible. They also showed that the system is stable at $\phi = 0$ but only for $\nu < -0.5^\circ$/day. So to evolve from a stable state with $\nu < 0$, the system would implausibly have to jump an unstable zone from $\nu = -0.5$ to ν_{crit}, in order to reach its present state. Moreover there exists a narrow zone of uncertain behavior around $\nu = 0$, where eccentricities are too large for conventional analytic methods to apply.

The objective of my current work is to understand the possible behavior of the system in deep resonance. One important recent result is that there do appear to be stable configurations of the satellites within the range $\nu = -0.5^\circ$/day to ν_{crit}, with values of ϕ intermediate between 0 and 180° and also between 360° and 180°. Thus it may have been possible for the system to have evolved through deep resonance after all.

These new apparent stability conditions were found in the following way. First, equations for variation of orbital elements were derived as described by Greenberg (1981), but extended to second order in eccentricity in order to include the instability discovered by Yoder and Peale. In order to understand better the nature of this instability, a numerical integration of an unstable case (with $\phi = 180^\circ$, $\nu < \nu_{crit}$) was performed. As expected the system diverged exponentially from the initial condition. Then, however, it began to oscillate about a state with $\phi \approx 135^\circ$. Similar behavior had occurred in a numerical integration by Wiesel (1981). I have now shown analytically that there is an equilibrium state at 135°. Moreover, a series of subsequent numerical experiments has revealed an apparently continuous range of stable conditions between 110° (with $\nu \sim 0.1^\circ$/day) to 180° (at $\nu = \nu_{crit}$. Symmetrical conditions are found on the other side of 180°.

It seems plausible that this range of stable configurations may connect the stable state at $\phi = 0^\circ$ ($\nu < 0$) with that at $\phi = 180^\circ$ ($\nu > 0$), thus allowing the continuous evolution through deep resonance. A number of uncertainties remain to be resolved before this conjecture is proven. First, the stable connection must be demonstrated all the way to $\phi = 0^\circ$. That will involve examining behavior in very deep resonance where expansions in eccentricity break down and direct numerical integration of orbits will be needed. (Eccentricities increase as ν goes to zero just as fast on the newly found stable track as where $\phi = 180^\circ$.) Also, results found so far need to be confirmed with analysis to higher order in eccentricities and stability checked with longer numerical integrations, or preferably proven analytically. Nevertheless, the probable existence of stable configurations with ϕ not 0 or 180° (an intriguing result for celestial mechanics) seems a strong argument for the possibility of evolution from deep resonance.

References

Greenberg, R. (1976) in Jupiter (T. Gehrels ed., Univ. of Arizona Press), p. 122.

Greenberg, R. (1981). Icarus **46**, 415.

Greenberg, R. (1982) in Satellites of Jupiter (D. Morrison, ed., Univ. of Arizona Press), p. 65.

Ojakangas, G.W., and Stevenson, D.W. (1984). DPS abstract.

Peale, S.J., Cassen, P., and Reynolds, R.T. (1979). Science **203**, 892.

Wiesel, W.E. (1981). Astron. J. **86**, 611.

Yoder, C.F. (1979). Nature **279**, 767.

Yoder, C.F., and Peale S.J. (1981). Icarus **47**, 1.

TOPOGRAPHIC EVIDENCE FOR SHIELD VOLCANISM ON IO

E.F. ALBIN, J.M. MOORE, and R. GREELEY
Department of Geology, Arizona State University, Tempe, Arizona, 85287

A volcano has been identified whose morphology, especially topography, supports and extends current evidence that shield volcanoes occur on Io. The feature is centered at 30°S, 246°W and lies in a region near the terminator. Previous work (Carr et al., 1979, and Schaber, 1982) has inferred the presence of shield volcanism on Io from the planimetric configuration of flows on such features as Ra Patera.

Slope and elevation information were determined photoclinometrically. Problems inherent in this technique can produce errors on the order of 10%. Figure 1 shows a planimetric presentation of the volcano in Mercator projection. Two components make up the feature: a central edifice roughly 40-50 km in diameter, and a broad, slightly elliptical base 75 by 90 km across. The boundary between the base and the surrounding terrain is defined by a scarp-like feature or flow front. Slopes on the western half of the central edifice range from approximately 10° to 14°, while those on the eastern half are much less, about 8°. 1° to 2° slopes are found on the outer apron. The summit stands slightly less than 2.5 km above the surrounding terrain. A crater 5 km in diameter and approximately 100 m deep is located at the summit. The feature is situated on intervent plains material. Plume deposits from Pele, 425 km to the northwest, mantle the volcano and produce a nearly uniform albedo. Several large mountains are found 150 km to the east, and a layered plains boundary scarp is 150 km to the southeast.

As shown in Figure 2, the size of this feature is comparable to large shield volcanoes found on Earth. In addition, the topography is similar to some terrestrial shield volcanoes that exhibit a change in slope; the steepening may be explained by shorter and/or thicker flows emplaced during late stage eruptions.

REFERENCES

Carr, M.H., Masursky, H., Strom, R.G., and Terrile, R.J. 1979, Volcanic features of Io, Nature 280, p. 729-733.

Schaber, G.G., 1982, The geology of Io: in Satellites of Jupiter, D. Morrison, Ed., p. 556-597.

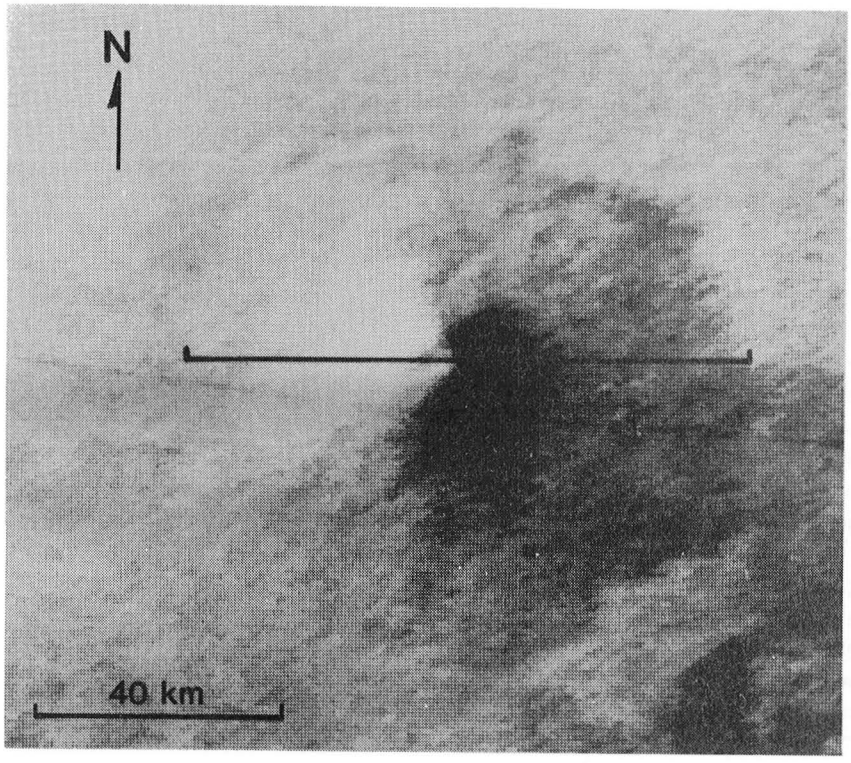

Figure 1. A shield volcano on Io and the line along which a topographic profile was constructed.

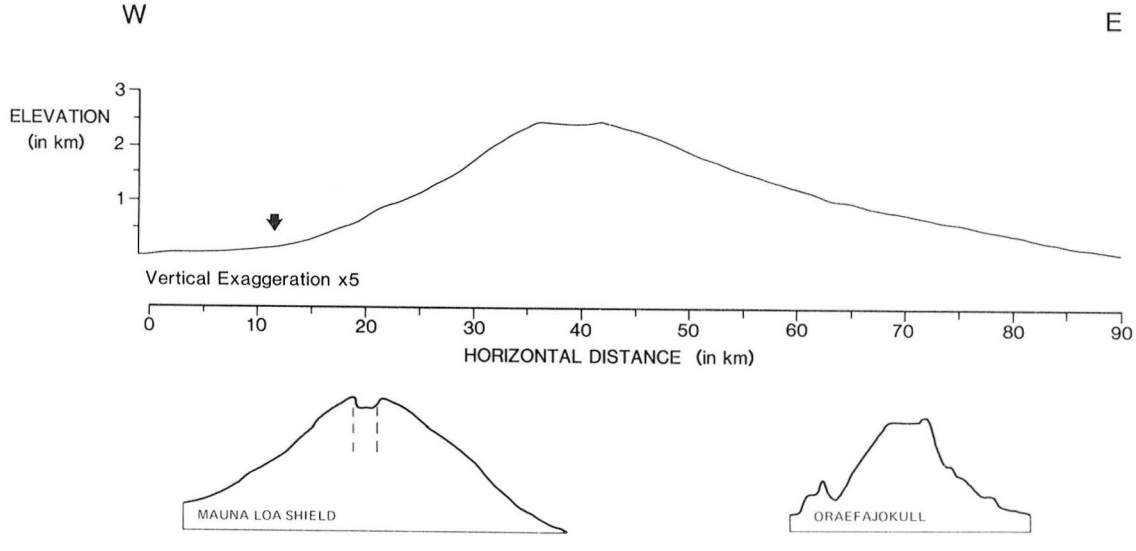

Figure 2. Profiles of the Ionian shield and two terrestrial shield volcanoes drawn at the same horizontal and vertical scale. The portion of the Ionian shield to the left of the arrow shows a typical slope for the outer base of the volcano.

SULFUR VOLCANOES ON IO?

R. GREELEY and J. FINK
Department of Geology, Arizona State University, Tempe, Arizona, 85287

The unusual rheological properties of molten sulfur, in which viscosity decreases ~four orders of magnitude as it cools from 170° to 120°C, may result in distinctive volcanic flow morphologies that allow sulfur flows and volcanoes to be identified on Io. Search of high resolution Voyager images reveals three features--Atar Patera, Daedalus Patera, and Kibero Patera--considered to be possible sulfur volcanoes based on their morphology. All three average 250 km in diameter and are distinguished by circular-to-oval central masses surrounded by irregular, widespread flows. Geometric relations indicate that the flows were emplaced after the central zone and appear to have emanated from their margins. The central zones are interpreted to be domes representing the high-temperature stage of sulfur formed initially upon eruption. Rapid quenching formed a crust which preserved this phase of the emplacement. Upon cooling to 170°C, the sulfur reached a low viscosity runny stage and was released as the thin, widespread flows. Drainage of the liquid from the domes' interiors caused subsidence of the crust, forming concentric fractures seen on Atar and Daedalus Paterae.

GEOMORPHIC CLASSIFICATION OF LAVA FLOWS ON IO

David Pieri, Jet Propulsion Laboratory, Pasadena, CA 91109

While no one has previously set out specifically to classify lava flows on Io, various authors have described the geomorphology of flows on Io, ranging from preliminary reconnaissance reports (Smith et al., 1979) to more detailed descriptions (Masursky et al., 1979; Carr et al., 1979; Schaber, 1980, 1982; Greeley et al., 1983). Table 1 shows a geomorphic classification scheme which is hoped to be more comprehensive and less genetic than previous ones. A comparison of this scheme with those of other researchers is shown in Table 2.

Broad flows occur throughout the surface of Io. They tend to broaden and spread out from dark circular calderas which appear to have little or no relief. They also appear to be thin, since they sometimes appear to abut pre-existing topography, which is itself quite subtle. Flow boundaries are often diffuse and ill-defined, also implying that the flows thin toward their boundaries or are merging with pre-existing material which may be of similar composition. Auras (Baloga et al., 1984) are not visible on the margins of broad flows, and the flows themselves appear orange to light red in Voyager Imaging Team data. Photometrically, broad flows at Ra Patera, where high resolution Voyager color data are available, appear to have a spectral response in Voyager color filters similar to laboratory values measured for orange sulfur (Clancy and Danielson, 1981; Pieri et al., 1984). Since these flows cover large areas, it is not surprising that there is moderate overlap between these flows.

Filamental flows are sharply defined, and are typically single-strand, relatively narrow flows. These flows have sharp margins and distinct boundary auras, and appear to be thick. Filamental flows at the Ra Patera complex appear to have photometric responses in the range of red or black sulfur allotropes, and in one case carries into the range for orange sulfur (Pieri et al., 1984; Clancy and Danielson, 1981). They appear to emanate from dark flat circular calderas throughout the equatorial regions of Io. Schaber (1980, 1982) attributes the strongly directional character of the filamental flows to their consequent emplacement of shield constructs ("shield crater flow units"). However, the simultaneous and interspersed presence of broad flows with filamental flows, which may be judged as being less directional by Schaber's criteria may weaken that argument and could be more consistent with a compositional or phase difference between these flow types.

Digitate flows have sharp margins, appear thick, and are distinguished by the finger-like flows emanating from what appears to be a single source. Digitate flows actually represent a continuum of flow types; at one end of the continuum they merge into the filamental flows class, with long separate thin digits emanating from a single dark flat caldera; at the other end of the continuum they merge into the broad flow category with equally spaced stubby digits emanating along a broad flow front like pahoehoe toes, but on a vastly larger scale. Sometimes inter-digit areas appear light and may consist of aura deposits. Digitate flows often emanate from small irregular calderas and may partly innundate them.

Intercalated flows are small thin flows which are almost completely overlapping. They appear dark and have little color variegation and appear to thin distally. Examples appear to be uniformly circumferentially distributed around steep-walled, stepped calderas.

Sheet flows/materials are large smooth intercaldera areas which cover a large percentage of the surface of Io. They embay massifs and fill pre-existing calderas. Occasionally they exhibit erosional margins (McCauley, 1979) which reveal multiple, relatively thin (~100 meters thick), stepped layers. They are associated with no obvious source, but we provisionally interpret them as flows because of subtle streamline markings on their surface and because of embayment relationships with pre-existing massifs. Sheet flows typically appear very light in Voyager images, and in most color versions they show up as light orange or yellow.

Contained flows occur within calderas, hence the name. They correspond to the "vent materials" of Greeley et al. (1983). These small flows appear to result from intra-caldera eruptions, their shape conforms to that of the caldera interior, and they appear to typically overlap one another. Occasionally small "jets" of white material appear to be associated with their margins, although there appear to be no conformal auras.

Io poses a unique and challenging problem for volcanic geomorphologists in that there is a serious controversy over the composition of Ionian volcanic flows. Various authors have explored the consequences of lavas with a predominately sulfur composition (Masursky et al., 1979; Carr et al., 1979; Schaber, 1980, 1982; Fink et al., 1983; Greeley et al., 1983), have pointed to evidence of the existence of sulfur lavas (Sagan, 1979; Pieri et al., 1984), have argued against sulfur being the predominant constituent of the surface materials of Io (Clow and Carr, 1980), and at least one other researcher, on the basis of spectral evidence, has completely rejected the idea of Ionian sulfur vocanism (Young, 1984). It is against that tapestry of uncertainty that an attempt was made to sort out the morphology of the flows and to isolate features within the flows which may be diagnostic of various compositional regimes.

REFERENCES

Baloga, S.M., D.C. Pieri, and D. Matson, 1984. Auras of volcanic flows on Io, submitted to Jour. Geophys. Res. (Red).

Carr, M.H., H. Masursky, R.G. Strom, and R.J. Terrile, 1979. Volcanic features on Io, Nature, 280, p. 729-733.

Clow, G.C., and M.H. Carr, 1980. Stability of sulfur slopes on Io, Icarus, 44, p. 268-279.

Clancy, R.T., and G.E. Danielson, 1981. High resolution albedo measurements on Io from Voyager I, Jour. Geophys. Res., 86, p. 8627-8634.

Fink, J.H., S.O. Park, and R. Greeley, 1983. Cooling and deformation of sulfur flows, Icarus, 56, p. 38-50.

Greeley, R., P.D. Spudis, and J.E. Guest, 1983. Geologic map of the Ra Patera quandrangle, Io (Ji2a), unpublished MS and presentation to Galilean Satellite Mappers, September 7, 1983 at the United States Geology Survey Astrogeology Branch, Flagstaff, Arizona.

Masursky, H., G.G. Schaber, L.A. Soderblom, and R.G. Strom, 1979. Preliminary geological mapping of Io, Nature, 280, p. 725-728.

McCauley, J., B.A. Smith, and L.A. Soderblom, 1979. Erosional scarps on Io, Nature, 280, p. 736-737.

Pieri, D.C., S.M. Baloga, R.M. Nelson, and C. Sagan, 1984. Sulfur flows at Ra Patera, Io, Icarus, in press.

Sagan, Carl, 1979. Sulfur flows on Io, Nature, 280, p. 750-753.

Schaber, G.G., 1980. The surface of Io: Geologic units, morphology, and tectonics, Icarus, 43, p. 302-333.

Smith, B.A. and the Voyager Imaging Team, 1979. The Jupiter system through the eyes of Voyager 1, Science, 204, p. 951-972.

Young, A.T., 1984. No sulfur flows on Io, Icarus. 58, p. 197-226.

TABLE 1. GEOMORPHIC CLASSIFICATION OF LAVA FLOWS ON IO

CHARACTERISTICS>>>

TYPE VVVV	Boundary Morph.	Thickness	Width Syst.	Area Size	Aura Morph.	Color	Caldera Morph.	Overlap Morph.
Broad Flows	Diffuse	Thin <1-10 m	Narrows toward source	Large ~5 x10^4 Km^2	None	Org.-Red	Circular dark flat	Occasional 30% est.
Filamental Flows	Sharp	Thick >10m	Unif to narrow upstream Variable down stream	Small ~10^3 Km^2	Usually have dstnct cnfrml auras	Bl--Red-Org-Yell W---	Circular dark flat	Little overlap (<10%)
Digitate Flows	Sharp	Thick >10m	Broad avoid Digits uniform width	Mod-large 1-5x 10^3 Km^2	Occas bright inter-digit areas	dark (?)	small irregular often partly innundted	Little overlap, appear to dominate source cal
Intercalated flows	Semi-diffuse	Thin <10m	Wedge-out distlly	Small ~10^3 Km^2	None	dark (?)	Steep-walled, deep (~500m) stepped	Almost complete overlap (~90%)
Sheet flows	Sharp crisp margins	Moderate 10-100 m	Avoid to irreg	Large >10^4 Km^2	None apparnt	Yell-Org-	None visible	Conformal layering (<~90%)
Contained flows	Sharp crisp margins	Thin to moderate <100 m	Avoid	Small to mod ~10^3 Km^2	Diffuse cnfrml; occas jet	Bl Red-Org-Yel-W--	Circular to scalloped	Often overlapped (~50%)

TABLE 2. COMPARISON OF CLASSIFICATION SCHEMES

This paper	Masursky et al 1979	Carr et al 1979	Schaber 1980,1982	Greeley et al 1983
Broad flows	Broad	Broad-dark; Light flows	Pit crater flow unit	Flows; Smooth flows
Filamental flows	Complex-digitate (Complexly-intersecting)	Long narrow dark flows	Shield crater flow unit	Flows
Digitate flows	Complex-digitate	Broad-dark; Long narrow dark flows	Pit crater flow unit; Shield crater flow unit; Fissure flow unit Mountain unit	Flows
Intercalated flows	Complex-digitate (complexly-intersecting)	Broad-dark; Long narrow dark flows	Shield crater flow unit	Flows
Sheet flows	Broad	Broad-dark; Light flows	Layered Plains materials	Plateau slows Plains materials;
Contained flows		Complex albedo patterns w/in calderas		Vent materials

SULFUR OXYGEN PROCESSES ON IO

Robert M. Nelson
William D. Smythe
Jet Propulsion Laboratory
Pasadena, CA 91109

Evidence for the presence of sulfur as a major constituent of the surface of Jupiter's satellite Io has been presented in the literature for many years. The evidence is based on the strong similarity between Io's spectral geometric albedo and the reflection spectrum of solid sulfur (Wamsteker et al., 1974; Sill, 1973). The detection of ionized sulfur in the Jovian magnetosphere (Kupo et al., 1976) and the development of the now widely accepted sputtering mechanism for the removal of ions from the Io surface and their transport to the magnetosphere (Matson et al., 1974); provides further support for the hypothesis that a condensed phase of sulfur is present on Io's surface and is being removed from the surface by sputtering from the energetic particles in the Jovian environment.

However, attempts to closely match the laboratory spectrum of elemental sulfur (S_8) with Io's spectral geometric albedo have not been successful and researchers have attempted to improve the agreement of either mixing other compounds with sulfur (Nash and Fanale, 1977) or by proposing that the elemental sulfur present on Io's surface is not S_8 (which is yellow) but instead is a mixture of the orange-red long chain allotropes of sulfur of the kind that are described throughout the sulfur chemistry literature (Nelson and Hapke, 1978). These allotropes can be made by heating sulfur above its melting point and quenching the melt to lower temperature (Meyer, 1968).

The detection by the Voyager spacecraft of sulfur dioxide gas over the Io hot spot (Pearl et al., 1979) and the identification of SO_2 as a condensed phase on its surface (Fanale et al., 1979; Smythe et al., 1979) has opened new areas for laboratory research involving sulfur and sulfur-oxygen compounds on Io's surface and in its atmosphere.

We have begun a series of laboratory experiments aimed at studying the physical and chemical properties of elemental and allotropic sulfur and sulfur-oxygen compounds in an environment that closely resembles that of Io's surface. This work involves the manufacture of sulfur glasses by heating ultrapure sulfur above the melting point and rapidly quenching the melt. If quenched sulfur glasses are present on Io's surface then it is also reasonable to expect that some very small fraction of Io's surface may consist of molten sulfur, and therefore we are also investigating the properties of molten sulfur.

We have measured the reflection spectrum of molten sulfur in a vacuum at a range of temperatures from its melting point to its boiling point and we have found that while there is a definite change in spectral reflectance as a function of temperature, the reflectance of a column of molten sulfur at any temperature is so low that it would appear as a 'black area' in the Voyager images. However, the thermal infrared data indicate that not all the black

areas could be molten sulfur spots. Thus, if molten sulfur were to be present on Io's surface it could only be present in some (not all) of the black spots. (Nelson et al., 1983).

We have designed and fabricated a glass manifold with suitable valves and vacuum system in order to study the bulk properties of allotropic sulfur alone and in the presence of controlled amounts of sulfur-oxygen compounds believed to be present on Io's surface. This is accomplished by first evacuating the chamber containing the sulfur and backfilling the chamber with the gaseous sulfur oxygen compound. After sealing, the tube can form a completely closed environment.

In the future, we plan to investigate the effect of various types of radiation on the color of ultrapure sulfur powders in the Io environment. To do this we may employ a variety of radiation sources including x-rays, electrons and protons (see e.g., Nelson, 1983).

It is hoped that these experiments will lead to a better understanding of questions regarding the presence of allotropic sulfur as a possible major constituent of Io's surface and the properties of sulfur in combination with various sulfur-oxygen compounds believed to be present on Io's surface and in its atmosphere.

REFERENCES

Fanale, F. P., R. H. Brown, D. P. Cruikshank, and R. N. Clark, Significance of Adsorption Features on Io's IR Reflectance Spectrum, Nature, 280, 1979, 761-763.

Kupo, I., Yu. Meckler, and A. Eviatar, Detection of Ionized Sulfur in the Jovian Magnetosphere, Astrophys. J., 205, L51-L53, 1976.

Matson, D. L., F. P. Fanale, and T. V. Johnson, Sodium D-Line Emission from Io: Sputtering and Resonant Scattering Hypothesis, Astrophys. J., 192, 1974, L43-L46.

Meyer, B., Elemental Sulfur in Inorganic Sulfur Chemistry, G. Nickless, ed., Elsevier, Amsterdam, 1968.

Nash, D. B., and F. P. Fanale, Io's Surface Composition Based on Reflectance Spectra of Sulfur/Salt Mixture and Proton Irradition Experiments, Icarus, 31, 1977, 40-80.

Nelson, R. M., and B. W. Hapke, Spectral Reflectivities of the Galilean Satellites and Titan, 0.23-0.86 Micrometers, Icarus, 26, 1978, 304-329.

Nelson, R. M., Colors of Irradiated Sulfur at Low Temperature: Implications for Io, Division for Planetary Sciences, American Astronomical Society Meeting, 1983.

Nelson, R. M., D. C. Pieri, S. M. Baloga, D. B. Nash, and C. Sagan, The Reflection Spectrum of Liquid Sulfur: Implications for Io, Icarus, 56, 1983, 409-413.

Pearl, J., R. Hanel, V. Kunde, W. Macguire, K. Fox., S. Gupta, C. Ponnamperuma, and F. Raulin, Identification of Gaseous SO_2 and New Upper Limits for Other Gases on Io, Nature, 280, 1979, 755-758.

Sill, G. T., Reflection Spectra of some Solids of Planetary Interest, Comm. Lunar Planet Lab., 10, 1973, 1-7.

Smythe, W. D., R. M. Nelson, and D. B. Nash, Spectral Evidence for SO_2 Frost or Adsorbate on Io's Surface, Nature, 280, 1979, 766-767.

Wamsteker, W., R. L. Kroes, J. A. Fountain, On the Surface Composition of Io, Icarus, 23, 1974, 417-424.

The Violet Absorber on Io: Disulfur Monoxide Derivatives

Bruce Hapke, Department of Geology and Planetary Science, University of Pittsburgh, Pittsburgh, PA 15260

Following the Voyager flybys of Jupiter it has been generally accepted that the surface of Io is covered with SO_2 frost and elemental sulfur. However, several difficulties have recently become apparent with this hypothesis. I had previously suggested (Hapke, 1979, Geophys. Res. Let., 6, 799) suggested that S_2O, which is readily formed under a variety of conditions from the dissociation of SO_2, may be an important compound on Io, but at that time no reflectance data on the frost was available. The reflectance spectra of S_2O/SO_2 mixtures as low temperature frosts and their derivatives, polysulfur oxides, were measured at a variety of temperatures. Specific features possessed by these frosts and identified on Io are bands at 340 nm and 440 nm and a maximum at 800 nm, with decreasing IR reflectance. Thus, this material can account for many of the features in the spectrum of Io. S_2O rather than elemental S is probably the reddening agent on Io, and there is presently no good evidence for S on the surface.

PATTERNS OF FRACTURE AND TIDAL STRESSES DUE TO NONSYNCHRONOUS ROTATION: IMPLICATIONS FOR FRACTURING ON EUROPA.

E.M. Parmentier and P. Helfenstein, Department of Geological Sciences, Brown University, Providence, RI 02912

Global lineaments on Europa (1,2) have been interpreted as fractures in an icy crust. A variety of lineament types have been identified (3,4), which appear to form a systematic pattern on the surface (3,4,5). For a synchonously rotating body, the pattern of fractures observed could be produced by a combination of stresses due to orbital recession, orbital eccentricity, and internal contraction (6). However, it has recently been suggested that the forced eccentricity of Europa's orbit may result in nonsynchronous rotation (7). This study examines the hypothesis that fractures in a thin icy crust may have formed in response to stresses resulting from nonsynchronous rotation.

Asynchronous rotation will result in a time-variable tide in which a biaxial distortion of figure moves relative to the body. Tectonic features produced by this deformation depend on the resulting horizontal stress field near the surface. The incremental horizontal stress $\Delta\sigma_{ij}$ due to a small angular displacement of the tidal axis $\Delta\theta$ can be calculated by the superposition of stresses due to removing an initial tidal distortion along the old tidal axis and creating a new tidal distortion of the same amplitude along the displaced tidal axis. With the tensor components of stress due to each deformation expressed in the same coordinate system, the superposition can be carried out by the addition of corresponding components of the two stress tensors. The surface distribution of stress due to a small, but finite, displacement of the tidal axis is simply $\Delta\sigma_{ij}=\dot{\sigma}_{ij}\Delta\theta$, where the infinitesimal stress increment $\dot{\sigma}_{ij}$ is a symmetrical tensor and can therefore be represented by the orientation of its principal axes and its most tensile and compressive principal values $\dot{\sigma}_1$ and $\dot{\sigma}_2$ respectively. These are shown on mercator projections in Figures 1 and 2.

Three types of lineaments, dark bands, triple bands, and ridges, digitized from high resolution Voyager 2 images, are also shown in Figure 1. Many of the longest and most linear dark bands and triple bands occur at high angles to the stress trajectories. As shown by the stress magnitudes in Figure 2, these bands occur primarily on an area of the surface where $\dot{\sigma}_1$ is tensile and $\dot{\sigma}_2$ is compressive. Fractures of this orientation, if produced by tidal stresses due to nonsynchronous rotation, must be tension cracks. Bands occuring in areas where $\dot{\sigma}_1$ and $\dot{\sigma}_2$ are both tensile are shorter and intersect other bands at high angles, having the general appearance of tension cracking in a nearly isotropic state of stress. Fractures which form in a nearly isotropic state of stress will not reflect stress orientations as well as those formed where the stresses are anisotropic. The long, linear bands which occur primarily at higher latitudes may therefore provide a better indication of stress orientations than the short, reticulate bands near the equator.

Ridges generally occur at high angles to the stress trajectories. If ridges are tectonic features that form perpendicular to the most tensile horizontal stress, those which can be observed are generally consistent with the stresses due to a westward displacement of the tidal axis. On areas of the surface where $\dot{\sigma}_1$ is tensile, ridges could be tension cracks. However, within the lightly shaded region in Figure 2 where both principal stress increments are compressive, ridges could not form by tension cracking. They may, alternatively, be dikes intruded perpendicular to the least horizontal compressive stress as suggested on the basis of their morphology (3). Ridges are observed on areas of the surface where the principal stress increment of greatest magnitude is compression parallel to the ridges. It is interesting to speculate that this may in some way account for their remarkably regular cycloidal form. The distribution of ridges on the surface is clearly an important constraint both on the mechanism by which they form and the surface stress field. However, this distribution cannot be accurately determined because ridges are visible in Voyager images only at oblique illumination near the terminator.

A moving tidal distortion would cause repetitive fracturing of the surface, and could produce tensional features with a range of orientations on the same area of the surface. Thus, it is important to establish whether the observed lineaments reflect stresses and deformation accumulated over a finite amount of tidal axis motion or only the last small increment of displacement. Ideally, the amount of tidal axis displacement required to form very young tectonic features should be reflected in the degree to which their orientation conforms to the predicted directions of incremental stress. Ridges, because they preserve their topographic expression, have been considered the youngest features observed on the surface (3). Therefore they may reflect the most recently accumulated stresses more accurately than the dark bands and triple bands. Dark bands and triple bands that extend into the lightly shaded region of Figure 2 where both principal stress increments are compressive may have formed when the tidal axis was located to the east of the present sub-Jove point. If the bands form progressively as the tidal axis moves westward, then the orientation of their westward ends should most closely reflect the incremental stresses with the tidal axis at the current sub-Jove point. The long, linear dark bands and triple bands shown in Figure 1 do appear to be more nearly orthogonal to stress trajectories at their western ends. Clear evidence for shear offset across dark bands can be observed in a number cases (e.g. 8). Tension fractures that form progressively could develop shear offset as the tidal axis moves westward thus creating a shear stress on the fracture plane. Further study is required to determine if the direction of fracture offsets are consistent with the predicted sense of shear stress.

Fracturing of the surface due to nonsynchronous rotation can potentially occur on short time scales relative to that due to orbital recession and planetary volume change. Very low crater densities suggest that the surface is geologically recent, although, at the resolution of Voyager images, viscously relaxed or highly degraded impact craters may be difficult to identify. Evidence for very rapid resurfacing based on the leading-trailing hemisphere asymmetry of surface spectral properties (9) and for active volcanism during the Voyager encounter (10) has recently been presented. If resurfacing is very rapid, lineaments may be very young and thus difficult to reconcile with stresses due to orbital recession or planetary volume change. Whether the resurfacing process completely obscures earlier-formed lineaments remains uncertain, and the rotation rate is not known; however, nonsynchronous rotation is a mechanism that can result in the very recent, possibly ongoing, formation of tectonic features. Volcanism may occur in response to tension cracking. If so, it is interesting to note that the smoothest area of the surface, the icy plains unit (3), occurs in a region where tension fracturing due to nonsynchronous rotation would be expected. Clearly, the mechanism(s) responsible for fractures on the surface of Europa cannot be unambiguously determined on the basis of currently available evidence. Therefore, in examining mechanisms for surface fracturing, it is only possible to require that plausible tectonic mechanisms for lineament formation be consistent with the predicted stress field. However, for plausible interpretations of the origin of lineaments based on currently available imaging data, fracturing due to nonsynchronous rotation is consistent with their distribution on the surface and may explain their very recent formation.

REFERENCES: (1) Smith, B. A., et al., **Science** 204, 951-972 (1979). (2) Smith, B. A., et al., **Science** 206, 927-950 (1979). (3) Lucchitta, B. K., and L. A. Soderblom, **Satellites of Jupiter,** Univ. of Arizona Press, 521-555. (1982). (4) Pieri, D. C., **Nature** 289, 17-21 (1981). (5) Helfenstein, P., and E. M. Parmentier, **Proc. Lunar Planet. Sci. Conf. 11th**, 1987-1998 (1980). (6) Helfenstein, P. and E. M. Parmentier, **Icarus** 53, 415-430 (1983). (7) Greenberg, R. and S. J. Weidenschilling, **Icarus** 38, in press (1984). (8) Schenk, P. M., **Advances in Planetary Geology,** NASA TM-86247, 3-111 (1984). (9) Squyres, S. W., et al. **Nature** 301, 225-226 (1983). (10) Cook, A. F., et al., submitted to **Icarus** (1984).

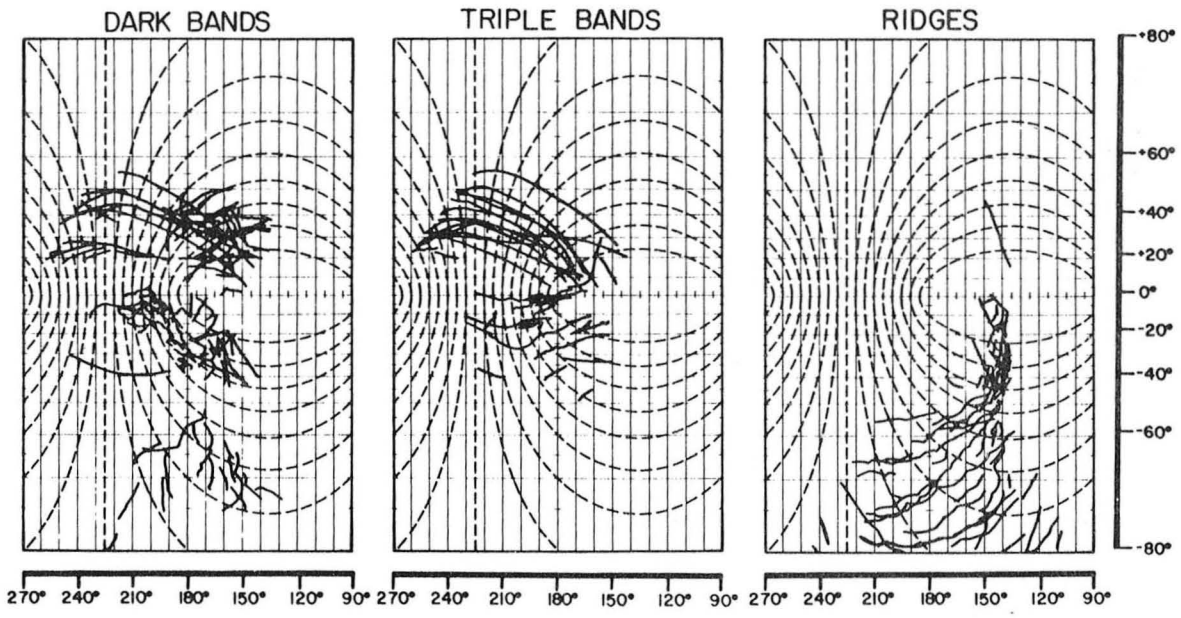

Figure 1. Stress trajectories (dashed) and lineaments (solid) digitized from Voyager 2 images (6). Stress trajectories are in the direction of the most tensile increment of horizontal surface stress due to an infinitesimal displacement of the tidal axis in the direction of increasing longitude. The instantaneous tidal axis is at 0 or 180^0 longitude and 0^0 latitude. The orientation of lineaments relative to stress trajectories provides a test of the hypothesis that lineaments are fractures produced by tidal stresses due to nonsynchronous rotation.

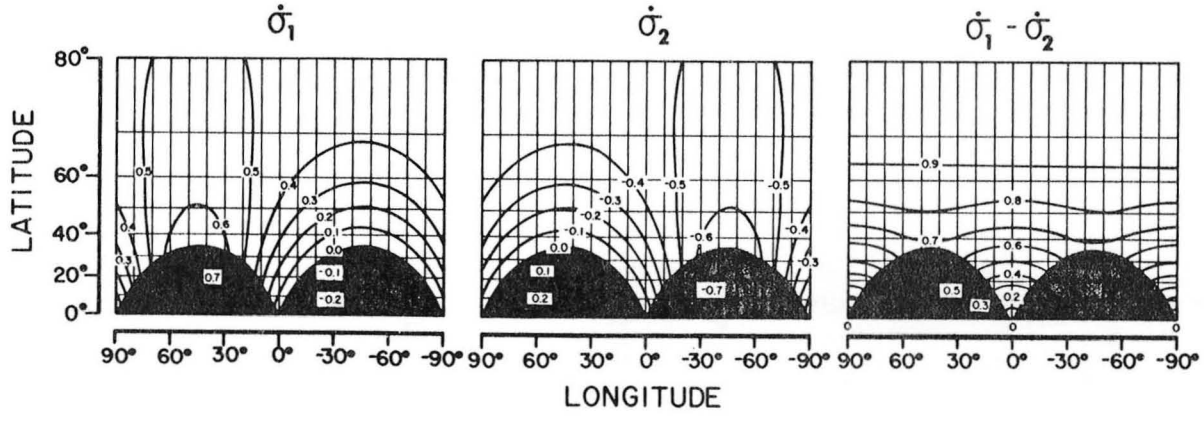

Figure 2. Incremental stress magnitudes due to an infinitesimal displacement of the tidal axis in the direction of increasing longitude. The orientation of the principal stress increments is given in Figure 1. Contours are plotted as fractions of the factor $8\mu A(1+\nu)/(5+\nu)$ where A is the tidal distortion amplitude, μ is the shear modulus, and ν is Poisson's ratio. Shaded regions correspond to areas of the surface where both principal stress increments are of the same sign. Dark and light shading corresponds to regions of tension and compression, respectively.

DARK HALO CRATERS AND THE THICKNESS OF GROOVED TERRAIN ON GANYMEDE

Paul M. Schenk and William B. McKinnon, Dept. Earth and Planetary Sciences and McDonnell Center for the Space Sciences, Washington University, Saint Louis, MO 63130.

Dark halo craters on grooved terrain on Ganymede represent potential probes of the subsurface geology. These craters are surrounded by a broad, diffuse low albedo annulus, or halo (Fig. 1) and have apparently lost the bright rim and ray deposits associated with very young craters. The halos are concentric about the crater and are symmetric, except where partially obscured by younger bright ray deposits. These craters are distinct from very dark, irregular, starburst-like dark ray craters described by Conca (1981). Dark halo craters have been identified only in bright terrain. The distribution of dark halo craters is not uniform, partly as a result of uneven Voyager imaging. They are much less frequent in Voyager 1 frames, which are of lower resolution and inherently lower contrast. Halos are less distinct or not recognizable near the terminator or limb in Voyager images, where phase angle and shadow effects are important. None have been recognized above 45° north or south latitude, where they may be masked by bright frost deposits. There is also no apparent dependence of frequency on longitude, or distance from the apex of motion or sub-jovian point. The greatest concentration is in Uruk Sulcus, the wide band of grooved terrain just southwest of Galileo Regio.

Halo diameter is correlated with crater diameter indicating the halo is related to ejecta deposits. The relationship between halo radius (R_h) and crater radius (R_c) is $R_h = (2.74 \pm 0.36)\ R_c^{1.01 \pm 0.05}$, roughly comparable to the relation between continuous ejecta radius and crater radius on the moon (Moore et al., 1974). The linear correlation of halo and crater diameter suggests that aging processes do not remove the halo with time. Continued impact gardening and exposure to the space environment should lead to a degrading of the halo if it is a photometrically related feature. As this is not observed, we conclude that halos are not the result of photometric effects in ejecta blankets, but are probably optically 'mature' and thus of compositional origin. Medium-resolution Voyager color images were examined for color variations that might indicate compositional differences between halos and target material. An orange/violet ratio image of several dark halo craters (Fig. 2), in which brightness gives the 'redness' of the visible spectrum at each location, shows that dark halos have an orange/violet ratio intermediate between the 'bluer', brighter grooved terrain and 'redder', darker cratered terrain. Only a minor amount of contaminant is required to alter the spectra of icy materials (Clark, 1982), so even if substantially diluted by the relatively pure water ice of grooved terrain material, spectrally and compositionally distinct halo ejecta is expected to alter the albedo and color of the ejecta deposit into which it is mixed. We conclude that the dark halos represent the excavation of darker, redder material and its incorporation into the ejecta deposits of grooved terrain craters.

No dark halos are associated with craters smaller than about 8 km. The five positively identified dark halo craters smaller than 12km are all located in a roughly 100-km-wide cluster, although the cluster is not restricted to any particular groove set or structural cell. Outside the cluster area, we take the transition diameter for dark halo craters in Uruk Sulcus to be ∿12km (Fig. 3).

A transition diameter for dark halo craters indicates that the darker, redder material incorporated into the ejecta occurs at a stratigraphic horizon the depth to which only a crater of sufficient size, in this case, approximately 12 km, can excavate. The depth of the inferred stratigraphic horizon can be derived from the observed transition diameter by reconstructing the geometry of the transient crater, and hence the excavation cavity, of the pre-modification crater. Craters in the 10-15km diameter range lie above the simple-to-complex crater transition diameter (~3-5km) (Passey, 1982), and thus have collapsed. As most of the dark halo craters in Uruk Sulcus appear to be flat-floored, we will assume this shape, with a steep inner rim slope. The average depth below the rim crest of a 12-km-wide crater in grooved terrain is 1.3 km ± 300 m, and rim crest heights are 300 ± 200 m (Passey, 1982), yielding crater depths below the ground plane of ~1 km for a 12 km wide crater. We adopt a value of 30° (near the angle of repose for talus) for the rimwall slope in our 12-km Ganymede crater. This is broadly consistent with the observed width of the rimwall (1-2 km). We assume a parabola for the form of the transient crater, with a depth to diameter ratio, measured with respect to the ground plane, of $(2\sqrt{2})$ (Dence, 1973). This approximate geometric model translates a collapsed, flat-floored 12-km-diameter crater on Ganymede into a parabolic transient crater of 9.3-km diameter and 3.6-km depth, or 8.6 km and 3.0 km, with respect to the ground plane. The depth of excavation is only ~30-50% of the transient crater depth (cf. Grieve et al., 1981), or ~0.97-1.55 km for a 12-km-wide crater on Ganymede.

The recognition of dark halo craters, almost all greater than 12 km in diameter, indicates that material darker and redder than grooved terrain material forms a stratigraphic horizon at about 1 km depth below the present surface of grooved terrain in Uruk Sulcus. This material is most likely downdropped cratered terrain material, which only larger craters have excavated into. This is most consistent with extensional tectonic models for grooved terrain formation whereby the lithosphere is stretched and blocks of ancient cratered terrain are downdropped along bounding faults, and subsequently resurfaced by a shallow layer of relatively clean icy material. Evidence for the preservation of cratered terrain material at shallow depth beneath grooved terrain material poses great difficulties for alternative grooved and smoothed terrain formation mechanisms. While some lateral motion along faults is probable (Lucchitta, 1980), there is no unequivocal evidence that dark cratered polygons were once together or have rotated over large angles with respect to one another (Parmentier et al., 1982). Wholesale stoping of cratered terrain into the interior (Shoemaker et al., 1982) is also not favored, and Parmentier et al. (1982) note that scattered 'outcrops' of cratered terrain within grooved terrain are mechanically inconsistent with this model.

This research was supported by NASA grant NAGW-432.

REFERENCES

Clark, R., Icarus, 49, 244-257 (1982); Conca, J., Proc. Lunar Planet. Sci. 12B, 1599-1606 (1981); Dence, M., Meteoritics, 8, 343-344 (1973); Grieve, R. et al., Proc. Lunar Planet. Sci. 12A, 37-58 (1981); Lucchitta, B., Icarus, 44, 481-501 (1980); Moore, M., et al., Proc. Lunar Sci. Conf. 5th, 71-100 (1974); Parmentier, E. et al., Nature, 295, 290-293 (1982); Passey, Q., Ph.D. thesis, Caltech (1982); Shoemaker, E. et al., in Satellites of Jupiter, pp. 435-520 (1982).

Figure 1

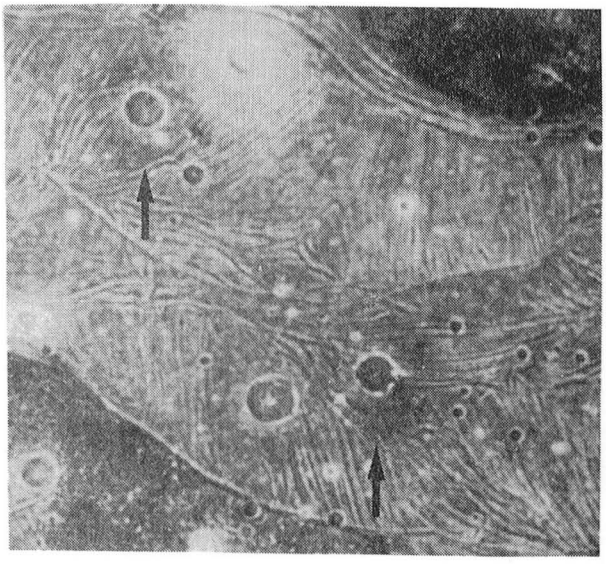

Figure 2

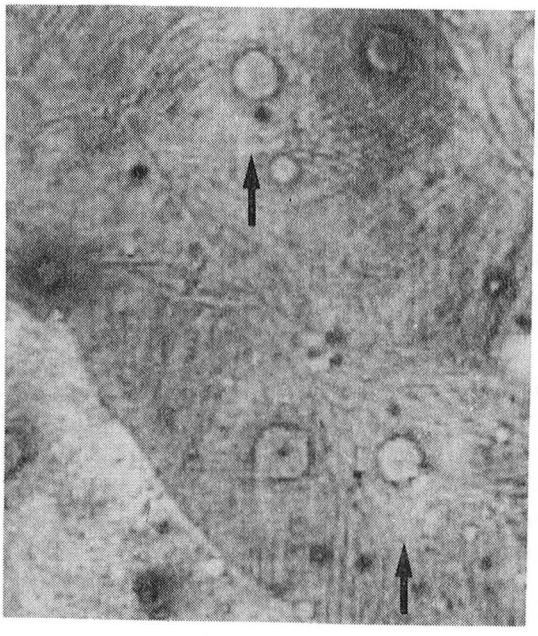

Figure 3

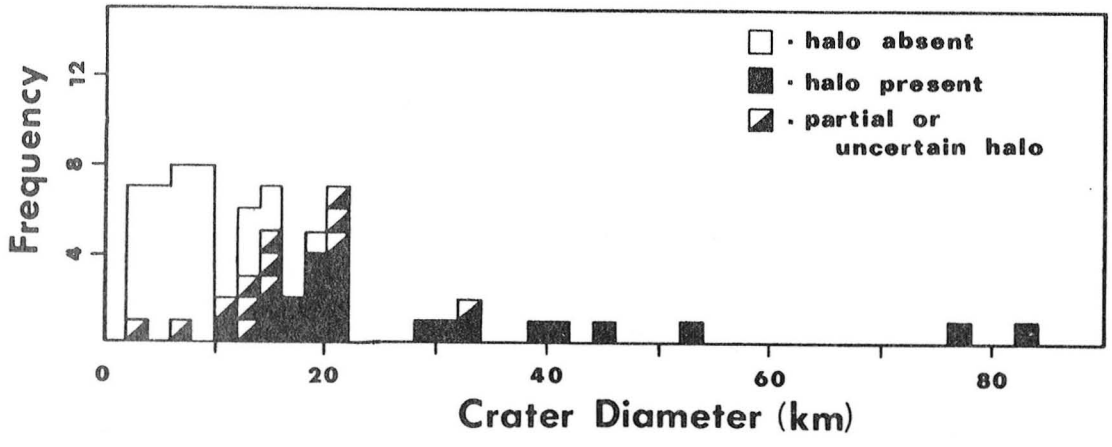

FORMATION OF BRIGHT TERRAIN BANDS ON GANYMEDE BY UNSTABLE LITHOSPHERE EXTENSION

M.T. Zuber and E.M. Parmentier, Department of Geological Sciences, Brown University, Providence, RI 02912

The surface of Ganymede, as seen in Voyager images, has been greatly modified by tectonic activity. Geologic evidence is consistent with the formation of younger bright terrain by the emplacement of icy material into rift zones formed in the older dark terrain (1, 2). To better understand the formation of both terrestrial rift zones and bright terrain bands on Ganymede, we are studying the mechanics of rift initiation by the growth of necking instabilities in an extending lithosphere. In particular, we are examining how an initial, small perturbation in lithosphere thickness at the lithosphere/asthenosphere boundary is amplified by uniform horizontal extension. The lithosphere is treated as a layer of power-law viscous fluid of thickness H overlying a weaker, viscous mantle substrate. In order to assess the relative importance of buoyant upwelling and mechanical instability in rift formation, both density and strength stratification have been incorporated into the model.

Previous studies have explained the width of rift zones and flanking uplifts as elastic flexure of the lithosphere (3) or as crustal viscoelastic deformation (4, 5) in response to graben subsidence. Figure 1a shows that characteristic rift zone topography can also be produced by the amplification of an initial thickness perturbation at the base of a ductile, deforming lithosphere. For small amplitudes, the magnitude of the surface topography is approximately proportional to the mean extension, but its shape is nearly constant. The topography is also relatively independent of the form of the initial thickness perturbation. The width of the rift zone is controlled by the growth rate spectrum, shown in Figure 1b, which is a function of the layer/substrate strength contrast, the density stratification, and the stress exponent describing ductile flow. The width of the rift zone thus directly reflects the mechanical structure of the lithosphere. For an initial perturbation that is narrower than the dominant wavelength, surface extension concentrates in a zone comparable in width to the dominant wavelength, and the resulting surface topography consists of a central depression and flanking uplifts. If the initial thickness perturbation is wider than the dominant wavelength, periodic instabilities form, as has been suggested to explain surface structures in the Basin and Range Province (6). On Ganymede, the distribution of bright terrain bands forms an irregular pattern on the surface, and preliminary observations show no systematic correlation of band width with sequence of emplacement. More detailed studies are presently underway to characterize the spatial and temporal distribution of bright bands on the surface, and to better quantify the relative contribution of density and strength contrasts in controlling rift zone morphology. On the basis of present results, the observed distribution of bright terrain may reflect global differences in the mechanical properties of Ganymede's lithosphere and/or variations in lithosphere thickness heterogeneities at which bands nucleate.

Structural relationships between bright bands, in particular the nature of their intersections, provide a basis for interpreting both Ganymede's global tectonic style as well as how the bands have formed. Intersections may most simply be classified into relationships where bands: 1) cross-cut, 2) form a terminating or "T"-structure, and 3) merge or bifurcate along strike. Schematic examples of these relationships are shown in Figure 2.

A cross-cutting relationship occurs where one band cuts across another and the discontinuous band is clearly older. In a T-relationship, one band sharply truncates against another, and it is presumed that the crossbar of the T formed first. We have measured the angles of intersection in cross-cutting and terminating bright bands from the highest resolution Voyager 2 images, and the results, summarized in Figure 3, show a mean intersection angle of about 70 degrees. The generally high angles of intersection are consistent with band formation by failure in response to tensional lithospheric stress. The first-formed band relieves stress perpendicular to its strike and the later band forms at a high angle to the first to relieve the other component of stress. If the widths of bright bands are related to the thickness of the lithosphere, then differences in widths of bands with known relative ages may indicate variations in Ganymede's geothermal gradient or lithosphere thickness with time.

Intersections in which bands merge or bifurcate, rather than being sharply truncated, can also be identified. The angles of intersection for these features are difficult to determine accurately but are generally less than 50 degrees. Because age relationships are often indeterminate, it is difficult to interpret the sequence of formation. Lithospheric inhomogeneities such as thickness variations or pre-existing structural weaknesses may have been involved in the formation of these intersections.

Knowledge of the amount of extension associated with the formation of bright bands would place an important constraint on the mechanism of rifting. The extension can be simply determined if the lateral offset of the older band in a cross-cutting relationship can be measured. The amount of extension can be best determined for intersections with wide younger bands and small intersection angles, unfortunately, most bands intersect at high angles. We have measured offsets from high resolution Voyager 2 images which indicate less than several tens of percent extension. While better estimates cannot be made at Voyager resolution, the current results are consistent with the hypothesis that Ganymede's lithosphere has not simply drifted apart, but failed by normal faulting which caused dark blocks to be down-dropped and flooded. In order to identify smaller amounts of extension, sub-kilometer resolution of surface features, which will be attainable in the Galileo mission, are required.

REFERENCES: (1)Shoemaker, E.M. et al., The Satellites of Jupiter, D. Morrison, ed., Univ. Arizona Press, Tuscon, 1982. (2)Parmentier, E.M. et al., Nature 295 290-293, 1982. (3)Vening Meinesz, F.A., Bull. Inst. R. Colon. Belge. 21 539-552, 1950. (4)Bott, M.H.P., Tectonophys. 36 77-86, 1976. (5)Bott, M.H.P., and Mithen, D.P., Tectonophys. 94 11-32, 1983. (6)Zuber, M.T. et al., submitted to Jour. Geophys. Res., 1984.

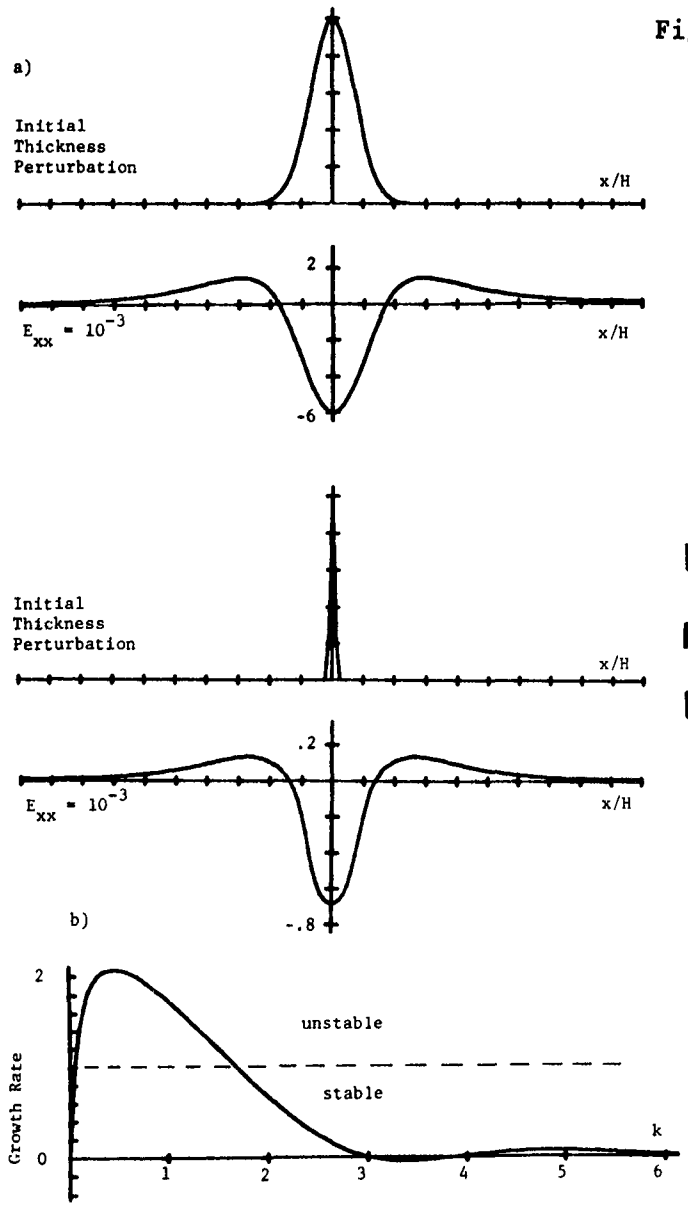

Figure 1. (a)Rift zone topography for two initial thickness perturbations. The initial perturbation, presumed to be small, is plotted with an arbitrary amplitude. Surface topography is normalized by the amplitude of the initial perturbation and the mean extension Exx. (b)Growth rate spectrum plotted as a function of wavenumber k normalized by the layer thickness.

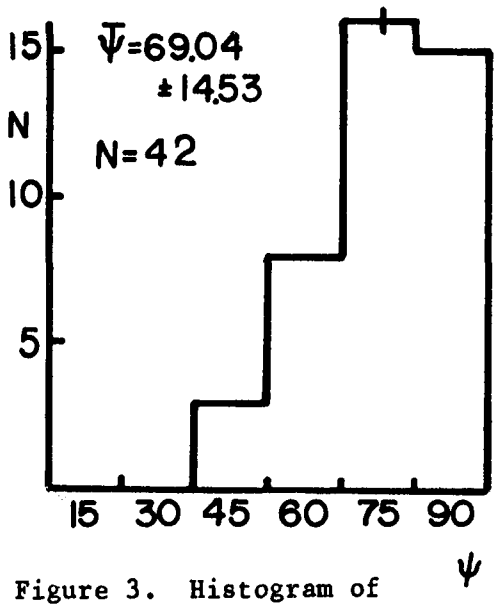

Figure 3. Histogram of intersection angles for cross-cutting and T-relationships.

Figure 2. The three types of bright band intersections: a) cross-cutting, b) T-relationships, and c) merging/bifurcating intersections.

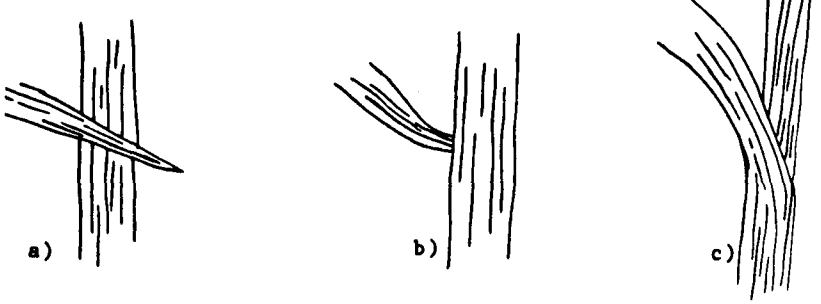

POLAR CAP FORMATION ON GANYMEDE

Carl B. Pilcher and Edward J. Shaya, University of Hawaii,
Institute for Astronomy

Since thermal migration is not an effective mechanism for water transport in the polar regions of the Galilean satellites (Purves and Pilcher, 1980 Icarus 43, 51), some other process must have been responsible for the formation of Ganymede's polar caps. We argue that the polar caps are probably the remnants of a more extensive covering of water ice that formed during a period in which the satellite was geologically active. Thermal migration would lead to the recession of such an ice layer, with the eventual formation of polar caps, but we show that the maximum thickness of a layer that could recede to the present boundaries of the polar caps over geologic time is at most a few meters. A thickness at least this great, however, is necessary to insure that the remnants of the ice sheet should still be visible today despite gardening to depths of tens of meters over Ganymede's polar regions. In particular, the remnant would be visible today if at least three conditions were fulfilled: (1) the initial thickness of the sheet must have been sufficiently large that the present regolith ice content is significantly greater than the original ice content of the underlying material, (2) the ice content of the optical surface of the regolith must not have been lowered significantly by evaporation or sputtering, and (3) the ice originally in the sheet must not have been so intimately mixed with the underlying material that it has little or no effect on the regolith's reflectance.

Albedo differences on the surface of Ganymede in general indicate that mixing of the type necessary to violate condition (3) is not the rule. We argue that condition (2) is fulfilled at latitudes poleward of ~50°. We have previously shown (Purves and Pilcher, 1980) that evaporation is unimportant at these latitudes. Sputtering also appears to be unimportant, as evidenced by ray lifetimes which are shortest on the leading hemisphere (Passey and Shoemaker, 1982, in Satellites of Jupiter, ed. D. Morrison, U. Ariz. Press, pg. 379), rather than on the trailing hemisphere as expected for sputtering. Further evidence is the dependence of the latitude of the polar cap margin on the nature of the underlying terrain (Squyres, 1980 Icarus 44, 502), a result unexpected if sputtering determines the margin latitude. Condition (1) is probably satisfied by an ice sheet initial thickness at least ~10% of the total regolith depth. This suggests an initial thickness of at least a few meters over the heavily cratered south polar grooved terrain, or correspondingly smaller values in the regions less heavily cratered.

Since it thus seems possible to fulfill all three conditions, we propose that Ganymede's polar caps are the optical manifestation of a process that began with the distribution of an ice sheet over the surface of Ganymede. The combined processes of impact gardening and thermal migration led, in regions at latitudes less than 40-45°, to the burial of some fraction of this ice, the migration of some to the polar cap margins, and a depletion of free ice in the optical surface. At higher latitudes, no process was effective in removing ice from the optical surface, so the remnants of the sheet are visible today. The absence of similar polar caps on Callisto

apparently reflects the absence of a process to form the initial ice covering. A likely candidate for a process operative on Ganymede, but not on Callisto, is one associated with the formation of Ganymede's grooved terrain.

INVESTIGATIONS OF PLANETARY RING PHENOMENA

Joseph A. Burns and Mark R. Showalter, Cornell U.

Our research this year has emphasized faint ring systems. (1) We have principally investigated the structure of Jupiter's ring (2,9,10,12-15) and tried to understand the processes (1,4,5,11) whereby that structure might be generated. We have also studied faint material in the Saturn system, discovering a new ring (12) and interpreting wavy features surrounding Encke's division in terms of perturbing moonlets (16,17). We have considered the interaction of faint rings and magnetospheres (3-5, 19) and have been able to identify some of the charged particle absorbers seen by Pioneer 11 in the neighborhood of the F ring. We have weighed whether the IRAS solar system dust bands might be asteroidal or cometary in origin (7), and developed a detailed dynamical model (6,8) to interpret the available data. Finally we have pointed out a new process, angular momentum drain, that might account for the slow rotations of intermediate-sized asteroids (18).

Our reanalysis (1,2,9,10,12-15) of the existing 25 Voyager images of the Jovian ring has fundamentally altered our understanding of the ring's properties. We have determined that three components make up the system: the main ring, the vertically-extended halo and an external "gossamer" ring. The interior disk reported by previous investigators is absent.

The bright ring has an abrupt (<200 km wide) outer boundary centered at orbital radius 129130±100 km, and a broader inner boundary at ∿122000 km. It reveals fine structure on scales of a few hundred km, some of which is associated with the embedded satellites Adrastea and Metis (1,11). It contains a large population of micron-sized grains, which obey a power-law size distribution $n(r) \propto r^{-p}$, with $p = 2.5 \pm 0.5$. Here $n(r)$ is the number of particles per unit ring area with radii between r and $r+dr$. These grains account for an optical depth $\tau = 1\text{-}6 \times 10^{-6}$ for $r < 100$ μm. The ring also contains a separate population of larger bodies, which are rough, dark and red, and have an optical depth $\sim 3 \times 10^{-6}$; these act as sources for the tinier grains.

The halo is a crudely toroidal cloud of material, running from the ring's inner boundary roughly halfway down to the Jovian cloudtops. It is symmetric about the ring plane, and extends for $\sim 10^4$ km above and below it. Its particle size distribution is not markedly different from the micron-sized population in the bright ring.

In addition, we have discovered a much fainter ring, which extends outward from the main ring to an orbit of ∿210,000 km, though with ever-decreasing brightness. Its mean intensity is ∿5% that of the main ring, and its only notable feature is a ∿20% brightness enhancement at synchronous orbit.

Much of the Jovian ring structure can be understood in terms of debris loss from satellites (1,11), rapid orbital evolution (1), resonances (5) and charged dust dynamics (4).

Papers and Abstracts Produced Under NAGW-310

1. Joseph A. Burns, Mark R. Showalter, and Gregor Morfill. The Ethereal Rings of Jupiter and Saturn. In Planetary Rings (R. Greenberg and A. Brahic, Eds.), pp. 200-272, University of Arizona Press, Tucson (1984).

2. Mark R. Showalter. Jupiter's Ring System Resolved: Physical Properties Inferred from the Voyager Images. Ph.D. Dissertation, Cornell University, January 1985.

3. Joseph A. Burns. Planetary Rings. In Dust-Magnetosphere Interactions, COSPAR Proceedings, Graz, Austria July 1984.

4. L. Schaffer and Joseph A. Burns. Dust Dynamics in Jupiter's Tilted Magnetic Field. Ibid.

5. Joseph A. Burns, L. Schaffer, R. Greenberg, and Mark R. Showalter. Numerology or Not: Jovian Ring Features Are Near Resonances. BAAS 16.

6. S.F. Dermott, P.D. Nicholson, Joseph A. Burns, and J.R. Houck. IRAS' Solar System Dust Bands: A Testable Hypothesis. Nature, submitted.

7. Joseph A. Burns, S.F. Dermott, P.D. Nicholson, J.R. Houck. IRAS' Solar System Rings: Collisional Debris from Asteroids or Cometary Dust? In Properties and Interactions of Interplanetary Dust (IAU Colloquium No. 85), Marseille.

8. P.D. Nicholson, S.F. Dermott, and Joseph A. Burns. A Dynamical Model for IRAS' Solar System Dust Bands. BAAS 16.

9. Mark. R. Showalter, Joseph A. Burns, J.N. Cuzzi, and J.B. Pollack. Re-examining Jupiter's Ring: Morphology. BAAS 15, 815 (1983).

10. Mark R. Showalter, Joseph A. Burns, J.N. Cuzzi, and J.B. Pollack. Re-examining Jupiter's Ring: Morphology. BAAS 15, 815 (1983).

11. Joseph A. Burns and Mark R. Showalter. Dust Rings from Satellites. BAAS 15, 814-815 (1983).

12. Joseph A. Burns, J.N. Cuzzi, and Mark R. Showalter. Discovery of Gossamer Rings. BAAS 15, 1013-1014 (1983).

13. Mark R. Showalter, Joseph A. Burns and J.N. Cuzzi. Fine Structure in Jupiter's Main Ring. BAAS 16, (1984).

14. Mark R. Showalter, Joseph A. Burns, and J.N. Cuzzi. Jupiter's Gossamer Ring. BAAS 16, (1984).

15. Mark R. Showalter, Joseph A. Burns, and J.N. Cuzzi. Particle Sizes and Properties in Jupiter's Main Ring. BAAS 16, (1984).

16. J.N. Cuzzi, J.D. Scargle, Mark R. Showalter, and L.W. Esposito. Saturn's Rings: Indirect Evidence for Moonlets Embedded within Encke's Division. BAAS 15, 813 (1983).

17. J.N. Cuzzi and Mark R. Showalter. Shepherding Moonlets: Detection by Adjacent Ring Radial Structure. BAAS 16 (1984).

18. A.R. Dobrovolskis and Joseph A. Burns. Angular Momentum Drain: A Mechanism for Despinning Asteroids. Icarus 57, 464-476 (1984).

19. J.N. Cuzzi and Joseph A. Burns. Charged Particle Absorption Signatures near Saturn's F Ring. In preparation.

20. Joseph A. Burns and Mark R. Showalter. The Puzzling Dynamics of Saturn's F Ring. In The Motion of Planets and Natural and Artificial Satellites. S. Ferraz-Mello and P.E. Nacozy, Eds. pp. 201-213. U. of São Paulo Press. (1983).

STUDIES OF PLANETARY RINGS

Jeff Cuzzi
NASA-Ames Research Center

This extended abstract covers observational and theoretical work performed under two separate proposals, and is therefore slightly longer than the length suggested for a single task. The problems involved in these separate proposals are highly interrelated, and are here discussed together for the sake of brevity. Also, as this is our first contribution to the P.G.G. annual report, we have included relevant 1983 papers in the appended bibliography.

I. Studies of dynamic processes in ring systems

a. Spiral density waves: The theory used for the analysis of spiral waves in Saturn's rings (Cuzzi et al, 1981) was initially developed by Goldreich and Tremaine (1978) for weak waves which do not strongly alter the local surface density; this is the so-called linear approximation. This theory has been used by Lissauer, Peale, and Cuzzi (1984) to demonstrate the possibility for transfer of large amounts of angular momentum and orbital energy from the ring system to the orbit of Enceladus, possibly amplifying Enceladus' orbital eccentricity and allowing tidal heating to have been important in the geologically recent past. The same effect leads, by conservation, to rapid loss of angular momentum by the rings and a correspondingly short lifetime. It had been hoped by some that the density wave transfer of angular momentum might become less effective for strongly forced, "non-linear" waves such as are, in fact, seen in the rings (see the review chapter by Cuzzi et al 1984). Research performed under this task by Shu, Yuan, and Lissauer (1985) has closed this loophole. This work consists of a fully self-consistent solution of the nonlinear spiral density wave problem, in the limit where viscosity is not important. The solutions are well-behaved, and are valid near resonance where the torque is actually deposited. The solutions are in good qualitative agreement with observed density waves (fig. 1a), and they demonstrate two important properties of strongly forced spiral waves: the effective torque is nearly the same as predicted by the linear theory (fig. 1b), and the wavelength may be slightly affected by nonlinearity. Thus, the timescale for ring evolution by this transfer remains disturbingly short (approx. 10^7 yr.), and ring surface mass densities estimated using the old linear theory may be high by about 20%. Current work is including viscosity and wave damping in the solution, and predictions will be compared with the observed behavior of density waves. Viscosity will decrease the huge amplitudes seen in the solutions of fig. 1a, and produce the damped envelope seen in observed waves (Cuzzi et al 1984).

b. Studies of the "shepherding" process: The idea of "shepherding", or gravitational torque, was first applied to the Uranian rings by Goldreich and Tremaine (1979). Most workers accept the principle implicit in this process, but many are unsatisfied with current understanding of its detailed workings. Until we better understand exactly how the momentum is transferred in these local interactions, we will not be able to apply our

knowledge to questions of ring origin and evolution or planetary formation. We have recently completed one phase of a two-part study which will demonstrate the workings of gravitational torque in one system of moderate optical depth: Saturn's A ring near the Encke gap. Cuzzi and Scargle (1985, see also Cuzzi et al 1984) present a detailed study of the distribution of wavy perturbations along the inner and outer edges of this gap (fig. 2). They conclude that these are radial oscillations induced by close passage of the ring material by a 10 km radius moonlet embedded near the center of the Encke gap. Their study demonstrates the damping of these edge waves with longitude in the frame of the moonlet; this damping is at the heart of the shepherding process (Greenberg 1983). Of course, the implied existence of such a large object within Saturn's Roche limit is of great cosmogonic interst in it's own right. Further studies are planned to search the edges of other empty gaps for similar edge waves. The second phase of this study, by Cuzzi, M. Showalter, and L. Esposito (in preparation) uses Voyager stellar occultation data near the edge of the Encke gap to strengthen the conclusions of the first study and add important information on the nature of the damping of edge waves and the location of the responsible moonlet. Theoretical work by Cuzzi, M. Showalter, Shu, and G. Stewart is proceeding on the physics of the momentum transfer process implied by the observed properties of this key region (e.g. Cuzzi and Showalter 1984).

c. Erosional transport and global redistribution of ring material: In studies supported under these tasks, a novel concept of ring structural evolution has been developed by Durisen et al (1982); for a recent review see Durisen (1984), and see also Lissauer (1984) for a simplified physical treatment. Basically, the idea is that the rings are continually bombarded by interplanetary meteoroids which are most effective in the mm size range. The ejecta, which are smaller chips and particles of total mass far greater than the mass of the projectile, travel large radial distances through the ring system on eccentric, inclined orbits before reimpacting the rings and being absorbed on the surface of a larger ring particle. In this process, both the mass and the angular momentum of the ejecta are transferred to the ring at the point of impact. To lowest order, adjacent inner and outer radial regions merely exchange ejecta and no net transport results; however, consideration of realistic effects (such as cylindrical geometry) produces a net effect to first order near ring edges and to second order elsewhere. To date, numerical calculations have incorporated the effects of both mass and angular momentum transfer on the redistribution of ring material. The results depend on the assumed angular and velocity distribution of ejecta. Typical model evolutions are shown in fig.3. There is a distinct similarity in the "pileups" at inner ring edges seen in the model evolutions with certain unexplained features seen in Saturn's rings, such as the fairly abrupt A and B ring inner edges. The evolutions are being upgraded in accuracy to allow longer runs, and to include treatment of realistic ejecta distributions and viscous transport of angular momentum. One intriguing aspect of erosional processes is that current estimates of the influx of meteoroids (Morfill et al 1983) imply extremely short timescales for ring erosion and evolution. The rings appear to absorb their own mass in meteoroids over the age of the solar

system; because the meteoroids carry zero net angular momentum in the frame of the planet, a substantial orbital decay is expected for the "accreting" system. An even more drastic decay is expected if even a small fraction of the ejecta is lost to the planet (ie, as ionized vapor). This research is continuing.

II. Primarily observational studies of planetary rings:

a. Jupiter's ring: An exhaustive new study of the structural and photometric properties of Jupiter's ring, primarily the thesis research of Mark Showalter of Cornell and initiated under this task, has just been completed. Many new results of interest have been obtained, and several misconceptions corrected. The ring has been found to consist of the well-known bright band and a roughly toroidal halo: the existence of a flat, diffuse disk, as previously suggested, has been ruled out (Showalter et al 1983a). A very faint, new "gossamer" ring has been discovered to lie between the known ring and the orbit of Amalthea (Burns et al 1983). Fine structure has been noted which may correspond to the orbits of Jupiter's several "ringmoons" Metis and Adrastea, or possibly certain resonances between the ring particle orbit periods and the period of the magnetic field. These would be able to affect the orbits of charged, micron-sized particles such as inhabit the visible ring. Detailed photometry of the ring has revealed that the usual characterization of "the" particle size as a few microns is oversimplified, and that a broad powerlaw distribution of sizes extends from submicron-sized dust particles to much larger radii (Showalter et al. 1983b), possibly all the way up to the macroscopic "mooms" believed to supply the visible ring dust. The "characteristic" micron size is an observational selection effect related to the observational geometry.

b. The nature of the F ring: Analysis by Cuzzi and Burns of the magnetospheric absorptions observed by Pioneer 11 (in preparation) implies that the region between the F ring shepherds may be replete with macroscopic clumps of material, ranging in size from cm to 10km. At least some of these clumps were not observed by Voyager imaging or occultation experiments. The implications of these results are being explored. Also, a faint new band of material has been discovered between the outer edge of Saturn's A ring and the visible F ring (Burns et al, 1983). The existence of this material may be due to erosional ejecta, as discussed in section Ic above.

c. Studies of the B ring irregular structure: The myriad features seen in Saturn's B ring, reminiscent of the grooves on a record, have received little attention to date; several hypotheses have been advanced to explain this complex structure, but none is completely satisfactory. Cuzzi and Luke Dones, a graduate student at U.C. Berkeley, have embarked on a thorough study of the photometric and morphological properties of this complex region. Several initial results are of interest (see, e.g., Cuzzi et al. 1984). First, the irregular structure seen in Voyager images may or may not be related to variations in ring optical depth. At least some of the features are due only to local variations in

particle albedo. Both global and local variations in color are also seen. There are also regional variations in the characteristic radial scale of observed features. Our study will attempt to fully integrate the various observed aspects of the irregular structure. We will also apply similar techniques in a more focussed study of the properties of the abrupt inner edges of the A and B rings, which are not currently well understood (see section Ic above). BIBLIOGRAPHY

Burns, J.A., Cuzzi, J.N., and Showalter, M.R. (1983) Discovery of gossamer rings; B.A.A.S., 15, 1013.

Cuzzi, J.N. (1983) Planetary ring systems; Revs. Geophys. Space Phys., 21, 173-186.

Cuzzi, J.N., Lissauer, J.J., and Shu, F.H. (1981) Density waves in Saturn's rings; Nature, 292, 707-707.

Cuzzi, J.N., Lissauer, J.J., Esposito, L.W., Holberg, J.B., Marouf, E.A., Tyler, G.L., and Boischot, A. (1984) Saturn's Rings: Properties and processes; In "Planetary Rings", R. Greenberg and A. Brahic, Eds., U. of Arizona Press.

Cuzzi, J.N. and Showalter, M.R. (1984) Shepherding Moonlets: Detection by adjacent ring radial structure; Hawaii DPS Meeting, Oct. 1984.

Durisen, R. (1984) Transport Effects due to particle erosion mechanisms; in "Planetary Rings", R. Greenberg and A. Brahic, Eds. U. of Arizona Press.

Durisen, R., Cramer, N.L., Mullikin, T.L., and Cuzzi, J.N. (1982) The evolution of Saturn's Rings due to Particle Erosion Mechanisms; "Saturn" Meeting, Tucson, Arizona, May 1982.

Epstein, E.E., Janssen, M.A., and Cuzzi, J.N. (1984) Saturn's Rings: 3.4mm Wavelength observations at low inclination; Icarus, 58, 403-411.

Esposito, L.W., Borderies, N., Goldreich, P., Cuzzi, J.N., Holberg, J.B., Lane, A.L., Pomphrey, R.B., Terrile, R.J., Lissauer, J.J., Marouf, E.A., and Tyler, G.L. (1983), Eccentric ringlet in the Maxwell gap at 1.45 R_S: Multi-instrument Voyager observations; Science, 222, 57-60.

Esposito, L.W., Cuzzi, J.N., Holberg, J.B., Tyler, G.L., Marouf, C.C., and Porco, C.C. (1984) Saturn's Rings: Structure, dynamics, and particle properties; in "Saturn", T. Gehrels, Ed., U. of Arizona Press.

Goldreich, P. and Tremaine, S. (1978), The formation of the Cassini division in Saturn's rings; Icarus, 34, 240-253.

Goldreich, P. and Tremaine, S. (1979), Towards a theory for the Uranian rings; Nature, 277, 97-99.

Greenberg, R. (1983), The role of dissipation in shepherding of ring particles; Icarus, 53, 207-218.

Lissauer, J.J., (1984) Ballistic transport in Saturn's rings: An analytic theory; Icarus, 57, 63-70.

Lissauer, J.J., Peale, S.J. and Cuzzi, J.N. (1984) Ring torque on Janus and the melting of Enceladus; Icarus, 58, 159-168.

Lissauer, J.J., Shu, F.H. and Cuzzi, J.N. (1984) Viscosity in Saturn's rings; In proceedings of IAU Colloquium 75, Planetary Rings; A. Brahic, Ed.

Morfill, G.E., Fechtig, H., Grün, E., and Goertz, C.K. (1983) Some Consequences of meteoroid impact on Saturn's rings; Icarus, 55, 439-447.

Showalter, M.R., Burns, J.A., Cuzzi, J.N. and Pollack, J.B. (1983a) Re-examining Jupiter's ring: Morphology; B.A.A.S., 15, 815.

Showalter, M.R., Burns, J.A., Cuzzi, J.N. and Pollack, J.B. (1983b) Re-examining Jupiter's ring: Photometry; B.A.A.S., 15, 815.

Shu, F.H., Cuzzi, J.N. and Lissauer, J.J. (1983) Bending waves in Saturn's rings; Icarus, 53, 185-206.

Shu, F.H., Yuan, C., and Lissauer, J.J. (1985) Nonlinear spiral density waves: An inviscid theory; Astrophys. J. (submitted).

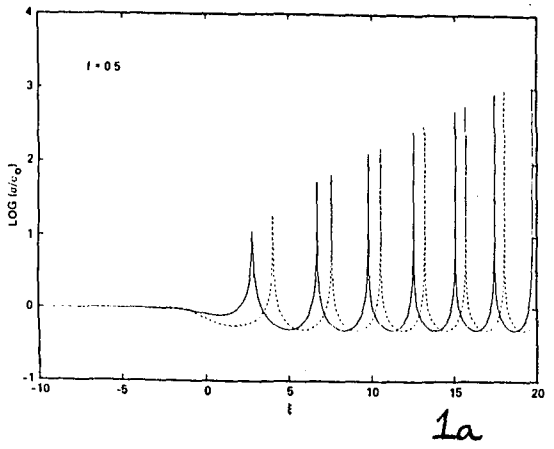

1a

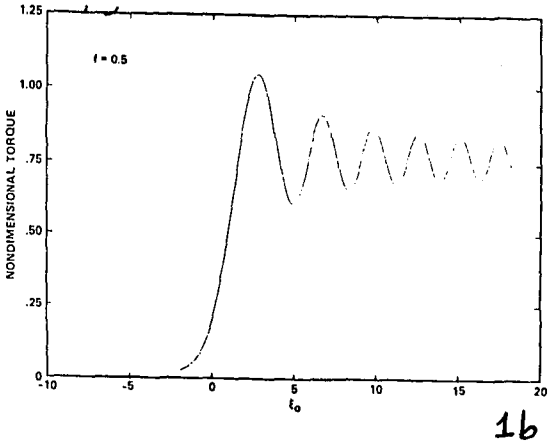

1b

Fig 1a: Theoretical density profiles for nonlinear density waves show the same "spiky" appearance as do waves observed in Saturn's Rings. The parameter ξ represents distance radially outward from a resonance at ξ =0. (Shu et al. 1985)

1b. The ratio of the torque transmitted to the rings in a strongly nonlinear density wave to the value calculated from standard linear density wave theory, as a function of distance from resonance, supports the linear results (Shu et al. 1985)

fig 2.

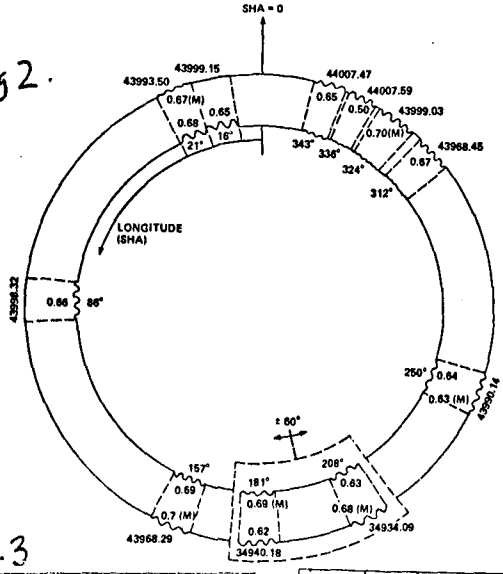

Fig 2: The angular distribution of edge waves along the inner and outer edges of the Encke gap in Saturn's A ring provides strong indirect evidence for the presence of an unseen moonlet of about 10 km radius embedded near the center of this clear gap (Cuzzi and Scargle 1985)

fig. 3

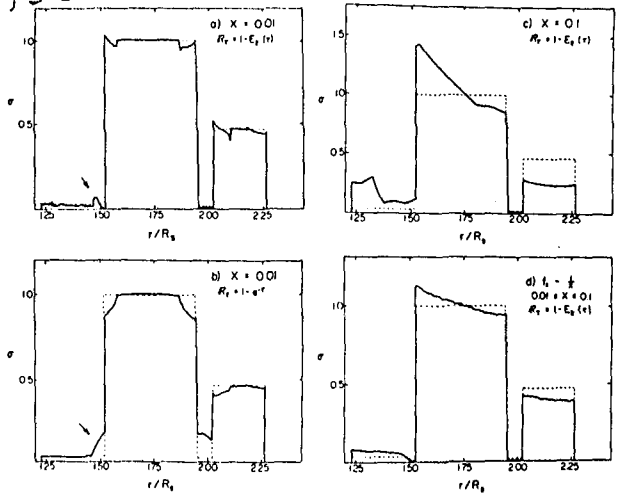

Fig 3: Numerical simulations of the structural effects of erosional redistribution of ring material. The dashed lines show the initial distributions, and the solid lines show the results for various choices of ejection velocity, which is given as a fraction X of the orbital velocity. Interesting similarities are seen to certain unexplained aspects of Saturn's ring structure (Durisen 1984).

DYNAMICAL STUDIES OF SATURN'S RINGS

Dr. Philip D. Nicholson, Dept. of Astronomy, Cornell University, Ithaca, NY 14853 and Dr. Carolyn C. Porco, Lunar and Planetary Lab, University of Arizona, Tucson, Az. 85721

The wealth of data returned by the Voyager investigations of the Saturnian system has revealed the structure of Saturn's ring system to be dominated by many abrupt transitions in optical depth, narrow well-defined ringlets and gaps, and spiral density and bending waves. A handful of these features have been attributed with reasonable certainty to the resonant influence of external satellites, but the vast majority of the structure in Saturn's rings remains unexplained.

A systematic study of the entire C ring has begun in which particular emphasis is placed on the search for as yet unrecognized eccentric or inclined features and the role, if any, played by satellite resonances in controlling C ring structure. The choice of the C ring for this study was governed by several principal considerations: 1) the apparent regularity and high degree of organization of C ring structure, as opposed to the chaotic appearance of the B ring; 2) the lack of existing models for this region, as opposed to the A ring where much of the structure is due to density wave trains; and 3) the comparatively low optical depth of the C ring, which has resulted in high quality occultation data being available from both the radio (RSS) and stellar (PPS) occultation experiments carried out by Voyagers 1 and 2. These occultation data, as well as ~ 30 photometrically calibrated and geometrically corrected Voyager images of the C ring, have been acquired and are currently being inter-compared over several noteworthy regions in the C ring. Though the occultation data are in general of much higher resolution than the imaging data, the more extensive ring longitude coverage provided by the images offers the opportunity to study azimuthal variations in position, width, and brightness of individual features.

Imaging data reduction has followed the pattern established in our earlier studies of eccentric features (Porco et al. 1984a, 1984b). Each image has been used to produce scans of brightness across the rings which are then reduced to an absolute scale of radial distance by reference to certain circular fiducial features whose radii are accurately determined by the occultation experiments. (Results from two such imaging scans showing regions of particular interest in the C ring are compared in Fig. 1 with the corresponding RSS 3.6 cm opacity profile.) New software has been written to increase the efficiency and accuracy of

this measurement process and has resulted in more precise estimates of the relative distances between ring features. In previous work, measurement uncertainties were ~ 3-5 km; in current work, these have been reduced to ~ 0.5-1.5 km. It is anticipated that deviations from circularity of ~ 5 km will be detectable in this analysis.

A catalogue of satellite resonances falling within the C ring has been generated to explore the possibility of other associations of resonances with ring features like that noted in Fig. 1b, and to make comparison between different resonances. As well as the inner Lindblad resonances (ILR), whose location and strengths were calculated by Lissauer and Cuzzi (1982), inner vertical resonances (IVR) and corotation resonances have been included. Fig. 2 shows the locations of the important families of resonances in the C ring, superimposed on a low resolution plot of the RSS occultation profile. Initial efforts in searching for eccentric and inclined features are being guided by this array of resonances.

The eccentric ringlet at 1.29 Rs, which was found by Porco et al. (1984a) to have an apsidal precession locked to the orbital motion of the satellite Titan, has provided an indirect but powerful constraint on Saturn's higher order gravity harmonics. This constraint has been combined with the gravity solution of Null et al. (1981), which was based on Pioneer 11 Doppler tracking and satellite secular precession rates, to derive new estimates for the gravity coefficients J2, J4, and J6. These results are currently in preparation for publication.

References

Franklin, F.A., Colombo, G., and Cook, A.F. (1982). Nature 245, 128-130.

Lissauer, J.J. and Cuzzi, J.N. (1982). Astron. J. 82, 1051-1058.

Null, G.W., Lau, E.L., Biller, E.D., and Anderson, J.D. (1981). Astron. J. 86, 456-468.

Porco, C., Nicholson, P.D., Borderies, N., Danielson, G.E., Goldreich, P., Holberg, J.B., and Lane, A.L. (1984a). Icarus (in press).

Porco, C., Danielson, G.E., Goldreich, P., Holberg, J.B., and Lane, A.L. (1984b). Icarus (in press).

Tyler, G.L., Marouf, E.A., Simpson, R.A., Zebker, H.A., and Eshleman, V.R. (1983). Icarus 54, 160-188.

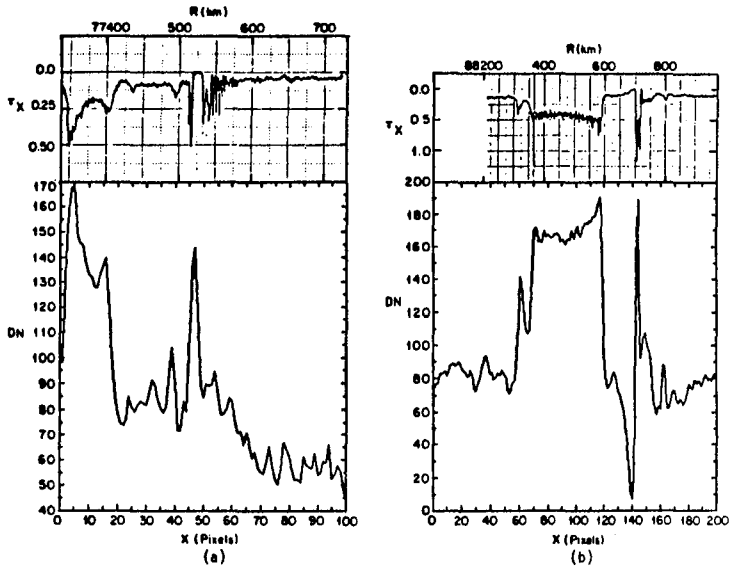

Fig. 1. Comparisons between radial scans of ring brightness, from Voyager 2 narrow angle frames, and X-band radio occultation profiles of the same regions. Image resolution is 4-5 km per pixel, while the RSS data have been deconvolved to a resolution of 1 km. (a) A portion of frame FDS 43995.28, showing the neighbourhood of a 15 km-wide gap at 1.2850 R_S and an associated wavelike feature. Note that the region of the peak image brightness actually corresponds to the gap in the RSS profile, rather than to either of the narrow features flanking it. The gap appears either to be discontinuous, or to be filled with highly optically reflective, very small particles. (b) A portion of frame FDS 43992.59, showing the 29 km-wide gap at 1.470 R_S and its narrow (17 km), embedded ringlet. The wavelike pattern outside the gap has an approximately constant wavelength of 4.5 km. The Mimas 3:1 IVR and 1980 S27 2:1 ILR are located at radii of 88703 and 88712 km, respectively. (Unpublished RSS data provided by G. L. Tyler.)

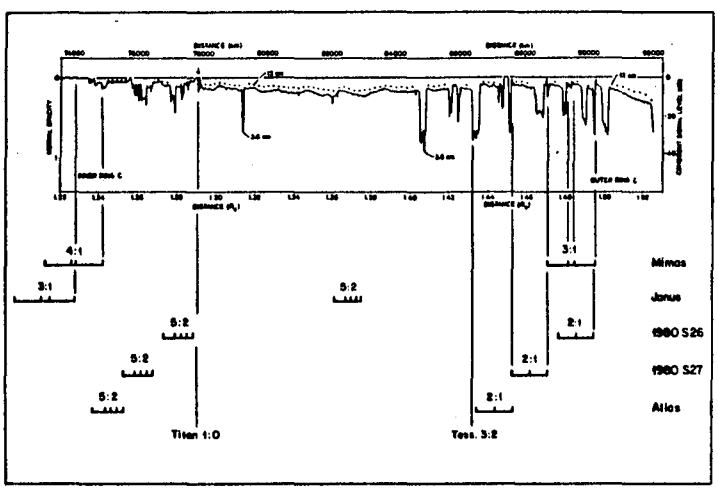

Fig. 2. A low-resolution view of the C ring, showing the locations of the principal families of resonances with known satellites. For each resonance group (e.g., Mimas 3:1), the individual resonances shown are, in order of increasing radius, the IVR, one or two corotation resonances, and one or two ILR's. Also included are the Titan 1:0, or apsidal, resonance and the hypothetical 3:2 tesseral resonance due to irregularities in Saturn's gravity field (Franklin et al., 1982). Optical depth profile at 3.6 cm from Tyler et al. (1983).

METEOROIDAL IMPACTS, PLASMA, FINE STRUCTURE OF RINGLETS AND SPOKES ON SATURN'S RING B

A.F. Cook, Herzburg Institute of Astrophysics, National Research Council of Canada, Ottawa, Ontario, Canada KIA OR6 and Harvard-Smithsonian Center for Astrophysics, Cambridge, Massachusetts., 02138
G.E.Hunt and Robert Barrey, Atmospheric Physics Group, The Blackett Laboratory, Imperial College, London, England SW7 2AZ

We consider the role of the bombardment of the rings by the dominant size (~90 μg of meteoroids believed to be arriving there. We show that the impact plasma is returned to the ring by magnetic mirroring over a sufficiently long interval and a correspondingly long track on the ring, which, in turn, causes an overlap in the effects of impacts. A result is that we expect this process to produce a pervasive background plasma north and south of the ring. This plasma, in turn, should deposit a nocturnal layer in Saturn's ionosphere and maintains a continuous electrical connection between the atmosphere and the ring. The plasma should maintain already levitated grains in that state, and thus provide the particles in the observed radial fine structure of ringlets, dark in back scatter and enhanced in forward scatter.

Impacts of large meteoroids can generate an extensive cloud of magnetically threaded enhanced plasma outside the primary plasma expansion cloud and diamagnetic cavity. Impact ionization of neutral atoms in the atmosphere of the ring by neutral atoms emerging from the primary plasma expansion cloud provides the source of this ionization. This circumstance explains the observed presence of spokes on both the illuminated and unilluminated faces of the ring.

A discrepancy exists between the distance at which the behavior of the spokes suggests that co-revolution about Saturn should occur and that at which it must occur. We suggest that a steady pattern in the ionospheric winds could well be the cause. A morning-evening asymmetry in these winds could be the ultimate reason for leading-trailing asymmetry in the behavior of the spokes.

Small grains levitated from the ring are expected to be warm enough in sunlight to be above the ferroelectric transition for ice. Upon immersion into Saturn's shadow they should cool, become ferroelectric electrets and begin to collect cancelling charges on their surfaces. Upon emersion, they will warm, should make the transition in reverse and release their charges, mostly into the trapped plasma above the north face of the ring. This process may contribute in some indirect way to leading-trailing asymmetry in the behavior of the spokes.

An instability associated with the expansion of narrow radial spokes in the gradient of the magnetic pressure is invoked as a possible explanation for the recently forward tilts in spokes.

INTERACTION OF THE MAGNETOSPHERIC IONS WITH THE SURFACES OF THE ICY SATELLITES OF SATURN

R. E. Johnson, University of Virginia

One of the most exciting recent developments of Planetary Science is the extraordinary connection between the compositions of the surfaces of the satellites and rings particles and the compositions of the magnetospheric plasmas in which they are imbedded. What may be even more exciting is this connection is being developed and understood via a combination of laboratory and satellite measurements. This interaction has not only exposed a new set of phenomena in Planetary Science, it has stimulated new research on radiation effects in materials which we in an engineering environment see will be technologically useful.

Laboratory measurements have begun to characterize the changes induced in ice by ion and electron bombardment. Most attention has been paid to measurements of the atoms and molecules ejected via ion bombardment, but work has been initiated at Virginia on changes in the spectral character of the ice. For a number of useful ion types and energies we have determined the ejection yields, energy, and angular distributions. Although there are huge gaps in this knowledge considerable progress is being made in characterizing the environment of the inner icy satellites and the E-ring of Saturn. In Figure 1, I give a calculation of the neutral cloud of O, OH, and H_2O co-orbiting with these satellites and icy particles. This cloud is supplied by ion bombardment of the surfaces of the icy satellites. It is noteworthy that close to the orbital plane of the satellites the number density of neutrals is larger than the plasma ion density, opposite to the situation at the Io plasma torus. In fact, recent laboratory measurements suggest these neutral densities should be increased. Although we have not as yet been able to demonstrate that this material is the source of the E-ring particles, it is evident that the relatively high density of water molecule products could be a source for such a feature. Further, using ionization rates we have produced source rates at fresh ions for the magnetosphere of Saturn. These source rates are being used to understand the anamolus properties of this plasma which bombards the inner satellites.

Recent results on CH_4 and mixtures of H_2O and CH_4 indicate that a considerable amount of chemistry is induced in such ices via ion bombardment. Methane does not erode simply as CH_4 rather the H is lost preferentially resulting in dramatic changes in the albedo of the residual material. Since methane may be expected to condense at the outer planets, possibly as a clathrate, such changes in albedo may account for the darkened surfaces of the rings at Uranus and darkening of surfaces of certain satellites.

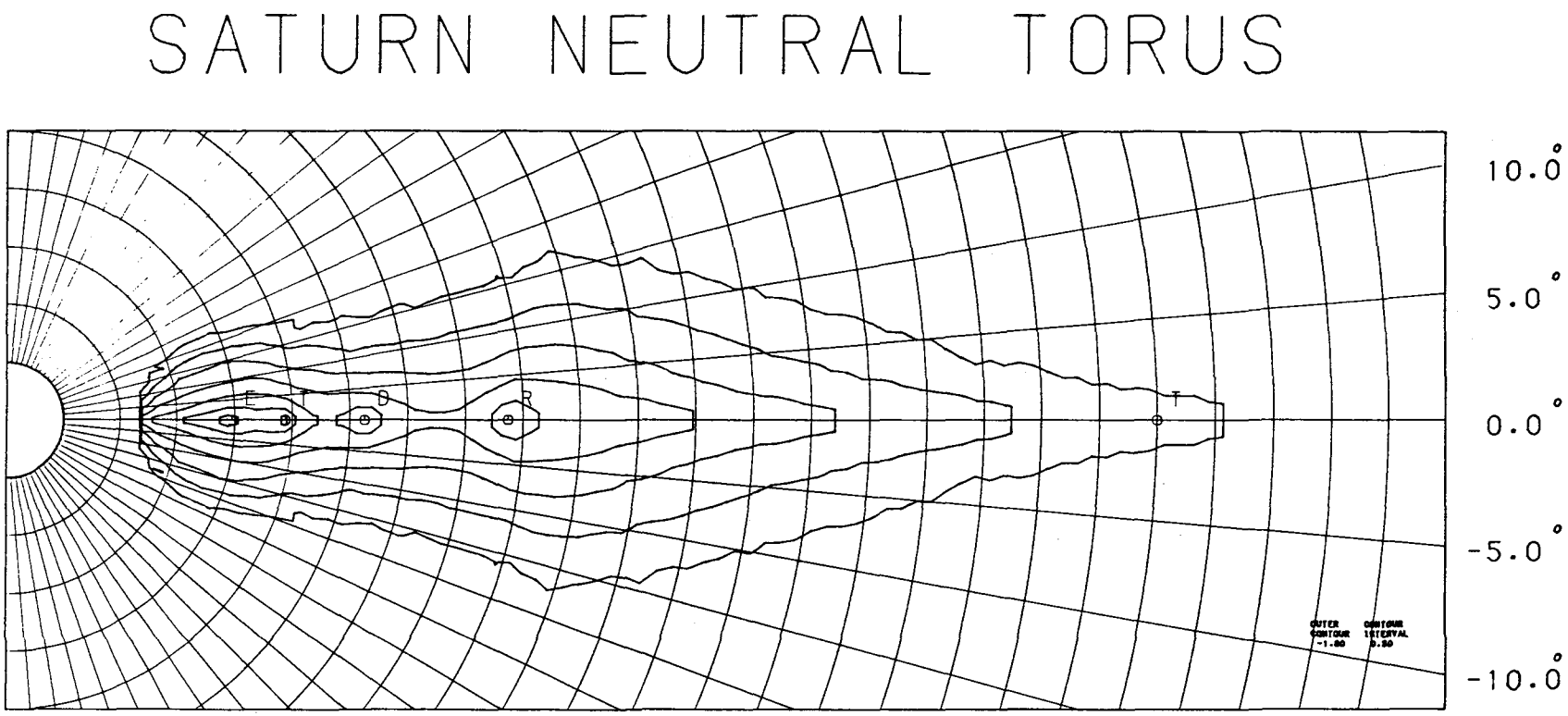

Figure 1. Neutral Torus Sputtered from the Inner Satellites: Outer Contour 10^{-1} oxygen/cm^3, Contour Steps in Half Powers of Ten

Plasma Production by Meteoroid Impact

P. K. Haff, Division of Physics, Mathematics, and Astronomy, Caltech 301-38, Pasadena, California 91125 and A. Eviatar, Department of Atmospheric Sciences, University of California, Los Angeles, California 90024

Material ejected from the surfaces of satellites in the outer solar system plays an important role in the magnetospheres of the outer planets, and may dominate the mass loading, as in the vicinity of the Jovian satellite Io.

At least four potential ejection mechanisms can be identified - intrinsic geologic activity, thermal sublimation, sputtering, and micrometeoroid impact vaporization. On all the icy satellites, except possibly Enceladus [Herkenhoff and Stevenson, 1984], sputtering and impact vaporization are the only two potentially important sources of magnetospheric plasma. Sputtering has been shown to be an important mass source at both Jupiter and Saturn (e.g., [Haff et al., 1979; Cheng et al., 1982; Barton, 1983; Johnson et al., 1983; Haff et al., 1983]). Here we assess the impact mechanism as a plasma source.

Two recent, and rather different, estimates of the micrometeoroid impacting mass flux are used to estimate vapor fluxes in the outer solar system. Morfill et al. [1983] have attributed the existence of the H atmosphere associated with Saturn's rings to vapor released by meteoroid impact on ring particles. If each impacting hypervelocity mass creates an amount of vapor comparable to the mass of the projectile, their studies imply an interplanetary flux of $\sim 3 \times 10^{-15}$ g cm^{-2} s^{-1} at Saturn. A more conservative estimate of the meteoroid flux derives from the work of Samuelson et al. [1983] who found the CO_2 abundance on Titan to be consistent with an interplanetary flux of $\sim 3 \times 10^{-15}$ g cm^{-2} s^{-1}. If we assume a vapor production efficiency of unity, then, taking into account the focussing of the meteoroid flux due to Saturn, the rate of vapor released from each satellite can be calculated and compared with estimates of the corresponding sputtering rate. Similar calculations may be applied at Jupiter, where a somewhat higher interplanetary flux is assumed, based upon Humes observation [Humes, 1980] of an essentially constant density of micrometeoroid material between 1 and 18 AU.

The results of these calculations are summarized in the Table. For the Morfill et al. [1983] flux values, impact vaporization is important at Amalthea, and it can apparently compete with sputtering at Europa, Ganymede, and Callisto. However, the numbers reported in the Table are the total vapor production rates, and because of the large size of these satellites perhaps only 1% of this will escape to space. At Saturn, the maximum vaporization rates could compete with sputtering at the Mimas-Rhea quintet, being dominant in fact at Rhea. For the more conservative Samuelson et al. [1983] numbers, the impact source can nowhere compete with sputtering, which then remains the principal source of magnetospheric mass at both Jupiter and Saturn.

One interesting problem is the non-observation of a significant heavy ion density associated with the orbit of Rhea [Frank et al., 1980], although either vaporization due to a Morfill-type flux or to a lesser degree the sputtering process would suggest that Rhea ought to be a significant source of mass. The lack of significant heavy ion plasma associated with the orbit of Rhea could be due to charge-exchange reactions with neutral hydrogen atoms. Eviatar et al. [1983] have attributed the absence of a prominent plasma torus at Rhea to this process.

REFERENCES

L. A. Barton, Magnetospheric Ion Erosion of the Icy Satellites of Saturn, Masters Thesis, Univ. of Virginia, unpublished (1983).

A. F. Cheng, L. J. Lanzerotti, and V. Pirronello, J. Geophys. Res., 87, 4567-4570 (1982).

A. Eviatar, R. L. McNutt, Jr., G. L. Siscoe, and J. D. Sullivan, J. Geophys. Res. 88, 823-831 (1983).

L. A. Frank, B. G. Burek, K. L. Ackerson, J. H. Wolfe, and J. D. Mihalov, J. Geophys. Res. 85, 5695-5708 (1980).

P. K. Haff, C. C. Watson, and Y. L. Yung, J. Geophys. Res. 86, 6933-6938 (1979).

P. K. Haff, A. Eviatar, and G. L. Siscoe, Icarus 56, 426-438 (1983).

K. E. Herkenhoff and D. J. Stevenson, Lunar and Planet. Sci. XV, 361-362 (1984).

D. H. Humes, J. Geophys. Res. 85, 5841-5852 (1980).

R. E. Johnson, J. W. Boring, C. T. Riemann, L. A. Barton, E. M. Sieveka, J. W. Garrett, K. R. Farmer, W. L. Brown, and L. J. Lanzerotti, Geophys. Res. Lett. 10, 892-895 (1983).

G. E. Morfill, H. Fechtig, E. Grun, and C. K. Goertz, Icarus 55, 439-447 (1983).

R. E. Samuelson, W. C. Macguire, R. A. Hanel, V. G. Kunde, D. E. Jennings, Y. L. Yung, and A. C. Aiken, J. Geophys. Res. 88, 8709-8715 (1983).

TABLE

Jupiter	Φ_1[a] ($g\ s^{-1}$)	Φ_2[b] ($g\ s^{-1}$)	Φ_{sputt}[c] ($g\ s^{-1}$)
Amalthea	210	2.1	22
Europa	10,000	100	8100
Ganymede	7,300	73	20,000
Callisto	11,000	110	1,800
Saturn			
Mimas	170	1.7	12
Enceladus	230	2.3	95
Tethys	850	8.5	990
Dione	780	7.8	2100
Rhea	1,100	11	170

a) Total satellite vapor loss rate, Morfill et al. [1983] impact flux.

b) Total satellite vapor loss rate, Samuelson et al. [1983] impact flux.

ORIGIN AND EVOLUTION OF THE SATURN SYSTEM

James B. Pollack, NASA Ames Research Center
Moffett Field, CA 94035

As was the case for Jupiter, Saturn formed either as a result of a gas instability within the solar nebula or the accretion of a solid core that induced an instability within the surrounding sola nebula. In either case, the protoplanet's history can be divided into three major stages: early, quasi-hydrostatic evolution (stage 1); very rapid contraction (stage 2); and late, quasi-hydrostatic contraction (stage 3). During stage 1, Saturn had a radius of several hundred times that of its present radius R_S, while stage 3 began when Saturn had a radius of 3.4 R_S. Stages 1 and 2 lasted 10^6-10^7 yr and 1- 10^4 yr, respectively, while stage 3 is continuing through the present epoch.

Saturn's current excess luminosity is due, in part, to the loss of thermal energy built up by a faster contraction that marked the earliest phase of stage 3. But, in contrast to the situation for Jupiter, this internal energy source fails by a factor of several in producing the observed excess luninosity. The remainder is most likely due to the gravitational separation of helium from hydrogen due to its partial immiscibility in the outer region of the metallic hydrogen zone.

The irregular satellite Phoebe was most likely captured by gas drag experienced in its passage through a bloated Saturn, just prior to the onset of stage 2. During stage 2, a nebular disk formed from the outermost portions of Saturn, due to a progressive increase in their rotational velocity as the planet contracted. This increase may have been enhanced significantly by a transfer of angular momentum from the inner to the outer regions of the planet. The nebular disk served as the birthplace of Saturn's regular satellites and probably the ring material. Viscous dissipation within the nebula caused an inward transfer of mass, and thus may have determined the nebula's lifetime, and an outward transfer of angular momentum. It is not clear what the relative roles of Saturn's luminosity and viscous dissipation were in determining the nebula's radial temperature structure and its evolution with time.

As Saturn's excess luminosity declined or less viscous dissipation in the nebula occurred during the early portion of stage 3, water was able to condense at progressively closer distances to the center of the system and water clathrates and hydrates were able to form throughout much of the nebula, especially in its outer regions. It is the likely presence of ices other than pure water ice in at least some of the regular satellites of Saturn that make them chemically distinct from the large icy satellites of Jupiter. If Saturn's nebula had a high enough pressure (greater than several tens of bars) in its inner region, a liquid solution of water and ammonia, rather than water ice, would have been the first "icy" condensate to form.

Despite the comparatively small size (hundreds to about a thousand kilometers) of the inner satellites of Saturn, a number (especially Dione and Rhea) may have exprienced significant expansion and melting during the first 1×10^9 yr due to the presence of substantial quantitites of ammonia monohydrate (10-20% by weight). The occurrence of the youngest known surfaces in the Saturn system on the comparatively small-sized Enceladus is most readily attributed to strong tidal heating created by its forced orbital eccentricity. But a significantly larger eccentricity is required at some time in its past for tidal heating to be quantitatively capable of initiating melting, with the current eccentricity being perhaps large enough to maintain a molten interior.

During the early history of the Saturn system, giant impact events may have catastrophically disrupted most of the original satellites of Saturn. Such disruption, followed by reaccretion, may be responsible, in part, for the occurrence of Trojans and coorbital moons in the Saturn system, the apparent presence of a stochastic component in the trend of satellite density with radial distance, and the present population of ring particles.

Titan's atmosphere formed from the hydrates and clathrates - especially ammonia monohydrate and/or nitorgen clathrate and methane clathrate - that consituted the satellite. Over the age of the solar system, a nontrivial amount of atmospheric nitrogen (about several tens of percent of the current atmospheric inventory) and much more methane than is presently in the atmosphere have been lost, through a combination of N and H escape to space and the irreversible formation of organic compounds. These considerations imply quasi-real time buffering of atmospheric methane by a near-surface methane reservoir and the existence of a layer of 0.1 to 1 km thickness of organic compounds close to or on Titan's surface.

GIANT PLANETS AND THEIR SATELLITES: COSMOCHEMISTRY, EVOLUTION AND STRUCTURE

D.J. Stevenson, California Institute of Technology

This work encompasses most aspects of the solar system beyond the asteroid belt, but with emphasis on the interplay of cosmochemistry and planetary physics. Four students are involved currently in the work reported here and collaboration continues with Jonathan Lunine (who is now a postdoc at the University of Arizona).

1. Titan

Our work on the likely surface state of Titan was published during the year.[1] In a follow-up to this effort, Jon Lunine and I examined how Titan's ocean and atmosphere would evolve through geologic time.[2] We conclude that the ancient (but post-accretion) Titan may have been colder than at present, possibly with a frozen surface. We also concluded that a hydrocarbon ocean is capable of substantially eroding water ice topography on a geological time scale -- ''Karst'' may result. In a more speculative analysis,[3] we have attempted to understand the origin and early evolution of Titan's atmosphere. We find that neither of the conventionally advocated origins of molecular nitrogen (clathrates or photochemical production from NH_3) is very satisfactory. The origin of CH_4 is also unclear but probably the result of outgassing. These problems are the subject of ongoing work.

2. Clathrates

Our thorough statistical mechanical treatment of clathrate hydrates is now complete and forms the major part of Jon Lunine's Ph.D. thesis. It has been accepted by Astrophysical Journal.[4] Main conclusions include predictions for noble gas ratios in the atmospheres of giant planets and Titan, predictions for the degree of double occupancy (CH_4 and H_2 in the same cage site), a prediction that clathrate is probably not present in comets (because of kinetic inhibition) and a prediction that clathrate undergoes decomposition at $P \gtrsim 12$-14 kbar, possibly relevant to the origin of methane on Titan (and perhaps Triton). This work is the first ever complete treatment of clathrate thermodynamics for solar system application.

3. Planetary Dynamos

I have discovered a new dimensionless number, called the energy flux number $\bar{\Phi}$, which characterizes the existence and nature of a planetary dynamo. In a paper in press in Astronomische Nachrichten[5] I show that a dynamo requires $\bar{\Phi} \gtrsim 1$ and can exist in one of three states: energy limited ($\bar{\Phi} \lesssim 10^{2.5}$), dynamically determined laminar ($10^{2.5} \lesssim \bar{\Phi} \lesssim 10^{5}$) and dynamically determined turbulent ($\bar{\Phi} \gtrsim 10^{5}$). Mercury, Earth, and Jupiter are probable examples of these three states, respectively.

4. Formation of the Giant Planets

A popular model for giant planet formation (Mizuno, 1980) involves

slow growth of a solid core followed by hydrodynamic collapse of gas. I have performed more detailed calculations[6] indicating that the collapse is initiated when the core is only ~ one Mars mass, because of the tendency for H_2O and H_2 to mix in the deep envelope and the probable lack of dust opacity in the upper envelope. The implications of this result are enigmatic. On the one hand, early collapse may hasten giant planet formation -- a desirable feature. On the other hand, it is not clear whether these objects -- dubbed ''superGanymedean puffballs'' -- are suitable precursors for giant planets.

5. The E-Ring

Ken Herkenhoff and I have examined whether the E-ring particles can originate from water-ammonia volcanism on Enceladus.[7] We find that condensation in an expanding NH_3 vapor cloud centered on a (probably rather quiescent) H_2O-NH_3 vent can lead to particles of the right size to explain the observed properties. This is a much more satisfactory explanation than meteoritic impact because it is specific to Enceladus and leads to a narrow range of particle sizes (as observed).

6. Uranian Satellites

Prompted by the Uranus-Neptune workshop held in February, 1984, I have analyzed a model in which the Uranian satellites are formed from a disk that is spun out in the giant impact that caused the 98° obliquity of Uranus.[8] The shock chemistry predicts depletion of H_2O (i.e., $CH_4 + H_2O \rightarrow CO + 3H_2$) and a corresponding density enhancement for the more distant satellites (Titania and Oberon), consistent with the tentative conclusions of Veillet (1983).

7. Uranian Atmosphere

Any plausible model for Uranus' formation, evolution, and structure leads to the expectation that the deep atmosphere is enormously enhanced in ices relative to cosmic abundance. I have analyzed the chemical and phase assemblage implications of this[9] and conclude that the observable atmosphere is probably rich in CH_4, slightly enriched in He, depleted in NH_3, and has small amounts of N_2, CO, and CO_2. Some of these predictions can be tested by Voyager in 1986.

8. Io Sulfur Lakes

Motivated by recent work by McEwen et al., Jon Lunine and I have been examining the thermodynamics and fluid dynamics of sulfur lakes.[10] We conclude that the ~450 K hot spot at Loki Patera may be a sulfur lava lake and the associated ~250 K feature may represent latent heat release (condensation) of the sulfur evaporating from this lake. Consideration of a two-layer (sulfur overlying silicates) convection system suggests that temperatures higher than ~450 K are not allowed for stable features, consistent with observation.

9. Episodic Tidal Evolution

Greg Ojakangas and I have almost completed an analysis of the coupled thermal and orbital evolution of a tidally heated satellite, allowing for the strong temperature dependences of convective heat flow,

tidal quality factor and Love number.[11] We find that a satellite such as Io has no steady state but oscillates through periods of high heat flow and volcanic activity ($\sim 10^7$ yr in duration) with quiet interperiods $\sim 10^8$ yr duration. Eccentricities and heat flows consistent with observation emerge from this model.

10. Resurfacing of Ganymede

Randy Kirk and I have examined further the question of whether groove formation can result from a slow process (gradual, global expansion as originally proposed by Squyres) or requires a fast process (eg., diapiric upwelling resulting from contact between ice I and ice III in the interior). Using a pseudo-Newtonian viscoelastic formulation for extension of the outer layers, we find that for the rheology inferred from the recent experiments of Durham et al. (1983), slow extension is accommodated by creep and no fracture. We conclude that the resurfacing of Ganymede required ''sudden'' (time scale $\lesssim 10^5$ yr) events.

11. Origin of the Moon

I have attempted to solve the ''second burn'' problem: How do you get a substantial amount of material into earth orbit after a giant impact? Three important factors were identified:[12] pressure gradient acceleration, non-central gravity and viscous effects. The latter is especially important in a model that involves spin-out of a massive, supercritical atmosphere to form a disk.

12. Other Papers

Other papers published during the year were on the viscosity of rock-ice mixtures[13] and the condensed matter physics of planets.[14] Review papers on giant planets[15] and satellite origins[16] are in press.

References

(1) Lunine, J.I., Stevenson, D.J., and Yung, Y.L. (1983) Science **222**, 1229-1230. (2) Lunine, J.I. and Stevenson, D.J. (1984) Proc. NATO Conf. ''Ices in the Solar System.'' (3) Lunine, J.I. (1984) Part III of Ph.D. Thesis. (4) Lunine, J.I. and Stevenson, D.J. (1984) to appear in Astrophys. J. Suppl. (5) Stevenson, D.J. (1984) Astron. Nachr. **305**, 257-264. (6) Stevenson, D.J. (1984) LPSC XV Abs 822-823. (7) Herkenhoff, K.E. and Stevenson, D.J. (1984) LPSC XV Abs. 361-362. (8) Stevenson, D.J. (1984) Proc. Uranus and Neptune Workshop. (9) Stevenson, D.J. (1984) Bull. Am. Astron. Soc. **16**, 658. (10) Lunine, J.I. and Stevenson, D.J. (1984) Bull. Am. Astron. Soc. **16**, 654. (11) Ojakangas, G.W. and Stevenson, D.J. (1984) Bull. Am. Astron. Soc. **16**, 661. (12) Stevenson, D.J. (1984) Origins of the Moon Abstract Volume (LPI), p. 60. (13) Friedson, A.J. and Stevenson, D.J. (1983) Icarus **56**, 1-14. (14) Stevenson, D.J. (1984) Mat. Res. Soc. Symp. Proc. **22**, 357-368 (publ. Elsevier). (15) Stevenson, D.J. (1984) The Solar System (Rubey Colloq. Vol.), ed. M. Kivelson. (16) Stevenson, D.J., Harris, A.W. and Lunine, J.I. (1984) In Planetary Satellites, Univ. Arizona Press.

THE STRUCTURE AND COMPOSITION OF URANUS AND NEPTUNE

Reynolds, R.T. and M. Podolak*, NASA Ames Research Center, Moffett Field, CA 94035

Uranus and Neptune form a special class of planetary objects; intermediate in mass and composition between the giant Hydrogen-rich planets, Jupiter and Saturn, and the small, rocky terrestrial planets. Their structure and composition are not only of intrinsic importance, but also should provide information as to the nature of the protoplanetary nebula and the processes of planetary formation. Many theoretical models have been constructed (using high pressure equations of state with the equation of hydrostatic equilibrium) in order to compare calculated results, for various assumed compositions and structural configurations, with the observational data (mass, radius, rotation rate, gravitational moments, etc.). While it is possible to obtain models which are consistent with known observational constraints, insufficient data has thus far precluded unique and definitive solutions. For a long time, Uranus' rotational period was determined as being close to 24 hours by some groups and close to 16 hours by others. This discrepency is only now in the process of being resolved (1). Another data set which places important constraints on the mass distribution within the planet is the set of moments of the gravitational field. For Uranus the quadrupole moment (J_2) is known with good precision, and the 16 pole moment (J_4) is known to within 30% (2). For Neptune J_2 is known to about 10%, whole J_4 has not yet been determined (3).

We have constructed a detailed set of theoretical models of these planets within the framework of two- and three-shell models (4), (5). The two-shell models consist of a core of "rock" (MgO, SiO, Fe, and Ni in solar proportions) surrounded by an evelope of "ices" (H_2O, CH_4, and NH_3 in solar proportions), H_2 and He. The ratio of ice and rock to H_2 and He is allowed to vary. The three-shell models have, in addition, a shell of ice between the rock core and the envelope. In order to match the density of Uranus, as well as the gravitational quadrupole (J_2) and 16-pole (J_4) moments with a rotation period of 16 hours (1), a three-shell model is required. The mass ratio of ice to rock (I/R) should be about 3 (1), (2); very close to the ratio expected in solar composition (6). As can be seen from figures 1 and 2, two-shell models produce too high a value of J_4 for a 16 hour period. For Neptune, an 18 hour rotation period (1) implies a mass ratio of ice to rock of about 3. Here, however, the ices are spread through the envelope, and a two-shell model provides a good fit to the observations (fig. 3). A three-shell model is also possible but the ice shell must be small, and most of the ices must reside in the envelope (fig. 4). Again the ice to rock ratio is about 3. For both Uranus and Neptune the ice to rock ratio will be well above 1. Such values are difficult to reconcile with a scenario in which N and C are accreted primarily in the form of N_2 and CO. In such a case $I/R \sim 0.5$ would be expected. $I/R \sim 3$ is consistent with most versions of both giant protoplanet theories and those equilibrium

accretion theories where N and C are accreted as NH_3 and CH_4.

It thus appears that, while Uranus and Neptune may have similar bulk compositions, the ices within the two planets are differently distributed. The nature of this difference and the question of the source of the large differences between the measured heat flows of the two planets must be related and be important to their evolutionary history. These questions are being actively investigated (7).

REFERENCES

1. Belton, M.J.S. and R. Terrile (1984). Rotational properties of Uranus and Neptune. In Uranus and Neptune (J.T. Bergstrahl, ed.). Workshop Proceeding, in press.

2. Elliot, J.L. and P.D. Nicholson (1984). The rings of Uranus. In Planetary Rings (R. Greenberg and A. Brahic, eds). U. of Arizona Press, in press.

3. Harris, A.W. (1983). Physical characteristics of Neptune and Triton inferred from the orbital motion of Triton. Abstract of talk given at I.A.U. Colloquium No. 77, Ithaca, NY, July 5-9.

4. Podolak, M. and R.T. Reynolds (1981). On the structure and composition of Uranus and Neptune. Icarus, 46, 40-50.

5. Podolak, M. and R.T. Reynolds (1984). Consistency tests of cosmogonic theories from models of Uranus and Neptune. Icarus, 57, 102-111.

6. Cameron, A.G.W. (1981). Elementary and nuclidic abundances in the solar system. In Essays in Nuclear Astrophysics (C.A. Barnes and D.N. Schramm, eds.) pp 23-43. Cambridge Press.

7. Podolak M. and R.T. Reynolds (1984). What have we learned from modeling giant planet interiors? In Protostars and Planets, II (D. Black ed.), U. of Arizona Press, in press.

*Permanent address: Dept. of Geophysics and Planetary Physics
Tel Aviv University
Ramat Aviv, Israel

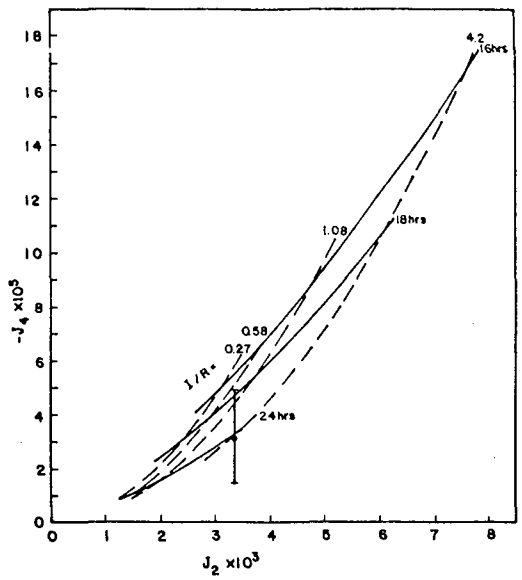

FIG. 1. Variation of J_2 and J_4 for Uranus two-shell models with fixed I/R (dashed curves) and fixed rotation period (solid curves).

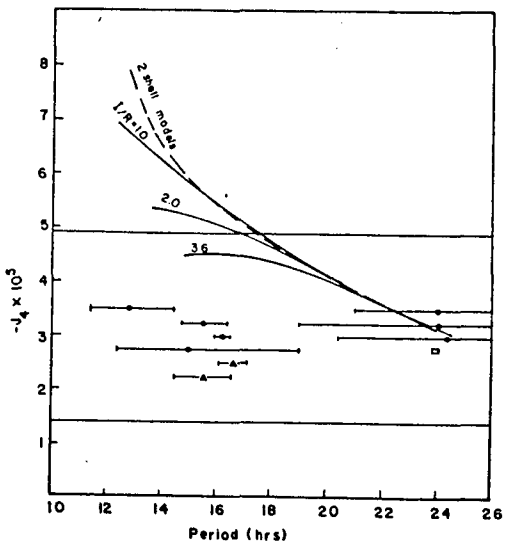

FIG. 2. Variation of J_4 for three-shell Uranus models with a rotation period chosen to give a fit to J_2. The solid curves are for three-shell models with total I/R of 1.0, 2.0, and 3.6. The dashed curve is for two-shell models. The points with error bars show the observations (circles for spectroscopy, triangles for J_2 oblateness, square for photometry). The solid horizontal lines show the limits on J_4.

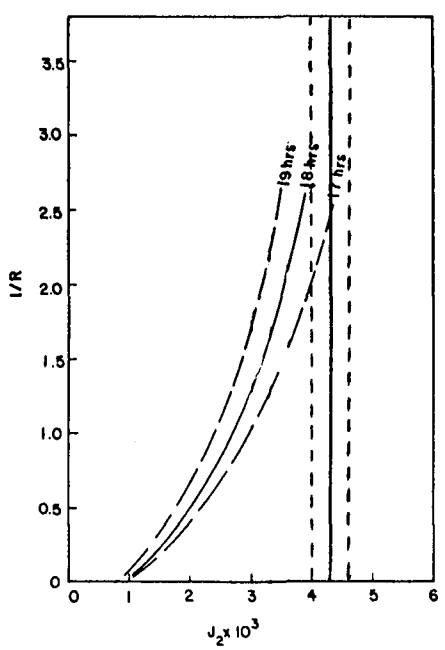

FIG. 3. Variation of J_2 with I/R for two-shell Neptune models. The vertical solid line shows the observed value for J_2, the dashed lines show the uncertainty. The solid curve shows the variation for a period of 18 hr, the dashed curves show the variation for 17- and 19-hr periods.

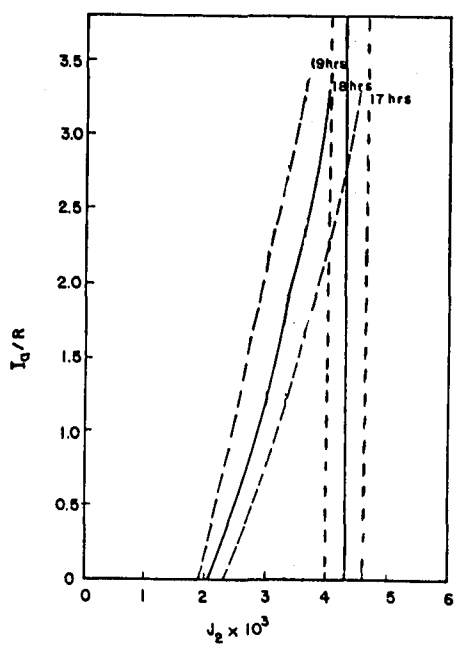

FIG. 4. Variation of J_2 with I_a/R for three-shell models of Neptune. I_a is the amount of ice in the atmosphere, otherwise the definitions are those of Fig. 3.

STUDIES OF ICY BODIES: URANIAN SATELLITES AND COMETARY NUCLEI

S.W. Squyres and R.T. Reynolds, NASA Ames Research Center,
Moffett Field, CA 94035

This report summarizes some recent studies in two areas of a continuing program of research on the evolution and structure of icy bodies of the solar system.

The Tidal Evolution of the Uranian Satellites

Observational measurements of the masses (1) and radii (2) of the Uranian Satellites only recently have become sufficiently reliable to permit investigation into the evolution and structure of these bodies. The orbits of the Uranian Satellites are quite regular and their eccentricities are small. The eccentricities are non-zero, however (1), and should be subject to tidal damping, provided that they are not maintained by a resonant forcing relation. The three inner-most Uranian Satellites are found to be almost, but not quite, in a three body resonance of the Laplacian type which is typified by Io, Europa and Ganymede. Such an inexact relation cannot maintain an eccentric orbit. Calculated decay times for the outer two satellites, Titania and Oberon, are of the order of the age of the solar system and their current eccentricities offer no problem. The inner satellites present a different picture; calculated decay times are of the order of 10^7-10^8 years (3,4). While Miranda is so small that it's physical parameters are not well determined, the calculated eccentricity damping times for Umbriel and especially Ariel are uncomfortably short. A detailed search for possible present day or even relatively recent, resonances which might have produced the observed eccentricities has not produced any satisfactory candidates (4).

This leaves us with several possible explanations: (a) The reported eccentricities are incorrect, and are in fact near-zero; (b) The reported mean motions are incorrect, and an exact commensurability exists; (c) Our assumed physical properties are grossly in error (e.g. dissipation function Q is in reality very large), or (d) The system is evolving very rapidly, perhaps from a previous state of higher eccentricity. Cases (a) and (b) are unlikely when one considers the quality of existing data. Case (c) would imply unexpected physical properties, and would be more consistent with non-icy compsitions. Case (d) might have resulted from passage through a chaotic zone surrounding the 5:3 resonance involving Ariel and Umbriel 2×10^8 years ago. Cases (b) and (d) would imply some tidal heating of the satellites, praticularly Ariel. Using the homogeneous tidal heating rate and ice-like physical properties, the tidal heat production for Ariel would be comparable to that produced by radioactive decay. Much higher rates can be generated from a body having a molten shell. The calculated homogeneous heating rates for Ariel are several times higher than similar rates for Enceladus, which has been suggested as a possible example of such enhanced tidal heating.

Although Ariel has a higher albedo than the three outer satellites, which can be indicative of a higher degree of geological activity, there is not nearly enough evidence to show that Ariel is currently or recently active. There is, however, an interesting discrepancy between tidal damping theory using expected physical properties and the observed eccentricities. As with the previous Voyager fly-bys of Jupiter and Saturn, the Uranus fly-by may also reveal some unexpected phenomena.

Temperatures Within Cometary Nuclei

While considerable theoretical attention has been given to the problem of the surface temperatures of icy comet nuclei; the near sub-surface temperature distribution has not been as well studied. Even if only pure ice models are considered, the effects of heat transfer within the body are highly dependent upon the physical structure of the icy material. Since most of the material properties, albedos and thermal emissivities of comet nuclei are either unknown or poorly constrained, it is not possible to calculate a unique temperature distribution for a cometary nucleus. It is possible, however, to develop a general approach which can explore the range of models inherent in the probable limits of values of key parameters.

Such a study is given further impetus by the possibility of in-situ measurement of the near surface properties of a cometary nucleus. The proposed comet rendzevous mission (5) could implant an instrumented penetrator directly into the nucleus, permitting measurement of composition, temperature and penetration resistance to a depth of 1 m.

A one-dimensional heat flow equation has been used to represent the near surface regions. It is solved for temperature dependent material properties and specified upper and lower boundary conditions. The thermal conductivity function provides for a two-phase medium consisting of an ice fraction and a pore fraction. The ice fraction conductivity is modified to include the effects of lowered fractional contact areas. The pore conductivity includes both radiative and vapor diffusion (Knudsen flow) components. The upper boundary condition describes the radiative balance of the surface with solar radiation (including radiative transfer effects in the coma), conduction from the interior and ice sublimation. The lower boundary condition is simply one of zero heat flux around an entire orbit.

The equation has been solved numerically for a grid of some 30 evenly spaced points extending from the surface to five thermal skin depths. Two sets of investigations were performed. First, the effects of variations in physical properties of the sub-surface materials were considered for three model materials; (a) solid ice, with a porosity of zero and a Hertz factor (the fractional area of contact for spherical particles) of unity, (b) porous ice, with variable pore size and a Hertz factor of unity

(equivalent to ice with bubbles) and (c) "frost", with variable pore size, variable porosity and variable Hertz factor. In the second set of calculations we considered the effects of variations in nucleus surface albedo and thermal emissivity. Both were varied over the entire range of 0-1. An extensive set of calculations have been performed for the case of the comet Kopf and the results are being prepared for publication (6).

The parameter that can actually be measured by temperature sensors on the comet penetrator is the difference in temperature between the surface and a depth of 1 m at aphelion. The steepness of the thermal gradient depends upon the thermal diffusivity. For solid ice the temperature difference is quite small, $\sim$1 K. For frosts of varying porosities and Hertz factors this difference can approach 30K. Temperature measurements can provide direct information on the thermal diffusivity and emissivity of a comet nucleus. In combination with thermal models, and measurements of composition and penetration resistance, they will permit a much more complete picture of the physical and chemical nature of the nucleus than is possible through remote measurements alone.

REFERENCES

1. Veillet, C. (1983). De l'observation et du mouvement des satellites d'Uranus. PhD thesis, University of Paris.

2. Brown, R.H., D.P. Cruikshank and D. Morrison (1982). Diameters and albedos of satellites of Uranus. Nature, 300, 83-92.

3. Squyres, S.W. and R.T. Reynolds (1983). Tidal evolution and the satellites of Uranus. EOS, 64, 746.

4. Squyres, S.W., R.T. Reynolds, and J.J. Lissauer (1984). On the tidal evolution of the Uranian Satellites. Icarus, submitted.

5. Morrison, D. and N.W. Hinners (1983). A program for planetary exploration. Science, 220, 561-567.

6. Squyres, S.W., C.P. McKay and R.T. Reynolds (1984) Temperatures within comet nuclei. Manuscript in preparation.

ON THE ORIGIN OF TRITON AND PLUTO

W.B. McKinnon, Dept. Earth and Planetary Sciences and McDonnell Center for the Space Sciences, Washington Univ., Saint Louis, MO 63130.

Lyttleton long ago hypothesized that Triton and Pluto originated as adjacent prograde satellites of Neptune (1). With the presently accepted masses of Triton and Pluto-Charon (2-3), however, the momentum and energy exchange required to set Triton on a retrograde trajectory is impossible. The mass of Triton has probably been seriously overestimated (4-5), but not sufficiently to relax this restriction. It is implausible that the present angular momentum state of Pluto-Charon has been significantly influenced by Neptune (6). It could not acquire such angular momentum during an ejection event unless a physical collision was involved, which is probabilistically quite unlikely. The simplest hypothesis is that Triton and Pluto are independent representatives of large outer solar system planetesimals. Triton is simply captured. Consequences of capture are potentially spectacular and include runaway melting of interior ices and release to the surface of clathrated CH_4, CO, and N_2 (7). Condensed remnants of this proto-atmosphere plausibly account for features in Triton's unique spectrum (8-11).

The dynamics of Triton's orbital evolution are considerably simplified by the fact that its specific dissipation function, Q, at tidal frequencies, is much less than that of Neptune ($Q_T << Q_N$). Accordingly, the monthly radial tide raised on Triton by Neptune dominates Triton's orbital evolution, except for orbits of very small eccentricity. The total angular momentum change over the age of the solar system is a few percent for $Q_N \sim 10^5$.

Lyttleton's hypothesis is evaluated in the following manner: Triton and Pluto originate as regular direct satellites of Neptune, in circular orbits; orbital evolution brings them into a range of significant gravitational interaction, say, within the sphere of influence of the more massive satellite, and Triton is sent into a retrograde orbit with the same angular momentum as it has today. Conservation of angular momentum requires that the angular momentum of Pluto increase. Pluto's post-encounter orbital energy is minimized for velocities perpendicular to its radius vector. The semimajor axis of the new orbit, a_P, with respect to Neptune is illustrated in Figure 1 for a range of plausible mass ratios m_T/m_P(the prsently accepted value is $\sim$10; lower values are possible but should be >1). All the a_P shown correspond to hyperbolic trajectories. orbits with $a_P < 1.62\ R_N$ (Neptune radii), however, are so energetic that once Pluto leaves Neptune's sphere of influence, it is not bound to the solar system. Only for $a_P > 54.9\ R_N$ is Pluto definitely bound. Thus, for plausible mass ratios momentum conservation alone determines that a Lyttleton-type interaction is not possible, unless the interaction takes place well outside the domain of regular satellites. This domain, $a \leq 60\ R_N$, is defined in analogy with the regular satellite systems of Jupiter, Saturn, and Uranus.

These arguments can be generalized to allow multiple encounters if conservation of energy is accounted for. The encounters are assumed to be conservative, with the only restriction on Triton's final energy being

that it exceed its present value. The final orbits of Triton and Pluto must be ∿intersecting ones, however, so for plausible mass ratios, a combination of orbital interactions to reverse Triton's motion cannot actually be found (12).

The present angular momentum state of the Pluto-Charon system (i.e., that contained in their mutual orbits and spins) is not consistent with a Neptune satellite origin either. If Pluto-Charon ever orbited Neptune with a semimajor axis a, tides raised on Pluto by Neptune would extract angular momentum from the system and cause the Pluto-Charon system to contract and eventually coalesce. The coalesced object would then be rapidly spun down to synchronous rotation (6) unless Pluto-Charon orbited Neptune at a great distance ($\tau \lesssim 100$ m.y. for $a < 45\ R_N$; $\tau \propto a^6$). These same arguments apply if the original state of Pluto-Charon was a coalesced, rapidly rotating proto-Pluto.

Only a physical collision could impart the requisite angular momentum to Pluto-Charon prior to its ejection from the Neptune system. A close pass to Pluto by a more massive object could exert an extremely large torque on Pluto but the timescale for the interaction would be severely limited, and the angular momentum imparted by a grazing pass of even an earth mass would be only a few percent of the present total. A larger transfer of angular momentum may be possible for the slowest encounters with a massive grazer, if tidally-induced fission occurs, but the restriction of slow encounters again requires Pluto to be in a distant orbit about Neptune initially. With regard to ejection dynamics, the reduction of the interaction cross- section from a gravitational one to approximately one of collision makes "rogue" planet hypotheses such as that of Harrington and Van Flandern (13) probabilistically untenable. Farinella et al. call upon a captured Triton to eject Pluto as its capture orbit decays (14), but this hypothesis still requires a physical collision with Pluto, following which, gravitationally bound Plutonian debris accretes into a binary and eventually reaches stable, resonant solar orbit. This is an unlikely series of events.

The preceding arguments effectively decouple the origin of Pluto from that of any Neptune satellite. Hence, for Triton to begin as a direct satellite and end up retrograde would require interaction with an unknown and ad hoc object. I propose a simple reversal of Lyttleton's hypothesis: instead of beginning as satellites of Neptune, Triton and Pluto originate as satellites of the sun. The existence of large, outer solar system planetesimals is consistent with the dynamics of planetary accretion and may even be necessary to explain planetary eccentricities, inclinations, and obliquities. Pluto-Charon's "binary" status is plausibly related to hypotheses regarding binary asteroid formation, and Triton's capture could be effected by the combination of a retrograde, temporary orbit about Neptune and a dissipative mechanism such as gas drag.

If Triton was captured, then it should have experienced a spectacular thermal event. As $Q_N >> Q_T$, nearly all of the orbital energy dissipated during post-capture orbital evolution is deposited in the body of Triton. Gas drag, while potentially important for capture, did not result in a major change in orbital elements, as the evolution of Triton's inclination has been moderate (15). Calculations (7) show that collapse of an elliptical post-capture orbit, extending to the edge of Neptune's sphere of

influence ($\sim$3500 R_N), to one where the semimajor axis is within a few percent of the present value requires $\sim$4 Q_T m.y., for constant Q_T. Most of the energy ($\sim$80%), however, is dissipated in an $\sim$1.5 Q_T m.y. period near the end. The equivalent surface heat flow, for reasonable Q_T, is far too great for solid-state convection in ice to transport, so it is extremely probable that the icy component of Triton completely melted during the latter phase of capture. Q_T itself would plummet as melting began, accelerating differentiation.

Catastrophic melting of Triton's ices should have released its inventory of clathrated gases to the surface, which for accretion outside a circumplanetary nebula would be CH_4,CO, and N_2 (16,17). A condensed fraction of this primordial atmosphere may be responsible for Triton's unique surface composition - present spectral identifications include liquid nitrogen (11) and methane ice.(9-11)

This research was supported by NASA Grant NAGW-432.

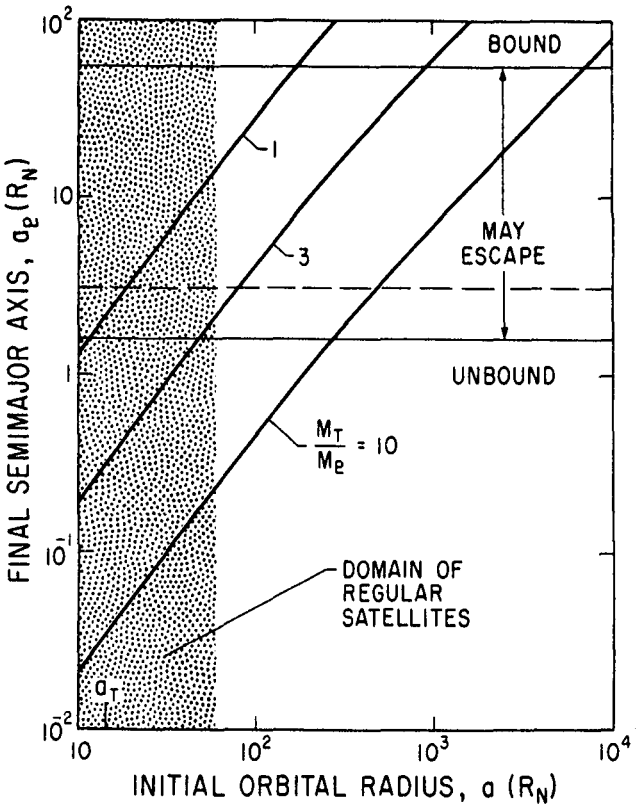

Fig. 1 Hyperbolic semimajor axis of Pluto, with respect to Neptune and after an interaction with Triton, as a function of initial orbital radius for three different mass ratios. These results, derived from angular momentum conservation alone, represent maximum values. Asymptotic velocities from Neptune of 2.25 and 13.1 km s^{-1} (a_P = 54.9 and 1.62 R_N) correspond to limits on bound or unbound solar trajectories, if Neptune's orbital velocity is taken into account. The dashed horizontal line is the minimum a_P for ejection into a direct, bound solar orbit. For plausible mass ratios, any interaction to reverse Triton's orbital motion and retain Pluto in the Solar System must take place well outside the domain of regular satellites (see text).

REFERENCES

(1) Lyttleton, R.A. Mon. Not. R. astr. Soc. 97, 108-115 (1936).
(2) Alden, H.L. Astr. J. 50, 110-111 (1943).
(3) Harrington, R.S. and Christy, J.W. Astr. J. 86, 442-443 (1981).
(4) Cruikshank, D.P., Stockton, A., Dyck, H.M., Becklin, E.E. and Macy, W. Jr. Icarus 40, 104-114 (1979).
(5) McKinnon, W.B. Bull. Am. astr. Soc. 14, 765 (1982).
(6) Lin, D.N.C. Mon. Not. R. astr. Soc. 197, 1081-1085 (1981).
(7) McKinnon, W.B. Bull. am. astr. Soc. 15, 857 (1983).
(8) Cruikshank, D.P. and Silvaggio, P.M. Astrophys. J. 223, 1016-1020 (1979).
(9) Rieke, G.H., Lebofsky, L.A., Lebofsky, M.J. and Montgomery, E.F. Nature 294, 59-60 (1981).
(10) Apt, J., Carleton, N.P. and Mackay, C.D. Astrophys. J. 270, 342-350 (1983).
(11) Cruikshank, D.P., Brown, R.H. and Clark, R.N. Abstr. Natural Satellites, IAU Coll. 77, 40 (1983).
(12) McKinnon, W.B. Nature 311, 355-358 (1984).
(13) Harrington, R.S. and Van Flandern, T.C. Icarus 39, 131-136 (1979).
(14) Farinella, P., Milani, A., Nobili, A.M. and Valsecchi, G.B. Moon Planets 20, 415-421 (1979); Icarus 44, 810-812 (1980).
(15) Pollack, J.B., Burns, J.A. and Tauber, M.E. Icarus 37, 587-611 (1979).
(16) Lewis, J.S. and Prinn, R.G. Astrophys. J. 238, 357-364 (1980).
(17) Prinn, R.G. and Fegley, B. Astrophys. J. 249, 308-317 (1981).

CHAPTER 2

ASTEROIDS AND COMETS

Page intentionally left blank

STUDY AND ESTIMATION OF PLANET-CROSSING ASTEROID POPULATIONS: DISCOVERIES AND ANALYSIS

Eleanor F. Helin and R. Scott Dunbar
Jet Propulsion Laboratory

The principal objective of this work is to evaluate the populations of the various classes of planet-crossing asteroids, based on the results of the systematic Planet-Crossing Asteroid Survey (PCAS) search program. Knowledge of the populations is crucial to the estimation of lunar and terrestrial planet cratering rates from asteroidal and cometary sources needed to establish the chronology of other surface features on those bodies. A secondary objective is to identify the sources of these crater-forming objects and their relative importance in producing the observed planet-crossing asteroid population. In this abstract we will briefly describe some key PCAS asteroid discoveries relevant to the population problem and the progress in using the available search data to update and refine earlier estimates of the planet-crossing asteroid population.

PCAS Discoveries Relevant to the Population Study

Three discoveries from the PCAS program in 1984 are particularly significant to the population analysis problem. Two of these represent previously unknown classes of asteroids with Mars-crossing orbits. The first of these new Mars-crossers, 1984 AB, occupies an orbit remarkably similar to that of Mars (Ref. 1). This object has a semimajor axis of 1.57 AU (only 3% larger than Mars') and a low orbital eccentricity for a Mars-crosser of e = .08. At first thought to be a possible Mars Trojan (at discovery it was very close to the Mars-Sun L5 equilateral Lagrange point), 1984 AB is nonetheless an unusual object. Its orbit is such that it never enters the main asteroid belt, indicating that it may have reached its present state through close

The second unusual Mars-crosser is 1984 BC, which has a decidedly cometary orbit but no evidence of cometary activity (Ref. 2). The orbit of 1984 BC crosses the orbits of both Mars and Jupiter, and a relatively close encounter with Jupiter is expected in 1986. Physical observations at visible and infrared wavelengths reveal an object with an albedo of 0.03, consistent with a carbonaceous composition expected for cometary material. The orbital and physical evidence points strongly to an interpretation of 1984 BC as an extinct comet. For the purposes of this work, this object highlights another problem which must be considered in any population and cratering rate analysis: What is the contribution of extinct cometary nuclei to the bombardment of the terrestrial planets?

The third and most recent discovery is that of 1984 QA, only the fourth Aten-type asteroid discovered (Ref. 3). This object has an orbital semimajor axis of 0.989 AU, the nearest value to Earth's of any known solar system object. It is also the first discovery of an Aten object in six years, since the discovery of 2100 Ra-Shalom. Estimates by Helin and Shoemaker (Ref. 4) in 1979 placed the Aten population at about 100 $\pm$ 50 to absolute magnitude 18, based on three discoveries from 1976 to 1978 made with the Palomar 18-inch Schmidt. The absence of Aten discoveries in the last six years, despite greatly expanded sky coverage with both the 18-inch and 48-inch Schmidts, suggests that the Aten asteroid population has been seriously overestimated.

Another 14 new asteroids, with orbits in the Hungaria and Phocaea regions of the inner main belt, were discovered in 1984. The Hungaria and Phocaea regions are considered to be likely sources of some planet-crossing asteroids. Members of these groups are in some cases Mars-crossing, while retaining the basic orbital characteristics identifiying them with those regions.

Population Analysis

We have initiated a review and update of the planet-crossing asteroid population which will include the results of the last 6 years of PCAS search and discovery statistics. The tasks now underway include the organization of our search data base for 1979-84 (independent search fields, limiting magnitudes, etc.) for use in the subsequent analyses, and an analysis of the orbital statistics of known planet-crossers. The objectives of the latter task include a detailed study of the discovery circumstances of known objects, a study of the distributions of the orbits to detect all possible search biases, and a preliminary investigation of alternative orbital classification schemes based on likely orbital phase space source regions and dynamical transport mechanisms. We have also begun a critical review of the theory of systematic search used to derive estimates of the planet-crossing asteroids from the PCAS observations.

The possibility of constructing a more "physical" classification scheme is being investigated in an attempt to form a link between planet-crossers and their origins. A simple plot of orbital inclination versus semimajor axis for the near-Earth asteroids, for instance, shows definite clustering in regions corresponding to the Flora, Phocaea, and Hungaria regions for about 50% of the known objects, and no clear associations for the rest. If we accept the hypothesis that secular resonances near these regions are responsible for large changes in eccentricity which cause these objects to become planet-crossing, we would expect that the part of the population which has not yet suffered a major planetary encounter would retain the orbital characteristics (with the exception of orbital eccentricity) of the source regions. Those which have experienced one or more encounters would be "randomized", with significant changes in all of their orbit elements and a loss of information as to origin. While these ideas are very preliminary, a complete study of the populations of the planet-crossing asteroids should consider the relative importance of their various possible sources if we are to gain insight into the long-term rate of terrestrial planet bombardment in the past.

We have begun a review and revision of the theory of systematic search used to estimate the populations of planet-crossing asteroids. This theory depends in part on the distribution of orbits, using the observed population as a representative sample, so we expect some refinement of the population estimates due to the doubling of the known planet-crosser sample since 1978. It also depends to some extent on the distribution of physical characteristics like albedos and especially phase functions, for which a great deal of new data has become available since the previous estimates were derived. There are also some mathematical problems with the earlier formulation of the theory itself, some of which may have a significant effect on the population estimates, and therefore on terrestrial planet cratering rates based on the estimated source populations. This work is still in its early stages, but we already expect that several important modifications to the theory will be required.

Other work

We have searched for asteroids in the Earth-Sun equilateral Lagrange point regions with the Palomar 48-inch Schmidt since 1980. On the basis of this search, and its null results to date, we have derived an observational upper limit on the population of Earth Trojans (Ref. 5). This upper limit is defined in terms of the brightest member of the population which should have been detectable by the search, given that only part of the region which can be occupied by Trojans could be searched to a limiting apparent magnitude of about 21 (photographic). The absolute magnitude of the "brightest" Trojan derived in this analysis is $V(1,0) > 18 \pm .5$, or a limiting diameter of about 1 km. Previous searches with the same telescope by Gehrels in 1973 and Shoemaker and Helin in 1978 have been reviewed and similarly analyzed (Ref. 6). Those searches, however, did not constrain the population as severely as the 1980-83 search. We conclude that the population of Earth Trojans, if it exists, consists of a small number of objects which are smaller in size than typical Apollo/Amor objects discovered in recent years.

REFERENCES

1 Helin, E. F. and R. S. Dunbar (1984) "1984 AB — A Unique Mars-Crossing Asteroid", Icarus (in press).

2 Helin, E. F., R. S. Dunbar, J. Gradie, L. A. Lebofsky, and D. J. Tholen (1984) "Asteroid 1984 BC — An Extinct Comet?", 1984 AAS/DPS meeting, Kona.

3 Dunbar, R. S., M. A. Barucci, E. F. Helin, and S. R. Swanson (1984) Discovery, observations, and orbit of 1984 QA. IAU Circular Nos. 3980, 3898, and Minor Planet Circular No. 9073.

4 Helin, E. F. and E. M. Shoemaker (1979) "The Palomar Planet-Crossing Asteroid Survey, 1973-1978", Icarus, v. 40, No. 3, pp. 321-328.

5 Dunbar, R. S. and E. F. Helin (1983) "Estimation of an Upper Limit on the Earth Trojan Asteroid Population from Schmidt Survey Plates", 1983 AAS/DPS meeting, Ithaca, Bull. Amer. Astron. Soc., vol. 15, no. 3, p. 830.

6 Dunbar, R. S. (1984) "Implications for the Population of Earth Trojan Asteroids from Schmidt Surveys", submitted to Icarus, June 1984.

Theoretical Results

An analytical study was made of the feasibility of using ranging data to a spacecraft lander on a synchronously rotating satellite to determine the satellite's orbit, the planet's orbit, the lander coordinates, and the principal term of forced physical librations. Synchronous rotation introduces difficulties not encountered with a freely rotating satellite. Useful results can be obtained, but observation time spans of the satellite's node and perifocus precession periods are necessary to separate the unknowns at the highest accuracy. Significant separation can also take place on the time scale of the earth-planet synchronous period. One of the lander coordinates becomes mixed with the satellite's semimajor axis and hence the masses of the planet and satellite. A second coordinate is badly mixed with the satellite's orbital longitude. The other parameters would separate cleanly, most interesting it should be possible to determine the tidal secular acceleration of the satellite and the principal libration term, the latter giving a fractional moment of inertia difference (B-A)/C.

The paper "Determining Asteroid Masses from Perturbations on Mars" was published in Icarus, vol. 57, pp. 1-13, 1984.

Data Analysis

Efforts are presently concentrating on proper elements and families. There are two unpublished data sets: asteroids numbered 1797-2065 (plus some additional objects, e.g. planet crossers), and the new and revised orbits in the Palomar-Leiden Survey II (PLSII) (Van Houten, Herget, and Marsden 1984). The proper elements and family assignments are ready for the former data set, but the final tables have not been generated. Preliminary results are available for the PLS material, but the final proper elements are still being generated. Ten new families have been identified with the two data sets. The most interesting may be associated with Vesta (a previous family is also associated with Vesta), the numbered members are 1933, 1959, 2024, 2029, and 2045. Proper elements and family identifications for objects numbered through 2065 will be provided as a file for the IRAS asteroid project and TRIAD.

Astrometry

The astrometry program is directed toward measuring and reducing positions on comets and the minor planets with less common orbits. Nearly all of the plate material during the

past year has come from a highly successful observing program on the Palomar 1.2 m Schmidt camera (the observing is a separate project, the measurement and reduction is done under this contract). This year for the first time we are also reducing CCD material from the Palomar 1.5 m telescope. Plate transfers are often needed due to a very narrow field of view. The comet plates are usually taken when the object is faint to extend the observed arc. The asteroids are the less common types, either follow up on recently discovered objects or recoveries of unnumbered bodies. During the past year positions have been published on 16 comets and 70 minor planets. The latter includes 14 planet crossers, 18 objects of high inclination, 3 distant (Cybele type) minor planets, 2 Hildas, 1 Hertha family member, and 32 more ordinary minor planets. The two IRAS earth crossers and several IRAS comets were included. The positions are reported on Minor Planet Circulars 8089, 8120, 8187, 8192, 8218, 8250, 8325, 8326, 8356, 8439, 8440, 8449, 8485, 8510, 8593, 8595-8597, 8622, 8698-8700, 8754, 8830, 8832, 8875, and 8876.

THE OLIVINE ASTEROIDS: DISCOVERY, MINERALOGY, AND RELATIONSHIP TO PALLASITES. J. F. Bell, B. R. Hawke, and M. J. Gaffey, Planetary Geosciences Div., Hawaii Inst. of Geophysics, Univ. of Hawaii, Honolulu HI 96822.

INTRODUCTION: Telescopic observations have recently revealed the existence of a new class of asteroids whose surfaces show the spectral signature of abundant olivine. The mineralogy of a well-observed example (446 Aeternitas) is discussed and the implications for the origins of olivine-rich meteorites and the thermal evolution of asteroids outlined.

DISCOVERY: Veeder et al. (1,2) demonstrated by means of broadband (JHK filter) spectrophotometry that the asteroids classed as type "R" in the taxonomy of Bowell et al (3) actually comprised two classes with widely different infrared spectra, and introduced the designation type "A" for the smaller group. R. N. Clark pointed out during discussion of ref. 1 at the 1982 DPS-AAS meeting that the A-type objects lie in an area of the JHK plot which is occupied only by olivine-rich mixtures (4). Cruikshank and Hartmann (5,6) recently obtained spectrophotometry of 246 Asporina and 289 Nenetta which revealed the distinctive deep multiple absorption bands of olivine, confirming this interpretation. At least 5 and possibly 13 (7) A-type asteroids are identifiable at present.

NEW OBSERVATIONS: We obtained high-resolution IR spectra of the A-type object 446 Aeternitas on 7 November 1983 with the NASA Infrared Telescope Facility on Mauna Kea, Hawaii. An average spectrum is shown in Fig. 1 as a ratio to the star 16 Cygni B which is spectrally similar to the sun. (Points plotted as crosses are existing photovisual data.) The individual spectra were taken over a period of about three hours during which the absolute brightness of the asteroid increased ≈20% indicating significant rotation; however no detectable variations in mineralogy across the the surface of Aeternitas are apparent in our preliminary analysis.

SURFACE MINERALOGY: Our spectrum of Aeternitas clearly indicates that this asteroid's optically visible surface is predominantly olivine. Although a significant amount of plagioclase could be present without being evident in this spectral curve, only pyroxene and metal are directly indicated as accessory minerals. The weak possible 2-micron absorption band may indicate a minor component of pyroxene. Application of a newly developed calibration of the spectral properties of olivine-pyroxene mixtures (8) indicates an abundance of about 5% pyroxene. Uncertainty in the location of the continuum makes it impossible to rule out abundances between 0 and 10% of orthopyroxene or clinopyroxene. If small, distinct pyroxene-rich areas exist on Aeternitas the upper limit may be somewhat higher. The spectral curve is somewhat redder than would be expected for a pure mafic assemblage, indicating either A.) a fayalitic olivine, or B.) a metallic iron phase with exposed non-oxidised surfaces. The latter is more plausible. The surface of this asteroid is nearly monomineralic olivine with possible accessory pyroxene and metal. The similarity of broadband colors (2) indicates that similar mineral assemblages dominate the surfaces of the other A-type asteroids. Only 289 Nenetta appears slightly unusual, as both J-K color (1) and spectrophotometry (6) indicate a significantly deeper olivine band than in 246 and 446.

ORIGIN OF OLIVINE-RICH ASTEROIDS: The mineralogy inferred above indicates that the surfaces exposed to space today on the A objects were once in the interior, and that this region was subject to extreme magmatic differentiation. The apparent presence of metallic nickel-iron suggests that the current surface was originally the mantle-core transition region. These objects can be either differentiated planetesimals which have been eroded down symmetrically to a deep layer rich in cumulate olivine, or small fragments of a >50 km thick cumulate accumulation on a much larger parent body. The former interpretation appears most probable, and implies that some very small planetesimals (D < 100 km) were once almost completely melted. A search for mineralogical variations on the surfaces of these objects may allow a choice to be made between these alternate models. In either case, the A asteroids must derive from thermally evolved and magmatically differentiated parent planetesimals.

RELATIONSHIP OF A-TYPE ASTEROIDS TO METEORITES: Only two meteorite classes could plausibly be derived from the currently exposed surfaces of the A asteroids: pallasites (olivine crystals in a metal matrix) and olivine achondrites (cumulate olivine + accessory pyroxene and plagioclase). The presence of a metal phase supports an analogy with pallasites. No reflectance spectra of pallasites exist due to sample preparation difficulties. A lab spectrum does exist for the olivine achondrite Chassigny. However it has an anomalously young crystallization age and is therefore considered a member of the "SNC meteorites" for which an origin on Mars has been proposed (9). The discovery in Antarctica of a meteorite from the Moon has seemingly overcome the physical arguments against ejection of meteorites from Mars and greatly enhanced the credibility of a martian origin for the SNC meteorites. Thus Chassigny is of doubtful relevance to the A asteroids. The other olivine achondrite (Brachina) may be derived from a more pyroxene-rich and metal-poor layer of an A-type parent body.

We have conducted laboratory studies to investigate the hypothesis that A-type asteroids are the parent bodies of pallasites. Olivine grains of three sizes (fayalite content similar to main-group pallasites) were scattered on a roughened iron background to simulate the multiple scattering expected in a regolith derived from pallasite bedrock. IR spectra were obtained for a variety of iron/olivine ratios within each olivine particle size. No simulation using 1mm olivine grains can reproduce the fine structure seen in the asteroid spectra; evidently the large olivine crystals found in pallasites do not survive regolith gardening. Simulations with 90-μm olivine grains provide excellent matches to the asteroids in band depth and shape, though continuum slopes indicate that the asteroidal metal phase has a more curved spectrum that does our artificial iron alloy. Apparent olivine content increases in the sequence Asporina-Aeternitas-Nenetta, from ~30% to ~40% to ~70%. A third series of simulations employing a broad range of particle sizes <250μm also provides acceptable matches with slightly higher olivine contents. (In the case of Nenetta a 100% olivine regolith may be consistent with the somewhat noisy data available.) These results fully support the interpretation of A-type asteroids as having pallasite-like surface mineralogy.

IMPLICATIONS FOR DELIVERY OF METEORITES TO THE EARTH: The identification of the A-type objects as analogs of the olivine-rich meteorites is of high uniqueness due to the distinctive nature of the olivine spectral features, comparable in certainty to the identification of basaltic achondrites with Vesta. The existence of two reliable matches between two very different meteorite types and well-observed asteroids provides a clue as to the magnitude of possible bias factors in the relative abundance of meteorite types relative to the abundances of their parent bodies. There are about 40 observed basaltic achondrite falls known, but only one possible source body among the large, well observed asteroids. The dozen or so known A-type objects have produced at most 3 meteorite falls. Thus a bias factor of at least 150 exists between these two meteorite classes. Clearly the statistical distribution of meteorite types reaching the Earth has no relation to the abundances of mineralogically similar main belt asteroids.

REFERENCES: 1) Veeder et al., Bull. AAS 14, 719. 2) Veeder et al., Icarus 55, 177. Bowell et al., Icarus 35, 313. 4) Clark, Icarus 49, 244. 5) Cruikshank and Hartmann, Bull. AAS 15, 825. 6) Cruikshank and Hartmann, Science, 223, 281. 7) King et al., Bull AAS 15, 825. 8) Cloutis et al., Bull. AAS 15, 826. 9) Wood and Ashwal, PLPSC XIIB, 1359.

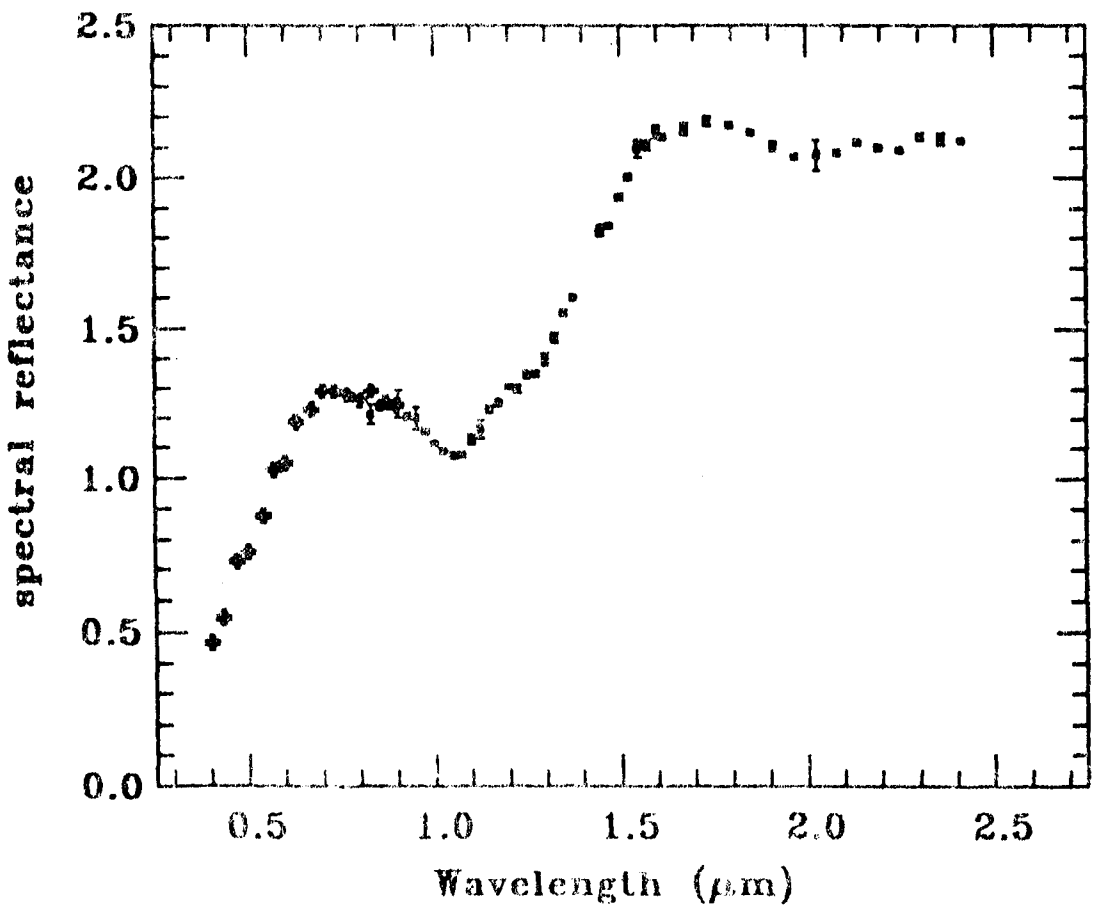

ASTEROID COLLISIONAL EVOLUTION STUDIES

Donald R. Davis, Clark R. Chapman, Stuart J. Weidenschilling, and Richard Greenberg, Planetary Science Institute, Tucson, AZ 85719

Understanding asteroid collisional evolution is important for characterizing the physical state of asteroids today and for learning about the processes that acted in this region of the solar system early in its history. We have previously studied asteroid collisional history using a numerical model to calculate the evolution of various hypothetical initial populations over the age of the solar system. Collisional outcomes were calculated by scaling laboratory impact experiments to asteroid-sized bodies, incorporating theoretical models for effects of gravitational binding. A crucial element of these studies was the gap between the energy required to shatter an asteroid and that required to disrupt it and disperse the fragments. The gap arose because of our assumption that the collisional energy density (called "impact strength") required to shatter a body is independent of size of the body, whereas the gravitational binding energy increases with size (1,2). We have recently described a new model for scaling the collisional energy required to shatter large asteroids, which predicts an increase in impact strength with size due to the strengthening effects of gravitational self-compression (3). This model predicts a fragmental size distribution for disruption of bodies hundreds of km in size which is in good agreement with that observed for Hirayama families.

We have now revised the collisional outcome algorithm in our numerical simulation of asteroid evolution to reflect pressure-strengthening, together with an improved treatment of asteroid collisions as a distribution of oblique impacts rather than as only head-on collisions. We have studied the evolution of hypothetical initial asteroid populations based on the revised collisional models to determine which populations lead to the observed asteroid belt. In addition to yielding a size distribution similar to that now observed, we also require that any viable scenario should produce (a) a Vesta-sized object which has not been collisionally shattered (in order to account for Vesta's global and presumably ancient crust) and (b) generate approximately the observed number of major Hirayama families.

The initial and evolved size distribution of a plausible asteroid population is compared with the observed asteroid size distribution in Fig. 1. The evolved population is in good agreement with the observed belt, including the presence of the well-known "bump" in the population at sizes 50-200 km. (Actually, the "bump" has different shapes for subsets of the main-belt population, based on the now partially obsolete bias-corrected statistics of Zellner (4), and further work is necessary to account for these and other variations of the size distribution within the belt.) In our studies, the bump arises as a natural consequence of the increasing collisional lifetime with asteroid size resulting from the increasing gravitational binding energy. Hence, at larger sizes a larger fraction of the initial population survives over the age of the solar system. The effect becomes important at sizes at which gravitational binding becomes important large compared with material strength. This interpretation would attribute the bump to being a natural consequence of collisional physics given sufficient collisional evolution, hence a steady-state feature rather than being the remnant memory

of a primordial asteroid distribution, as suggested by Kuiper et al. (5). On the other hand, if the belt is only minimally evolved, then the bump could be a primordial remnant.

The degree of asteroid collisional evolution in our current models has an upper bound due to the existence of Vesta, while the number of Hirayama families provides a lower limit on the degree of collisional evolution. These conditions imply that there has been only a modest degree of collisional evolution since the time Vesta differentiated. Large initial asteroid populations containing a planetary mass and distributed in either (a) power-laws of the type used by Safronov (1969), (b) bell-shaped distributions as proposed by Kuiper et al. (1958), or (c) runaway growth distributions like those found by Greenberg et al. (1978), result in all surviving large asteroids being thoroughly shattered in our present collisional models. Thus, we conclude there has been only a modest collisional evolution of the belt population since the time of Vesta's differentiation. The runaway growth population distribution containing 3 timmes the current belt mass best satisfies all constraints in our current collisional models. Subsequent collisions have produced the observed Hirayama families but left Vesta's crust largely intact, although just barely so. Gravitationally-bound rubble piles are formed at sizes $\lesssim$400 km, although the degree of shattering is considerably less than that predicted for massive initial belts. For example, bodies 50-200 km in size are hit by projectiles delivering a cumulative collisional energy ~10 times their impact strength over the age of the solar system. Therefore, most asteroids larger than 100 km would become gravitationally-bound rubble piles, with the degree of collisional shattering decreasing rapidly for bodies $\lesssim$400 km. There would be virtually no original bodies <25 km in size remaining. The current population of smaller asteroids would consist of fragments from larger collisions, partially reaccumulated cores, and eroded larger asteroids in varying proportions. Disruption of large asteroids to produce Themis-like families requires that the parent bodies have large effective impact strengths that we attribute to gravitational self-compression. Large asteroids which are shattered prior to being disrupted may have their impact strength restored due to compressive annealing acting over long times.

Our result that there was a small mass initial belt implies significant mass loss from this region of the solar system prior to the formation of Vesta's basaltic crust, which presumably formed early in solar system history. Studies of asteroid accretion times and reconstruction of the primordial solar nebula suggest that there must have been significantly more mass in this part of the solar system when asteroids were accreting; probably the total mass was ~1 $M_\oplus$. Quite possibly, the same mechanism that pumped up asteroid orbits to produce the ~5 km/s mean collision speed also produced the mass depletion.

References

(1) Chapman, C.R., Davis, D.R., and Greenberg, R., Reports of Planetary Geology Program, 1977-78, NASA TM-79729, 25-27.
(2) Davis, D.R., Chapman, C.R., Greenberg, R., Weidenschilling, S.J., and Harris, A.W. (1979), in Asteroids, 528-557.
(3) Davis, D.R., Chapman, C.R., Greenberg, R., and Weidenschilling, S.J., LPSC XIV Abstracts (1983).
(4) Zellner, B. in Asteroids, 783-806.

(5) Kuiper, G.P., Fugita, Y., Gehrels, T., Groeneveld, I., Kent, J., van Biesbroeck, G., and van Houten, C.J. Astrophys. J. Suppl. 3, 289-428 (1958).

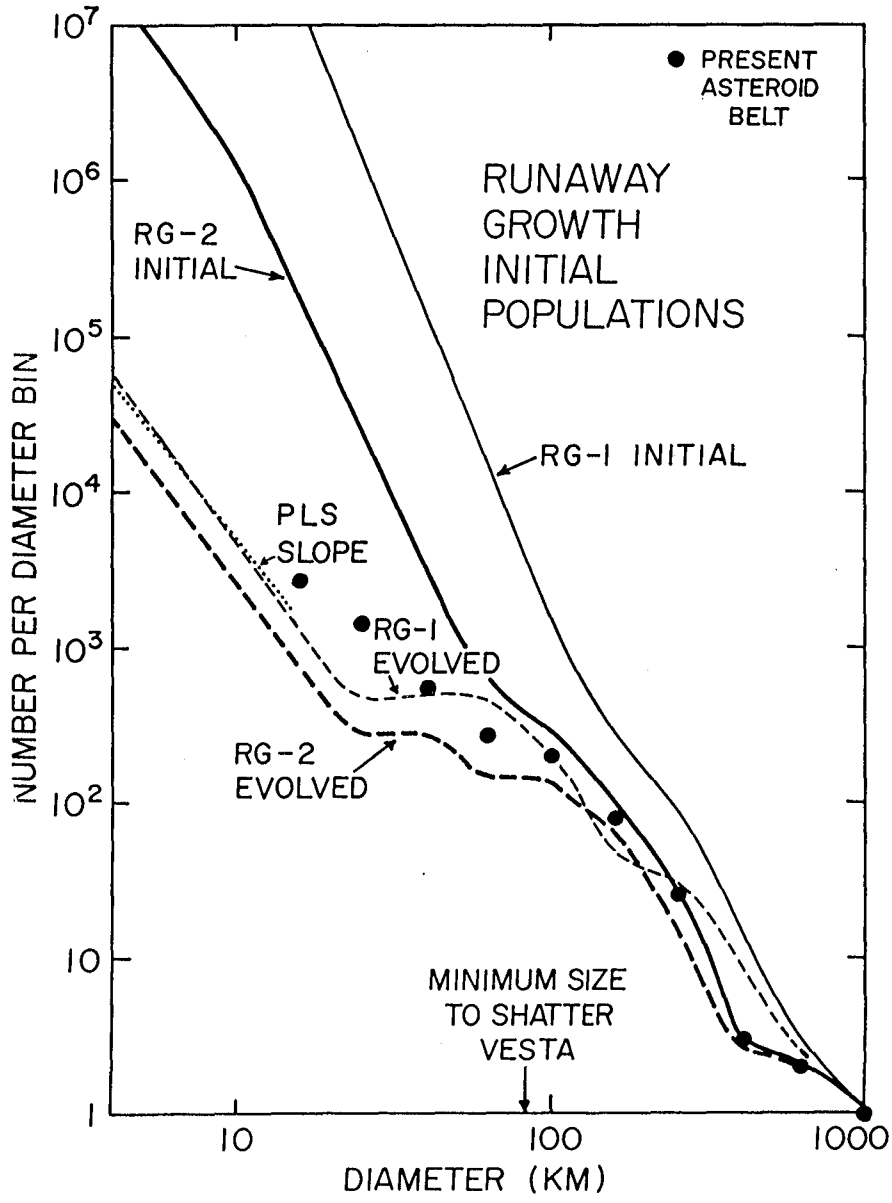

Figure 1: The initial and the collisionally evolved size distribution after 4.5 b.y. for an initial asteroid belt about 3 times as massive as the present belt (RG-2) and a Mars-mass initial distribution (RG-1). The initial distribution has a shape of a runaway growth distribution similar to that used in (2). There are a few large (500-1000 km) bodies, and most of the distribution mass is contained in bodies 25-100 km in diameter.

CONVEX-PROFILE INVERSION OF ASTEROID LIGHTCURVES

Steven J. Ostro* and Robert Connelly**, Departments of *Astronomy and **Mathematics, Cornell University, Ithaca, NY 14853

Asteroids appear as unresolved point sources when viewed through even the largest Earth-based optical telescopes, and most of our current knowledge of asteroid sizes and shapes has been inferred indirectly from disk-integrated, VIS/IR measurements. Under special circumstances, the modern techniques of occultation timing, delay/Doppler radar, and speckle interferometry can yield direct estimates of dimensions, but the primary observational constraints on shapes per se are optical lightcurves.

The lightcurve of a rotating asteroid is completely determined by the asteroid's shape, its light-scattering behavior, and the viewing geometry. As Russell (1906) noted, even if lightcurves were available for an asteroid at all physically possible Sun-Earth-asteroid configurations, it would be "quite impossible to determine the shape of the asteroid" because of the difficulty of separating albedo variations from curvature variations. Fortunately, the bulk of available photometric and polarimetric data indicate that the forms of most broadband optical lightcurves seem less sensitive to surface heterogeneity than to gross asteroidal shape. Within this framework, many researchers have examined the dependence of lightcurve shape on viewing geometry, asteroid shape, and scattering law. Most of these studies have invoked a mathematically simple figure, such as a triaxial ellipsoid, whose shape is completely parameterized by the two ratios b/a and c/a, where $a \geq b \geq c$ are the semiaxis lengths. However, analyses based on such simplified shapes ignore much of the interesting information that distinguishes individual lightcurves (e.g., all odd Fourier harmonics).

Ostro and Connelly (1984) have developed a new approach, called convex-profile inversion (CPI), to lightcurve analysis. CPI obtains a convex profile, $\underline{P}$, from an asteroid's lightcurve. The number of parameters that characterize the profile is limited only by the number of Fourier harmonics used to represent the parent lightcurve, so CPI can preserve much (if not all) of the salient information contained in the parent lightcurve. Whenever certain ideal conditions are satisfied, $\underline{P}$ is an estimator for the asteroid's "mean cross section" $\underline{C}$, a convex set defined as the average of all cross sections $\underline{C}(z)$ cut by planes a distance z above the asteroid's equatorial plane. $\underline{C}$ is therefore a 2-D average of the asteroid's 3-D shape. The ideal conditions are that (A) all intersections of the asteroid's surface with planes perpendicular to the spin axis are convex; (B) the asteroid's scattering law is geometric, i.e., brightness is proportional to projected, visible, illuminated area; (C) the astrocentric declinations δ_E, δ_S of the Earth and Sun are zero; and (D) the solar phase angle ϕ is known and nonzero. CPI's geometrical conventions (Fig. 1) are such that for any given Sun-Earth-asteroid configuration, the sign of ϕ will correspond to either retrograde or direct rotation.

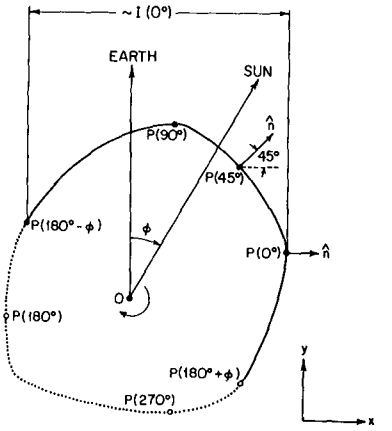

Fig. 1. Geometry for 2-D asteroid lightcurve inversion. The asteroid is a convex profile rotating clockwise, and is shown at rotational phase $\theta = 0°$. The solar phase angle ϕ is indicated, as are the asteroid's illuminated (solid) and unilluminated (dotted) portions. The asteroid's brightness is proportional to the orthogonal projection, in the direction of the Earth, of the visible, illuminated portion of the profile.

To obtain a profile from a lightcurve, we first find the lightcurve's Fourier series: $I(\theta) = \Sigma\, \underline{c}_n e^{in\theta}$ and define the radius of curvature function: $r(\theta) = \Sigma\, \underline{d}_n e^{in\theta}$, where $\underline{d}_n = \underline{c}_n/\underline{v}_n$ and $\underline{v}_n$ is a known function of ϕ and n. The profile is determined by $r(\theta)$ and will be closed and convex only if the N linear constraints, $r(2\pi k/N) \geq 0$ for $1 \leq k \leq N$, are satisfied. In practice, CPI finds that profile $\underline{P}$ which provides the least-squares estimator for $\underline{C}$ by finding that vector of Fourier coefficients which satisfies the constraints and is closest to the vector of unconstrained Fourier coefficients.

We have tested CPI by inverting lightcurves generated analytically for geometrically scattering ellipsoids (GSE's). When $\delta_E = \delta_S = 0$, the inversion yields an ellipse with axis ratio b/a independently of ϕ. When $\delta_E \neq 0$ and/or $\delta_S \neq 0$, the resulting profile is not necessarily an ellipse and has breadth extrema not necessarily in the ratio b/a; the degree to which $\underline{P} \neq \underline{C}$ depends on each of the five free parameters. We have calibrated the deviation of $\underline{P}$ from $\underline{C}$ for GSE's as a function of b/a, c/a, lightcurve noise level, rotation-phase sampling interval $\Delta\theta$, and departure from ideal conditions. The coupling between these factors is considerable. If the rms noise due to all sources is ~ 3% of the lightcurve's peak-to-valley amplitude, then $\underline{P} \approx \underline{C}$ if $\Delta\theta < 5°$. If $|\delta_E|, |\delta_S| > |\phi|$, then distortion of $\underline{P}$ is minimal when δ_E is between 0 and $-\delta_S$ but severe when δ_S is between 0 and δ_E.

To permit quantitative comparison of profiles, we use a scale-invariant, rotation-invariant, Euclidean distance Ω between two profiles $\underline{P}$ and $\underline{P}'$. We also define the "noncircularity" Ω_C as the distance between a given profile and a circle, and β as the ratio of a profile's maximum breadth to its minimum breadth. The lightcurve amplitude Δm is often taken as a measure of an asteroid's noncircularity and elongation. This approach would be justified if every asteroid were a GSE and every lightcurve were obtained at $\phi = \delta_E = \delta_S = 0$. For the purpose of using actual lightcurves to compare the shapes of real asteroids, the statistics Ω_C and β incorporate all the information in a parent lightcurve, and as such are *a priori* preferable to Δm. They also permit a distinction between noncircularity and elongation.

Figure 2 shows results of convex-profile inversion of two lightcurves of 15 Eunomia, obtained at $\phi = -12°$ and $\phi = -21°$ by Groeneveld and Kuiper (1954) and van Houten-Groeneveld and van Houten (1958). These authors argue that Eunomia's pole is nearly normal to the ecliptic. If this is the case, then, since Eunomia's orbital inclination is only 12°, Condition C might have been close to being satisfied during the photometric observations. The negative signs for ϕ correspond to retrograde rotation, as deduced by the cited authors. Although the two Eunomia lightcurves were taken at very different solar phase angles, the profiles do seem similar. Under the ideal conditions, $\bar{P}$ should not depend on ϕ, so the profiles in Fig. 2 might be valid approximations to Eunomia's mean cross section despite possible departures from our ideal conditions.

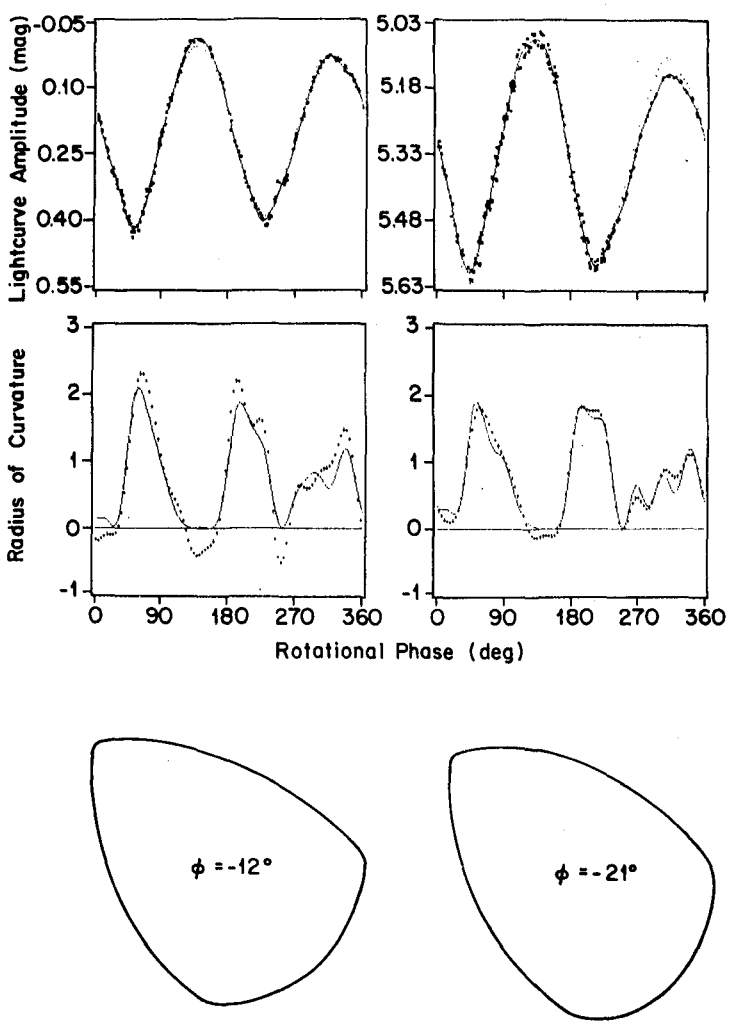

Fig. 2. Convex profiles for asteroid 15 Eunomia. In the top figures, the large symbols are the lightcurve data, the solid curve represents the lightcurve derived from the unconstrained fit, and the tiny dots represent the lightcurve derived from the constrained fit, i.e., from the convex-profile inversion. In the middle figures, the unconstrained and constrained radius-of-curvature functions are represented by symbols and solid curves, respectively. The profiles are shown at rotational phase $\theta = 0°$ as in Fig. 1.

REFERENCES:

Groeneveld, I., and G. P. Kuiper (1954). Astrophys. J. 120, 200-220.

Ostro, S. J., and R. Connelly (1984). Icarus 57, 443-463.

Russell, H. N. (1906). Astrophys. J. 24, 1-18.

SURFACES OF ASTEROIDS AND COMETARY NUCLEI

Michael C. Malin, Department of Geology, Arizona State University, Tempe, AZ 85287

Introduction

With the likely return of high resolution images of the surfaces of asteroids and cometary nuclei within the next ten years, it is perhaps appropriate to begin discussion of the types of landforms and processes that may exist on these types of bodies. Such discussions serve both as exercises in predictive science (i.e., proposing hypotheses to be tested by the future data) and to stimulate additional research that could be performed prior to the anticipated data return, in order to hone interpretational skills. Acknowledging that some asteroids may be cometary nuclei in disguise, asteroids will be treated here as a simpler case than comets, owing to their more limited response to the space environment. Larger bodies ($D > 100$ km) will not be discussed, even though they are recognized to be extremely important. This limitation permits only processes depending on exogenic phenomena to be considered (excluding processes such as volcanism on Vesta, for example), thus focusing discussion on the more unique aspects of these bodies, namely, their size and number.

Asteroids

What processes shape asteroidal surfaces? Certainly the most important must be impact cratering. However, as cratering probability scales with size for several reasons, including the increase in gravitational cross-section, asteroids are likely to be less cratered than, for example, similarly sized areas on the Moon or Mars. They are also likely to be less cratered than Phobos and Deimos, as those bodies owe their crater populations in no small way to their proximity to Mars. Collisions between asteroids are probably rare, as they are for the most part in similar orbits—comets and Apollo/Amor objects are probably responsible for much of the cratering of asteroids. Material ejected from a given asteroid has a statistically high chance of re-impacting that asteroid because their orbits share common points of intersection. These considerations suggest that cratering histories of asteroids may show considerable variability, reflecting more the statistical occurrences in an asteroid's past than solar system wide events.

Other asteroidal processes are problematical. Solar radiation (particulate or electromagnetic) may create small scale physical or chemical changes, but are unlikely to create major landforms visible in spacecraft photographs. Surface manifestations of internal processes (e.g., volcanism) are unlikely on small objects, although effects of early heating events (associated with short-lived radioactivity or external heating events) might still be preserved. Phenomena involving volatiles (degassing from impact-generated thermal or pressure gradients; e.g., Thomas, et al. 1979) may occur, again limited by the impact and/or thermal history.

Comets

Comets hold the potential for considerably greater diversity in surface processes and landforms than asteroids, owing to their greater observed surface activity. This activity, resulting from volatilization of constituent ices, may lead to many features for which terrestrial counterparts exist. For example, size dependent ejection of dust and ice grains (e.g., Probstein, 1968; Finson and Probstein, 1968; Sekanina and Schuster, 1978a, 1978b) could lead to sorting processes both for materials left on the surface (lags) (Brin and Mendis, 1979) and for material transported into the coma, some of which may be re-implanted onto the cometary surface (Wallis and Macpherson, 1981). Thus crude analogies may be drawn to terrestrial sedimentology (in part the study of the concentration and redistribution of particles under the influence of an entraining fluid). Additional insight can be gleaned from terrestrial studies of the interaction of fine-grained particles (of various compositions, including silicates and hydrocarbons) with snow and ice (e.g., Nakawo and Young, 1981; Driedger, 1980). These works provide emperical observations that supplement and support theoretical models of sublimation of volatile/dust mixtures, or volatiles under dust blankets. Landforms that develop in snow and ice (e.g., Muller and Coulter, 1957; Drozdowski, 1977; Gardner, 1978; Hall, 1978) may bear considerable resemblence to hypothecated features on comets (e.g., Whipple and Huebner, 1976).

Cratering on cometary nuclei may be even more limited than on asteroids, since comets spend so little time in the "dirtier" neighborhood of the solar system (both because of their large semi-major axes and inclinations). Short period comets have considerably greater chance of impacting and being impacted than do long period comets. Impacts may play an important role in the evolution of volatiles on comets. They may provide "windows" into the interior of the nucleus, where different volatiles may be present (a possible explanation for jetting associated with the initial activity of comets approaching the sun). Further, if larger grains are not initially present in the material from which comets accrete, cratering can make such particles through impact lithification and induration.

Conclusion

The preceding is less a presentation of what is to be seen on asteroids and cometary nuclei than a call for discussion of the potential attributes of these objects that may be examined using instruments on existing or proposed missions. Currently, U. S. planners are concentrating on the Mariner Mark II Comet Rendezvous/Asteroid Flyby mission: what instruments should be flown on this mission, what should be the goals and/or objectives of these instruments, and what specific design criteria should be applied to these experiments? Leading candidate instruments include devices to determine composition and its spatial distribution (visible, near-infrared, and thermal or mid-infrared) and morphology (e.g., cameras). As our experience with these bodies is so limited (i.e., we've yet to spatially resolve a comet's nucleus), these questions are especially difficult to address. ESA's Giotto mission to Comet Halley should provide the first specific opportunity to test such ideas as expressed above. Now is the time to

make predictions...anyone else out there want to come out on the limb?

References

Brin, G. D. and Mendis, D. A. (1979) Dust release and mantle development in comets: Astrophys. J. 229, 402-408.

Drieger, C. L. (1981) Effect of ash thickness on snow ablation: in The 1980 Eruptions of Mount St. Helens, Washington, P. W. Lipman and D. Mullineaux, Eds., U. S. Geol. Surv. Prof. Paper 1250, 757-760.

Drozdowski, E. (1977) Ablation till and related indicatory forms at the margins of Vestspitsbergen glaciers: Boreas 6, 107-114.

Finson, M. L. and Probstein, R. F. (1968) A theory of dust comets. I. Model and equations: Astrophys. J. 154, 327-352.

Gardner, J. (1978) Wenkchemna Glacier: ablation complex and rock glacier in the Canadian Rocky Mountains: Can. J. Earth Sci. 15, 1200-1204.

Hall, K. (1978) Ablation hollows on melting snow surfaces: A proposed classification and observations on formation: Norsk geogr. Tidsskr. 32, 143-151.

Muller, E. H. and Coulter, H. W. (1957) The Knife Creek Glaciers of Katmai National Monument, Alaska: J. Glaciology 3, 116-122.

Nakawo, M. and Young, G. J. (1981) Field experiments to determine the effect of a debris layer on ablation of glacier ice: Ann. Glacio. 2, 85-91.

Probstein, R. F. (1968) The dusty gasdynamics of comet heads: in Problems of Hydrodynamics and Continuum Mechanics, M. A. Leverent, Ed. (Soc. for Indust. and App. Math. Pub., Philadelphia), 568-583.

Sekanina, Z. and Schuster, H. E. (1978a) Meteroids from Periodic Comet d'Arrest: Astron. Astrophys. 65, 29-35.

Sekanina, Z. and Schuster, H. E. (1978b) Dust from Periodic Comet Enke: Large grains in short supply: Astron. Astrophys. 68, 429-435.

Thomas, P., Veverka, J., Bloom, A., and Duxbury, T. (1979) Grooves on Phobos: Their distribution, morphology, and possible origin: J. Geophys. Res. 84, 8457-8477.

Wallis, M. K. and Macpherson, A. K. (1981) On the outgassing and jet thrust of snowball comets: Astron. Astrophys. 98, 45-49.

Whipple, F. L. and Huebner, W. F. (1976) Physical processes in comets: Ann. Rev. Astron. Astrophys. 14, 143-172.

AN IDEALIZED SHORT PERIOD COMET MODEL: SURFACE INSOLATION, H_2O FLUX, DUST FLUX AND MANTLE EVOLUTION

Fraser P. Fanale and James R. Salvail (Planetary Geosciences Division, Hawaii Inst. of Geophys., Univ. of Hawaii)

A model of cometary activity is developed which integrates the feedback processes involving heat, gas and dust transport, and dust mantle development. The model includes the effects of latitude, rotation and spin axis orientation. Results are obtained for various grain size distributions, dust to ice ratios, and spin axis orientations. Attention is focused on the development, change of structure and distribution of dust mantles and their mutual interaction with ice surface temperature and gas and dust production. In this model the dust mantle controls the mechanism of gas transport not only by its effect on the temperature but, more importantly, by its own dynamic stability.

Results suggest that an initially homogeneous short period comet with a "cosmic" dust-to-water ice ratio, typical orbit, rotation rate, and grain size distribution would develop at most only a thin ($<$ 1mm) cyclic mantle at all points on the nucleus. Such a fully developed temporary mantle would exist throughout the diurnal cycle only beyond $\sim$ 4 A.U. Thus, cyclic behavior would be expected for such an idealized comet, at least for most of its lifetime. Long term irreversible mantle development on comets with typical rotation rates was not found except regionally on Encke and also on objects with perihelia $\gtrsim$ 1.5 A.U. Even in these cases, free silicate exists, after a few cycles, only as relatively rare large grains and agglomerates with radii $\sim$ 1 cm. scattered over exposed ice. Full mantle development would require hundreds to thousands of cycles. In the case of an initially homogeneous comet Encke, this slow incipient mantle development is shown to be the direct result of its peculiar axial orientation. High obliquity appears required for long term mantle development for typical rotation rates and perihelia $\lesssim$ 1.5 A.U.

Heat conduction into the nucleus for an incompletely mantled or bald comet has been found to be very important in maintaining relatively higher ice surface temperatures, and hence fluxes, during those portions of the diurnal and orbital cycles which would otherwise be cooler. It is also shown to be at least one cause of post perihelion brightness asymmetries, especially in lower obliquity comets. Maximum heliocentric distances at which 1μm dust, sand, pebbles, cobbles and boulders can be permanently ejected from the subsolar point by H_2O (CO_2) are, in A.U.: 6.9 (16.8), 5.2 (11.5), 1.8 (3.0), 0.21 (0.34) and 0.07 (0.11) respectively. A detailed anatomy of temperature, gas and dust flux vs. latitude and longitude for a homogeneous rotating comet with fixed axis is given for comparison with future observation.

Most H_2O flux histories deduced from brightness data are found to be in reasonable agreement with the model, allowing for uncertainty in radius and albedo. A clear exception is Encke. It is shown that the large discrepancy between Encke's observed and model predicted fluxes, based on radar cross section, can be used to evaluate the extent of exposed ice ($<$ 10%). The model is then used to place an active area so as to explain a reported sharp drop in flux on approach to the sun at 0.78 A.U. An active area or areas, $<$ 10% of the comet's surface, centered near 65°N latitude

appears indicated.

Although cyclic mantles are generally indicated for the set of parameters we used, our results show that a global mantle only one to three centimeters thick (depending on the orbit) consisting of the full range of grain sizes can cause irreversible evolution to a noncometary body. We investigated the long term evolution of such a postulated initially thinly mantled cometary object. It was found that after the first few passes and until the end of its dynamic lifetime the object averaged $< 3 \times 10^{-13}$ $gcm^{-1} sec^{-1}$ H_2O flux. Therefore, if cometary objects evolve into Apollo asteroids, ice should always be accessible within 10 meters of the surface despite numerous close perihelion passages. The possible impact of factors not included in the model, such as initial inhomogeneities, coma scattering of radiation, and global redistribution of ejected silicate around the nucleus are discussed.

Comet Thermal Modeling

Paul R. Weissman, Earth and Space Sciences Division, Jet Propulsion Laboratory, Pasadena, CA 91109, and Hugh H. Kieffer, Astrogeology Branch, U.S. Geological Survey, Flagstaff, AZ 86001

Past thermal models of cometary nuclei have tended to be restricted to hemispherical averages and have ignored many important effects such as surface heat flow, rotation period, or coma opacity. We have developed a new computer based model called KRC/COM which includes these and many other important effects to give a more accurate physical model of sublimation from icy cometary nuclei. Halley's Comet has been used as a test case (Weissman and Kieffer, 1984a, 1984b) because of the high interest in the 1986 perihelion passage of that comet. Future work will seek to generalize the results to all long-period comets.

One of the more interesting results of this work is that as the comet approaches the sun the generation of the cometary dust coma causes a net increase in the total energy reaching the nucleus. Although geometric shadowing by the dust decreases the direct solar radiation at the nucleus surface, multiple scattering and thermal emission by the coma dust more than compensate for it. The maximum energy feedback occurs for an opacity of about 0.8 when 2.6 times as much energy reaches the nucleus surface as for a bare nucleus with no dust coma. For greater opacities the energy feedback decreases because multiply scattered radiation can no longer penetrate to the nucleus surface.

The coma feedback mechanism has several interesting effects on the nucleus during its perihelion passage. In the case of Halley the total sublimation is increased by a factor of about two, and a surface ice layer with an average thickness of about 5 meters will be removed during the perihelion passage. Maximum subsolar temperatures at perihelion on the nucleus surface are buffered by the energy going into sublimation and are far below that expected for a non-sublimating body with the same albedo. Minimum temperatures on the nucleus nightside are raised considerably by the coma feedback mechanism. Near perihelion the diurnal and latitudinal temperature range on the Halley nucleus is reduced to less than 10 K, with a maximum dayside temperature of about 208 K, and a uniform nightside temperature of about 198 K. This may have the effect of reducing the generation of nongravitational forces on the nucleus, since such forces require a substantial day-nite temperature difference, as well as a thermal lag between maximum insolation (local noon) and maximum sublimation rate. Another effect is an enhanced gas production rate near perihelion, an effect that has already been observed in several recent comets. Predictions of the gas production rate for Halley as a function of solar distance are in good agreement with Newburn's (1981, 1984) estimate of Halley gas production pre-perihelion in 1910.

Dynamics of Long-Period Comets

Paul R. Weissman, Earth and Space Sciences Division, Jet Propulsion Laboratory, Pasadena, CA 91109

Dynamical studies of the origin and evolution of long-period comets in the Oort cloud during the past year have concentrated on four areas: 1) interpretation of IRAS observations of dust shells around Vega and some 40 other main sequence stars as evidence for cometary clouds around each of these stars; 2) the dynamical plausibility of an unseen solar companion star orbiting in the Oort cloud and causing periodic cometary showers which result in biological extinction events on the earth; 3) a review of the current hypotheses for cometary formation with particular attention to how each mechanism supplies the required mass of comets to the Oort cloud; and 4) development of new dynamics software to simulate the passage of individual stars directly through the Oort cloud. Each of these efforts is described in detail below.

Aumann et al. (1984) reported the discovery of an 85 K dust shell around Vega at a distance of 85 AU from the star. Subsequent analysis found dust shells around approximately 40 stars, about 10% of all stars, within 25 parsces of the sun, many of them F and G type stars like the sun. Weissman (1984a) showed that the observations were consistent with the dust that might be expected from comets in inner Oort clouds around each of these stars. The shells are at distances from each star where the primary condensate from a proto-stellar nebula would be volatile ices, principally water ice. Settling of ice and dust grains to the nebula mid-plane and collapse due to Goldreich-Ward gravitational instabilities would result in icy conglomerate planetesimals, analgous to the way comets are thought to have formed in our own solar system. It is not possible to discriminate between nonvolatile dust and dirty ice particles using the IRAS data. The lack of warmer dust closer to each star may indicate that the near-star region has been swept clean by planets which have formed in that zone. Thus, the IRAS results may be useful in determining which stars are good candidates for also having planetay systems. The detection of Oort clouds around other stars also gives us a means of estimating the number and production rate of interstellar comets escaping from each of these clouds.

Whitmire and Jackson (1984) and Davis et al. (1984) have proposed that the 26 Myr periodicity found by Raup and Sepkoski (1984) in the terrestrial biological extinction record can be explained by cometary showers caused by an unseen solar companion star in a distant, long-period orbit passing through the Oort cloud every 26 Myr. The idea of repeated cometay showers is supported by Alvarez and Muller (1984) who found a period of approximately 28 Myr for the occurrence of large craters on the earth over the last 225 Myr. A study of the dynamical stability of the orbit of the proposed "death star" (Weissman, 1984b) has shown that it has a half life of about 600 to 800 Myr, and thus could not have been in its presently proposed orbit over the history of the solar system. A recent capture event is highly unlikely because of the low capture cross-section for the solar system, so the proposed star would have to have been in a more tightly bound orbit in the past. Also, random fluctuations in the period of the hypothesized star would be about 10% per orbit.

The consequences of repeated cometary showers from the Oort cloud has been examined. A single cometary shower is equivalent to 500 Myr of steady state cometary flux in the terrestrial zone. With a 28 Myr period the "death star" would have caused at least 140 showers since the end of the late, heavy bombard-

ment 4.0 Gyr ago. This would raise the post-mare cratering on the earth and moon by a factor of between 5 and 18, depending on what fraction of terrestrial and lunar cratering is cometary versus asteroidal. This prediction is inconsistent with the observed rate derived from craters counted on dated surfaces. The shorter orbital period of a more tightly bound original orbit for the star would only make the matter worse. Also, the repeated passes of the star through the Oort cloud would seriously deplete the number of comets there, implying a much greater original mass for the Oort cloud.

Also, analyses of meteoritic debris in many of the terrestrial craters used to establish the 28 Myr period indicate that the impactors were highly differentiated objects, similar to iron, stony-iron, or achondrite meteorites. This result is inconsistent with a cometary source; the nonvolatiles in comets are believed to be relatively primitive and undifferentiated agglomerations of interstellar dust. Thus, the idea of a hypothetical solar companion star causing cometary showers and craters associated with biological extinctions is refuted on a number of different fronts.

A review of the major (and minor) theories of cometary origin was completed. The three most widely accepted hypotheses all assume a primordial origin for the comets, having them form at the same time as the sun and planetary system. The minor theories all tend to assume some type of episodic formation, often quite recently, and often involving cataclysmic events such as encounters between the solar system and giant molecular clouds. The primordial hypotheses differ in the distance from the sun at which the comets form. Kuiper (1951) suggested that the comets formed as icy planetesimals in the Uranus-Neptune zone; Cameron (1978) suggested that they formed in an extended solar nebula accretion disk up to 10^3 AU from the sun; while Cameron (1973) suggested cometary formation in subfragments of the proto-solar nebula, already orbiting at Oort cloud distances. Each of the hypotheses is dynamically plausible but only the first has been the subject of any detailed physical and dynamical analysis. The Uranus-Neptune zone does not seem capable of providing the total mass of comets required to populate the Oort cloud, so some combination of the three hypotheses may be required.

There has been a growing consensus recently that there exists a massive "inner Oort cloud" extending from just beyond the orbit of Neptune to perhaps 10^4 AU from the sun. The inner cloud was presumably populated by planetesimals ejected on moderately elliptical orbits from the Uranus-Neptune zone, and comets formed in the extended solar nebula accretion disk, and has a total population of perhaps 10^{14} comets. Its existence can help to solve several important problems in cometary dynamics, such as providing a more efficient source for the short-period comets, a source for the complex cratering histories of the Galilean and Saturnian satellites, or a source for replenishing the dynamically active outer Oort cloud after a close encounter between the solar system and a GMC. IRAS observations of clouds of cool dust in close proximity to the solar system (Low et al., 1984) may be the first actual detection of material in the inner Oort cloud.

Finally, during the past year development has proceeded on a new program called PENETRATE which simulates the perturbations on a hypothetical cloud of comets caused by a star passing either through or just outside the Oort cloud. This program can be used to determine the detailed distribution of stellar perturbations as a function of stellar mass, velocity, and encounter distance, or can find the fraction of comets ejected from the cloud or thrown into the

planetary region by each close stellar passage. The results from these studies will in turn be used to better model the long-term dynamical evolution of comets in the Oort cloud, or to study the interstellar flux of comets produced by the solar system.

Page intentionally left blank

CHAPTER 3

VENUS

Page intentionally left blank

VOLCANISM AND RIFT FORMATION IN BETA REGIO, VENUS: NEW RADAR RESULTS. D. B. Campbell[1], J. W. Head[2], J. K. Harmon[1], and A. A. Hine[1]. (1) Nat'l Astronomy and Ionosphere Ctr., Arecibo Observatory, Arecibo, PR 00612; (2) Dept. Geological Sciences, Brown Univ., Providence, RI 02912.

Beta Regio is an oval-shaped highland region centered near 25° N latitude and 280° longitude. It extends for about 2500 km in a N-S direction, and is approximately 2000 km wide, rising as high as 5 km above mean planetary radius (1). Early Earth-based radar observations of Venus revealed the presence of two radar-bright features in this region which are now known as Rhea and Theia Mons. Saunders and Malin interpreted these two features to be large volcanic constructs similar to those of the Tharsis region of Mars (2). Masursky et al. (1) noted that Beta Regio has complexly varying radar brightness values, elevations, and rms slopes. The two irregularly-shaped shield-like features Rhea and Theia Mons dominate the topography and lie adjacent to a central N-S trending canyon which appears to be a northern extension of a complex disrupted region of en echelon ridges and troughs south of Beta Regio. Masursky et al. (1) interpret the central Beta Regio trough to be a rift and Rhea and Theia Mons to be constructional volcanic features. McGill et al. (3) have drawn topographic analogies between Beta Regio and the East African rift system on Earth.

In August and September of 1983 we obtained a high-resolution (about 2 km) image (Fig. 1) of central Beta Regio which reveals geologic details of Rhea and Theia Mons and the central chasm. The image was obtained using the 12.6-cm wavelength radar system at Arecibo Observatory in Puerto Rico. The image maps the backscatter cross section per unit area (surface reflectivity). The angle at which the surface is illuminated by the incident radar wave is less than 40° at these latitudes. In this image, variations in brightness are related to differences in small-scale (wavelength-size) surface roughness values (bright, high values; dark, low values).

Most of the bright and dark linear features in Fig. 1 are 25-100 km long, are arranged with their long axes parallel to sub-parallel, trending north to northeast (Fig. 2), and are closely related to the central topographic depression. The bright bands are interpreted to be areas of enhanced roughness associated with faults and the collection of faults related to the central depression are interpreted to be a rift system as inferred previously on the basis of topographic data. Theia Mons rises over 5 km above the planetary datum and 1.5 to 2.5 km above the surrounding crest of Beta Regio. A circular area of high radar backscatter (Fig. 3) and approximately 320 km in diameter is situated directly on the topographic high. A smaller irregular 50-90 km diameter region of low backscatter is located approximately at the center of the bright area. These two features are centered on the extension of the western edge of the rift system (Figs. 1-3), suggesting a correlation of the location of a major volcanic center and a significant fault. Thus, additional support for a volcanic origin for Theia Mons comes from its superposition on the western bounding fault of the rift, the extremely close correlation of topography and the major brightness variation, and lobate flow-like features extending radially away from the central area for several hundred km in a downslope direction. Theia Mons interrupts the topography and structure of the rift system, strongly suggesting that it is superposed on the rift structure and is therefore younger. Several other areas characterized by bright regions of various shapes and central dark spots (Fig. 3) are often related to an elevated area. The most prominent of these, Rhea Mons, is located along the western edge of the rift system, rises 0.5 to 1.0 km above the surrounding terrain, but has a sharp boundary along its eastern margin. Similarities to Theia Mons suggest a volcanic origin; however, the feature appears more extensively modified by rift faulting and is adjacent to one of the deeper portions of the rift. The large number of these features and their relationship to the rift valley suggest that extensive volcanism has accompanied rift formation in Beta Regio and that a significant portion of the rim topography of the rift (1-2 km) may be locally due to the construction of volcanic edifices.

Schaber (4) has pointed out the global distribution of chasmata on Venus and has suggested that they represent global rift systems comparable to continental-type rifts (3) on Earth. These data provide important new information on the nature of rift formation on Venus and the nature and role of volcanism in this process.

References: 1) Pettengill, G.H. et al., JGR, 85, 8261, 1980; Masursky, H. et al., ibid, 8232, 1980. 2) Saunders, R.S. and Malin, M.C., GRL, 4, 547, 1977. 3) McGill, G. et al., GRL, 8, 737, 1981. 4) Schaber, G., GRL, 9, 499, 1982.

Fig. 1

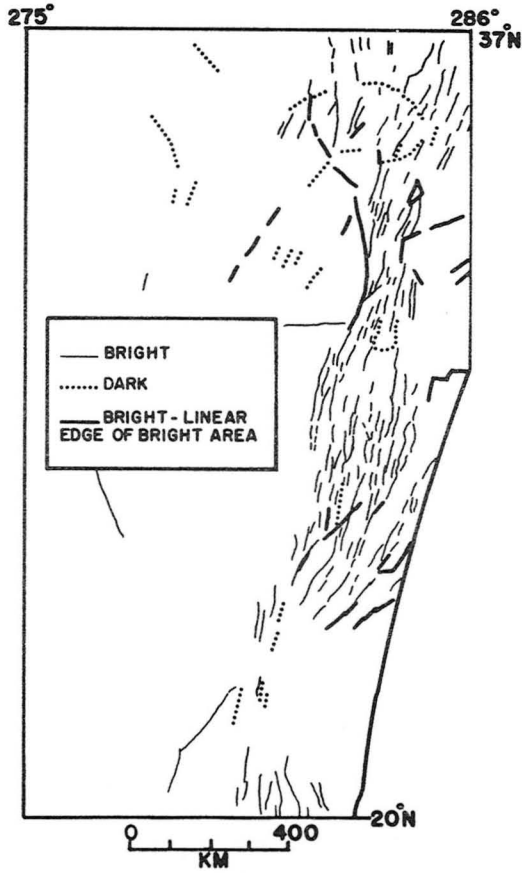

Fig. 2

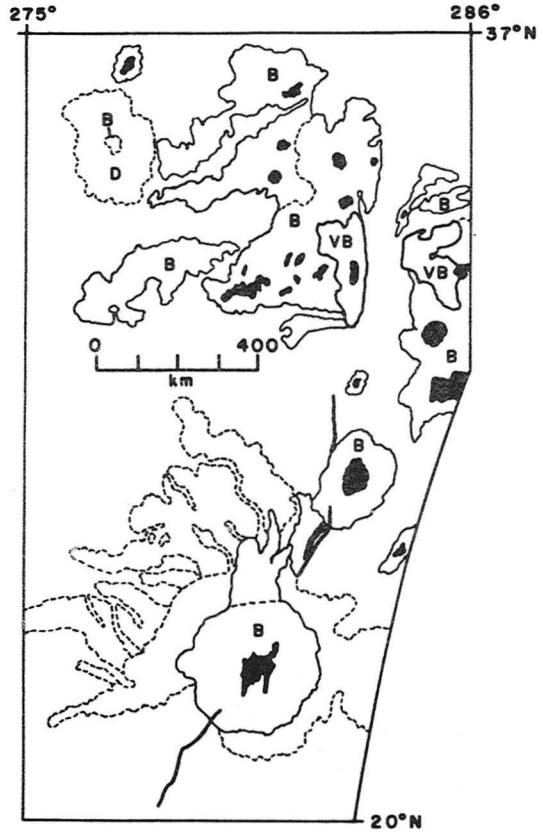

Fig. 3

CHARACTERISTICS OF BASALTIC LAVA FLOWS ON VENUS. Lionel Wilson[1,2], James B. Garvin[2], and James W. Head[2]. (1) Dept. Environmental Sciences, Univ. of Lancaster, Lancaster LA1 4YQ, U.K.; (2) Dept. Geological Sciences, Brown Univ., Providence, RI 02912.

We review some ideas relating to the formation of lava flows on Venus with particular relevance to understanding the surface morphological features seen in the panoramic images made by the Venera 13 and 14 landers (1). The major element compositions measured by the Soviet probes indicate that the surface rocks at the Venera 13 site resemble a terrestrial tholeiite compositio whereas the Venera 14 rocks are similar to terrestrial alkali basalts. Few data exist on the rheological properties of such magma types on Earth; these properties are a strong function of magma volatile content, and there are important gaps in our knowledge of the typical volatiles to be associated with the magmas on Venus. However, the suggestion that venusian magmas may be water-poor (2), together with consideration of the fact that the high venusian surface temperatures may cause magmas to experience up to 50 K less cooling during their rise to the surface than corresponding terrestrial counterparts, leads to the finding that venusian magmas may typically have plastic viscosities, E, up to a factor of three greater than terrestrial counterparts on eruption. A similar analysis of yield strength variations with temperature, magma composition and volatile content suggests that temperature will exert the main control and that venusian magma yield strengths, Y, may be a factor of several times smaller than those of terrestrial equivalents. We suggest that (Y = 1 Pa, E = 300 Pa s) and (Y = 100 Pa, E = 3000 Pa s) will probably define extremes of the rheology range, at least for venusian tholeiites. Substitution of this range of properties into various expressions relating the rise velocity of magmas in the crust to the widths of open and closed crustal fissures shows that there is no obvious reason to expect the range of mass or volume eruption rates of basaltic magmas on Venus to be systematically different from that of terrestrial basalts.

On Earth, many basaltic magmas form fire-fountains over the vent. In some cases this is just a consequence of the high rise speed of the magma through the crust, but in other cases the high eruption velocity is due mainly to the expansion of exsolved magmatic gas (3). Both the process of gas exsolution itself (4), and the cooling of clasts which takes place in the optically-thin, outer parts of the fire-fountain, lead to an increase in Y and E for the erupted magma. The high Venus surface pressure suppresses gas exsolution completely unless the total magma volatile content exceeds about 3 wt. % (5). If gas exsolution does occur, the upward velocity imparted to magmatic pyroclasts will typically be 2.5 times less on Venus than on Earth due to the reduced gas expansion, leading to a similar reduction in pyroclast flight time. Thus we expect venusian magmas to suffer minimal cooling as a result of emerging through the vent, and take the above ranges of magma properties to be typical of lava flows forming on the surface.

Subsequent cooling is a consequence of radiation and convection from the surface of a flow and conduction into the substrate over which it moves. The high venusian surface and atmospheric temperatures act to reduce radiative and conductive losses relative to the Earth, but the high atmospheric density enhances convective losses so effectively that the total heat loss rates are typically two to three times greater at temperatures above about 800 K (6). As a consequence, surface temperatures on a venusian lava flow will take less time to approach the ambient temperature than on a terrestrial flow and the initial rate of growth of a cooled crust on a lava moving in a laminar fashion will be greater for venusian flows. If we define the cooled crust to be the layer at the base of which the solidus is reached solely as a result of conductive cooling and use a treatment of heat loss (7) which takes account of the buffering effect of latent heat release (8) we find crustal thicknesses as a function of time as shown in Table 1. At times longer than about three hours after eruption, however, crustal thicknesses become greater on terrestrial flows, mainly due to the much lower absolute temperatures which the terrestrial flow surfaces will have reached by this time. For flows which continue to move for times in excess of three hours, progressively greater relative mobility is ensured for venusian flows.

The Venera 13 and 14 images show layered structures in surface rocks with layer thicknesses of the order of 0.1 m. We have considered the possibility that these layers may represent the cooled upper parts of lava flows; there are at least two plausible models. In the first we assume that the lava moves as a Bingham plastic over topography consisting of channel-like depressions which any new flow can partially fill. In such cases, a central plug of unsheared lava forms, the thickness and width of which are dictated by the lava yield strength and the channel geometry (9). The exact form of the relationship depends on the detailed cross-sectional shape of the channel but we have found that, for a wide range of width to depth ratios in both rectangular and elliptical channels, the central plug occupies roughly one-fifth of the depth of the channel.

If we attempt to interpret layers seen in the Venera images to be the cooled versions of such plugs, we have to explain why several layers of similar thickness are often seen in immediate succession. It is sometimes observed during terrestrial eruptions that rigid, plate-like sections of cooled plugs become detached from the underlying flow when a sudden change in flow direction occurs, and we can imagine scenarios in which a number of such plates become stacked one above another. But such sequences might only be expected to form a very small fraction of the total area of the flow field resulting from the eruption, and so we do not currently favor this interpretation.

In the second mode of cooled-crust formation, we assume that a flow moves as a Bingham plastic in an unconfined manner on an infinite plain. In this case the flow will form lateral levees and assume an equilibrium depth proportional to its yield strength (10). Shear will take place only at the base of the central channel and there will be no internal deformation of the lava within the channel; the obvious cooling unit will be the full thickness of the flow. We explore the consequences of this model using equations relating the geometrical and material properties of the flow (11). If the central channel is much wider than its levees and has depth D, then the yield strength is $Y = Dg\rho\alpha$ where the gravity, g, = 8.8 m/s^2, and the lava density, ρ, is taken as 3000 kg/m^3. If the slope, α, over which the lava moves is taken to be 0.01 radians, then D = 0.1 m implies Y = 26 Pa, well within the above range of estimates. The corresponding levee width is $L = D/2\alpha = 5$ m. If the volume effusion rate of the lava is F then the central channel width W is given (11) by $W^{11} = (24FE)^4\, g\rho/Y^5\alpha^6$. The mean flow velocity, U, is found from U = F/WD and the ultimate length of the flow, limited by cooling, is X approximated by X = FD/150WK where K is the thermal diffusivity of the lava, about 7×10^{-7} m^2/s. A suitable value of E from the above range of estimates is 1000 Pa s; while analogy with effusion rates deduced for terrestrial (and lunar) basaltic eruptions indicates that F may lie in the range 10 to 10^5 m^3/s. Table 2 gives some sets of values of F, W, U, and X. The pattern which emerges involves flows which are typically much wider than they are long; indeed, unless the magma is erupted from an elongate fissure source, it is not clear that an individual flow unit can attain its equilibrium width before cooling limits its motion. The values given in the table can be changed by assuming other values for α and E; however, even if E were reduced to 300 Pa s (the lower limit estimated above) and α were increased to 0.05, the resulting decrease in W and corresponding increases in U and X would involve only a factor of 3.7, making the flow widths and lengths equal at F = 10^3 m^3/s. More important is a result which follows from the nature of the above equations: any one flow unit must come to rest after a time $T = X/U = D^2/150K$ which depends only on the flow thickness. Thus, T for all the flows in the table is 95 seconds! Clearly, most eruptions -- certainly those represented by the larger values of F -- would be expected to last much longer than this; this analysis implies that the resulting deposits would consist of many overlapping, thin units: Table 2 shows the numbers of layers required to accomodate an (arbitrary) erupted volume of 10^6 m^3. Such a result is not inconsistent with what is seen in the Venera images, but we stress that this model requires that the spacecraft be located within a few hundred meters to a very few km of a major vent.

Table 1. Thicknesses of lava crusts.

time since eruption	crust thickness/mm Venus	Earth
1 second	0.48	0.27
1 minute	7.9	6.2
1 hour	75	71
1 day	355	380

Table 2. Properties of 0.1 m thick lava flows.

F/(m^3/s)	W	U/(m/s)	X	# of layers for 10^6m^3
10	640 m	0.16	15 m	1000
100	1.5 km	0.68	65 m	100
1000	3.4 km	3.0	280 m	10
10	7.8 km	12	1.2 km	1
10	18 km	55	5.3 km	1

References: (1) C.P. Florensky et al., Pis'ma v AZh 8, 429, 1982; (2) K. Goettel (1982) Proc. Lunar Planet. Sci. Conf. 13th, 265; (3) L. Wilson and J.W. Head, JGR 86, 2971, 1981; (4) R.S.J. Sparks and H. Pinkerton, Nature 276, 385, 1978; (5) J.W. Head and L. Wilson (1982) Proc. Lunar Planet. Sci. Conf. 13th, 312; (6) J.W. Head et al., Int'l Conf. on Venus Envir., Palo Alto, 1981; (7) D. Turcotte and G. Schubert, Geodynamics, Wiley, 1982; (8) M. Settle (1979) Proc. Lunar Planet Sci. Conf. 10th, 1107; (9) A.M. Johnson, Physical Processes in Geology, 1970; (10) G. Hulme, Geophys. J. R. Astr. Soc., 39, 361, 1974; (11) L. Wilson and J.W. Head, Nature 302, 633, 1983.

VENUS SURFACE COMPOSITION FROM RADIO/RADAR MEASUREMENTS

Gordon H. Pettengill, Peter G. Ford and Bruce M. Chapman
Center for Space Research
Massachusetts Institute of Technology

We have applied three quite different radio techniques to the study of the electrical properties of the surface of Venus. First, using radar, primarily from the Pioneer Venus Orbiter (PVO) spacecraft, we have studied the reflectivity of the surface at near-normal incidence and from these measurements have inferred the corresponding dielectric constants. Second, using measurements of thermal emission brightness temperature obtained both from spacecraft and from the ground we have calculated surface emissivities and from these also have inferred dielectric constant. Finally, we have observed the degree of linear polarization associated with thermal energy emitted from the surface at various angles, and again have attempted to solve for the dielectric constant. In the first and second of these we have been quite successful; the latter technique, on the other hand, appears to have complications that have so far resisted unraveling.

The radar data have provided the highest surface resolution of the three techniques, and were the first to show the unusually high values of Fresnel reflection coefficient (approaching 0.40 in extreme cases) that are associated with many of the elevated regions of Venus[1]. We have refined the interpretation of these data, using large-angle diffuse scattering observations (radar images) to estimate the distribution of small-scale surface roughness. Since the surface containing small-scale roughness cannot contribute to the quasi-specular component which dominates the echo when looking at near-normal incidence, the quasi-specular results must be renormalized for the "missing" surface area when calculating the Fresnel reflection coefficient.

We have completed the analysis for planetary zones lying between -10° and $+45^{\circ}$ latitude, and are attempting to extend the correction into those regions where good Arecibo coverage is available. The major surprise from this work is that the corrected reflectivity shows a largely bimodal distribution over the surface, with about 95 percent of the area exhibiting values near 0.15. The remaining 5 percent shows values ranging upwards to about 0.40, primarily in the mountainous regions.

The thermal emission data obtained from the PVO mission[2] have been supplemented by ground-based observations from the Very Large Array (VLA). With an angular resolution of 1.2 arc sec at a wavelength of 20 cm, the VLA data have a Venus surface resolution of between 200 and 500 km diameter in the sub-earth region, depending on planetary distance. While having lower resolution than most of the spacecraft data, the VLA observations are useful in two respects: they provide better surface resolution at high latitudes, (where PVO was at higher altitude) and they provide better thermal intensity resolution throughout. The combined thermal data set provides powerful confirmation of the radar reflectivity results, showing fairly uniform values of emissivity of about 0.85 over most of the planet, but reduced values (minimum about 0.60) in just those regions where the radar reflectivity is highest. Figure 1 shows an example of VLA results for the Aphrodite Terra region of Venus.

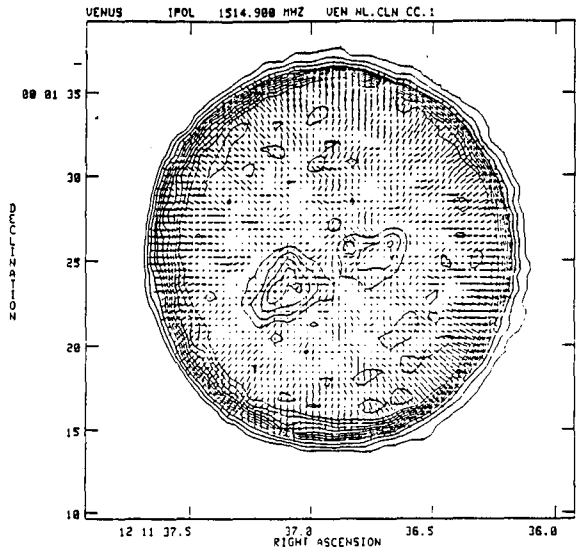

Figure 1. Thermal brightness of Venus at 20 cm wavelengths as observed with the VLA on 12 November, 1983. The central meridian longitude was 108° and the cool features seen near the center of the disk (where the contour interval is 35K) correspond to Aphrodite Terra. The short line segments show the degree and direction of emitted linear polarization.

The polarization of the surface emission has been measured only with the VLA. The extreme roughness and relatively small size of the anomalously reflective regions renders the method useless against them, but we had hoped to gain confirmation of the dielectric properties of the large, relatively uniform areas characteristic of most of the planet. At a wavelength of 20 cm, however, the observed polarizations fall far short of the values predicted for a surface dielectric constant of 5 (as implied by a reflection coefficient of 0.15), even after correcting for surface roughness and beam convolution. At present we are searching for clarification of the reasons behind this discrepancy.

We feel the most likely explanation for the regions of high apparent dielectric constant (in the absence of liquid water on the planet) is given by the assumption of small conducting particles embedded in a matrix of "normal" rock. Measurements made at M.I.T. show that a volume fraction of 5 to 8% conducting material can yield bulk dielectric constants of 20 or more as required by the extreme values of reflectivity/emissivity. While our radio/radar observations must be silent on the identification of the conducting material, consideration of the surface and atmospheric chemistry[3] suggests that iron pyrites (FeS_2) are an extremely likely candidate.

REFERENCES

(1) Pettengill, G.H., P.G. Ford and S. Nozette, "Venus: Global Surface Radar Reflectivity", Science, 217, 640 (1982).

(2) Ford, P.G. and G.H. Pettengill, "Venus: Global Surface Radio Emissivity", Science, 220, 1379 (1983).

(3) von Zahn, V., S. Kumar, H. Niemann and R. Prinn, "Composition of the Venus Atmosphere", in Venus, p. 398, D. Hunten et al., eds., Univ. Ariz. Press, Tucson (1983).

SURFACE UNITS ON VENUS DERIVED FROM PIONEER-VENUS ALTIMETRY, ROUGHNESS, AND RELECTIVITY MEASUREMENTS. A.R. Peterfreund, J.W. Head, J.B. Garvin, Dept. Geol. Sci., Brown Univ., Providence, RI 02912, and S.A. Zisk, Haystack Observ., Westford, MA 01886.

The nature of the venusian surface has been revealed by Pioneer-Venus (PV) observations to be diverse at scales from tens to hundreds of kilometers. In this study [1], we investigate the spatial correlation of elevation, surface roughness, and radar reflectivity as a means of assessing the degree of homogeneity of surface radar properties within topographic provinces and develop a map of possible geologic boundaries. Correlations were performed in a supervised fashion whereby unit boundaries were selected on the basis of statistical and empirical studies of the individual data sets [2,3,4]. Interpretations of these units in terms of geologic characteristics are based on the determination of physical units which are model dependent.

Topographic divisions follow those of previous studies [4,5]: 1) lowlands, <6051.0 km radius; 2) rolling plains, 6051.0 to 6053.0 km; 3) highlands, 6053.0 to 6055.5 km; and 4) mountainous regions, >6055.5 km. The planetary mean radius, 6051.5 km, is within the rolling plains, which covers ~75% of the planet. These divisions define topographic provinces that are spatially distinct and serve to outline specific geographic regions. The topographic divisions may be geologically significant in that chemical and physical weathering processes are likely to be pressure-temperature and thus elevation dependent [6]. Divisions for radar roughness and reflectivity were chosen on the basis of statistical distribution and physical interpretation [7,8]. RMS surface slope is indicative of small-scale (0.1 to 10m) roughness averaged over the radar field of view [3]. Three divisions in RMS slope were made: 1) 1^{o} to 2.5^{o}, smooth; 2) 2.5^{o} to 5.0^{o}, transitional from smooth to rough; and 3) $>5.0^{o}$, relatively rough. Boundaries were chosen such that a sharp distinction could be made between smooth and rough surfaces. The transitional range, which comprises ~45% of the observed surface area of the planet, is probably inhomogeneous and contains a mixture of both smooth and rough elements. Three divisions in reflectivity were chosen: 1) < 0.1, low bulk density (< 2.0 g/m^3) and absence of materials with high dielectrics; 2) 0.1 to 0.2, moderate bulk density (2.0 - 3.2 gm^3) and minor amounts of high-dielectric material (<1%); and, 3) >0.2, either high bulk density (<3.2 g/m^3) and/or the presence of high-dielectric materials. The three divisions were chosen to discriminate between regions that could be described as containing predominantly porous and unconsolidated fine material (soil), predominantly rock, or significant percentage of high-dielectric material. The moderate range, which contains ~67% of the observed venusian surface, is unlikely to be representative of surfaces with a significant unconsolidated regolith typical of the Moon and much of Mars.

Spatial correlations of roughness and elevation show a pattern of increasing roughness with elevation. Most lowlands are smooth or transitional from smooth to rough. Within these regions the low- and moderate-roughness units are spatially well-defined, while high-roughness units are isolated (i.e, single cell-sized equivalent to 10^4 km^2). Small topographic depressions (<10^6 km^2) tend to have moderate roughness values, while broader lowlands are both smooth and transitional. Rolling plains display broad regions of both smooth and transitional roughness. Rough units occur as either small regional clusters or isolated features. Many of the small elevated plateaus (e.g., Alpha Regio) contained within this topographic unit have transitional to high roughness values. Chasmata contained within Aphrodite Terra appear to be

relatively rough. Highlands appear mostly transitional in roughness. Smooth regions can be seen in Lakshmi Planum, near mountains in Ishtar Terra, and in isolated sections of Aphrodite. Rough regions occur adjacent to mountainous terrain within highlands, as seen, for example, in western and central highlands of Aphrodite and eastern Ishtar Terra. Mountainous regions are mostly transitional to rough, with only isolated occurrences of smooth surfaces.

Correlations of radar reflectivity and elevation show a less distinctive relationship than those for elevation and roughness. For a given elevation interval a full range of reflectivity can be observed. Spatially, reflectivity units appear to be better defined than roughness units (i.e. more contiguous). Lowlands are mostly moderate in reflectivity, suggesting a predominantly rock surface, with small patches and a few isolated occurrences of lower and higher reflectivity areas. Rolling plains are also mostly moderate in reflectivity, implying a predominance of surface material with an average bulk density of rock. Low-reflectivity units tend to be adjacent to highland regions, such as Beta and Aphrodite Terra, but are not evenly distributed around the entire highlands. Chasmata appear to contain some material with low reflectivity. High-reflectivity units occur mostly as isolated small areas with the notable exception of the region west of Atalanta Planitia. Highland regions show a pattern of highest reflectivity adjacent to mountainous terrain, with decreasing reflectivity away from these peaks. This pattern is well illustrated in the western and central highlands of Aphrodite. In Ishtar Terra, the pattern of reflectivity units follows a more regional pattern than the circumscribed pattern around Beta and Aphrodite Terra. Mountainous regions contain the highest reflectivity values observed on Venus [9]. These high-reflectivity values are in excess of what would be expected based on bulk density, and as such are inferred to contain considerable percentage of high-dielectric material. Not all mountainous terrains, however, are characterized by high-reflectivity values; for example, most of Akna and Freyja Montes and Rhea Mons have surface materials with moderate to low reflectivities.

Roughness-reflectivity spatial correlations result in a map of spatially distinct units. Of the 9 defined roughness-reflectivity units, 90% of the observed surface is clustered into 4 units; two low-reflectivity units, which are smooth and transitional in roughness and account for ~25% of the observed venusian surface; and two moderate-reflectivity units, which are also smooth and transitional, and make up ~65% of the observed surface. The low-reflectivity units most likely contain >50% soil and generally surround highland regions. This suggests that lateral sediment transport could be an important geologic process on Venus. The widespread distribution of moderate-reflectivity units suggests extensive exposures of relatively smooth rock. The distribution of high-reflectivity units indicates that high-dielectric materials occur in a wide range of localized environments and that altitude-dependent chemical reactions may not be the only factor responsible for the occurrence of these materials.

References: 1) Peterfreund, A.R. et al. (1983) JGR (in press). 2) Pettengill, G.H. et al. (1980) IEEE Trans. Geo. Rem. Sens., GE-18, 28. 3) Pettengill, G.H. et al. (1980) JGR, 85, 8261. 4) Masursky, H. et al. (1980) JGR, 85, 8232. 5) McGill, G. et al. (1983) Venus, Chpt. 6, 69. 6) Nozette, S. and Lewis, J. (1982) Science, 216, 181. 7) Garvin, J.B. et al. (1983) LPSC XIV, 239. 8) Garvin, J.B. et al. (1983) Bull. Am. Astron. Soc., 15, 818. 9) Pettengill, G.H. et al. (1982) Science, 217, 640.

CLASSIFICATION OF CIRCULAR FEATURES ON VENUS. E. R. Stofan, J. W. Head, and R. Grieve, Dept. of Geological Sciences, Brown Univ., Providence, RI 02912.

Among the unanswered questions concerning Venus are the age of its surface and the mechanisms of lithospheric heat transfer (conduction, plate recycling, and hot spot volcanism). The presence or absence of impact craters is germane to these questions. If there is a large population of impact craters, then the surface is ancient and Venus is characterized by conduction like the Moon, Mars, and Mercury, rather than plate recycling and hot spot volcanism. Alternatively, if there is a large population of volcanic craters, then the surface is younger and other mechanisms of heat transfer likely dominate (1). If there are both types of features then mechanisms of heat transfer may vary areally, and/or with time. Thus, development of criteria to distinguish the origin of circular features on Venus is an important task. This is made difficult by the relatively low-resolution radar images and lack of high-resolution global coverage available for Venus. Previous studies (2-9) have emphasized various aspects of the observational, theoretical, experimental, and comparative planetological studies of cratering on Venus, and several have reached divergent opinions concerning the age of the Venus surface. Masursky et al. (1980) conclude that the density of circular features of likely impact origin in the Venus rolling plains is comparable to the ancient cratered terrain of the Moon, Mars, and Mercury (9), while Campbell and Burns (2,3) suggest that the surface may be relatively young, in the range of 600 m.y. to 1000 m.y. A major source of uncertainty in both studies is the possible inclusion of circular features of non-impact (volcanic or tectonic) origin in the so-called impact crater population. The purpose of this study is to continue the development of a classification scheme of circular features on Venus in order to further distinguish their origin and distribution.

Previous studies (2,3) have described two major types of circular features: large, radar dark, quasi-circular regions with diameters 200-1300 km; and well-defined circular areas of low backscatter surrounded by an area of high-contrast rough terrain, less than 300 km diameter. These studies have concentrated on the nature and distribution of the second type because of their similarity to impact craters seen in lunar radar images. In our classification scheme, we build on previous studies but include the full range of circular features, including those with a very high likelihood of volcanic origin. By examining the full range of circular features, and incorporating new high-resolution radar data, we hope to clarify the origin of these features and the distribution of the associated geologic processes on Venus.

The range of radar characteristics associated with circular features is shown in Figure 1. Four basic classes have been delineated. Class I features are characterized by a bright patch with a dark center, with the dark-to-bright radius $r_D < 0.75\ r_B$. The bright patch has a diffuse outer boundary and is generally quite circular (Fig. 1). The central dark area is less circular and has a somewhat diffuse boundary with its bright surround. The primary example of this class is Theia Mons (23°N, 281°), from which apparent flow-like patterns extend radially outward from its bright surround in high-resolution radar images (11). The feature corresponds to a topographic high; it is located in a region characterized by other bright areas with dark central patches which are thought to be of volcanic origin (e.g., Rhea Mons, 33°N, 283°). These factors have led to the interpretation that Theia is a volcanic feature (11), indicating a possible volcanic origin for other Class I features.

The circular features in Class II were described by Campbell and Burns (1980) as large, dark, quasi-circular regions of large diameter (> 200 km). This type of feature was also observed in Pioneer-Venus radar data (12). Two

examples are located at 18°N, 325° and 29°N, 336°. Many Class II features contain a bright spot or spots, which are not necessarily centrally located. Features in this class were not included by Campbell and Burns in their crater counts. In general, the Class II features are considered enigmatic in origin.

We further define a subclass (IIA) characterized by a bright topographically high ring located in a large, dark, irregularly shaped area that is of relatively low topography compared to the surrounding area. An example is located at 74°N, 315°, directly west of Freyja Montes. The bright ring in this depression has an approximate diameter of 200 km, with the depression close to 500 km across. The large topographic depression suggests an origin at least partially influenced by tectonic processes.

Class III features contain a single bright ring with a dark interior, where $r_D > 0.75\ r_B$. Class III approximately corresponds to the second group described by Campbell and Burns (1980), with diameters < 300 km. The bright rings have a distinct outer boundary, and a highly circular interior. Subclass IIIA features appear in radar images as bright rings with a centrally located bright spot. The location of the outer boundary of the bright ring can vary significantly as a function of radial direction. The general appearance and central bright spot point to a possible impact origin. An example is located at 27°S, 340°.

The last group (Class IV) is comprised of multiple ring features, in which two or more bright rings encircle a dark area which varies in size. The feature at 63°S, 322° is a concentric ring structure with ring diameters of 155 and 265 km and may be similar to multi-ringed impact basins of the Moon, Mars, and Mercury. The feature Cleopatra may also fall into this class, although its origin is not well understood (13).

The classification system described above is preliminary. Further studies are being made on the size ranges of the classes, location relative to province and elevation, and correlation with topography. An improved classification of circular features will aid in determining whether a feature is of volcanic, impact, or tectonic origin, enabling better estimates to be made of the age and geologic evolution of the surface of Venus.

References: 1) Solomon, S.C. and Head, J.W. (1982) JGR, 87, 9236-9246. 2) Campbell, D.B. and Burns, B.A. (1980) JGR, 85, 8271-8281. 3) Burns, B.A. (1982) Ph.D. Thesis, Cornell Univ., 206 pp. 4) Cutts, J.A. et al. (1981) Icarus, 48, 428-452. 5) Saunders, R.S. and Malin, M.C. (1976) Geol. Romana, 15, 507-515. 6) Schaber, G. and Boyce, J. (1977) Impact and Explosion Cratering, Pergamon, 603-612. 7) Grieve, R.A.F. and Head, J.W. (1982) LPSC XIII, 285-286. 8) Schultz, P.H. (1981) Conf. on Venus Environment (abstract), 6. 9) Masursky, H. et al. (1980) JGR, 85, 8232-8260. 10) Settle, M. (1980) Icarus, 42, 1019. 11) Campbell, D.B. et al. (1984) Proc. Lunar Planet Sci. Conf. XV, this volume. 12) Pettengill, G.H. et al. (1979) Science, 205, 90-93. 13) Peterfreund, A.R. et al. (1984) Proc. Lunar Planet Sci. Conf. XV, this volume.

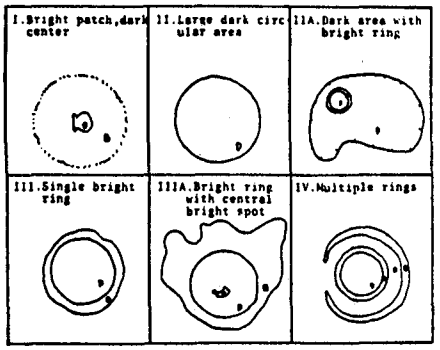

FIGURE 1. Classification of circular features on Venus

Venus Gravity: Global field results

N.A. Mottinger, JPL; W.L. Sjogren, JPL; B.G. Bills, L.P.I.

The Pioneer Venus Orbiter has provided a vast amount of gravity data, since March 1979. High resolution results were first to be extracted (Phillips et al., 1979; Sjogren et al., 1980; Reasenberg et al., 1981). They revealed the high correlation between topography and gravity. These data were acquired at relatively low spacecraft altitudes (150km) where atmospheric effects and high frequency variations were significant and modelling with global spherical harmonics was difficult. During 1982 data were acquired over a complete Venus rotation where the lowest altitudes were 1000km or more, thus removing atmospherics and high frequency gravity effects. It is these data that have been reduced to produce a tenth degree and order spherical harmonic model of the global gravity field of Venus (publication now in press, J. Geophysical Research).

The gravity information is extracted from the orbiting spacecraft Doppler radio signals as it is tracked by earth-based radar antennae. The system is capable of measuring spacecraft speeds to 1mm sec^{-1} over 10 second periods, producing acceleration profiles accurate to a few milligals. There were 78 orbits of data which were uniformly distributed in longitude to provide 40,000 observations.

The reduction technique used a least squares approach where 78 independent arcs of data were combined in a simultaneous inversion. The Williams et al. (1983) gravity field was used as the base model with very large apriori uncertainty. Only one iteration of forming the partial derivatives and residuals was necessary, for the new gravity model essentially removed all systematic signatures in the data. Initially the residuals were systematic with 50mm sec^{-1} signatures, but these were reduced to 1-2mm sec^{-1} which is comparable to plasma effects and the high frequency noise in the system.

The tenth degree and order gravity field solution has 117 parameters describing the spherical harmonic coefficients. This provides approximately 1800km feature resolution. These coefficients are presented as a geoid map in figure 1 (i.e. 20m contours of equal potential off a reference sphere). The uncertainties in the contours are largest in the high latitude regions (15-30m) due to the large eccentricity of the orbiter. The uncertainty near the equator is 5-10 m.

The geoid contours overlay a topographic map produced by the radar altimeter (Pettengill et al., 1980). It is not entirely obvious from figure 1 that the gravity highs correspond to topographic highs and the lows similarly correspond. However, the colored topography version in Pettengill et al. makes it clearly evident. Features such as Beta Pegio (25N,285E), Aphrodite (5S,90E), Atla (0,200E), Ishtar (65N,0E), Sedna Planitia (45N,320E) and Niobe Planitia (20N,130E) are all within definitely defined contoured areas. This agrees with previous results by Sjogren et al., 1980, 1983, and Reasenberg et al., 1981, 1982. The amplitudes are reduced due to the smoothing of the spherical harmonic resolution. Evaluation in the polar regions reveals nothing unusual. There is a sizeable positive anomaly near 75S,240E. suggesting a highland area.

This new reduction now allows one to investigate isostasy on a global scale. An Airy type compensation model was assumed and the spectral admit-

tance (i.e. the ratio of gravity to topography) was computed for each degree. The best match of the Airy model to the spectral admittance profile occurred near a 200±40km depth of compensation. Compensation at such great depth almost surely implies a significant contribution from dynamic processes since the temperature regime would seem to preclude sufficient long term strength for purely static support over geologic time. The isostatic anomaly map which shows regional departures from the global average indeed reveals that there are many departures above and below the 200km average. Beta and Atla have large positive departures whereas parts of Aphrodite and Ishtar has negative departures. Both of these results are consistent with previous local anomaly studies (Esposito et al., 1982, and Sjogren et al., 1984).

The oblateness of Venus is given by the second degree harmonic $J_2 = (4.52 \pm .15) \times 10^{-6}$. This is consistent with the Russian value of $(4.0 \pm 1.5) \times 10^{-6}$ (Akim et al., 1978). Other second degree harmonics determine the orientation of the principal axes of the moments of inertia. It is determined that the axis of greatest moment of inertia is 2.6° off the spin axis of Venus. Although this seems large it is energetically equivalent to the Chandler wobble on Earth. There is also the near alignment of the axis of least inertia with the location of the sub-Earth point at the time of the next particularly close inferior conjunction with Earth on December 16, 2101. This may indicate a high order spin-orbit resonance with Earth.

References

Akim, E.L., Z.P. Vlasova, and I.V. Chuiko, Determination of the dynamical flattening of Venus from measurements of the trajectories of its first artifical satellites, Venera 9 and 10, Sov. Phys. Dokl. 23, 313-315, 1978.

Esposito, P.B., W.L. Sjogren, N.A. Mottinger, B.G. Bills, and E. Abbott, Venus Gravity: Analysis of Beta Regio, Icarus 51, 448-459, 1982.

Pettengill, G.H., E. Eliason, P.G. Ford, G.B. Loriot, H. Masursky, and G.E. McGill, Pioneer Venus radar results: Altimetry and surface properties, J. Geophys. Res. 85, 8261-8270, 1980.

Phillips, R.J., W.L. Sjogren, E.A. Abbott, J.C. Smith and R.N. Wimberly, Gravity Field of Venus: A preliminary analysis, Science, 205, 93-96, 1979.

Reasenberg, R.D., Z.M. Goldberg, P.E. MacNeil, and I.I. Shapiro, Venus gravity: A high resolution map, J. Geophys. Res., 86, 7173-7179, 1981.

Reasenberg, R.D., Z.M. Goldberg, and I.I. Shapiro, Venus: Comparison of gravity and topography in the vicinity of Beta Regio, Geophys. Res. Lett., 9, 637-640, 1982.

Sjogren, W.L., R.J. Phillips, P.W. Birkeland, and R.N. Wimberly, Gravity anomalies on Venus, J. Geophys. Res. 85, 8295-8302, 1980.

Sjogren, W.L., B.G. Bills, P.W. Birkeland, P.B. Esposito, A.R. Konopliv, N.A. Mottinger, R.J. Phillips, and S.J. Ritke, Venus gravity anomalies and their correlations with topography, J. Geophys. Res. 88, 1119-1128, 1983.

Sjogren, W.L., B.G. Bills, and N.A. Mottinger, Venus: Ishtar Gravity Anomaly, Geophys. Res. Lett. 11, 489-491, 1984.

Williams, B.G., N.A. Mottinger and N.D. Panagiotacopulos, Venus gravity field: Pioneer Venus Orbiter navigation results, Icarus 56, 578-589, 1983.

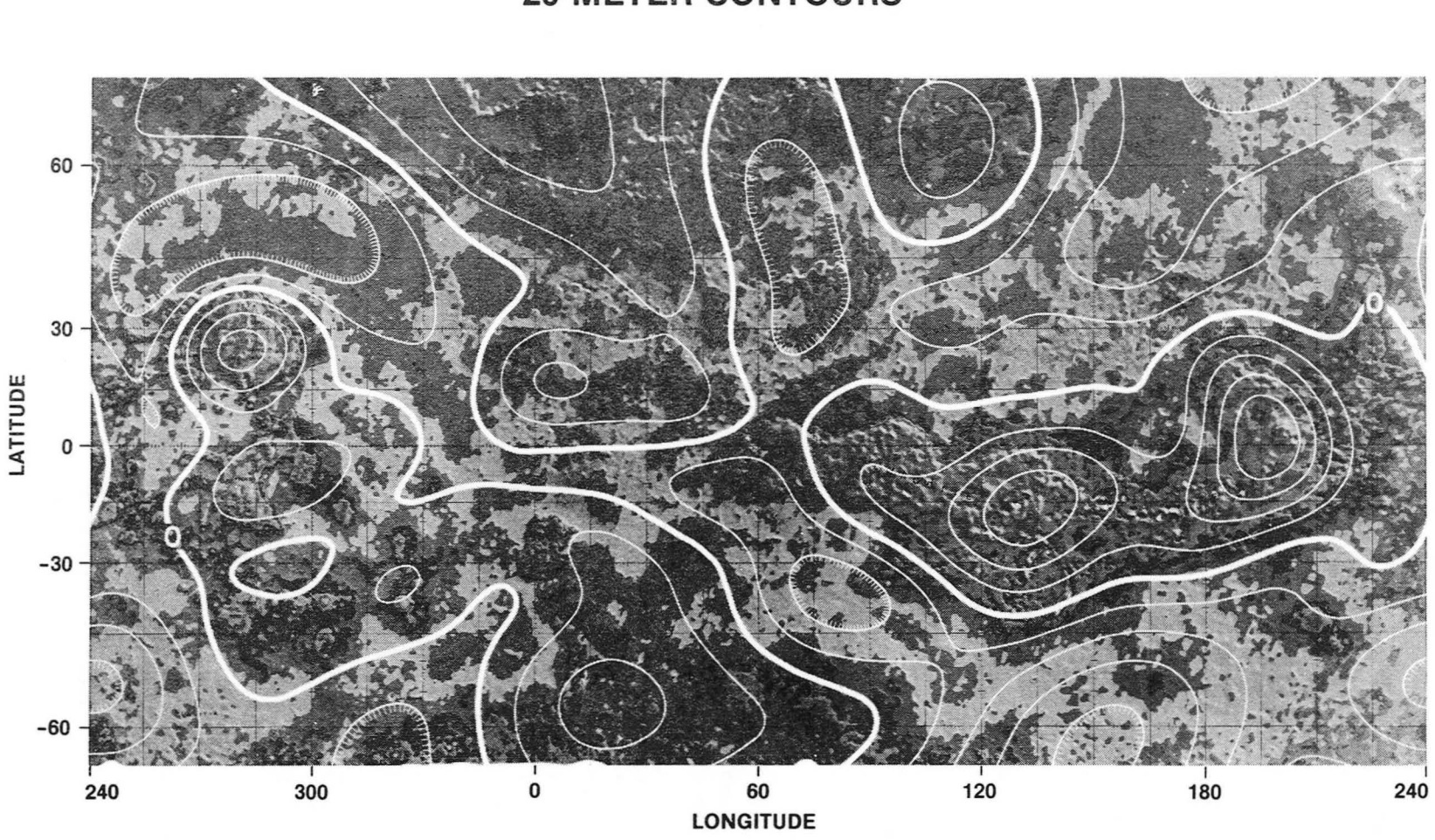
VENUS GEOID
20 METER CONTOURS
60
30
0
-30
-60
LATITUDE
240
300
0
60
120
180
240
LONGITUDE

Figure 1

GEOPHYSICAL INTERPRETATION OF VENUS GRAVITY DATA

R. D. Reasenberg, Smithsonian Astrophysical Observatory

Our principal scientific objective remains the investigation of the subsurface mass distribution of Venus through the analysis of the data from Pioneer Venus Orbiter (PVO). In particular, we use the Doppler tracking data to map the gravitational potential, which we compare to the topographic data from the PVO radar (ORAD). In order to obtain an unbiased comparison, we filter the topography obtained from the PVO-ORAD to introduce distortions which are the same as those of our gravity models.

Both the gravity and filtered-topography maps are derived by two-stage processes with a commond second stage. In the first stage, the PVO Doppler tracking data are analyzed by a Kalman filter which solves the nonlinear spacecraft state estimation problem. The filter can analyze a long span of data without the accumulation of model error and thus avoids the two usual problems of short-arc analysis: (a) The orbital element estimates tend to absorb the gravity signatures of interest; and (b) There is a tendency toward degeneracy and unstable solutions such that some good data must be discarded. The residuals from the Kalman filter are sequentially differenced to yield Doppler-rate residuals which are needed for the second stage. Also in the first stage, the topography is used to calculate a corresponding spacecraft acceleration under the assumptions that the topography has a uniform given density and no compensation. In the second stage, the acceleration measures found in the first stage are passed through a linear inverter to yield maps of gravity and topography. Because these maps are the result of the same inversion process, they contain the same distortions; a comparison between them is unbiased to first order.

We have applied our analysis system to a region covering approximately the longitude range from 125 to 350 deg E longitude at the equator. Over this range we now have a gravity map and a correspondingly smoothed topography map. (Figure 1.) We have found the spectral admittance $Z(\lambda)$ in 40 x 40 deg windows between -5 and 35 deg N latitude and at 10 deg longitude intervals over the region studied.

Throughout the analysis range, we find a strong positive correlation between topography and gravity. However, the details of the correlation change with longitude (Reasenberg and Goldberg, 1984). In a 50 deg longitude span west of Beta Regio, we find $Z(\lambda)$ is consistent with Airy compensation at a depth of 50 km (See Figure 2) [Goldberg and Reasenberg (1984a)]. Some aspects of this work were presented at the May 1984 Meeting of the AGU in Cincinnati [Goldberg and Reasenberg, 1984b; Reasenberg and Goldberg, 1984]. It is shown in Goldberg and Reasenberg [1984a] that our inversion technique produced a relatively undistorted gravity map in this region, notwithstanding that the observing geometry was particularly poor: As seen from the sub-spacecraft point, Earth was never more than 30 deg above the horizon.

We have used the Airy model to determine the "effective compensation depth" d_c as a function of wavelength λ and longitude. With the exception

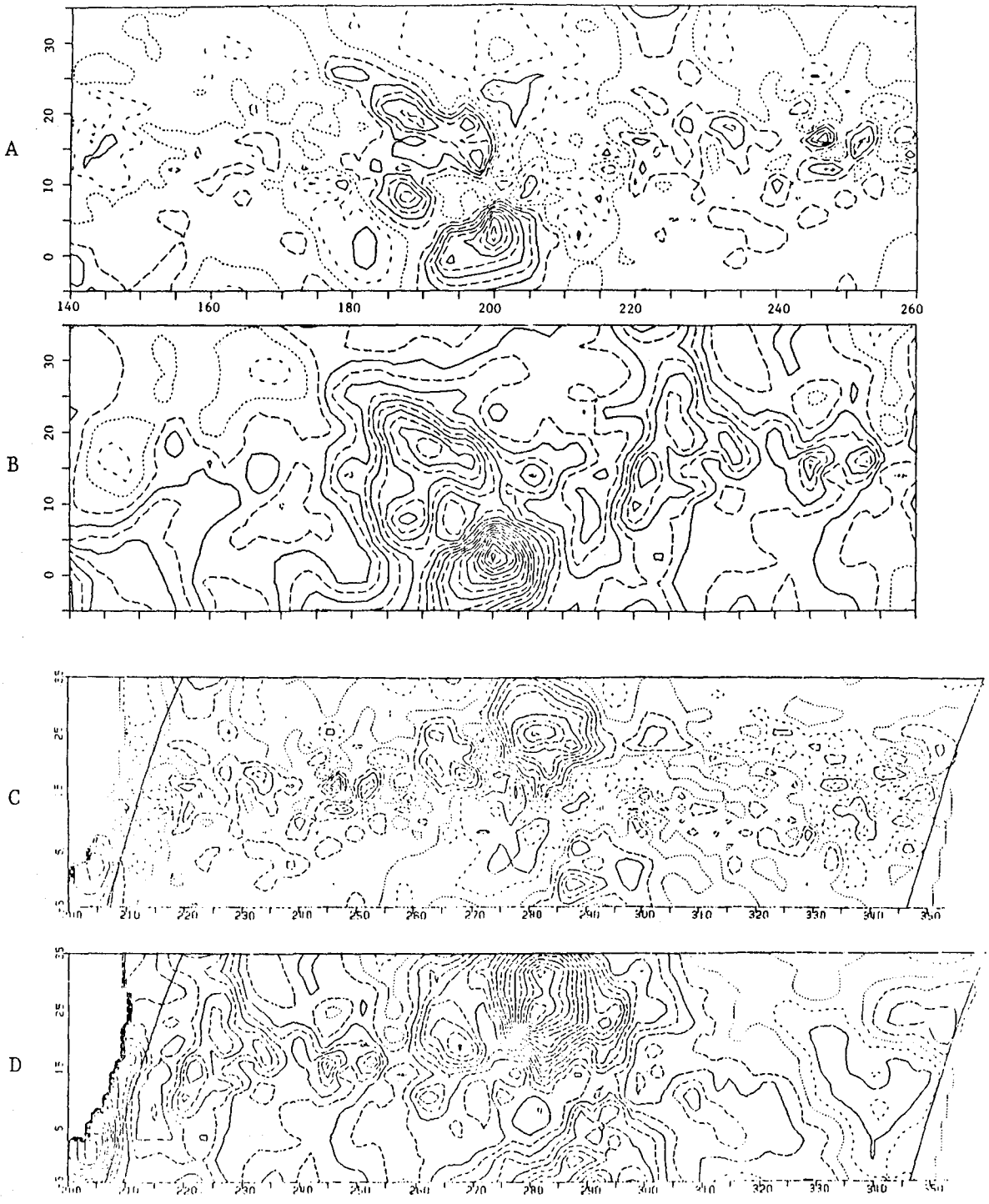

Figure 1. Contour maps of gravity (A and C) and smoothed topography (B and D) for the region of Venus near the PVO periapsis. The zero contours are represented by finely dotted lines, the odd positive contours by long dashes, and the odd negative contours by shorter dashes.

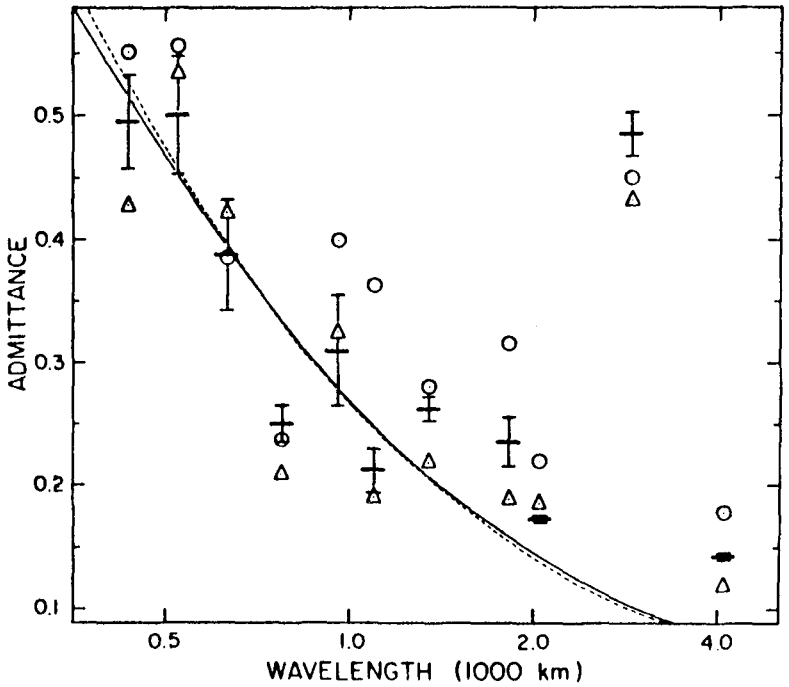

Figure 2: Spectral admittance for a region west of Beta Regio. The long horizonal bars show the admittance; the shorter bars, the standard deviation due to data noise, as determined by a Monte Carlo simulation. The variance due to geophysical "noise" is suggested by the open circles (triangles) which show the admittance taken from a region of identical size and shape, but shifted 5 deg to the east (west). The solid curved line is the theoretical admittance due to Airy compensation at a depth of 50 km, assuming the density of the surface material has the nominal value of 2.6 g/cm^3. The dashed curve is for Airy compensation with surface material of density 3.0 g/cm^3, at a depth of 42 km. An increase (decrease) in the depth of compensation would correspond to a shift of these curves to the right (left).

of the 50 deg span mentioned above, we find that d_c varies monotonically with λ. The most plausible explanation for this signature seems to be that there is an inhomogeneous upwelling of material providing "dynamic support" for the topography. Further interpretive work is in process with a detailed model as its objective.

References

Goldberg, Z. M. and R. D. Reasenberg, Venus Gravity West of Beta Regio, submitted to Icarus, 1984a.

Goldberg, Z. M. and R. D. Reasenberg, Venus: High Resolution Gravity Map for the East End of Aphrodite Terra, EOS, 65, 232, 1984b.

Reasenberg, R. D. and Z. M. Goldberg, Spectral Admittance of East Aphrodite, Comparison with Other Regions of Venus, EOS, 65, 232, 1984.

GRAVITY FIELD OF VENUS AND COMPARISON WITH EARTH

Carl Bowin, Geoffrey Abers and Loren Shure
Woods Hole Oceanographic Institution, Woods Hole, MA 02543

The acceleration (gravity) anomaly estimates by spacecraft tracking, determined from Doppler residuals, are components of the gravity field directed along the spacecraft-earth line-of-sight (LOS). These data constitute a set of vector components of a planet's gravity field, the specific component depending upon where the earth happened to be at the time of each measurement, and they are at varying altitudes above the planet surface. From this data set we have solved for the gravity field using the method of harmonic splines (Shure, Parker and Backus 1982; Parker and Shure, 1982; Shure, Whaler, Gubbins and Hobbs, 1983) which imposes a smoothness criterion to select a gravity model compatible with the LOS data. To apply the exact method is computationally unfeasible. It requires the solution of a square system of equations which has dimensions equal to the number of data (D). Since there are approximately 140,745 points over most of Venus between -45 and +70 latitude, manipulation of a matrix of nearly 20 billion elements would be required for the most rigorous solution. Even the reduced LOS data set of 9,364 measurements used in this study would require manipulation of a system of over 87 million elements which also is not practical with our computers. A modification in which the number of basis functions is reduced (to P) requires the solution of a D x P system, then iteratively P x P systems. The resolution at the planet's surface resulting from reducing the model to a few hundred of these functions would be about 5000 km. Clearly, the data have more detailed valuable information, thus leading us to a piecewise solution instead of a more satisfying single global solution. In this piecewise solution, we find models region by region which are piecewise harmonic and sub-optimally smooth. Given the piecewise model it is now possible to upward and downward continue the field quantities desired with a few parameters unlike some other methods which must return to the full dataset for each desired calculation.

Although the total range of anomalies at 300 km altitude is similar for both the earth ($\pm$20 mgal) and Venus ($\pm$25 mgal), their relationships to topographic features are markedly different. On the earth, the large broad gravity and geoid anomalies show little relationship to the locations of continents, the planet's largest topographic features. This is especially clear in geoid maps. These relations on the

earth have been explained (Jordan, 1978; Bowin, 1983, in press) by mass anomalies deeper than 600 km in the lower mantle and at the core-mantle boundary region that contribute most significantly to geoid anomalies, and lithosphere mass anomalies contributing most significantly to gravity anomalies. On Venus, however, virtually all the positive gravity and geoid anomalies correlate well with positive topographic features, which results in a positive mgal/km slope. For Venus the geoid and gravity anomalies appear to be due principally to mass anomalies associated with surface topographic features. Thus, mass anomalies in about the outer 600 km (26.9% of volume) of Venus are inferred to be the source for its geoid and gravity anomalies, whereas the earth's geoid and gravity anomalies may result from mass anomalies in the outer 2900 km (83.8% of volume) of the planet. If the mass anomalies of Venus occur principally in the outer 200 km, as we suggest in this study, then Venus' geoid and gravity anomalies principally arise from only 9.6% of the volume of the planet. Possible contributions from deep mass anomalies unrelated to surface structures must be minor.

Gravity to topography relations for twelve regions on Venus were analyzed and all show positive slopes of gravity and topography. The magnitudes for the slopes lie in two groups. One has high slopes of 12 to 18 mgal/km, and the other has lower slopes ranging from 5 to 9 mgal/km. Beta Regio Sappho, North Atla, and South Atla all lie within the high slope group, and Beta and South Atla also have the largest magnitude positive anomalies in the constant altitude maps.

The mass anomalies of the high-slope group are greater than would be anticipated from their topographic expression relative to that for Aphrodite and the other features of the low-slope group. The larger gravity anomalies that occur on Venus for the low-slope group, relative to those on earth for similar sized features, can be explained in the case of Aphrodite by a much thicker crust (70-80 km) on Venus than on earth (5-40 km) (Bowin, 1983). The eclogite transition would be expected to be depressed to a greater depth than on earth because of the higher crustal temperatures for Venus, thereby perhaps permitting a greater thickness of basaltic crust to develop.

A possible explanation for the high-slope group, which we consider likely, leads to the assumption that the features of the high-slope group are younger than the rest of the positive topographic features. A viscous relaxation response

to new surface loads, from recent eruptions, for example, would result in the crust temporarily sustaining a greater load than at eventual equilibrium. During that time, those features would have higher admittance relations than for features that previously attained isostatic equilibrium. Lightning in the vicinity of Beta Regio and south Atla suggests that they are volcanic constructs presently active (Bowin, 1983), as possibly do the recent variations in the abundance of atmospheric sulfur dioxide (Esposito, 1984). A combination of broad surface uplift from thermal expansion at depth and recent volcanic surface loading, may explain the high gravity anomalies observed at Beta Regio and south Atla.

References

Bowin, C.O., Depth of principal mass anomalies contributing to the Earth's geoidal undulations and gravity anomalies. Mar. Geodesy, 7, 61-100, 1983a.

Bowin, C.O., Global gravity maps and the structure of the earth, In: The Utility of Regional Gravity and Magnetic Anomaly Maps (SEG), in press.

Bowin, C.O., Gravity, topography and crustal evolution of Venus. Icarus, 56, 345-371, 1983

Esposito, L.W., Sulfur dioxide: episodic injection shows evidence for active Venus volcanism. Science, 223, 1072-1074, 1984.

Jordan, S.K., Statistical model for gravity, topography, and density contrasts in the earth, J. Geophys Res., 83, 1816-1824, 1978).

Parker, R.L. and L. Shure, Efficient modeling of the earth's magnetic field with harmonic splines. GRL 9, No. 8, 812-815, 1982.

Shure, L., R.L. Parker, and G.E. Backus, Harmonic splines for geomagnetic modeling. PEPI, 28, 215-229, 1982.

Shure, L., K. Whaler, D. Gubbins, and B. Hobbs, Physical constraints for the analysis of the geomagnetic secular variation. PEPI, 32, 114-131, 1983.

THE SUPPORT OF LONG WAVELENGTH LOADS ON VENUS.

W. Bruce Banerdt and R. Stephen Saunders, Jet Propulsion Laboratory, California Institute of Technology, Pasadena, CA 91109

One of the great surprises of the Pioneer Venus mission was the high degree of correlation between topography and gravity found at all wavelengths [1]. This implies a close relationship between topography and lateral subsurface density anomalies, such as those due to passive or dynamic compensation [2], and indicates that sources at great depth do not contribute significantly to the gravity field [3].

If all density anomalies are assigned to the crust and upper mantle and lateral movements (such as plate tectonics) are excluded, global stress trajectories can be computed for various modes of topographic support. These stress trajectories can then be compared with observed tectonic features in order to constrain models of the planet's interior [4].

Assuming a Sleep-Phillips [5] type compensation model with a variable crustal thickness and a variable upper mantle density, we have used thin shell theory [6] to investigate three "end member" cases: 1) loading by topographic construction, resulting in a downward deflection of the surface (no mantle support); 2) completely compensated support of a constructional load (no surface deflection); 3) topography due entirely to upward deflection of the surface supported by a low-density upper mantle (no surface load). Case 2 can be further subdivided into lithospheric compensation, for which the elastic lithosphere must be thick enough to include the upper mantle density anomaly (typically a few hundred kilometers), and sub-lithospheric compensation in which only normal stresses from upper mantle buoyancy are transmitted across the bottom of the lithosphere. All models were required to simultaneously satisfy the observed Venusian topography [7,8] and gravity [9] through harmonic degree and order 7. Figures 1, 2, and 3 show the stress field, upper mantle density anomaly, and crustal thickness anomaly for a completely compensated sub-lithospheric support model with a crustal thickness of 50 km, lithosphere thickness of 100 km, and upper mantle thickness of 300 km.

The stress patterns generated for these three cases are markedly different, and should provide some clear diagnostic information on types of support when coupled with tectonic observations. Unfortunately, global resolution at present is sufficient to delineate only the largest rift systems. What observations are available tenatively suggest that Venus falls somewhere between case 2 and case 3, implying some degree of dynamic or thermal support [10,11,12]. It is not yet possible to confidently rule out lithosphere-only compensation based on correlations of stress trajectories with tectonic features alone. However, the data do suggest that the sub-lithospheric component of support is important, perhaps even dominant. This conclusion is strengthened by thermal and mechanical constraints on Venus' elastic lithosphere thickness [10,13,14] which indicate thicknesses of 10-100 kilometers. In general our models imply relatively thick crust and dense upper mantle for Ishtar Terra and Ovda Regio (western Aphrodite), thinned crust and buoyant upper mantle for Tethus Regio and regions near Sappho and Alpha Regio, and a nearly uniform crust with a buoyant upper mantle for Beta Regio and Atla Regio (eastern Aphrodite).

These findings are consistent with the interpretation of lightning bursts observed over Beta and central and eastern Aphrodite (but not western Aphrodite) being associated with active volcanism [15]. Western Aphrodite, although elevated, appears to have a thicker crust and higher density (colder) mantle and thus would not be a likely site of recent volcanism under our

interpretation of these models. Atla, Thetis, and Beta Regione overlie low density (hotter) mantle, making active volcanism more likely. This type of reasoning would also lead one to expect volcanic activity in Tethus and Eisila Regione.

Ishtar Terra appears to have no appreciable mantle density anomaly. Together with the thicker crust, this would seem to indicate a low probability for recent volcanic activity. However, our stress models predict generally radial tensile features, while Maxwell, Akna, and Freyja Montes are indicative of a concentric compressive regime. Thus our models probably do not apply to Ishtar.

Passive and dynamic support do lead to different regional stress systems; with passive support stresses are determined by the geoid [5], while dynamic support implies topographically controlled stresses. Since there are significant deviations from a one-to-one correlation of gravity and topography on Venus (even though the overall degree of correlation is high) it should be possible to constrain models for various regions using high resolution images from earth-based radar, Venera 15/16, and Venus Radar Mapper as they become available.

REFERENCES: [1] Sjogren et al., JGR, 85, 8295, 1980; [2] Phillips et al., Science, 212, 879, 1981; [3] Kaula, GRL, 11, 35, 1984; [4] Banerdt et al., JGR, 87, 9723, 1982; [5] Sleep and Phillips, GRL, 6, 803, 1979; [6] Vlasov, General Theory of Shells, NASA TT F-99, 1964; [7] Pettengill et al., JGR, 85, 8261, 1980; [8] Bills and Kobrick, man. in prep., 1984; [9] Mottinger et al., EOS, 64, 865, 1983; [10] Phillips and Malin, Venus, 159, 1983; [11] Morgan and Phillips, JGR, 88, 8305, 1983; [12] Spohn and Schubert, Tectonophys. 94, 67, 1983; [13] Anderson, GRL, 7, 101, 1980; [14] Solomon and Head, JGR, 89, 6885, 1984; [15] Scarf and Russell, GRL, 10, 1192, 1983.

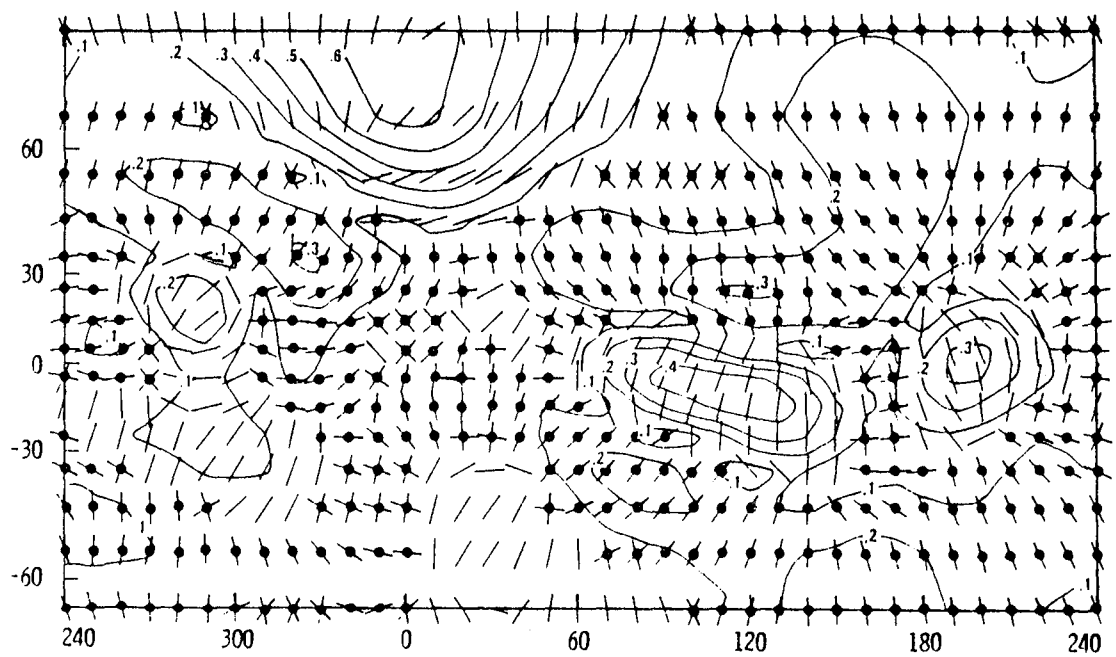

FIGURE 1. Stresses for a completely compensated sub-lithospheric support model. Lines with filled circles indicate compression, those without indicate tension. Contours show magnitude of maximum stress difference in kbar.

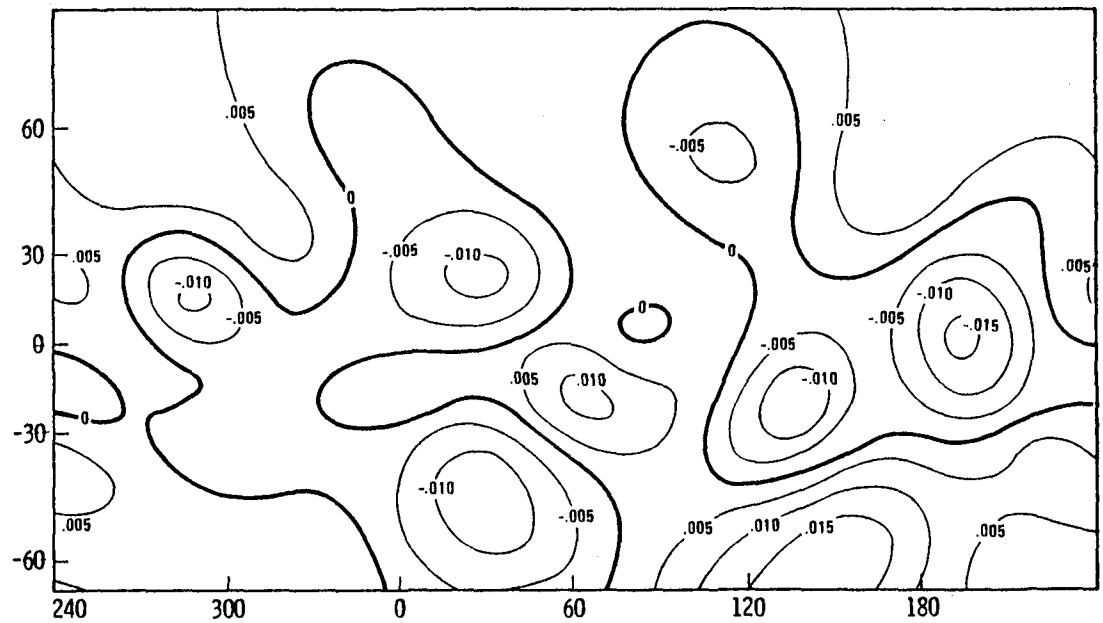

FIGURE 2. Mantle density anomaly for model of figure 1. Units are gm/cm^3.

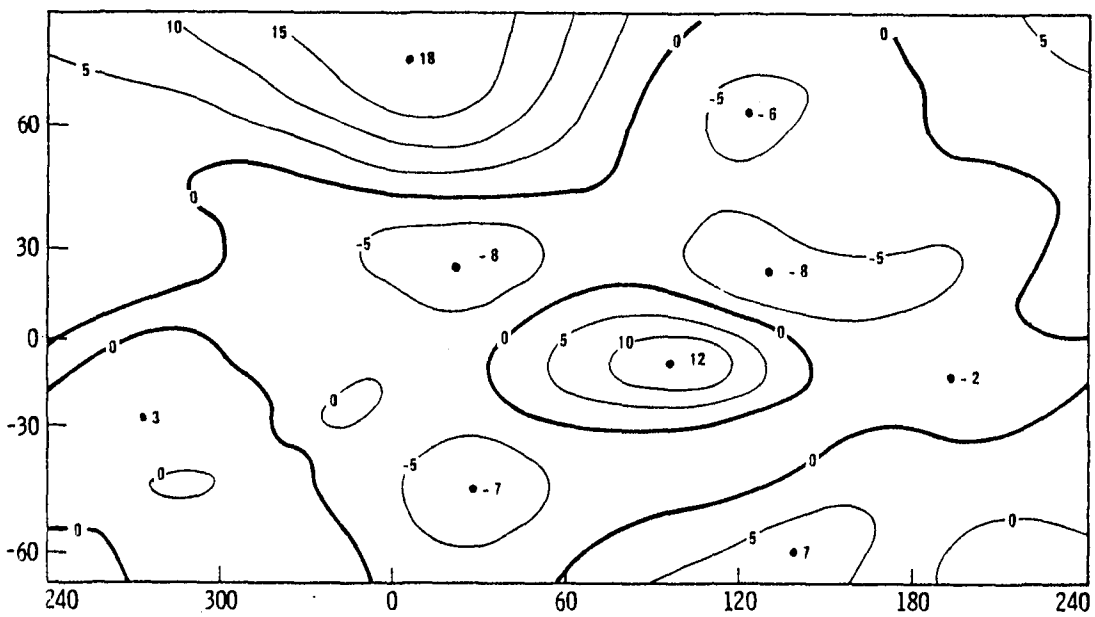

FIGURE 3. Crustal thickness anomaly for model of figure 1, including contributions from both surface and "Moho" relief. Units are kilometers.

VENUS CHASMATA: A LITHOSPHERIC STRETCHING MODEL. Sean C. Solomon, Dept. of Earth, Atmospheric, and Planetary Sciences, Massachusetts Institute of Technology, Cambridge, MA 02139; and James W. Head, Dept. of Geological Sciences, Brown University, Providence, RI 02912.

Introduction. An outstanding problem for Venus is the characterization of its style of global tectonics, an issue intimately related to the dominant mechanism of lithospheric heat loss [1]. Among the most spectacular and extensive of the major tectonic features on Venus are the chasmata, deep linear valleys generally interpreted to be the products of lithospheric extension and rifting [2-5]. Systems of chasmata and related features can be traced along several tectonic zones up to 20,000 km in linear extent [5]. We have developed a lithospheric stretching model to explain the topographic characteristics of Venus chasmata and to constrain the physical properties of the Venus crust and lithosphere.

Chasma Characteristics. Major systems of chasmata, readily identified from Pioneer Venus topographic data [2,3], are located in the Beta and Phoebe highland regions [4] and along the Aphrodite-Beta and Themis-Atla tectonic zones in the Venus equatorial highlands [5]. Smaller chasms have been identified elsewhere on the basis of radar imaging data [6]. Among the principal highland regions of Venus [7], Ishtar Terra may be distinguished as the only large highland area apparently lacking major rift structures.

Topographic profiles across major chasmata have similar characteristics from region to region [2-5]. The rift valleys are typically 75-100 km in width. The floors of the chasmata are up to 2.5 km deeper than ambient terrain levels, and the rims of the rifts are generally raised by 0.5 to 2.5 km. Because of the large footprint and spacing of the altimetry data [3], the rift widths may be slightly overestimated, and the maximum relief of rims and chasma floors may be somewhat greater than indicated here.

A major question is the relative contribution of volcanic construction and thermal uplift to the observed rim heights. New high-resolution radar images of the rift system in central Beta Regio have allowed the tentative identification of a number of individual volcanic constructs along the boundaries of the rift [8] and an assessment of their relationship to local topography [4]. On the basis of these new data, the regions of maximum rim height appear to coincide with volcanic constructs; and rim heights are no more than 1-1.5 km in areas without discernible constructional contribution [8].

Previous Models. The principal model proposed in the literature to explain the characteristics of Venus chasmata is the Vening-Meinesz graben model [5]. For this model to predict the correct width of the rift valley or graben, however, the local thickness of the elastic lithosphere must be 45-70 km [5]. Such a great thickness for the elastic lithosphere of Venus is extremely unlikely; on the basis of laboratory data and the high surface temperature of Venus, the elastic lithosphere can be shown to be no more than a few kilometers in thickness [9].

Lithospheric Stretching Model. We therefore propose a lithospheric stretching model to explain the topographic characteristics of highland rifts on Venus. Such models have been applied successfully to explain the structures and subsidence histories of continental basins and rifted continental margins on Earth [10-12]. We adopt the two-layer lithospheric stretching model of Turcotte [11]. According to this model, a crust of thickness C_o and density ρ_c and a lithosphere of thickness L_o (including the

crust) is stretched under extension to new crustal and lithospheric thicknesses C and L. There is a resulting subsidence

$$s = \frac{(\rho_m - \rho_c)}{\rho_m} C_o (1 - \beta_c) - \frac{\alpha}{2} (T_m - T_o) L_o (1 - \beta_L) \quad (1)$$

where $\beta_c = C/C_o$ and $\beta_L = L/L_o$ are thinning factors for the crust and lithosphere, T_m and ρ_m are the temperature and density of the asthenosphere, T_o is the surface temperature, and α is the volumetric coefficient of thermal expansion for the lithosphere. The first term in (1) represents the isostatic result of crustal thinning; the second term represents the thermal result of lithospheric thinning.

We adopt the view that the width of the region of thinned lithosphere beneath a Venus rift is greater than the width of the region of significantly thinned crust; rifts on the Earth appear to be consistent with this premise [12]. By this view, the total rim-to-floor relief, excluding volcanic construction, across a rift on Venus is a measure of crustal thinning. Setting the first term in (1) equal to 3.5 to 4 km, and assuming $\rho_m = 3.4$ g/cm^3 and $\rho_m - \rho_c = 0.4$ g/cm^3, gives $C_o(1-\beta_c) = 30$-34 km. Since $\beta_c \geq 0$, a minimum thickness for the pre-rift highland crust on Venus is 30 km. A rift developed in a region of significantly thinner crust, perhaps including the Venus lowlands and midland plains [7], would be expected to display lesser relief than do the highland chasmata.

The height of the non-constructional portion of the raised rim of a chasma is, by the present model, a measure of lithospheric thinning and associated thermal uplift [13]. Setting the second term in (1) equal to 1 to 1.5 km, and adopting $\alpha = 3 \times 10^{-5}$°K^{-1} and $T_m - T_o = 10^3$°K, gives $L_o(1-\beta_L) = 70$ to 100 km. Since $\beta_L \geq 0$, the pre-rift thermal lithosphere is at least 70 km thick. It should be noted that the uplift attributed here to lithospheric thinning is in addition to any thermal contribution to the broad topographic rise of highland topography [14]; i.e., the thermal lithosphere would have to exceed 70 km in thickness if a portion of the topographic rise of a rifted highland is attributed to a broad area of heating and thinning of the thermal lithosphere.

Conclusions. A lithospheric stretching model can account for the topographic characteristics of Venus rift structures and, in addition, provides new bounds on the thickness of the crust and thermal lithosphere in the Venus highlands. Unresolved by this study is the causative mechanism for rift formation, but the great length of ridge systems and the inferred thermal component of uplift point to a global-scale and currently active tectonic process. The lack of major rift structures in Ishtar Terra provides additional support for the hypothesis [9] that the most recent tectonic activity in that highland area has been dominantly compressional.

References: [1] S.C. Solomon and J.W. Head, JGR, 87, 9236, 1982; [2] G.H. Pettengill et al., Science, 205, 90, 1979; [3] G.H. Pettengill et al., JGR, 85, 8261, 1980; [4] G.E. McGill et al., GRL, 8, 737, 1981; [5] G.G. Schaber, GRL, 9, 499, 1982; [6] D.B. Campbell et al., Science, 204, 1424, 1979; [7] H. Masursky et al., JGR, 85, 8232, 1980; [8] D.B. Campbell et al., Science, submitted, 1984; [9] S.C. Solomon and J.W. Head, JGR, in press, 1984; [10] D. McKenzie, EPSL, 40, 25, 1978; [11] D.L. Turcotte, J. Geol. Soc. Lond., 140, 1983; [12] S.J. Hellinger and J.G. Sclater, JGR, 88, 8251, 1983; [13] T. Spohn and G. Schubert, Tectonophysics, 94, 67, 1983; [14] R.J. Phillips and M.C. Malin, in Venus, Ariz., 159, 1983.

A STATISTICAL TREATMENT OF THE REGIONAL SLOPE CHARACTERISTICS OF VENUS AND EARTH. V. L. Sharpton and J. W. Head (Department of Geological Sciences, Brown University, Providence, Rhode Island 02912)

Introduction. Regional slope is a scale-dependent parameter that describes the planar gradient over some (relatively broad) area of topography. As such, it has a fundamental relevance to the geological evolution of a planetary surface: it is controlled by the interaction of those processes which tend to increase or reduce surface relief (e.g. tectonism, volcanism, impact cratering, weathering, viscous relaxation) and in turn, exerts control on the erosion, transportation and deposition of surface materials. We have calculated the regional slope values, measured over 3° by 3° regions, for Venus and Earth. In a companion paper[1], we have presented the regional slope characteristics for the major topographic features discernable at *PV* resolution[2], and compare these with slope features associated with terrestrial landforms. Here we analyze the regional slope frequency distribution information for Venus and Earth and examine the effects on terrestrial regional slope resulting from the removal of the ocean load from sea floor topography. To aid in understanding the nature of the Venus surface, we calculate the *mean* regional slope value of each elevation interval of the *PV* topography.

Method. The method used to calculate the regional slope values for Venus and Earth and the data limitations are summarized in Sharpton and Head[1]. Topography of the *unloaded* Earth was derived in a manner outlined in Head *et al.*[3], using relationships presented in Parsons and Sclater[4] to describe ocean floor elevation as a function of age and distance from the spreading ridge. This topography was then processed in the same manner as the previous topographic data sets. These regional slope data were then used to generate the statistical relationships that follow.

Slope-frequency relationships. Fig. 1 gives the relationship between regional slope and percent surface area for Earth, unloaded Earth, and Venus. The general shape of these curves can be described by a function relating regional slope and percent area of the form $A = k S^{\alpha}$, where A is percent area (expressed as a fraction), S is regional slope in degrees, and k and α are constants. Table 1 gives the values of these constants, as well as the correlation coefficient, mean, median and range for each curve.

The modal regional slope value for the Earth curve is 0.0°, where ~26% of the surface area occurs. For Venus, the mode occurs between 0.07° to 0.1° and includes ~23% of the surface, whereas only ~20% fall in the 0.0° to 0.07° range. The non-zero mode and the lower proportion of 0.0° surfaces in the Venus curve are indicative of a global deficiency in regionally flat surfaces compared to Earth. Surfaces of 0.07° to 0.24° are substantially more abundant on Venus than on Earth. About 66% of the surface of Venus and ~48% of the terrestrial surface have regional slopes falling in this range. The region beyond ~0.24° contains ~14% of all Venus surfaces and ~26% of all Earth surfaces.

The characteristics of the unloaded Earth curve are even less like those of Venus. About 33% of unloaded Earth's surface has 0.0° slope, exceeding the Venus value by ~13%. In the range of 0.07° to 0.24°, there is little variation between the two terrestrial curves; Venus has a significantly larger percentage (~66%) of its total surface within this interval than does the unloaded Earth (~47%). It is only for slopes greater than ~0.3° that the differences between the Venus and Earth distributions are lessened slightly from ~8% (loaded) to ~6% (unloaded).

Mean regional slope vs. elevation. The plot of the Venus mean regional slope (calculated from all regional slope values at a given elevation) as a function of elevation is shown in Fig. 2. Within the lowermost elevations are a few small regions of high mean slope associated with the *chasmata*, and a narrow zone between -1.8 km and -1.0 km where mean slope values increase sharply from ~0.0° to 1.0°. This zone is followed by an elevation range characterized by constant regional slope (~0.1°) extending to elevations of ~0.3 km. From 0.3 km to 3.5 km the regional slope increases consistently with increasing elevation. Above 3.5 km mean regional slope varies widely with elevation but a slight depression in slope is apparent between 3.5 km to 5.0 km corresponding to high plateau regions associated with western Aphrodite, Lakshmi Planum and eastern Ishtar. In the

range 0.3 km to 2.4 km (Fig. 2) the systematic increase of regional slope with elevation can be separated into two zones: a lower zone from -0.3 km to 1.4 km and an upper zone from 1.4 km to 2.4 km. The incorporation of relatively steep highland margin slopes[1] appears to explain the increase in mean slope in the upper zone. The systematic trend across the lower zone, however, reflects the addition of more 0.1° to 0.2° slopes as elevation increases. These slopes are typical of the lowlands and upland rolling plains provinces, and are arranged in systematic patterns separating small zones of 0.0° slope; they appear to be most similar in shape, size and magnitude to the regional slope characteristics of some older folded mountain belts on Earth.[1]

Conclusions. There are significant distinctions between the regional slope frequency distributions of Venus and Earth. Although these differences could be influenced by the presence of a hydrosphere on Earth, they do not appear to be related to the depression of the terrestrial seafloor due to ocean loading. When a correction for ocean loading is applied to the terrestrial data, the variations in the low slope range become more pronounced. The shortage of flat regional surfaces on Venus relative to Earth, suggests that degradation and aggradation processes (e.g. erosion, deposition, volcanic infilling) are relatively ineffective. In addition, the abundance of regional slopes on Venus between 0.07° and 0.24° implies either that surface processes are not effective at reducing slopes beyond this range or that some geological process operates to preferentially generate regional slopes in this range. We are presently comparing Venus regional slopes to those of cratered terrain and volcanic plains on the moon, Mars, and Mercury.

Table 1. Regional Slope-Frequency Distribution Statistics

	k	a	R^2	Mode	Mean	Median	Range
Earth	$10^{-3.11}$	-2.87	0.88	0.00°	0.21°	0.12°	0.0 - 2.4°
Unloaded Earth	$10^{-3.37}$	-3.01	0.89	0.00°	0.16°	0.08°	0.0 - 2.4°
Venus	$10^{-3.81}$	-3.32	0.90	0.09°	0.14°	0.12°	0.0 - 2.4°

Figure 1

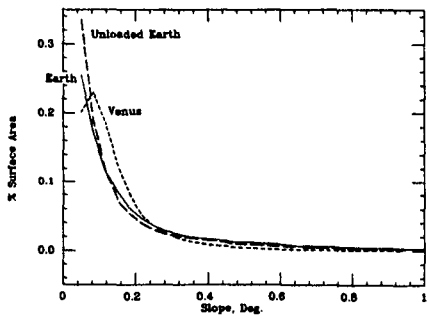

Figure 2. Venus Mean Slope

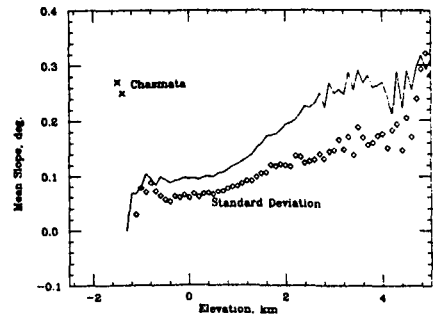

Fig. 1. Slope-frequency curves for Venus, Earth, and Unloaded Earth join discrete groups of data. The first group extends from 0.0° to 0.07° (where curves begin), all other groups are 0.03° wide. *Fig. 2.* Mean slope vs. elevation curve for Venus is represented by solid line. Diamonds give magnitude of standard deviation associated with each mean slope calculation.

References. [1] Sharpton and Head (1984) *this volume.* [2] Pettengill *et al.* (1980) J.G.R. *85*, 8261-8270. [3] Head *et al.* (1981) Am. Scientist, *69*, 614-623. [4] Parsons and Sclater (1977) J.G.R., *82*, 803-827.

RESPONSE OF EARTH'S ATMOSPHERE TO INCREASES IN SOLAR FLUX AND IMPLICATIONS FOR LOSS OF WATER FROM VENUS

James F. Kasting, James B. Pollack, and Thomas P. Ackerman, NASA Ames Research Center, Moffett Field, CA 94035

A one-dimensional radiative-convective model is used to compute temperature and water vapor profiles as functions of solar flux for an Earth-like atmosphere. The troposphere is assumed to be fully saturated, with a moist adiabatic lapse rate, and changes in cloudiness are neglected. Predicted surface temperatures increase monotonically from -1°C to 111°C as the solar flux is increased from 0.81 to 1.45 times its present value. Surface temperatures corresponding to high solar fluxes may be underestimated, however, owing to neglect of H_2O continuum absorption outside of the 8- to 12-μm window region.

These results imply that the surface temperature of a primitive water-rich Venus should have been at least 80°-100°C and may have been much higher. The existence of liquid water at the surface depends on poorly known aspects of H_2O continuum aborption and on uncertainties concerning relative humidity and cloudiness. In any case, water vapor should have been a major atmospheric constituent at all altitudes, leading to the rapid hydrodynamic escape of hydrogen. The oxygen left behind by this process was presumably consumed by reactions with reduced minerals in the crust. Both the loss of oxygen and the presently observed enrichment of the deuterium-to-hydrogen ratio are most easily explained if oceans of liquid water were initially present.

Page intentionally left blank

CHAPTER 4

LUNAR ORIGIN AND SOLAR SYSTEM DYNAMICS

Page intentionally left blank

LUNAR ORIGIN: ROLE OF GIANT IMPACTS*

William K. Hartmann, Planetary Science Institute, Tucson, Arizona 85719.

The impact flux required to accrete Earth's mass during accretion time T = 0.03 to 150 m.y. ranges from some 10^7 to 10^{12} x the present flux.[1] In 1975, Hartmann and Davis[2] suggested that impacts of a large planetesimal(s?) during this period ejected "iron-deficient crust and upper mantle material, forming a cloud of refractory, volatile-poor dust that could form the moon."

The high primordial flux implies 1 impact/week of bodies ranging about 2-50 km across and about 10^{13} to 10^{17} kg. A small fraction of the resulting ejecta reaches near-Earth space, with sub-orbital stay-times of the order of a week. (In fast-accretion models, the "weekly impactors" have dimensions larger than the present atmospheric thickness; they are especially efficient in ejecting debris into near-Earth space.) Therefore, the "weekly impactors" maintain a time-varying circum-Earth swarm or disk; its density needs further evaluation. The swarm may have interacted with incoming material, or accreted onto a small proto-moonlet already (captured?) in orbit.

Less frequent 100+ km impactors ejected transient surges of mass into the circum-Earth swarm. The largest impactors probably approached or exceeded lunar size. One or more giant impacts may have added enough heated, volatile-depleted upper-mantle material (from a magma ocean?) to contribute much of the moon's mass. Lunar formation in such a swarm is supported by Thompson and Stevenson, possibly within 100 yr.[3] If Earth spun rapidly, as in fission models, the largest impact may have introduced enough angular momentum and energy to trigger the ejection/fission event. Impact-induced fission thus overcomes certain problems of classical fission models.

The suggestion by Hartmann and Davis[2] and later by Cameron and Ward[4,5] that lunar origin involved giant impacts remains attractive. Large planetesimals are consistent with current accretion models, and may have been widely scattered in the early solar system; their existence is a reasonable, if not necessary, assumption in moon-origin models. Furthermore, isotopic data require the moon's formation primarily from local material resembling Earth's upper mantle, not material from elsewhere in the solar system. Giant impacts are stochastic, class-predictable events that would provide the required type of ejected Earth-mantle material without requiring large moons to form near other planets (a problem with less stochastic processes). Such material may have mixed with incoming meteorites during lunar formation, affecting lunar chemistry. Further work on this hypothesis should include dynamical studies of whether: (1) some ejected material in each large impact would remain in orbit, causing growth of the swarm; (2) a small moonlet captured or accreted in the swarm could serve as a nucleus to catalyze lunar accretion; (3) spontaneous accretion could yield a moon without a catalyst-moonlet; (4) tidal action could help the primordial moon move outward instead of spiraling in due to drag; (5) Earth's rotation rate or an oblique impact is critical in launching the swarm; and (6) the swarm helps differentiate incoming material, preferentially capturing low-density silicate dust.

*Research conducted in conjunction with the Tucson Lunar Origin Consortium.

References
(1) Hartmann, W.K. (1980) Proc. Conf. Lunar Highland Crust, p. 155-171.
(2) Hartmann, W.K. and Davis, D.R. (1975) Icarus 24, p. 504-515.
(3) Thompson, A. and Stevenson, D. (1983) Lunar Planet. Sci. XIV, p. 787-788.
(4) Cameron, A. and Ward, W. (1976) Lunar Sci. VII, p. 120-122.
(5) Ward, W. and Cameron, A. (1978) Lunar Planet. Sci. IX, p. 1205-1207.

A CIRCUM-TERRESTRIAL COMPOSITIONAL FILTER*

Clark R. Chapman and Richard Greenberg, Planetary Science Institute, Tucson, Arizona 85719.

A major question about the moon is its under-abundance of iron. We seek (as others have before) to understand whether a metal-silicate fractionation of heliocentrically orbiting bodies can be achieved through collisional interactions with a circum-terrestrial swarm. Large, dense metallic cores of disrupted, differentiated planetesimals could pass through such a swarm relatively unimpeded, while silicate fragments would be filtered out and captured by the cloud, which might subsequently accrete into a metal-depleted moon. We envision planetesimals left over during the very late stages of accretion of the Earth, with heliocentric orbits extending a few tenths of an AU beyond the Earth's orbit. These planetesimals may have been heated and geochemically differentiated into silicate bodies with iron cores, just as has apparently happened to a major fraction of the asteroid population. Such bodies would diffuse toward the near-Earth environment. We consider the rates of such diffusion and of the mutual collisional destruction within the population. We then consider the interaction of these differentiated planetesimals and their collisional products (both silicate mantle-fragments and iron cores) with a swarm of Earth-orbiting lunesimals (perhaps ejecta from the Earth) of km-scale, totaling a mass of order 0.1 lunar mass, extending out 10 or 20 Earth radii. We find that such a small near-Earth population of lunesimals can filter out silicate-rich material, while passing iron cores, and form a moon composed partly of terrestrial material, but more substantially of the captured silicate-rich portions of the planetesimals. This silicate-separation process and accretion of lunesimals into the moon must go to completion in a time short compared with 10^7 yr, which is the timescale for the planetesimals to be swept up by, or scattered away by, the Earth.

Our quantatative conclusions are: (1) Silicate fragments will be trapped, while iron cores can pass through the circum-terrestrial swarm dozens of times, taking at least 10^6 yr before being trapped. (2) Until the supply of planetesimals is depleted, it may prevent the circum-terrestrial swarm from accreting: planetesimals larger than 100m in size could fragment rocky-strength lunesimals and would impact them on a timescale shorter than the timescale for accretion of lunesimals (1 year). (3) The iron cores are large and strong enough to withstand collisions with the lunesimal population. (4) If collision velocities among the planetesimals are <300 m/sec, as expected if they are governed chiefly by gravitational interactions with each other (rather than with larger planets), then the planetesimals and iron cores will survive long enough for the segregation process to go to completion. (5) The planetesimals apparently can diffuse toward the Earth's orbit on a timescale of 10^7 yr by their own collisional dissipation; they interact with the circum-terrestrial swarm at velocities of several km/sec, as required for the segregation process. (6) During the course of 10^7 yr, the iron cores will be swept up by the Earth and Venus (or gravitationally scattered away), so little metal will remain for accretion by the moon once the moon forms; the stirring-up of the circum-terrestrial swarm will slow as the cores are depleted, and the moon will accrete. (7) The whole scenario works only if there is a way to maintain the hypothesized circum-terrestrial swarm, which otherwise would collisionally diffuse (much of it collapsing on

the Earth) on a timescale of 10^3 yr; the source of angular momentum to maintain the swarm remains a mystery.[2,3]

*Research conducted in conjunction with the Tucson Lunar Origin Consortium.

References

(1) Greenberg et al. (1978) Icarus 35, 1.
(2) Davis, D.R. and F. Herbert (1984). This conference.
(3) Weidenschilling, S.J. (1984). This conference.

MODELS OF ANGULAR MOMENTUM INPUT TO A CIRCUMTERRESTRIAL SWARM FROM ENCOUNTERS WITH HELIOCENTRIC PLANETESIMALS*

Donald R. Davis and Richard Greenberg, Planetary Sci. Inst., Tucson, AZ 85719
and Floyd Herbert, Lunar and Planetary Lab., Univ. Arizona, Tucson, AZ 85721

Models of lunar origin in which the Moon accretes in orbit about the Earth from material approaching the Earth from heliocentric orbits must overcome a fundamental problem: the approach orbits of such material would be, in the simplest approximation, equally likely to be prograde or retrograde about the Earth, with the result that accretion of such material adds mass but not angular momentum to circumterrestrial satellites. Satellite orbits would then decay due to the resulting drag, ultimately impacting onto the Earth.

In the present work, we investigate one possibility for adding both material and angular momentum to Earth orbit: imbalance in the delivered angular momentum between pro- and retrograde Earth-passing orbits which arises from the three-body dynamics of planetesimals approaching the Earth from heliocentric space. The existence of this imbalance for planetesimals directly striking the Earth and its tendency to be of prograde sense was first demonstrated by Giuli (1968) in numerical computations and later in analytic work by Harris (1977).

In order to study angular momentum delivery to circumterrestrial satellites, we have numerically computed near-Earth velocities as a function of distance from the Earth for a large array of orbits systematically spanning heliocentric phase space. The resulting distribution $f(\underline{v},r,a,e)$ of Earth-passing velocities $\underline{v}$ at each distance r resulting from orbits at each heliocentric a and e together with one of the various plausible assumed heliocentric planetesimal number densities $n(a,e)$ determines the mean velocity near the Earth of all planetesimals from all parts of the feeding zone by $\langle\underline{v}\rangle = \int \underline{v}\, f(\underline{v},r,a,e)\, n(a,e)\, d^2\underline{v}\, da\, de / \int f(\underline{v},r,a,e)\, n(a,e)\, d^2\underline{v}\, da\, de$.

The results of this experiment for most assumed planetesimal distributions produced mean tangential Earth flyby velocities that were positive (prograde) both near the Earth's surface and at distances up to 40 R_E. A constant $n(a,e)$ yielded mean flyby tangential velocities of only a few percent of local circular Earth orbit speed $v_c(r)$, whereas a quasi-thermal distribution around heliocentric eccentricity of 0.03 gave flyby tangential velocities varying from a few to 10% of v_c (at 40 R_E). Raising the mean thermal eccentricity to 0.05 and assuming that planetesimals crossing the Earth's orbit without terrestrial perturbations are reduced in frequency by a factor of 10 produced a mean flyby tangential velocity 20% of v_c at 1 R_E and 30% of v_c at 40 R_E (but about zero at 2.5 R_E). The significance of heliocentric feeding zone weighting is shown in Figs. 1 and 2, which are histograms of the sign of the zonal statistic $\langle\underline{v}(a,e)\rangle$ at 4 R_E, computed by evaluating the above expression over small a and e bins with $n(a,e)$ constant. Figure 2 values are relative to $v_c(r)$, while Fig. 1 refers to a nonrotating frame. These diagrams indicate the heliocentric phase space source regions for significant angular momentum input to the near-Earth region. Therefore, while other weightings of the heliocentric population might increase angular momentum input, Fig. 2 suggests that there is no simple

weighting that would spin up the circumterrestrial swarm.

These preliminary experiments show that heliocentric planetesimals passing through the Earth environment possess significant angular momentum. However, it also appears that these same planetesimals impacting a circularized circumterrestrial planetesimal swarm would likely remove angular momentum (though possibly increasing mean kinetic energy), presumably promoting both swarm infall upon the Earth and escape to heliocentric space. Only a distribution of highly eccentric satellite orbits with mean tangential velocities of a few tens of percent of local circular velocity would be immune against angular momentum loss to passing heliocentric planetesimals.

Another critical issue in the study of planet growth is the statistics of the outcomes of gravitational encounters among planetesimals. These encounters govern the relative velocities among planetesimals that are so critical in determining collision and accretion rates. Gravitational encounters similarly control evolution within the asteroid belt and delivery of meteorites to the terrestrial planets, in effect the last, on-going stage of planetary accretion.

Most analyses of the effects of gravitational encounters have involved statistical treatments in which a swarm of planetesimals is treated as a gas with some thermal velocity representing the relative velocities among the bodies (Greenberg et al., 1978). Another approach has been to integrate numerically the evolution of a swarm of test bodies (Cox et al., 1978). A complementary approach is to consider the full range of geometrical encounters possible for two bodies on intersecting orbits with fixed a, e, and i, but distributed values of the orbital phase angles (Greenberg, 1982). This approach is viable as long as orbital encounters are not tangential (i.e., encounters at an apse of both orbits). In that case, there are difficult analytical singularities. Nevertheless such cases are potentially very important for a number of reasons. For example, a planetary embryo's feeding zone, a region which still needs to be defined meaningfully, is bounded by planetesimals which approach tangentially. Also, asteroidal fragments and new Apollos probably follow orbital evolutionary tracks that remain nearly tangent with the Earth's.

The statistics of tangential encounters need to be developed using numerical integration of the encounter trajectories, both because of the inherent analytical singularities and the slow encounters which tend not to be approximatable by two-body encounters. In cooperation with A. Carusi and G. Valsecchi, we have begun a systematic numerical study of encounter outcomes. For example, we have investigated the case of a Mars-sized planetary embryo at 1 AU interacting with a planetesimal with a = 0.755 AU, e = 0.3, and i = 0.3. Aphelion of the planetesimal is only 1/2 a "Hill sphere" (sphere of influence) radius beyond the embryo's circular orbit. We have mapped the outcomes of over 20,000 numerically integrated encounters, representing a distribution of initial argument of pericenter and mean anomaly. Each integration covered the entire encounter within 50 Hill spheres. Preliminary results indicate a systematic tendency of tangential encounters to reduce orbital inclination. Consideration of properties of the Tisserand invariant suggest this process may play a role in increasing orbital overlap and promoting accretion of planetesimals (or of meteorites at present). Results of this first case are still being interpreted and additional cases, with vary-

ing a, e, i, and mass, are being integrated.

Acknowledgments

The authors thank C.P. Sonett for making computer time available. This work was funded in part by NASA under grant number NASW-3516.

*Research conducted in conjunction with the Tucson Lunar Origin Consortium.

References

Cox, L.P., Lewis, J.P., and Lecar, M. (1978). Icarus **34**, 417.
Giuli, R.T. (1968). Icarus **8**, 301.
Greenberg, R. (1978). Icarus **35**, 1.
Greenberg, R. (1982). Astron. J. **87**, 184.
Harris, A.W. (1977). Icarus **31**, 168.

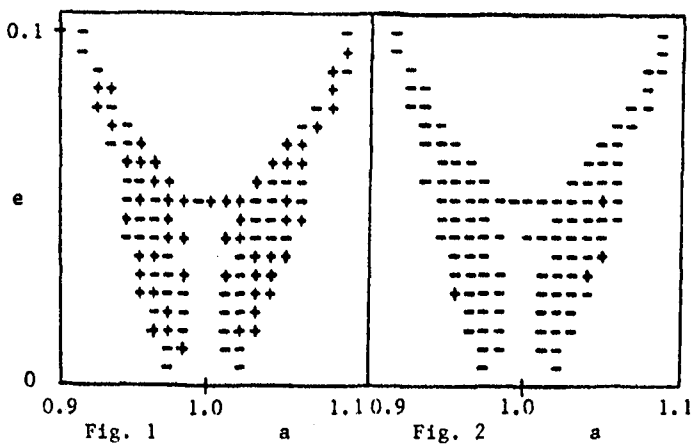

Fig. 1 Fig. 2

Figure 1: A 2-D histogram of the sign of the mean tangential velocity of heliocentric planetesimals passing through the Earth neighborhood at a distance of 4 R_E, expressed as a function of a and e for the heliocentric source orbits. Symbols only appear at positions corresponding to orbits capable of reaching the 40 R_E circumterrestrial disc.

Figure 2: A 2-D histogram the same as Fig. 1, except that the zero of velocity is taken to be (prograde) circular orbit velocity at 4 R_E.

CAPTURE OF PLANETESIMALS INTO A CIRCUMTERRESTRIAL SWARM*

Stuart J. Weidenschilling, Planetary Science Institute, Tucson, Arizona 85719

The lunar origin model considered by the Tucson Consortium[1,2] involves processing of proto-lunar material through a circumterrestrial swarm of particles. Once such a swarm has formed, it can gain mass by capturing infalling planetesimals[3] and ejecta from giant impacts on the Earth,[4] although the angular momentum supply from these sources remains a problem. Here we examine the first stage of formation of a geocentric swarm by capture of planetesimals from initially heliocentric orbits.

The only plausible capture mechanism that is not dependent on very low approach velocities is the mutual collision of planetesimals passing within Earth's sphere of influence. The dissipation of energy in inelastic collisions or accretion events changes the value of the Jacobi parameter, allowing capture into bound geocentric orbits. Ruskol[5] noted that this process is most effective for small bodies with larger area/mass, possibly allowing compositional sorting (e.g., if mean Fe content varies with size).[1,5] She assumed that planetesimals captured in this way would bring net prograde angular momentum sufficient to ensure stable orbits about the proto-Earth.

We have tested this capture scenario directly by many-body numerical integration of planetesimal orbits in near-Earth space. Initial orbits are chosen randomly from a uniform distribution in $\underline{a}$ outside the sphere of influence. The program can integrate up to 200 trajectories simultaneously. For a reasonable chance of collision with this limited number, only the planar case is considered, with approaches within 4×10^9 cm scored as collisions. All collisions result in coagulation. A particle's status, free or bound, is determined by the value of the Jacobi parameter. Collisions within the sphere of influence are scored as free-free, free-bound, or bound-bound. The number of events is severely limited by computer time, but allows some useful conclusions.

With no initial random velocities ($\underline{e} = 0$), 78 free-free collisions yielded 27 captures (35%), 9 prograde and 18 retrograde. A uniform distribution of random velocities up to 0.05 times the heliocentric circular velocity yielded 68 free-free collisions with 14 captures (21%), evenly divided prograde-retrograde. In both cases, free-bound collisions tend to cause captured bodies to spiral inward until accreted by Earth. These results agree with those of Davis and Herbert[3] that the systematic contribution of angular momentum is insufficient to maintain an orbiting swarm under heavy bombardment. Thus, a circumterrestrial swarm can be formed rather easily, but is hard to sustain because the mean net angular momentum of a many-body swarm is small. The requisite angular momentum can be supplied by a single collision (or a few, at most) of large bodies within Earth's sphere of influence. A swarm formed in this way could have subsequently accreted up to several times its original mass without collapsing onto the planet, possibly allowing enough processing of proto-lunar material to produce iron-silicate fractionation.

*Research conducted in conjunction with the Tucson Lunar Origin Consortium.

References
1. Chapman, C. and R. Greenberg (1984). This conference.
2. Greenberg, R. et al. (1984). This conference.
3. Davis, D.R. and F. Herbert (1984). This conference.
4. Hartmann, W.K. (1984). This conference.
5. Ruskol, E. (1972). Izv. Earth Phys. **7**, 99.

ORBITAL RESONANCES AND PLANETARY ACCRETION IN THE SOLAR NEBULA

S.J. Weidenschilling and D.R. Davis , Planetary Science Institute, Tucson, AZ 85719

We have studied planetesimal orbital evolution in a resisting medium near an accreting protoplanet to explore mechanisms for capture into Trojan and satellite orbits. Various mechanisms for capture into libration have been proposed (1), e.g., increase in Jupiter/Sun mass ratio, change in jovian orbital radius, and collisions of asteroids with interplanetary dust. Our studies include effects of solar nebula gas drag on orbital evolution. Since Jupiter is largely composed of gases thought to have been accreted from the solar nebula by a proto-Jupiter core of ~15 $M_\oplus$, any model that considers effects of a growing Jupiter on nearby planetesimals must also consider the effects of the gas on those same bodies. In general, the gas deviates from keplerian motion, causing secular decay of planetesimal orbits, as well as damping eccentricity. We have numerically explored motion of bodies near Jupiter under the effect of a resisting medium. We integrate the equations of motion, using the formalism of the planar restricted three-body problem, modified to include effects by gas drag and a growing Jupiter.

In our tentative scenario for the origin of Trojan asteroids, bodies are first trapped in horseshoe-type libration, then into orbits around a single Lagrange point by an increase in Jupiter's mass. Gas drag causes planetesimals to move inward on decaying orbits until they approach that of Jupiter, providing a steady-state population of temporary horseshoe librators. Accordingly, our numerical experiments started bodies in drag-perturbed orbits outside Jupiter's orbit. An unexpected result was that only a few cases reached Jupiter's orbit; most became trapped in stable resonances. Viewed in the rotating reference frame, the resonant orbits display stationary multi-lobed patterns. They are clearly commensurabilities of the type j:(J+1), with j an integer (the number of lobes = j). Figure 1 shows examples for $\mu = 10^{-4}$, a secondary mass 1/10 that of Jupiter. The phase of each pattern is such that closest approach occurs after conjunction. Each encounter thereby gives the particle additional heliocentric angular momentum that compensates for that lost by drag during a synodic period. As seen in Fig. 1, higher drag tends to yield higher-order resonances for a given μ. These allow closer approaches and a larger angular momentum increment per encounter, which compensates for the longer synodic period. We have also explored the effect of different drag parameters on a single resonance (3:4), at $\mu = 10^{-3}$ (Fig. 2). As drag is increased, the phase of the pattern shifts, decreasing the closest approach distance. The resonance is stable at least over a factor of eight in drag parameter (corresponding to a range of planetesimal size or gas density). The combination of different resonances, and variable phase within each resonance, ensures trapping for a wide range of conditions. As an extreme example, we found a stable orbit in 14:15 resonance for a secondary of 1 $M_\oplus$.

These orbits are examples of an effect predicted by Greenberg (2), who showed that damping of eccentricity near a commensurability would produce a secular change in semimajor axis, pushing a small body away from its perturber. Greenberg considered explicitly only resonances inside the perturber's orbit, to explain the origin of Cassini's division, but the same

formalism applies to external resonances. When there is a secular decrease in semimajor axis due to gas drag, an equilibrium state can be attained in which drag and gravitational torques balance. This equilibrium is stable since the gravitational torque increases closer to exact resonance.

We have performed an analytic investigation of the resonant perturbations, following Greenberg's approach. This reveals that resonantly trapped planetesimals attain equilibrium values of eccentricity, $e \simeq \sqrt{(\Delta V/V_k)(j+1)}$, where ΔV is the deviation of the gas from the Keplerian velocity V_k. Typical nebula models imply $\Delta V/V_k \sim 10^{-2}$, yielding significant values of e. Surprisingly, this result is independent of the perturbing mass, planetesimal size, or gas density. However, all those quantities are important in determining whether a planetesimal can attain equilibrium at any given resonance. In order to be trapped, a planetesimal must exceed a minimum size. For a perturber of 1 $M_\oplus$, bodies $\gtrsim$ a few km in size can be trapped in low-order resonances. For one Jupiter mass, bodies larger than a few meters in size can be trapped.

Our results have important implications for cosmogony. One scenario (3) assumes that the terrestrial planets accreted in the presence of the gaseous nebula, as drag delivered planetesimals into their feeding zones. It might seem that trapping in stable resonances would inhibit planetary growth by preventing planetesimals from approaching the embryos. However, the net effect is the opposite: resonances speed accretion. The reason for this is the large eccentricities of the resonant planetesimals, which lead to relative velocities ~1 km/s in Earth's zone for bodies in different resonances or between resonant and non-resonant objects. Collisions among these bodies result in catastrophic disruption, with fragments small enough to pass through resonances and reach the embryo. Figure 3 shows that all orbits with $j>1$ overlap. Thus, the first-formed embryo will dominate a zone extending outward to at least the 2:3 resonance ($\simeq$1.3 orbital radii). This effect prevents formation of too many small planets that are too closely spaced, compared to the actual solar system. Resonances also lead to shorter accretion timescales. Planetesimal orbits do not need to evolve under the influence of drag all the way to the vicinity of the embryo. Instead, they need only reach the nearest resonance in order to be disrupted; the orbital evolution supplying the fragments to the embryo is much more rapid.

A detailed account of this work has been submitted for publication (4).

References: (1) C.F. Yoder, Icarus 40, 341 (1979). (2) R. Greenberg, Icarus 33, 62 (1978). (3) C. Hayashi, K. Nakazawa, I. Adachi, Pub. Astr. Soc. Japan 29, 163 (1977). (4) S.J. Weidenschilling, and D.R. Davis, Icarus, submitted.

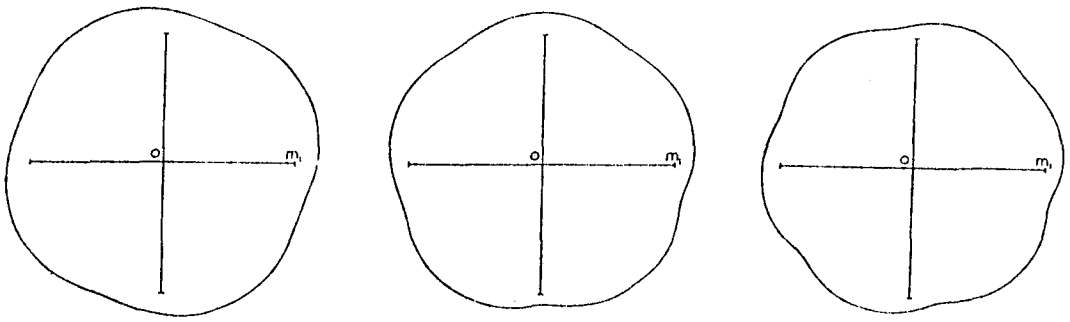

Figure 1: A series of resonant orbits viewed in a rotating frame. In all figures, the sun is at the origin and the perturbing embryo appears fixed on the x-axis at the point labeled m_1. The planetesimal appears to circulate in the clockwise direction. Left to right: 4/5, 5/6, and 6/7 resonances.

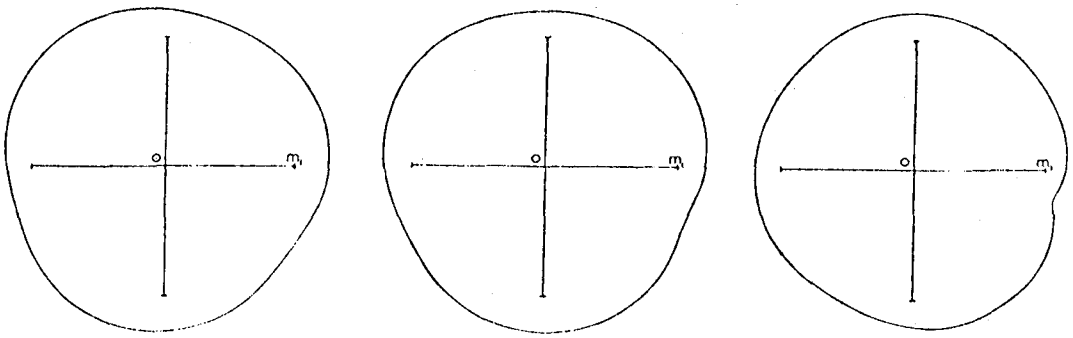

Figure 2: 3/4 resonant orbits with different values of the drag parameter. From left to right, the drag increases by a factor of two at each step. Increasing drag produces a phase shift, allowing closer approaches to the embryo; another doubling of drag results in collision.

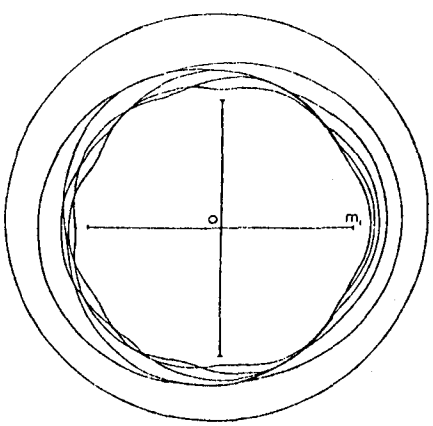

Figure 3: Superimposed orbits of resonances from 1/2 to 6/7. Overlapping orbits lead to collisions between bodies in different resonances.

Accumulation of the Terrestrial Planets
G. W. Wetherill, DTM, Carnegie Institution of Washington

A. The validity of the two-body approximation in calculations of planetary growth. Use of this approximation is essential to practical 3-dimensional "simulations" of planetary growth. There is no reason to believe it is valid at very low velocities. Understanding the range of validity of the approximation, both for gravitational perturbations and impact rates, is therefore essential.

With regard to gravitational perturbations, the changes in semi-major axis, eccentricity, and inclination resulting from close planetesimal encounters (near 1 A.U.) out to 10 Tisserand sphere of influence radii were calculated by two- and three-dimensional numerical integration. These were compared with the results of treating the encounter as a two-body problem, as is customary in Monte Carlo calculations of orbital evolution and in numerical and analytical studies of planetary accumulation. It is found that for values of $(V/V_e) \lesssim 0.35$ (V = relative velocity, V_e = escape velocity of largest body), the two-body approximation fails to describe the outcome of individual encounters. In this low velocity region, the two-body "gravitational focusing" cross-section is no longer valid; "anomalous gravitational focusing" often leads to bodies on distant unperturbed trajectories becoming close encounters and vice versa. In spite of these differences, average perturbations given by the two-body approximation are valid within a factor of two when $V/V_e > 0.07$. In this same velocity range the "Arnold extrapolation", whereby a few very close encounters are used to estimate the effect of many more distant encounters, is found to be a useful approximation.

In addition the validity of the two-body approximation in calculating collisions between planetesimals has been evaluated as a function of the ratio of unperturbed planetesimal velocity (with respect to a circular orbit) to mutual escape velocity when their surfaces are in contact (V/V_e). Impact rates are calculated by numerical integration of the equations of motion. It is found that when $V/V_e > 0.4$, the two-body approximation is a good one. In contrast, at low velocities $(V/V_e < 0.1)$ two-body "collision course" trajectories fail to lead to impacts. On the other hand, at these low velocities many impacts result from encounter trajectories with unperturbed separation distances far beyond the two-body gravitational radius. As a consequence of this "anomalous gravitational focusing" planetesimals will continue to interact even when their orbits are non-crossing. This will tend to reduce the difficulty with premature isolation of planetesimal embryos during accumulation. Quantitatitively, when $0.06 \lesssim V/V_e \lesssim 0.2$, the impact rate varies approximately with the fifth power of the radius of the larger body, and is about a factor of 3 above that predicted using the conventional two-body gravitational cross-section formula. At lower values of V/V_e, the impact rate increases less rapidly. Finally, at the lowest values of V/V_e (<.02), the impact rate increases only in proportion to the geometric cross-section, as a consequence of the swarm being essentially two-dimensional for large unperturbed encounter distances. The gravitational enhancement in

effective cross-section is limited to a value of about 3000. This leads to an optimal size for growth of planetesimals from a swarm of given eccentricity, and places a limit on the extent of runaway accretion. In the range of velocities found in modelling the late (but not necessarily the early) stages of planetary accumulation, the approximation is found to be an acceptable one.

B. The neon inventory of the Earth as predicted by gas-rich accumulation (with H. Mizuno).

For models of planetary accumulation in the presence of solar nebular gas, the initial surface temperature of the Earth is controlled by the grain opacity of the atmosphere. The surface temperature in turn controls the quantity of neon dissolved and trapped within the interior of the Earth. In order to compare accumulation theory with observation calculations have been made of the grain opacity expected to be associated with accumulation in a gaseous nebula. There are two parameters that are in principle determined by the theory, but actually are at present uncertain: the mean eccentricity e of the planetesimal swarm, and the fraction ξ of the accretional energy that is expended in the release of grains into the atmosphere by ablation of the incoming planetesimal. It is found that if the eccentricity of the swarm is low (10^{-1}), rather low values of ξ (10^{-5}) are required to match the observed neon data. In contrast higher values of ξ are required (10^{-1}) for the most probable case, intermediate eccentricity (10^{-2}). For the high eccentricity case ($e = .1$) ξ must be 10^{-2}. The results show that avoidance of excess trapped neon of solar composition places restrictive, but not necessarily impossible, conditions on the parameters of the accumulation theory.

C. The asteroidal source of ordinary chondrites.

A very fundamental question relevant to the era of planetary formation is that of the source of meteorites. Meteorites represent the principal detailed source of knowledge of the solar system during its formation. Identification of the sources of meteorites is required in order to place this knowledge in its planetological context. In this investigation it is shown that asteroids near 2.50 A.U. (3:1 Kirkwood gap) are the probable source of the most abundant class of meteorites, the ordinary chondrites.

The orbital evolution of asteroidal fragments with diameters ranging from 10 cm to 20 km, injected into the 3:1 Kirkwood gap at 2.50 A.U., has been investigated using Monte Carlo techniques. It is assumed that this material can become Earth-crossing on a time scale of 10^6 years, as a result of a chaotic zone discovered by Wisdom, associated with the 3:1 resonance. This phenomenon, as well as close encounter planetary perturbations, the $\dot{\nu}_6$ secular resonance, and the ablative effects of the Earth's atmosphere are included in the determination of the orbital characteristics of meteorites impacting the Earth derived by fragmentation of this asteroidal material. It is found that the predicted meteorite orbits closely match those found for observed ordinary chondrites, and the total flux is in approximate agreement with the observed fall rate of ordinary chondrites. About 10% of the predicted impacting bodies are meteorite-size bodies originating directly from the asteroid belt. The

remainder are obtained by subsequent fragmentation of larger (~1 m to 20 km diameter) Earth-crossing asteroidal fragments. The largest of these fragments are observable as Apollo-Amor objects. Thus the apparent paradox between the orbital characteristics of observed ordinary chondrites and those predicted from Apollo object sources is reconciled. Both appear to be complementary aspects of the same phenomena. No other asteroidal resonance is found to be satisfactory as a source of ordinary chondrites. These meteorites are therefore most likely to be derived from asteroids in this limited region of the asteoridal belt, the largest of which are 11 Parthenope, 17 Thetis, and 29 Amphitrite.

EVOLUTION OF GRAINS IN A TURBULENT SOLAR NEBULA

S.J. Weidenschilling, Planetary Science Institute, Tucson, AZ 85719

Planetesimal formation by gravitational instability of a dust layer requires a non-turbulent solar nebula. Motions of the gas at more than a few cm/s would stir up the dust layer too much. Safronov (1) maintained that there was no energy source to drive turbulent motion. His conclusion has been challenged by others (2-5) who model the solar nebula as a turbulent, convective accretion disk. Self-consistent models of a convective disk depend on high opacity of the disk material, which must be provided by grains. Models using opacity coefficients that are functions of temperature only involve the implicit assumption that the dominant mass is in particles small compared to the relevant wavelengths of radiation. Coagulation of grains could render that assumption invalid. Grain coagulation is implied by the requirement of forming planetesimals, as the turbulent velocities (~ 1/3 sound speed) in the accretion disk would disrupt any dust layer. Planetesimal formation must commence during the turbulent stage; otherwise, by the time the disk became optically thin due to viscous spreading, it would not contain enough mass to form the planetary system. Two scenarios are possible: Collisional coagulation could form large planetesimals, simultaneously leaving a sufficient fraction of matter in small grains to maintain the nebula's opacity. Or, coagulation of grains into small (~cm) aggregates could lower the opacity enough for turbulence to decay. Larger bodies would then form by low-velocity collisions or gravitational instability in the quiescent disk.

I have calculated numerically the evolution of a population of grains in a turbulent solar nebula. A detailed description of the method and results is in press (6). This is a 1-D calculation of coagulation and vertical transport. The disk is divided into discrete layers; in each, the grain size distribution is represented by the population in a series of discrete size bins. During each timestep, changes in the size distribution due to collisions are computed for each layer. Then particles in each size range are transported between layers by vertical mixing. In the nonturbulent case, the transport is downward only, due to settling toward the central plane. Turbulence allows the possibility of upward motion as well.

The vertical structure of the nebula is assumed adiabatic. Calculations were performed at two radii, r = 2 AU and 30 AU, well away from major condensation boundaries. The central temperature and surface density were chosen to match the evolutionary model of Lin and Bodenheimer (4). The opacity is due to solid grains, which are primarily water ice at 30 AU, and an iron-silicate mixture at 2 AU. For grains smaller than $\lambda_c = 0.29/T$ cm, the wavelength of peak block-body flux at temperature T, opacity is proportional to mass concentration of grains, independent of their size distribution. I adopt expressions for opacity that are equivalent to those used by Lin and Bodenheimer in the limit of small grains. However, grain aggregates larger than λ_c contribute to opacity by geometric extinction, which does depend on the size distribution. The effective IR absorptivity is chosen empirically so that the opacity is continuous when the particle size equals λ_c. Thus, the opacity remains constant until some particles grow to a critical size, and then begins to drop as coagulation produces still larger aggregates.

The turbulent velocity Vt of the gas is parameterized as a function of

the local sound speed. The turbulence has a finite range of scales. The largest eddies are ~disk thickness H in size, with turnover time ~1/Ω. Their energy cascades through a spectrum of smaller eddies to a size where viscous dissipation is important. Dimensional arguments (7) give an energy dissipation rate that sets the length, time, and velocity scales of the smallest eddies. In the model nebula, these are of the order of a few km, a few hours, and tens of cm/s, respectively.

Turbulence gives the particles random motion with respect to the mean gas flow. Völk et al. (8) express the rms velocity as a function of the ratio of the response time of the particle to gas drag, te, to the timescale of the largest eddies, tk~1/Ω. For te/tk <<1, the particle velocity ⟨Vd⟩ governing turbulent diffusion is ~Vt, while for te>> tk, ⟨Vd⟩ ~Vt(tk/te). Systematic motions become important for bodies large enough that te/tk is not negligible. Mass transport between levels is due to both systematic and random velocities. When te/tk is not too small, the transport rate is computed explicitly. When te/tk <<1, this procedure is subject to numerical instabilities (the net turbulent flux is the small difference between large quantities). To avoid this, when te/tk <0.1, the dust/gas mixing ratio in that size range is simply assumed constant. In practice, this means aggregates must reach sizes >1 cm before they begin to concentrate toward the central plane.

Relative velocities between grains control the rate of collisions and their outcomes. I use expressions for relative velocity as a function of particle size and turbulent gas velocity developed by Völk et al. (8). Their expressions are valid when the grain response time t_e, exceeds the eddy lifetimes. We note that the smallest eddies have lifetimes ~hours, so their results are not valid for grains or aggregates smaller than ~100 μm. I have developed an expression valid in that regime, based on the fact that the gas is continually accelerated by the eddies. Particles of different sizes experience differential accelerations due to drag as the gas changes velocity. This effect dominates over thermal motion, systematic settling, or laminar shear in producing relative velocities.

Collisional outcomes are modeled more realistically than in earlier calculations of this type, which assumed coagulation or some arbitrary "sticking efficiency". The present model includes catastrophic disruption of aggregates when collisional energy exceeds a selected impact strength, and erosion in subcatastrophic collisions. The collision strength of aggregates is estimated from unpublished data of W.K. Hartmann for impacts into powdery regoliths.

Results: Numerical simulations show that turbulence greatly increases the rate of collisions over that in a similar but non-turbulent disk. The coagulation rate for small grains is increased accordingly. Aggregates reach sizes ~0.1-1 cm in a few tens of orbital periods. Relative velocities increase with size, so erosion and disruption prevent formation of larger bodies when plausible impact strengths (10^4-10^5 erg cm^{-3}) are assumed. The aggregates are too small to settle to the central plane of the disk, so planetesimal formation is impossible while turbulence persists. However, the formation of aggregates reduces the opacity of the disk. Some combinations of opacity law and surface density make the disk optically thin, which would cut off turbulence produced by the convective instability mechanism. Thus, the solar nebula may have experienced alternating periods of turbulence and quiescence, as grains were depleted by coagulation and replenished by infall from the presolar cloud.

References: (1) V.S. Safronov, NASA TTF-677 (1972). (2) D. Lin, J. Papaloizou, MNRAS 191, 37 (1980). (3) D. Lin, Ap. J. 246, 972 (1981). (4) D. Lin, P. Bodenheimer, Ap. J. 262, 768 (1982). (5). G. Morfill, W. Tscharnuter, and H. Völk, Ap. J., in press (1984). (6) S.J. Weidenschilling, Icarus 44, in press. (7) H. Tennekes, J. Lumley, A First Course in Turbulence, MIT Press (1972). (8) H. Völk, F. Jones, G. Morfill, S. Röser, Ast. Ap. 85, 316 (1980).

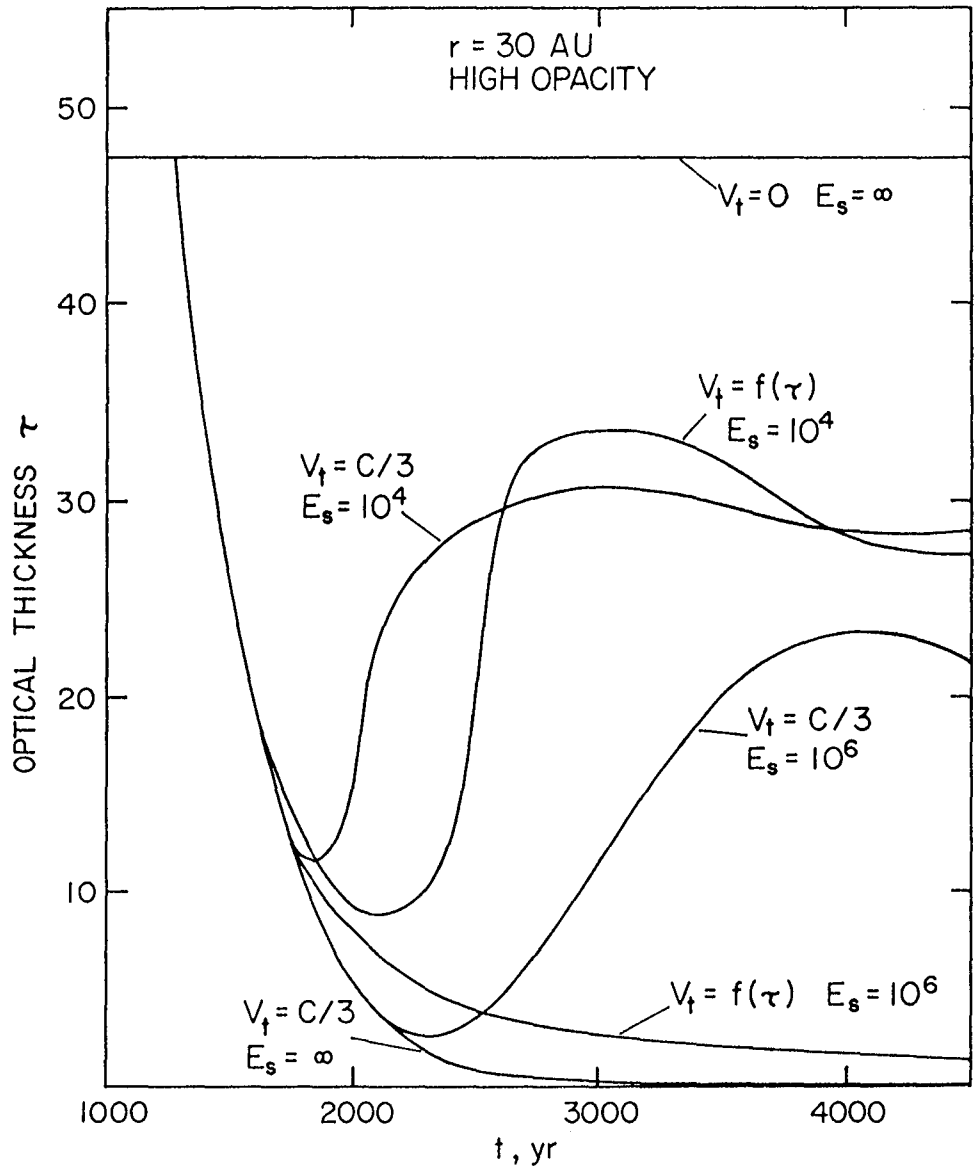

Figure 1: Evolution of the disk optical thickness at r = 30 AU, for various assumptions as to turbulent velocity V_t and aggregate impact strength E_s (erg cm^{-3}). V_t is expressed in terms of the sound speec C. $V_t = f(\tau)$ corresponds to an assumed functional dependence for which the turbulent velocity decreases with decreasing optical thickness.

THE FORMATION OF PREPLANETARY DISKS FROM THE COLLAPSE OF ROTATING MOLECULAR CLOUD CORES

Patrick Cassen, Theoretical Studies Branch, NASA-Ames Research Center, Moffett Field, CA 94035; Frank H. Shu and Susan Terebey, Astronomy Dept., University of California, Berkeley, CA 94720.

An understanding of the origin of the Solar System will require a theory of the formation of protostellar disks that can be tested by astronomical observations of young stellar objects and protostars. Such a theory should, of course, be consistent with known properties of the Solar System, but should also provide a guide for future observations and form part of a general theory of star formation. In view of the lack of concensus regarding the general properties to be expected of a nebular disk, in spite of the many numerical treatments of hydrodynamic collapse that have been published in the last decade, our approach was to design and solve a problem that is physically realistic but amenable to rigorous analysis without resort to cumbersome numerical effort. The solutions that we found describe the collapse of a molecular cloud core that is initially in unstable equilibrium, embedded within an envelope of uniform density, and rotating at the same rate as the envelope. The calculations provide a self-consistent description of dynamical collapse from intestellar dimensions to those of the Solar System (see Terebey et al., 1984). We exploited the facts that (1) the densest parts of these cores contain sufficient mass to make stellar objects, but contain much less rotational energy than gravitational energy, so that a "small rotation" limit is appropriate, and (2) an exact analytic solution for the non-rotating collapse has been previously worked out (Shu, 1977). Thus, we have solved the problem by performing a perturbational analysis valid in the limit of slow rotation. The hydrodynamic equations, including self-gravity, are reduced to a set of ordinary differential equations, which is solved by the method of matched asymptotic expansions.

The problem thus formulated and solved has several advantages over previous treatments of protostellar cloud collapse. First, the calculation starts from an exact equilibrium which appears to be a realistic representation of cloud cores as determined by observations of CO and NH3 molecules. Second, since we consider the collapse of an embedded core, the problem of artifically imposed outer boundary conditions does not arise, as it does in calculations that consider the collapse of a cloud fragment. The mass of the star being formed is assumed to be limited by the onset of a stellar wind, which overcomes the accretion when the protostar's energy of differential rotation is released. Third, solutions are easily found for a wide variety of cloud parameters without recourse to extensive numerical computations. Indeed, one of the primay goals of this work was to be able to identify the conditions under which different types (i.e., massive or low mass) of disks and stars would form. This can be done because the collapse solutions have inner limiting forms that attach smoothly to our previously derived solutions for the buildup of protostars and protostellar disks (Cassen and Moosman, 1981, and Cassen and Summers, 1983, Cassen, et al., 1983).

The main results of these calculations can be summarized as follows:

(1) There is a natural limiting mass to the components of a stellar (or star plus planetary) system, related to the angular velocity and sound speed of the molecular cloud from which the system forms, and to the protostellar radius, a quantity that has been fairly well-constrained by recent work on protostellar structure (e.g., Stahler et al., 1980 and Mercer-Smith et al., 1984). The range of stellar masses so derived seems to correspond to realistic ranges of observed stellar masses and interstellar cloud parameters.

(2) In highly dissipative disks there is a tendency to concentrate the angular momentum of the system into a small fraction of the mass, thereby favoring the formation of planetary systems, such as the Solar System. In systems for which the dissipation rate is low, division of the mass into comparable fractions (e.g., binaries) is favored. The proper measure of dissipation rate is the ratio of accretion time to viscous diffusion time.

(3) The pressure distribution on the surface of an accreting protostar is nonuniform in a way that favors the channeling of a stellar wind into a bipolar flow preferentially directed along the rotation axis. The energy of differential rotation within the protostar is sufficient to power such a wind upon rearrangement of internal angular momentum (as induced, for instance, by the onset of convection due to deuterium burning).

(4) The angular momentum of an accreting protostar grows to a value of the order necessary to cause dynamic instability to non-axisymmetric modes. The importance in this is that a distorted, rotating protostar could lose angular momentum to its surrounding disk by gravitational torques associated with spiral density waves. In such circumstances, the disk material would spread as it gained angular momentum from the protostar. Such a mechansim would effectively reduce the dissipation time in the disk, and therefore lead to conditions favoring the formation of planets, as mentioned in (2) above.

REFERENCES

Cassen, P. and Moosman, A. (1981) On the formation of protostellar disks, Icarus, 48, 353-376.

Cassen, P and Summers, A.L. (1983) Models of the formation of the solar nebula, Icarus, 53, 26-40.

Cassen, P., Shu, F.H., and Terebey, S. (1985) Protostellar disks and star formation. To be published in "Protostars and Planets II," Univ. of Arizona Press.

Mercer-Smith, J.A., Cameron, A.G.W., and Epstein, R.I. (1984) On the formation of stars from disk accretion. Astrophys. J., 279, 363-366.

Shu, F. (1977) Self similar collapse of isothermal spheres and star formation, Astrophys. J., 279, 363-366.

Stahler, S.W., Shu, F.H., and Taam, R.E. (1980) The evolution of protostars. I. Global formulation and results. Ap. J., 241, 637-654.

Terebey, S.; Shu, F.H.; and Cassen, P. (1984) The collapse of the cores of slowly rotating isothermal clouds, Astrophys. J. (in press).

RESEARCH ON THE EARLY HISTORY OF THE SOLAR SYSTEM

A.G.W. Cameron, Harvard-Smithsonian Center for Astrophysics

The principal scenario for the early history of the solar system which I have been considering had its genesis in my calculations of the evolution of a dissipating turbulently viscous disk of gas and dust formed during the collapse of an interstellar cloud fragment.

During the last two years William Cabot has been a postdoc here doing research on the turbulent properties of an accretion disk. Cabot showed in his thesis that meridional circulation currents are not very strong and that they can give rise only to a very weak turbulence. More recently, since he has come here, he has shown also that turbulence can only very weakly arise from baroclinic instabilities. [3] The probability now seems to be that none of the instabilities that are known to be possible in subadiabatic regions of stellar interiors will give rise to vigorous turbulence.

Meanwhile, Vittorio Canuto and some of his colleagues in New York have developed a new theory which relates the rate of turbulent dissipation to the growth rates of the largest eddies in the disk, and the results support a high value for the "alpha" dissipation parameter used in accretion disk theory (Astrophys. J., **280**, 55L, 1984). Bill Cabot was drawn into this work some time ago and has gone beyond the Canuto results in that he has investigated the effects of nonaxisymmetric modes in the development of thermal convection, finding that they tend to be somewhat more effective than the axisymmetric modes investigated by Canuto et al. This raises the probable value of alpha above the Canuto value.

Based on these results and on the new insight into the disk dissipation processes that depend on these results, I have recently carried out some new calculations on modelling the inner parts of the primitive solar nebula subject to the assumption of a steady inward mass flow. The results show a very hot inner region of the nebula at the peak rates of mass dissipation and allow the categorization of the evolution of the primitive solar nebula to be made in terms of three main evolutionary stages. The first stage is cool and dispersed, the second stage is hot and mass flow is rapid, and in the third stage mass flow ceases and the nebula tends to resemble the low mass nebula which has been popular among other workers in recent years. These results were reported at the Protostars and Planets II conference and the last Lunar and Planetary conference, and they are given in detail in a chapter for the Protostars and Planets II book.

Let me digress for the moment to mention some recent work on the early evolution of the sun carried out by J.A. Mercer-Smith in collaboration with me. Although these calculations were carried out using a one-dimensional stellar evolution code, boundary conditions were imposed to roughly simulate the accretion of a star from an accretion disk. These conditions were a time scale for mass accumulation onto the star and an assumption about how the rotational energy transported into the star was divided between being radiated away from the surface and being carried away by the mechanisms that transport angular momentum out of the star. The observational condition to be matched was the present distribution of T Tauri stars in the Hertzsprung-Russell diagram. A successful matching of these observations occurred if it was assumed that the rate of mass accumulation was much higher at the end of the process than at the start (we actually assumed in this case that the rate of mass accumulation was proportional to the elapsed time up until the end of accretion). The luminosity of the protosun was at least 20 times the present value throughout most of the latter part of its accumulation. In the most meaningful cases the outer convection zone of the sun did not develop until accumulation ceased. Thus it is reasonable to assume that the T Tauri stage of the sun started at the end of the accumulation process. [1,10]

These various developments have led me to the following picture for the evolution of the primitive solar nebula. When material starts to accumulate in the nebula from the collapse

of a fragment of an interstellar cloud, there is little mass present and the material is spread out and subject to large fluctuations due to the turbulent motions of the infalling material. This is when gravitational instabilities have a chance to form giant gaseous protoplanets in this inner region. Any such protoplanets will be thermally stripped of their envelopes, but cores of precipitated solid materials may survive. As the infall proceeds, the solar nebula becomes more regularized, turbulence develops throughout, and dissipation to form the sun takes place. As the inward flow of mass near the center occurs, the gravitational bonds there are strengthened, and material of given specific angular momentum spirals inwards, thus increasing the surface density of the disk. The rate of dissipation appears to be a strong function of the surface density for most temperature-density regimes, so that the rate of mass flow to form the sun rapidly increases. When the infall of material from the interstellar cloud abates, the dissipation of the solar nebula runs the surface density down to a fairly low level at which the characteristic time for further dissipation becomes quite long. At this time the high luminosity of the protosun, which is embedded in a dusty environment in which gaseous infall has not entirely ceased, will begin to impose quite high surface temperatures on the upper surfaces of the nebula. I expect that this will become sufficient to suppress superadiabatic gradients in the interior of the nebula, and hence to suppress the turbulence, and hence to stop the dissipation of the nebula. There should then follow a fairly long period in which a thermally-stabilized solar nebula of one percent or less of a solar mass (in the planetary region) exists until removed probably by the effects of the T Tauri solar wind. [5,6,7]

Some time ago, Bill Ward and I discussed a scenario involving the formation of the Moon as a result of a major collision with the protoearth. As the result of the collision, much of the rocky mantles of both the protoearth and the projectile will be vaporized, condensing into small particles upon vapor expansion, with a fraction of these small particles being left in orbit about the protoearth as a flattened disk. Fluctuations within the disk can lead to tidal interactions and significant evolution of the structure of the disk in quite a short time. This should lead to the spreading of the disk beyond the Roche limit of the Earth, where gravitational instabilities should lead to a rapid collection to form the Moon. Because of the expected condensed cores within the protoearth and the projectile, and the high thermal bath in which this entire process takes place, the Moon so formed should be greatly depleted in both metallic iron and more volatile elements. [2,9,11]

A major question in this scenario is the efficiency for putting collision products into the orbiting disk about the protoearth. I have investigated this by generalizing to three dimensions a code which does a particle simulation of hydrodynamics with dissipation, and using it to simulate the expansion of the vaporized component of the rocky mantles that takes place during the collision. After expansion and recondensation of the vapor into small particles the mean free path of the particles remains quite small, and so hydrodynamic methods can still be used to examine the motion for some time after the collision. A large number of cases has been calculated, in which the parameters that were varied included the initial geometric distribution of the vaporized rock, the collision velocity, the internal energy of the vapor, and the extent to which the surviving projectile mass may exert a gravitational pull on the vapor cloud. It was found that an adequate amount of mass and angular momentum to form the moon were easily placed into the orbiting disk in a large fraction of the calculated cases. [8]

I have also done a multidisciplinary study which relates processes in dense interstellar molecular clouds with the properties of one solar mass stars in the late stages of evolution, with the formation of the primitive solar nebula and with the presence of extinct radioactivities in it. This study started with a consideration of the dense cores present throughout the interiors of dense molecular clouds and asked how such cores were likely to be made. A consideration of the various types of stellar-induced disturbances that can arise

in the interior of such clouds indicated that the primary candidate of interest for an event leading to the formation of the sun would be an asymptotic giant branch star of approximately one solar mass in the last stages of its evolution, when it casts off a planetary nebula. Such a star is likely to produce significant quantities of all of the extinct radioactivities whose decay products we study in solar system materials, including those which had hitherto been considered to be primarily products of supernova explosions. The mass ejected from this star is redirected along the magnetic field lines within the cloud, forming a pair of cores. After collapse and internal star formation, the early T Tauri wind from the newly-formed stars can similarly induce the formation of additional cores within the cloud. Each generation of star formation dilutes the fraction of the extinct radioactivities (then live) within the gas. After some five or six generations of this star formation the abundances of the radioactivities are down to the level found in the solar system. The calculated abundances of the extinct radioactivities are in satisfactory mutual agreement and the observed abundances of these radioactivities are plausibly reproduced. [4]

RELEVANT REFERENCES

1. Cameron, A.G.W., and Mercer-Smith, J.A. 1983. "Behavior of the Sun during growth from the primitive solar nebula", Lunar and Planetary Science XIV, p. 88.

2. Cameron, A.G.W. 1983. "Origin of the atmospheres of the terrestrial planets", Icarus, **56**. 105.

3. Cabot, W., 1984. "The nonaxisymmetric baroclinic instability in thin accretion disks", Astrophys. J., 277, 806.

4. Cameron, A.G.W., 1984. "Star formation and extinct radioactivities", Icarus, in press.

5. Cameron, A.G.W., 1984. "Formation and evolution of the primitive solar nebula", Protostars and Planets II, University of Arizona Press, in press.

6. Cameron, A.G.W., 1984. "The Rapid Dissipation Phase of the Primitive Solar Nebula", Lunar and Planetary Science XV, The Lunar and Planetary Institute, Houston, TX, p. 118.

7. Cameron, A.G.W., 1984. "Conditions during formation of the earth", Workshop on the Early Earth, Lunar and Planetary Institute, Houston, TX, p. 11.

8. Cameron, A.G.W., 1984. "Formation of the prelunar accretion disk", Conference on the Origin of the Moon, Lunar and Planetary Institute, Houston, TX, p. 58.

9. Cameron, A.G.W., and Ward, W.R. 1976. "The origin of the moon", Lunar Sci. VII, 120-122, LSI, Houston.

10. Mercer-Smith, J.A., Cameron, A.G.W., and Epstein, R.I. 1984. "On the formation of stars from disk accretion", Astrophys. J., 279:363-366.

11. Ward, W.R., and Cameron, A.G.W. 1978. "Disc evolution within the Roche limit", Lunar Planetary Sci. IX, 1205-1207, LPI, Houston.

VIKING RADIO SCIENCE DATA ANALYSIS AND SYNTHESIS

I.I. Shapiro and R.D. Reasenberg
Smithsonian Astrophysical Observatory
Harvard-Smithsonian Center for Astrophysics

The principal scientific objectives of our analysis of the Viking radio tracking data fall into three classes: (i) the study of Mars, its rotation, topography, and internal structure; (ii) the development of a general dynamical model of the solar system; and (iii) tests of the fundamental laws of gravitation. Tables 1 and 2 contain recently determined estimates of planetary masses and some relativistic parameters. These results and supporting material were presented at the June 1984 meeting of the AAS Division of Dynamical Astronomy [Babcock et al., 1984; Chandler et al., 1984]. In general, our mass estimates agree well with the latest values published in the Astronomical Almanac.

The central element in our data analysis is the Planetary Ephemeris Program (PEP) which embodies our mathematical models of the solar system and observables. It functions as a weighted-least-squares fitting (and Kalman filtering) facility for observations related to the positions, velocities, rotations, etc. of solar-system bodies, natural and manmade.

Table 1. Planet Mass Estimates[1] Presented at the DDA Meeting, May 1984

Planet[2]	Mass Estimates: Analysis at CfA	Mass Estimates: Astron. Almanac(1984)	Differences Between Estimates	Standard Deviation (CfA)
Mercury	6,023,700	6,023,600	100	1000
Venus	408,523.1	408,523.5	0.4	1
Earth + Moon	328,900.554	328,900.550	0.004	0.003
Mars[3]	3,098,750	3,098,710	40	60
Jupiter	1,047.3482	1,047.350	0.0018	0.002
Saturn	3,497.90	3,498	0.10	0.3
Uranus	22,830	22,960	130	300
Neptune	19,480	19,314	166	500
Earth/Moon	81.300565	81.300588	2.3×10^{-5}	1.5×10^{-5}

[1] All planet masses in inverse solar mass units.
[2] The data are not sensitive to the mass of Pluto.
[3] The CfA estimates of the mass of Mars do not use the spacecraft encounter data which dominate the estimate given in the Astronomical Almanac (1984, US Government Printing Office).

Table 2. Relativity Results Presented at the DDA Meeting, May 1984

Quantity	GR Nominal	Estimates[1] #1	Estimates[1] #2	Estimates[1] #3	Units
J_2	N/A	-3 ± 3			10^{-6}
$\beta-1$	0	-0.025 ± 0.05	-0.01 ± 0.02		
$\gamma-1$	0	$0.\ \pm0.002$	$0.\ \pm0.0015$		
$\dot{G}/G$	N/A[2]			0 ± 2	$10^{-11}\ yr^{-1}$

[1] Each column represents a summary of results from a large number of solutions of the least-squares normal equations. The errors shown are realistic estimates of the standard deviation.

[2] Although general relativity does not address the possible time dependence of the relation between atomic and gravitational times, one normally assumes $\dot{G}/G = 0$ in classical physics.

We have made a multifaceted upgrade to our analysis of the dynamics of the solar system. We have iterated the estimator a total of four times to obtain a stable, converged solution. In connection with the iteration, we added new "cross partial" terms to some of the variational equations and reintegrated all of the variational equations; we increased the number of outer-planet orbital elements that could be estimated by including the required additional variational equations, and recalculated the entire sensitivity matrix. Also, we included in our working set of data the outer-planet NPs (Earth-planet time-delay pseudo-data derived from the Doppler and ranging observations of spacecraft at encounter with the planet) and optical observations which permitted us to estimate an enlarged set of outer-planet orbital elements.

In another phase of the upgrade, the asteroid model in PEP was changed. We had been able to estimate the mass of a fictitious uniform ring and the masses of eight separate asteroids. (In an earlier modification, the latter had been increased from four.) It is now also possible to estimate the densities of asteroids in up to five classes. This new model serves to include, at least approximately, the effects of up to 200 asteroids which are too small to consider individually but which may be important collectively. For each, the mass is the product of the density estimated for its class and an externally provided volume. Although this model has serious shortcomings, the dearth of applicable auxiliary data makes it a reasonable compromise. In our recent numerical experiments with the data, we have made use of the ability to estimate the larger number of individual asteroid masses and densities for the different asteroid classes.

To investigate the results of this upgrade, we performed a series of numerical experiments; we found our solutions to show more stability and the postfit residuals to show less systematic signature than before. Before the upgrade, we had been unsuccessful in including in our solutions

the Viking Lander delay data taken after 5 August 1980: When included, these data showed, and caused the other Lander delay data to show, a large systematic signature; their prefit residuals had a systematic signature with about a 5 μs peak. (The same problem was encountered at JPL.) After the upgrade, the systematic signature was lost in the noise.

In addition to precession and nutation [Reasenberg and King, 1979], our model of the rotation of Mars includes a secular rate of change of the period and both annual and semiannual variations in the phase of rotation [Williams, 1977, private communication; Philip, 1979; Reasenberg and King, 1979]. Our preliminary investigation with a 400-day set of Lander delay data provided a marginal detection of the semiannual terms [Reasenberg et al., 1979] and showed that these could not be clearly distinguished from the annual terms with such a small span of data. A better result came from our study with an 800-day data set to which we applied the improved plasma estimates and data weights: The annual terms are found to be small and only moderately correlated in the estimator with the semiannual terms. The semiannual terms have an amplitude (expressed as an equatorial surface displacement) and a phase (11.5 $\pm$5 m, -2° $\pm 25^{\circ}$) consistent with the model of Davies et al. [1977] (10.5 m, -36°), but not so consistent with the model of Philip [1979] (9.6 m, -58°). The use of the Viking data to determine the amplitude and phase of the annual and semiannual terms in the rotation of Mars will provide one of the few independent constraints on global models of the circulation and condensation of the atmosphere of Mars.

Recently, we modified our model of the rotation of Mars. In the old model, the seasonal irregularities were added to a spin rate that was constant in ephemeris time. In the new model, that spin rate is constant in Mars proper time, and therefore varies by about $\pm 10^{-9}$ in ephemeris time. The associated rotational phase shift is of the same order and approximate phase as the predicted annual effect of the atmospheric condensation at the poles. The new relativistic correction is thus critical for the accurate determination of the amplitudes and phases of the proposed meteorological effects.

References

Babcock, R. W., J. F. Chandler, R. D. Reasenberg, and I. I. Shapiro, "Limits on Metric Parameters β and γ," BAAS, in press, 1984.

Chandler, J. F., R. W. Babcock, R. D. Reasenberg, and I. I. Shapiro, "New Limit on $\dot{G}$," BAAS, in press, 1984.

Davies, D. W., C. B. Farmer, and D. D. LaPorte, "Behavior of Volatiles in Mars' Polar Areas: A Model Incorporating New Experimental Data," J. Geophys. Res., 82, 3815-3822, 1977.

Philip, J. R., "Angular Momentum of Seasonally Condensing Atmosphere, with Special Reference to Mars," Geophys. Res. Letters, 6, 727-730, 1979.

Reasenberg, R. D. and R. W. King, "The Rotation of Mars," J. Geophys. Res., 84, 6231-6240, 1979.

Reasenberg, R. D., R. B. Goldstein, P. E. MacNeil, and I. I. Shapiro, "Mars Rotation: Bound on Seasonal Variation," BAAS, 11, 571, 1979.

Gravity Field of the Jovian System from Pioneer and Voyager Tracking Data

J. K. Campbell, S. P. Synnott
Jet Propulsion Laboratory, California Institute of Technology, Pasadena CA 91109

The flights of the Voyager spacecraft through the Jovian system in 1979 provided the opportunity to improve the knowledge of the gravity field of the planet and satellites beyond that determined from the Pioneer encounters (Null (1976). The Pioneer spacecraft had much closer flybys of the planet than did Voyager, allowing more accurate determinations of Jupiter's gravity field. However, the Voyager spacecraft had closer approaches to the Galilean satellites and therefore provided complementary Doppler experiments from which to determine gravity coefficients.

Two fundamentally different types of data were processed together in the present analysis: earth based radio tracking data from Pioneer and Voyager obtained by the JPL/NASA Deep Space Net (DSN) and Voyager-based optical measurements obtained with the imaging system. The radio data measure the range and range rate of the spacecraft as viewed from tracking stations on the surface of the earth. The optical data consist of cross line-of-sight measurements of the positions of the Galilean satellites as viewed from the spacecraft (Synnott, et al (1984)). These data types are thus complementary and were acquired essentially continuously over the last 30 days of the Voyager approach, all post encounter data consisted of earth-based radio tracking only.

The gravity solutions were obtained by simultaneously fitting the radio metric distance and velocity measurements and the optical position measurements in the Jet Propulsion Laboratory Orbit Determination Program (ODP) (Moyer 1971). In general, parameters describing the planet barycentric positions of the spacecraft and the four Galilean satellites were estimated along with the masses of Jupiter and the satellites, the instantaneous right ascension and declination of the pole of the planet, planet gravity harmonic coefficients, the earth tracking stations, and the locations of the Jupiter barycenter and the earth-moon barycenter with respect to the solar system barycenter. The solar barycenter coordinates of the Jupiter barycenter and the earth-moon barycenter, and the masses of the Sun and the remaining planetary systems are taken from JPL Development Ephemeris 118 (Newhall et al,(1983)). The a priori Jupiter centered coordinates of the Galilean satellites are taken from the theory developed by Lieske (1980). Partial derivatives with respect to constants of the theory have also been developed by Lieske to allow improvements as new position data become available. An error covariance matrix on these theory constants Galileans was provided by Lieske (private communication) and used as a priori information in the present analysis.

The Voyager and Pioneer S-band doppler data used in the gravity parameter estimation process were corrected for the perturbing effects of various components of the intervening media: the earth's troposphere and ionosphere, the interplanetary plasma and the Io torus. In addition the

effects of the Jovian plasmasphere radially inward from the Io torus were also evaluated and found to be insignificant for the gravity solutions.

The sensitivities of the gravity solutions to the effects of four small components of the Jovian gravitational environment were also tested and found to be insignificant. The four effects were Jovian tides raised by the satellites, the Io second order gravity field, the small inner satellites and an assumed mass concentration at the Great Red Spot.

The inherent accuracy in the Doppler data that makes estimation of gravity parameters possible, also imposes the requirement that nongravitational accelerations or impulsive spacecraft velocity changes be carefully modelled. Null (1976) has described the sources of nongravitational acceleration and velocity impulses acting on the spin-stabilized Pioneer spacecraft. In general, only a few spin axis orientation maneuvers were performed on each spacecraft, at epochs sufficiently removed from periapse to allow separation of these effects from gravitational signatures. Velocity impulses representing each of these maneuvers were included as solution parameters. The Voyager spacecraft is particularly difficult to deal with in this regard. Impingement of some of the ejected gas on parts of the spacecraft structure causes net ΔV's to be imparted when certain pairs of the thrusters are fired. In addition, when the spacecraft orientation is changed by large angles significant net ΔV's may be imparted. In the present analysis, larger velocity increments are explicitly modelled and the components are estimated along with the gravity coefficients. The much lower level velocity impulses incurred in attitude maintenance are modelled as small stochastic accelerations in the estimation filter algorithm, (Campbell et al, (1983)).

Estimates for satellite and planet masses, in units of $km^3\ sec^{-2}$, Jupiter gravity harmonics and the orientation of the rotational pole, as obtained from the complete set of Pioneer and Voyager measurements are as follows: the Galilean satellite masses are (5961 $\pm$ 10) for Io, (3201 $\pm$ 10) for Europa, (9887 $\pm$ 3) for Ganymede, and (7181 $\pm$ 3) for Callisto. The mass of the Jupiter system is (126712767 $\pm$ 100). A mass for Amalthea could not be reliably estimated. The second, third, fourth, and sixth zonal harmonic coefficients of Jupiter are $J_2 = (14736 \pm 1) \times 10^{-6}$, $J_3 = (1.4 \pm 5) \times 10^{-6}$, $J_4 = (-587 \pm 5) \times 10^{-6}$, and $J_6 = (31 \pm 20) \times 10^{-6}$, at an equatorial radius of 71398 km. The sectorial harmonics are $C_{22} = (-0.03 \pm 0.05) \times 10^{-6}$, $S_{22} = (-0.007 \pm 0.05) \times 10^{-6}$. The right ascension and declination of the pole of Jupiter relative to the mean Earth equator and equinox of 1950.0 are $268^\circ.001 \pm 0^\circ.005$ and $64^\circ.504 \pm 0^\circ.001$ respectively. All error estimates are standard errors and are our evaluation of real as opposed to formal errors. These error bars either span the range of solutions obtained from different missions, or the range of solutions obtained from sensitivity experiments with one data set.

For comparison to our results we note that Standish (1984) has obtained a value of (126712610 $\pm$ 120) $km^3\ sec^{-2}$ for GM_S from reduction of photographic plates of the planets and Earth-Viking lander range measurements, which is in reasonable agreement with our result. In addition Lieske (private communication, 1984) has obtained values for α_p and δ_p from reduction of an extensive series of Galilean satellite observations dating from the year 1650. His solutions are $\alpha = 286^\circ.002 \pm$

0.004, $\alpha_p = 64^{\circ}.503 \pm 0.002$ which are consistent with our results.

The results for J_3, C_{22}, and S_{22} are not signficantly different from zero and thus are consistent with a model of a rotating planet in hydrostatic equilibrium.

This work essentially confirms the results reported by Null for the Jovian zonal harmonic coefficients J_2 and J_4, and offers significantly tighter bounds on J_6, J_3 and the tesseral coefficients C_{22} and S_{22}. The results for J_3, C_{22} and S_{22} are expected for a fluid planet in hydrostatic equilibrium. The tighter error bound we place on J_5 may allow further constraints to be placed on models of Jupiter's interior (Hubbard and Slattery, (1976)). We note that future large reductions in the uncertainty of J_6 will probably not result from analysis of radio tracking data (because there is no mission planned with a low Jupiter orbit), but may come from Galileo spacecraft optical observations of the precessions of the lines of nodes or apsides of the small inner satellite (if they have observable eccentricities and inclinations).

The error bars reported here for the masses of the Galilean satellites range from factors of 3 to 12 smaller than those found by Null from the Pioneer data alone. These reduced mass uncertainties may allow improved estimates of the libration amplitude and period of the Io-Europa-Ganymede resonance lock from an analysis of 300 years of earth-based optical observations (Lieske and Yoder, private communication). The improved period and amplitude values may provide information either on the epoch of the formation of the resonance or on the frequency of excitation impacts since its formation. Doppler measurements from the Galileo spacecraft flybys of the Galilean satellites are expected to further reduce the error bars on satellite massed by at least an order of magnitude.

References

Campbell, J. K., Synnott, S. P., and Bierman, G. J., (1983). IEEE Trans. AC-28, 3, 156.

Hubbard, W. B., and Slattery, W.L., (1976), in Jupiter, (University of Arizona Press).

Lieske, J. H. (1980). Astron. Astrophys. 82, 340.

Moyer, T. D. (1971), Mathematical Formulation of the Double-Precision Orbit Determination Program (DPODP) Jet Propulsion Laboratory, Pasadena, TR 32-1527.

Newhall, XX, Standish, E. M., and Williams, J. G., (1983). Astron. Astrophys. 125, 165.

Null, G. W., (1976). Astron. J. 81, 1153. Astron. Astrophys. 125, 150.

Peters, C. F. (1980). Numerically Integrated Galilean Satellite Ephemeris (IAU) Colloquim No. 57).

Synnott, S. P. et al, (1984). In preparation.

CHAPTER 5

CRATERING PROCESSES

Page intentionally left blank

"Impact and Collisional Processes in the Solar System"

Thomas J. Ahrens, Seismological Laboratory,
California Institute of Technology, Pasadena, California 91125

We are carrying out a program of experimental research dealing with the mechanical and thermodynamic aspects of shock impact cratering and accretionary processes on solid planets and satellites.

1. Impact Spall and the Spall Strength of Rocks

The recently proposed model of Melosh (1984), describing the physics controlling the size and velocity of only lightly shocked spalled ejecta surrounding the crushed rock region of an impact crater, has provided a model for possibly delivering meteorites such as ALHA81005 (the "lunar meteorite") from the Moon to the Earth.

The model appears to provide a good framework for relating dynamic tensile (spall) strength to crater spall thickness for gabbro. Gabbro, the only rock-type for which we have tested the theory (Lange et al., 1984A) has given results which provide strong impetus for further experimentation.

In an attempt to provide experimental data to test the Melosh (1984) spallation model, a series of experiments has been developed to determine spall velocities and to map the shape of the detached shock wave for impacts into competent rock.

We have started to carry out some spall velocity measurements. Our work carried out at the Ames gun has demonstrated that impact spalls could be easily obtained on that facility in a "recovery" mode. At Caltech our first simple experiments employed projectiles of aluminum and lead fired from a rifle at targets of San Marcos gabbro. The impact velocity in these experiments was near 1 km/sec.

The resulting velocities were 11 m/sec and 17 m/sec for the lead and aluminum bullets, respectively. This is approximately 2% of the impact velocity and 5-80 times lower than the velocity predicted by the Melosh model. However, there are a number of reasons which could explain this discrepancy.

We are presently carrying out a series of impact spall experiments for use in the vertical gun facility to be impacted in a 4 to 6 km/sec range. Initial targets are of anorthosite and gabbro.

2. Shock Temperatures in the Heterogeneous Regime

Because knowledge of shock and post-shock temperatures are crucial to construct complete equations of state of planetary materials, we are

carrying out measurements based on radiative techniques of shock temperatures of silicates and volatile-bearing minerals.

Quantitative knowledge of shock and post-shock temperatures provide the physical basis for describing the melting and partial vaporization and phase transitions associated with planetary accretion and impact.

New spectra and radiative temperatures of shear bands (which we believe are at the melting point) have been acquired for shocked minerals. Also simultaneous framing camera images acquired for calcite, both fused and crystal quartz and sodium chloride. Because quasistatic melting data for Mg_2SiO_4 are available to 15 GPa we have recently prepared a series of high quality peridot samples for shock temperature, shear band measurements. The hypothesis that shear bands are at the melting point needs rigorous testing. If we can show that this is the case, this technique has promise to allow determination of the melting point of quite a large number of minerals and cosmochemical interest at high pressures. We have acquired samples of a series of solar system materials and expect to carry out experiments during the next year.

3. Impact Devolatilization of Minerals and Accretion of Planetary Atmospheres

Volatile-bearing minerals, especially phyllosilicates, carry much of the water of carbonaceous chondrites, and control their oxidation state and contribute to the atmosphere of planets (Earth, Venus, Mars, and Titan) during accretion. We have been obtaining the first release adiabat data for this class of materials. Shock compression Hugoniot data for serpentine, brucite, gypsum, calcite, and aragonite have demonstrated that these minerals undergo shock-induced phase changes to high pressure phases. Although the compression behavior of these materials was approximately known, the shock pressures, which correspond to various infall velocities required to cause incongruent vaporization upon adiabat release and produce volatile release, were previously unknown or poorly defined (Lange and Ahrens, 1982).

During the last year we have carried out new measurements of the release isentropes of $CaCO_3$ (both polycrystalline and porous), as well as new Hugoniot and release isentrope experiments on $Mg_3Si_2O_5(OH)_4$ (chrysotile) to 22 GPa. In this recent work we have improved on the earlier buffer-method of laboriously obtaining one or two release datum or data per experiment. We are now constructing multiple particle velocity electromagnetic gauge targets and measuring wave profiles upon release in several positions in the targets. This method permits continuous release isentrope measurements to be carried down to pressures of 2 to 3 GPa in a single experiment where we can begin to see the effect of the partial pressure of the volatile in the post-shock environment.

We have also carried out more recovery experiments on porous calcite in addition to the single crystal experiments, these data and an

accompanying model, at least in a simple way, the range of planetary sizes which control the generation and occurrence of CO_2-rich atmospheres on the Hadean earth, Venus, and Mars via the following reactions which may occur upon accretion of carbonaceous chondrites. We also carried out some recovery experiments on the Murchison chondrite to compare volatile release with data for phyllosiliate minerals.

We have started to examine the effect on the water budgets of the planets, of reactions which occur when metallic iron, which would be present in chondritic material, is introduced in a simple accretion model. Reactions such as

$$Mg_3Si_2O_5(OH)_4(serp.) \xrightarrow{shock} 2H_2O + Mg_2SiO_4 + MgSiO_3 \quad (1)$$

$$2H_2O \rightarrow 2H_2 \text{ (escape)} + O_2 \quad (2)$$

$$MgSiO_3 + Fe + H_2O \rightarrow 1/2Fe_2SiO_4 + 1/2\ Mg_2SiO_4 + H_2 \text{ (escape?)} \quad (3)$$

may control the total fayalite (or ferrosilite) budget of planetary mantles. Ringwood has pointed out the importance of reaction (3) in the evolution of the terrestrial planets. We believe our study is the first serious quantification of this issue.

Publications:

Impact cratering and spall failure of gabbro, by Manfred A. Lange Thomas J. Ahrens, and Mark B. Boslough, Icarus, 58, 383-395, 1984.

Shock effects on hydrous minerals and implications for carbonaceous matter, by Manfred A. Lange, Philippe Lambert, and Thomas J. Ahrens, submitted to Geochim. Cosmochim. Acta.

CO_2 loss in shock-loaded calcite and implications for primary atmospheres, by M. A. Lange and T. J. Ahrens, to be submitted to Earth and Planetary Science Letters, 1984.

FeO and H_2O and the homogeneous accretion of the Earth, by M. A. Lange and T. J. Ahrens, Earth and Planetary Science Letters, in press, 1984.

Shock wave techniques for geophysics and planetary physics, by T. J. Ahrens, submitted to Methods of Experimental Physics; Geophysics, ed by C. G. Sammis and T. L. Henyey, Academic Press, 1984.

"Impact Cratering Calculations"

Thomas J. Ahrens and John D. O'Keefe, Seismological Laboratory
California Institute of Technology, Pasadena, California 91125

Understanding the physical processes of impact cratering on planetary surfaces and atmospheres is vitally important to planetary science. Aside from the often made observation that the craters themselves are the most ubiquitous landform on the solid planets and the satellites, there are several other reasons to understand the impact process.

Our objectives are to describe and understand impact cratering, both normal and oblique, on planetary surfaces and to determine energy partitioning, ejecta distribution, (both with regard to size, velocity, energy content, and size sorting), the condensation physics of impact induced vapor and the loss of planetary atmospheres during accretion of terrestrial and icy planets.

1. Oblique impact and possible origin of SNC meteorites

The major problem with the hypothesis that the shergottites, (S), nakhlites, (N), and Chassigny, (C), are samples of the Martian surface is the difficulty of accelerating them as part of the ejecta plume from an impact to an excess of the Martian escape velocity (5 km/sec) without melting. As pointed out by Wood and Ashwal (1981) and others, previous calculations (O'Keefe and Ahrens, 1977a) indicate that on the average, silicate ejecta escaping a planetary surface at 5 km/sec are completely melted. Moreover, ejecta in the 2 to 3 km/sec range, on the average, contain sufficient internal energy for incipient melting.

Nyquist (1983, 1984) suggested that very oblique impacts on Mars might generate asymmetric impact vapor clouds of sufficient density and duration to entrain and accelerate unshocked or lightly shocked surface materials to speeds in excess of the escape velocity. To test this hypothesis, we carried out a series of 2-dimensional normal and oblique impact calculations. We considered the impact of infinite cylinders (axis parallel to Martian surface and axis perpendicular to the impact direction) impacting a hypothetical Martian surface composed of (92% enstatite and 8% water) at a range of angles at speeds of 7.5 and 20 km/sec (O'Keefe and Ahrens, 1984aA). Our results are as yet preliminary. The normal impact calculations of a rod give similar flow fields to our previous calculations of the normal impact of a sphere. However, for oblique impacts, although the amount of low angle trajectory ejecta is increased by the oblique impact, (in agreement with Gault and Wedekind, 1978; Zook et al., 1984) especially in the case of the 7.5 km/sec impact, this material is not accelerated to very high speed and contains the internal energy comparable to normal ejecta traveling at those velocities. As shown in our new calculations, oblique impacts with angles of $\gtrsim 25^{o}$, at the two speeds examined, generated very little highly shocked ejecta and did not achieve the asymmetric jet

conditions which could accelerate surface materials to velocities > 5 km/sec, as speculated by Nyquist. Thus shallow angle impacts do not produce the horizontally directed gas cloud which Nyquist (1983) suggested might entrain Martian surface material. However, due to jetting, for impacts $\gtrsim 25^{o}$, at least in the geometry of the present impacts, such a gas cloud is produced and has a velocity on the order of 20 km/sec. It consists of vaporized hypothetical Martian and impactor material (assumed to have an enthalpy of vaporization of 3.3 kJ/g) with a density of $\sim 5 \times 10^{-4}$ Mg/m^3. This material exists at distances of up to ~50 projectile diameters from the impact point for projectiles in the diameter range of ~1 to 10 km. We speculate that such a flow could easily entrain and accelerate 1 m diameter unshocked boulders to speeds > 5 and < 20 km/sec in distances on the order of 1 to 10 projectile diameters. We need to apply the criteria for jet formation for asymmetric impact to a wider range of possible impactors and martian surface materials in our next effort. A more complete study of energy partitioning associated with oblique impact, melting, and vaporization and the study of entrainment dynamics is under way.

2. Ejecta sizes and velocity spectra

Because of a need to describe the relation between ejecta-size distributions and velocity-size distributions, we have attempted to synthesize a testable model from the following:

(1) Numerical calculations and experimental data prescribing the cumulate mass of ejecta traveling faster than a certain velocity, versus ejecta velocity.

(2) A fit to the maximum ejecta particle size versus crater diameter from laboratory and natural impact structures and large explosions.

(3) A very limited number of data relating maximum ejecta fragment size versus ejecta velocity.

(4) Using cumulate mass of ejecta versus particle mass (or diameter) data, a self-consistent model can be constructed from laboratory impact experiments, experimental data, and from chemical and nuclear explosion data.

The model parameters so derived then predict the degree of sorting of particle size versus velocity, as well as the dependence on maximum size of ejecta fragments, versus ejecta velocity. The latter depends on crater dimensions and planetary gravity as proposed by Housen et al. (1983). Both of the above predictions of our model are experimentally measurable and we intend to test this model on small scale impact experiments this year using the Ames vertical gun facility.

3. Impact into porous regolith

Many questions have arisen as to how such partitioning of energy and attenuation of impact pressures depends on planetary surface porosity as, for example, on a regolith or on a megaregolith. There are two competing effects here. The porosity decreases the target impedance and lowers the shock energy density that can be initially coupled from the projectile into the target. However, the porosity causes irreversible compaction to occur, and hence, more local dissipation into heat takes place in the vicinity of the impacted region. We have carried out the first cratering calculations or impact into a 28 halfspace target and although the calculations do not yet extend to sufficient time to yield the total partitioning result, the shock attenuation determined relative to solid anorthosite being impacted at various speeds, is very similar.

4. Study of the equation of state of water and ice, and a possible model for the accretion of the Jovian and Saturnian satellites

We have, however, fit the available shock wave, thermodynamic and phase diagram data for ice, porous ice, and water into the framework of the Rice and Walsh (1957) and Bakanova et al. (1976) equation of state to define critical release isentropes. In the case of solid ice at initially 70 and 263 K, we determined using the Mollier diagram of Bosnjakovic et al. (1970) that the shock pressures required for incipient melting (IM) of ice to the liquid water-Ice III - Ice V triple point varied from 7.6 to 6.2 GPa (76 to 62 kbar). Achievement of sufficient entropy for the release isentrope to pass through the liquid-vapor critical point (CP) required 25.5 and 26.7 GPa and temperatures of 1756 and 1779 K, respectively. We found that the minimum impact velocity onto ice required to induce IM, CM, and isentropic release through CP is 2.1, 3.0, and 4.5 km/sec for silicate impactors. For icy (cometary) projectiles, these critical velocities are 3.4, 4.4, and 7.2 km/sec. Thus, in contrast to the terrestrial planets, the infall (escape) velocities onto the solid icy satellites are too low to induce melting or vaporization. These statements are true for non-porous surfaces.

In contrast to the Lunine and Stevenson (1982) model, we assume accretion at a low H_2O partial pressure (below the 6 millibar, 273 K critical point) where water-ice sublimes directly to vapor). We demonstrate that if the larger satellites accreted from the same group of planetesimals which formed the smaller Saturnian satellites, impact vaporization of water upon accretion of porous icy planetesimals can account for an increase in mean planetary density from 1.35 g/cm^3 for water-silicate objects like Ganymede, Titan, and Callisto. Our model does not deal with the resulting shock vaporized water atmosphere which would also coaccrete. However, we believe that Cameron's (1983) atmospheric impact erosion model may provide a means of disbursing these ephemeral atmospheres from some of the icy satellites.

(5) Condensation of impact produced vapor

In attempting the describe the amount and size of very fine particulate ejecta which resulted from condensation of the impact induced vapor which may be produced upon impact of the Cretaceous-Tertiary bolide (Ahrens and O'Keefe, 1981a,b) we discovered that the only related existing work on the subject was that of Raizer (1960) which was pertinent only to the free-molecular field regime. We applied the theory of Pesthy et al. (1981) to account for the rapid expansion of an impact induced vapor sphere to describe the condensation growth equation in the continuum regime.

A paper summarizing our description of the impact induced vapor sphere expansion from the earth and predicting condensate size as a function of impactor radius is in preparation.

Bibliography

1. Ahrens, T. J. and O'Keefe, 1983, Impact of an asteroid or comet in the ocean and extinction of terrestrial life, Proc. Lunar and Planetary Science Conf. XIII, Part 2, J. Geophys. Res. 88, A799-A806.
2. Lange, M. A. Ahrens, T. J., and Boslough, M. B., 1984, Impact cratering and spall failure of gabbro, Icarus, 58, 383-395.
3. O'Keefe, J. D. and Ahrens, T. J., 1984, Impact and explosion crater ejecta, submitted to Icarus.
4. Lange, M. A. and Ahrens, T. J., 1984, FeO and H_2O and the homogeneous accretion of the earth, Earth and Planetary Science Letters, in press.
5. Ahrens, T. J. and O'Keefe, J. D., 1984, Shock vaporization and the accretion of the icy satellites of Jupiter and Saturn, The Proceedings of the NATO Research Conference on Ices in the Solar System, ed. by P. Klinger, A. Dollfus, and R. Smoluchowski, submitted, 1984.
6. O'Keefe, J. D. and Ahrens, T. J., 1984, Oblique impact, a process for providing meteorite samples of other planets, to be submitted.

PROGRESS REPORT
IMPACT CRATER SCALING LAWS

K.A. Holsapple, University of Washington
Seattle, WA 98195
October, 1984

A combined theoretical/numerical study to discover the dependence of an observed impact crater on the conditions of the impact has been underway for the last two years. These studies have focused on the effects of the impactor size and velocity, of the material properties of the impactor and impacted body, and of the gravitational field strength. The understanding of these fundamental "scaling laws" are of primary importance to the planetary sciences.

It has been discovered that a great variety of observed effects can be predicted and correlated by a theory based upon a point-source solution characterized by a single measure of the impactor size, velocity, and material called the coupling parameter [1]. A number of applications of the theory have been reported recently, these are summarized in [4].

A relatively new application [2] considered the application of the concept to the dynamical history of the crater growth in a variety of materials. These studies are of particular interest since not only do they test the coupling parameter theory at the late stages of the crater growth, but also give insight into the relative time at which it begins to dominate the cratering mechanics.

A typical result of this study is shown in figures 1 and 2. Fig. 1 shows the unreduced data of crater depth versus time for various cases, ranging over many decades in different sizes and times. Fig. 2 is the same over many decades in different sizes and times. Fig. 2 is the same data normalized in the way that the theory predicts will superimpose the data along a common power-law line in the intermediate stages. It is seen that indeed the data superimposes well, and matches the predicted slope. Additional results are give in [2].

More recent efforts have been directed to discovering how the form of the coupling parameter (and thus the scaling) depends on the material of the impacted body. It has been suspected for some time that the material's air-filled porosity is the dominant property that governs the scaling laws. Numerical code calculations have been designed to test this hypothesis.

In a first series of calculations, impacts at several impact velocities, from 2 to 100 km/sec, have been run using a non-porous equation of state for the target material. The properties were actually those of a metal, but were also characteristic of a strong rock. The model included specific melt and vapor phase changes. These runs were to determine whether a governing coupling parameter could be recognized in such a calculation, how to determine its form, and to test for ranges of applicability. Fig. 3 shows a typical result, a superposition of three cases of the kinetic energy of the downward moving material of the flow

field versus the momentum of that same material, where problem time is a parameter increasing from the left to the right. The good superposition along the power-law slope predicted from the theory is noted.

In addition to those studies, studies were designed to test the dependence of the coupling parameter on the Gruniesen parameter and the u_s/u_p slope values that characterize a Tillotson material model. As expected and consistent with the results of the crater growth study described above, no reasonable changes in those values had any effect on the observed scaling [3].

The present work is focused on porous materials. The first goal was to determine if a code calculation could recover the scaling exponents that can be derived theoretically (see [4] for such a derivation) for an idealized "perfectly-porous" material that crushes at zero strength and subsequently is incompressible. A model that was close to the idealized case was generated in a form suitable for code calculations and utilized for a series of one-dimensional calculations. The code calculation did in fact demonstrate the theoretical coupling parameter.

Two efforts are presently underway. A large number of calculations of impacts using a "physically real" porous material model have been obtained from S. Shuster of California Research and Technology. These runs are being analyzed for evidence of a coupling parameter. A typical result is presented in fig. 4, showing the superposition of a number of cases in a way determined from the coupling parameter theory. Surprisingly, these calculations seem to indicate a coupling parameter of the same form applicable to a non-porous material, distinctly different from that expected from other theoretical and experimental results for porous materials.

The other continuing effort is to extend the one-dimensional calculations for the idealized porous model to two-dimensional impacts, to compare the idealized with the "real" porous models. To date this has proven to be a formidable task, because of the numerical stability problems of the code for the highly idealized model. However, preliminary results are now being obtained, and will be analyzed soon.

The reference [4] gives an extensive discussion of the theory and applications of the couplilng parameter concept. It has just been completed and is ready for submission for publication.

REFERENCES

[1]. Holsapple, K.A., "Coupling parameters in cratering" (abstract). EOS 62, p. 949, 1981.

[2]. Holsapple, K.A., "On crater dynamics: Comparisions of results for different target and impactor conditions." Lunar and Planetary Science XV, pp. 367-368, 1984.

[3]. Bjorkman, M.D. and Holsapple, K.A., "Plane hypervelocity impact and source similitude dependence on a Tillotson EOS", Proc. 3d APS Conf. on Shock Waves, 1983.

[4]. Holsapple, K.A. and Schmidt, R.M., "Point source solutions and coupling parameters in cratering mechanics", submitted for publication, 1984.

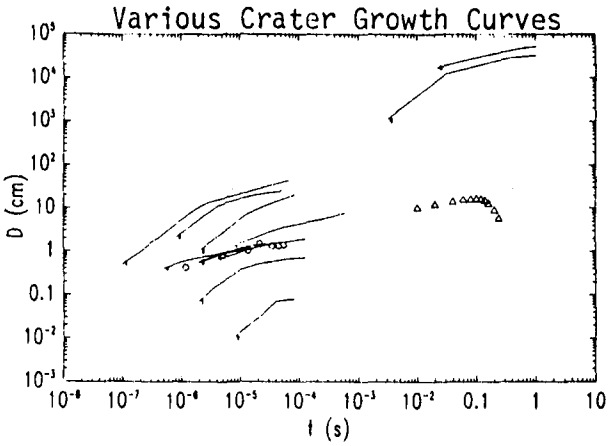

Figure 1. Crater Growth Histories

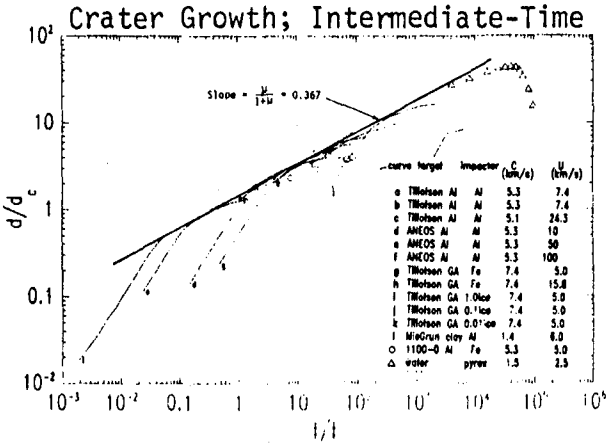

Figure 2. Scaled Crater Growth Histories

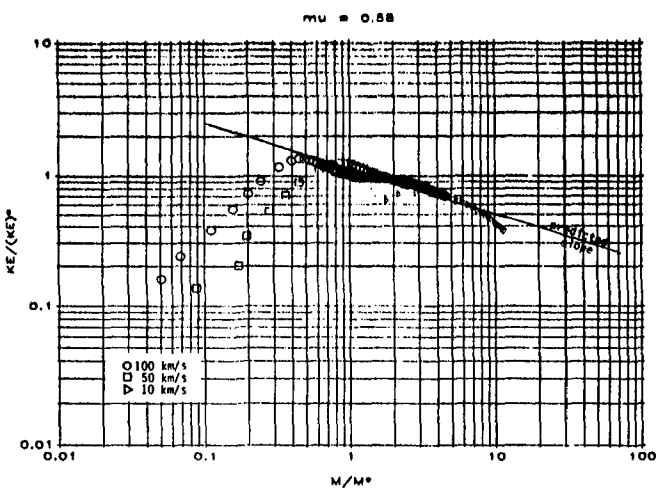

Figure 3. Impacts Into A Non-porous Material

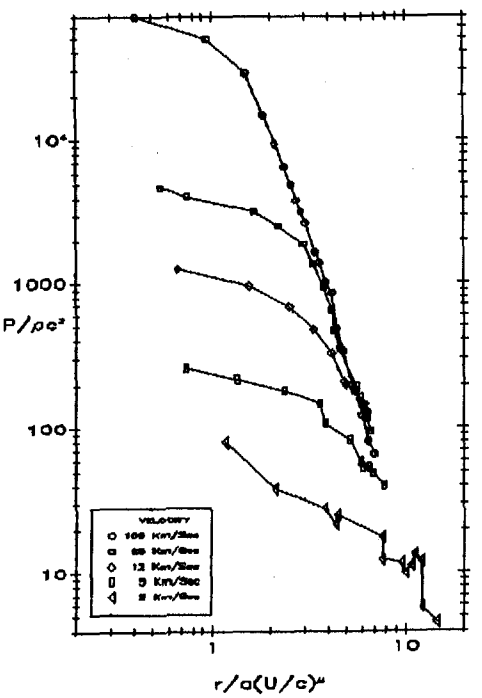

Figure 4. Impacts Into A Porous Material

CENTRIFUGE IMPACT CRATERING EXPERIMENTS

Robert M. Schmidt, Kevin R. Housen, Michael D. Bjorkman, Keith A. Holsapple
Boeing Aerospace Company, Mail Stop 13-20, Seattle WA 98124

Previous arguments based on a source coupling parameter theory have elucidated many aspects of our observed experimental results for impact cratering. In some special cases, the theory has provided explicit functional relations of interest. Recently, our efforts have been focused on experiments to determine the kinematics of crater growth, impact-induced target flow fields and the generation of impact melt.

Crater Growth

If for any time subsequent to source energy and momentum coupling, crater growth is independent of gravity, material strength and wave speed, then crater dimensions should grow as a simple power-law in time[1]. Furthermore, the exponent for this power-law growth regime is related to the gravity scaling exponent for final crater dimensions versus source size.

Previous examination of experimental results from both impacts and explosions in water show good agreement with the coupling parameter theory[2,3]. These experiments were performed using a quarter-space target tank on a centrifuge. Transient cavity formation was recorded on 16mm film at a framing rate of 5000/sec. Crater growth histories were obtained for various gravities over the range of 10-500G. When plotted in a non-dimensional form, the growth histories were found to be kinematically similar. The rate of cavity growth, the dependence of maximum cavity size and time of formation upon gravity are all in agreement with a value of 0.65 for the gravity exponent, α.

Obtaining comparable measurements for granular target materials has been difficult because of attendent experimental constraints and labor intensive data reduction requirements. A preliminary test (shot 307-QXE) was conducted at 400G in a quarter space tank in order to record the growth and possible collapse of the transient crater in nearly saturated moderately dense fine grained Ottawa Banding sand. Crater floor uplift("collapse") was observed to occur on the same time scale as the radial motion of the ejecta

plume. The high speed film records indicate that the final shape of the apparent crater stabilized by the time the ejecta plume reached the vicinity of the final crater radius. Crater volume deplayed power-law growth until maximum transient depth was reached. More interestingly, crater radius showed power-law growth nearly all the way out to the final radius. Both the volume and radius time exponents, interpreted with the assumption of a unique coupling parameter, are in good agreement with the gravity exponent, α=0.65, measured for water. This value may be applicable for all non-porous geological targets.

However, preliminary results from our 1-G impact experiments conducted at Ames[4] indicate that the simple power-law growth regime may not develop under certain conditions. Furthermore, a 1-G explosive experiment in wet sand also shows the inconsistency observed for the impact experiment. Results of a second experiment in wet sand are currently being reduced as are results from a pair of dry sand control experiments. Previous dry sand experiments performed by Piekutowski (1980) are in good agreement with the theory. Crater volume, radius and depth all show power-law growth with time exponents that are in agreement with a value of the gravity exponent equal to 0.45-0.50. This value has been determined separately from numerous cratering experiments in dry sand for both impact and near surface explosives.

Investigations of Cratering Flow Fields

The concept of a source coupling parameter was used to develop a general nondimensional scaling relation for impact induced material motions (i.e. cratering "flow fields"). The utility of such a model is twofold. First, it provides a useful methodology for analysis of experimental measurements of particle motions, e.g. those obtained from numerical simulations of impacts or from quarter-space measurements of actual (laboratory) cratering events. Second, it provides a framework for evaluating the generality of other flow models, in particular Maxwell's Z model.

Preliminary examinations of available measurements of particle motions showed consistency with the coupling parameter model. Three cases were considered: (1) A finite-difference calculation of a deeply buried explosion in rock (by Maxwell), (1) a calculation of an impact in plasticene clay

(by Austin et al) and (3) a small explosion in a quarter-space of dry sand.

The Z model, even in it's most general form, was shown to be inconsistent with a coupling parameter except in the special cases of steady flow or where the time dependence of radial velocity is power law in form. The observation that the Z model is a special restricted form of a coupling parameter implies that the Z model cannot be expected to hold as a general rule. We anticipate acquiring additional data on particle motions (e.g. from our centrifuge quarter-space experiments) in order to provide more definitive tests of the coupling parameter model and of the generality of the Z model.

Impact Melt

A study on the feasiblility of using scaling relationships for impact melt and crater dimensions to determine impactor size and velocity was discussed at the Lunar and Planetary Science XV Conference. A fundamental conclusion drawn from the analysis is that a coupling parameter determines both the quantity of melt and the crater dimensions for impact velocities greater than 10km/s. As a result one can not determine impactor radius, a, or velocity, U, individually, but only as a product in the form of a coupling parameter, aU^{μ}. The melt volume and crater volume scaling relations were applied to Brent crater. Scaling relations imply that 7% of the total apparent volume was melted while drill cores suggest that only 0.6% melted and remained in the crater. Thus either 90% of the melt was ejected or the melt volume scaling relation determined from hydrocode calculations is inaccurate. We are currently examining the transport of melt and the validity of the melt volume scaling relations.

1) Holsapple and Bjorkman, **EOS**, Vol 64, No 45, p 747, Nov 83.
2) Schmidt, **EOS**, Vol 62, No 45, p 944, Nov 81.
3) Schmidt, **EOS**, Vol 64, No 45, p 747, Nov 83.
4) Schmidt and Piekutowski, **EOS**, Vol 63, No 43, p 1020, Nov 82.
5) Piekutowski (unpublished data, 1984).
6) Schmidt, Lunar and Planetary Sci XV, Houston, p 722, Mar 84.
7) Housen, Lunar and Planetary Sci XV, Houston, p 377, Mar 84.

PROGRESS ON EXPERIMENTAL IMPACT STUDIES

W.K. Hartmann, D.R. Davis, and S.J. Weidenschilling, Planetary Science Institute, Tucson, AZ 85719

A broad-based program of experimental impact studies has been continued, based primarily on our experimental impact work at Ames Research Center's Vertical Gun Facility during recent years.

Hartmann has submitted a paper to Icarus entitled "Impact Experiments 1: Ejecta Velocity Distributions and Related Results from Regolith Targets." This derives the velocity distributions, energy partitioning, and related properties from 14 impacts at speeds 5 to 2321 m/s in vacuo into regolith-like fine powders (Hartmann, 1984, submitted for publication).

Additional data are still being analyzed from various other experiments already performed. These include data on velocity and mass distributions as a function of azimuth around the crater during oblique impacts, catastrophic disruption of spherical targets of variable strength, and catastrophic disruption of irregular-shaped natural rock targets and artificial granular aggregate targets. Periodic reports on our results in some of these areas have been published in Lunar and Planetary Science Abstracts (Davis and Weidenschilling, 1982; Hartmann, 1980; 1983). Data analysis is continuing.

An important area of the work is deriving information applicable to studies of early planetary accretion and asteroid collisions. Reports on these continuing efforts have been published in recent Lunar and Planetary Science Abstracts (Davis, Chapman, Greenberg, and Weidenschilling, 1983; Davis, Chapman, Weidenschilling, and Greenberg, 1984).

References

Davis, D.R. and S.J. Weidenschilling, 1982. Catastrophic Disruption and Momentum Transfer in High-Speed Impacts, Lunar. Planet. Sci. 13, 142-143.

Davis, D.R., C.R. Chapman, R. Greenberg, and S.J. Weidenschilling, 1983. Asteroid Collisions: Effective Body Strength and Efficiency of Catastrophic Disruption, Lunar Planet. Sci. 14, 146-147.

Davis, D.R., C.R. Chapman, S.J. Weidenschilling, and R. Greenberg, 1984. Asteroid Collisional Evolution Studies, Lunar Planet. Sci. 15, 192-193.

Hartmann, W.K., 1980. Continued Low-Velocity Impact Experiments at Ames Vertical Gun Facility: Miscellaneous Results, Lunar Planet. Sci. 11, 404-406.

Hartmann, W.K., 1983. Energy Partitioning in Impacts into Regolith-Like Powders, Lunar Planet. Sci. 14, 281-282.

Hartmann, W.K., 1984. Impact Experiments 1: Ejecta Velocity Distributions and Related Results From Regolith Targets, submitted to Icarus.

PROGRESS ON STUDIES OF EARLY INTENSE CRATERING

William K. Hartmann, Planetary Science Institute, Tucson, AZ 85719

Research on the existence and effects of "saturation" cratering throughout the solar system was completed. A paper was given at the LPSC XV, and is in press in Icarus (Hartmann, 1984).

Some researchers, including Voyager analysts, have concluded that saturation equilibrium cratering exists nowhere in the solar system, and therefore that diameter distributions in even the most heavily cratered provinces reveal initial production functions related to impacting bodies. Based on this premise, they identify different populations of impactors in different epochs and regions of the solar system. These hypotheses are clearly crucial to interpreting planetary history and need further independent examination.

Comparing my own crater counts on heavily cratered surfaces throughout the solar system, as shown in Figs. 1 and 2, I found that the most heavily cratered regions of the lunar highlands, the lunar maria at small crater diameters, Mercury, Mars, Phobos, Deimos, Callisto, Mimas, Tethys, and Rhea all cluster around (within a factor 2) the same -1.83 power law for crater densities ($0.06 < D < 1448$ km). This envelope is well below the theoretically proposed saturation equilibrium values of Woronow, Strom, and Gurnis (1982) by a factor of about 2 to 6. A striking coincidence would be needed if all these surfaces were unsaturated but all had about the same crater density. Instead, I propose that the data points in Figs. 1 and 2 define an empirical saturation level reached on some surfaces in different parts of the solar system.

Particular support to this view comes from the curve for small lunar mare craters, which ascends steeply toward small diameters below 2 km, but levels off at about the same "saturation" level below about 300 m. Further studies of these craters may illuminate questions of saturation or non-saturation.

The crater counts on frontside lunar uplands, used by Strom and co-workers as a basic reference curve identified with one of their populations of early impactors, are confirmed by my counts. However, this area is contaminated with ancient, ejecta-masked basalts (Hawke, Bell, and Clark, 1983). This crater population is deficient in 1-16 km craters, which may be obliterated by the lavas. Thus, this curve is not representative of heavily cratered highlands, and is of questionable value as a standard comparison curve. The "pure" highlands show a "flatter", less structured curve, as shown in Fig. 1.

There is evidence of a turndown at large diameters in these populations. The production function in the outer solar system may differ from that in the inner solar system, as proposed by Woronow, Strom, and Gurnis (1982), but it is also possible that viscous relaxation of ice craters or immediate flooding of craters that penetrate through an ice lithosphere into watery substrate may explain the greater deficiency of large craters on icy moons. This problem is controversial and needs more study.

Further work has begun on the role of giant impacts during the intense early bombardment period. In particular, giant impact(s) on the primeval Earth may have initiated lunar formation, as pointed out by Hartmann and Davis (1975) and Cameron and Ward (1976). This hypothesis is receiving increased attention by various researchers, as reflected in the 1984 Lunar Origin Meeting in Kona. I will present new work on this hypothesis at that meeting.

References

Cameron, A.G.W. and W.R. Ward (1976). The Origin of the Moon, Lunar Sci. VII, 120 (abstract).

Hartmann, W.K. (1967). Lunar Crater Counts II: Two Lunar Type-Areas, Comm. Lunar Planet. Lab. **6**, 39-41.

Hartmann, W.K. (1973). Martian Cratering 4. Mariner 9 Initial Analysis of Cratering Chronology, J. Geophys. Res. **78**, 4096-4116.

Hartmann, W.K. (1984). Does Crater "Saturation Equilibrium" Occur in the Solar System?, Icarus **59**, in press.

Hawke, B.R., J. Bell, and P. Clark (1983). Very Ancient Lunar Volcanism: Implications for Crustal Composition and Evolution, in Natural Satellites, IAU Colloq. 77, abstracts, Cornell University, 36.

Passey, Q.R. and E. Shoemaker (1982). Craters and Basins on Ganymede and Callisto: Morphological Indicators of Crustal Evolution, in Satellites of Jupiter (D. Morrison and M. Matthews, eds.), University of Arizona Press, Tucson.

Woronow, A., R. Strom, and M. Gurnis (1982). Interpreting the Cratering Record: Mercury to Ganymede and Callisto, in Satellites of Jupiter (D. Morrison and M. Matthews, eds.), University of Arizona Press, Tucson.

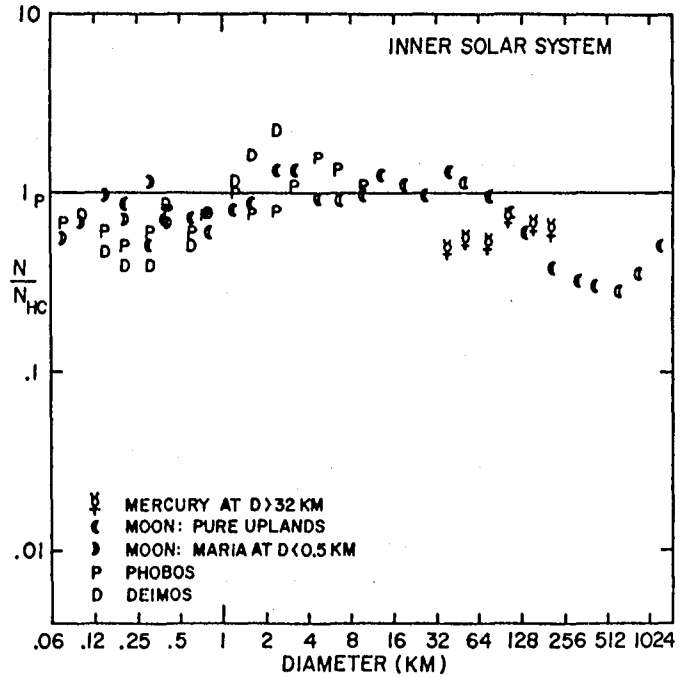

Fig. 1. Crater densities on the most heavily cratered surfaces in the inner solar system, including regions on Mercury, Moon, Phobos, and Deimos. The graph is a relative plot, showing observed number of craters/km^2 in each $\sqrt{2}$ diameter bin (N), relative to an estimated best fit for heavily cratered regions (N_{HC}). The solid horizontal line represents N_{HC}, which is a power law with exponent -1.83. Observed clustering of most counts from heavily cratered regions within a factor of 2 of this line suggests an empirical identification of saturation equilibrium cratering.

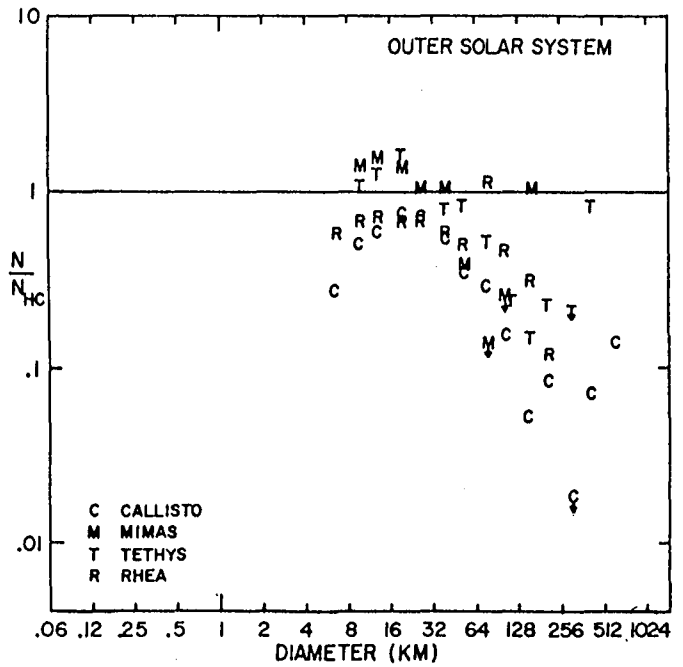

Fig. 2. Same as Figure 1, for four heavily cratered moons in the outer solar system. Coincidence of the maximum crater densities within factor 2 of values in inner solar system reinforces the suggestion of an empirical saturation equilibrium crater density, shown by the horizontal line. This line is well below the saturation equilibrium densities proposed theoretically by Woronow and co-workers, with consequent important implications about planetary surface evolution.

WHY NOT A CONSTANT EARLY LUNAR IMPACT RATE?

Don E. Wilhelms, U.S. Geological Survey (MS 946), Menlo Park CA 94025

It has long been clear that at least two distinct episodes of impacting are recorded on the Moon's surface [1,2]. An early episode marked by an intense barrage that included basin-forming projectiles ended about 3.8 aeons ago when the Orientale basin was created (the close of the Early Imbrian Epoch [3]). The second episode, after 3.2 or 3.3 aeons ago, was marked by a much lower impact rate (during the Eratosthenian and Copernican Periods). These very different rates are separated by a short transition period during the Late Imbrian Epoch [2,3,4].

Whether the Eratosthenian and Copernican impact rate was constant or variable continues to be debated [4]. I have found that a constant rate is consistent with a widely accepted 0.8-aeon age for Copernicus [5] if mare and crater substrates respond differently to the same impacts [3,6]. Here I suggest that the rate during the early episode could also have been approximately constant, at least from the time the lunar crust solidified. This is contrary to the opinion of most investigators, who either ascribe most basins and radiometric terra ages to a "terminal cataclysm" [7] or conclude that the impact rate declined with a (probably varying) half life of about 0.05 to 0.2 aeon [e.g. 8]. All our estimates for the early impact rate are limited by the lack of well-constrained astronomical models, the imprecision of relative ages based on crater frequencies, and the paucity of pre-mare radiometric ages for lunar rocks.

My suggestion is based on the observed numbers and ages of basins rather than of craters and on the relative and radiometric ages of the Imbrium and Nectaris basins. Of the 44 basins $\geq$300 km in diameter whose existence I believe is securely or tentatively established [3], 2 are giant pre-Nectarian basins (South Pole-Aitken and Procellarum), 28 formed later in pre-Nectarian time, 11 are Nectarian, and 3 are Imbrian. The problem with estimating relative ages of densely cratered terra surfaces is that the limiting diameter of the steady state of craters increases progressively for older and older surfaces, and for the oldest units appears to be on the order of 50 km [3]. Consequently, the size-frequency relations of craters smaller than 50 km differ little among old pre-Nectarian units. Ages of the old units are distinguished mainly by subtle differences in the position of the "rollover" of size-frequency curves from the leg representing crater production, whose slope is approximately -1.8 cumulative [2], to the leg representing the steady state, whose slope is approximately -1 cumulative [3] (much shallower than the -2 for small craters [9]).

Because no pre-Nectarian stratigraphic units have been radiometrically dated, the duration of the Nectarian Period (the time between the Nectaris and Imbrium impacts) is the best geologic basis for estimating the early impact rate. Imbrium is the only pre-mare feature whose relative and radiometric ages are both well established. It is also the best lunar stratigraphic unit for correlating frequencies created by the older and

younger impact fluxes, because its deposits are both sufficiently extensive to have enough $\geq$20-km craters for comparison with those on older basins [3] and sufficiently young to have small craters above the steady-state diameter [10] for comparison with those on radiometrically dated mare units [11]. I accept an age for Imbrium of 3.85±0.02 aeons, based on radiometric ages of 3.83 aeons for a group of probable Imbrium impact-melt rocks from the Apollo 14 site [12], 3.85 aeons for KREEP-rich basalt from the Apollo 15 site that are contemporaneous with or younger than the basin [13], and 3.86 aeons for black-and-white breccia from the Apollo 15 site that is probably part of the Imbrium ejecta [14]. Unfortunately, Imbrium formed almost at the end of the basin-forming barrage, so these relatively good data alone do not tightly constrain the very ancient cratering frequencies.

The Nectaris basin has extensive deposits, a statistically good crater frequency, and a favorable stratigraphic position between 13 younger and 30 older basins [3]. Unfortunately, its radiometric age is less certain; it has been estimated as either 4.1 aeons [8] or 3.92 aeons [15,16] on the basis of small dated Apollo 16 samples tentatively believed to be part of the Nectaris ejecta. Based on the petrologic arguments of James [15] and Spudis [16], I favor 3.92±0.03 aeons [3]. If these ages for Imbrium and Nectaris are correct, the Nectarian Period lasted about 0.07 aeon.

The severest problems in determining the early impact rate by geologic means arise in extrapolating the Nectarian rate backward in time. The oldest cratered surface I detected lies within the limits of the possible Al Khwarizmi-King basin [3], which, if not a basin, at least represents very old terra. Exponential extrapolation from the Imbrium age of 3.85 aeons to the Nectaris age of 3.92 aeons gives an age for this surface of 4.03±0.03 aeons. The oldest preserved basins, including Al Khwarizmi-King, predate this surface. The exponential extrapolation suggests that a very large number of now-obliterated basins also formed after the crust solidified between 4.3 and 4.2 aeons ago [17,18] and before 4.03±0.03 aeons ago.

Baldwin [19] objects to such steeply declining exponential rates because they imply that a mass as great as that of Jupiter has struck the Moon. Although such a large impacting mass is not impossible, I agree that an alternative should be sought and therefore examined the implications of a constant impact rate. If the impacts after crustal solidification occured at the Nectarian rate (11 basins in 0.07 aeon, or 157 basins per aeon), the 28 pre-Nectarian basins younger than the 2 giant basins started to form about 4.1 aeons ago and about 16 basins formed every 100 m.y. before that time. South Pole-Aitken and Procellarum (2,500 and 3,200 km in diameter, respectively) must have obliterated many of the smaller basins older than 4.1 aeons. If craters between 30 and 300 km formed at the Nectarian rate of 19,000 per aeon, then about 3,400 were formed between 4.1 and 3.92 aeons ago. About 1,200 pre-Nectarian craters of this size--probably younger than 4.1 aeons--are still visible [3]. I believe that these results show that the large numbers of basins and craters observed on the lunar terrae are just as readily explained by a constant as by a steeply declining impact rate.

Discovery of mare basalt about 4.23 aeons old in the Imbrium ejecta [20], which was derived from the Procellarum basin, may help date Procellarum. If this age is correct and if the sample was derived from intact flows or dikes in Procellarum, the Procellarum impact and crustal soldification both predated 4.23 aeons. This relatively old age for a still-observed (though faint) basin is consistent with the idea that the number of basin impacts does not greatly exceed the observed number of basins.

In summary, a constant pre-Imbrian impact rate--although far from being established--is at least consistent with all the relevant observations of which I am aware and with the following lunar historical scenario: (1) Crustal solidification between about 4.3 and 4.25 aeons ago; (2) formation of Procellarum, South Pole-Aitken, about 22 now-obliterated basins, and about 2,850 now-obliterated 30-300 km craters between 4.25 and 4.1 aeons ago; and (3) formation of 39 still-preserved basins, 1,200 still-preserved craters (30-300 km), and 2,200 now-obliterated craters between 4.1 and 3.85 aeons ago (late pre-Nectarian and Nectarian). At the constant rate, the amount of mass that impacted the Moon since crustal solidification would not greatly exceed the amount that has left a permanent visible record.

---

[1] Shoemaker E. M., Hackman R. J., & Eggleton R. E. (1962) Advances in Astronaut. Sci. 8, p. 70-89. [2] Basaltic Volcanism on the Terrestrial Planets (1981) LPI, Houston, chap. 8. [3] Wilhelms D. E. (1985) The Geologic History of the Moon: USGS Prof. Paper 1348. [4] Grieve R. A. F. (1984) JGR 89, suppl. 2, p. B403-B408. [5] Eberhardt P., Geiss J., Grögler N., & Stettler A. (1973) The Moon 8, p. 104-114. [6] Schultz P. H. & Spencer J. (1979) LPS X, p. 1081-1083 (abs.). [7] Tera F., Papanastassiou D. A., & Wasserburg G. J. (1974) EPSL 22, p. 1-21. [8] Wetherill G. W. (1981) Multi-ring basins (PLPSC 12A), p. 1-18. [9] Trask N. J. (1966) Caltech-JPL Tech. Rpt. 32-800, p. 252-263. [10] Trask N. J. (1971) USGS Prof. Paper 750D, p. 138-144. [11] Neukum G., König B., & Arkani-Hamad J. (1975) The Moon 12, p. 201-229. [12] Papanastasssiou D. A. & Wasserburg G. J. (1971) EPSL 12, 36-48. [13] Carlson R. W. & Lugmair G. W. (1979) EPSL 45, p. 123-132. [14] Alexander E. C. & Kahl S. B. (1974) PLSC 5, p. 1353-1373. [15] James O. B. (1981) PLPSC 12B, sec. 1, p. 209-233. [16] Spudis P. D. (1984) LPS XV, p. 808-809 (abs). [17] Carlson R. W. & Lugmair G. W. (1981) EPSL 56, p. 1-18. [18] Taylor S. R. (1982) Lunar Science: A lunar perspective: LPI, Houston, p. 246. [19] Baldwin R. B. (1983) Oral commun. [20] Taylor L. A., Shervais J. W., & Hunter R. H. (1983) LPS XIV, p. 777-778 (abs).

Martian Terrain Ages

Robert G. Strom and Nadine G. Barlow, Lunar and Planetary Laboratory
University of Arizona, Tucson, Arizona 85721

The cratering record in the inner Solar System shows two crater populations based on their size/frequency distributions. The heavily cratered surfaces of the Moon, Mercury and Mars all show a similar multi-sloped crater size distribution which represents the period of heavy bombardment. In the diameter range 8 to about 70 km the population index has a -2 slope. On the younger plains units of the Moon and Mars the crater size/frequency distribution has about a -3 slope over the same diameter range. This different crater population represents the accumulation of craters since the end of heavy bombardment. On the Moon the end of the period of heavy bombardment has been dated at about 3.8 BY ago. At this time the family of objects responsible for the period of heavy bombardment became extinct and the subsequent cratering record was caused by a second family of objects which has impacted up to the present time. These two families of impacting objects may have overlapped in time but the high flux of the early objects dominated the cratering record prior to 3.8 BY. The time at which heavy bombardment ended on Mars is model dependent. If heavy bombardment was primarily the result of comets (1) or a disrupted planetesimal (2), then heavy bombardment ended simultaneously on all of the inner planets. If, on the other, heavy bombardment was caused by accretional remnants, then it may have extended as much as 1 BY later on Mars than on the Moon and other terrestrial planets (3). Thus, on Mars, the transition from a highlands-like crater size distribution to a plains-like size distribution represents a time horizon at about 3.8 or 2.8 BY depending upon ones assumptions concerning the origin of the impacting objects. Martian surfaces, however, can be dated relative to the end of heavy bombardment by the type of crater population superposed on them. Furthermore, the relative ages of surfaces within these two time divisions can be determined by crater densities.

About 87% of the Martian surface has been divided into about 25 major geologic units based on published geologic maps and revisions from Viking 1:2M photomosaics. Only the north polar region and the southern half of the Argyre basin have not yet been included. Crater measurements and classifications on the units are complete down to a diameter of 8 km.

Martian surface units show a wide range of crater densities indicating a large spread in relative ages. At a crater density equivalent to about -2 on a Log R plot (Figure 1) the crater population changes from a highlands-like to a plains-like size/frequency distribution, thus marking the end of heavy bombardment. Figure 2 is a map showing the ages of generalized terrains relative to the end of heavy bombardment. Each general terrain may contain several geologic units of different relative ages which will be delineated later on more detailed maps.

In general about 60 percent of the Martian surface dates from the period of heavy bombardment and is situated primarily in the southern hemisphere. This area includes large tracks of volcanic plains (~10%) in and around the Hellas basin and bordering the highlands in the Lunae Planum and Syrtis Major regions. The crater density and size distribution on these surfaces are similar to those on the plains within and surrounding the Caloris basin on Mercury. About 40 percent of Mars post-date the period of heavy bombardment and primarily occupies the northern hemisphere. About 30 percent of this area is covered by plains with a crater density similar to the lunar maria. The remaining 10 percent consists of younger volcanics (Tharsis and Elysium), canyons and layered deposits. Since we are dealing only with the large crater population and therefore large areas, these dates should be considered as average ages only. Individual geologic units may contain smaller areas that are either older or younger than the average age of the unit.

Some local geologically significant units have to be studied in more detail. Almost all small volcanic constructs date from near the end of heavy bombardment. These include Hecates, Ceraunius and other volcanoes with channelled flanks suggesting the channelling process was an ancient event. The major episode of outflow channel formation is roughly contemporaneous with the emplacement of northern plains. The youngest terrains on Mars are the large Tharsis volcanoes and Elysium Mons, the volcanic plains surrounding the Tharsis and Elysium constructs, the canyon deposits, and equatorial and polar layered deposits.

(1) Shoemaker, E., (1980) Satellites of Jupiter, U. of Ariz., p.277
(2) Wetherill, G.W., (1975) Proc. Lunar Planet. Sci. Conf. 6, p.1539-1561
(3) Wetherill, G.W., (1977) Proc. Lunar Planet. Sci. Conf. 8, p.1-15

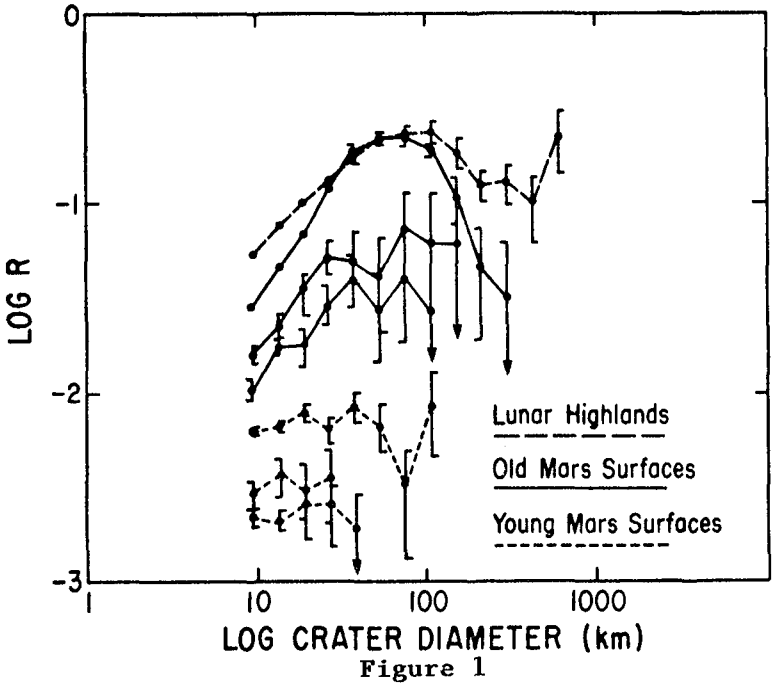

Figure 1

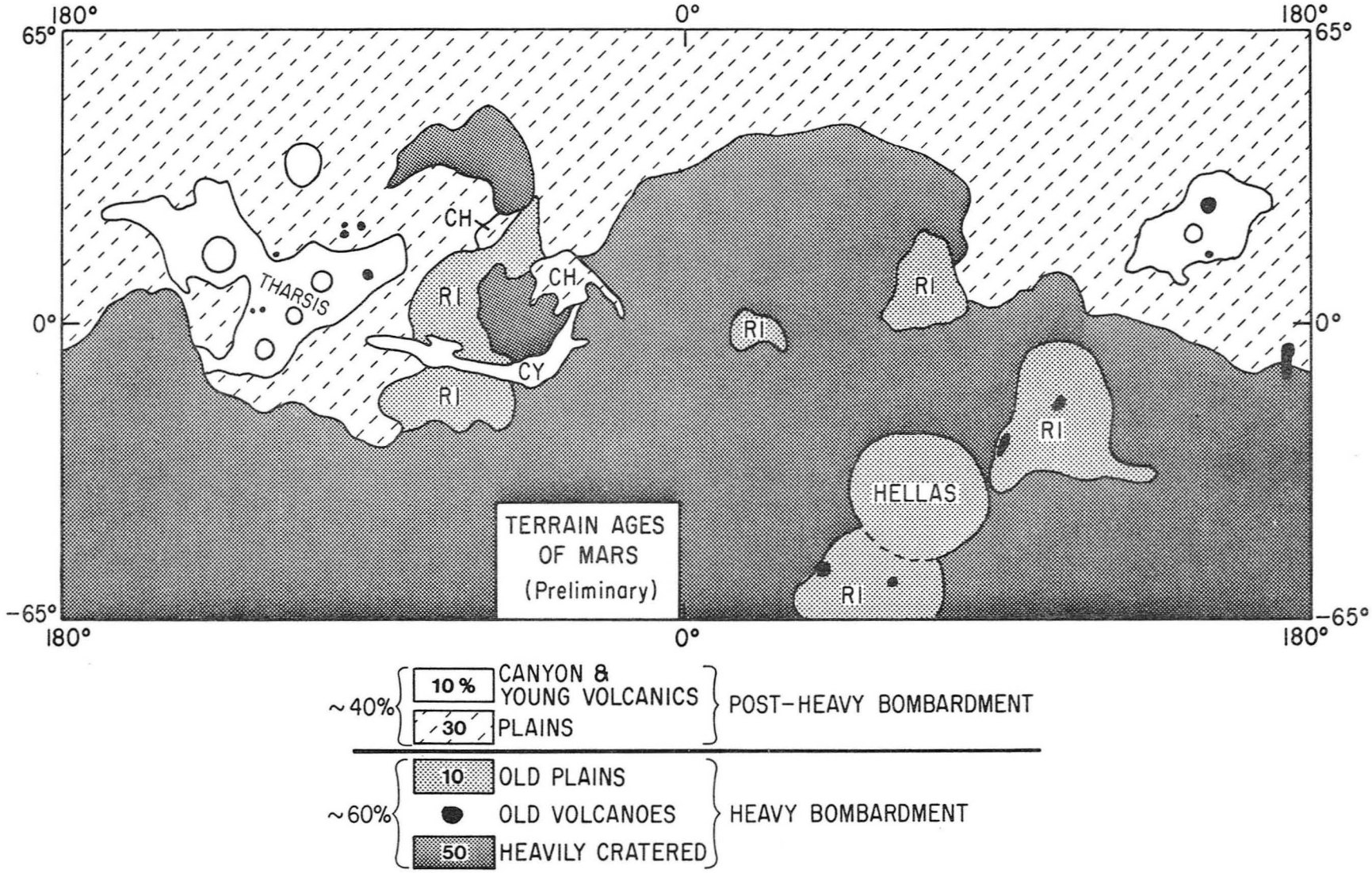
180°
0°
180°
65°
65°
0°
0°
-65°
-65°
180°
0°
180°
CH
CH
THARSIS
RI
RI
RI
RI
RI
CY
HELLAS
TERRAIN AGES
OF MARS
(Preliminary)
~40%
10 %
CANYON &
YOUNG VOLCANICS
30
PLAINS
POST-HEAVY BOMBARDMENT
~60%
10
OLD PLAINS
OLD VOLCANOES
50
HEAVILY CRATERED
HEAVY BOMBARDMENT

Figure 2

IMPACTS IN ICE: COMPARISONS OF SOLAR SYSTEM CRATER POPULATIONS

W.B. McKinnon, Dept. Earth and Planetary Sciences and McDonnell Center for the Space Sciences, Washington Univ., Saint Louis, MO 63130

The "classical" phases of cratering are compression, excavation, and modification. Recent theory and experiments, however, support an alternative sequence of physical events: (1) Coupling - energy and momentum are transferred, and the cratering flow field is set up; (2) Power-law-growth - the flow field expands, with transient cavity dimensions expressible as a simple power-law function of time; and (3) Late-phase - some combination of gravity, strength, and viscosity limits cavity growth, initially causing a deviation from power-law behavior and eventually determining the size and shape of the final (transient) crater (cf. ref. 1). The dominant mechanism that limits cavity growth defines a cratering regime and a single variable, the coupling parameter, determines the scaling laws in the various regimes. The coupling parameter is intermediate in dimensionality between energy and momentum and its exact form is determined by experiment. For simple materials with rate- and scale- independent strength, the transition crater diameter between the strength and gravity regimes is, within reasonable bounds, independent of velocity. Even the smallest craters observed by Voyager appear to be gravity dominated (2,3; Fig. 1). The role of viscous scaling, however, is unclear at present.

Crater populations on the Jovian and Saturnian satellites can be compared after applying "gravity-scaling" correction factors (3; see Table). The external populations of Shoemaker (comets and asteroids) create craters on the Saturnian satellites of up to twice the diameter as those of Ganymede and Callisto. This differential is reversed if the Saturnian craters are due to a lower velocity, internal (i.e., planetocentric) population. In all cases, the transient craters created on these icy bodies are larger than those on the moon. For craters larger than a threshold diameter that varies from satellite to satellite, however, the transient crater is not in mechanical equilibrium and collapses under the influence of gravity. The final crater diameter increases with respect to the transient value and a host of crater structures are created. A critical issue is the mode of collapse: how much is due to rim collapse (terracing) and how much to a more distributed style of failure (subsidence) that does not widen the crater. While the latter is not believed to be important for the moon, the failure mechanism for craters in ice may be different. Model-dependent corrections for the degree of collapse can be calculated if the threshold diameter for collapse can be estimated. Ideally, depth-diameter statistics should be used but estimates of the transition from bowl-shaped to central-peak craters are essentially equivalent. The transition diameters lie in the intervals 3-5, 10-20, 15-25, 20-35, 10-20, and 20-35 km for Ganymede, Rhea, Dione, Tethys, Enceladus, and Mimas, respectively (3,6; Fig. 2). The effect of these corrections is to further increase the diameters of craters on the icy satellites with respect to the moon. Indeed, the increases for Ganymede

and Callisto may be sufficiently great so that final craters due to external bombardment are larger there than on all the Saturnian satellites save Mimas and Enceladus. Unfortunately, even taking all the above into account, it is not possible to rigorously compare crater populations on different objects without a thorough study of the possible "saturation-equilibrium" effects of hypothetical production functions. Certain tentative conclusions can be drawn, however, especially when coupled with inferences from the dynamics that govern projectile population evolution (3,7).

(1) The "Jovian" population (comets) is deficient to some degree in large impactors compared to terrestrial accretion-zone planetesimals; this difference imples that two populations do indeed exist.

(2) As comets must have bombarded the terrestrial zone, these impacts were overprinted by residual terrestrial-zone planetesimals.

(3) Identification of the Jovian population with Saturnian population II is unpalatable.

(4) Identification of the Jovian population with Saturnian population I is possible; in this case population II is internal.

(5) Heavily cratered terrains on Ganymede, Callisto, and the Saturnian satellites may predate inner planet "late heavy bombardment".

The research was supported by NASA Grant NAGW-432.

REFERENCES

1) Holsapple, K.A. Lunar Planet. Sci. XV, 367-368 (1984).
2) McKinnon, W.B. Eos Trans AGU 64, 747 (1984).
3) Chapman, C.R., and McKinnon, W.B. Chapter to appear in Natural Satellites (1984).
4) Shoemaker, E.M., and Wolfe, R.F. Lunar Planet. Sci XII Suppl. A., 1-3 (1981).
5) Shoemaker, E.M., and Wolfe, R.F. In Satellites of Jupiter, 277-339 (1982).
6) Passey, Q.R., and Shoemaker, E.M. In Satellites of Jupiter, 379-434, (1982).
7) McKinnon, W.B. Ices in the Solar System, Abs. NATO Adv. Res. Workshop, 43 (1984).

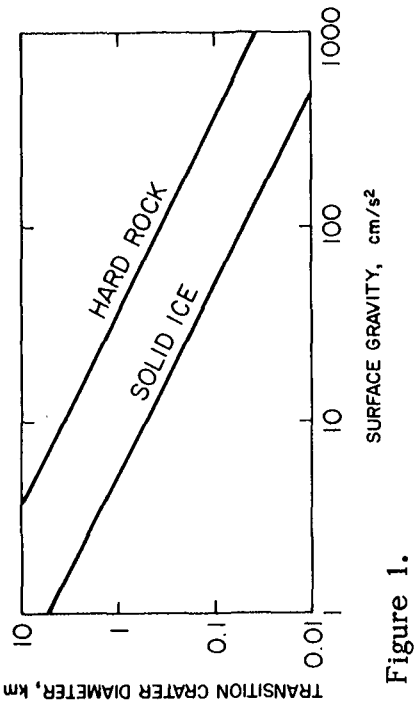

Figure 1.

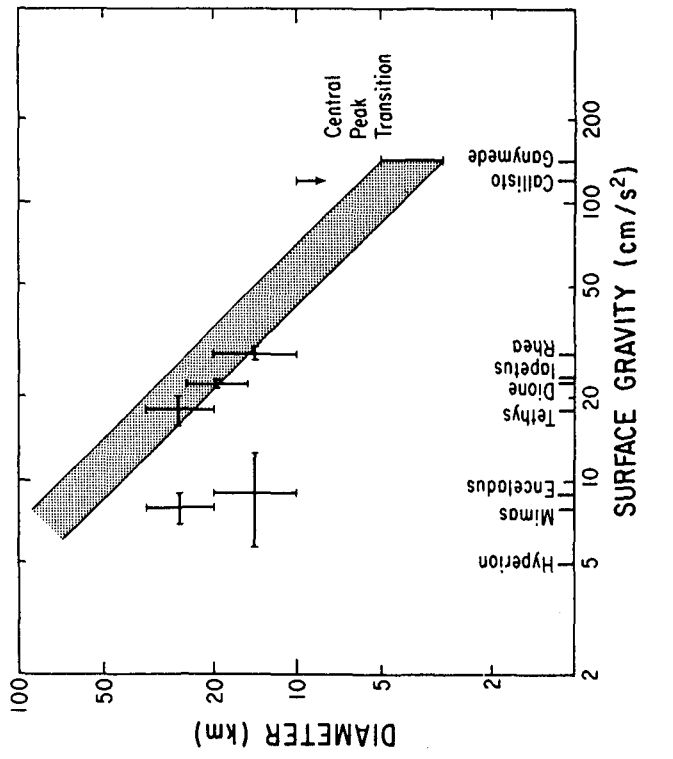

Figure 2.

TABLE . Crater Diameters on Different Satellites for Physically Similar Projectiles

Satellite	External Projectiles				Internal Projectiles[a]	
	Impact[b] Velocity (km/s)	Transient[c] Diameter (km)	Simple-to-Complex[d] Transition Diameter (km)	Collapsed[e] Diameter (km)	Transient[c] Diameter (km)	Collapsed[e] Diameter (km)
Moon	20	1	~15	1	1	1
Phobos	13	3.2	unobserved			
Ganymede	17.4	1.4	~4	3.2	0.8	1.5
Callisto	14.5	1.4	(f)		0.9	
Rhea	15.2	1.9	~15	2.5	1.2	1.3
Dione	17.1	2.1	~20	2.6	1.2	1.2
Tethys	18.3	2.2	~27.5	2.5	1.3	1.1
Mimas	21.9	2.9	~27.5	3.6	1.5	1.4

(a) A representative velocity of 5 km/s is assumed for Jovian and Saturnian satellites; comparison is to 20 km/s lunar impacts.

(b) Mean values; velocities for Jovian and Saturnian satellites based on Shoemaker and Wolfe (1981; 1982), velocities for Moon and Phobos from C. Chapman.

(c) Transient craters are assumed to be geometrically similar.

(d) From Figure 16.

(e) Crater volume is modeled as a right cylinder, with depth ratios taken from simple-to-complex transition diameters.

(f) Below resolution limit.

PROBLEMS IN RECOVERING CRATER PRODUCTION FUNCTIONS.

Alex Woronow. Geosciences Depart., U of Houston, Houston, TX 77004

Two techniques proposed for the recovery of the crater-production functions on densely cratered surfaces have been appraised. The first technique classifies craters according to their degree of rim preservation, then interprets the statistics of the freshest craters as closely mimicing the full population's production function. Although commonly practiced, in fact, this method is demonstrably misleading for densely cratered surfaces. In second technique each crater diameter measured is weighted by the fraction of the crater that remains unoverlapped by subsequent impacts. While this method is theoretically sound even at saturation crater densities, it too fails at high densities, due to practical difficulties.

A major effort of crater analyses involves attempts to recover the crater-production functions. The "production function" gives the relative frequencies of different diameter craters being formed on a surface. For sparsely cratered surfaces, the observed relative frequencies of crater diameters must closely resemble the proportions in which crater sizes were formed. But as crater densities increase, progressively greater numbers of craters may be obliterated by subsequent overlapping impacts, and the relative proportions of crater diameters observed on the surface may deviate increasingly farther from the proportions in which they are produced. Ultimately, the deviation becomes so severe that the production function may be fully obscured.

Technqiue: In order both to assess the reliability of using crater classes, and to examine the feasibility of using Mullins's method for recovering production functions, a Monte Carlo computer code was written. The code accounts obliteration of craters by mutual overlaps of the crater bowls and annular ejecta blankets. A most important feature of the code is the manner in which it maintains information on the integrity of crater rims during successive overlaps. Rims are represented as perfect circles of no width with successive overlaps removing all or portions of the rim. A rim may, therefore, either be fully or partially obliterated in a single, large overlapping impact, or be progressively fragmented and slowly obliterated by many small overlapping impacts, or be in any intermediate condition due to any combination of successive large and small impacts.

Throughout this study, the analyses of the computer-generated data were made at very high crater densities, that is, at saturation. The simulation was run well beyond the point where the long-term rate of cratering was balanced by the rate of obliteration. This balance was assured for all crater classes; therefore, craters of all states of degradation were present in their equilibrium abundances.

Production Function Recovery from Crater Classes: This method is quite simple to apply, and has been frequently (e.g. Chapman, 1968; Chapman et al., 1970; Strom, 1977; Woronow, et al., 1982). One simply classifies craters according to their degree of rim degradation and then interprets the most pristine class as closely reflecting the size-frequency distribution of the production function. Although this method has had frequent application and has even been extended to interpreting the more degraded classes as

representing the production function of geologic processes at previous epochs, it has never been demonstrated to be a reliable procedure.

Figure 1 provides a guide to interpreting crater classes. Considering the solid lines, and the abscissa as a scale of crater degradation, then the rightmost portion of the graph represents slope indices gleaned from a class of quite fresh (relatively unoverlapped) craters. More toward the left-hand side of the graph, this "fresh" crater class is broadened to include successively more degraded craters in the resulting slope index.

The -2 and -4 production functions produce a family of fresh craters that, if used by themselves, would badly under-estimate the production slope index; the -3 production function yields fresh craters that over-estimates the slope index.

Production Function Recovery from Weighted Counts: Mullins (1976) demonstrated that the production function could be recovered from even a saturated surface if one employs the following weighting scheme: first, measure the fraction of a crater rim or bowl that is free of overlapping impacts, second, measure the diameter of the crater, and then, rather than simply recording one crater of that size, record the unoverlapped fraction just obtained. This weighting adjusts for the effects of diameter-dependent obliteration.

The dashed lines in Figure 1 are slope indices derived by this means For cases where the resolution does not impede identification of craters having rim fragments down to a few percent of the whole (the left-hand side of the figure), this method does yield a good estimate of the production function (except for the -3 production function). If, however, one cannot recover such small fragments of rims (and accurately measure the diameter of the parent crater), either because of resolution limits or just because practical limits of feature recognition and measurement, then the method yields less accurate estimates of the production function. If only very fresh craters can be measured then, as expected, Mullins's technique converges to the integer-counting method.

Figure 1 also shows that integer counts of craters having greater than about 25% of their rims intact fortuitiously yield the production slope indices for the -2 and -4 cases. One might be tempted, therefore, to use this means to recover the production function. However, the -3 production function does not abide this same rule, and more complex (non-power law) production functions may not either. Probably one would not be at all justified in freely using craters with greater than 25% rims remaining to define the production function.

For the -3 case, the production function can almost be approximated by analysis of the freshest craters if one allows for the overall offset of the observed slope index away from that for the production function. However, notice that the -2 production function approaches the same observed slope index as that of the -3 for the freshest craters. Again, therefore, in practice, one probably could not remove this ambiguity between the two populations in order to reliably recover the correct production function.

REFERENCES

Chapman, C.R., Interpretation of the Diameter-Frequency Relation for Lunar Craters Photographed by Rangers VII, VIII, and IX, Icarus, 9, 1-22, 1968.

Chapman, C.R., J.A. Mosher, and G. Simmons, Lunar Cratering and Erosion from Orbiter 5 Photographs. J. Geophys. Res., 75, 1445-1466, 1970.

Mullins, W.W., An Estimator of the Underlying Size Distribution of Overlapping Impact Craters, Icarus, 29, 113-123, 1976.

Strom, R.G., Origin and Relative Age of Lunar and Mercurian Intercrater Plains, Phys. Earth and Planet. Interiors, 15, 156-172, 1977.

Woronow, A., R.G. Strom, and M. Gurnis, Interpreting the Cratering Record: Mercury to Ganymede and Callisto, In Satellites of Jupiter (D. Morrison, ed.), 237-276, 1982.

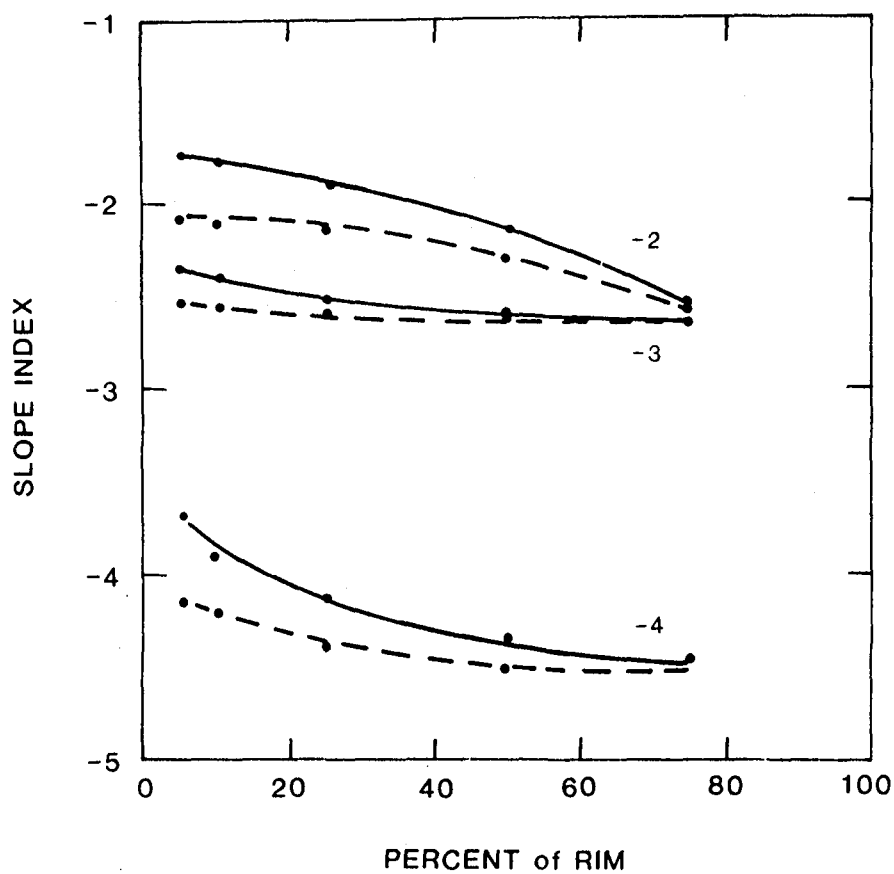

A PARAMETRIC STUDY OF CRATER-SATURATION SIMULATIONS. Alex Woronow, Geoscience Depart., U. of Houston, Houston, TX 77004.

Computer models of cratered surfaces often use inputs of uncertain nature and importance. This work evaluates the sensitivity of the resulting crater-saturation estimates to the input parameters, principally applicable to the study of craters upward from 8km diameter. In order of decreasing importance, crater saturation simulations are found to be sensitive to 1) the dynamic range of crater diameters used, 2) the effectiveness of ejecta-blanket obliteration assumed, and 3) the number of points taken to describe the crater rim. The size of the largest crater in proportion to the size of the simulated surface has no effect on the results when the edges of the simulated surface are correctly treated and craters are counted by the fraction of the crater within the simulated area. A similar procedure is recommended when gathering crater size-density data from images.

The individual parametric studies represent only pieces of the whole model and the exact LOG(R) values derived from these pieces have no significance by themselves. Instead, the **relative** importance, and **relative** behavior of the pieces is what should be gleaned from the figures.

Dynamic Range: Usually held as the most important factor in determining the validity of a particular crater simulation, dynamic range commands first consideration. Figure 1 gives the results of a series of runs made with dynamic ranges from less than (1.5 : 1) to (724 : 1). The densities are reported for the single, central square root of 2 bin. That is, dynamic range was increased by adding both smaller and larger craters to the simulation in a symmetrical manner. Each data point represents the density of craters having at least 10% of their rims remaining, averaged over 20 samples. This plot undoubtedly indicates the maximum effect limited dynamic range can have on computer simulations. In producing the data for Figure 1, craters, no matter how small, overlapping the rim of a larger crater obliterated the overlapped portion of the rim. In reality, any parasitic crater must be some substantial fraction of the size of the host crater in order to render the overlapped portion of the rim fully unrecognizable.

Ejecta Blanket Effects: The simplest model for an ejecta blanket consists of an annulus concentric to the crater bowl within which all craters or pieces of craters are considered annihilated. One could achieve any arbitrary depression in the final saturation density by allowing the annulus to assume any arbitrarily large radius. Figure 2 illustrates the effects. Here the abscissa is a multiplicative factor applied to the crater diameter to determine how far from the crater center the ejecta extends. That figure shows that as the ejecta annulus increases in radius the saturation density is depressed, approximately congruently for all production slope indices. The rate at which this depression of the saturation density occurs depends upon the degree of rim preservation required for crater recognition. In Figure 2 the solid lines depict the effect for craters with greater than 5% rims remaining while the dashed line depicts an example where craters must have greater than 50% rims remaining.

As an alternative approach, the model incorporated ejecta blankets with exponentially decaying thickness (with a -3 exponent) from a thickness at the rim equal to 10% of the crater radius. After each new crater was formed, the program searched radially outward to other craters, and determined if the

thickness of the ejecta at those craters exceeds the crater depth (taken to be 15% of the diameter). If this condition was met, then the proportion of the rim lying under that ejecta was obliterated. No accounting was made of multiple ejecta overlaps wherein each individual ejecta blanket was by itself insufficient to remove the crater rim, but together they may have been substantial enough to achieve obliteration. Probably such cooperative ejecta obliteration is relatively rare in comparison to direct overlap of craters and their thicker ejecta facies. The arrows on Figure 2 indicate the results of this modeling procedure where one may read the LOG (R) value from the curves.

Crater Size to Surface Size: The ratio of the area occupied by the largest crater to the area of the surface being simulated may plausibly be one controlling factor determining the saturation density. Marcus (1970) postulated that the largest crater governs the ultimate saturation limit in a study region. In fact, when craters are counted by integers, the crater/surface area ratio can somewhat bias the end results. A standard procedure in collecting crater statistical data is to include within the data set any crater whose center lies within the counting boundaries, counting it as a whole regardless of whether a portion of it lies beyond the boundaries or not. Conversely, any crater lying partially within the counting boundaries, but having its center outside the boundary is ignored. Actually, one should count craters by the fraction that lies within the area of interest. Figure 3 illustrates the analytical solution for the correction factor for the case of a circular counting surface.

Rim Preservation and Recognition: Generally, craters are recognized by the presence of elements of topographic relief arranged in circular plan. These circular elements are usually pieces of the crater's rim. Although no studies exist on how much rim must be present, or how fragmented the segments could be and yet have a crater to be recognized and measured, most practitioners of the art arrive at about the same total number of craters for any particular study area (Hartmann, et al., 1981). Figure 4 depicts the dependency of saturation density on rim percent needed for recognition of a crater. Fortunately, the dependency is nil for a slope index of -2, and minimal for slope indices as great as -4 when considered over the most likely range of perhaps 10% to 30%. This low dependency of results on degree of rim preservation required for crater recognition may partially explain why workers with divergent experience and patience tend to get remarkably similar counting results.

The behavior is readily understood in terms of the obliterative mechanism of crater and ejecta overlap; namely, for -2 and -3 slope indices, craters larger than the host are the most effective obliterators. Under such a circumstance, a larger crater is most likely to totally obliterate a small crater, if it hit it at all, rather than only partially overlap it. Therefore, most craters are either pristine or totally obliterated, few are partially obliterated. If the production slope index is -4, however, then craters smaller than the host do most of the obliteration, and more than one impact is usually required to totally obliterate a crater. Therefore, partially obliterated craters are common, and one would expect a higher correlation between the degree of obliteration and the observed density of craters having that degree of obliteration or less then for the less negative production slope indices.

REFERENCES

Hartmann, W.K., et al. (1981) Chronology of Planetary Volcanism by Comparative Studies of Planetary Cratering. Basaltic Volcanism on the Terrestrial Planets, Pergamon Press,

Marcus, A.H. (1970) Comparison of Equilibrium Size Distributions for Lunar Craters. J. Geophys. Res. 75, 4977-4984.

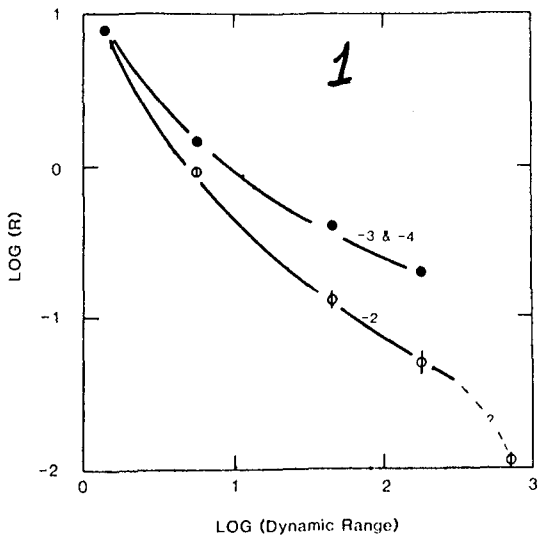

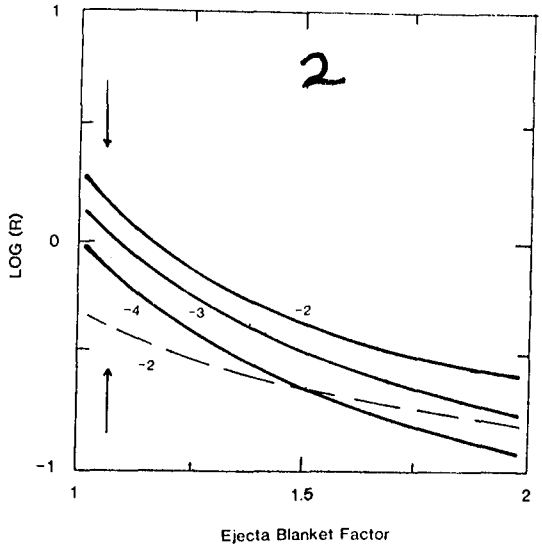

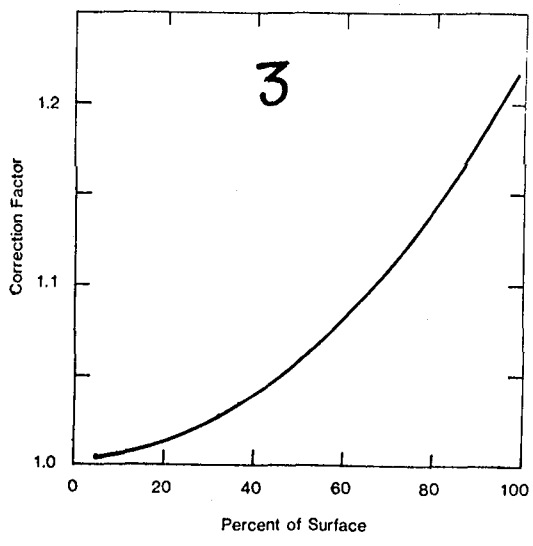

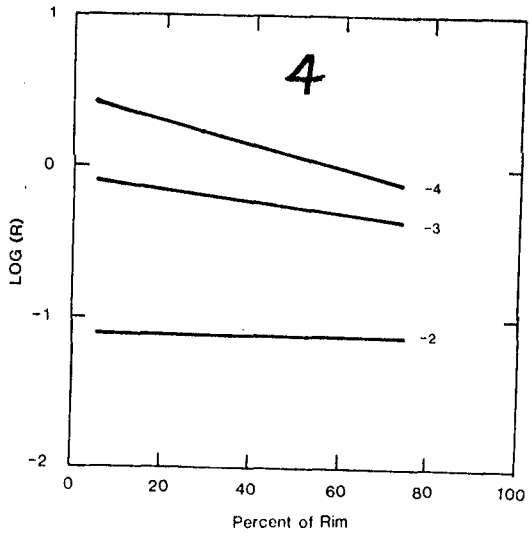

AVERAGE SPACING FOR RINGS OF INDIVIDUAL MULTI-RING BASINS IS $2.0^{0.5}D$

R. J. Pike*, P. D. Spudis†, and G. D. Clow*, U. S. Geological Survey: *Menlo Park, CA, 94025; †Flagstaff, AZ, 86001, also Dept. Geology, Arizona State Univ., Tempe, AZ, 85287.

Introduction — This report continues our enquiry into the mathematically regular spacing of the concentric rings of planetary impact basins, a concept originating with [1] and [2]. The most recent results have shown that a constant radial increment of $x^{0.5}D$, where x is about 2.0 and D is ring diameter, separates adjacent statistical groups of rings and arcs of multi-ring basins on Mars, Mercury, and the Moon [3,4]. Here, we present statistics of spacing for adjacent rings of individual basins on the three planets, and revise earlier work on single basins [5,6] from ring measurements of newly-recognized basins on Mercury and Mars [3,4]. Analysis of ring rank:ring diameter for adjacent rings of individual basins also yields an average spacing of about $2.0^{0.5}D$, specifically $(2.01 \pm 0.26)^{0.5}D$.

Data — Basin rings are recognized and mapped by photogeology [1,7,8]. Measurements of average ring diameters for the 64 basins in Table 1 are ours [3,4]; center coordinates of many newly mapped basins are given in [7,8]. Many basin names are informal. The numerical ranking of rings from I (innermost) to VII (outermost) by graphical analysis, a necessary prelude to all subsequent statistical work, is described by [3]; see also [4,5,6,].

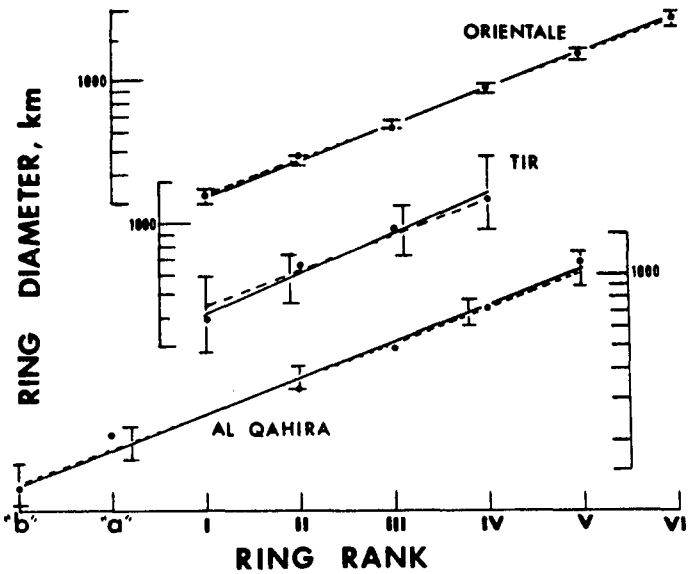

Figure 1. Basin ring diameter as a function of ring rank for three representative basins (dots): Orientale (Moon), Tir (Mercury), and Al Qahira (Mars). Solid lines, linear fits; error bars, 95% C.I.; dashed lines, fit for spacing model where slope = $2.0^{0.5}D$. Provisional ranks "a" and "b" are infrequently occupied by rings.

Procedure — A functional dependence of $\log_{10}$ ring size (Y) upon radial ring position, or rank (X), was established by linear least-squares fits for each basin on Mars (n = 24 basins, 108 rings), Mercury (n = 22, 85), and the Moon (n = 18, 85) that has three or more rings. The equations, after [6] from [2], are of the form $\log D_n = \log D_{IV} + (n-4) \log b$, where D_n is diameter of a ring of any rank n and D_{IV} is diameter of the main ring ("topographic rim") both in km, ranks are similarly spaced integers in arbitrary units, and b is slope. Diameters were weighted 1,2, or 3 in the correlations according to quality of the photogeologic observations. Figure 1 shows three examples of the observations and the resulting lines. Fits of the equation to each basin yield statistical estimates of the slope b* and diameter of the main basin ring D_{IV}* (Table 1). The average spacing increment for adjacent ranked rings, x, is $(b^*)^2$. Rings III and V, which lie farther from ring IV than the nominal 2.0 spacing increment in grouped-data results [4], were not separated from the

Table 1 Least-Squares Fits to Ring Rank & Diameter for Multi-Ring Basins

BASIN†	rings	r	D_{IV}*	b*	x, 95% C.I.
MOON					
Orientale	6	0.999	924	1.420	2.016 +0.103 -0.098
Imbrium	6	0.999	1137	1.427	2.036 +0.095 -0.091
Nectaris	5	0.994	871	1.403	1.967 +0.292 -0.255
Moscoviense	5	0.998	432	1.428	2.040 +0.196 -0.179
Mendel-Rydberg	4	0.999	428	1.458	2.126 +0.220 -0.199
Hertzsprung	4	0.992	548	1.419	2.013 +0.639 -0.485
Humorum	6	0.996	424	1.386	1.920 +0.166 -0.152
Smythii	5	0.999	760	1.431	2.047 +0.123 -0.116
Crisium	5	0.999	524	1.443	2.081 +0.111 -0.105
Grimaldi	3	0.995	432	1.383	1.913 +2.610 -1.104
Humboldtianum	6	0.996	684	1.420	2.016 +0.179 -0.164
Coulomb-Sarton	4	0.996	461	1.406	1.977 +0.420 -0.347
Serenitatis South	5	0.999	895	1.462	2.137 +0.111 -0.105
Korolev	4	0.999	429	1.388	1.927 +0.154 -0.143
Ingenii	4	0.999	320	1.412	1.994 +0.211 -0.191
Apollo	3	0.999	491	1.435	2.060 +0.935 -0.643
Balmer	3	0.999	393	1.497	2.241 +1.319 -0.831
Keeler-Heaviside	4	0.996	493	1.476	2.179 +0.521 -0.420
MARS					
Al Qahira	6	0.994	742	1.420	2.017 +0.221 -0.199
near Newcomb crater	4	0.996	853	1.459	2.129 +0.517 -0.416
Ladon	5	0.994	579	1.356	1.838 +0.234 -0.208
Chryse	5	0.999	1282	1.482	2.196 +0.174 -0.162
Mangala	3	0.988	694	1.442	2.080 +6.995 -1.603
Sirenum	4	0.992	497	1.507	2.270 +0.855 -0.621
so. of Hephaestus Fossae I	4	0.991	458	1.465	2.145 +0.766 -0.565
so. of Hephaestus Fossae II	3	0.996	1053	1.399	1.958 +2.174 -1.030
southeast of Hellas	3	0.996	535	1.398	1.954 +2.379 -1.073
south of Renaudot crater	4	0.999	651	1.446	2.090 +0.110 -0.104
south of Lyot crater	5	0.996	389	1.400	1.961 +0.228 -0.204
Cassini	5	0.998	444	1.452	2.108 +0.168 -0.155
Deuteronilus-B	4	0.999	194	1.451	2.105 +0.140 -0.131
Deuteronilus-A	5	0.997	207	1.370	1.876 +0.173 -0.158
near South crater	5	0.974	774	1.359	1.846 +0.555 -0.426
near Schiaparelli crater	5	0.993	428	1.434	2.056 +0.338 -0.291
near Le Verrier crater	4	0.999	474	1.348	1.818 +0.093 -0.088
Noctis Labyrinthus	5	0.999	1851	1.451	2.105 +0.103 -0.098
South Polar	3	0.986	872	1.405	1.975 +6.770 -1.529
Argyre	6	0.996	803	1.330	1.768 +0.134 -0.124
Isidis	4	0.998	1451	1.422	2.022 +0.287 -0.252
Hellas	7	0.999	2252	1.378	1.898 +0.071 -0.069
Huygens	3	0.999	468	1.392	1.937 +0.571 -0.441
near Cassini	6	0.999	356	1.443	2.083 +0.103 -0.098
MERCURY					
Borealis	3	0.997	1567	1.358	1.843 +1.519 -0.833
Gluck-Holbein	3	0.999	487	1.411	1.990 +0.929 -0.633
Sobkou	3	0.984	900	1.374	1.889 +6.100 -1.442
Brahms-Zola	4	0.999	609	1.362	1.854 +0.169 -0.155
Donne-Moliere	4	0.999	1066	1.414	1.999 +0.113 -0.107
Hiroshige-Mahler	3	0.997	336	1.475	2.176 +2.265 -1.110
Mena-Theophanes	4	0.996	788	1.466	2.150 +0.504 -0.409
Tir	4	0.988	1333	1.482	2.198 +1.024 -0.699
Budh	3	0.997	827	1.407	1.979 +1.980 -0.990
Ibsen-Petrarch	4	0.994	624	1.430	2.044 +0.564 -0.442
Andal-Coleridge	5	0.986	1329	1.396	1.948 +0.440 -0.359
Matisse-Repin	4	0.999	857	1.448	2.096 +0.069 -0.067
Bartok-Ives	4	0.993	1125	1.341	1.800 +0.426 -0.345
Hawthorne-Riemenschneider	4	0.999	537	1.410	1.987 +0.155 -0.144
Vincente-Yakolev	4	0.992	710	1.412	1.993 +0.598 -0.460
Eitoku-Milton	4	0.999	1189	1.420	2.017 +0.088 -0.085
Sadi-Scopas	4	0.993	909	1.374	1.888 +0.469 -0.376
Tolstoi	4	0.993	499	1.439	2.072 +0.615 -0.474
Caloris	6	0.997	1330	1.438	2.067 +0.171 -0.158
Chong-Gauguin	4	0.992	900	1.407	1.979 +0.615 -0.469
Shakespeare	3	0.996	438	1.511	2.282 +3.512 -1.383
Van Eyck	4	0.995	286	1.372	1.884 +0.382 -0.317

† - Many names are provisional, and do not constitute official nomenclature

others. We had anticipated that inclusion of rings III and V (see those of Al Qahira, Figure 1) would yield fits with slopes uniformly greater than $2.0^{0.5}$. The average observed excess, 0.012, is small and may not be statistically significant.

Results — Mean values of x for each planet lie close to the model spacing increment of 2.000 postulated by [2] for the Orientale basin: Mars, 2.004 +0.523 -0.449; Mercury, 2.006 +0.677 -0.579; and Moon, 2.034 +0.323 -0.299. However, the dispersion of slope, b*, given by the 95% confidence interval (C.I.), is high. We examined C.I. values as a function of the number of rings in each basin, and found an inverse, but strongly nonlinear, dependency (Figure 2). The relation between sample size and dispersion of slope is approximately linear for $4 \leq n \leq 7$ rings per basin, but at n = 3 rings the dispersion is about 4X that expected from an extrapolation from basins with four or more rings. Thus diameter:rank fits to three-ring basins are too poorly constrained to yield meaningful estimates of the dispersion for slope of the equations (and hence basin-ring spacing). Accordingly, we have deleted the 14 three-ring basins and recalculated mean slope and its C.I. for the remaining 50 basins (233 rings). The resulting values for $\bar{x}$ are: Mars, 2.008 +0.260 -0.217 (n = 19 basins, 93 rings); Mercury, 2.000 +0.394 -0.312 (n = 16, 67); and the Moon, 2.029 +0.220 -0.192 (n = 15, 73).

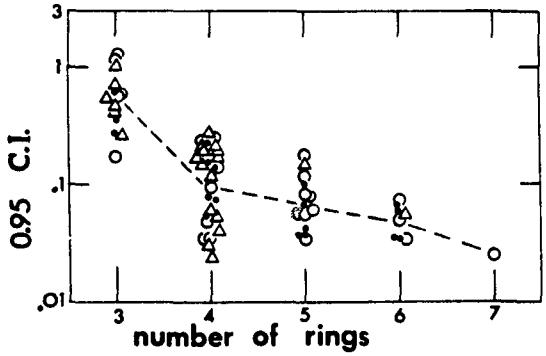

Figure 2. Nonlinear inverse dependency of 0.95 C.I., the dispersion of slope for least-squares fits to basin ring diameter and ring rank, upon number of rings per basin. Dots, Moon; circles, Mars; triangles, Mercury. Dashes connect geometric means of 0.95 C.I.

Discussion — The revised average-spacing increments for single basins are barely changed from the initial ones. However, the values of dispersion are substantially reduced, and are thus closer to the intrinsically lower values derived from analyses of grouped basins [3,4]. The weighted mean x and C.I. values for all three bodies are $2.012^{+0.286}_{-0.236}$. This observed 95% C.I., 1.776 to 2.298, lies well within one $2.0^{0.5}D$ interval, 1.414 to 2.829, defined by distances midway between $\log_{10}$ model ring-spacing values, 1.0, 1.414, 2.0, 2.828, etc. Whether or not the observed mean 95% C.I. — although narrow — is small enough to differ significantly from one that might arise from random processes (cf. [6]) remains to be tested. We are devising formal statistical procedures to answer this question.

Interpretation — A constant spacing of basin rings, both inside and outside the main ring (IV) and on three different planets, carries some weighty genetic implications [3,4]. We do not repeat these arguments here save to emphasize that ring location, and perhaps ring formation, are more likely controlled by mechanics of the impact event itself than by crustal properties such as layering or thickness.

References — [1] Hartmann, W.K., & Kuiper, G.P., 1962, Comm. Lunar Planet. Lab. 1, 55-66; [2] Fielder, G., 1963, Nature, 198, 1245-1260; [3] Pike, R.J., & Spudis, P.D., 1984a, NASA TM-86246, 90-92; [4] Pike, R.J., & Spudis, P.D., 1984b, Lunar Planet. Sci. XV, 647-648; [5] Pike, R.J., 1981, NASA TM-84211, 123-125; [6] Clow, G.D., & Pike, R.J., 1982, Lunar Planet. Sci. XIII, 123-124; [7] Spudis, P.D., & Strobell, M.E. 1984, Lunar Planet. Sci. XV, 814-815; [8] Schultz, P.H., Schultz, R.A., & Rogers, J., 1982, J. Geophys. Res. 87, 9803-9820.

RING-DIAMETER RATIOS FOR MULTI-RING BASINS AVERAGE $2.0^{0.5}D$

R. J. Pike, U. S. Geological Survey, Menlo Park, CA, 94025, and P. D. Spudis, U. S. Geological Survey, Flagstaff, AZ, 86001 and Dept. Geology, Arizona State Univ., Tempe, AZ, 85287.

The Problem — This note broadens our study of the spacing of the concentric rings of planetary impact basins, an idea from [1] and [2]. The most recent findings show that a radial increment of $x^{0.5}D$, where x is about 2.0 and D = ring diameter, separates both (1) adjacent least-squares groups of rings and arcs of multi-ring basins on Mars, Mercury, and the Moon [3,4], and (2) adjacent rings of individual basins on the three planets [5,6,7]. Here, we present statistics for ratios of ring diameters, the first and most-applied parameter of ring spacing [1,2,8-10]. We find that ratios excluding rings flanking the main ring also have a mean spacing increment of about 2.0. Ratios including such rings, as for the least-squares groups, [3,4] and (1) above, have a larger increment, averaging 2.1. The F-test indicates, with 95% confidence, that these spacings did not arise by chance.

Observations — Photogeology is used to recognize and map planetary basin rings. We measured average diameters for rings of 67 basins (see [7] for list of 64). The numerical ranking of rings from I (innermost) to VII (outermost) by graphical analysis, a prelude to statistical work, is described by [3], also [4-6]. Table 1 summarizes the scope of our observations. The basic data are ratios of diameters of adjacent observed basin rings, D_n/D_{n-1}, where n is ring rank, an integer usually 1-7. The observed ratios fall into the two clusters of values found by [1], about 1.4 to 1.5 — usually for adjacent ranks, and about 2.0 — usually for alternate ranks (Figure 1). To supplement the few latter ratios we generated a second set of "alternate ring-rank" ratios by deliberately skipping one observed ring (Table 1, Figure 1). The three subsets of ratios were grouped according to inclusion of rings III or V. We also included for comparison our ratios for two-ring basins that lack central peaks.

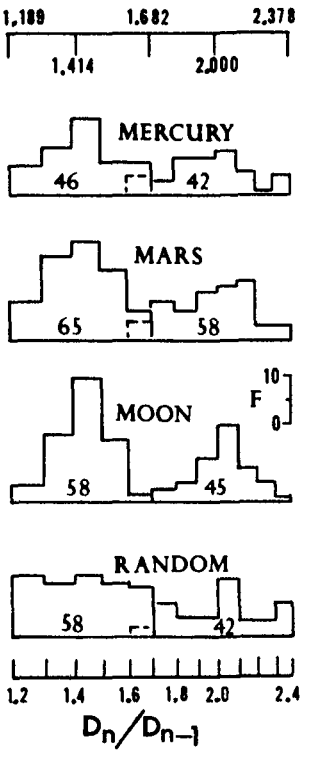

Figure 1. Frequency, F, of basin-ring ratios for adjacent (L) and alternate (R) ranks. No breakdown by ranks III,V. No two-ring basins. $\log_{10}$ s for both sets of random ratios is the same: 0.045.

Analysis — Mean ($\bar{x}$) and standard deviation (s) were calculated, in the $\log_{10}$ domain (basin-ring ratios are lognormally distributed) for each of the 18 groups of observed ratios (Table 2). Nine other groups had too few (<10) ratios for stable statistics. We repeated the statistics for two sets of ratios drawn from a table of random numbers [13], one corresponding to ring ratios for adjacent ranks (1.189 to 1.682), the other to ratios for alternate ranks (1.682 to 2.378). The intervals are defined by distances midway between two $\log_{10}$ model ring-spacing values, respectively 1.0, 1.414, and 2.0 and 1.414, 2.0, and 2.828. We transformed all values of $\bar{x}$ and s to the domain of the spacing increment, x, so that statistics for both adjacent and alternate ranks are directly comparable (Table 2).

Table 1. **NUMBERS OF BASINS, RING DIAMETERS & THEIR RATIOS FOR THREE PLANETS**

Planet	multi-ring basins	rings as mapped	rings as ranked	ratios: rings in adjacent ranks	ratios: rings in alternate ranks	
					No observed ring skipped	One observed ring skipped
Moon	18	85	82	58	6	39
Mars	26	119	112	65	21	40
Mercury	23	92	87	46	18	24
Totals	67	296	281	169	45	103

Table 2 **RATIOS OF BASIN RING DIAMETERS: STATISTICS OF CENTRAL TENDENCY AND DISPERSION**

Groups of Ring Ratios §	Mean, ± Standard Deviation†, (Number of ratios) [results for raw ratios below, and their x equivalents above]		
	Moon	**Mars**	**Mercury**
	ADJACENT RING RANKS		
Randomly-chosen values from 1.189 to 1.682	– – – – – – – – – – – –	2.069 +0.475 -0.387 (105) [1.438 +0.157 -0.141]	– – – – – – – – – – – –
II/I, VII/VI (spacing neither wide nor close)	– – ¶ – –	2.016 +0.383 -0.323 (14) [1.420 +0.129 -0.119]	– – ¶ – –
III/II, VI/V (close spacing)	1.994 +0.256 -0.225 (20)* [1.412 +0.088 -0.082]	1.929 +0.412 -0.371 (19) [1.389 +0.141 -0.128]	1.888 +0.359 -0.298 (12) [1.374 +0.125 -0.113]
IV/III, V/IV (wide spacing)	2.117 +0.224 -0.204 (30)* [1.455 +0.075 -0.072]	2.137 +0.356 -0.306 (32)* [1.462 +0.117 -0.109]	2.097 +0.327 -0.283 (30)* [1.448 +0.109 -0.101]
	ALTERNATE RING RANKS: NO OBSERVED RING SKIPPED ¶¶		
Randomly-chosen values from 1.682 to 2.378	– – – – – – – – – – – –	2.020 +0.460 -0.375 (42) [2.010 +0.217 -0.196]	– – – – – – – – – – – –
IV/II, VI/IV (spacing neither wide nor close)	– – ¶ – –	1.887 +0.352 -0.297 (13) [1.943 +0.174 -0.159]	1.961 +0.339 -0.288 (13) [1.981 +0.164 -0.152])
III/I, VII/V (close spacing)	– – ¶ – –	– – ¶ – –	– – ¶ – –
D/D_i for two-ring basins §§	2.108 +0.169 -0.157 (10)* [2.053 +0.081 -0.078]	2.249 +0.519 -0.422 (22)†† [2.121 +0.232 -0.209]	2.048 +0.259 -0.230 (31)* [2.024 +0.124 -0.117]
	ALTERNATE RING RANKS: ONE OBSERVED RING SKIPPED		
IV/II, VI/IV (spacing neither wide nor close)	2.044 +0.240 -0.214 (20)* [2.022 +0.115 -0.109]	1.997 +0.345 -0.294 (19) [1.999 +0.166 -0.153]	1.897 +0.237 -0.211 (12)* [1.948 +0.118 -0.111]
III/I, VII/V (close spacing)	– – ¶ – –	1.849 +0.421 -0.342 (11) [1.923 +0.208 -0.188]	– – ¶ – –
Rings V/III (wide spacing)	2.263 +0.306 -0.269 (12)* [2.127 +0.139 -0.131]	2.316 +0.603 -0.478 (10) [2.152 +0.264 -0.235]	– – ¶ – –

† calculations in $\log_{10}$ domain, ratios weighted 1 to 5 according to quality of data
§ include ratios formed from a few rings ranked below I ("a","b")
* dispersion of observed ratios is significantly less than that of ratios selected randomly within one $2^{0.5}$ interval, according to one-sided F-test carried out in the $\log_{10}$ domain at the 0.95 confidence level
¶ too few data for stable statistics
§§ no central peaks; D equivalent to ring IV, D_i to ring II
¶¶ no wide spacings (rings V/III)
†† preliminary data

Results: Central tendency — The 267 observed ratios (x equivalents) in the 15 multi-ring categories (Table 2) cluster around the model spacing increment of 2.000 postulated by [2] for the Orientale basin. The combined weighted mean for all three planets is 2.039 +0.382 -0.284, close to our values obtained for individual basins [7]. The net excess of observed over model, +0.04, is statistically insignificant. Weighted means for individual planets are 2.091 +0.248 -0.221 (Moon, n = 82 ratios), 2.027 +0.393 -0.333 (Mars, n = 118), and 1.997 +0.319 -0.274 (Mercury, n = 67). The difference among "close," "wide," and "neither close nor wide" ring ratios, although not statistically significant, is strong enough to show up clearly in averaged x values of these groups: respectively 1.928 +0.353 -0.305 (n = 62 ratios), 2.117 +0.304 -0.265 (n = 92), and 1.976 +0.314 -0.270 (n = 91). The spacing for rings V/III is expectedly large, 2.287 +0.441 -0.364 (n = 22). However, because $\bar{x}$ for randomly-chosen ratios within one $2.0^{0.5}$ interval also is 2.0 (Table 2), observed values for average spacing have no meaning unless their dispersion occupies limits too narrow to have occurred by chance.

Results: Dispersion — The spread of basin-ring ratios about the mean is significantly less than dispersion that might arise from random processes, with qualifications noted below. This difference indicates that the $2.0^{0.5}D$ ring spacing is real. We compared, by an F-test at the 95% confidence interval [14], the standard deviation, s, of each subset in Table 2 with s from one of the two sets of randomly-generated ratios [13]. Results of the test are highly systematic by sample size and by planet (Table 2): For six of seven subsets of ≥ 20 ratios, observed dispersion is significantly less than random dispersion (i.e., a "pass"). Of the 11 subsets containing ≤ 19 ratios, only three pass. Clearly, when the sample is adequate, dispersion of ring ratios is significantly less than that due to chance. Most subsets "failing" the test simply are too small — so small that their difference from random is "not proven" rather than disproven, a critical distinction. All five lunar subsets pass the test; three of the five mercurian subsets pass; only one martian subset passes, partly because the sample (n = 32) is large. The $2.0^{0.5}D$ spacing is strongest on the Moon — where basin rings are best known and displayed, weakest on Mars — where mosts rings are severely degraded, and intermediate (but still much weaker than on the Moon) on Mercury — where degradation is slow but the rings are not strongly developed or well displayed.

Discussion: — We demonstrate here by a formal statistical test that the $2.0^{0.5}D$ spacing of basin rings on three planets is not accidental. The degree of certainty is 95%. A similar spacing of concentric rings, both within and without the main ring (IV) of basins on three disparate planets, prompts some interesting genetic speculations [3,4]. We need not reiterate these arguments at length here, except to note that basin ring location, and perhaps mode of ring formation, are probably controlled more by the mechanics of the impact event itself than by crustal properties such as layering or thickness.

References — [1] Hartmann, W.K., & Kuiper, G.P., 1962, Comm. Lunar Planet. Lab. 1, 55-66; [2] Fielder, G., 1963, Nature, 198, 1245-1260; [3] Pike, R.J., & Spudis, P.D., 1984a, NASA TM-86246, 90-92; [4] Pike, R.J., and Spudis, P.D., 1984b, Lunar Planet. Sci. XV, 647-648; [5] Pike, R.J., 1981, NASA TM-84211, 123-125; [6] Clow, G.D., & Pike, R.J., 1982, Lunar Planet. Sci. XIII, 123-124; [7] Pike, R.J., Clow, G.D., and Spudis, P.D., 1984, this volume; [8] Hartmann, W.K., and Wood, C.A., 1971, Moon, 3, 3-78; [9] Howard, K.A., Wilhelms, D.E., & Scott, D.H., 1974, Rev. Geophys. Space Phys., 12, 309-327; [10] Wood, C.A., & Head, J.W., 1976, Proc. Lunar Sci. Conf. 7th, 3629-3671; [11] Schultz, P.H., Schultz, R.A., & Rogers, J., 1982, JGR 87, 9803-9820; [12] Spudis, P.D., & Strobell, M.E., 1984, Lunar Planet. Sci. XV, 814-815; [13] Rand Corp., 1955, A Million Random Digits, Free Press; [14] Natrella, M.G., 1963, Experimental Statistics, NBS Handbook 91, U.S.G.P.O.

Morphology and Mechanics of Terraces in Lunar Craters

Steven K. Croft, Lunar and Planetary Laboratory
University of Arizona, Tucson, Arizona 85721

The morphology and morphometry of terraces provide information on the mechanical conditions of failure and enlargement of impact craters. A simple, perfect plasticity model for terrace formation was proposed by (1), but the preliminary terrace width measurements used to support the model were insufficient to provide a rigorous test. Thus a more thorough morphometric study of lunar crater terraces was made. Roughly 1,000 terraces in 53 (reasonably) fresh lunar craters were measured using Apollo and Lunar Orbiter vertical stereo photography. Terrace widths and their order inward from the rim were measured along eight equally spaced radials in each crater. A list of the craters including rim diameters and geologic data is given in (2).

Results. Figure 1 shows the dependence of the largest terrace width, W_1, on the crater rim diameter, D_r. W_1 is defined as the average of the three largest terrace widths measured in any single crater. W_1 increases approximately linearly with rim diameter: $W_1 \simeq 0.06 D_r$. The symbols with error bars at lower left are not measured terrace widths, but calculated thicknesses of sheets of crater wall material required to account for the debris deposits found on the floors of several simple and flat-floored craters (see ref. 2). Figure 2 is a plot of terrace width as a function of distance from the crater center, both quantities normalized to the crater rim radius. Each point represents a terrace; points of zero width correspond to debris deposits. Each connected set of points represents the cumulative inward widths of terraces along a single radial. Though there is large variablility from radial to radial and from crater to crater, there is a clear trend of decreasing terrace width towards the crater center. Figure 3 shows the average cumulative terrace width subtracted from the rim diameter (defined as the Terrace Reconstruction Diameter, see ref. 2) of each crater as a function of rim diameter and the geologic nature of the substrate. The normalized terrace reconstruction diameter decreases as $D_r^{-0.15}$ with increasing D_r from the simple-complex transition at 15 km to 40-50 km, above which it asymptotically approaches ~0.8. Thus the cumulative terrace width increases rapidly from zero (no terraces) at D_r = 15 km, and approaches a maximum width of about 0.2 the crater radius at large diameters. Cumulative terrace widths also tend to be larger in craters formed on lunar maria. Summarizing, in an average terraced rimwall, the widest terrace of width ~0.06 D_r (figure 1) is the first one inside the crater rim, with successive terraces of decreasing width (figure 2) descending to a debris deposit at the edge of the crater floor at a cumulative terrace width of ~0.2 D_r (large craters).

Discussion: According to the theory of terrace formation of (1), the terrace width: $W = c/(g\rho \sin^2\varphi)$, where c is cohesion, g is surface gravity, ρ is material density, and φ is the slope of the failure scarp. A constant cohesion was assumed in (1), leading to a prediction of constant terrace width regardless of crater diameter. This

prediction, however, is inconsistent with the data presented here: W_l increases linearly with D_r and larger terraces tend to occur in larger craters. The simple model of (1) also predicted a much larger zone of terrace failure than is observed (figure 3), a problem noted later (3). The framework of a new model to explain the new terrace data is shown in figure 4. In an impact, a roughly hemispherical shock wave expands outward from the point of impact. The pressure, P, in the shock decreases with increasing range from the point of impact. Based on observation and models of the strength degradation of material subjected to shock (4), the cohesion of material subjected to shock pressures above some upper limit, P_u, is reduced to zero; the cohesion of material subjected to shock pressures below some lower limit, P_l, remains essentially unchanged. Between P_u and P_l at a constant normalized radial distance from the point of impact (figure 4) is a transition zone where cohesion increases from zero to the ambient value. Since the width of a terrace depends on the effective cohesion, terraces of zero "width" (cohesionless debris) will form in material subjected to pressures above P_u, and terraces of increasing width, (due to increasing cohesion) will form at increasing radial distances in the cohesion transition zone, until the cohesion becomes great enough to prevent further failure. Due to different scaling relations (5), the excavation cavity (gravity scaled) extends beyond the transition zone (strength scaled) in small craters, thus no terraces form. At larger absolute diameters, the excavation cavity shrinks relative to the transition zone, eventually reaching a point where part of the transition zone is beyond the excavation and terraces can form (the simple-complex transition). As the absolute diameter continues to increase, larger portions of the transition zone remain in the crater, producing an increasingly wider zone of terrace formation. Finally, at large enough absolute diameter, portions of the zero cohesion zone remain in the crater, producing a zone of constant width of visible terraces bordered by loose debris next to the crater floor. Further decrease of the excavation cavity relative to the transition zone (represented by the $\varepsilon/\alpha = 0.85$ line in figure 3) leaves only increasing amounts of debris inside the constant width terrace zone. This model explains the data in figures 2 and 3. One possible explanation for the linear dependence of W_l on D_r is obtained by assuming the effective cohesion within the terrace zone is governed by acoustic fluidization (6), which predicts an effective cohesion that scales linearly with D_r. Substitution of this cohesion into the terrace width equation above produces the desired linear relation. With modest extrapolation, the data and model presented here can be applied to basins, providing a new physical and empirical model for the formation of asymmetric basin rings such as the Cordillera of Orientale.

References. 1) Melosh H.J., in Impact and Explosion Cratering, p. 1245-1260, 1977. 2) Croft S.K., J. Geophys. Res., in press, 1984. 3) Melosh H.J., J. Geophys. Res. 87, 371-380, 1982. 4) Swift R.P., in Impact and Explosion Cratering, p. 1025-1042, 1977. 5) Croft S.K., in Multiring Basins: PLPS 12A, p.227-257, 1981. 6) Melosh H.J. and E.S., Gaffney J. Geophys. Res. 88, A830-A834, 1983.

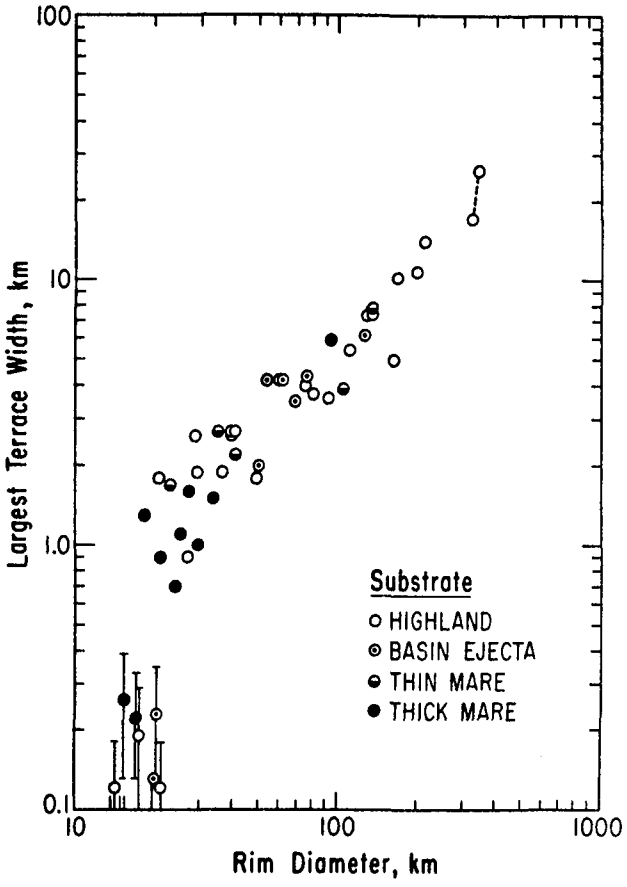

Figure 1

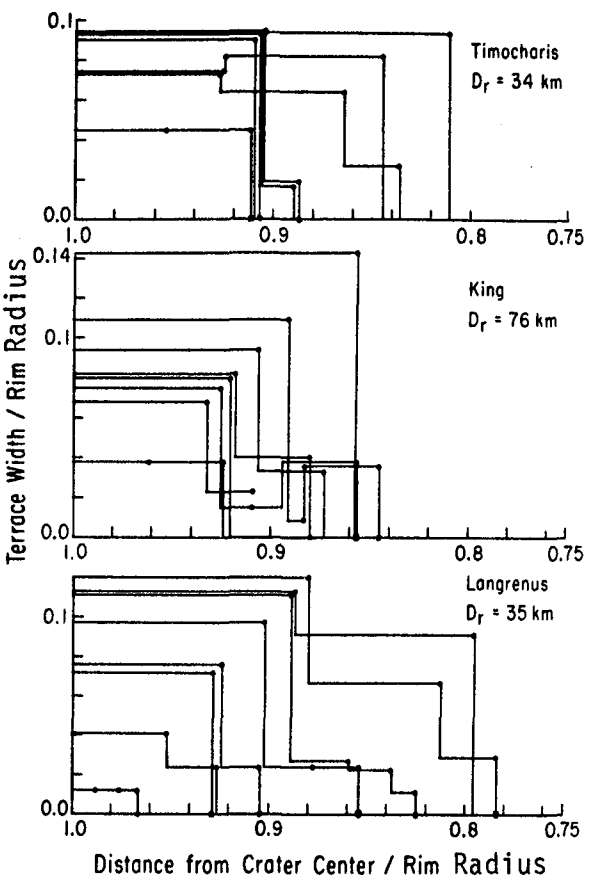

Figure 2

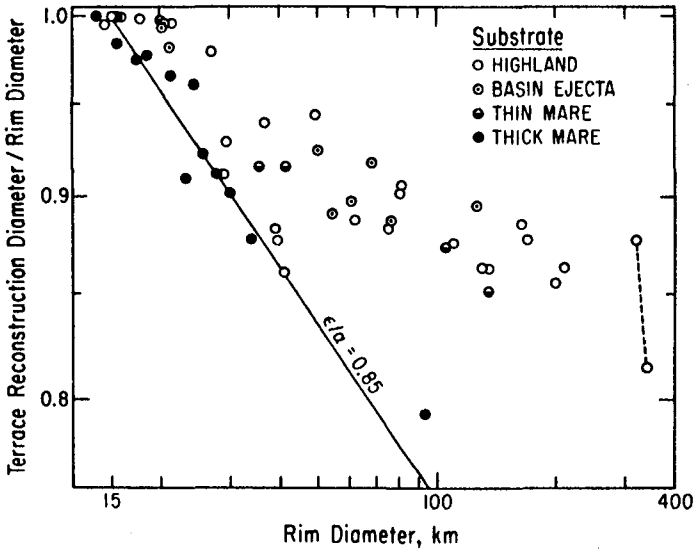

Figure 3

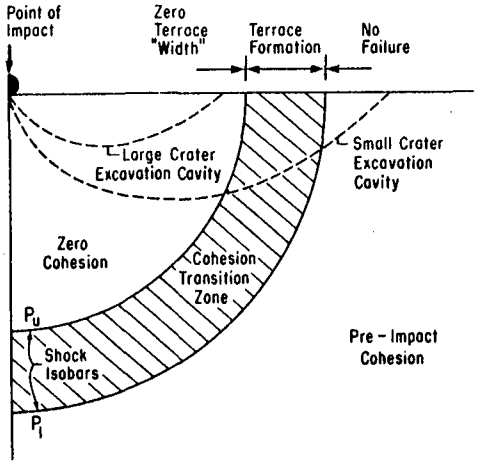

Figure 4

ACCUMULATION OF TOPOGRAPHIC DATA FOR CRATERS ON MARS AND THE JOVIAN AND SATURNIAN SATELLITES: A PROGRESS REPORT

P. A. Davis, L. A. Soderblom, D. J. Roddy, U.S. Geological Survey, Flagstaff, Arizona 86001, and A. S. McEwen, U.S. Geological Survey, Flagstaff, Arizona 86001 and Department of Geology, Arizona State University, Tempe, Arizona 85287

The computer procedure for simultaneous derivation of topography and albedo from calibrated vidicon images along radial profiles within craters [Davis and Soderblom, 1984] is now being used to accumulate topographic data for a statistically large number of simple and complex craters on Mars, as well as on the satellites of Jupiter and Saturn. Existing photoclinometric methods are of two types: (1) the most widely used, the "asymmetric method", requires an estimate of the brightness of a flat field within the profile; (2) the "symmetric method" uses two radial profiles to solve for topography and albedo simultaneously. During data acquisition for Martian craters [Pike and Davis, 1984], we found that both methods, regardless of photometric function, have inherent sensitivities for their solutions. The sensitivites are a function of surface slope, solar incidence angle, and emission angle (hence phase angle) [Davis and McEwen, 1984]. These sensitivities, which translate to measurement errors, have been briefly discussed by Davis and McEwen [1984]. We are currently re-acquiring the data of Pike and Davis [1984], with emphasis on the associated errors in photoclinometry, to determine whether these inherent sensitivities produce the scatter in graphic presentations of crater characteristics such as rim-depth versus rim-diameter plots. If the scatter is merely a product of data acquisition, then more accurate surface characterizations by these crater data can be obtained by weighted consideration of the error associated with each data point. We have chosen the surface of Mars on which to perform this evaluation because it is the best understood planetary surface for which we have acquired calibrated vidicon imagery.

For the Jovian and Saturnian satellites, we have empirically determined by the multiple-image technique of McEwen [1984] that the photometric function of these surfaces is best represented by a Lommel-Seeliger function, consistent with the results of Squyres and Veverka [1981]. We are now commencing systematic topographic data acquisition of all craters shown on Voyager 1 and 2 vidicon images. Once all these data acquisitions are completed, the data will be used with similar data that have been previously obtained for the Moon and Mercury to examine such differential effects as target materials and gravity on cratering mechanics and crustal processes.

REFERENCES

Davis, P. A., and A. S. McEwen, 1984, Photoclinometry: Analysis of inherent errors and implications for topographic measurements. Lunar and Planetary Science XV, Lunar and Planetary Institute, Houston, Texas, p. 194-195.

Davis, P. A., and L. A. Soderblom, 1984, Modeling crater topography and albedo from monoscopic Viking Orbiter images I. Methodology. Journal Geophysical Research, 89, p. 9449-9457.

McEwen, A. S., 1984, Multiple-image techniques for solution of planetary photometric functions: Applications to Europa. Submitted to Journal Geophysical Research.

Pike, D. J., and P. A. Davis, 1984, Toward a topographic model of Martian

craters from photoclinometry. Lunar and Planetary Science XV, Lunar and Planetary Institue, Houston, Texas, p. 645-646.
Squyres, S. W., and J. Veverka, 1981, Voyager photometry of surface features on Ganymede and Callisto. Icarus, 46, p. 137-155.

NEWLY DISCOVERED MARTIAN IMPACT BASINS

Marianne Stam, Department of Geology and Geography,
University of Massachusetts, Amherst, MA 01003

Three previously unrecognized martian impact basins have been discovered through detailed mapping of landforms, structures and terrains near Cassini and Al Qahira basins. These include Al Qahira A (183.5W,13.2S), Al Qahira B (181.3W,26S) and Cassini A (323.7W,13.7N) (fig.1).

Al Qahira A lies on the martian dichotomy boundary and intersects the older basin, Al Qahira. It has four rings that are expressed by a variety of landforms (table 1). The three inner rings are expressed by massifs, knobs and both inward- and outward-facing scarps. The outermost ring is inferred from the concentric distributions of wrinkle ridges, outward-facing scarps and flat-topped massifs. Other evidence that supports the existence of these rings includes an abrupt change in the orientation of Ma'adim Vallis when the first and second rings are crossed. Furthermore, the northern tip of this channel follows a concentric path along the first ring; and an unnamed 'intermediate channel' (Baker, 1982) is found at the intersection between this basin's fourth ring and Al Qahira's outermost ring. Southwestward, Al Qahira A is cut by a younger Basin, Al Qahira B.

Al Qahira B is a highly degraded basin with one identifiable ring (table 1). Its ring is expressed by a few massifs, knobs and inward-facing scarps, but is recognized mainly by the distributions of wrinkle ridges and plains units. Further evidence for the existence of this ring is a change in orientation of Ma'adim Vallis approximately where the channel crosses it. Southward, Al Qahira B is intersected by basin number nine on table 2 of Schultz et al. (1982).

Cassini A lies southward of the younger Cassini Basin and is intersected by it. It probably has four rings (table 1), but the second ring is so poorly expressed that its existence must be considered tentative. The first ring is the most prominent and consists of inward-facing scarps, ridges and a few massifs and knobs. The outer rings, in contrast, are expressed by the distributions of furrowed terrain and the approximately concentric orientations of narrow valley networks. Furthermore, a large 'longitudinal channel' (Baker, 1982) to the south abruptly changes orientation from an east-west to a north-south direction where it crosses the fourth ring. This same channel follows an approximately concentric orientation along the third ring.

These findings demonstrate the importance of detailed mapping of various types of landforms and terrains to the discovery of basins on Mars and suggests that there are probably more that await identification.

References Cited

Baker, V.R. (1982) The Channels of Mars. University of Texas Press, Austin.

Schultz, P.H. (1982) The Structure and Evolution of Ancient Impact Basins on Mars. JGR 87(B12): 9803-9820.

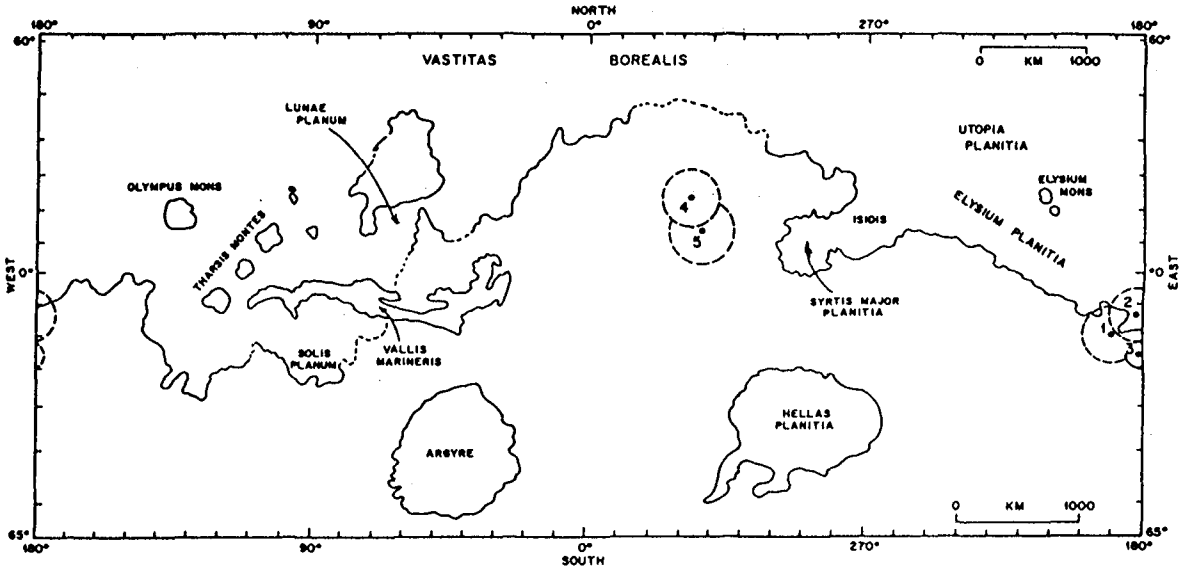

Fig. 1: Locations of new basins. Only outermost rings are shown.
1 = Al Qahira, 2 = Al Qahira A, 3 = Al Qahira B,
4 = Cassini, 5 = Cassini A.

TABLE 1: Basin Features

Basin Name	Location	Ring Number	Ring Diameters (Km)
Al Qahira A	183.5W,13.2S	1	335
		2	530
		3	731
		4	994
Al Qahira B	181.3W,26S	1	545
Cassini A	323.7W,13.7N	1	354
		2(?)	653
		3	928
		4	1204

THE NATURE OF MARTIAN FLOW EJECTA CRATERS

V.M. HORNER and R. GREELEY
Department of Geology, Arizona State University, Tempe, Arizona, 85287

Ejecta with flow features and discrete termini surround many fresh martian craters (1,2 and others). Several morphologies of the flow-like ejecta are observed (2,3,4 and others); they are found globally and in nearly all terrains (5). Numerous studies suggest that the morphology of flow ejecta craters is related to the amount of subsurface volatiles (2,3,4) and/or to atmospheric drag effects (6,7). Although several studies have attempted to constrain factors which could contribute to the ejecta morphology such as latitude, elevation, and terrain unit (3,8,9,10,11), these involved only one or two constrained variables or used global data sets based on Mariner 9 information. Viking-based data sets are becoming available and may provide a better base from which an understanding of the factors which govern ejecta morphology may be obtained. In addition, block sizes of martian flow ejecta may provide clues to the ejecta emplacement process.

Over 500 flow ejecta craters have been measured and classified from Viking subquadrangle photomosaics. The position, ejecta morphology class, crater and ejecta diameters, central features, elevation, and terrain units were recorded for each crater. Several geologic maps of Mars (12,13,14) are used to identify terrain units to compare Mariner 9 and Viking unit definitions. Elevations are from (12) and from Earth-based radar elevations obtained by Mouginis-Mark and Downs (15). Data have been obtained primarily from photomosaics covering the equator to ±25° latitude, which is the area covered by the Mouginis-Mark and Downs (15) data set. Craters within a swath roughly 45° wide from the poles to the equator will be included in the study to investigate latitudinal differences among ejecta morphologies. The main data set will be sorted to create subsets constrained by a number of parameters, and the results will be plotted with respect to the other unconstrained parameters.

Details of ejecta emplacement may be discernable from the block sizes of crater ejecta. The maximum block size for craters ranging from centimeters to kilometers in size is generally within a factor of two of the equation: $S_{max} = 1/2\ D^{2/3}$, where S = block size and D = crater diameter in centimeters (16). However, it does not necessarily follow that the entire ejecta size distribution shifts to larger sizes by this relation as impact energy, and thus crater size, increases. Schultz and Mendell (17) used data from the Apollo 17 Scanning Infrared Radiometer (resolution ~2 km) to study the ejecta deposits of several lunar craters. Thermal signatures were lower than expected for ejecta >0.5 -1.0 crater radii from the crater rim, implying an average ejecta size <30 cm for deposits 1-3 crater radii from craters the size of Aristarchus. The Viking Infrared Thermal Mapper (IRTM) data set contains groundtracks of sufficient resolution (to a resolution cell size of 2x8 km) to surrounding terrain. This data set is currently being examined for high resolution tracks crossing large, fresh craters. Several craters have already been located which show distinct yet complex ejecta signatures. The spatial extent of this signature seems to match the visual extent of the continuous ejecta deposits. Before the IRTM data can be properly interpreted, other contributions to the detected signal (e.g., dust, duricrust) must be taken into account.

REFERENCES

1. Head, J.W. and R. Roth, Papers Presented to the Symposium on Planetary Cratering Mechanics, Flagstaff, AZ, p. 50, 1976.

2. Carr, M.H. et al., J. Geophys. Res. 82: 4055, 1977.

3. Mouginis-Mark, P.J., J. Geophys. Res. 84: 8011, 1979.

4. Johansen, L.A., NASA TM 80339: 123, 1979.

5. Allen, C.C., Icarus 39: 111, 1979.

6. Schultz, P.H. and D.E. Gault, J. Geophys. Res. 84: 7669, 1979.

7. Schultz, P.H. and D.E. Gault, Lunar Planet. Sci. XV, 1984.

8. Blasius, K.R. et al., NASA TM 84211: 93, 1981a.

9. Blasius, K.R. et al., NASA TM 84211: 96, 1981b.

10. Saunders, R.S. and L.A. Johansen, NASA TM 82385: 150, 1980.

11. Mouginis-Mark, P.J. and E.A. Cloutis, Lunar and Planet. Sci. XVI: 532, 1983.

12. Scott, D.H. and Carr, M.H., Map I - 1083, USGS, 1978.

13. Greeley, R., 1984 (in preparation).

14. Scott, D.H. and Tanaka, K., U.S.G.S. Open File Rpt. 84-659-A, 1984.

15. Mouginis-Mark, P.J. and G.S. Downs, Lunar and Planet. Sci. XIII: 182, 1982.

16. Moore, H.J., NASA SP-232: 26, 1971.

17. Schultz, P.H. and W. Mendell, Proc. Lunar Planet. Sci. Conf. 9th: 2857, 1978.

INTERACTION OF MARTIAN FLOW EJECTA BLANKETS WITH PRE-EXISTING IMPACT CRATERS: MORPHOLOGICAL OBSERVATIONS

David Pieri and Michael Hurick, Jet Propulsion Laboratory, Pasadena, CA 91109
Stephen Baloga, 3490 Adgate Drive, Ijamsville, MD 21754

The evidence of interaction between impact flow ejecta blankets and pre-existing landforms such as craters, scarps, and wrinkle ridges may yield important clues as to the nature of the ejecta emplacement process (Pieri et al., 1984). During the past year we have made progress in the morphological characterization of flow ejecta blankets and the interactions of these blankets with pre-emplacement impact craters. In particular, we have reconnoitered about 80 small "satellite" craters (pre- and post-blanket emplacement) (0.5-12 diameter) on or in 3 well-expressed flow ejecta "parent" impact craters (21-39 km in diameter; Viking picture numbers 612A42, 032A28, 087A11). We looked closely for evidence for interaction of the blanket with pre-existing structures, and were able to describe several types. These are:

(1) **Infilling:** many small craters appear to have been infilled by the ejecta material as it moved away from the parent impact. Some appear to have been gently filled, perhaps by airfall, while others appear to have experienced rapid filling by flow. This observation may be able to constrain the velocity field of the ejecta flow as decribed by Pieri et al. (1984).

(2) **Encroachment:** some of the larger satellite impacts appear to have presented an obstacle to hydrodynamic flow. They appear to have been "encroached" by the flow and there appears to be upstream deformation of the blanket resulting from the flow feeling the influence of the crater wall upstream from the crater. Sometimes this influence is substantial and extends two or three crater diameters away from the obstacle. Also there appear to be flow structures preserved within the deposit. This observation may help in constraining the velocity field and viscosity-distance dependency of the blanket.

(3) **Overflow:** some of the satellite craters appear to have been filled and overflowed by the ejecta blanket. This is particularly common near the distal edges of the blankets for smaller craters--sometimes only a very faint upper rim is visible. Of course it is impossible to say how many of the small craters have been totally buried. This observation may constrain the thickness of the blankets.

(4) **Breaching:** there is clear evidence of wall-breaching in some of the larger satellite craters. This implies strong erosional interactions and appears to be most prevalent where scouring has occurred near the rim of the parent crater. Breaching is often associated with visible radial striations in very thin parts of the ejecta blanket.

Detailed examination of the overall morphology of three ejecta blankets reveals a range of thicknesses, from depths sufficient to completely bury craters in the 5 km diameter range in distal areas of the blankets, to very thin blankets which allow subtle pre-existing topography (e.g., polygonal cracks) to be visible within a half the diameter of the parent crater. Radial and azimuthal symmetries appear to exist within the blankets over a range of morphologies. It also appears that there is a weak linear correlation between the diameter of craters with nearly 100% infilling and distance from the

center of the parent crater. We are in the process of further developing this data set and are beginning to make quantitative data-theory comparisons as a test of our flow ejecta emplacement models. Ultimately, we hope to be able to use the data from flow-ejecta blankets and landslide deposits to help constrain the nature, state, and history of volatiles present during their formation.

REFERENCE

Pieri, D.C., S.M. Baloga, and M. Norris, 1984. Geomorphic clues to the martian volatile inventory: I. Flow ejecta blankets, p. 116-118 in Reports of the Planetary Geology Program--1983, NASA TM-86246, Holt, ed., 376 pages.

Ripple Ring Basins on Ganymede and Callisto

Steven K. Croft, Lunar and Planetary Laboratory,
University of Arizona, Tucson, Arizona 85721

The unusual morphology of the Valhalla multiple- or ripple-ring (1) basin on Callisto was totally unexpected in light of the morphologies of large impact structures on the terrestrial planets, and its discovery prompted a short but intensive burst of descriptive and interpretive studies (1-7). Two other ripple-ring basins (RRB's), Asgard (2) and a smaller structure near the crater Adlinda (4, 6), were also briefly described. In the course of this study, several additional RRB's were found on Callisto, an example of which (inner pair of arrows) is shown in figure 1. A previously unrecognized RRB on Ganymede was also found. An image and geologic sketch map of this RRB are shown in figure 2a, b. Morphometric and positional data for all known RRB's are given in table 1.

Structure and Morphology. The geologic structure of the Valhalla basin can be divided into four concentric zones (3, 5, 6, 7): 1) a central plain, 2) an annulus of sinuous and "ropy" ridges, 3) a transition zone, and 4) a broad zone of scarps and grabens. The concern in this study is with basin structure, thus the 300 km diameter Central Plain is considered in place of the 600-700 km Bright Central Zone of most previous studies (3, 5, 7), because the latter is an albedo feature rather than a structural one. In addition, comparable central plains are found in basins and palimpsests on both satellites (6, 8, 9). Asgard exhibits all four zones, though zone 4 consists of only 2-3 rings as compared to the several 10's of rings in zone 4 of Valhalla. The Anarr-Balkr basin (figure 1) also shows a single outer scarp (outer arrow), though this may be a ring of Valhalla (at left) structurally controlled by the prior presence of the smaller basin. The heavily cratered state and low resolution available for the rest of the smaller callistoan basins make unambiguous morphological identification impossible, but the smaller RRB's appear to have only a central plain and surrounding zone of bright ridges, and lack the transition and scarp zones. This conclusion is corroborated by the structure of n. Osiris on Ganymede, which appears similar to the callistoan RRB's in low resolution frames (e.g., FDS# 20631.25), but which is seen in high resolution (figure 2a, b) to consist only of a central plain and sub-concentric ridges morphologically similar to the plain and sinuous ridges of Valhalla. Some of the deep grooves surrounding n. Osiris appear to be structurally controlled by the basin, but apparently post-date it.

Morphometry. The Ridge and Scarp zone diameters in table 1 are plotted as functions of the Central Plain diameter in figure 3. Though the data are sparse and the error bars (generally not shown) are large (the boundaries of all the zones are broad and diffuse), a roughly linear Ridge/Plain diameter relation definitely exists and a much steeper, nearly quadratic Scarp/Plain relation is indicated. In addition, the spacing between structures in the Ridge zone is 20-40 km, independent of basin diameter; the spacing of 50-100 km in the scarp zone is also apparently independent of basin diameter, but clearly larger than in the Ridge zone.

Distribution. Most of the known RRB's on Callisto occur in the leading hemisphere, though this may in part be due to variable resolution and lighting conditions in the available imagery. On Ganymede, the Galileo Regio Furrow system has been suggested to be impact derived (2, 4), but subsequent studies (10, 11) lean towards internal origins. It is included in table 1 for completeness. Thus there is only one definite and one possible RRB on Ganymede, and both occur in the leading hemisphere.

Discussion. 1) Basin structure: Ridge zones and Scarp zones differ morphologically and morphometrically, and the latter apparently form only around the largest basins. This suggests different mechanisms are responsible for forming structures in the two zones. If it is assumed that ejection angles and velocities in RRB's are not too different from other basins on Ganymede and Callisto, and if Valhalla's zone of crater depletion (diameter ~2500 km, ref 2) is due to the ejecta blanket, then an approximate diameter of 1500 km for the tectonic rim of Valhalla is predicted from the tectonic rim/continuous ejecta diameter relation for basins on Ganymede (9). This diameter corresponds roughly with the ridge zone, suggesting that ridges form by processes active within the tectonic rim. By contrast, the scarps are suggested to form exterior to the tectonic rim, possibly by the asthenosphere-lithosphere traction mechanism proposed by (7). Assuming this mechanism, the lack of scarps around smaller RRB's suggests the necessity of a transient crater or ejecta thickness of some minimum size to generate stresses large enough to initiate scarp formation. The origin of the central plain has been suggested to be associated with a central melt zone (8, 9).

2) Thermal Structure: The existence of at least one RRB on Ganymede implies that at one time crustal or impact conditions were the same on both satellites. The presences of RRB's on Callisto suggests that these particular conditions were not directly related to the conditions that brought about resurfacing on Ganymede. The paucity of RRB's on Ganymede relative to Callisto almost surely does not represent differing impact conditions, but is consistent with the restricion of RRB formation to early in the thermal history of both satellites and the subsequent obliteration by the resurfacing on Ganymede (n. Osiris is largely obliterated) suggested by comparative crater counts (12).

References: 1) Wood C.A., in Multi-ring Basins, PLPS 12A, p. 173-180, 1981. 2) Smith B.A., et al., Science 204, 951-972, 1979. 3) Hale W., et al., LPI Contr. 414, 30-32, 1980. 4) McKinnon W.B. and H.J. Melosh, Icarus 44, 454-471, 1980. 5) Remsberg A.R., LPS XII, p. 874-876, 1981. 6) Passey Q.R. and E.M. Shoemaker, in Satellites of Jupiter, p. 379-434, 1982. 7) Melosh H.J., J. Geophys. Res. 87, 1880-1890, 1982. 8) Croft S.K., J.Geophys. Res. 88, B71-B89, 1983. 9) Croft S.K., Icarus, submitted, 1984. 10) Shoemaker E.M., et al., in Satellites of Jupiter, p. 435-520, 1982. 11) Casacchia R. and R.G. Strom, J. Geophys. Res. 89, B419-B428, 1984. 12) Strom R.G., et al., J. Geophys. Res. 86, 8659-8674, 1981.

Table 1. Ripple-Ring Basin Morphometry

Name*	Lat.	Lng.	FDS Image #	Diameter of Central Plain	Diameter of Ridge Zone	Diameter of Scarp Zone	Ring Spacing Ridges	Ring Spacing Scarps	Confidence Level†
On Callisto:									
Valhalla	13°N	56°	16422.11	300 km	1400 km	4000 km	25-35 km	70-100 km	1
Asgard	31°N	139°	20602.21	150	1170	1500	~30	50-80	1
Adlinda-Buri	50°S	29°	16418.14	≤100	670	-	25-35	-	1
Alfr-Loni	4°S	231°	20614.30	≤150	650	-	30-40	-	1
Anarr-Balkr	34°N	359°	16421.43	≤120	640	840†	20-30	-	1
Har-Tindr	2°S	355°	16421.30	-	520	-	-	-	2
n. Grimr	39°N	199°	20602.25	-	450	-	-	-	2
Fadir-Jumo	61°N	12°	16422.03	-	340	-	-	-	2
On Ganymede:									
n. Osiris	30°S	150°	20637.35	70	460	-	20-30	-	1
Galileo Regio	~20°S	~165°	20636.41ff	-	-	>4000	-	50-100	3

* All but first two names are suggested, following basin designation system suggested by Wilhelms & El-Baz (1977).
† Confidence levels: 1 = definite, 2 = probable, 3 = possible.

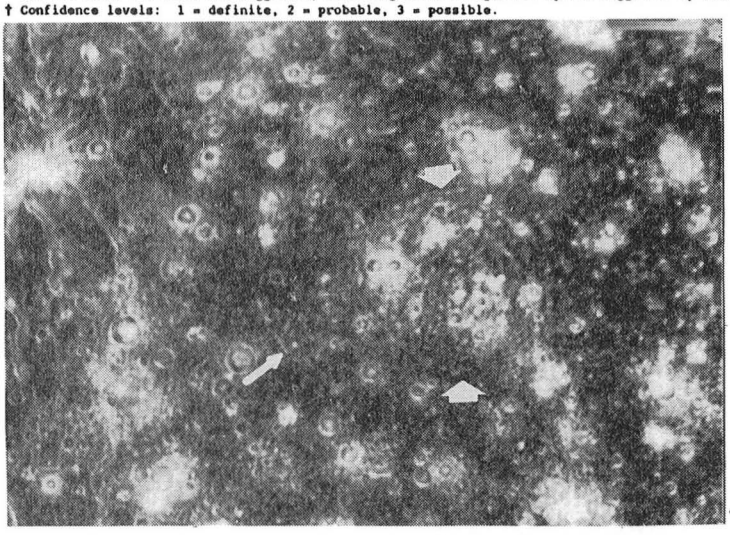

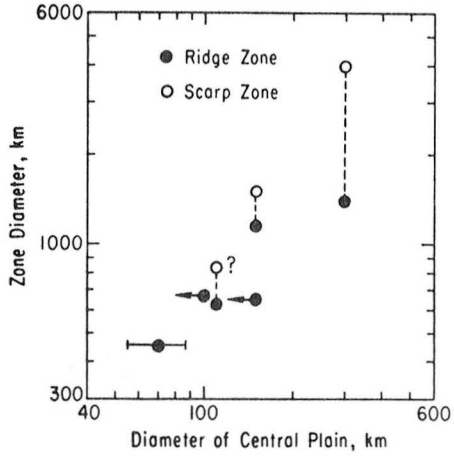

Figure 1 Figure 3

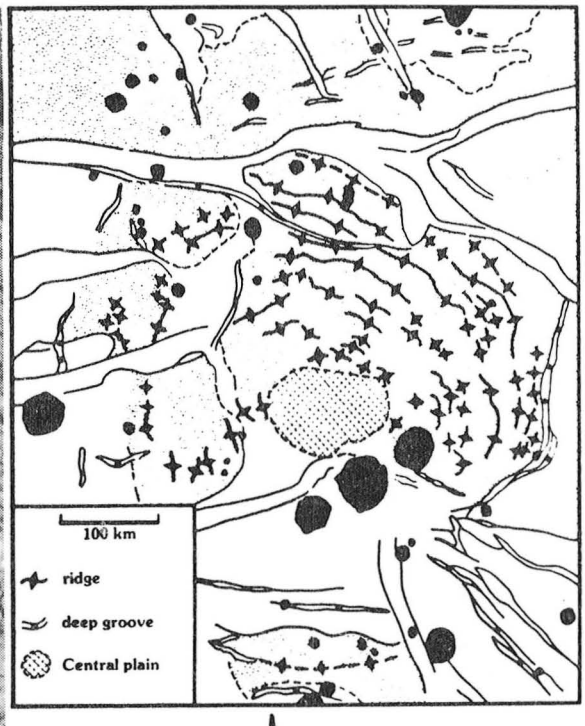

Figure 2a Figure 2b

CHAPTER 6

PLANETARY INTERIORS, PETROLOGY AND GEOCHEMISTRY

Page intentionally left blank

Implications of Convection in the Moon and the Terrestrial Planets

Donald L. Turcotte, Department of Geological Sciences, Cornell University, Ithaca, NY 14853

During the past year the work carried out under this grant has emphasized studies of the early evolution of the moon and its implications for the early evolution of the earth. This work has been divided into two parts:

1) Studies of core formation. Cosmochemical studies strongly favor a near-homogeneous accretion of the earth. These studies also show that core segregation probably occurred within the first 10^5 years of earth history. Mechanisms of core formation have received relatively little attention. Turcotte and Emerman (1) examined dissipative melting as a possible mechanism for core segregation. For a large iron body migrating through the mantle, the potential energy lost by the body is dissipated by frictional heating. If the body has a radius greater than about 30 km, the frictional heating is sufficient to melt a path through which the body can fall. If the iron body is liquid (as expected) with a low viscosity, it would penetrate the mantle as a diapir. The problem of an immiscible liquid body melting its way through a solid is solved, and a family of diapir shapes is obtained. We find that dissipative heating may be a viable mechanism for core segregation if sufficiently large bodies of liquid iron can form.

2) Early thermal evolution of the earth and moon. The energy associated with the accretion of the earth and the segregation of the core is more than sufficient to melt the entire earth. In order to understand the thermal evolution of the early earth it is necessary to study relevant heat transfer mechanisms. Turcotte and Pflugrath (2) have postulated the existence of a global magma ocean and carry out calculations of the heat flux through it in order to determine its depth. The increase in the mantle liquidus with depth (pressure) is the dominant effect influencing heat transfer through the magma ocean. We find that a magma ocean with a depth of the order of 100 km would have existed as the earth accreted. We conclude that this magma ocean zone refined the earth resulting in the simultaneous formation of the core and the atmosphere during accretion. The resulting mantle was a well-mixed solid with a near pyrolite composition.

(1) D.L. Turcotte and S.H. Emerman, Dissipative melting as a mechanism for core formation, Proc. 14th Lunar Plant. Sci. Conf., J. Geophys. Res. 88, B91-B96 (1983).

(2) D.L. Turcotte and J.C. Pflugrath, Magma oceans and the zone refining of the accreting earth, Proc. 15th Lunar Plant. Sci. Conf., Submitted for publication, (1984).

HIGH PRESSURE COSMOCHEMISTRY OF MAJOR PLANETARY INTERIORS: LABORATORY STUDIES OF THE WATER-RICH REGION OF THE SYSTEM AMMONIA-WATER

Malcolm Nicol, Mary Johnson, and Andrea S. Koumvakalis
Department of Chemistry and Biochemistry
University of California, Los Angeles, CA 90024

Existing models of the major planets and their satellites are simple in the sense that they make rather arbitrary assumptions concerning the deep interiors. "Rock" cores or "ice" (water-ammonia-methane) layers are often invoked without considering whether these are thermodynamically consistent. However, the behavior of "gas-ice" mixtures at very high pressures is very poorly understood; when this project began, virtually no measurements had been made on binary or multicomponent gas-ice systems at pressures of the order of tens of thousands of atmospheres. The purpose of this project, thus, is to determine some relevant pressure-temperature-composition (P-T-X) regions of the hydrogen (H_2)-helium (He)-water (H_2O)-ammonia (NH_3)-methane (CH_4) phase diagram. Such experimental studies, and theoretical modeling of the relevant phases, are needed to interpret the compositions of ice-gas systems at conditions of planetary interest.

This project is the first attempt to characterize the compositions and structures of a multi-phase, multi-component system at very high pressures. At room temperature, this challanges existing technology; and our goal is to characterize this system over a wide range of low and high temperatures. Thus, our initial task was to demonstrate that the necessary measurements reasonable precision. We worked with NH_3-H_2O compositions that are relevant to planetary problems yet are easy to prepare. Another reason for this choice was that a few parts of the relevant P-T-X space had already been determined. The P-T surface of water has been examined by several groups, most recently by Mishima and Endo [1]; and Mills et al. [2] have determined the corresponding surface for NH_3. Rollet and Vuillard [3] studied the T-X diagram of ammonia-water at atmospheric pressure and found two water-rich phases, $NH_3 \cdot 2H_2O$ (ammonia dihydrate), which melts incongruently, and $NH_3 \cdot H_2O$ (ammonia monohydrate), which is nonstoichiometric and melts at a higher temperature than the dihydrate.

These results suggested that we should begin by determining a P-T surface at approximately the monohydrate composition and the P-X surface at room temperature. The latter conditions also were studied by Boehler in our laboratory with a large-volume piston-cylinder apparatus in order to identify problems that arise from metastability and sample size. At room temperature, five phases were observed, including: the liquid; ice VI and ice VII (which resembled their descriptions in the literature); a high-relief apparently isotropic ammonia monohydrate phase; and a low-relief, strongly anisotropic ammonia dihydrate phase. In all cases, the phases were identified visually, usually both with and without crossed polarizers. The ice phases resembled their descriptions in the literature. The dihydrate phase had less relief than the liquid, was anisotropic under crossed nicols, and tended to form two networks of cracks at about a 70° angle to each other at low pressures. When squeezed

above 3.3 GPa, dihydrate reconstituted into myrmekitic intergrowths of Ice VII with a higher-relief phase which appeared to be isotropic. From calculation of the area of the diamond cell occupied by the various phases, the low-pressure phase was shown to have a composition near $NH_3 \cdot 2H_2O$, and the high-pressure phase to have composition near $NH_3 \cdot H_2O$.

Nucleation problems were found to be severe, with ice VI being especially difficult to nucleate: in 24 separate measurements between 0 and 30 mole percent NH_3 where ice VI should have occured, it was detected only 8 times, only twice at compositions other than 5 mole percent NH_3, and never observed at the pure water composition. Similar nucleation problem has also been described for pure water by both Yamamoto [4] and Piermarini et al. [5]. Boehler's work also indicates that the ice VI-liquid field extends further into the liquid region than we found at several compositions. An issue that must still be examined is whether the low-temperature and high-pressure hydrates are equivalent.

Near the composition $(NH_3)_{0.5}(H_2O)_{0.5}$, the melting curve of the solid has been studied to 50 kilobars and nearly 400 K. These observations have been interpreted in terms of congruent melting of the monohydrate melts However, Lunine [6] has suggested an alternative interpretation in terms of incongruent melting to dihydrate plus liquid at room temperature. Thus, we are working to identify the phases present by visual methods with polarized optics, vibrational spectroscopy, or x-ray diffraction.

A more detailed report of this work is being published elsewhere. [7] We are continuing these studies by extending the low-ammonia phase diagram to other interesting temperatures, investigating the structures and stoichiometries of the high-pressure hydrates, and determinating the densities (and, possibly, viscosities) of the solids and fluids in the NH_3-H_2O system.

REFERENCES

1. O. Mishima and S.J. Endo (1980), **J. Chem. Phys. 73**, 2454.
2. R.L. Mills, D.H. Liebenberg, and Ph. Pruzan, Ph. (1982), **J. Phys. Chem. 86**, 5219.
3. A.-P. Rollet and G. Vuillard (1956), **Comptes. rendus Acad. Sci. Paris 243**, 383.
4. K. Yamamoto (1980), **Jpn. J. Appl. Phys. 19**, 1841.
5. G.J. Piermarini, R.G. Munro, and S. Block (1983) **IX AIRAPT Conf. High Pressure Res. Abstracts**, AF2-1.
6. J. Lunine (1984) [personal communication].
7. M.L. Johnson, M. Nicol, and A. Schwake (1985), **Proceedings of the NATO Workshop - Ice in the Solar System** (In press).

THEORETICAL THERMODYNAMICS OF MIXTURES AT HIGH PRESSURES
NASA Grant NAGW-192

W. B. Hubbard, Lunar and Planetary Laboratory, University of Arizona

Developing an understanding of the chemistry of mixtures of metallic hydrogen and abundant, higher-Z material such as oxygen, carbon, etc., is important for our understanding of fundamental processes of energy release, differentiation, and development of atmospheric abundances in the Jovian planets. It provides a significant theoretical base for the interpretation of atmospheric elemental abundances to be provided by atmospheric entry probes in coming years. We are still in the very earliest phases of such a study, and even the most rudimentary information about the phase diagrams of such important binary mixtures as hydrogen and carbon, hydrogen and helium, and hydrogen and oxygen, is largely lacking. Although low-Z mixtures such as H-He can in principle be investigated by perturbation-theoretic techniques, in practice significant differences are found when non-perturbative approaches such as Thomas-Fermi-Dirac (TFD) theory are used. For mixtures of hydrogen and high-Z material (such as C, N, O), perturbation theory fails completely. We are engaged in an initial mapping of the phase diagrams of such binary mixtures in the pressure range from $\sim$10 Mbar to $\sim$ 1000 Mbar, using results from three-dimensional TFD calculations carried out here.

Derivation of a general and flexible thermodynamic model for such binary mixtures in the relevant pressure range has been greatly facilitated by the following breakthrough. There exists an accurate and fairly simple thermodynamic representation of a liquid two-component plasma (TCP) (DeWitt and Hubbard 1976, Hubbard and DeWitt 1984), in which the Helmholtz free energy can be represented as a suitable linear combination of terms dependent only on density and terms which depend only on the ion coupling parameter. We have found that the crystal energies of mixtures of H-He, H-C, and H-O can be satisfactorily reproduced by the same type of model, except that an effective, density-dependent ionic charge must be used in place of the actual total ionic charge. We will call this model the "effective potential" (EP) model. It follows that the liquid-state Helmholtz free energy for such a mixture is then immediately available, and can be used to map out the phase diagram. The results are in good agreements with calculations made using hard-sphere perturbation theory to obtain the mixture thermodynamics.

The following figures show recent results for binary phase diagrams obtained using the described approach. Fig. 1 shows the critical temperature for onset of immiscibility in a hydrogen-helium liquid mixture, as a function of pressure. The top solid curve (marked "unscreened") shows the predicted onset of immiscibility for the unrealistic case of a mixture in which the electron density is presumed to be entirely uniform. This curve does not differ substantially from the curve computed using perturbation theory (Stevenson 1975). In contrast, the lower curves show the predicted onset of immiscibility as calculated from the 3-D TFD results using hard-sphere perturbation theory with lowest-order quantum corrections (HSPT) and the effective potential representations respectively. These curves actually fall below the helium melting curve as calculated from EP theory.

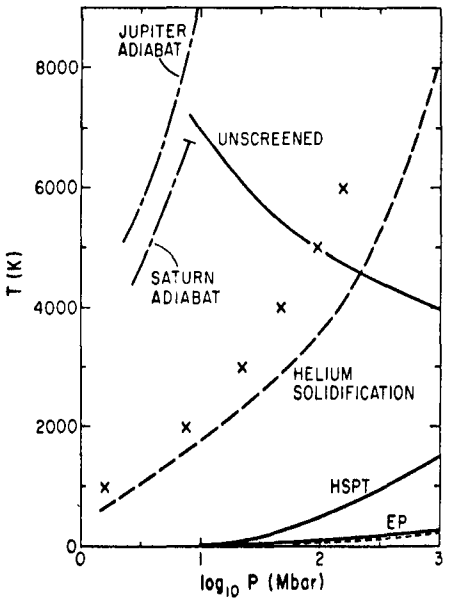

Fig. 1 - Critical temperatures (solid curves) of liquid hydrogen-helium mixtures in various approximations. Also shown is a Jovian adiabat for a solar-composition mixture of hydrogen and helium, and the melting curve of pure helium.

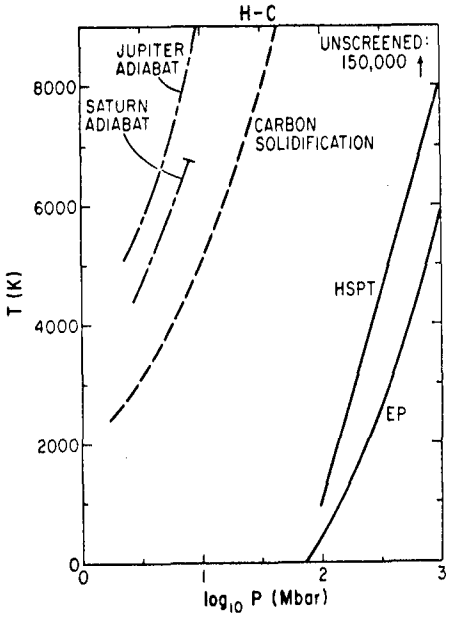

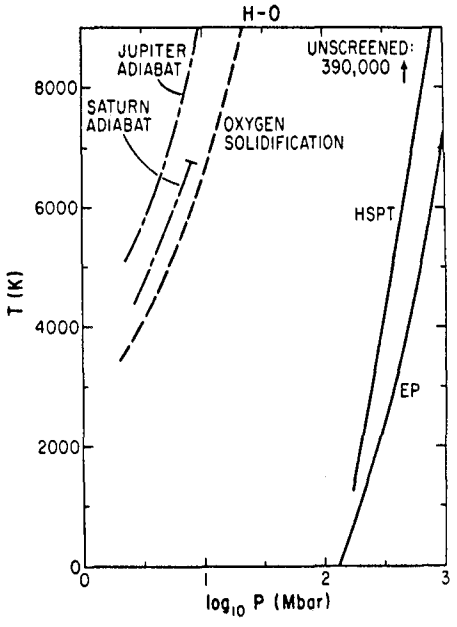

Figs. 2 (left) and 3 (right) - Critical temperatures (solid curves) of liquid hydrogen-carbon (left) and hydrogen-oxygen (right) mixtures in various approximations.

Figs. 2 and 3 show comparable results for mixtures of hydrogen and carbon, and hydrogen and oxygen. A calculation neglecting electron screening would predict that these mixtures would be totally immiscible under Jovian interior conditions, but the EP model predicts that both mixtures are miscible under Jovian conditions. According to the results of this calculation, there is no immiscibility at pressures below about 100 Mbar (which spans the entire Jovian interior). Even where a miscibility gap does exist, it appears only in very carbon- or oxygen-rich mixtures, and would not appear in a fluid of solar or near-solar composition.

These results are important because they imply that the abundant species He, C, N, and O are fully soluble in the deep Jovian interior. Thus if there is a discrepancy between measured atmospheric abundances and presumed primordial abundances, it is to be attributed to initial inhomogeneous accretion (possible) or perhaps to a major phase transition in hydrogen itself (e.g. the proposed first-order phase transition from molecular to metallic hydrogen).

REFERENCES

DeWitt, H. E., and Hubbard, W. B. (1976) Statistical mechanics of light elements at high pressure. IV. A model free energy for the metallic phase. Astrophys. J. 205, 295.

Hubbard, W. B. , and DeWitt, H. E. (1984) Statistical mechanics of light elements at high pressure. VII. A perturbative free energy for arbitrary mixtures of H and He. Submitted to Astrophys. J.

Hubbard, W. B. , and MacFarlane, J. J. (1984) Statistical mechanics of light elements at high pressure. VII. Thomas-Fermi-Dirac theory for binary mixtures of H with He, C, and O. Submitted to Astrophys. J.

Stevenson, D. J. (1975) Thermodynamics and phase separation of dense fully ionized hydrogen-helium fluid mixtures. Phys. Rev. B12, 3999-4007.

SHOCK COMPRESSION OF LIQUID HELIUM TO 56 GPa (560) KBAR*

W. J. Nellis, N C. Holmes, A. C. Mitchell, R. J. Trainor,
G. K. Governo, M. Ross, and D. A. Young

University of California, Lawrence Livermore National Laboratory
Livermore, California 94550

We present shock-wave data for liquid He that has been compressed to densities up to 0.7 g/cm^3, five times greater than the normal liquid, and heated to temperatures up to 21000 K. The maximum pressure attained is 56 GPa (560 kbar). These are the first shock data ever reported for liquid He and the conditions attained are more extreme than any achieved in other experiments. The highest static pressure so far attained in He is 16 GPa on the melting curve.[1]

The equation of state and intermolecular potential for dense He and H_2 have been widely studied because they are the simplest and most abundant of the elements. Their properties are important for modeling the giant planets where they are the major constituents and are subjected to pressures up to 4.5 TPa (45 Mbar) and temperatures up to 20000 K in Jupiter and to about 1 TPa and 14000 K in Saturn.[2] Saturn is of particular interest because studies have suggested that it has an internal energy source that is associated with unmixing and gravitational separation of the hydrogen-helium fluid at pressures below 1 TPa.[2] The existence of this phase transition depends very sensitively on the hydrogen and helium equations of state. In a series of recent papers we have reported shock-wave data[3] and theoretical calculations[4] for liquid D_2 shock-compressed to 76 GPa and 7000 K. This paper reports the results of a similar study for He.

Strong shock waves were generated by the impact of planar projectiles into cryogenic specimen holders. Projectiles were accelerated to velocities of 3-7 km/s by means of a two-stage light-gas gun.[5,6] Shock pressure, density, and specific internal energy were derived from the measured impactor velocity, shock velocity, and initial liquid density by means of the Hugoniot equations. The He specimens were initially in the liquid state at 4.3 K. The specimen holders[7,8] and coolant fill system[3] were similar to that used for liquid H_2. Several refinements were necessary to adapt the cryogenic design for He. The specimen holder was made from pure Al for improved thermal coupling between the liquid He coolant and the specimen cavity. The sample cavity was filled by condensing He gas by flowing the gas through a heat-exchange coil located in the coolant chamber. More than 100 layers of aluminized Mylar were wrapped on the assembly for thermal radiation shielding. The impact surface, which could not be covered, was an infrared mirror, diamond-turned and Au-plated for high reflectivity. A liquid N_2-cooled radiation shield was positioned in front of the impact surface to shield thermal radiation from all directions except the axis of the launch tube. Aluminum foil was contoured to the surrounding black inner wall of the gun target chamber. Specimen

temperature was measured by a calibrated Ge resistance thermometer. Initial specimen density was liquid saturation density[9] at the measured temperature.

Our theoretical analysis combines a statistical-mechanical theory of liquids with an effective pair potential. The liquid theory used here is a modified hard-sphere variational perturbation theory.[10] We have tested the adequacy of various potentials and constructed one which fits the data optimally. Three useful potentials for comparison with data are: 1) molecular beam,[11] 2) Aziz, et al.,[12] and 3) linear muffin-tin-orbitals (LMTO).[13] The LMTO potential was derived from pair potential fit to LMTO band structure calculations on solid He up to 25 TPa. The first two potentials are strictly two-body, but the third, is an effective potential which incorporates many-body effects. The LMTO and beam potentials are purely respulsive exponential functions. However, because of the very high temperatures along the Hugoniot, short-range repulsive contributions dominate, and the error due to omitting the attractive potential is negligible except at the lowest experimental point.

The theoretical curves are compared with experiment in Fig. 1. It is clear that the beam and Aziz potentials are too stiff, while the LMTO potential is somewhat too soft. These tendencies are strongly amplified in the calculation of the double-shock curves. This shows that many-body contributions to the effective potential have the effect of softening the two-body repulsion, and are very important in dense He. We have chosen an optimum potential with the same slope as the LMTO, but which has a larger preexponential coefficient. We find this potential to be $\varphi(r) = 1.1 \cdot 10^5 \varepsilon \exp(-11 r/r_m)$, where ε/k = 10.8 K and r_m = 2.9673 Å. For the highest experimental point on the principal Hugoniot, the liquid model predicts a temperature of approximately 12000 K, and for the double-shock point, the prediction is approximately 21000 K.

In conclusion, the high densities and temperatures reached in the shock-wave experiments have determined the effective He pair potential in a previously unexplored region and confirm the importance of many-body effects. This potential can now be used to generate a He equation of state for the study of planetary interiors.

*This work performed under the auspices of the U.S. Department of Energy by Lawrence Livermore National Laboratory under contract #W-7405-Eng-48, with partial support from the U.S. National Aeronautics and Space Administration under contract 83-033.

REFERENCES

1. P. Loubeyre, J. M. Besson, J. P. Pinceaux, and J-P. Hansen, Phys. Rev. Lett. 49, 1172 (1982).
2. D. J. Stevenson, Annu. Rev. Earth Planet. Sci. 10, 257 (1982).
3. W. J. Nellis, A. C. Mitchell, M. van Thiel, G .J. Devine, R. J. Trainor, and N. Brown, J. Chem. Phys. 79, 1480 (1983).
4. M. Ross, F. H. Ree, and D. A. Young, J. Chem. Phy. 79, 1487 (1983).

5. A. H. Jones, W. M. Isbell, and C. J. Maiden, J. Appl. Phys. 37, 3493 (1966).
6. A. C. Mitchell and W. J. Nellis, Rev. Sci. Instrum. 52, 347 (1981).
7. W. J. Nellis and A. C. Mitchell, J. Chem. Phys. 73, 6137 (1980).
8. W. J. Nellis, F. H. Ree, M. van Thiel, and A. C. Mitchell, J. Chem. Phys. 75, 3055 (1981).
9. R. D. McCarty, National Bureau of Standards Technical Note 631 (unpublished).
10. M. Ross, J. Chem. Phys. 71, 1567 (1979).
11. P. B. Foreman, P. K. Rol, and K. P. Coffin, J. Chem. Phys. 61, 1658 (1974).
12. R. A. Aziz, V. P. S. Nain, J. S. Carley, W. L. Taylor, and G .T. McConville, J. Chem. Phys. 70, 4330 (1979).
13. D. A. Young, A. K. McMahan, and M. Ross, Phys. Rev. B 24, 5119 (1981).

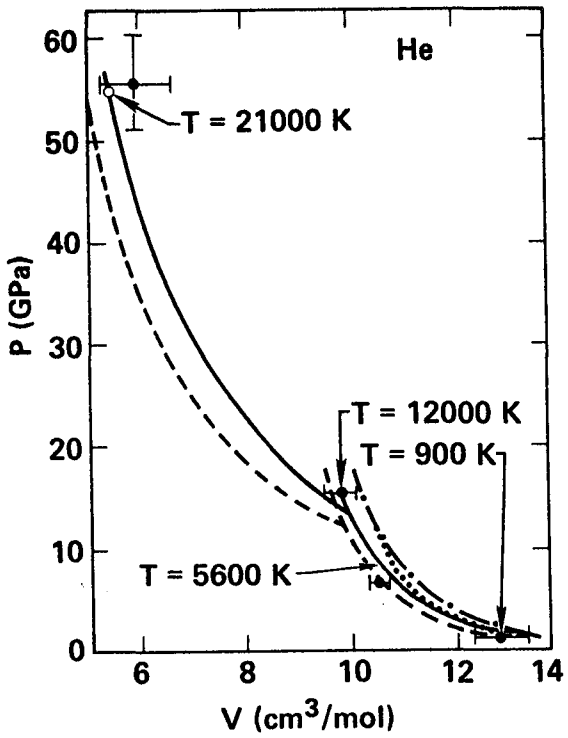

FIG. 1 Comparison of experimenal (points with error bars) and theoretical (curves) helium Hugoniots. Calculations with four different pair potentials are compared with the single-shock data, but only the best two potentials are compared with the double-shock point. The solid curve was calculated using the optimized potential, the dashed curve with LMTO, the dots with Aziz, and the dot-dash with the beam potential. The open circle on the theoretical curve at 55 GPa is the double-shock point predicted by the theory for the experimental conditions (10 GPa = 100 kbar).

MODELLING EQUILIBRIUM AND FRACTIONAL CRYSTALLIZATION IN THE SYSTEM MgO-FeO-CaO-Al_2O_3-SiO_2

Floyd Herbert, Lunar and Planetary Laboratory, U. Arizona, Tucson AZ 85721

This report concerns a mathematical modelling technique for use in petrogenesis calculations in the system MgO-FeO-CaO-Al_2O_3-SiO_2. Semi-empirical phase boundary and elemental distribution information has been combined with mass balance to compute approximate equilibrium crystallization paths for arbitrary system compositions (however the available laboratory data restrict the domain of acceptable accuracy to high-olivine compositions). Because the calculation is applicable to a range of system compositions, fractionation calculations are also possible.

The goal of the calculation is the computation of the composition and quantity of each phase present as a function of the degree of solidification. Formally, the degree of solidification is parameterized by the heat released by the solidifying phases.

The mathematical requirement for the solution of this problem is: (1) An equation constraining the composition of the magma for each solid phase in equilibrium with the liquidus phase, and (2) an equation for each solid phase and each component giving the distribution of that element between that phase and the magma. The phase boundary constraints may be written formally as $F_{\gamma\beta}(\underline{X}_L) = 0$, where γ is the liquidus phase and β runs over the other solid phases. The vector $\underline{X}_L = (X_L^{MgO}, \cdots, X_L^{SiO_2})$ is the oxide composition of the liquid. The relations $F_{\gamma\beta}$ have been given in terms of the Ol-Qtz-Wo-An-Fe/(Mg+Fe) system[1] and converted to the oxide representation here. Mass conservation is given by $\underline{N}_L = \underline{N}_T - \sum_{\alpha \neq L} \nu_\alpha \underline{X}_\alpha N_\alpha$ and $\underline{X}_L = \underline{N}_L / \|\underline{N}_L\|$, with $\underline{N}_L$ and $\underline{N}_T$ being the component mole number vectors of the magma and system, respectively and $\|\underline{N}_L\| = \sum N_i^L$. The stochiometric coeficient ν_α gives the total number of moles of oxide per mole of phase α. The component distribution is given formally by the mole fraction vector $\underline{X}_\alpha$, a function only of the magma composition $\underline{X}_L$. Semi-empirical formulas have been given by a number of authors[2]. Thus the composition and quantities of the various phases are determined self-consistently from mutual constraints.

Self-consistency is enforced in the following manner. Writing the equation for degree of solidification as a function of heat release Q as $F_Q = \sum_{\alpha \neq L} N_\alpha H_\alpha - Q = 0$ and collecting it together with the phase boundary equations into the vector relation $\underline{F}(\underline{N}) = 0$, with $\underline{F} = (F_Q, F_\alpha, \cdots)$ and $\underline{N} = (Q, N_\alpha, N_\beta, \cdots)$ leads to the Newton's method iteration:

$$\underline{F}(\underline{N}) + \frac{\partial \underline{F}}{\partial \underline{N}} \cdot \Delta \underline{N} = 0. \qquad (1)$$

Given a state near the desired solution, this equation can be repeatedly solved, updating $\underline{N}_{new} = \underline{N}_{old} + \Delta \underline{N}$. Since the completely liquid state is always a solution for $Q=0$, the equation (1) can be iterated while increasing Q to the desired degree of solidification. Since $\underline{X}_L$ and $\underline{X}_\alpha$ are continually recomputed as this procedure is followed, the desired solution can be found even though new solid phases come into and drop out of equilibrium.

With $\underline{N}(Q)$, $\underline{X}_L(Q)$, and $\underline{X}_\alpha(Q)$ now calculatable for equilibrium crystallization, it remains to model fractional crystallization. This requires the specification of the fractionation rules; usually the loss of

one or more phases as they form. If component β is the one lost, the computation proceeds as before. This time, however, one stops the calculation at the point where N_β has become slightly larger than zero. At this point one redefines $\underline{N}_T(\text{new})=\underline{N}_T(\text{old})-\nu_\beta N_\beta \underline{X}_\beta$. Since this step changes the system composition $\underline{X}_T=\underline{N}_T/\|\underline{N}_T\|$, sucessive recalculations track the evolution of the system due to the gradual loss of the components of phase β.

The procedure for fractional melting is similar to that for fractional crystallization, except that in the former case the system is allowed to crystallize under the rules for equilibrium solidification until the liquid is nearly exhausted. This reproduces the state of a small degree of equilibrium melting and allows the track through composition space to pick the phases and their compositions in equilibrium at the point of complete solidification. Now the liquid phase is removed, leading to the new system composition $\underline{N}_T(\text{new})=\underline{N}_T(\text{old})-\underline{N}_L=\sum_{\alpha\neq L}\nu_\alpha N_\alpha \underline{X}_\alpha$. As before, the system composition changes each time the small amount of fractionated phase is lost.

The code described above for computation of fractional melting and crystallization was used to compute models of the following lunar magma ocean evolutionary scenario. It has been suggested that the outer portion of the Moon was molten shortly after its formation. The heat source responsible is unknown, though a number of candidates exist. A number of these heat sources (^{26}Al decay, electromagnetic heating by a T Tauri-like solar wind, pressure-release magma generation in solid state convection) are relatively slow (on the order of 10^6 years). Since the segregation of magma is generally quicker than this, one would expect these heat sources to produce magma by fractional melting. This magma, as it erupted to the surface and began to solidify, would be expected to insulate itself via a floating plagioclase-rich crust[3]. Thus the heat loss and magma crystallization process would also be slow[4]. This scenario results in doubly fractionated cumulates -- as fresh fractionated magma arrives in the magma ocean it would undergo a second fractionation as it solidifies. Depending on the relative densities, the newly erupting magma would either mix with the magma ocean magma or else overlie it (the magma Mg number would be expected to increase with time and hence new magma would be less dense).

Models constructed on the basis of the first alternative have been constructed. Because of the extra degree of freedom (the relative rates of melt generation and cumulate solidification) the suite of possible models can be quite complex. Interesting results include the early deposition of high-Fe cumulates (reversing the usual order) with delay of crystallization of high-Ti minerals until the last stage of the magma ocean. This decoupling of Fe and Ti in the magma ocean cumulates, a proposed mare basalt source region, may be related to a lack of correlation noted[5] of Fe and Ti in these basalts. Additionally, there is a qualitative similar between the behavior of the correlation between Na/(Ca+Na) in plagioclase and Mg number in co-crystallizing mafics and the behavior found in lunar rocks[6].

Although no claim is made here as to the completeness of this model for early lunar evolution, it is proposed that certain aspects of the magma ocean stage may be understood in these terms.

REFERENCES

(1) J. Longhi, Proc. Lunar Planet. Sci. Conf. 8th, 601, 1977; J. Longhi, Proc. Lunar Planet. Sci. Conf. 9th, 285, 1978; J. Longhi and L. D. Ashwal, Lunar Planet. Sci. XV, 491, 1984; J. Longhi, Proc. Lunar Planet. Sci. Conf. 12th, 1001, 1981.

(2) The references in (1) and also: M. J. Drake, Geochim. Cosmochim. Acta, 40, 401, 1976; M. J. Drake, Geochim. Cosmochim. Acta, 40, 457, 1976.

(3) J. V. Smith et al., J. Geology, 78, 381, 1970; J. A. Wood et al., Proc. Apollo 11 Lunar Sci. Conf., 965, 1970.

(4) F. Herbert et al., Proc. Lunar Planet. Sci. Conf. 9th, 249, 1978.

(5) S. E. Kesson and A. E. Ringwood, Earth Planet. Sci. Lett., 30, 155, 1976.

(6) J. L. Warner et al., Lunar Science VII, 915, 1976.

QUENCHING EFFECTS ON IRON SITE PARTITIONING IN THE APOLLO 17 ORANGE GLASS COMPOSITION

M. Darby Dyar, Department of Earth, Atmospheric, and Planetary Sciences, Massachusetts Institute of Technology, Cambridge, MA 02139

Past studies of the composition and structures in lunar glasses have contributed greatly to our understanding of mare petrogenesis and the structure of the lunar interior (1,2,3). In particular, analyses of the spectral signatures of glasses have proven extremely useful to remote sensing applications in areas of the moon where glass is in significant proportions in the lunar soil. Such studies have also provided information on Fe site occupancies in glasses, which are used to construe oxygen fugacities at the lunar surface (4). Much of this data has been obtained through work on synthetic analogues of lunar glasses. However, recent Mossbauer studies of an Apollo 15 green glass composition (5) have shown that synthetic glasses are extremely sensitive to variations in quenching media (6). Glass structure and Fe^{3+}/Fe^{2+} ratios are strongly controlled by quenching conditions, which may mask the effects of the original glass' formation temperature or oxygen partial pressure. Furthermore, synthetic glasses were often run at low fugacities on Pt wires, (which may result in considerable Fe loss from the sample and misleading phase equilibrium data. These problems suggest that previous investigations of lunar glass structure ought to be reconsidered.

The purpose of this report is to critically consider the effects of quench media on the Apollo 17 orange glass composition: 39.42(wt.)% SiO_2, 22.48% FeO, 9.04% TiO_2, 6.32% Al_2O_3, 7.74% CaO, and 14.97% MgO (7). Aliquots of 30mg each were equilibrated at 1400°C, log f_{O_2} = -11.3, using Fe-alloyed Pt wire loops (8) in a gas mixing furnace. Each identical sample was equilibrated for one hour and then quenched into one of three different quench media: a brine/ice eutectice mixture (-21°C), silicone oil (25°C) or air (25°C). Each experiment was repeated at least three times. ^{57}Fe Mossbauer spectra were measured on all runs; spectra were fit with a combination Lorentzian/Gaussian peak shape (9).

The three quenchants may be ranked in order of efficiency as brine/ice (fastest quench)>silicone oil>air (slowest quench). Because cooling rate is related to molar volume, the fastest quenched glasses will have the least dense structures, and vice versa (6). The iron site occupancies shown by the Mossbauer spectra (Figs. 1-3) follow this trend. The least dense glasses have the lowest Fe^{2+} isomer shifts; the densest (air quenched) glasses have the highest isomer shifts, indicating that iron is favoring higher coordination. Quadrupole splitting also increases in the densest glasses. The fits also show that the proportion of octahedral to tetrahedral iron varies with quench medium.

These results can be compared against the Mossbauer spectrum of lunar sample 74220 (orange glass) examined by Vaughan and Burns (2). The lunar sample can be fit with a four-fold Fe^{2+} doublet and at least one six-fold Fe^{2+} doublet, suggesting a relatively ordered glass comparable to the slowest cooled, air-quenched synthetic glass. A similar result was determined for the Apollo 15 green glass composition (6). More rapid quenching, such as that provided by the brine/ice mixture leads to a glass with a significantly different type and proportion of oct/tet Fe^{2+} sites. Therefore, past studies which employed rapid quench media such as water or liquid Hg may have drawn suspect conclusions regarding the structure of lunar glasses.

This work also underscores the fact that quenched glasses have undergone drastic structural changes upon passing through the glass transition temperature at differing rates. It is doubtful that these quenched glasses are in any way structurally representative of their original melts (10).

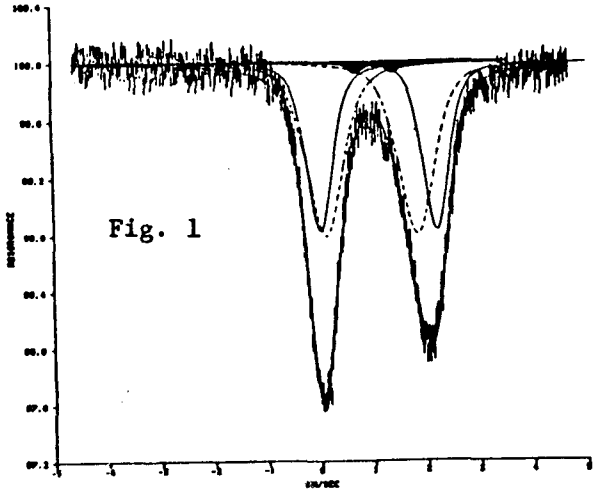

Fig. 1

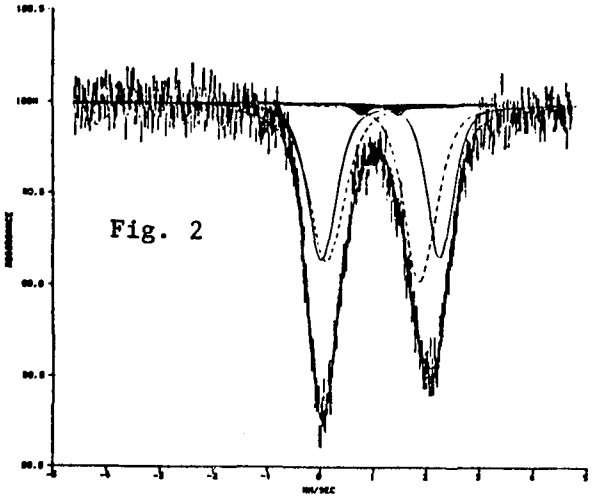

Fig. 2

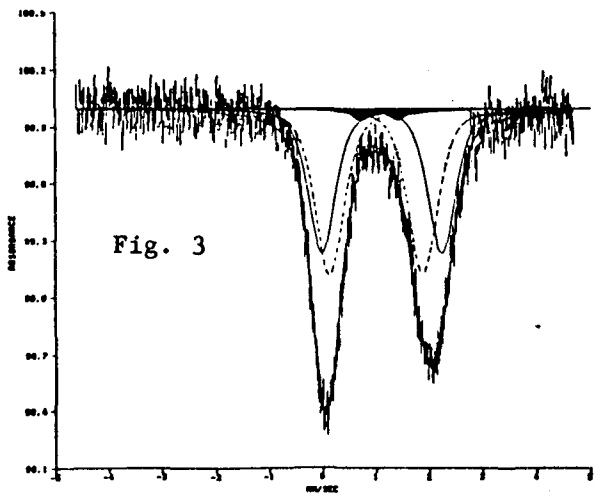

Fig. 3

Figures 1-3 show the orange glass composition as quenched in brine/ice (#1), silicone oil (#2), and air (#3). All samples have 1-2 % of total Fe in the form of ilmenite, δ = 1.060 and Δ = 0.678 (shaded peaks). Tetrahedral Fe^{2+} peaks are shown with dashed outlines. Mossbauer parameters for the fits are as follows, relative to an Fe foil calibration:

	δ_{tet}	δ_{oct}	Δ_{tet}	Δ_{oct}
Brine-ice	0.975	1.109	1.717	2.183
Oil	0.978	1.120	1.755	2.217
Air	1.008	1.124	1.813	2.295

(1) Delano J. (1979) Proc. Lunar Planet. Sci. Conf. 10th, 275-300.
(2) Vaughan D. J. and Burns R. G. (1973) EOS, 54, 618-619.
(3) Dyar M. D. and Burns R. G. (1981) Proc. Lunar Planet. Sci. Conf. 12th, 695-702.
(4) Mao H. K., et al. (1973) Proc. Lunar Planet. Sci. Conf. 4th, 397-412.
(5) Burns R. G. and Dyar M. D. (1983) Proc. Lunar Planet. Sci. Conf. 14th, B221-228.
(6) Dyar M. D. and Birnie D. P. (1984) J. Non-Cryst. Solids, (in press).
(7) Bell P. M., et al., (1976) Proc. Lunar Planet. Sci. Conf. 7th, 2543-2559.
(8) Grove T. L. (1981) Contrib. Mineral. Petrol., 78, 298-304.
(9) Stone A. J., et al., (1984) DECUS Publication, (in press.).

(10) Research supported by NASA grant no. NSG-7604.

EXPERIMENTAL METHODS FOR QUENCHING STRUCTURES IN LUNAR-ANALOG SILICATE MELTS: VARIATIONS AS A FUNCTION OF QUENCH MEDIA AND COMPOSITION

M. Darby Dyar, Department of Earth, Atmospheric, and Planetary Sciences
Massachusetts Institute of Technology Cambridge, Massachusetts 02139

Compositions analogous to lunar green, orange, and brown glasses were synthesized under consistent conditions, then quenched into a variety of different media when the samples were removed from the furnace. Iron valence and coordination are a direct function of quench media used, spanning the range from brine/ice (most effective quench), water, butyl phthalate, silicone oil, liquid nitrogen, highly reducing CO-CO_2 gas, to air (least efficient quench). In the green and brown glasses, Fe^{3+} in four- and six-fold coordination is observed in the slowest quenched-samples; Fe^{2+} coordination varies directly with quench efficiency. Less pronounced changes were observed in the Ti-rich orange glass. Therefore the remote-sensed spectrum of a glass-bearing regolith on the Moon may be influenced by the process by which the glass cooled, and extreme caution must be used when comparing spectra of synthetic glass analogs with real lunar glasses.

HIBONITE: CRYSTAL CHEMISTRY AND ORIGIN OF BLUE COLORATION IN METEORITIC ASSEMBLAGES

Roger G. Burns and Virginia Mee Burns, Department of Earth, Atmospheric, and Planetary Sciences, Massachusetts Institute of Technology, Cambridge, Massachusetts 02139

Introduction. The blue color and optical spectra of hibonite, a common constituent of refractory inclusions in carbonaceous chondrites, are features of topical interest because they may be manifestations of exotic cation species stabilized in unusual coordination sites in the hibonite crystal structure. Hibonite, ideally $CaAl_{12}O_{19}$, is conducive to atomic substitution of host Ca^{2+} and Al^{3+} ions by a variety of lanthanide and first series transition elements. The latter cations are responsible for the colors of many rock-forming minerals as a result of intraelectronic (crystal field) or intervalence (charge transfer) transitions. Indeed, the visible-region spectra of most oxide and silicate minerals are generally well understood. Problems remain, however, over assignments of absorption bands in meteoritic hibonite optical spectra due to uncertainties of cation valencies and complexities in the crystal structure. We review here the crystal chemistry of hibonite, describe results of Mossbauer spectral measurements of iron-bearing hibonites, and discuss electronic transitions that may be responsible for the blue coloration of meteoritic hibonites.

Structure and Chemistry. Hibonite is isostructural with magnetoplumbite, $PbO.6Fe_2O_3$, and synthetic $CaO.6Al_2O_3$ [1]. Trivalent cations occur in five distinct sites, three of which provide octahedral coordination; their designations, multiplicities and average metal-oxygen distances are: Al(I), Al(III) and Al(IV); 6:2:1; and 1.91Å, 1.88Å and 1.88Å, respectively. The remaining two sites, Al(II) and Al(V), have tetrahedral and trigonal bipyramidal (5-fold) coordinations, multiplicities of 2:1, and mean interatomic distances of 1.81Å and 1.99Å, respectively. The Ca^{2+} ions occupy 12-fold coordination sites and are replaced by lanthanide ions in terrestrial hibonites. A Mossbauer spectral study [2] of synthetic $CaAl_{12-x}Fe_xO_{19}$ ($6.0>x>0.1$) demonstrated that Fe^{3+} ions are strongly enriched in the tetrahedral and 5-fold sites (Fig. 1). While large divalent cations (e.g. Fe^{2+}, Cr^{2+}, V^{2+}, Mg^{2+}) should favor the larger, distorted 5-fold sites, trivalent cations acquiring high crystal field stabilization energies (e.g. Cr^{3+}, V^{3+}, Ti^{3+}) might be expected to occupy the octahedral sites. Chemical analyses of meteoritic hibonites [3] reveal significant concentrations of V, Cr and Ti. They also have higher Ca and Mg, lower Fe, and comparable Ti contents compared to terrestrial hibonites [4]. Although blue colorations of meteoritic hibonites have been attributed to V^{3+} [3] and Ti cations [5], no specific coordination site or type of electronic transition were identified.

Mossbauer Spectra. Measurements were made on hibonite, from a metamorphosed limestone from Madagascar, the chemical formula of which [4] is $(Ca_{0.94}REE_{0.05})(Al_{10.49}Ti_{0.55}Mg_{0.49}Fe_{0.41}Si_{0.07})O_{19}$. Its Mossbauer spectrum is shown in Fig. 2. The three doublets resolved in the synthetic hibonite spectrum (Fig. 1) were assigned [2] to Fe^{3+} ions in 5-fold (peaks XX^1), tetrahedral (peaks YY^1) and octahedral (peaks ZZ^1) sites. The Madagascan hibonite spectrum is more complex due to additional contributions from Fe^{2+} ions. Computer-fitting of the spectrum profile enabled five doublets to be resolved: peaks XX and YY: Fe^{3+} ions in tetrahedral and 5-fold sites; and peaks AA, BB, and CC: Fe^{2+} ions in tetrahedral, octahedral and 5-fold sites. The site occupancy factors (calculated from % area/site multiplicity) indicate that Fe^{2+} ions are also enriched in the 5-fold site. Surprisingly, the iron cations appear to discriminate against the octahedral sites. The large proportion of ferric iron implies that titanium predominates as Ti^{4+} ions in

this terrestrial hibonite. Such a cation assemblage accounts for its brown color, by analogy with terrestrial augites, hornblendes and biotites.

Interpretation of Optical Spectra. Reported measurements [5] of visible-region spectra of natural and synthetic blue hibonites with approximate composition $Ca_{1.02}Al_{11.16}Ti_{0.35}Mg_{0.34}V_{0.10}Cr_{0.01}Si_{0.02}O_{19}$ (based on the Blue Angel inclusion from the Murchison meteorite [3]) show two absorption bands centered near 14500 and 25000cm^{-1}. Heat treatment at elevated oxygen fugacities produced orange hibonites and the disappearance of the 14500cm^{-1} band. These energies differ significantly from those obtained from optical spectra of Al_2O_3 [6,7] doped with V^{3+} (25000 and 17500cm^{-1}), Cr^{3+} (24500 and 18400cm^{-1}) or Ti^{3+} (20300 and 18450cm^{-1}). These cations readily substitute for octahedral Al^{3+} ions in the corundum structure [7]. The optical spectra of blue hibonites corroborate, therefore, the site occupancy data for iron and indicate that trivalent cations such as V^{3+}, Cr^{3+}, and Ti^{3+}, if present in hibonite, are not concentrated in the octahedral sites. By analogy with iron, these trivalent cations would favor the 5-fold Al(V) sites, so that the optical spectra must be assigned to crystal field transitions within cations occurring in a trigonal bipyramidal coordination site. Furthermore, the observation [5] that hibonite's blue color is induced at low oxygen fugacities raises the possibility that low valence cations such as Ti^{3+}, V^{2+} and Cr^{2+} might be stabilized by the Jahn-Teller effect in the distorted trigonal bipyramidal Al(V) site. Such site occupancy stabilization of reduced cation species and its influence on element partitioning in coexisting refractory phases need to be considered in condensation calculations involving solar nebula [8]. A complete assignment of blue hibonite optical spectra awaits measurements on single crystals in polarized light and calculations of the electronic structures of transition metal cations in 5-fold coordination sites [9].

References

[1] Kato K. and Saalfield H. (1968) Neues Jahrb. Min., Abh., 109, 192.
[2] Glasser F. P., et al. (1972) J. Solid State Chem., 5, 255.
[3] Armstrong J. T., et al. (1982) Geochim. Cosmochim. Acta, 46, 575.
[4] Maaskant P., et al. (1980) Mineral. Mag., 43, 995.
[5] Stolper E. and Ihinger, P. (1983) Lunar Planet. Sci., XIV, 749.
[6] McClure D. S. (1962) J. Chem. Phys., 36, 2757.
[7] Burns R. G. and Burns V. M. (1983) Adv. Ceramics, 12, (in press).
[8] Fegley M. B. (1982) Lunar Planet. Sci., XIII, 211.

[9] Research supported by NASA grant no. NSG-7604.

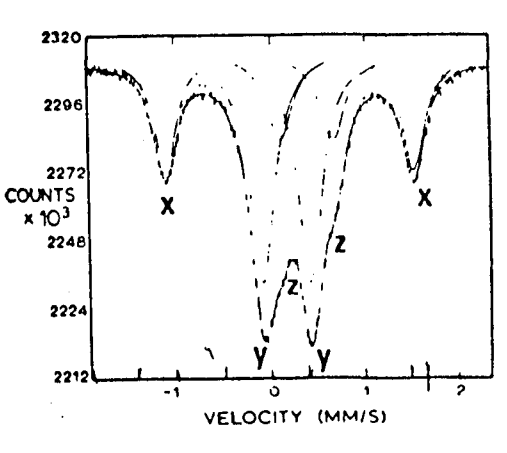

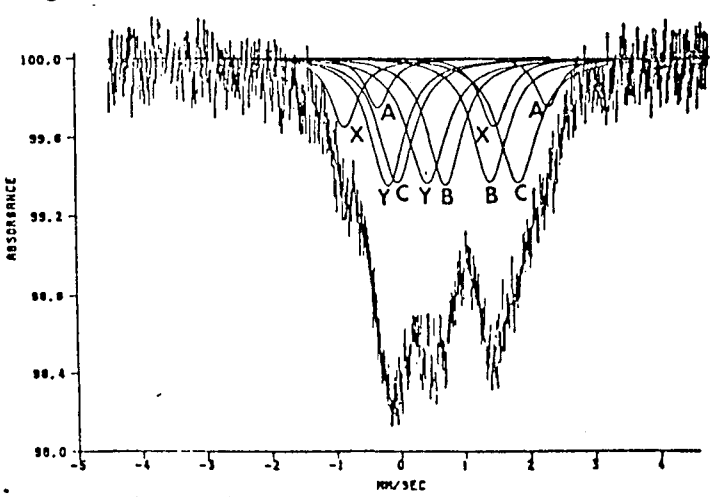

Figure 1. Mossbauer spectrum of synthetic $CaAl_{10.8}Fe_{1.2}O_{19}$ (ref. [2]).
Figure 2. Mossbauer spectrum of Madagascar hibonite.

CRYSTAL CHEMISTRY OF METEORITIC HIBONITES

Roger G. Burns and Virginia Mee Burns, Department of Earth, Atmospheric, and Planetary Sciences, Massachusetts Institute of Technology, Cambridge, Massachusetts 02139

Structural features influencing relative enrichments, cation stabilities, and colors of vanadium-, titanium-, and iron-bearing hibonites ($CaAl_{12}O_{19}$) in meteorites are examined. These transition elements may substitute for Al^{3+} ions which occur in five different coordination sites in the hibonite crystal structure, including three distinct octahedra [Al(1), Al(3), and Al(4) positions], one tetrahedron [Al(2) position], and an unusual trigonal bipyramid [the Al(5) position] providing five-fold coordination by oxygen ions. Mossbauer spectral measurements of terrestrial and synthetic iron-bearing hibonites demonstrate that although Fe cations occur in four-, five-, and six-fold coordinations, they are relatively enriched in the trigonal bipyramidal Al(5) site which provides the largest average Al^{3+}-oxygen distance. Similarities with Mossbauer spectra of blue sapphires indicate that some Fe^{2+} ions are also located adjacent to Ti^{4+} cations in hibonite's face-sharing Al(3) octahedra.

Arguments based on ionic radius and crystal field stabilization energy criteria are used to explain the enrichment of Fe^{2+} ions in the five-fold coordination Al(5) site of hibonite. Similar electronic stabilities apply also to V^{3+} and Ti^{3+}, but not to Cr^{3+}, providing an explanation for the fractionation of vanadium into meteoritic hibonites. Three mechanisms are proposed for the blue colors of these hibonites, the visible-region spectra of which show minima at 550 nm (blue) between two absorption bands at about 400 nm and 700 nm. One assignment of these bands is to crystal field transitions within V^{3+} and Ti^{3+}, respectively, which are located in the symmetry D_{3h} trigonal bipyramidal Al(5) site. A second assignment of the 700 nm band is to an intense $Fe^{2+} \rightarrow Ti^{4+}$ intervalence transition between traces of these cations located in adjacent face-shared Al(3) octahedra. The orange color and disappearance of the 700 nm produced by the heat treatment of hibonite at elevated oxygen fugacities may then be the result of oxidation of either Ti^{3+} to Ti^{4+} or Fe^{2+} to Fe^{3+}. A third explanation of the blue-orange color change involves color centers induced when primoidal ^{26}Al decays to ^{26}Mg, or from trapped electrons in the lattice as a result of non-stoichiometry and structural defects in hibonite.

Magmas as Selective Filters of Volatiles Between Planetary Mantles and Surfaces

John R. Holloway and Sigurdur Jakobsson
Depts. of Chemistry and Geology
Arizona State University, Tempe, AZ 85287
October 1, 1984

Of paramount importance in understanding the composition of early planetary atmospheres and biospheres is a knowledge of the relationship between mantle volatiles and volcanic gases. In the case of Earth it appears that volcanic rocks and gases are relatively oxidized compared to the upper mantle. In the case of the C-O-H volatiles (H_2O, CO_2, CO, CH_4, H_2) the volcanic gases are enriched in H_2O and CO_2 while the volatiles in the mantle may be dominated by H_2O, H_2 and possibly CH_4 (1).

In the past three years we have perfected an experimental technique for phase equilibrium studies in the 5-30 kbar range which allows accurate control of volatile species activities in the fluid phase (2). In these experiments a silicate sample is placed in a graphite crucible, iron + wustite + C-O-H fluid is placed outside the graphite, and the entire assemblage is sealed inside a platinum capsule. At constant pressure and temperature the assemblage graphite + iron + wustite fixes the amounts of O_2, H_2, H_2O, CH_4, CO and CO_2 in the fluid. The buffering capacity of the system is such that run durations of the experiments range from 24 to 6 hours at temperatures from 1050°C to 1200°C. These times are sufficient for the system to attain equilibrium.

We have used this system to measure the relative solubilities of H_2O, CO_2, CO, CH_4 and H_2 in magmas at 10 kbar pressure. Most of our data has been collected on model magma of albite composition, but preliminary experiments show our conclusions are similar for magmas from basnite (SiO_2 = 45 wt%) to latite (SiO_2 = 68%) in composition. During the experiments the magma equilibrated with the fluid at 1200°C. At the end of an experiment the liquid silicate magma was quenched to a glass. The glass was placed in a furnace attached to a quadrupole mass spectrometer (QMS) and rapidly heated (< 5 minutes) to 1200°C at sub-atmospheric pressure. The molar ratios of released gases are determined by the QMS. Actual abundances of the dissolved gases are calculated by normalizing to the H_2O content of the glass determined by infrared spectrometry. Total C and H were measured in some of the glasses. Those results agree well with the IR and QMS results.

The results of fluid phase calculations and glass analyses are shown in Table 1. These results are the first of their kind for CH_4, CO, and H_2. Also shown in the Table are molar ratios of each species in the magma relative to their abundance in the fluid. These ratios give the relative solubilities of the species in the magma. Because the fluid phase species activities appear to be similar to their mole fractions (3), the relative solubility results will also predict the order of activity coefficients. That is, a high relative solubility implies a low activity coefficient and vice-versa. This means that the following conclusions will hold regardless of the presence or absence of a fluid phase in the mantle.

Table 1. Volatile Compositions in Coexisting Melt and Fluid at 1200°C, 10 kbar in Mole %

	H_2O	CO_2	CO	CH_4	H_2	log 10 fO_2
Fluid phase	21.5	0.7	1.1	65.6	11.1	-11.9
Magma volatiles	83.1	0.5	9.5	2.0	4.9	-11.9
Normalized Magma*	33.0	0.2	3.8	0.8	2.0	"
Relative solubilities**	4	1	9	0.03	0.4	----
Magma volatiles at 1200°C, 1 atm***	82.6	7.0	1.1	4.4	4.8	-10.1

* Normalized magma volatiles calculated using the measured value of 3.60 wt% H_2O in melt.

** These values calculated by assuming magma volatile compositions are in equilibrium at atmospheric P and 1200°C.

*** Relative solubilities calculated as: Magma volatiles/fluid.

The results tell us that, at upper mantle conditions, volatile species will dissolve in a magma in the order $CO > H_2O \gg CO_2 \approx H_2 \gg CH_4$. The actual amount of a volatile species which dissolves in the upper mantle magma depends on its abundance in the source region are well as on its relative solubility. Under conditions more reducing than those equivalent to the quartz-fayalite-magnetite (QFM) buffer, the abundance of CO and CO_2 will be very low compared to H_2O while H_2 and CH_4 are comparable to H_2O (3). The values shown in Table 1 are an example of this case. Even though CH_4 and H_2 are abundant in the mantle in this case, their very low solubilities relative to H_2O means the magma acts like a semipermeable membrane to the surface, so the volcanic gases will be H_2O rich and more oxidized than the mantle.

In mantles relatively oxidized (compared to QFM), H_2O, CO_2 and CO will be abundant, H_2 a minor species and CH_4 insignificant (3). CO_2 will be more abundant than CO, but because CO is relatively much more soluble than CO_2 the CO/CO_2 ratio in the magma will be much higher than in the mantle source region. This will cause volcanic gases evolved from this magma to be more reduced than the mantle source.

Thus mantle magmas will selectively screen volatiles from planetary surfaces, forcing volcanic gases towards the "neutral" QFM oxidation state where H_2O is the dominant species. There is no suggestion in this model that volcanic gas compositions should change significantly with time.

References

(1) Eggler, D. H. and Baker, D. R. (1982) Reduced volatiles in the system C-O-H: Implications for mantle melting, fluid formation, and diamond genesis. Adv. Earth. Planet. Sci. High Pressure Research Geophysics, 237-250. D. Reidel, Tokyo.

(2) Jakobsson, S. and Holloway, J. R. (1984) Melting Experiments with graphite-C-O-H fluid-iron-wustite: A buffered system without iron-loss. Monash Univ. Workshop on Experimental Geochemistry. Monash Univ., Australia.

(3) Holloway, J. R. (1981) Volatile-melt interactions. Adv. Phys. Chem. 1, 266-296. Springer-Verlag, New York.

THE EVOLUTION OF CO2 ON MARS

Ralph Kahn, McDonnell Center for the Space Sciences, Dept. of Earth and Planetary Sciences, Washington University, St. Louis, MO 63130

At an average location on the surface of Mars, the pressure of CO2 (PCO2) varies seasonally between about 6 and 8 mb. Outgassing models suggest that at least 140 mb, and possibly as much as 3000 mb of CO2 have been placed in the atmosphere over geologic time. Neither the polar caps nor the regolith alone appear to be adequate repositories for the CO2, and mechanisms associated with storing carbon in these reservoirs do not account for the particular range and stability of PCO2 found on Mars today.

I have explored the consequences of the hypothesis that the evolution of CO2 is directly linked to the occurrence of at least transitory pockets of moisture (Kahn, submitted to Icarus, 1984). While current conditions preclude the existence of open bodies of liquid water, the formation of moisture in disequilibrium is not excluded by any known constraints. To a first approximation, the water evaporation rate is inversely proportional to PCO2, and I postulate the existence of a limiting value (P*) for which liquid water can form in the Mars environment. According to the scenario, the evolution of PCO2 is controlled largely by relatively rapid aqueous chemistry forming carbon-containing sedimentary rocks, perhaps during early history in open water, but more recently in transitory pockets of moisture in the soil. Once the total atmospheric pressure is reduced to near P*, the occurrence of transitory moisture is inhibited, and atmospheric CO2 is no longer depleted by an efficient mechanism. The role of the carbonate reservoir in the current overall carbon budget on Mars, according to this scheme, is illustrated in Figure 1.

The triple point pressure of water is the minimum equilibrium partial pressure of water above the pure liquid, and is equal to 6.1 mb. P* is unlikely to be lower, but need not be much higher, than the triple point pressure of water. [Factors including soil absorbtivity, solute abundance, heating rate, and local elevation affect the actual value of P*.] The hypothesis thus provides an explanation for the current value of PCO2 which is apparently consistent with existing chemical and physical constraints, and is supported by arguments showing that formation of liquid water in disequilibrium is difficult but not impossible on Mars today.

The exact value of P* is poorly constrained by existing data, and probably varies with time and location. The degree to which PCO2 is tuned to P* is also unknown. Additional laboratory work under simulated Martian conditions could better establish the dependence of P* on PCO2 and heating rate, and might aid in assessing the plausibility of the proposed mechanism. If a large fraction of the outgased CO2 resides in a rock reservoir, substantial carbon-containing sedimentary deposits should occur, though they may be buried by other material. One bar of CO2 could form a layer of calcite about 20 meters thick, or could be stored, for example, as 5 percent of soil particles within a 700 meter regolith. If these deposits are found, for example, by multispectral

mapping of the Mars surface by MGCO, their spatial distribution should contain clues about the way heat and water needed for sedimentation are supplied.

The hypothesis has profound implications for the history of the Mars surface and atmsophere. It suggests that unless rapid outgassing events occurred subsequent to early Mars times, the climate of the planet has evolved linearly, rather than in the cyclic manner allowed by polar cap and regolith adsorption reservoirs. The linear pattern is shown in Figure 2, which illustrates schematically how PCO2 might have evolved over geologic time, possibly decreasing rapidly during an early period when the surface temperature may have been high enough to sustain stable bodies of liquid water, and later decreasing more slowly when transitory pockets of moisture form, either on a seasonal basis, or due to local geothermal activity.

Acknowledgements: This work is supported in part by NASA grant NSG 7612 to Cornell University and NASA grant NAGW 660 to Washington University, St. Louis, under the Planetary Atmospheres Data Analysis Program.

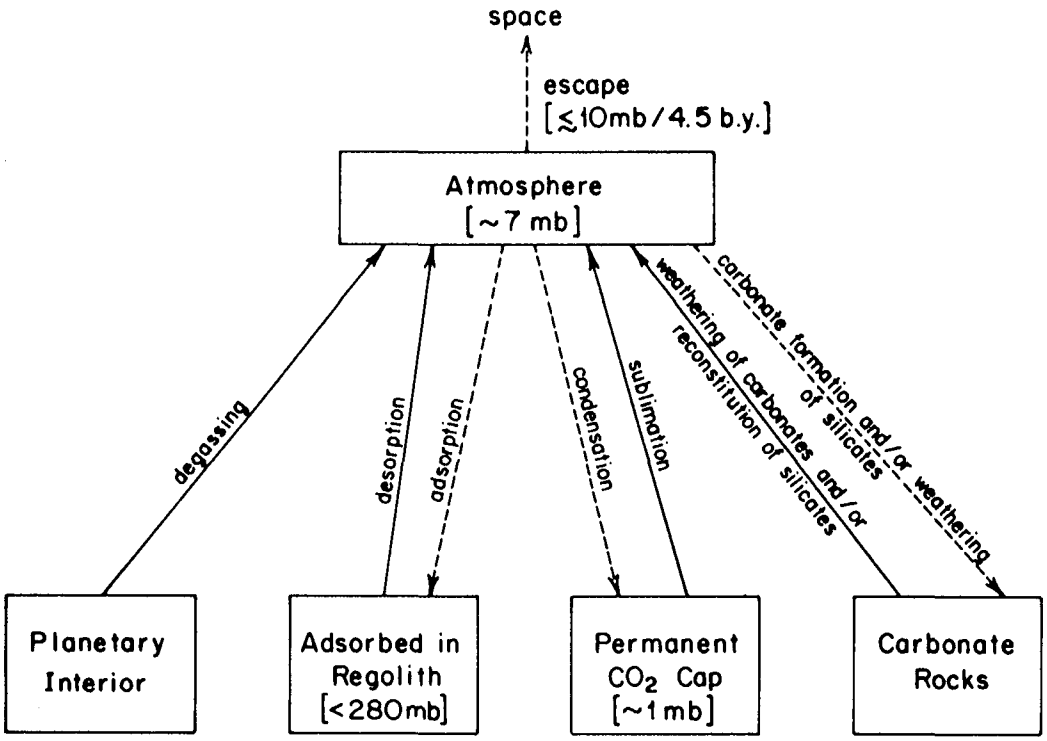

Figure 1. A representation of the CO2 cycle on Mars.

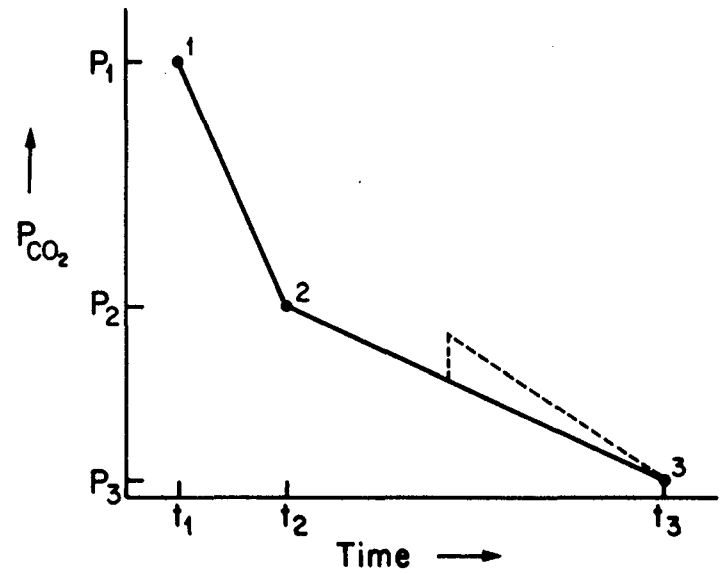

Figure 2. Some possible scenarios for the evolution of PCO2. The dashed line illustrates the effect of a rapid outgassing event.

CHAPTER 7

VOLCANIC PROCESSES

Page intentionally left blank

RIDGED PLAINS OF LUNAE PLANUM: THICKNESS DISTRIBUTION REVISED

R. A. De Hon, Department of Geosciences,
Northeast Louisiana University, Monroe, LA 72109

The thickness of ridged plains-forming materials on the eastern flank of the Tharsis Dome was previously estimated (1) using the buried crater technique based on mercurian crater dimensions. In that paper, it was recognized that "imprecise knowledge of crater morphology limits the technique to generalized estimates of regional thickness trends(1)." Now that a working relationship of martian crater trends is formulated (2), new data are used to revise the isopach of plains-forming material in the Lunae Planum region (Fig. 1A). The distribution of data points in the region has not increased; consequently, the new map is still valid for generalized thickness trends only.

The isopach map (Fig. 1A) is based on a total of 65 points; 32 points represent thickness estimates at partially buried craters. The remaining 33 points define the limits of plains-forming materials (zero thickness). Suitable buried craters are randomly distributed and sparse near the western edge and northern portion of the area. The overall thickness trend is similar to the previously mapped distribution (1), but there is a significant reduction in thickness values. The maximum measured thickness, near the western limit of exposed materials, is 660 m. The average thickness of exposed materials is 310 ± 110 m, but the distribution is best described as a wedge of material thinning to the west and south. A 5th order trend surface (Fig. 1B) provides a reasonably good match to the isopach (coefficient of correlation = 0.7224, standard deviation = 0.15). The 5th order residuals (Fig. 1C) indicate local lenses that deviate from the general trend.

Materials exposed at Lunae Planum form an eastward sloping plateau on the east flank of the Tharsis Dome. The exposed ridged plains-forming material is a remnant of a larger body of volcanic flows that thickens to the west and norhwest toward the source area near the crest of the dome. The materials are, in part, covered by younger flows associated with the central Tharsis volcanoes; and they are, in part, removed by processes responsible for the formation of Kasei Vallis and the northern plains. The total area of presently exposed ridged plains in Lunae Planum is approximately 5×10^6 km^2. The volume is estimated to be roughly 1.5×10^6 km^3.

References

(1) De Hon, R. A. (1982) J. Geophys. Res. 87, 9821-9828.
(2) Pike, R. J. and Davis, P. A. (1984) Lunar and Planet. Sci. XV, 645-646.

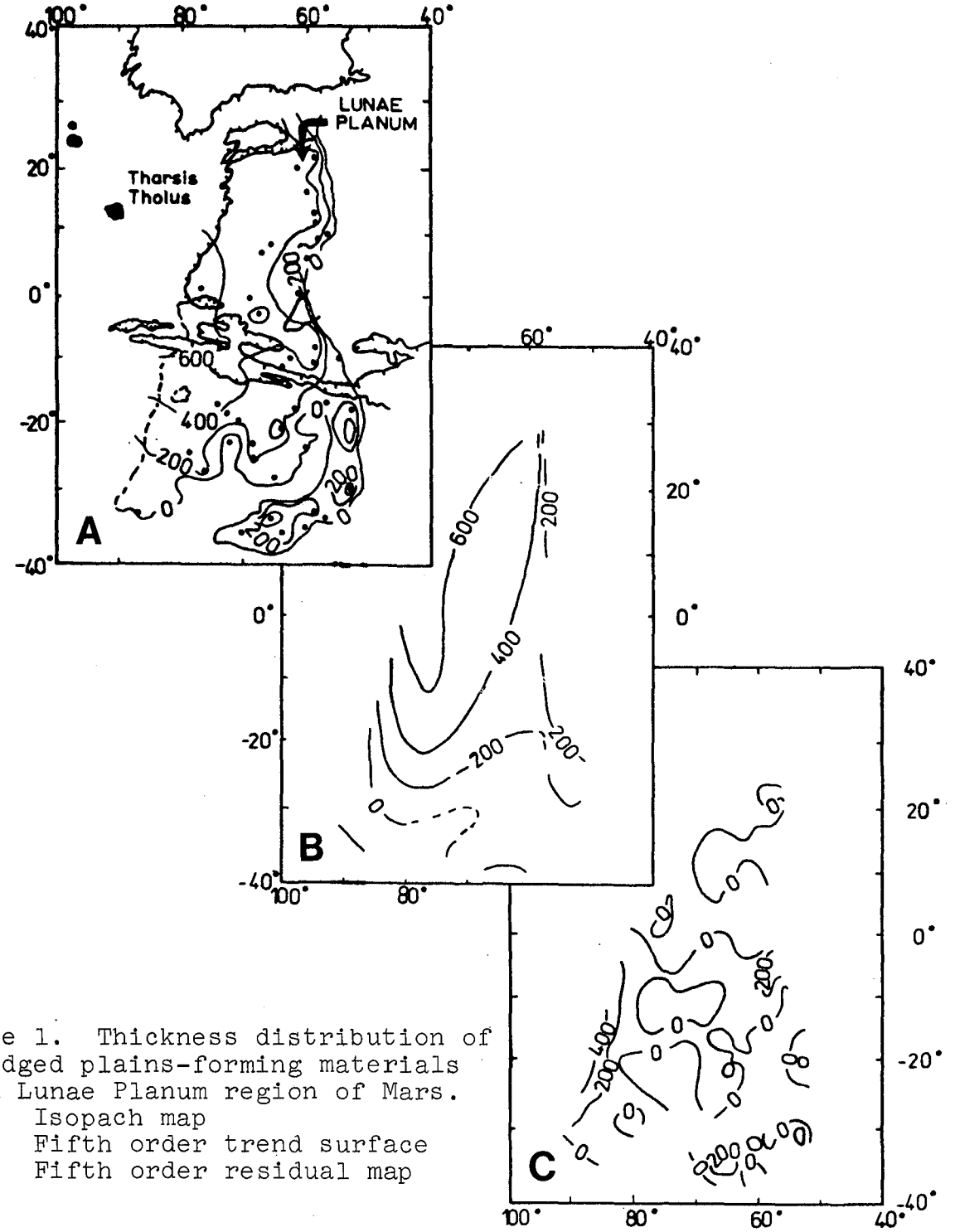

Figure 1. Thickness distribution of ridged plains-forming materials in Lunae Planum region of Mars.
A. Isopach map
B. Fifth order trend surface
C. Fifth order residual map

VOLCANIC DEBRIS FLOWS IN THE ELYSIUM REGION OF MARS

Eric H. Christiansen and Michael P. Ryan
Department of Geology, University of Iowa, Iowa City, Iowa 52242

Many investigators have suggested that magma-ice interaction was important for the generation of the fluids which produced the martian channels, but in general there is little evidence to link volcanism and channel formation. Photogeologic studies of the Elysium volcanic province appear to provide a specific example of the importance of volcano-ice interaction to produce the channels of Hrad and Granicus Valles. In addition, these studies have shown that the channels lie on the surface of a large sedimentary deposit which is interpreted here as an accumulation of volcanic debris flows or lahars. In spite of some similarities with martian "outflow" channels, this latter difference may distinguish the Elysium channels from other types of martian channels.

The three large volcanoes of the Elsium province, Elysium Mons, Albor Tholus, and Hecates Tholus are all located on a regional system of WNW-trending fractures and graben called Elysium Fossae. Apparently, these fractures have served as magma conduits periodically throughout the evolution of the volcanic field. In the northwestern Elysium volcanic province, the earliest discernible volcanism related to these fractures was the eruption of flood-type lavas which flowed to the northwest down the regional slope. Lava flows can be traced for 600 km away from their vents. In a sense, these eruptions were parasitic in that they formed late in the evolution of Elysium Mons, and in that they are displaced away from the main volcanic edifice along a structural trend as is the usual case for terrestrial parasitic eruptions. The usual martian problem of scale poses some problems as the eruptions originated about 300 km from the summit of Elysium Mons and created an accumulation of lavas that cover over 10,000 cubic kilometers. The greatest volume of these lavas appear to have been derived from two fracture systems which have been enlarged to troughs 4 to 10 km wide and 150 to 200 km long.

The Granicus and Hrad Valles channels issue from a set of fractures which are parallel to those described above, but situated to the south and north respectively. These troughs, similar to those from which the lavas erupted, have formed on the steep western slopes of the Elysium dome. A vast deposit with a channeled surface spreads out onto the adjacent plain from the mouths of these troughs. The deposits extend down the regional slope toward the northwest and cover approximately 1,000,000 square km. It is these mass flow features which we regard to be lahars. The lahars drop about 5 km over their 1000 km course, much of it in the first 100 km (Downs et al. 1982) where the debris coursed down the narrow troughs of Elysium Fossae. The margins of the deposit consist of lobate flow fronts which are locally dissected by irregular depressions and short sinuous valleys. In a few cases, discrete channels emerge from the bases of these lobate masses and extend several tens of kilometers further. The latter two observations

strongly suggest that the flows were wet debris flows in which water separated from the granular matrix (Wright and Schmincke 1984) by percolation (to create fluvial seepage channels) and evaporation (to create irregular depressions). This inference and the intimate association of these flows with the volcanism associated with Elysium Mons have lead to their interpretation as vast volcanic debris flows, or lahars, derived from the melting of ground ice beneath the volcanic region and its consequent escape through the same fracture system from which the flood lavas erupted (Christiansen and Greeley, 1981). Near the sources at Granicus Valles, the deposit is smooth and thin. (The rims of small craters protrude indicating a thickness of less than 200 m--using the crater diameter to rim height measurements of Lee, 1984). Fluids in the channels scoured the margin of the flood-lava plain described above. Further from the source, the deposit spills over the lava plain obscuring the southern extent of the lavas. At even greater distances, the debris flows cover the polygonally fractured plains which are typical of Utopia Planitia. In this area, the ejecta blankets of pre-existing craters are not completely buried. Proximal channels form a well-defined anastomose system of distributaries with wide lateral deposits. Locally, teardrop-shaped islands occur on the channel floors. To the northwest, the channels become shallower and less distinct. Some channels disappear by merging with the surrounding debris plains; broad shallow channels reappear further along the same trends and have short tributaries similar to the seepage channels described by Higgins (1984). Considerable portions of the distal lahars are dissected by narow reticulate valleys which also resemble seepage or sapping valleys. Some high-standing knobs and pre-existing craters are gullied by similar, but broader, systems of valleys. In distal regions, the interchannel regions are hummocky and irregular depressions are common.

The lahars associated with Hrad Valles merge with the Granicus lahars to the south near the northern extent of the flood-lava plain. In the region south of the crater Mie, interchannel deposits are dark and bear a striking resemblance to terrestrial basaltic lavas in that their margins are digitate, fissures occur on the crests of small lava toes at flow margins, and depressions on flow surfaces are common. For terrestrial lava flows, many of these features are the result of the formation of a rigid skin or rind on the flow which experiences brittle deformation as the underlying lava moves or drains. The emplacement characteristics of a wet lahar at the surface of Mars may be analogous to that of a terrestrial lava flow. It is conceivable that a stiff surface layer could develop on a lahar by freezing of included water. Thus although the origin of these flow features is ambiguous, they may have formed on the surface of a lahar.

A third set of debris flows also issue from the NW-trending fractures burying the central part of the lava plain. These flows are shorter (100 to 200 km) and have pitted, hummocky central areas, smooth lateral deposits and steep lobate margins. Shallow sinuous channels issue from their bases. Other flow deposits, interpreted to be lavas because they

lack evidence for the removal of liquid water, emanate from this same set of fractures. The lavas appear to have formed contemporaneously with this set of lahars.

The geologic relations described above demonstrate that the debris flows formed amdidst other volcanic activity in the Elysium region. Thereby suggesting that the magmatism was important to the generation of the mobilizing liquid. Thus we prefer to explain the origin of the lahars as the result of the melting of ground ice and liquefaction of subsurface materials. The possible contact of magma with liquid water may have resulted in hydrovolcanic explosions which produce large quantities of easily mobilized fine-grained material (Sheridan and Wohletz 1983). The intersection of this fluid reservoir with the regional fracture system lead to the rapid expulsion of a muddy slurry down the steep western slope of the province.

REFERENCES

Christiansen, E.H., and Greeley, R. (1981) Mega-lahars(?) in the Elysium region, Mars: Lunar and Planetary Science XII, p. 138-140.

Downs, G.S., Mouginin-Mark, P.J., Zisk, S.H., and Thompson, T.W. (1982) New radar-derived topography for the northern hemisphere of Mars: J Geophys Res 87, p. 9747-9754.

Higgins, C.G. (1984) Piping and sapping: development of landforms by groundwater outflow. in R.G. LaFleur (ed), Groundwater as a geomorphic agent, Boston, Allen and Unwin, p. 18-58.

Lee, S.W. (1984) Wind streaks on Mars: Comparisons of production models with observations of bright streaks. NASA Tech Mem 86246, p. 155-157.

Sheridan, M.F., and Wohletz, K.H. (1983) Hydrovolcanism: Basic considerations and review: J Volcanol Geotherm Res 17, p. 1-29.

Wright, R.V., and Schmincke, H.U. (1984) Pyroclastic Rocks: Berlin, Springer-Verlag, 472p.

THICKNESS OF RIDGED PLAINS MATERIALS IN HESPERIA PLANUM, MARS

R. A. De Hon, Department of Geosciences,
Northeast Louisiana University, Monroe, LA 71209.

Hesperia Planum is a region of ridged plains-forming materials on the northeast flank of the Hellas Basin. The region is dominated by Tyrrhena Patera, a large shield volcano. Hesperia Planum and Tyrrhena Patera are part of a grand alinement of volcanic features from Amphitrites Patera on the southwest flank of Hellas, through Hadriaca Patera on the northeast Hellas rim, to Elysium Mons and Hecates Tholus. The ridged plains materials exhibit characteristics in common with plains materials of Lunae Planum and mare materials of the moon. Hesperia Planum plains materials are presumed to be volcanic flows that originated from Tyrrhena Patera (1). The Hesperia ridged plains occupy a roughly elliptical region 1200 km by 1800 km. Tyrrhena Patera is eccentrically located on the west central portion of the plains. Hesperian ridged plains materials are superposed on older cratered terrain except in the southwest where they overlie older plains-forming materials associated with Hadriaca Patera.

The thickness distribution of plains-forming materials in Hesperia Planum is determined by the diameter of partially buried craters (2). Martian rim height to crater diameter relationships used for the thickness estimates were determined by Pike and Davis (3). As with all martian thickness studies, the distribution of measured thicknesses is sparse due to a low number of suitable partially buried craters. The resulting isopach of plains materials (Fig. 1A) has a low level of confidence but is sufficient for generalized thickness trends. The isopach is based on 72 thickness measurements, and 83 points define the edge (zero thickness) of the plains-forming material. The mean of the thickness estimates is 360 $\pm$ 120 m. The maximum measured thickness, 640 m in the southwest (Fig. 1A), may be erroneous due to the presence of older plains-forming materials related to Hadriaca Patera. Another thick lens is presumed to be associated with Tyrrhena Patera, but no craters survive in this portion of the plains. An arbitrarily high value of thickness is used to complete the contouring program.

The isopach of plains-forming materials exhibits an uneven thickness distribution. Average thickness, determined by grid sampling over the region, is 216 $\pm$ 153 m. Local lenses exceed 500 m. A fifth order trend surface provides a partial match (coefficient of correlation = 0.657) to the isopach. The trend surface (Fig. 1B) provides a rather simple elliptical

distribution with the center of mass southeast of Tyrrhena Patera. Major zones of significant deviation from the trend are shown in the map of residuals (Fig. 1C). These include Tyrrhena Patera, the thick lens associated with Hadriacan materials, and large lenses along the eastern and southern margins.

Hesperia Planum contains an extensive ridge system. Ridges are radial to Tyrrhena Patera near the shield with strongest development northeast and southwest of the shield. Farther from the shield, the dominant pattern is that of two intersecting ridge systems. The intersecting sets are best developed in the southeastern portion of the plains. The origin of ridges on plains-forming materials remains problematic. Both igneous and structural origins have been proposed. Lunar observations of similar appearing mare ridges suggest that some ridges are tectonic features. They may be localized over buried topographic prominences by concentration of the local stress field during regional subsidence (4,5). Ridge spacing may be controlled by the thickness of plains-forming materials and the viscosity ratio of the plains and substrate materials (6,7). Thickness is a critical value in these calculations. Values determined in this paper and for Lunae Planum (8) provide important constraints to estimates of strain and physical properties of the plains and substrate materials.

References

1. King, E. A. (1978) U.S. Geol. Surv. Misc. Inves. Map. I-1073.
2. De Hon, R. A. (1982) J. Geophys. Res. 87, 9821-9828.
3. Pike, R. J. and Davis, P. A. (1984) Lunar and Planet. Sci. 15, 645-646.
4. De Hon, R. A. and Waskom, J. D. (1976) Proc. Lunar Planet. Sci. Conf. 7, 2935-2955.
5. Sharpton, V. L. and Head, J. W. (1981) Lunar Planet. Sci. 12, 962-963.
6. Saunders, R. S. and Gregory, T. E. (1980) NASA Tech. Mem. 82385, 93-94.
7. Watters, T. R. and Maxwell, T. A. (1982) NASA Tech. Mem. 85127, 279-281.
8. De Hon, R. A. (1985) this volume.

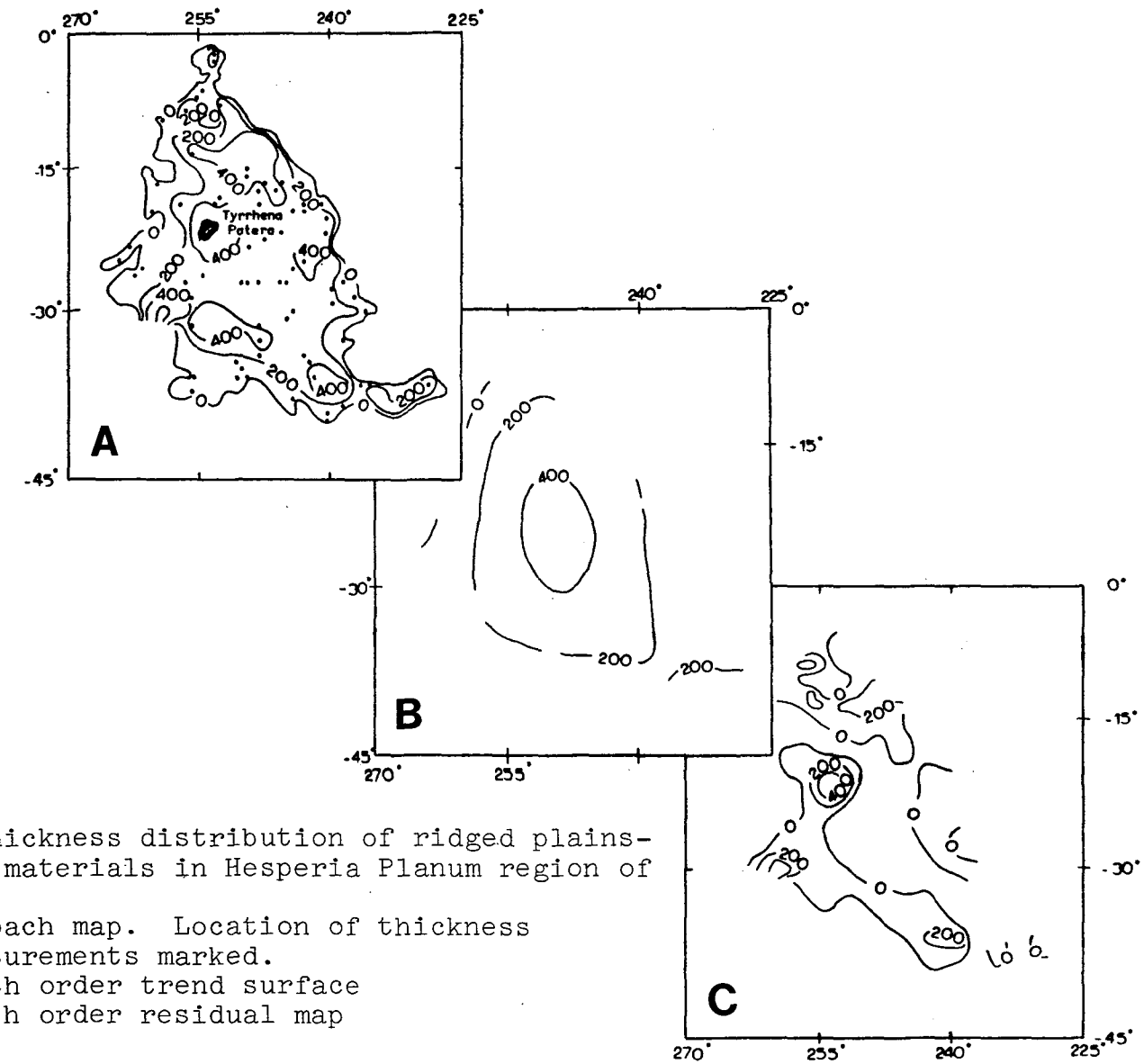

Figure 1. Thickness distribution of ridged plains-forming materials in Hesperia Planum region of Mars.

A. Isopach map. Location of thickness measurements marked.
B. Fifth order trend surface
C. Fifth order residual map

ESTIMATES OF LAVA ERUPTION RATES AT ALBA PATERA, MARS

Stephen M. Baloga, 3490 Adgate Drive, Ijamsville, MD 21754 and
David C. Pieri, Jet Propulsion Laboratory, Pasadena, CA 91109

The martian volcanic complex Alba Patera exhibits a suite of well-defined, long and relatively narrow lava flows qualitatively resembling those found in Hawaii. Even without any information on the duration of the martian flows, eruption rates (total volume discharge/duration of the extrusion) estimates are implied by the physical dimensions of the flows and the likely conjecture that Stephan-Boltzmann radiation is the dominating thermal loss mechanism.

The ten flows is this analysis emanate radially from the central vent and have had recent measurements of the length, plan areas, and average thicknesses determined by shadow measurement techniques (R. Lopez, PhD. dissertation). The dimensions of interest are shown in Table 1, below. Although perhaps morphologically congruent to certain Hawaiian flows, the dramatically expanded physical dimensions of the martian flows argues for some markedly distinct differences in lava flow composition for eruption characteristics.

It is widely believed that Stephan-Boltzmann radiation is the dominating thermal loss mechanism for terrestrial silicate lava flows (see e.g., Williams and McBirney, 1979; Shaw and Swanson, 1974; Pieri and Baloga, 1984) and there is evidence that (sulfur) lava flows at Ra Patera, Io exhibit the same behavior (Pieri et al., 1984). In a current study of selected Hawaiian lava flows (Pieri and and Baloga, 1984a,b), we have found that eruption rate is well-correlated with flow plan area provided the data is appropriately presorted to remove compositional and eruption process differences. In addition, the slope of the linear relation between Q, the eruption rate, and A, the plan area of the flow, is bounded quantitatively by:

$$Q_m = 3\,[T_s^{-3} - T_o^{-3}]^{-1} \cdot b \cdot A, \qquad (1)$$

and,

$$Q_u = T_s^{4}[T_o - T_s]^{-1} \cdot b \cdot A, \qquad (2)$$

where T_s is the solidus temperature of the flow, T_o is the eruption temperature and $b = \varepsilon\sigma/\rho C_p$. Here ε is the emissivity, σ is the Stephan-Boltzmann radiation constant, ρ is the density, and C_p is the specific heat. Equation (1) evokes the assumption of "thermal mixing", that is, the radiating surface of the lava is continuously renewed and is characteristic of the internal flow temperature at all points downstream. The thermally "unmixed" case described by equation (2) presumes the flow material is shielded by a solid skin or roof that must perforce, radiate at the solidus temperature as a maximum. Both derivations assume the terminal plan area of the flow is attained when the flow temperature reaches lava solidus.

It has been suggested that the Alba Patera flows are basaltic or possibly ultra-mafic in composition (e.g., Kaula, et al., 1981 or Head et al., 1981). Consequently, we have taken $\rho = 2.7$ gm/cm^3, $C_p = 8.4 \times 10^6$ ergs/gm K, and assumed $\varepsilon = 1$ for estimation purposes. The eruption rates associated with Alba Patera flow plan areas are shown in Table 1 for a common solidus (1200 K) and two plausible eruption temperatures (1500 K and 1700 K).

TABLE 1.

ALBA PATERA ERUPTION RATE ESTIMATES

Flow No.	Length (km)	Area (km^2)	(T_o=1500 K) Qu	Qm	(T_o=1700 K) Qu	Qm
			($x10^3$ m^3/s)			
1.	68	332	58	90	35	68
2.	128	444	78	120	47	90
3.	206	824	145	223	87	168
4.	220	860	151	233	91	175
5.	40	156	27	42	16	32
6.	54	236	42	64	25	48
7.	138	356	63	96	38	73
8.	44	212	37	57	22	43
9.	80	296	52	80	31	60
10.	98	300	53	81	32	61

These eruption rates are clearly enormous by comparison, for example, with Hawaii, where an effusion rate of 5 x 10^3 m^3/sec would be at the high extreme of the range of observed data. (e.g., Malin, 1980). The values in the table dramatically illustrate the consequences of the vast plan areas of the Alba Patera flows. It should be noted that the elevation of the eruption temperature substantially decreases the eruption rate requirements and additionally extends the results for thermally mixed and unmixed flows. Differences between eruption and solidification temperatures, of the order of 100-200 K, as might be found in Hawaiian lava flows, elevate the Alba Patera eruption rates to incredible (but not rigorously excludable) values. It is also parenthetically interesting, to note that the larger Alba Patera flows engender theoretical eruption rate requirements comparable to those calculated for flows at Ra Patera on Io. Although the latter flows are even more extensive, the eruption rates appear to be mitigated by the physical compositional parameters for elemental sulfur (Pieri et al., 1984).

We presently favor eruption temperatures in excess of 1500 K for the Alba Patera flows consistent with a mafic or ultramafic lava composition. Although our studies are guided by the results above, we are also investigating the Alba Patera flows using models for the temporal evolution of lava flow thickness profiles with spatially dependent viscosities. It is hoped that this additional theory and data comparison will impose further constraints on admissible eruption parameters and compositions for these flows.

REFERENCES:

Malin, M.C., 1980, The lenghts of Hawaiian lava flows, Geology, 8, p. 306-308.

Pieri, D.C. and S.M. Baloga, 1984a. Effusion rates, areas, and lengths of some Hawaiian lava flows, submitted to Journal of Volcanology and Geothermal Research.

Pieri, D.C. and S.M. Baloga, 1984b. Effusion rates, areas, and lengths for some lava flows on Hawaii and Mount Etna with planetary implications, p. 141 in Reports of Planetary Geology Program-1983, NASA TM 86246, Holt, ed., 376 pgs.

Pieri, D.C. S.M. Baloga, R.M. Nelson, and C. Sagan, 1984. Sulfur flows at Ra Patera, Io, Icarus, in press.

Shaw, H.R. and D.A. Swanson, 1974. Eruption flow rates of flood basalts, Proc. 2nd Columbia River Basalt Symposium, p. 271-299, East Washington State College Press.

Williams, H. and A.R. McBirney, 1979. Volcanology, Freeman and Cooper & Co., San Francisco, CA, 396 pgs.

Kaula, W.M., F.P. Fanale, and D.L. Anderson, 1981, "Implications of basaltic volcanism for the evolution of planetary bodies," p. 1238 in Basaltic Volcanism of the Terrestrial Planets Basaltic Volcanism Study Project, Pergammon Press, New York, 1286 pp.

Head, J.W. III, W.B. Bryan, R.G. Greeley, J.E. Guest, P.H. Schultz, R.S.J. Sparks, G.P.L. Walker, J.L. Whittford-Stark, C.A. Wood, M.H.Carr, 1981, "Distribution and morphology of basalt deposits on planets," p. 701, ibid.

EMPLACEMENT OF LONG LAVA FLOWS ON MAUNA LOA (HAWAII) AND ALBA (MARS)

P.J.Mouginis-Mark, G.P.L.Walker, L.R.Gaddis and S.Rowland Hawaii Institute of Geophysics, Univ. Hawaii, Honolulu, HI 96822; and L. Wilson, Univ. Lancaster, Lancs., LA1 4YQ England.

Spacecraft images have revealed that extremely long lava flows (more than 200 km long) exist on the surface of Mars[1] and Io[2]. Compared to terrestrial volcanic eruptions, the occurrence of these long flows is very unusual, and may hint at a different style of either magma production or eruption[3]. Attempts to model the emplacement of the long flows on other planets, using a Bingham rheological model, have been only partially successful[4,5,6]. Such analyses led to the idea that another alternative emplacement mechanism exists which to date has not been documented on the Earth[7,8,9]. The objective of our analysis is to conduct field measurements on long lava flows in Hawaii (where individual flows such as those of 1859 and 1881 exceed 40 km in length) in order to document and interpret their flow characteristics. In this way, we hope to understand better the formation of long lava flows and to determine if the Mauna Loa flows are terrestrial analogs to the long flows seen on Mars (e.g., the Arsia Mons[1,8] and Alba Patera[10] flows) and Io.

Several hypotheses exist to help explain the formation of long lava flows. These hypotheses include the influence of local slope and lava rheology (Newtonian flows vs. Bingham flows)[4,11], effusion rate[12], and the relative importance of tube-fed flows[13]. We are attempting to determine the emplacement mechanism for long flows by first focusing on the 1859 Mauna Loa flow (Fig. 1). This flow originated at an altitude of about 2,800 m on the northwest flank of the volcano and flowed about 47 km into the ocean. Observations made at the distal end of the flow (> 40 km from the vent) show that no prominent lava channel is present there, and no large lava tubes have been located. Together with the dominance of aa and the presence of various other structures, these observations argue for a Bingham rheology for this flow at least close to its terminus.

In the analysis of lava flows on other planetary surfaces, one of the most reliable measurements that can be made is the width of each lava flow. A major limiting factor when investigating the rheology of martian lava flows is the absence of local topographic data (although some correlations between flow morphology and local slope have been made[8,10]). We are studying the interrelationships between flow morphology and topography using the U.S. Geological Survey's 1:24,000 series photomaps of Hawaii. Slope and width for the 1859 flow have been measured at 240 m intervals along its length (Fig. 2). Local slopes vary from 0° to 10°, and the width varies from 200 m to 2,800 m. Within 10 km of the vent, slopes decrease from 10° to 4°, while the flow width varies from 500 m to 1,200 m; numerous small lava channels exist within 3.5 km of the vent. Maximum flow widths (up to 2,800 m) are attained between 10 and 20 km from the vent, and correlate with unusually low slopes between 1° and 4°. No lava channels are evident in this portion of the flow. Beyond 20 km, a prominent lava channel (20-65 m wide) does, however, exist. This channel has a significant amount of lava spatter on the channel sides, which probably indicates that the flow was turbulent in this area. Where this channel occurs, the flow width remains fairly constant (between 300 m and 1,200 m) despite moderate changes in local slope (2° to 8°).

As a continuation of this study, we are currently conducting field studies on the 1859 flow to search for possible associations between flow lobe morphology and lava rheology[14], and between the rate of response of flow thickness to changes in local slope. In addition, we are studying the diversity of lava flow morphologies that exist elsewhere in Hawaii, since changes in surface texture of the flows provide further information on its deformation history and its changing rheology with increasing distance from the vent[15,16,17]. With respect to investigations of volcanoes on Mars, we have identified several lava flows more than 100 km long which erupted close to the summit caldera of Alba Patera. While lacking topographic data for this volcano, the well-defined flow units, used in conjunction with our data from Hawaii, may permit us to place constraints on the local topography of martian volcanoes.

References: 1) Schaber, G.G. et al. (1978). PLPSC 9th, p. 3433-3458. 2) Schaber, G.G. (1982). In: The Satellites of Jupiter, Ed. D. Morrison, Univ. Arizona Press, p. 556-597. 3) Wilson L. and Head (1983). Nature 302, p. 663-669. 4) Hulme G. (1974). Geophys. J. Roy. Astron. Soc., 39, p. 361-383. 5) Moore, H.J. et al., (1978). PLPSC 9th, p. 3351-3378. 6) Greeley R. et al., (1981). NASA TM-84211, p. 38-40. 7) Malin M.C. (1980). Geology, 8, p. 306-308. 8) Roth L.E. and Saunders R.S. (1983). LPS XIV, p. 652-653. 9) Settle M. (1978). LPS IX, p. 1047-1049. 10) Cattermole P. and Reid C. (1984). The summit calderas of Alba Patera, submitted to: Icarus. 11) Hulme G. (1976). Icarus 27, p. 207-213. 12) Walker G.P.L. (1973). Phil. Trans. R. Soc. Lond. 274, p. 107-118. 13) Carr M.H. et al., (1977). JGR 82, p. 3985-4015. 14) Wadge G. (1982). LPS XIII, p. 829-830. 15) Fink J.H. and Fletcher R.C. (1978). J. Volc. Geotherm. Res., 4, p. 151-170. 16) Peterson D.W. and Tilling R.I. (1980). J. Volc. Geotherm. Res., 7, p. 271-293. 17) Kilburn C.R.J. (1981). J. Volc. Geotherm. Res., 11, p. 373-382.

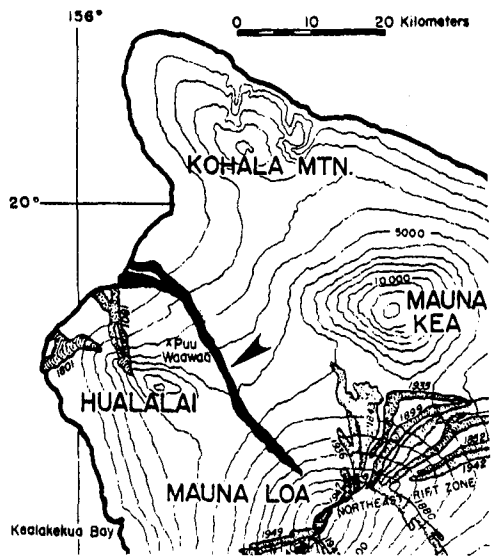

Fig. 1: Map of the northwestern portion of the Big Island of Hawaii, showing the location of the 1859 lava flow (arrowed) for which the morphometric measurements have been made.

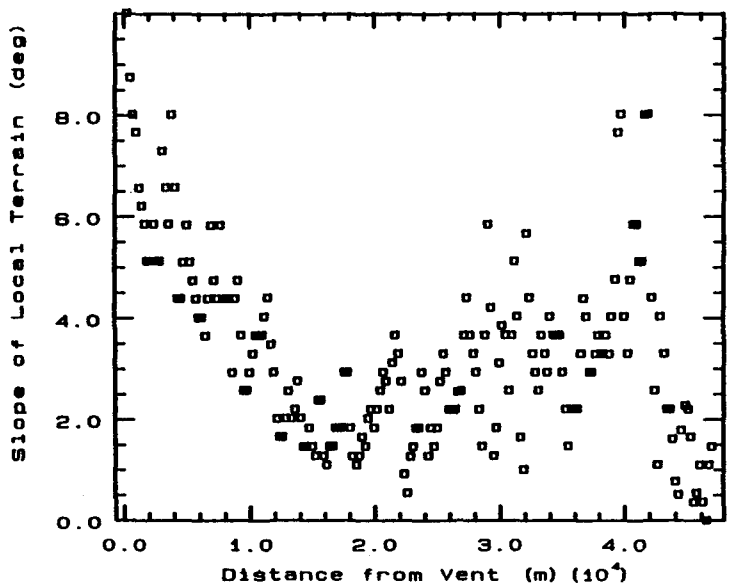

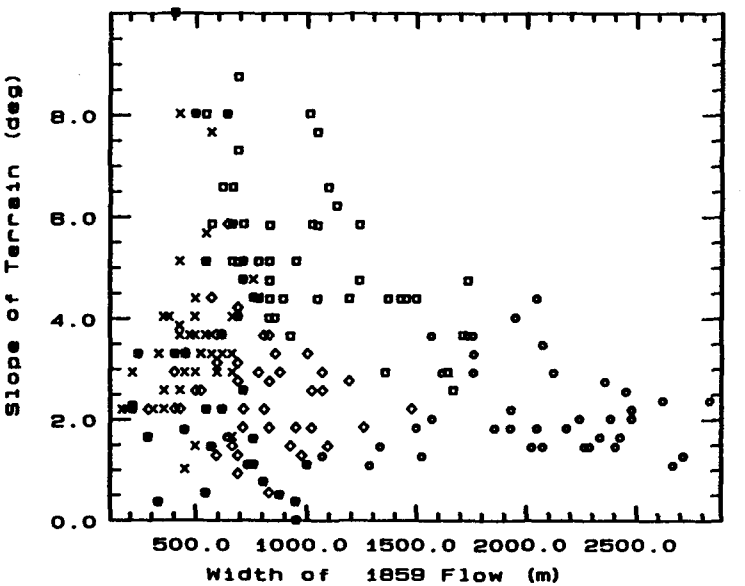

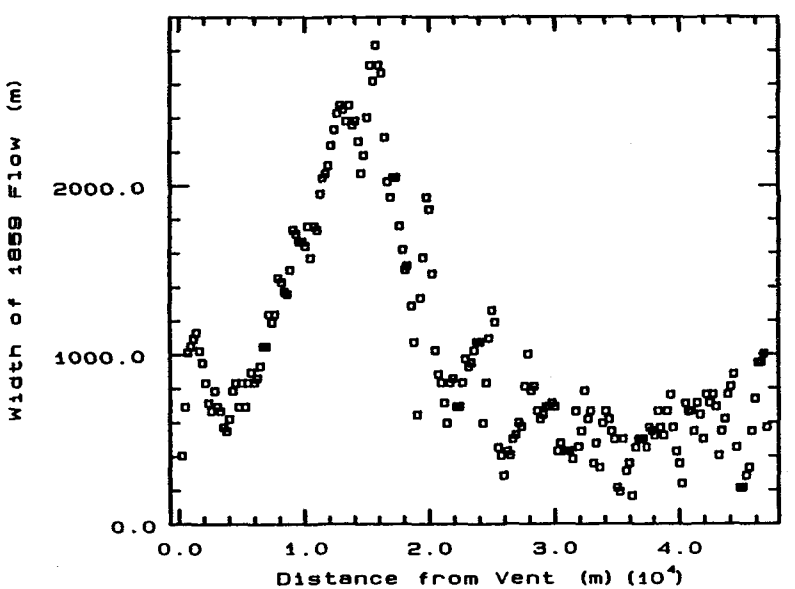

slope: points 1 to 42 (0 to 10 km)
slope: points 43 to 84 (10 to 20 km)
slope: points 85 to 126 (20 to 30 km)
slope: points 127 to 168 (30 to 40 km)
slope: points 169 to 197 (40 to 46.8 km)

Fig. 2: Morphometric data for the Mauna Loa 1859 lava flow. Measurements presented are for flow width and local slope as a function of distance from the vent, made at 240 m intervals along the flow length. Different symbols denote dimensions of flow at different distances from the vent.

THERMAL INFRARED OBSERVATIONS OF LAVA FLOWS DURING THE 1984 MAUNA LOA ERUPTION

David Pieri, Alan R. Gillespie, Ann B. Kahle, Jet Propulsion Laboratory, Pasadena, CA 91109
James Kahle, California Division of Mines and Geology, Los Angeles, CA
Stephen M. Baloga, 3490 Adgate Drive, Ijamsville, MD 21754

Volcanism is perhaps the most important constructional geomorphological process throughout the solar system, with active volcanism witnessed on the earth, Io, and suspected for Venus. But the quantitative study of active volcanism, however important, is fraught with difficulty. Even "simple" measurements of such parameters as flow effusion rate (mass/unit time), flow surface and subsurface temperatures, and flow thickness have been hard because active flows provide a hostile working environment for the volcanologist. In addition, until recently, quantitative physical models were not detailed enough to demand more precise and (most importantly) systematic measurements during the emplacement process. Such parameters as effusion-rate versus time, viscosity as a function of distance from the vent, surface flow velocity profiles, and systematic measurements of velocity and depth all along the flow as a function of time, become important boundary conditions for models of the physics of lava flows (e.g., Walker, 1973; Booth and Self, 1973; Wadge, 1981; Pieri and Baloga, 1984). Such emplacement models are important, not only for their application to terrestrial flows, but also for their application to planetary lava flows where remote sensing imaging is the main or only source of data (e.g., Pieri et al., 1984a).

In April of this year the authors were fortunate enough to have the use of a thermal infrared scanning television system for measurements on active basalt flows at Mauna Loa, Hawaii (Pieri et al., 1984b). Through the gracious assistance of the Inframetrics Corporation, the United States Geological Survey (Hawaii Volcano Observatory), and the United Kingdom Infrared Telescope Facility (Hilo), we were able to helicopter over the actively erupting #1b, #1c and #1d flows for about 8 hours at a range of ~30 m, making thermal infrared videotape images of the flowing lava streams and the vent areas at 10.6 μm, as well as some broadband images in the 8-12 μm range (for gas plume detection). We calibrated these data with on-site hand held radiometer measurements, in-flow thermocouple measurements (courtesy of N. Banks, USGS), and with later laboratory kiln measurements (courtesy of J. Stephens, JPL). An example of a single frame of these data (courtesy of JPL Audio-Visual Group) is shown in upper figure 1, along with a normal visual picture of the same vent area.

The infrared frame in figure 1 was taken from a range of about 200 meters on approach to the vent area in the Northeast Rift Zone of Mauna Loa at about the 9000 foot level. It shows the erupting vent area on the morning of April 7, 1984. The lava fountain is about 50 meters high, and the white zone is the hottest at about 1150 degrees C. The darkest tones are the coolest and are about 700 degrees C or less. Intermediate gray levels scale approximately linearly. This particular version of the data was taken from a false color version showing 8 color levels, however the master data tape contains 255 gray levels, and thus is far richer and more appropriate for quantitative analysis of temperatures and gradients. To our knowledge, thermal infrared data of this quality, thermal range, and level of precision has never been available before (R. Williams--oral communication). Also, since the data are output to standard commercial VHS or Beta format video tape, they are extremely

convenient to view, although quantative analysis presents some logistical problems because of the newness of the data medium.

The infrared video data are useful in quantitatively assessing the pattern and mode of flow thermal losses, particularly with regard to radiative losses from established/incipient floating crust. The general cooling of the flows downstream was readily apparent. Upper reaches of the active flow exhibited nearly crust-free main channels, radiating at about 700-800 degrees C. Below about the 7500 foot level (about 8 km from the vent) the flows formed nearly continuous crust and tended to spread, become less well-defined and founder due to a reduction in slope. Nevertheless, in thermal IR observations, the surface trace of the active subsurface channel was visible, radiating at about 500 to 700 degrees C. At the active flow front, most solid crust radiated at temperatures less than 500-600 degrees C, however bright high temperature interiors (~900-1000 degrees C) were clearly visible though evolving fissures. Breakout flows, breaching levees along the upper reaches of the main confined flows, appeared to be roughly 100 to 200 degrees cooler at their surface than the main, fast moving channels.

Channel interior morphology and thermal characteristics were dynamic, but surprisingly regular. Flows appear ~100 degrees C cooler along the center axis of the channel. Apparently, channel walls exert drag on the viscous flow, thereby initiating a roller action (as described by Booth and Self (1973) for Mt. Etna flows), apparently entirely in the laminar regime, despite an estimated flow velocity in excess of 20 miles/hour. As the flow rolls over at the margin, warmer material is brought to the surface, and the flow becomes more well-mixed thermally (Pieri and Baloga, 1984). Thermal stratification becomes more pronounced as solid crust eventually covers the channel entirely. An intermediate stage is reached as en-echelon plates follow each other down narrow channels, as described by Greeley (1971). Even before solid independent plates form, however, incipient regular thermal and spatial periodicities in the plastic surface layer are apparent.

Such data on the relationship between thermal and kinetic flow parameters should help answer questions about the modes of heat loss from the surface of a lava flow. In particular, knowledge about the rate and mode of lava flow heat loss coupled with measurements of flow velocity and characteristic dimension, is important in ascertaining the relationship between effusion rate and flow length and area, as well as in determining the viscosity scale length of the flow. An understanding of the interactions of these various parameters are important in assessing the eruption histories and compositions of volcanic flows on Mars, Io and possibly, Venus.

REFERENCES

Booth, B. and S. Self, 1973. Rheological features of Mount Etna lavas, Phil. Trans. R. Soc. Lond. A. 274, p. 99-106.

Pieri and Baloga, 1984. Effusion rate, area, and length relationships for some Hawaiian lava flows. Submitted to Journ. Volcan. and Geotherm. Res.

Pieri, D. C., S. M. Baloga, R. M. Nelson, and C. Sagan, 1984a. Sulfur flows at Ra Patera, Io, Icarus.

Pieri, D. C., A. R. Gillespie, A. B. Kahle, and S. M. Baloga, 1984b. Thermal infrared observations of lava flows during the 1984 Mauna Loa eruption, GSA Abstracts with Programs 1984, 16, p. 623.

Wadge, G., 1981. The variation of magma discharge during basaltic eruptions, J. Volcan. and Geotherm. Res. 11, 139-168.

Walker, G. P. L., 1973. Lengths of lava flows, Phil. Trans. R. Soc. Lond., A-274, p. 107-118.

CAPTION: FIGURE 1a.

Scene of active vent area on Mauna Loa on April 7, 1984. At least four active vents are visible. Smooth bright continuous, light gray swath across the middle of the picture is an active lava flow, about 100 meters wide, 5 meters thick, moving at about 25 miles per hour to the left. The spatter cones are about 40 meters high, with fountaining up to 50 or 60 meters. The lava temperature at the vent is about 1100 degrees Centigrade. Vent with arrow is the vent shown in infrared in Figure 1b.

CAPTION: FIGURE 1b.

Thermal infrared image of the central vent shown in Figure 1a. This is a frame grabbed from 1/2 inch video tape (VHS format) taken with the Inframetrics 525 thermal IR scanner. The original data were taken in 8 bit format (255 gray levels) which were, in turn, quantized into 8 false colors, which is a convenient format for qualitative analysis. That false-color image is reproduced here in black and white. The brightest gray tones here correspond with about 1100° C. The darkest gray (above black background) is about 700° C. Note the ejected in-flight glowing lava bomb (white arrow--upper center of picture) at about 800° C. Black darts indicate direction of flow in approximate centers of lava channels. This kind of spatially detailed quantitative thermal data for an active eruption is, to our knowledge, unique.

(Readers who would like to view the original false color and/or standard visual video tapes of this eruption are invited to contact the authors).

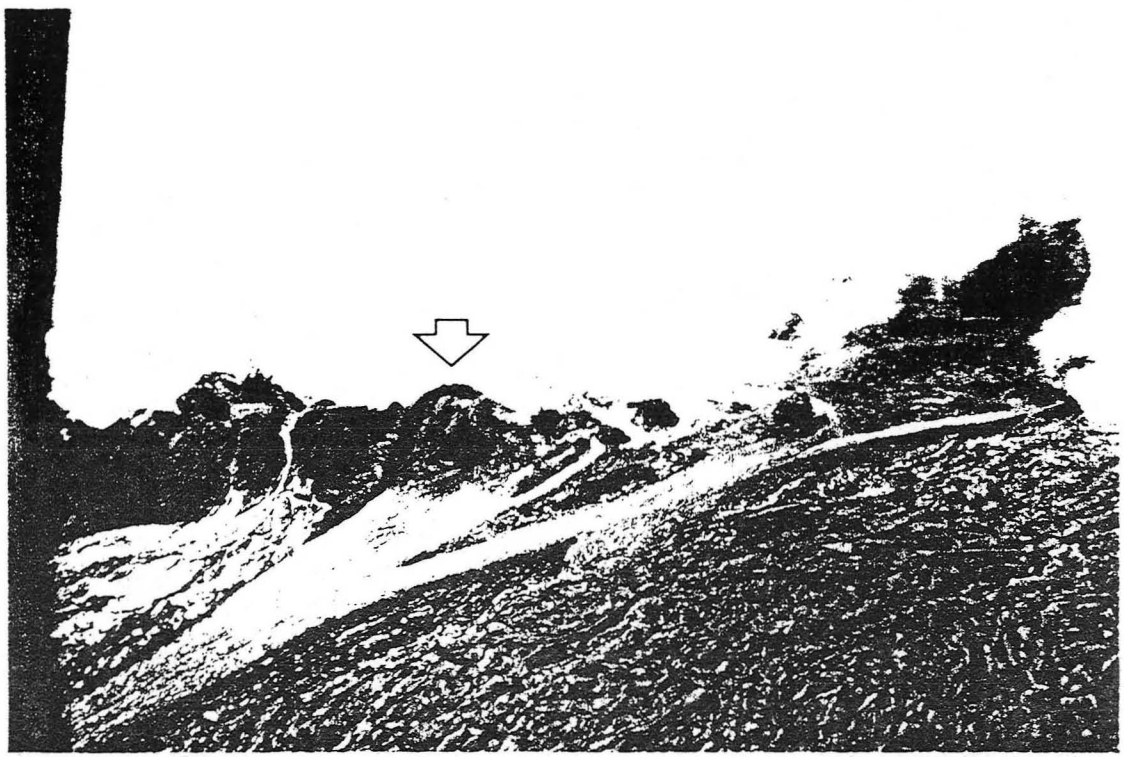

Fig. 1a

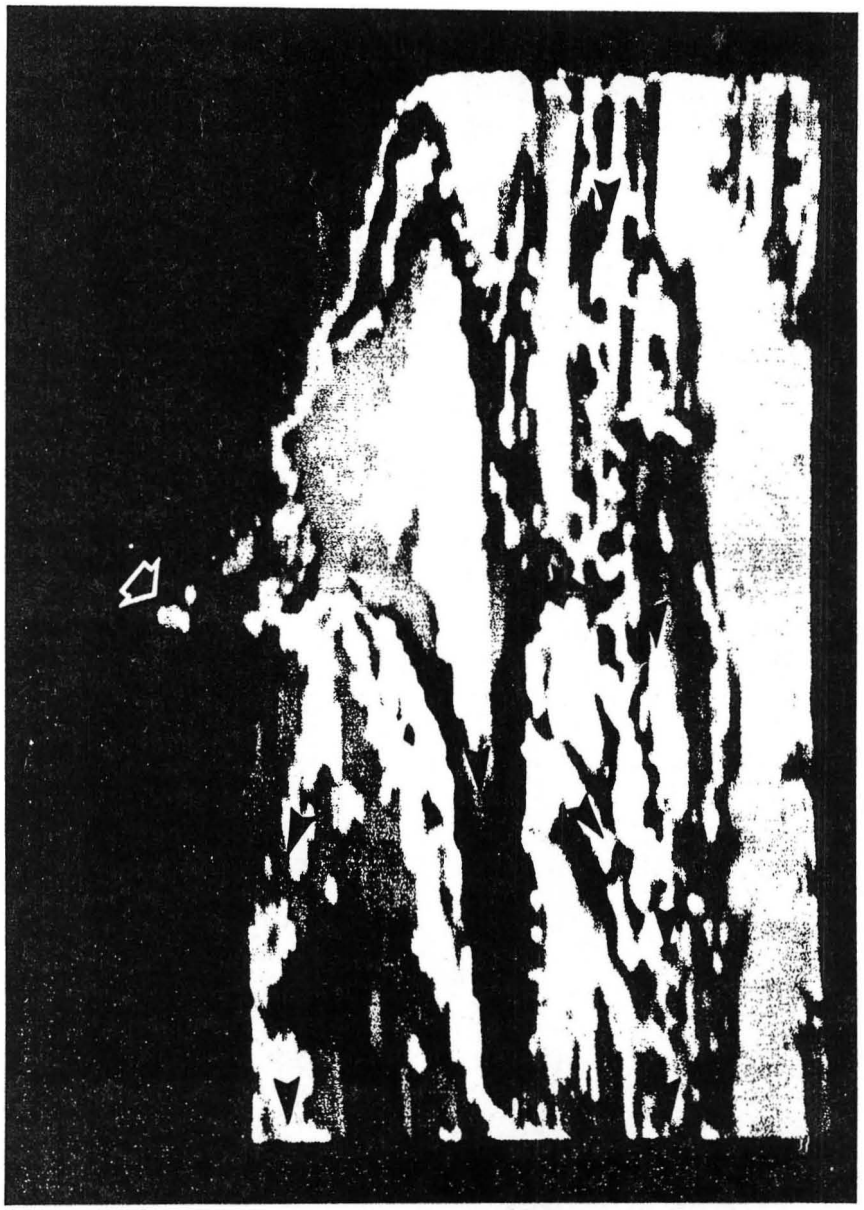

Fig. 1b

Field Measurements of the 1983 Royal Gardens Lava Flows, Kilauea Volcano, and 1984 Mauna Loa Lava Flow, Hawaii.

Jonathan Fink and Jim Zimbelman, Geology Dept., ASU, Tempe, AZ 85287

Introduction

Theoretical models used in the remote determination of lava flow rheology and compositions (e.g., Hulme, 1974; Moore et al., 1978; Fink, 1980; Park and Fink, 1981) rely on estimates of such geometric and flow parameters as volume flow rates, levee heights, and channel dimensions, as well as morphologic and structural patterns on the flow surfaces. Quantitative measures of these variables are difficult to obtain, even under optimum conditions. For flows whose emplacement was not witnessed, including those on other planets, the task of inferring these parameters can be nearly impossible.

In order to test various flow emplacement models used in planetary studies, we surveyed detailed topographic profiles across several Hawaiian lava flows that had been carefully monitored by the U.S. Geological Survey during their emplacement in 1983. Twenty two accurate channel cross sections were constructed by combining these profiles with digitized pre-flow topographic measurements. Levee heights, shear zone widths, and flow depths could then be read directly from the cross sections and input into the models. The profiles were also compared with ones constructed for some martian lava flows.

The Royal Gardens basalt flows

Beginning in January, 1983, a series of lava flows advanced through the Royal Gardens subdivision on the east flank of Kilauea Volcano. The housing development sits astride several N-S trending normal faults (down-dropped to the east) and has a nearly rectilinear street plan with major streets running parallel, and cross streets trending normal to the downslope direction. The streets, which are about 50 m wide, bisect 200 m wide, brushy areas cleared of trees. This layout served to funnel several of the flows down the tree-less areas and over the cross streets (Figure 1). Because of the relatively simple topography of the subdivision, it was possible to compare post-emplacement profiles constructed across the cooled surface of the flows with pre-flow topography and arrive at accurate estimates of cross sectional areas and final flow thicknesses.

Figure 2 shows accurate cross sections of the Phase 5 (6/29-7/3/83) flow taken at three successive downslope positions (sections shown on Figure 1). If we assume that the maximum levee heights represent the thickness of the moving flow, we can use the following formulae (Moore et al., 1978) to estimate yield strength (ty):

$$ty = p\ g\ H \sin B \qquad (1)$$

$$ty = p\ g\ (H^2/w) \cos B \qquad (2)$$

$$ty = 2\ p\ g \sin^2 B\ (wb) \qquad (3)$$

where p=density, g=gravity, H,w,wb=flow depth, width, and levee width, respectively, and B is the underlying slope. Using a density of 2500 kg/m^3 we obtain yield strength values for the highest cross section of 4.0, 7.3, and 1.5 kPa from the three equations above. The middle cross section gives values of 4.5, 7.1, and 2.1 kPa. The lowest cross section had values of 2.8, 3.4, and 1.5 kPa. These values are all relatively consistent and comparable to those calculated by Moore et al. (1978) for basalt flows.

Observations of active flows on Kilauea and Mauna Loa Volcanoes in the past two years have emphasized the complications involved in estimating the dimensions and properties of active flows. Multiple levee sets, surges, and expanding and contracting marginal shear zones all serve to thwart the efforts of later investigators who want to determine a unique set of rheological parameters for a given flow. Furthermore, measurements of lava density taken along the Mauna Loa flows of 1984 showed significant increases with time and with downstream position (Norm Banks, unpub. data, 1984). As an example of the problems these complications present, consider the yield strength estimates for the lowest cross section in Figure 2 (2.8, 3.4, 1.5 kPa). The cross section shows at least three pairs of nested levees. During the four day life of the flow these levees could have been activated and abandoned dozens of times before they finally came to rest in their present positions. If we use the dimensions of the inner levees and a lower value for lava density (1500) we get significantly lower yield strength values of 1.1, 1.4, and 0.2 kPa.

Another, more serious factor that complicates modeling of remotely observed flows is the lack of knowledge of underlying topography. Again taking the lowest cross section as an example, and assuming that the pre-flow surface was flat, the yield strength estimates from the first two equations would drop to 0.3 and 0.1 kPa, while the third equation would still give a value of 1.5 kPa. One of the ongoing goals of our study is to seek functional relationships between pre- and post-flow topography, so that more accurate estimates of flow and levee depths can be made for extra-terrestrial flows. We are also applying our measurements to a model developed by Park (1981) that takes into account the cooling, cross sectional shapes, and velocities of flows, important factors that are ignored by the yield strength models used above.

Ascraeus Mons flows

Application of any of the above models to extra-terrestrial flows requires images of high enough resolution to show the essential topographic features. The summit area of Ascraeus Mons on Mars shows numerous lava flows at a resolution of up to 22 m/pixel (Zimbelman, 1984). Figure 3 shows one of these flows for which we used shadow lengths to determine flow front and levee heights at three positions. Figure 4 shows the profiles at these locations. Assuming (1) a slope of 5 degrees, (2) lava density of 2500 (m-k-s) and (3) that the topography underlying the flow has a similar form to those measured in Royal Gardens, we obtain yield strength estimates for the upper cross section of 2.7, 4.6, and 0.7 kPa using the three equations listed above. The middle (3.0, 7.4, 1.5 kPa) and lower (3.7, 11.2, and 1.1 kPa) cross sections yield similar values. All of these calculations are subject to the same qualifications as the Hawaiian estimates. In addition, there are uncertainties of up to 50% in levee heights, 20% in flow thickness, 10% in flow widths, and 50% in topographic gradient.

Comparisons with features in the 1984 Mauna Loa flows

Images of the high resolution seen on Ascraeus Mons and Olympus Mons allow qualitative as well as quantitative comparisons to be made with terrestrial flows. The flow in Figure 3 shows several features that resemble structures observed forming in response to surges during the Mauna Loa eruptions of 1984. After surges subsided they commonly left behind dome-like mounds several tens of meters in diameter and height in the

center of the channel above breaks in slope. Subsequent surges were funnelled between these mounds and eroded their sides, streamlining them somewhat. The resulting subparallel "islands" were also seen in the Royal Gardens channels. Such features appear to be characteristic of aa basalt flows, having not been reported from more fluid pahoehoe flows nor for lavas of more silicic composition. A second type of construct seen forming in the Mauna Loa flows were dams of crust that piled up at constrictions above increases in slope. These dams caused ponding and the overflow of many short flows, forming a type of delta. In most cases these dams would eventually break, resulting in a new surge downstream, but they would leave behind wide areas with many short flows. Such constructs can be recognized on air photos of basalt and basaltic andesite flows, but not on more viscous rhyolite and dacite flows.

Both of these types of structures can be seen on the Ascraeus Mons flows, lending further support to the suggestion, based on yield strength estimates, that they are of basaltic or basaltic andesite composition.

References

Fink, J.H., 1980, Geology 8:250-254.
Hulme, G., 1974, Geophys. J. Roy. Astron. Soc. 39:361-383.
Moore, H.J. et al. (1978) Proc. LPSC 9th: 3351-3378.
Park, S.O., 1981 (PhD thesis), Iowa State University, Ames, Iowa.
Park, S.O. and Fink, J.H., 1981, GSA Abs. w. Prog. 13:525.
Zimbelman, J.R., 1984, (PhD thesis), Arizona State University, Tempe, AZ.

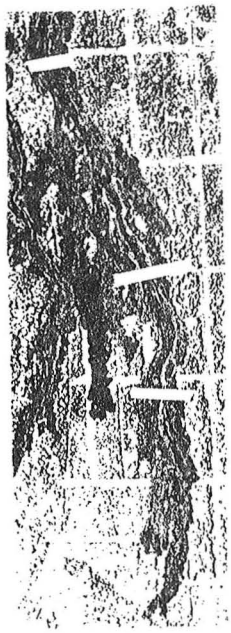

FIGURE 1

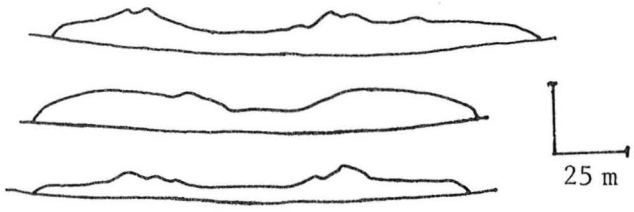

FIGURE 2 ↑

FIGURE 3 →

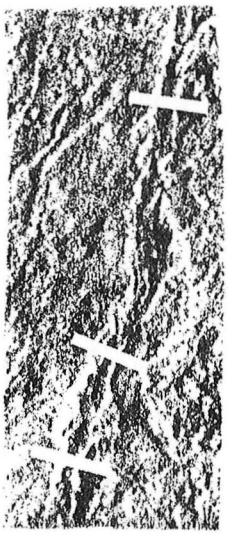

FIGURE 4 →

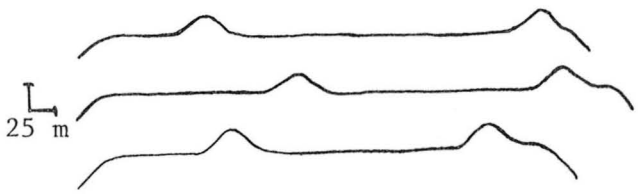

SURFACE STRUCTURES OF HAWAIIAN LAVAS

Scott K. Rowland and George P.L. Walker, Hawaii Institute of Geophysics, Honolulu, HI 96822.

Surface and internal lava structures can be valid indicators of lava viscosity and rheology, provided that care is taken to identify and eliminate structures which are strain-rate-dependent (Pinkerton & Sparks, 1976; Peterson & Tilling, 1980; Kilburn, 1981). We find a spectrum of types among Hawaiian basaltic flows, ranging from pahoehoe to a'a, that we interpret to mark a progression in lava viscosity and a change in rheology. The most fluid type in this spectrum is normal pahoehoe that has a smooth but commonly wrinkled or folded (ropy) surface. The next type, distinctly more viscous and, we think, probably non-Newtonian in rheology, is spiny pahoehoe which is characterized by a spinose surface and an absence of ropy structures. This type is sometimes termed "toothpaste lava", presumably because of its tendency to be squeezed out of openings (secondary boccas) on the surface or around the edge of a lava flow, and to retain on its surface any scrapemarks imposed by irregularities in the mouth of the bocca. Shearing of spiny pahoehoe generates a'a-type rubble, and all gradations are found between spiny pahoehoe and typical a'a. Drained-out lava tubes, very common in normal pahoehoe, are very scarce in spiny pahoehoe and a'a lavas and we think that tubes, if they form at all, are unstable structures in any lava which has a yield strength.

Here we single out two features which vary with the perceived viscosity, namely the sizes of surface undulations and the relief of surface textures. As the perceived viscosity rises, the size of undulations that can be generated and preserved on the surface of the flow also increases. This is caused partly by a thickening of the "skin" or solid portion of lava overlying the liquid interior and partly by a change in the liquid itself. The surface of a normal pahoehoe flow can be easily deformed into tightly folded "ropes" from one to a few cm wide. Spiny pahoehoe cannot deform so easily so that surficial folds have amplitudes exceeding 10 cm, and pressure ridges (ogives) often measured in meters are common on a'a flows.

While this decrease in the ability to form finer scale folding occurs, there is an enhanced ability to form and retain fine textures. The glassy surface of normal pahoehoe is often smooth on a cm scale and has almost no bumps or spines. A spiny pahoehoe surface has abundant cm-scale spines, and the clinker on a'a likewise maintains surface irregularities on the same scale.

These features relate directly with viscosity and yield strength of the lava at the time of eruption. Normal pahoehoe

undoubtedly gets pulled into spiny shapes as toes form, overflows occur, etc. However the fluidity of the lava allows these spines to be re-absorbed. The weight of any small scale perturbations is enough to cause them to sink back to the surface without being preserved, or surface tension causes their retraction before the skin solidifies. Indeed, some pahoehoe is unable even to preserve ropy structure. In spiny pahoehoe, the fluid portion of lava is strong enough to support the spines and they are preserved.

The net result is that with varying viscosity and rheology the scale of both the structural relief and the textural relief progressively change.

On aerial photos we note that pahoehoe flows have a high albedo and are rather featureless (they are unable to support large scale structure). A'a however has a low albedo and structural features such as channels and pressure ridges are preserved and show up clearly.

An important part of our work consists in correlating structural features of the lava with the measured distribution of olivine phenocrysts, since the extent to which these crystals have settled out from the upper half of the lava enables us to impose constraints on the viscosity/yield strength values within the spectrum of types. We are also measuring the distribution and sizes of spherical vesicles with the same objective. We are concentrating our observations at present on lavas containing olivine phenocrysts because they provide us with the opportunity of quantifying the properties of the flowing lavas, and we plan to proceed to aphyric lavas only when we have gained sufficient experience on the porphyritic ones.

Our preliminary studies on the long lavas of Mauna Loa indicate, perhaps surprisingly, that there is no clear-cut correlation of lava length with type in this spectrum of lavas, indicating that viscosity/yield strength of the basaltic lavas per se are not the primary controls determining flow length. Flowage of the lava through lava tubes, while it may help to account for the long flow distance of some lavas, is not a generally applicable explanation for long flow length.

References

Kilburn, C.R.J., 1981 Pahoehoe and aa lavas: a discussion and continuation of the model of Peterson and Tilling. J. Volcanol.Geotherm. Res., 11, 373-382.

Pinkerton, H., and Sparks, R.S.J., 1976 The 1975 sub-terminal lavas, Mount Etna: a case history of the formation of a compound lava field. J.Volcanol.Geotherm.Res., 1 167-182.

Peterson, D.W., and Tilling, R.I., 1980 Transition of basaltic lava from pahoehoe to aa. J.Volcanol.Geotherm.Res.,7,271-293.

BASALTIC PRESSURE RIDGES: FORMATION AND RELATIONSHIP TO FLOW EMPLACEMENT

E. THEILIG
Department of Geology, Arizona State University, Tempe, AZ, 85287

Pressure ridges and pressure plateaus are common but not ubiquitous surface features on terrestrial basaltic lava flows and may reflect a specific flow emplacement mechanism. Since pressure ridges and pressure plateaus are similar in morphology, occur in association with each other, and probably formed by the same mechanism, they will both be referred to as "ridges" to simplify the discussion. Many of the ridges are large enough to be detected on high-resolution orbital images; therefore, understanding these features could provide a means for interpreting volcanic flows on other terrestrial planets. The objective of this study is to determine the mechanism of pressure ridge formation and how their formation relates to flow emplacement. To provide insight into the timing of ridge formation and mechanism(s) of flow emplacement, detailed field maps were made of parts of two lava flows (Wapi Flow, Idaho, and McCartys Flow, New Mexico) to determine: 1) the relationship of ridges and plateaus to various flow units; 2) the presence or absence of squeeze-ups or addition of new material to the primary flow and their relation to ridges; 3) the orientation of ridges with respect to general and localized flow direction; 4) the association of ridges to other surface features; and 5) the progression of ridge forms.

Pressure ridges and plateaus are associated with flows characterized by multiple-flow units of pahoehoe with a few isolated patches of slab or aa lava, the presence of collapse depressions, and the absence of identifiable lava tubes. Field mapping was initially done in areas where flow direction could clearly be defined, few flow units and ridges were present, and constraints could be placed on ridge formation and flow emplacement. Even though the areas were not as complex as other parts of the flows, they contained all of the general flow characteristics. More complicated areas with numerous flow units, ridges, and plateaus were also mapped to verify the results obtained from the special cases.

The relationship between ridges and various flow units is complex in even the most simple areas. Flow units can be divided into primary and secondary units on the basis of surface texture and occurrence. Primary units exhibit either a smooth and filamented or knobby and lineated surface texture and have a generally consistent flow direction, whereas secondary lava consists of numerous interfingering toes with inconsistent flow directions. The secondary units represent lava which was extruded when either the internal pressure of a flow exceeded the crustal strength or when cracks in the crust migrated downward and intersected the molten lava. In the latter case, the extent of lava erupted was dependent on crack width, the timing of intersection with the lava, and the internal pressure of the flow. No definitive age relationship for primary and secondary lava can be established for the entire flow, since secondary material may either embay or be buried by primary lava from another major flow unit. However, for each main flow unit the primary lava was emplaced first, followed by the break-out and embayment by one or more secondary units. Important observations from the mapping are that ridges can be composed of either primary or secondary units and that each ridge (and, in some cases, series of attached ridges) consists of an individual flow unit or lobe. As such, they are parallel to localized flow direction but may be oblique or transverse to overall flow direction. The relationship between adjacent ridge-containing flow units is complex because secondary material

that erupted from one ridge embays or partly covers an adjacent ridge, indicating some time separation in ridge formation. Therefore, the whole flow is characterized by interfingering flow lobes (each major unit represented by a ridge or plateau) that formed penecontemporaneously.

Several lines of evidence indicate an inflation mechanism for formation of ridges: 1) as observed from the mapping, ridges form the central parts of individual flow units. This is inconsistent with both a collapse mechanism in which ridges are formed by the partial collapse of a flow, and a compression mechanism, in which compressive stress is applied to the flow crust; 2) secondary material erupted from the base of one ridge can extend to the top of an adjacent ridge (this would not be unusual if the secondary flow had a very high velocity; however, since the secondary units appear to be emplaced as tube-fed flows this should not be the case), indicating emplacement of the secondary material at a lower level which was later uplifted; and 3) the break-out of secondary material from the top of the ridge indicates that the interior of the flow unit was under pressure; this would not be consistent with the simple draining of a flow associated with collapse.

From the field mapping a progression of ridge forms has been identified on the basis of size, surface texture, and setting. The smallest ridges are composed entirely of secondary lava erupted as a flow unit from the base of larger ridges. Their surfaces are characterized by short toes and tilted crustal slabs indicating initial emplacement of a thin-crusted flow which may have been toe-fed. The build up of pressure within the initial flow and subsequent inflation is indicated by the uptilted slabs which represent parts of the initial crust that were broken and pushed up when more toes were erupted and flowed down the side of the ridge. Intermediate ridges extend from major ridges (discussed below) and are usually slightly lower than the major features. They exhibit a mixture of surface textures, with secondary textures prominent near the terminus and primary textures near the "source." In many cases, ropes indicate flow direction toward the minor ridge. These ridges formed as flow lobes from the major ridges and advanced by the extrusion of toes and by break-out from underneath a crust. Major ridges form the dominant features on the flow and consist almost entirely of primary pahoehoe with only patches of secondary pahoehoe and aa. These features were probably initially emplaced as relatively thin flow units with some large ropes and were subsequently uplifted.

From the three ridge forms a progression of ridge formation and flow emplacement may be established: Formation of a new flow lobe is initiated by the break-out of toe-fed secondary lava which may then coalesce to form a single flow. Continued eruption of material behind a slowly advancing flow front causes the flow to inflate with subsequent eruption of secondary material. The longer a flow is channeled through this lobe the more it shows transition to the larger primary ridges. The mechanism for the formation of each of the ridge forms is probably the same, and the different forms and surface textures are a function of the duration and volume of material moving in the flow lobe. The longer a flow lobe is active and the higher the volume moving through it, the larger and more dominant it will become.

Results from detailed field studies indicate that pressure ridges and plateaus 1) are emplaced as individual flow lobes, 2) can be composed of primary or secondary material, 3) are dependent on duration and volume of activity within the flow unit, 4) are penecontemporaneous in formation, and 5) are indicative of slowly advancing flows with numerous flow lobes continuously forming and overriding each other.

MORPHOLOGIC EVOLUTION OF THE MOUNT ST. HELENS CRATER AREA, WASHINGTON

Gary L. Beach, Dept. of Geography, Oregon State U., Corvallis, OR 97331

INTRODUCTION

The large rockslide-avalanche that preceded the eruption of Mount St. Helens on 18 May 1980 removed approximately 2.8 km^3 of material from the summit and north flank of the volcano (Voight et al., 1983), forming a horseshoe-shaped crater 2.0 km wide and 3.9 km long (Lipman and Mullineaux, 1981). A variety of erosional and depositional processes, notably mass wasting and gully development, have since acted to modify the topographic configuration of the crater area. To document this morphologic evolution, a series of annual large-scale topographic maps is being produced as a base for comparitive geomorphic analysis.

METHOD

To date, four topographic maps of the Mount St. Helens crater area at a scale of 1:4000 have been produced by the National Mapping Division of the U. S. Geological Survey. Stereo aerial photography for the maps was obtained on 23 October 1980, 10 September 1981, 1 September 1982, and 17 August 1983. A fifth map based on August 1984 photographs is also planned. A 5 m contour interval was used to define the crater floor and breach, talus cones, and lava dome; a 10 m interval was used on the steep crater walls and upper volcano flanks. The maps extend from the south crater rim northward to the depositional Pumice Plain at the northern base of the volcano. A visual comparison of the southern half of the 1980 and 1983 maps illustrates the rapid erosion and deposition that occurred during that interval (Figures 1 and 2).

To quantify topographic changes in the study area, each topographic map is being digitized and corresponding X, Y, and Z values from successive maps are being computer-compared. For example, comparison of the 1980 and 1981 maps yields information on elevation and volumetric changes that occurred during that 1 year interval. Nagative values indicate erosion; positive values mark areas that have experienced deposition (e. g., talus accumulation or lava extrusion) or upwarping (owing to intrusion beneath and into the dome). Analysis of the resulting difference-maps will provide information on the rates of talus cone development, backwasting of the crater rim owing to rockfalls and rockslides, and fluvial erosion of the crater floor. To date, the 1980, 1981, and 1982 maps have been digitized and the software necessary to produce and analyze the difference-maps has been identified and tested.

The 1980 crater at Mount St. Helens presents scientists with a rare opportunity to examine the evolution of a unique assemblage of terrestrial landforms produced and modified by volcanism in a mountain environment. Equally important, a better understanding of the endogenetic and exogenetic processes that are shaping the Mount St. Helens crater provides a basis for extrapolation to similar situations on other planets - for example, degradation of crater forms by mass wasting, or development of fluvial channels on Mars.

References

Lipman, P. W. and Mullineaux, D. R., 1981. The 1980 Eruptions of Mount St. Helens, Washington. U. S. Geological Survey Professional Paper 1250, U. S. Government Printing Office, Washington, D. C., 844 pp.

Voight B., Janda, R. J., Glicken, H., and Douglass, P. M., 1983. Nature and mechanics of the Mount St. Helens rockslide-avalanche of 18 May 1980. Geotechnique, v. 33, pp. 243-273.

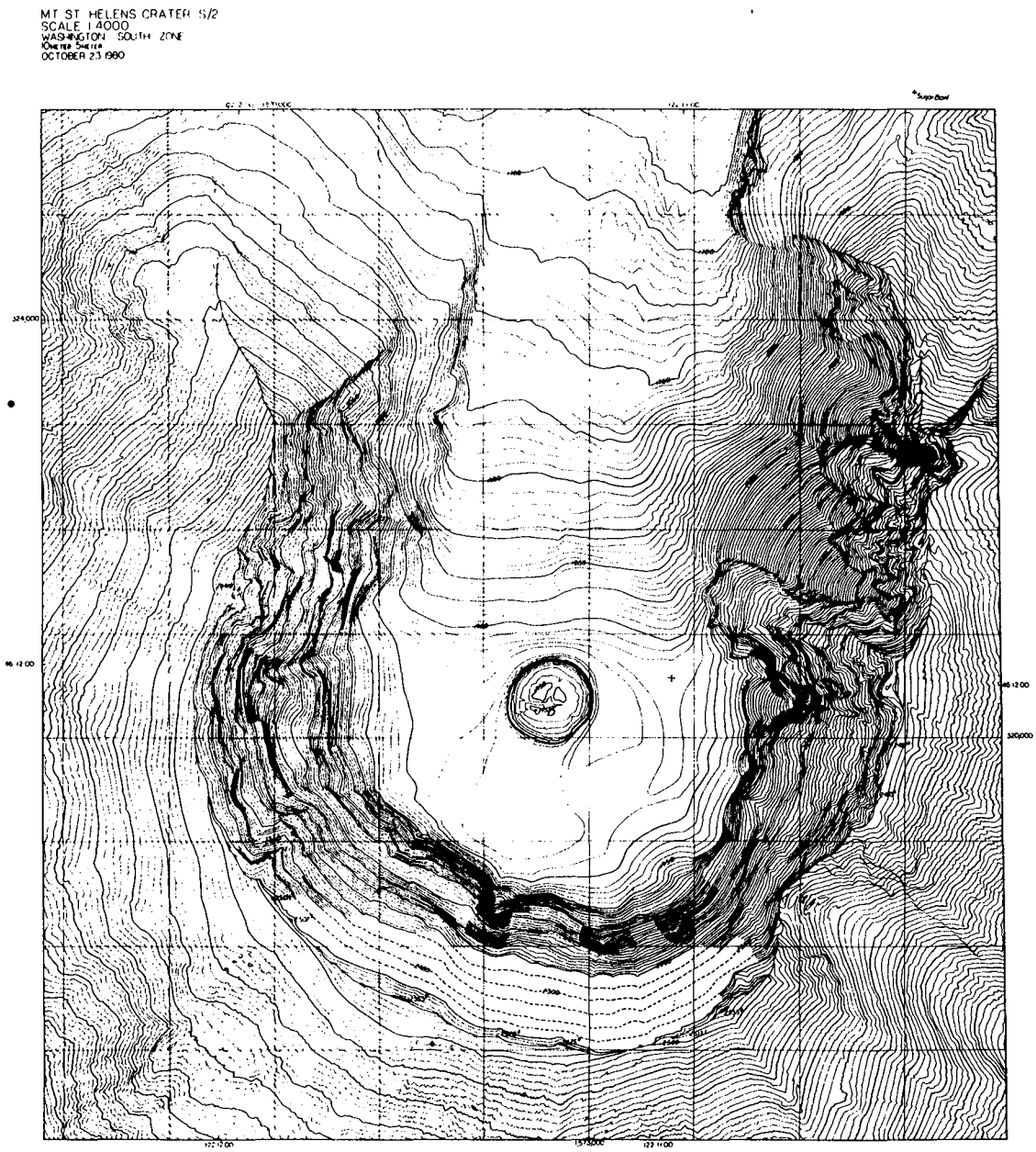

Figure 1. Mount St. Helens crater on 23 October 1980. Reduced from original 1:4000 scale. Note the small size of the central lava dome and the general smoothness of the contours on the crater floor. Vertical relief from the crater floor to the rim exceeds 600 m. The rectilinear SPC grid is spaced at 1000 ft. (305 m) intervals.

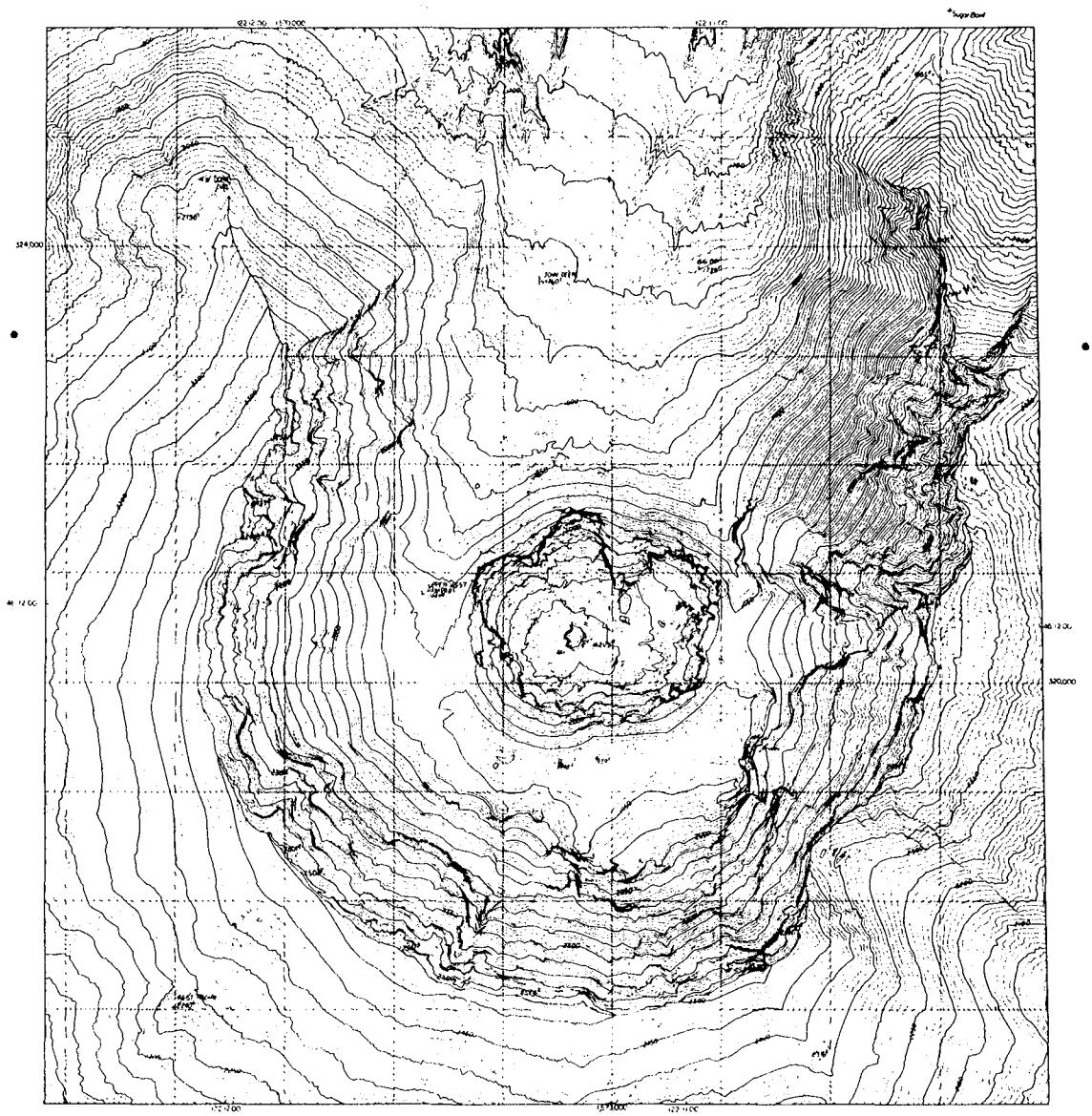

Figure 2. Mount St. Helens crater on 17 August 1983. Compared with Figure 1, the dome has grown considerably, rockfalls and snow accumulation have extended the talus cones at the base of the crater walls, erosion has modified the crater walls, and a gully system has developed on the crater floor north of the dome.

Volcanism of the Colorado Plateau - Basin and Range Transition: Implications for Crustal Processes

Christopher D. Condit, Wolfgang E. Elston, Dept. of Geology, University of New Mexico, Albuquerque, NM 87131.

On the Colorado Plateau-Basin and Range transition in Arizona and New Mexico, basaltic volcanism takes two physiographic forms: (1) Major central composite volcanoes (e.g. San Francisco Peaks, Fig. 1a) in which basaltic magma differentiates at shallow crustal levels to siliceous end members (Wenrich-Verbeck, 1979), and (2) large numbers of small cinder cones and a few domes that result from numerous discrete magma batches which apparently had little opportunity for differentiation (e.g. Springerville volcanic field, Fig. 1b; Condit, 1984). Similar features occur on Mars (e.g. Hecates Tholus region, Fig. 2; Elston, 1979). The hummocks of the terrain north-northwest of Hectes Tholus were tentatively interpreted as inselbergs by Elston (1979); they could be reinterpreted as a volcanic field of the Springerville type.

In the Springerville volcanic field, mapping in the 1000 km^2 western one-third of the field has documented 162 volcanic units, 19 of mixed lithologies and/or multiple vents. The flows can be characterized into four types, following the usage of Basaltic Volcanism Study Project (1981, p. 717-723). These include: (1) sheet flows with flood basalt characteristics, (2) basaltic plains flows with areas <40 km^2, (3) shield flows, and (4) one dome.

About 72 percent of the units of the western part of the Springerville field are alkali-olivine basalt, 26 percent hawaiite; one mugearite and one benmorite unit complete the suite. Field and chemical data suggest a large number of discrete magma batches generated by partial melting followed by fractional crystallization. No overall pattern of chemical evolution over time can be determined, but patterns emerge if flows from closely spaced vents are modeled. Major elements of 37 fine-grained rocks from all parts of the field have generalized trends consistent with fractional crystallization. Correlation coefficients for oxides vs. SiO_2 are: $FeTO_3$= -0.90, MgO=-0.72, Al_2O_3=0.36, CaO=-0.90, Na_2O=0.75, K_2O=0.81, TiO_2=-0.87. Trends of Ni, Cr, Ba, and Sr vs. differentiation index (Thornton and Tuttle, 1960) from 9 rocks representative of total chemical variation from scattered locations also suggest fractional crystallization, but combined major element-mass balance and Rayleigh fractionation models demonstrate that these 9 rocks cannot be related by fractional crystallization from commom magma batches. However, major element models suggest that selected adjacent flows are related by fractional crystallization.

REE patterns are typical of alkali basalts; light-REE are enriched 60-300 times chondritic, heavy-REE abundances range 10-14 times chondritic, suggestive of an enriched source. Seven initial $^{87}Sr/^{86}Sr$ ratios between 0.70356-0.70533 suggest crustal contamination and/or mantle heterogeneity. High Ce/Yb ratios (14.6-47) and garnet-bearing xenoliths 100 km north and south imply a mantle source with less than about 10 percent partial melting. Increasing concentrations of Y and Yb with higher SiO_2 values support localized fractional crystallization in the upper crust as the dominant differentiation process rather than increasingly small degrees of partial melting.

This study represents the first look at the petrogenesis of one of these Plateau-bounding volcanic fields, based on rigorous stratigraphic controls, in combination with major- and trace-element constraints.

Greely and Spudis (1981) suggest that lithospheric thinning in the Tharsus region have concentrated volcanism in this area. The Springerville volcanic field, and five other Late Tertiary-Quaternary volcanic fields (the Western Grand Canyon, San Francisco, Mormon Mountain-Hackberry, Zuni-Bandera and Mount Taylor fields) rim the southern margin of the Colorado Plateau, at or near the Transition Zone between the Colorado Plateau and Basin Range Provinces. Geophysical data (Warren, 1969; Sumner, 1976; Julian and others; 1970, Keller and others, 1979) indicate that the crust of the Basin and Range Province is about 22 km thick; that beneath the Colorado Plateau is about 40 km thick. The emerging pattern of large volcanic constructs associated with shallow fractional crystallization, and numerous cinder cones associated with limited or no shallow differentiation may provide an analogue for interpreting petrogenetic patterns and/or tectonic settings on Mars.

REFERENCES CITED

Basaltic Volcanism Study Project, 1981, Basaltic volcanism on the terrestrial planets: Pergamon Press, Inc., New York, 1286 p.

Condit, Christopher D., 1984, The geology of the western part of the Springerville volcanic field, east-central Arizona: Ph.D. dissertation, Univ. New Mexico, Albuquerque, NM., 453 p.

Elston, Wolfgang E., 1979, Geologic map of the Cebrenia Quadrange of Mars: U.S. Geol. Survey Misc. Inv. Map 1140.

Greeley, R., Spudis, P. D., 1981, Volcanism on Mars: Rev. Geophys. Space Phys., 19, p. 13-41.

Julian, B. R., 1970, Regional variations in the upper mantle structure in North America: Trans. Am. Geophys. Union, v. 51, p. 359.

Keller, G. R., Braile, L. W., and Morgan, P., 1979, Crustal

structure, geophysical models and contemporary tectonism of the Colorado Plateau: Tectonophysics, v. 61, p. 131-147.

Sumner, J. S., Schmidt, J. S., Aiker, C. L. V., 1976, Free-air gravity anomaly map of Arizona: Ariz. Geol. Digest v. 10, p. 7-12.

Thornton, C. P., and Tuttle, O. F., 1960, Chemistry of igneous rocks I. Differentation index: Am. Jour. Sci., v. 258, p. 664-684.

Warren, D. H., 1969, A seismic refraction survey of the crustal structure in central Arizona: Geol. Soc. Am. Bull. v. 80, p. 257-282.

Wenrich-Verbeek, K. J., 1979, The petrogenesis and trace element geochemistry of intermediate lavas from Humphreys Peak, San Francisco volcanic field, Arizona: Tectonophysics, v. 61, p. 103-129.

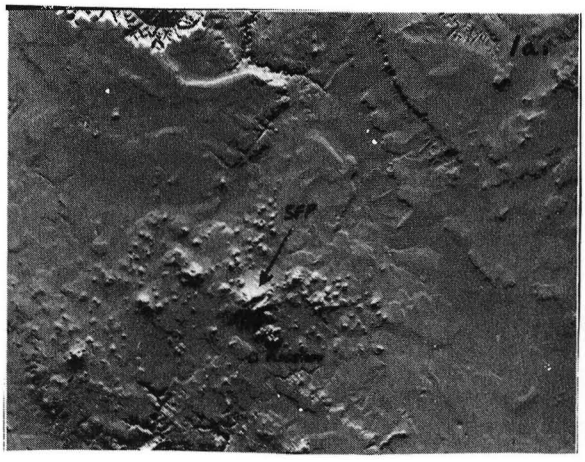

Figure 1a. Computer generated shaded relief image of San Francisco volcanic field and surrounding area. SFP=composite cone of San Francisco Peaks. Approximate scale 1:2M Image from U.S. Geol. Survey Flagstaff Image Processing Facility.

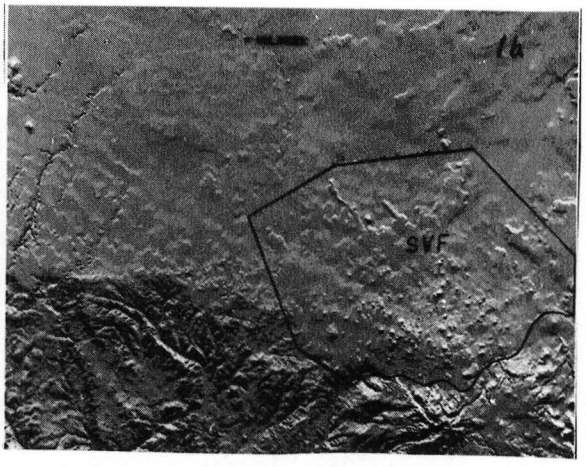

Figure 1b. Computer generated shaded relief image of Springerville volcanic field. Note cinder cones which make up most of the 384 documentated vents of the field. Approximate scale 1:2M. Image from U.S. Geol. Survey Flagstaff Image Processing Facility.

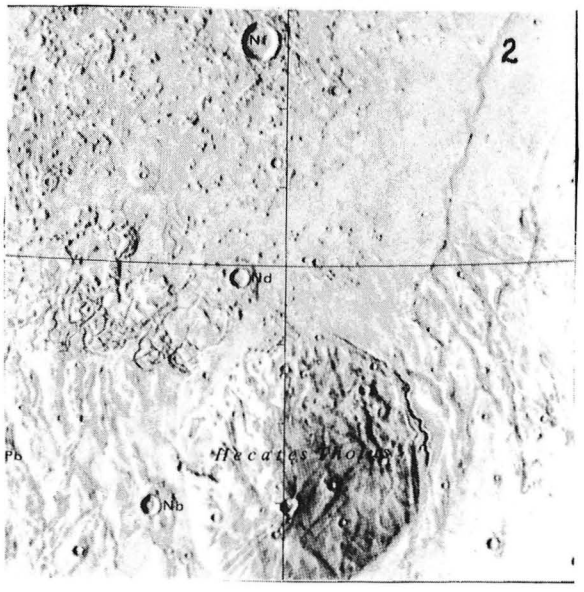

Figure 2. Shade relief map of Hecates Tholus and hommocky terrain north-northwest of Hecates Tholus. Approximate scale 1:7M.

THE GEOLOGY OF EAST BUTTE, A RHYOLITIC VOLCANIC DOME ON THE EASTERN SNAKE RIVER PLAIN, IDAHO

John E. Bretches and John S. King, Department of Geological Sciences, State University of New York at Buffalo, 4240 Ridge Lea Road, Amherst, NY 14226

East Butte is a prominent volcanic dome located on the eastern Snake River Plain (ESRP). It is situated 51 km west of Idaho Falls in the southeast corner of the Idaho National Engineering facility. East Butte rises 350 meters above the Quaternary basalt flows which encircle its 2.4 kilometer diameter base. Its maximum elevation is 2003 meters above sea level.

East Butte is composed dominantly of rhyolite. Armstrong and others (1975) determined a K-Ar age of 0.6 +/- 0.1 m.y. for a rhyolite sample from East Butte.

Previous investigations dealing with the three conspicuous Buttes of the ESRP (Big Southern, Middle, and East Buttes) have yielded various interpretations for their origin. East Butte and Big Southern Butte were first thought to have been steptoes - ancient rhyolitic volcanoes surrounded by a sea of basalt (Russell, 1902). Stearns and others (1938) proposed that faulting was the key in the development of East and Middle Buttes. Faulting generated a mountain range which was later differentially eroded because of the existence of both silicic and mafic lavas. Two prominent highs were the result of these processes. Only in the last 20 years were the Buttes identified as rhyolitic domes.

In the present study, detailed geologic mapping revealed East Butte to be a single, large cumulo-dome composed dominantly of rhyolite. The rhyolite can be classified into three main groups based on macroscopic characteristics such as color and structure. The first group, which makes up the largest volume of East Butte, consists of a massive, light to moderate gray rhyolite. The second group is also massive, but is pinkish gray in color. The third group, which is more abundant than the second, is flow-layered with pinkish gray bands.

Major element geochemical analyses indicate that the rhyolite of East Butte is mildly peralkaline (molecular excess of Na_2O and K_2O over Al_2O_3) and compositionally homogeneous. Color variations in the East Butte rhyolite result from varying amounts of chemical and physical weathering and to the degree of devitrification that the glass in the groundmass of the rhyolite has undergone. The rhyolite of East Butte is aphanitic with phenocrysts of sanidine and quartz which vary from 1 to 5 millimeters in length.

Vesicular reddish black inclusions of basalt up to 10 cm long are found in small amounts throughout all varieties of the East Butte rhyolite. Most of the inclusions contain

plagioclase phenocrysts. These phenocrysts measure up to 1 to 2 centimeters in length and have a typical euhedral, tabular habit.

Major element mixing diagrams indicate that the basalt inclusions in the East Butte rhyolite originated from the mechanical mixing of the rhyolitic magma of East Butte with a mafic magma having an SiO_2 content of about 49 percent. Petrographic observations such as zoned and embayed phenocrysts of plagioclase and sanidine and quartz crystals mantled by reaction rims of clinopyroxene in the basalt inclusions also support this hypothesis.

It has been suggested by previous investigators (e.g.: Bonnichsen and others, 1975; Doherty and others, 1979; Kuntz and Dalrymple, 1979) that East Butte, Big Southern Butte, and Middle Butte resulted from rhyolitic volcanism associated with major ring fractures of a large caldera now buried beneath approximately 1 km of younger basalt flows and sediments. This volcanism would correlate with Smith and Bailey's (1968) theory on the evolution of resurgent cauldrons. The rhyolitic magma originated from the emplacement of hot basaltic magma into granitic crustal rocks causing them to undergo partial melting and subsequent fractional crystallization at depths of 10 to 16 kilometers.

East Butte is believed to have developed predominantly by endogenous growth and internal expansion of rhyolitic magma which ascended through the ring fractures of the caldera. The early period of East Butte's development is believed to have been intrusive, and to have occurred beneath a thin (50 to 100 meters thick) layer of surficial basalt flows. This early phase was followed by a more extensive phase of extrusive evolution at the surface of the ESRP. Nearly all of the growth of East Butte occurred by endogenous internal expansion. A shallow 250 meter diameter depression near the summit of East Butte suggests the withdrawal of a portion of rhyolitic magma down a central conduit. Three small (3 to 5 meters in height) mounds of massive rhyolite which border the summit depression indicate the only occurrence of viscous rhyolitic magma to be extruded onto the surface of East Butte.

Volcanic morphologic features such as domes are not unique to earth. Two lunar domelike features are located near the shores of northeastern Oceanus Procellarum and about 30 km north of the crater Gruithuisen. These are identified as Gruithuisen γ and Gruithuisen δ. Gruithuisen γ is generally circular in plan, with a diameter of 20 km and a height of over 1.2 km. Gruithuisen δ covers an area of approximately 13 by 33 km and is about 1.6 km high. It has a broad, flat top with a relatively smooth texture without any large summit craters. Slopes on the flanks of these lunar domes range up to 30^{o} and have many ridges and furrows extending downslope. The convex profile of these domes has led Smith (1973) to conclude that the structures are cumulo-domes. Head and

McCord (1978) suggest that Gruithuisen δ may be composed of several coalesced domes.

Although larger and petrologically different, these lunar domes are morphologically quite similar to East Butte and other Buttes like it on the ESRP. These lunar domes may have been created by processes similar to those which have occurred on the ESRP and in other terrestrial volcanic provinces. A theory explaining the existence of lunar domes is a more viscous mafic lava, with possibly a slightly higher silica content due to parental magma differentiation or fractionation, being extruded to form a steep-sided volcanic construct.

References Cited

Armstrong, R.L., W.P. Leeman, and H.E. Malde, 1975, K-Ar dating, Quaternary and Neogene volcanic rocks of the Snake River Plain, Idaho: Amer. Jour. Sci., v. 275, no. 3, p. 225-251.

Bonnichsen, B., W.B. Travers, and G. Citron, 1975, Rhyolitic volcanism and structural evolution of the Snake River Plain: Geol. Soc. Amer. Rocky Mountain Section Meeting, Abstracts with Programs, v. 7, no. 5, p. 589-590.

Doherty, D.J., L.A. McBroome, and M.A. Kuntz, 1979, Preliminary geological interpretation and lithologic log of the exploratory geothermal test well, INEL-1, Idaho National Engineering Laboratory, eastern Snake River Plain: U.S. Geological Survey Open-File Report 79-1248, 9 pp.

Head, J.W. and T.B. McCord, 1978, Imbrian-age highland volcanism on the Moon: The Gruithuisen and Marian domes: Sci., v. 199, March 31, p. 1433-1436.

Kuntz, M.A. and G.B. Dalrymple, 1979, Geology, geochronolgy, and potential volcanic hazards in the Lava Ridge-Hells Half Acre area, eastern Snake River Plain, Idaho: U.S. Geological Survey Open-File Report 79-1657.

Russell, I.C., 1902, Geology and water resources of the Snake River Plains of Idaho: U.S. Geological Survey Bull. 199, 192 pp.

Smith, E.I., 1973, Identification, distribution, and significance of lunar volcanic domes: The Moon, v. 6, p. 3-31.

Smith, R.L. and R.A. Bailey, 1968, Resurgent cauldrons: Geol. Soc. Amer. Mem., no. 116, p. 613-662.

Stearns, H.T., L. Crandall, and W.G. Steward, 1938, Geology and groundwater resources of the Snake River Plains in southeastern Idaho: U.S. Geological Survey Water Supply Paper 774, 268 pp.

THE GEOLOGY OF MT. HOPE, A SILICIC VOLCANIC CENTER IN WEST CENTRAL ARIZONA

Ardyth M. Simmons and John S. King, Department of Geological Sciences, State University of New York at Buffalo, 4240 Ridge Lea, Amherst, NY 14226

Mt. Hope is located 4.5 miles east of the Mohon Mts., about 70 miles northwest of Prescott, Arizona. The Mohons occupy 36 square miles and rise to an elevation of 7500 feet above sea level with 1500 feet of local relief. Mt. Hope stands as a prominent, isolated silicic center 7263 feet in elevation, 1700 feet above surrounding basalt flows and tuffs.

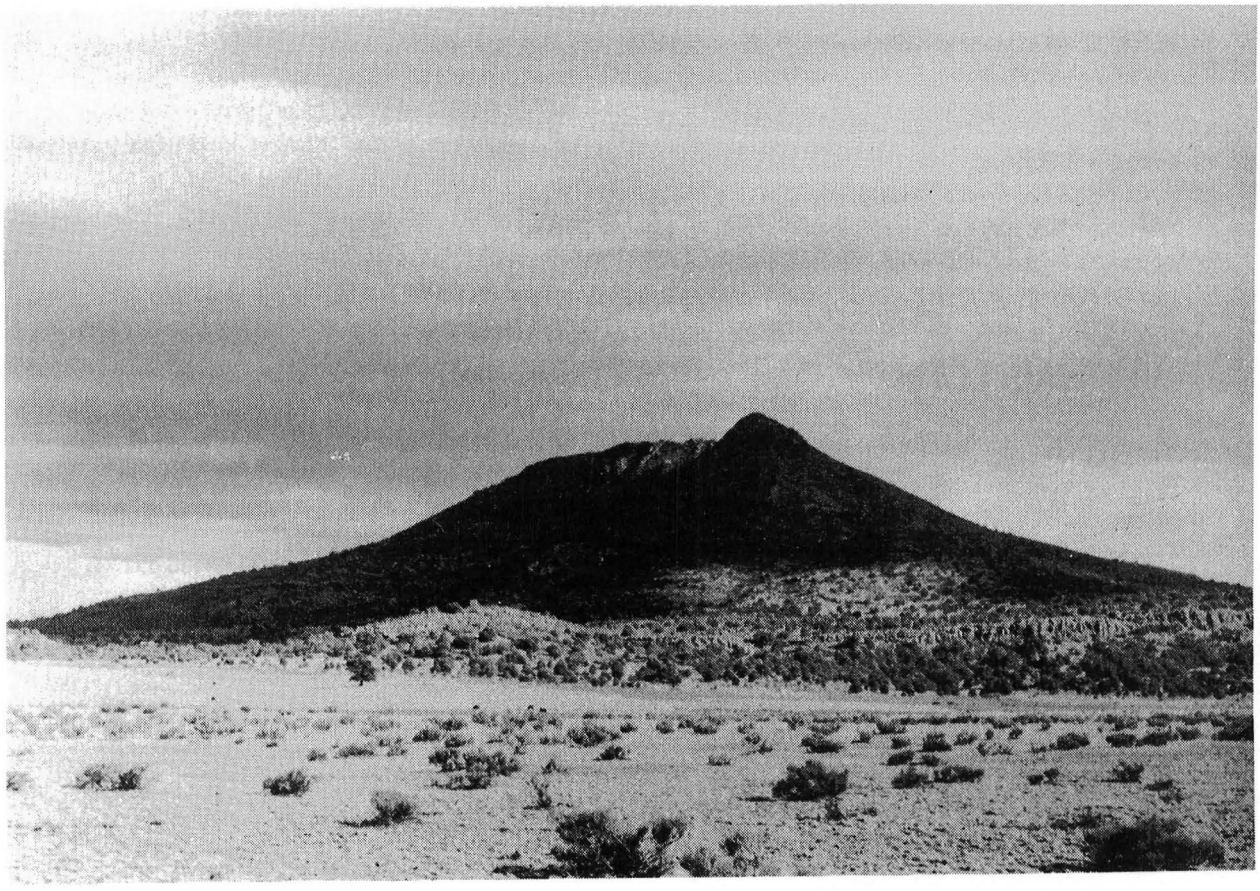

Figure 1. View of Mt. Hope to the south at a distance of 1.9 miles.

Young (pers. comm., 1984) obtained a K-Ar age of 24.3 $\pm$ 0.8 m.y. for a basalt sample from the Mohons. No age has been designated for the rhyolites and other silicic rocks of Mt. Hope.

The Mohon Mts. have not been investigated previously. They are of geologic interest because they occur in the transition zone between the Basin and Range and Colorado Plateau physiographic and structural provinces. This 62.5 mile wide strip forming an arc around the southern edge of the Plateau exhibits characteristics of both provinces, north-south normal faults of the Basin and Range as well as monoclinal folds typical of the Colorado Plateau.

Styles of volcanism in the transition zone vary from basalt flows to explosive eruptions of more silicic composition, with bimodal suites observed frequently (Lucchitta, 1974). Bimodal refers to volcanic fields in which intermediate rocks are scarce while basalt and rhyolite were erupted at about the same time and place.

The purpose of the present study is to establish a detailed history of the sequence of geologic events which occurred at Mt. Hope and an area 6.8 miles in diameter surrounding it. The final result will be comprised of information collected during field mapping, with data from petrographic studies and wet chemical analyses. From this it should be possible to suggest relationships to other volcanic regions, particularly bimodal suites in the transition zone, and gain a clearer picture of the petrologic nature of this area. Since bimodal suites are often associated with extensional tectonism (Christiansen and Lipman, 1972) and since the Miocene marks a shift from a compressional to an extensional regime in the crust of western North America (Atwater, 1970), it might be possible using petrologic and isotopic data to suggest a model for interpretation of source region(s) for the volcanic material of Mt. Hope and the Mohons. In addition, an analog study of lunar and/or martian features will relate the terrestrial volcanic morphologies to features found on these bodies which may have formed from similar processes.

Field work conducted this past summer has confirmed the bimodal nature of volcanism at Mt. Hope. The symmetrical, radial cone is comprised of several rhyolites with numerous intrusions of intermediate-composition dikes and two breccia pipes near the summit. Two pink, one gray, and one lavender flow-banded rhyolite were identified, which appear to be sequentially related with the lower pink flow followed by the gray, and gradational pink and lavender flow-banded rhyolites capping the peak. A secondary, dome-shaped feature, 644 feet lower than the summit, shows gray rhyolite cropping out stratigraphically higher than the banded and pink rhyolites, suggesting a possible separate origin or sequence of events from those which produced the Mt. Hope rhyolites.

Surrounding the peak to the south and west are massive basalt flows. These extend four miles south to Burro Creek and may be correlated beyond the map boundary to the Sanders basalt described by Anderson et al. (1955) in the Bagdad area. They are not macroscopically distinct from basalts found to the west of Mt. Hope, extending more than five miles into the foothills of the Mohons. To the east of Mt. Hope Quaternary alluvium and gravels extend 1.9 miles and beyond the map boundary to Ferguson Mesa and the Juniper Mts. This coarse, clastic material is over a foot thick in some places and contains pebbles of chert, granite, and possibly Tapeats sandstone washed down from ridges five miles away (Krieger, 1967). To the north a series of tuffs spread 4.8 miles and continue past the northern map boundary. These include chunks of obsidian and pumice up to two inches in diameter as well as numerous xenoliths of reddish vesicular basalt. Stratigraphic position indicates the tuffs are older than the basalt flows to the south and west.

Two interesting features are found north of Mt. Hope. The first is a nearly circular shaped basin 1.5 miles in diameter rimmed by horizontal basalt flows. It is truncated at the north and east by rhyolites possibly related to those of Mt. Hope. No evidence suggests it was formed by explosive activity; instead it might have collapsed when magma in the source withdrew and

migrated laterally, perhaps preceding the activity of Mt. Hope.

The second feature is a small tuff ring 0.2 miles in diameter located 1.5 miles northeast of Mt. Hope. Its shallow dipping slopes are comprised of a grayish tuff containing large fragments of obsidian. The ring is depressed an average of three feet at its rim; the central depression is filled with red basaltic cinders. This feature might take its shape as a result of collapse as well.

The relationship of events which occurred at Mt. Hope to those in the Mohon Mts. and to those of the transition zone at large has not yet been determined. Future work should indicate whether Mt. Hope is the youngest of volcanic centers in the Mohons and how the eruptive style and geochemical composition of the erupted material changed spatially and temporally.

References Cited

Anderson, C.A., Scholz, E.A., and Strobell, J.D., Jr., 1955, Geology and ore deposits of the Bagdad area, Yavapai County, Arizona: U.S. Geol. Survey Prof. Paper 278, 103 p.

Atwater, Tanya, 1970, Implication of plate tectonics for the Cenozoic evolution of western North America: Geol. Soc. Am. Bull. 81, p. 3515-3534.

Christiansen, R.L., and Lipman, P.W., 1972, Cenozoic volcanism and plate tectonic evolution of western United States, part 2, Late Cenozoic: Royal Soc. London Trans., v. 271, p. 249-284.

Krieger, M.H., 1967, Reconnaissance geologic map of the Camp Wood quadrangle, Yavapai County, Arizona: U.S. Geol. Survey Misc. Geol. Invest., Map I-502.

Lucchitta, Ivo, 1974, Structural evolution of northwest Arizona and its relation to adjacent Basin and Range province structures, in: Geology of northern Arizona with notes on archaeology and paleoclimate, Part 1: regional studies: Geol. Soc. Amer., Rocky Mt. Sect. Mtg., Flagstaff, p. 336-354.

A SILICIC SHIELD VOLCANO IN BOLIVIA

P.R. CHRISTENSEN and R. GREELEY
Department of Geology, Arizona State University, Tempe, Arizona, 85287

In the fall of 1981, the Shuttle Imaging Radar (SIR-A) experiment obtained a 50-km-wide image across the Altiplano in Bolivia (1,2). These data provide estimates of surface textures, at scales equal to and larger than the radar wavelength (23.5 cm), that are useful for assessing geologic processes and surface modification (3). The SIR-A groundtrack covered several volcanic structures within the Altiplano and the western cordillera of the Andes. Of particular interest is Volcan Quemado, located at -18° 37' S, 68° 45' W. This feature is a low, broad volcano with a series of explosion craters and an extrusive dome at the summit. It has a basal diameter of 8 km and rises 360 m above the surrounding valley floor, with a summit elevation of 4215 m. The flank slopes vary from 4° to 15°, generally increasing towards the summit. The summit region comprises a series of pit craters, with evidence for at least four separate explosive events. These craters create a crater chain 4.5 km long and 2.6 km wide along a line oriented nearly N-S. The diameter of each crater is ~1.5 km. Within this crater complex an extrusive dome, 1.6 km by 1.0 km at its base and elongated parallel to the crater chain, rises approximately 200 m above the floor of the central crater.

In June, 1983, an overflight of Volcan Quemado was carried out to provide closer inspection of the crater, dome, and flank morphology. Layered bedrock units, presumably flows, exposed in the crater walls pre-date crater formation. Based on its superposition, the summit dome appears to be younger than all explosive events. No surface expression of lava flows on the flanks was observed on this flight. The southern and western portions of the crater complex are covered by bright, unvegetated material that appears to have mega-ripples with wavelengths of 2 to 4 m. This material may be sand-to granule-sized pumice fragments that are being reworked by aeolian processes.

In July, 1984, a field study of Volcan Quemado was conducted to permit a more detailed investigation of this feature and to collect rock samples and study surface textures that relate to the SIR-A observation. This investigation focused on the eastern flank and summit-dome region. The dome is composed of glassy to fine-grained rhyolite; samples collected from within the explosion craters are rhyolitic, as are the pumice and glass fragments that cover much of the surrounding terrain.

At the summit of the dome is a series of ridges approximately 8 m high and spaced approximately 100 m apart. The surface rocks are heavily jointed and fractured; joint spacings are approximately 0.5 m apart. Much of the surface is covered by loose blocks that are typically 25-50 cm in diameter but range up to 1.5 m. As seen on the SIR-A image, the dome has a very high radar reflectivity, indicating a rough surface. This agrees well with the field observations of rocks and jointing, and with the observation of slopes of up to 60° in some locations.

The surface surrounding the summit craters is covered by pumice particles ranging from 1 mm to 10 centimeters. Layered ash and pumice beds are exposed within small gullies on the flanks of the volcano. No evidence for flows exposed at the surface was found during the surface traverses, although only a small fraction of the flank surface was studied. The radar return from the flank regions is very low; this is again consistent with field observations of particles smaller than the SIR-A radar wavelength. This region of low radar

return extends 20 to 30 km radially from the volcano summit. Extrapolating the field observations suggests that this entire region is covered by fine-grained pumice deposited during explosive eruptions at the summit.

Previous studies have described radar observations of basaltic flows (4,5). Volcan Quemado and its environs provides an excellent site to study the radar signature of a silicic volcanic construct. This feature differs from basaltic terrains primarily by the evidence of explosive eruptions associated with silica-rich magmas. These explosions produced a complex of distinctive craters that are visible on radar because of their steep inner walls and exposed bedrock units. Explosive events have also generated surface deposits of fine (1 mm to 10 cm) material that mantles the region around the volcano to a distance of 20 to 30 km from its center. These features are very different from those observed on basaltic flows, which typically lack violent, explosive events. In these terrains, the surface is dominated by radar-rough flows with steep, lobate flow fronts. Craters are less common, although maars are found in some regions. These comparisons suggest that spaceborne radar may be able to distinguish surface characteristics that can be used to identify volcanic eruptive styles on Venus, Mars, and other solar-system bodies.

REFERENCES

1) Settle, M. and J.V. Taranik, 1982, Science, 218, 993-996.
2) Ford, J.P., J.B. Cimino, and C. Elachi, 1983, Jet Prop. Lab. Publ., 82-95, 179 p.
3) Elachi, C. et al., 1982, Science, 218, 996-1003.
4) Masursky, H., 1982, Jet Prop. Lab. Publ., 4(19-21).
5) Greeley, et al., 1984, NASA Contractor Report, in press.

SUBMARINE VOLCANIC ERUPTIONS AND POTENTIAL ANALOGS FOR VENUS

L. Wilson, Univ. Lancaster, Lancs., LA1 4YQ England; P.J.Mouginis-Mark, P.Fryer and L.R.Gaddis Hawaii Institute of Geophysics, Univ. Hawaii, Honolulu, HI 96822.

As part of an analysis program to better understand the diversity of volcanic processes on the terrestrial planets[1,2], we have initiated an investigation of the volcanic landforms which exist on the Earth's ocean floor. In part, this analysis is focused toward gaining a better understanding of submarine volcanic landforms in their own right, but also it is hoped that these features may show similarities to volcanic landforms on Venus, due to the high ambient water (Earth) and atmospheric (Venus) pressures[3]. In conjunction with an analysis of data derived by a new side-scan sonar system called SeaMARC II[4], we have therefore been performing a series of numerical modelling experiments to investigate the relative importance of such attributes as water pressure and temperature on the eruption process, and to determine the rate of cooling and emplacement of lava flows in the submarine environment.

In a recent investigation of three volcanic seamounts in the western Pacific Ocean[4], Hussong and Fryer showed that numerous lobate flows exist on the flanks of these seamounts and on the adjacent abyssal plains. These flows, at least some of which are known to be lava flows (based on grab samples taken from the ocean floor), have a variety of outlines and exhibit a wide range of acoustic backscatter values as measured by SeaMARC II. This variation in the backscatter properties of the volcano flanks was interpreted to be due to both lava flows and volcaniclastic debris on some of the flanks, suggestive of effusive and explosive eruptions. Additional circumstantial evidence to support the idea of explosive activity lies in the occurrence of numerous parasitic cones (that have basal diameters of 0.3 - 3.0 km and heights up to 600 m). Such features can occur in water depths as great as 4 km, indicating that confining pressures (although much greater than those that occur on Venus), may not preclude explosive eruptions in this environment.

The factors known or suspected to be of importance in triggering and driving subaerial eruptions presumably also play the same role for submarine eruptions. These factors include: the opening of fissure systems extending for tens of kilometers into the crust as a result of large scale tectonic adjustments[5]; the over-pressurising of magma chambers at various depths in the lithosphere as a result of magma crystallization, gas exsolution, or injection of new magma at the base of the chamber[6]; and the propagation of dikes from magma sources at depth as a result of the bouyancy of the magma[7]. Dike widths are the major control on the rate at which magma migrates beneath an eruption site, determining the relative importance of friction and inertia forces[1] and of cooling[5] and heating[8]. The widths of dikes are in turn controlled by the local stress regime[9]; the range of tectonic environments in which oceanic volcanoes occur is at least as diverse as that in which subaerial volcanoes are found[10,11], and so it seems probable that the range of stress regimes will be

similar in these two environments.

There are, however, very important differences between the effects of absolute pressure on the exsolution of volatiles from magma erupting in subaerial and submarine environments[10]. The ambient pressures at water depths of 1 to 3 km (the range over which many submarine eruptions occur[12]) are the same as those at depths of 0.3 to 1 km in the subaerial lithosphere, and it is over just this range of pressures that the bulk densities of most magmas decrease and their ascent velocities increase significantly as a result of the nucleation and growth of bubbles containing the volatiles which exsolve as the pressure decreases[1,13]. Our calculations show that the fact that magmas erupting on the sea floor emerge at these higher pressure levels ensures that they must do so at systematically lower velocities and with lower gas vesicle contents (both in terms of the sizes and volume fraction of vesicles) than magmas of similar bulk composition and volatile content emerging on land. A second important difference between the submarine and subaerial environments is dictated by the high density of water relative to that of air. When lava is erupted in air, a negligible error is made by ignoring the mass of the air that it displaces; however, this is not true for lava erupted in water. This bouyancy effect means that even a non-vesicular lava (bulk density, say, 2800 kg/m^3) erupted under water will behave as though it had a density of about 1800 kg/m^3, i.e., as though it had a vesicle volume fraction of 35% in air. The difference will be even more important for a submarine lava which is itself vesicular; it can be shown that a submarine lava having a vesicle volume fraction of 30% (a common occurrence for lavas erupted in less than 2 km depth of water[14]) will behave as though its bulk density were just over one half its actual value. As a result of this bouyancy effect, our models for submarine lava flow emplacement show that both the shape and the lengths of submarine flows could be significantly different from that predicted from a simple analogy with their subaerial equivalents.

The final characteristic of submarine volcanism that we have considered to date is the form that an explosive eruption cloud or fire fountain would take in an underwater eruption. In many circumstances, sub-aerial explosive eruptions of basaltic magma produce fire-fountains in which the pyroclastic clots of magma are sufficiently closely packed that they suffer minimal heat loss, except at the edge of the fountain[1]. These conditions are favored by a low ejection velocity and coarse size distribution for the pyroclasts. At higher ejection velocities, smaller clasts are more likely to become entrained in a strongly convecting eruption cloud, driven by the transfer of magmatic heat to entrained air, and then are deposited to form a plinian air-fall deposit[15]. The situation will be more complex in an underwater eruption of this kind. On the one hand, the much lower eruption velocities of pyroclasts produced under 1 to 3 km of water (mainly in the range 1 to 10 m/s) would encourage accumulation of relatively uncooled magma clots within a few meters of the vent to form a lava flow. However, such clots may have a significant vesicularity, and this will make them behave as if they were in a low-gravity environment permitting longer flight times and greater cooling and dispersion. Additionally, the low effective density of the clasts make it much more likely that they

will be entrained into any convective system which forms in the water over the vent, ultimately producing a widely dispersed pyroclastic deposit.

Thus our investigations to date show that the confining water pressure and the bouyancy effects of the surrounding water significantly affect the styles of volcanism on the ocean floor. In the case of venusian volcanism, confining pressures will not be as great as that found at the ocean's abyssal plains, but nevertheless the general trend toward reducing magma vesiculation will hold true for Venus as well as the ocean floor. Furthermore, other analogs may also be found between submarine volcanism and venusian activity; currently we are exploring the emplacement process for submarine lava flows on Earth, based on rheological models for sub-aerial eruptions[1,16] in the hope that these models may offer useful insights into effusive activity on Venus.

References: 1) Wilson L. and Head J.W. (1981). J. Geophys. Res. 86, p. 2971-3001. 2) Wilson L. and Head J.W. (1983). Nature 302, p. 663-669. 3) Mouginis-Mark P.J., Fryer P., Hussong D. and Zisk S.H. (1984). LPS XV p. 577-578. 4) Hussong D.M. and Fryer P. (1983). EoS 64, no. 45, p. 627-632. 5) Fedotov S.A. (1978). Intl. Geol. Rev. 20, p. 33-48. 6) Blake S. (1981). Nature 289, p. 783-785. 7) Johnson A.M. and Pollard D.D. (1973). Tectonophysics 18, p. 261-309. 8) Hardee H.C. and Larson D.W. (1977). J. Volcanol. Geotherm. Res. 2, p. 299-308. 9) Shaw H.R. (1980). In: Physics of Magmatic Processes (ed. R. Hargraves), Princeton Univ. Press. 10) McBirney A.R. (1971). Revs. Geophys. Space Phys., 9, p. 9. 11) Batiza R. (1982). Earth Plan. Sci. Lttrs. 60, p. 195-206. 12) Basaltic Volcanism on the Terrestrial Planets. Pergamon Press, Inc. New York, pp 727-744. 13) McGetchin T.R. and Ullrich W.G. (1973). J. Geophys. Res. 78, p. 1833-1853. 14) Macpherson G.J. (1984). J. Geol., 92, p. 73-82. 15) Walker G.P.L., Self S. and Wilson L. (1984). J. Volcanol. Geotherm. Res. 21, p. 61-78. 16) Hulme G. (1974). Geophys. J. Royal. astro. Soc. 39, p. 361-383.

HYDROVOLCANISM

Michael F. Sheridan, Department of Geology, Arizona State University, Tempe, AZ 85287 and Kenneth H. Wohletz, ESS1, Los Alamos National Laboratory, Los Alamos, NM 87545

Hydrovolcanism is a common phenomena produced by the interaction of magma or magmatic heat with an external source of water, such as a surface body, an aquifer, or a glacier. The effects include hydrofracture of existing rock units in the subsurface and the formation of hyaloclastites in a subaqueous environment. Hydroexplosions originate within a few kilometers of the surface. They may be relatively small, phreatic events (Muffler et al., 1971) or devastating complex blasts.

The industrial phenomena of fuel-coolant interaction (FCI) is one model for understanding similar natural explosive processes (Peckover et al., 1973; Buchanan, 1974). The propagation of detonation waves through as mass of melt and water is another possible cause of extreme melt fragmentation. The actual mechanism of melt rupture and mixture with water prior to decompression is still poorly known.

Large-scale experiments at LANL (Sheridan and Wohletz, 1983; Wohletz and McQueen, 1983) have determined that the optimal mixing ratio of water to basaltic melt (thermite plus silicates) for efficient conversion of thermal energy into mechanical energy is in the rage of 0.1 to 0.3. For experiments near this optimum mixture, the grain-size of explosion products is extremely fine (less than 50 um); the particles are much larger (greater than 10 mm) for explosions at relatively low or high ratios (Wohletz, 1983). Morphology of particles ejected in the experiments suggest that several mechanisms of melt fragmentation were operative.

The spectrum of volcanic phenomena indicate that there is a wide range in the amount of external water that is involved in explosive eruptions. Very few volcanoes exhibit no hydrovolcanic characterisitcs. Based on our experimental results, eruptions can be classsified as dominantly magmatic if the ratio of external water to magma is less than 0.2. Eruptions with water/melt ratios in the range of 0.2 to 1.0 are highly explosive and carry tephra in a hot vapor that contains dominantly superheated (dry) steam. If the ratio of water to melt is higher than 1.0 the vapor consists of dominantly saturated (wet) steam. At very high ratios of water to melt little or no vapor is produced.

The morphology and texture of natural pyroclasts (Heiken, 1972; Sheridan and Marshall, 1973) are very similar to those of the experimental fragments produced by hydroexplosions (Wohletz, 1983). Blocky, equant grains dominate in SEM micrographs. Glassy clasts formed from fluid magma have low vesicularity, thick bubble walls, and drop-like form.

Microcrystalline essential clasts result from chilling of magma during or shortly following explosive mixing. Crystals commonly exhibit perfect faces with patches of adhering glass or large cleavage surfaces. Edge modification and rounding of pyroclasts is slight to moderate. Grain surface alteration (pitting and secondary mineral overgrowths) are a function of the initial water to melt ratio as well as age. Their deposits are typically fine-grained and moderately sorted, having distinctive size distributions compared with those of fall and flow origin.

Hydrovolcanic materials typically are dispersed in dilute density currents rich in steam vapor (Wohletz and Sheridan, 1979). The deposits of volcanic blast or surge eruptions are generally cross-stratified and thin bedded (Fisher and Waters, 1970; Crowe and Fisher, 1973). They may show a lateral transition from dry types near the vent to wet types in the distal reaches. In some cases there may be a transition from surge deposits to lahars or even hyper-concentrated stream deposits as the steam condenses into water and the promary deposits become remobilized (Sheridan and Wohletz, 1981).

The morphology of hydrovolcanic constructs is highly variable. Hyaloclastite volcanoes are steep sided and flat topped. Their structure and stratigraphy of pillow lava, pillow breccia, and stratified tuffs is related to their subaqueous origin (Sigvaldasson, 1968). Small phreatic craters may be only a few hundred meters in diameter and thier pyroclastic apron is only a few meters thick. The most common hydrovolcanic edifice is either a tuff ring or a tuff cone (Wohletz and Sheridan, 1983), depending on whether the surges were dry (superheated steam media) or wet (condensing steam media). The morphology of these two types are easily distinguished on aerial photographs allowing a remote means to estimate the amount of water in the subsurface at the time of volcanic activity.

Hydrovolcanic products are also a characteristic component of eruption cycles at larger volcanoes. Hydrovolcanism may be the main cause of sector collapse, debris avalanche, and volcanic blast phenomena. Two types of paterns of products are common at polygenetic volcanoes: 1) a sequence of dry to wet products (Vesuvius type, Sheridan et al., 1981) or wet to dry products (Vulcano type, Frazzetta et al., 1983) characterizes deep processes and the evolution of water/melt interaction with time at many volcanoes. Reconstruction of eruption cycles in terms of water-melt mixing is extremely useful in modeling volcanic phenomena and evaluating risk at active volcanoes.

REFERENCES

Buchanan, D.S., 1974. A model for fuel-coolant interactions. J. Phys. D.: Appl. Phys., 7:1441-1457.

Crowe, B.M. and Fisher, R.V., 1973. Sedimentary structures in base-surge deposits with special reference to cross bedding, Ubehebe Craters, Death Valley, California. Geol. Soc. America Bull., 84: 663-682.

Fisher, R.V. and Waters, A.C., 1970. Base-surge bed forms in maar volcanoes. Am. J. Sci., 268: 157-180.

Frazzetta, G., La Volpe, L., and Sheridan, M.F., 1983. Evolution of the Fossa cone, Vulcano. J. Volcanol. Geotherm. Res., 17:1-29.

Heiken, G., 1972. Morphology and petrography of volcanic ashes. Geol. Soc. America Bull., 83:1961-1988.

Muffler, L.J.P., White, D.E., and Truesdell, A.H., 1971. Hydrothermal explosion craters in Yellowstone National Park. Geol. Soc. America Bull., 82:723-740.

Peckover, R.S., Buchanan, D.J., and Ashby, D.E.T.F., 1973. Fuel-coolant interactions in submarine volcanism. Nature, 245:307-308.

Sheridan, M.F., Barberi, F., Rosi, M., and Santacroce, R., 1981. A model for the eruptions of Vesuvius. Nature, 289: 282-285.

Sheridan, M.F. and Marshall, J.R., 1983. Interpretation of pyroclast surface features using SEM images. J. Volcanol. Geotherm. Res., 16: 153-159.

Sheridan, M.F. and Wohletz, K.H., 1981. Hydrovolcanic explosions: the systematics of water-pyroclast equilibration. Science, 212:1387-1389.

Sheridan, M.F. and Wohletz, K.H., 1983. Hydrovolcanism: Basic conderations and review. J. Volcanol. Geotherm. Res., 17: 1-39.

Sigvaldason, G., 1968. Structure and products of subaquatic volcanoes in Iceland. Contr. Mineral. and Petrol., 18:1-16.

Wohletz, K.H., 1983. Mechanisms of hydrovolcanic pyroclast formation: grain-size, scanning electron microscopy, and experimental studies. J. Volcanol. Geotherm. Res., 17:31-63.

Wohletz, K.H. and McQueen, R., 1981. Experimental hydromagmatic volcanism. In: F.R. Boyd (Editor), Explosive volcanism: inception, evolution, and hazards. Studies in Geophysics, National Academy of Sciences.

Wohletz, K.H. and Sheridan, M.F., 1979. A model of pyroclastic surge. Geol. Soc. America Spec. Paper, 180:177-194.

Wohletz, K.H. and Sheridan, M.F., 1983. Hydrovolcanic explosions II. Tuff rings and tuff cones. Am. J. Sci., 283: 385-413.

CHAPTER 8

AEOLIAN PROCESSES AND LANDFORMS

Page intentionally left blank

OBSERVED CHANGES AT VIKING LANDER 1

Henry J. Moore, U.S. Geological Survey, Menlo Park, CA 94025

A local dust storm raged in Chryse Planitia, Mars, in June 1981. The changes wrought in the vicinity of the lander (Mutch Memorial Station) by this storm sometime near Sol 1742 have been partly described (1,2,3). This note itemizes changes related to the storm, cites evidence for wind directions during the peak of the storm, and notes two observations unrelated to the storm. Locations of itemized changes can be found by reference to figures in refs. 4 and 5.

Lander Grid. A substantial amount of material moved to the right-hand side of the grid area where little was previously present.

Footpad 2 area. The rim-like region beyond the buried footpad perimeter was rounded and locally reduced in elevation; clods and platy fragments of drift material were destroyed; cm-high scarps were subdued to obliterated by erosion and deposition of fines.

Footpad 3. Material was locally redistributed, removed, and added to the footpad walls and floor; a skiff of material was deposited on the skirt.

Engine Exhaust Crater. Scouring by the wind increased the area of exposed duricrust and etched-out fragments on the crater rim; deposition of fines reduced the slopes of the crater walls and covered areas beyond the rim. New miniature wind tails of "soil" that formed on the lee sides of clods suggest a local wind from N. 17° E.

Shroud Impact Crater. Crater rim was locally destroyed and floor was filled with a few mm of dark fines. Dark fines were deposited around the crater.

Sandy Flats. The trench (XRFS-7) in the wind tail of "soil" behind Sponge rock appeared unaltered on Sol 1728. Later, trench rims and tailings were subdued and rounded; trenches were partly filled. The flat, steep triangular face of the wind tail, originally behind Sponge rock, was rounded and the crest of the wind tail retreated 5 or 6 cm. Images of conical pile 1 were not acquired after the dust storm.

Conical pile 4. Pile was partly eroded; movement of materials

suggests that the eroding winds came from the east. Isolated fragments 0.4 to 0.5 cm across disappeared because they were either entrained or eroded by the wind.

Rocky Flats. Conical pile 2 on Metate 1 rock was destroyed. Conical pile 3 was removed except for a thin, sparse residue of fragments as large as 0.7 cm. Conical pile 5 was partly demolished; a mound 6 or 7 cm across and 2 cm high composed of fragments up to 0.7 cm remained after the storm. Rims of backhoe touchdown trenches were partly removed and the trench floors were partly filled. A small crater produced during landing was filled on its eastern sides and eroded on its western sides; nearby, new miniature wind tails of "soil" that formed on the lee sides of clods indicate the wind was from N. 35° E. Previously formed small wind tails were exposed by removal of fines deposited by engine exhaust gases, the surface sampler, and global dust storms. The deep hole trench tailings and nearby excavations were eroded by Sol 1757.

Grumpy Rock Disturbed Area. About 1.5 cm of fines were removed from top surfaces of disrupted blocks of "soil"; relief of piles of fines was reduced 0.5 cm or so; clods in the eastern area were reduced in size and the local relief decreased about 0.5 cm; a 3 cm rock perched on a block was chiefly rotated, but translation was inhibited by a block to the west; some deposited fines almost buried a fragment 1.5 cm high at the basal edge of disturbed area.

XRFS-11 Trenches. Fines were deposited beyond trenches along axes away from the lander; two clods 7 cm across were destroyed; trench tailings crests were deflated and altered with virtually no lateral shifts; trench floors were partly filled. Changes imply a wind from roughly N. 50° E.

Far field. An "active dune" about 18 m away from the lander shows no evidence of being active. Some of the many possible far field changes include the formation or exhumation of ripple marks with a wavelength of several cm.

Miscellaneous. A small slope failure of part of the wall of the excavation in the deep hole tailings (XRFS-16,17,18) occurred sometime between Sols 1313 and 1387. No evidence was found for a global dust storm during the third fall season by visual examination of the images.

Interpretations. The observations suggest that (a) the eroding winds of the Sol 1742 storm were more easterly (N. 35° to 90° E.) than those (N. 5° - 11° E.) that formed the large wind tails; (b) fragments in erosional residues are 0.7 cm and

larger, but smaller ones may be present. Some fragments 0.4 to 0.5 cm and smaller were somehow removed, at least locally; (c) wind speeds of the 1742 local storm were probably greater than those of a previous local dust storm (25-30 m/s) that occurred during the same season on Sol 423 (6) because the earlier storm did not alter the surface; (d) the major, if not entire, amount of erosion by the storm occurred between Sols 1728 and 1757; and (e) erosion chiefly occurred where the surface configuration and material properties were altered by the lander and its sampler.

References

1. Moore, H. J., 1982, Erosion of surface materials at the Mutch Memorial Station (Lander 1, Mars: Reports of Planetary Geology Program, NASA Tech. Memo. 85127, p. 180-181.

2. Wall, Stephen D., 1982, Viking Lander monitor mission imaging investigation status report: Reports of Planetary Geology Program, NASA Tech. Memo. 85127, p. 379-381.

3. Arvidson, Raymond E., Guinness, Edward A., Moore, Henry J., Tilman, James, and Wall, Stephen D., 1983, Three Mars Years: Viking Lander 1 imaging observations: Science, v. 222, no. 4623, p. 463-468.

4. Moore, H. J., Spitzer, C. R., Bradford, K. Z., Cates, P. M., Hutton, R. E., and Shorthill, R. W., 1979, Sample fields of the Viking landers, physical properties, and aeolian processes: Jour. Geophys. Res. v. 84, no. B-14, p. 8365-8377.

5. Moore, Henry J. and Dowey, Elizabeth M., 1981, Maps of the sample fields and summary of surface activities of Viking Landers 1 and 2, U.S. Geological Survey informal communication presented at the Third Mars Colloquium, Pasadena, CA., Aug. 31- Sept. 2, 1981, 50 p.

6. Ryan, J. A., Sharman, R. D., and Lucich, R. D., 1981, Local Mars dust storm generation mechanism: Geophys. Res. Lttrs., v. 8, p. 899-901.

REGIONAL LINEAR STREAKS ON MARS

P. Thomas, P. Gierasch, E. Alvarez, Laboratory for Planetary Studies, Cornell University

The most unusual albedo markings on Mars are long, narrow streaks that occur in sets of nearly parallel members (Fig. 1). We define these features, which attain lengths of 400 km, as regional linear streaks. Their distribution, shapes, time variability, contrasts, and meteorologic associations have been studied from Viking Orbiter images.

Linear streaks longer than 50 km occur in only three areas of Mars: Amazonis Planitia, Acidalia Planitia, and southwest of Mare Erythraeum (referred to below by quadrangle name, Argyre). All areas are 23-38° latitude, relatively smooth, and have only slight regional slopes. They occur at elevations of -2 to +6 km, nearly a scale height in range. Background albedos (Mars Consortium data) are 0.15 to 0.25 and thermal inertias span 4 to 11 inertia units.

Nearly all high resolution data of these streaks are of the Amazonis group. These streaks are generally 100-400 km long and 2-10 km wide, spaced 12-18 km apart. The streaks are not perfectly parallel, and at least two sets of differing orientations cross each other. The Argrye and Acidalia streaks are nearly the same dimensions but are fewer in number and less sharply bounded. There are no visible source obstacles. In Argyre and Acidalia nearby dark, crater related streaks are parallel to the linear streak trends, and suggest formation by east winds. In Amazonis there are bright linear streaks which follow a slightly different trend from the dark linear streaks. The bright streaks may originate at a series of low scarps; if this interpretation is correct, they formed during east winds.

The streaks are time variable. The Amazonis dark streaks were stable from L_S = 37° to L_S = 159°. Between L_S = 159° and L_S = 32° the streaks were erased and two or more new sets were formed. The streaks were stable through L_S = 80°. In Argyre at L_S = 101° there were no streaks. At L_S = 16° the streaks were well formed; at L_S = 32° they were somewhat reduced in extent.

Contrast of the streaks with the surrounding plains is small, and is comparable to that of dark, crater-related streaks. Such streaks can result from removal of thin dust layers from only a few percent of the ground area in the streaks.

The primary characteristics of the streaks that must be explained are the restricted latitude occurrence, the long, nearly parallel forms, their probable formation by easterly winds, and consistent pattern of lines convex to the equator. We are investigating problems of general circulation at these times and latitudes, as well as related cloud forms that may bear on atmospheric stability at the times the streaks probably formed.

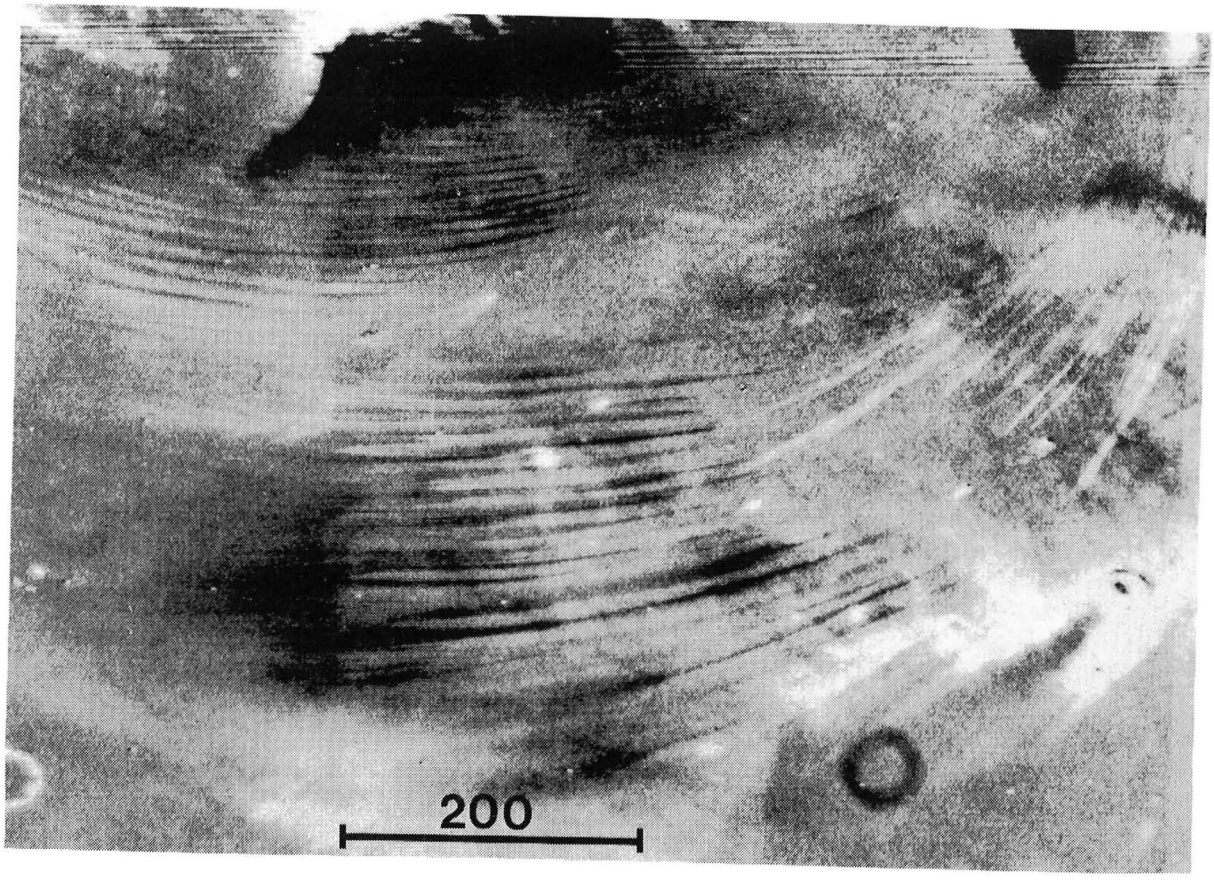

FIG. 1. Regional linear streaks in Amazonis Planitia, Image 323S76. Centered at 32°N, 160°W.

SEASONAL AND SECULAR VARIATION OF THE SOLIS LACUS ALBEDO FEATURE: RELATION TO THE MARTIAN DUST-TRANSPORT CYCLE

Steven W. Lee, Lab. for Planetary Studies, Cornell Univ., Ithaca, NY 14853
Present affiliation: Dept. of Geology, Arizona State Univ., Tempe, AZ 85287

As documented over the course of thirty-six martian years, dramatic seasonal and secular variations occur in albedo features in the Solis Planum region of Mars; the most striking of these is the classical dark albedo feature, Solis Lacus. This region is also known as a source area for local and global dust storms. Telescopic observations beginning in 1907 (de Mottoni, 1975) indicate that Solis Lacus is generally most distinct during southern spring and summer, and less distinct in southern fall and winter. Mariner 9 and Viking Orbiter images reveal that Solis Lacus contains and is surrounded by a conspicuous pattern of bright and dark wind streaks. Sketch maps of albedo features in this region as viewed by Viking over the course of one martian year are shown in Figure 1.

A seasonal dust-transport cycle is proposed to explain these observations. 1) During late southern spring or early summer, dust is eroded from the surface and transported from the region by local dust storms which may become a global dust storm. Removal of dust over a wide area results in the dark Solis Lacus feature. The presence of bright streaks throughout the year indicates that the surface is not swept completely clean of dust. 2) During the cessation stage of global dust-storm activity (typically mid- to late-southern summer), enhanced deposition in the lee of obstacles forms the prominent patterns of bright streaks (Veverka et al., 1981; Lee, 1984) observed within and around Solis Lacus. 3) As the year progresses (southern fall and winter), sedimentation from the atmospheric dust load occurs over the entire region, decreasing the contrast of the albedo features to their surroundings. 4) Dust-storm activity the following year renews the cycle by again removing dust from the region. Differences in the time of occurrence, severity (local or global), and longevity of dust-storm activity may lead to the observed year-to-year variability of albedo features.

For the following reasons, these observations exclude the possibility of significant deposits of dust (many cm in thickness) being transported into or out of the region on a seasonal basis. 1) The production of wind streaks is thought to involve as little as a few μm of dust covering a few tens of percent of the surface (Thomas et al., 1984; Wells et al., 1984). The observed persistence of the streak patterns is not consistent with the presence of thick dust deposits. Experimental studies (Wells et al., 1984) indicate that deposition of more than a few tens of μm of dust would obliterate the observed albedo features. 2) Integrating the deposition possible from the observed atmospheric dust loading (Pollack et al., 1979), an annual accumulation ~30 μm thick would result if no erosion took place. 3) The regional thermal inertia values are $\sim 8 \times 10^{-3}$ cal/cm^2/sec$^{1/2}$/°K and are indicative of a surface covered by particles larger than ~100 μm in size (Kieffer et al., 1977). Several cm of dust would exhibit a much lower thermal inertia signature. As suggested by Peterfreund (1982), a saltation triggering mechanism may effectively eject surface dust into suspension and result in the observed local dust storms.

Cycling of at most a few tens of μm of dust through this region could easily be accomplished by annual deposition followed by erosion during local dust storms. Such levels of eolian activity adequately explain the noted occurrence and variability of the regional albedo features. Deposition or erosion of large quantities of dust are not required nor are they consistent with the observations.

REFERENCES:

De Mottoni, G. (1975). The appearance of Mars from 1907 to 1971: Graphic synthesis of photographs from the I.A.U. Center at Meudon. Icarus 25, 296-332.

Kieffer, H. H., T. Z. Martin, A. R. Peterfreund, B. M. Jakosky, E. D. Miner, and F. D. Palluconi (1977). Thermal and albedo mapping of Mars during the Viking primary mission. J. Geophys. Res. 82, 4249-4295.

Lee, S. W. (1984). Mars: Wind streak production as related to obstacle type and size. Icarus 58, 339-357.

Peterfreund, A. R. (1982). Dust storm activity on Mars during the Viking mission. NASA TM-85127, 177-179.

Pollack, J. B., D. S. Colburn, F. M. Flasar, R. Kahn, C. E. Carlston, and D. Padek (1979). Properties and effects of dust particles suspended in the martian atmosphere. J. Geophys. Res. 84, 2929-2945.

Thomas, P., J. Veverka, S. Lee, and A. Bloom (1981). Classification of wind streaks on Mars. Icarus 45, 124-153.

Thomas, P., J. Veverka, D. Gineris, and L. Wong (1984). "Dust" streaks on Mars. Icarus, in press.

Veverka, J., P. Gierasch, and P. Thomas (1981). Wind streaks on Mars: Meteorological control of occurrence and mode of formation. Icarus 45, 154-166.

Wells, E. N., J. Veverka, and P. Thomas (1984). Mars: Experimental study of albedo changes caused by dust fallout. Icarus 58, 331-338.

Figure 1 (following page). Sketch maps of albedo features in Solis Planum. The features were digitized from Viking Orbiter images obtained during the first two consecutive martian years of the mission. No suitable images were available outside of the indicated boundaries. The shaded region corresponds to the Solis Lacus albedo feature. Wind streak classification follows the scheme of Thomas et al. (1981). The topographic base (contours in km shown in Fig. 1a) was digitized from the USGS 1:25M global topographic map.

a) Early southern winter (Year 1).
b) Late southern spring (Year 1).
c) Late southern summer (Year 1).
d) Mid-southern autumn (Year 2).

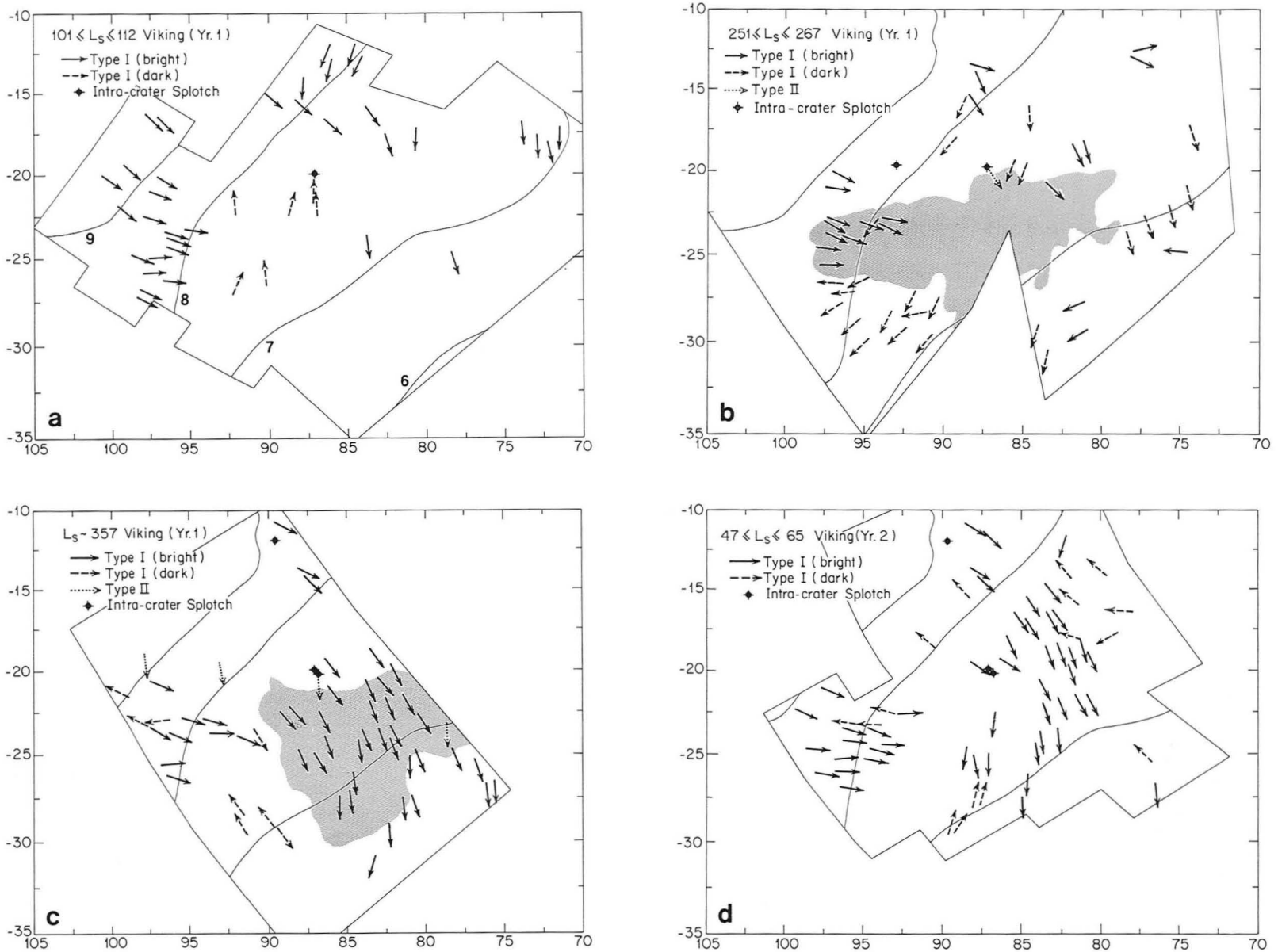
101 ≤ Ls ≤ 112 Viking (Yr. 1)
Type I (bright)
Type I (dark)
Intra-crater Splotch
9
8
7
6
a
251 ≤ Ls ≤ 267 Viking (Yr. 1)
Type I (bright)
Type I (dark)
Type II
Intra-crater Splotch
b
Ls ~ 357 Viking (Yr. 1)
Type I (bright)
Type I (dark)
Type II
Intra-crater Splotch
c
47 ≤ Ls ≤ 65 Viking (Yr. 2)
Type I (bright)
Type I (dark)
Intra-crater Splotch
d
-10
-15
-20
-25
-30
-35
105
100
95
90
85
80
75
70

Figure 1.

EOLIAN EROSION ON MARS: THREE SCALES

P. Thomas, Laboratory for Planetary Studies, Cornell University

Formation and erosion of deposits on Mars with vertical scales of 10^2-10^3 m and horizontal scales of $>10^2$ km may have occurred at rates very different from present ones. Evidence for the rates on small scales comes from observations of dust storms (Pollack et al., 1979) and photometry of wind streaks (Thomas et al., 1984). These observations cover scales less than 1 cm vertically and time scales less than 10 years (Table). Intermediate scale features such as yardangs and sand dunes are more difficult to evaluate, but for dunes, plausible rates of transport may be calculated (White, 1979; Thomas, 1982) (Table). Net eolian action in some areas may be so low (Arvidson et al., 1979) that in order to study the large features one needs to select those likely to have been modified more rapidly and that exhibit distinctive contrasts with surrounding areas. Best suited for such study are relatively soft deposits overlying more resistant substrates. Viking Orbiter images of four of the largest such areas on Mars (both poles, Zephyria (0°N, 180°W), and northeast Arabia (30°N, 300°W) have been examined to test how the erosional features correlate with patterns attributable to winds, properties of deposits, or non-eolian erosion, and for constraints on erosion and transport rates. Although these areas have many features that are superficially similar (especially the sinuous troughs), topography on the deposits visible at the higher resolutions (<200m/pxl) are often spectacularly varied, do not lend themselves to convenient comparison of morphologic maps of the different areas, and indicate that wind erosion is only one of several major processes modifying the deposits. The sinuous troughs so prominent in the polar deposits appear in many cases to follow or be terminated by structures within the deposits, such as faults, intrusions, or buried topography. In particular, some south pole troughs are extensions of aligned collapse features. The troughs in Zephyria may also follow structures, but have better expressed yardangs than do the polar regions. Yardang-like forms and mesas in the two non-polar deposits occur in close association with channels and various collapse features. Yardang locations and orientations are for the most part not well correlated with upwind supply of sand or with present wind directions. Inasmuch as formation times of most features visible in the deposits should be greater than 25,000 years, wind directions changing with season of perihelion (Arvidson et al., 1979) should not be recorded in these deposits. Some deposit boundaries may be related to slope winds from the Tharsis region that parallel the margins of the segments of the Zephyria deposits and yardangs near these margins. However, channel and collapse features are prominent in these areas, and the erosion represented by the yardangs is probably very small compared to the channel and collapse features.

The rates of eolian erosion for these deposits are of course very uncertain (Table 1), because both the times (from crater preservation) and depths of erosion are poorly constrained. The important conclusion is that no spectacularly high or low rates need apply to any of these deposits. The average rates may be comparable to the present dust storm activity or to the rates calculated for saltation transport. However, the

prominent role of collapse and channel formation in many areas and of cyclic activity at the poles suggest that eolian erosion may have been much less important than eolian removal of weathered material.

References

Arvidson, R. E., Guinness, E., Lee, S. (1979). Nature 278, 533-535.
Pollack, J. B., Colburn, D. S., Flasar, M., Kahn, R., Carlston, E., and Pidek, D. (1979). Jour. Geophys. Res. 84, 2929-2945.
Thomas, P., Veverka, J., Gineris, D., and Wong, L. (1984). Icarus, in press.
White, B. R. (1979). Jour. Geophys. Res. 84, 4643-4651.

TABLE 1: Eolian Erosion/Transport on Mars, Three Scales

	Wind Streaks	Dunes (Intracrater Splotches)	Thick Regional Deposits
Time scale	<10y	10^4-10^6 y	10^6-10^8 y
Depth	~10^{-3} cm	~100 m	0.1-3 km
Rates	Photometry 10^{-5}-10^{-3} gm/cm^2/y	m^2/y (horiz. flux) <10^{-1} cm/y vertical	10^{-4}-10^{-2} cm/y (craters)

THE ORIGIN OF REGIONAL DUST DEPOSITS ON MARS

P.R. CHRISTENSEN
Department of Geology, Arizona State University, Tempe, Arizona, 85287

There are three distinct regions on Mars characterized by very low thermal inertia (1) and high albedo (2). These regions, located around Tharsis (-15° to 45° N, 60° to 200° W), Arabia (0° to 30° N, 300° to 360° W), and Elysium (15° to 30° N, 210° to 230° W), cover a total of nearly 24 x 10^6 km^2 of the surface and represent an important class of surface deposit. The thermal properties indicate that these regions are covered by at least 3 to 5 cm of very fine (~ 50 μm) dust and their origin from dust storm fallout has been suggested by several investigators (1,3,4). However, their age, history, and the dynamical processes that have led to their formation remain uncertain.

Recently, additional evidence has been derived from the Viking Infrared Thermal Mapper (IRTM) observations that allows a more complete model for the formation of these regions to be proposed. The first observation is that dust appears to be currently accumulating in the low thermal inertia regions (4). Following each global dust storm a thin layer of dust is deposited globally, as evidenced by an increase in surface albedo seen from orbit (2,5) and from the Viking Lander sites (6). During the period following the storm, the bright dust fallout is subsequently removed from low albedo regions, as indicated by the post-storm darkening of these surfaces (5) and by an increase in the atmospheric dust content over dark regions relative to the bright, low thermal inertia regions (4). Thus, the fine dust storm material is removed from dark regions but not from the bright regions, resulting in a net accumulation within the bright, low thermal inertia regions. Once deposition has begun, the covering of exposed rocks and sand and the accumulation of fine material on the surface make removal of material increasingly difficult, thereby enhancing the likelihood that material will accumulate within the low thermal inertia regions.

A second result concerning the origin of the low thermal inertia regions is the observation that these areas have fewer rocks exposed at the surface than found elsewhere, indicating that some degree of dust mantling has taken place (4). There is, however, good evidence for the occurrence of some rocks at the surface (4,7), implying that the mantling is incomplete and has therefore been extremely slow or has begun relatively recently.

The minimum thickness of fine material required to produce a low thermal inertia surface is approximately 3 to 5 cm. Assuming that the global dust load of the 1977 storm was uniformly deposited over the surface gives a sedimentation rate of 10^{-3} cm $year^{-1}$ (8). This rate is probably an upper limit because the 1977 storm was unusually large and the dust may be preferentially deposited in the polar regions (8). However, at this rate only 5 x 10^3 years would be required to deposit the minimum amount of dust. An upper limit on the amount of dust present can only be inferred, but the occurrence of some rocks on the surface suggests that the mantle may only be several meters thick. A deposit of this thickness would only require 10^5 to 10^6 years to accumulate at the present rate.

Finally, localized deposits of coarse material have been observed within numerous craters on Mars, but these intracrater deposits are absent within the cores of the low thermal inertia regions. They do, however, occur around the edges of these regions (9). One possible explanation is that these deposits were once exposed on the surface in low thermal inertia regions, but have since been buried, providing additional evidence for mantling in these

regions. Their existence around the perimeter, together with the occurrence of active deposition, suggests that the low thermal inertia regions may be expanding. The mantle thickness is deep enough in the center to completely bury coarse deposits and thins toward the margin.

The explanation proposed for the origin of the low thermal inertia regions, which occur predominately in the northern hemisphere, is that they represent cyclic oscillations in dust deposition and removal. In this model, these regions would have formed during the most recent cycle of the 10^5 to 10^6 year north-to-south oscillation of the insolation maximums (10). In this case, fine material would currently be removed from the southern hemisphere, where wind velocities are presently the highest, and redeposited in the north. When the insolation maximum occurs in the north, the opposite may be true. This mechanism could therefore account for the observed active deposition, the occurrence of fines on the surface and for the incomplete mantling of the surface rocks and deposits of coarse material because the mantling has only recently begun.

In summary, the low thermal inertia, bright regions on Mars represent major deposits whose origins provide important information on the dynamics and history of martian sedimentary cycles. Results derived primarily from the IRTM data provide important constraints on the surface characteristics of these regions and allow a model for their formation to be developed. In this model, dust is preferentially deposited in the low thermal inertia regions, with positive feedback mechanisms act to increase deposition once it has been initiated. Deposition is actively occurring and these regions appear to be expanding at the present time. The current accumulation of fine material, however, probably represents only the most recent cycle of deposition and erosion associated with the cyclical variations in insolation and the resulting changes in wind patterns and velocity.

References

1. Palluconi, F.D. and H.H. Kieffer (1981) Icarus, 45, 415-426.
2. Pleskot, L.K. and E.D. Miner (1981) Icarus, 45, 179-201.
3. Zimbelman, J.R. and H.H. Kieffer (1979) J. Geophys. Res., 84, 8239-8251.
4. Christensen, P.R. (1982) J. Geophys. Res., 87, 9985-9998.
5. Pleskot, L.K. and E.D. Miner (1981) Third Intern. Colloq. on Mars.
6. Guinness, E.A., C.E. Leff, and R.E. Arvidson (1982) J. Geophys. Res., 87, 10051-10058.
7. Thorpe, T.E. (1982) Icarus, 49, 398-415.
8. Pollack, J.B., D.S. Colburn, F.M. Flasar, R. Kahn, C.E. Carlston, and D. Pidek (1979) J. Geophys. Res., 84, 2929-2945.
9. Christensen, P.R. (1983) Icarus, 56, 496-518.
10. Ward, W.R. (1974) J. Geophys. Res., 79, 3375-3386.

ON THE LATITUDINAL DISTRIBUTION OF DEBRIS IN THE NORTHERN HEMISPHERE OF MARS

E. A. Guinness, C. E. Leff and R. E. Arvidson, McDonnell Center for the Space Sciences, Department of Earth and Planetary Sciences, Washington University, St. Louis, MO 63130

Examination of Mariner 9 images showed evidence of debris mantling on Mars. The evidence included craters that appeared to be filled with debris and an apparent lack of small craters. Based on such data, it has been suggested that a circumpolar debris mantle exists poleward of about 30N and 30S latitudes (1). The presence of a debris layer has important implications for the modulation over time of atmospheric pressure by the cap-regolith-atmosphere system. Several studies (e.g., ref. 2) have modelled the effects of the regolith as a storage reservoir for volatiles. Each of these studies, however, has lacked a quantitative assessment of the thickness and distribution of debris mantling. In this abstract we discuss our preliminary efforts in providing constraints on the thickness and distribution of debris. Our initial approach is to examine crater size-frequency data for selected regions on Mars, later expanding the study to include an inventory of aeolian features and other direct indicators of debris deposition.

Thus far we have determined the crater size-frequency distributions for ten regions between latitudes 20N and 80N and covering a range of longitudes (Table 1). Crater data were derived from Viking Orbiter images with resolutions of between 26 and 75 meters/pixel. Data for the Viking One (VL1) landing site (3) and a similar crater distribution for a region northeast of VL1 (28N, 46W) were used as a standard distribution for a crater production population. Viking Orbiter images of these regions show no buried or filled craters. Viking Lander images show that the surface at VL1 is free from a thick, fine-grained debris layer. Thus, the VL1 data provide a reasonable sample of a production population.

Assuming that the debris deposits are young relative to the craters and that the debris simply filled or buried craters, the crater size-freqeuncy distribution curves for debris-mantled areas should show a reduction of slope compared to unmantled areas (4). Small craters can also be lost due to the modulation transfer function of the imaging system. Thus, any slope reduction occurring at diameters of less than about six times the image resolution were ignored. We would also expect atmospheric hazes would reduce the slope of the crater size-frequency distribution at small crater sizes because the modulation transfer function of the atmosphere would preferentially reduce the contrast of small craters. Evidence of atmospheric obscuration was checked by using the cloud and haze catalog generated by Kahn (5).

Five of the count areas provide a generally north-south trend north of our control areas in Chyrse Planitia. Two areas are in Acidalium Planitia (37N and 47N latitude). Both of these areas have crater size-frequency distributions that parallel the VL1 data, but suggest a somewhat younger surface (Figure 1). The other three areas in the north-south transect are at latitudes between 71N and 78N. The crater size-frequency distributions for these three areas show a reduction in

slope for small crater sizes (Figure 2). The frames used to acquire crater data, however, were taken during the northern early spring and mid-summer seasons, times that have a reasonable probability of haze, as suggested by the cloud and haze data base. In fact, a large cloud can be seen to the north of one of the count areas. Thus, there is a reasonable possibility that the slope reductions are due to atmospheric obscuration.

In order to check whether the results from the previous transect are representative of the northern hemisphere, we examined several areas in the mid-latitudes and polar regions at a variety of longitudes. Two of the areas east and west of the Elysium volcanic province have crater size-frequency distributions that are very similar to VL1 (Figure 3). A third count area north of Elysium (33N, 238W) has a distribution that shows a lack of small craters. The images of this region show clear indications that the region is partially covered by younger lava flows, which could have removed small craters by burial. As an additional check on atmospheric effects in the crater data, we determined crater size-frequency distributions for an area (75N, 167W) at two different seasons, mid-spring and early summer. Both distributions show a slope reduction for small craters, but the break in slope occurs at different diameters. The cloud and haze data base suggests that both times have a reasonable chance for hazes. In fact, the images at both times have streak-like structures that are suggestive of atmospheric clouds or haze.

In general, the crater data discussed in this abstract show no indications of a wide-spread increase in debris thickness with increasing latitude. The high resolution of the images examined (26-75 meters/pixel) suggests that a recently mobile debris layer of greater than several hundred meters is not likely. Still, our small sample size cannot rule out the possibility of a longitudinally-complex system for the distribution of debris. Clearly, examples of craters that appear to be filled with debris can be found throughout the planet. One possibility that our crater data cannot address is the presence of a thick regolith that pre-dates the majority of impact events. Finally, atmospheric haze can be an important factor in modifying the shape of crater size-frequency distributions.

REFERENCES CITED

1. Soderblom, L. A., Kreider, T. J., and Masursky, H. (1973), J. Geophys. Res., 78, 4117-4122.
2. Fanale, F. P., Salvail, J. P., Banerdt, W. B., and Saunders, R. S. (1982), Icarus, 50, 381-407.
3. Dial, A. L. (1978), NASA Tech. Mem. 79729, 179-181.
4. Chapman, C. R. and Jones, K. L. (1977), Ann. Rev. Earth Planet. Sci., 5, 515-540.
5. Kahn, R. (1984), J. Geophys. Res., 89, 6671-6688.

TABLE ONE

REGION	LAT/LON	Ls	SCALE (m/pix)	NUM CRATERS	AREA (sq. km)	Frames
Chryse	28N/46W	74.2	45	1160	19799	668A34-42
Acidalium I	37N/27W	20.9	59	484	34933	225S01-7,9,10
Acidalium II	47N/23W	141.2	75	77	1195	71B71-76
Polar I	71N/60W	38.4	26	71	4730	525B01-07
Polar II	76N/93W	141.2	58	22	18253	71B42-46,61-64
Polar III	78N/72W	140.7	58	11	35952	70B06-10,27-34
Elysium I	24N/216W	65.9	32	612	9733	649A38-45
Elysium II	26N/180W	67.6	35	489	12714	653A34-42
Elysium III	33N/239W	49.6	72	225	31510	612A43-47
Vastitas I	75N/167W	50.0	35	103	10186	551B83-87
Vastitas II	75N/167W	117.3	75	15	23183	703B40-43

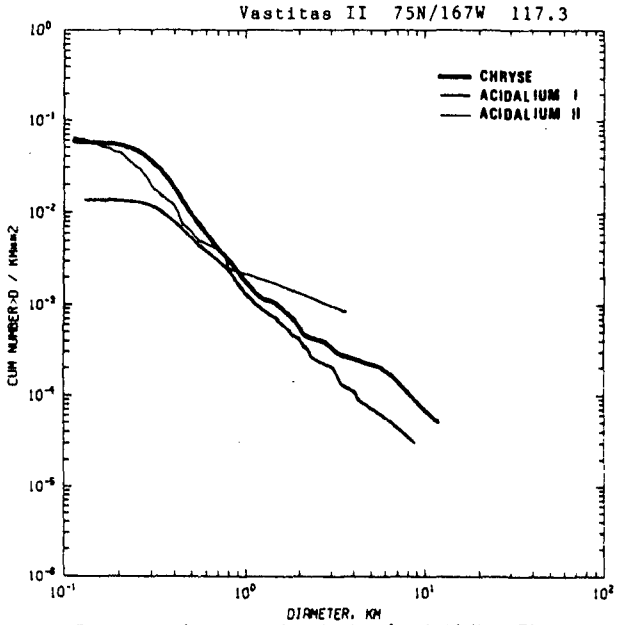

Figure 1. Crater size-frequency distribution for Acidalium Planitia are compared to Chryse Planitia (northeast of VL1). The distribution for Acidalium II is highly uncertain between diameters of 1 and 10 km because of the small number of craters counted.

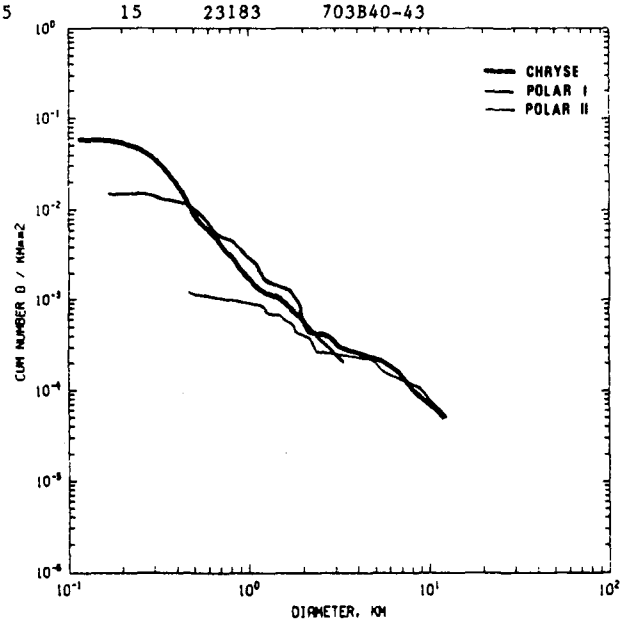

Figure 2. Crater size-frequency distribution for two polar regions are compared to the Chryse data. The data for the polar regions show a slope reduction at different diameters.

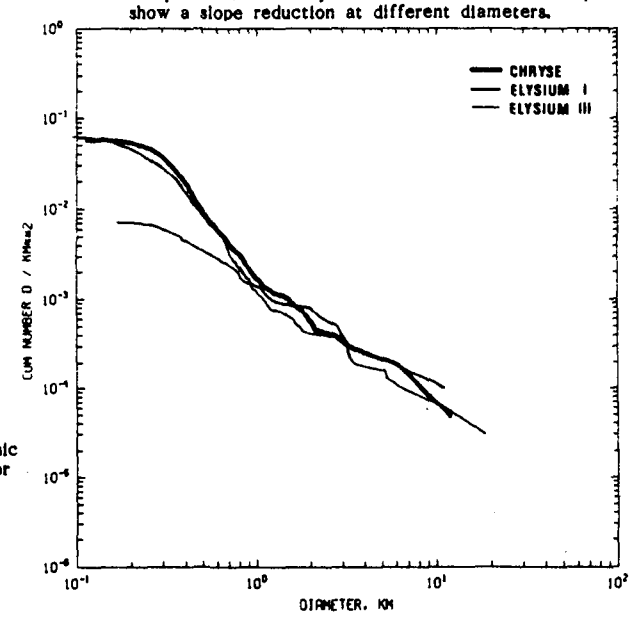

Figure 3. Crater size-frequency distributions for the Elysium volcanic province are shown Again, the Chryse data are shown for comparison.

TRANSFORMATION OF POLAR ICE SUBLIMATE RESIDUE INTO MARTIAN CIRCUMPOLAR SAND

R. Stephen Saunders, Timothy J. Parker, James B. Stephens, Eric G. Laue, Jet Propulsion Laboratory; **Fraser P. Fanale,** University of Hawaii

The experimental demonstration that a credible Martian "sand" may be formed from dust-bearing ice provides a new set of possible explanations for some of the observed Martian aeolian landforms. If a set of coherent experimental evidence can be developed that will be consistent with all other observations pertinent to Martian sand phenomena, then one of the great enigmas of the Martian surface may be resolved.

Aggregates of fine particles have been suggested to explain at least some of the vast circumpolar dune fields (Thomas, 1982), with the polar deposits providing the material. But Thomas doubted that the particles would have enough strength to survive the saltation distances invoved and argued that the dark color of the dunes indicates a distinctly different composition from the light-colored polar dust and a source other than the poles. For the "sand" to be credible it should be of low density and be mechanically soft so that it would produce little aeolian erosion of geologic features even over billions of years (Arvidson et al, 1979; Greeley et al, 1984). Yet the "sand" must also be able to survive transportation over hundreds of kilometers without disintegrating. Its color must be that of the relatively dark circumpolar dunes and intra-crater dunes found on Mars (Thomas, 1984; Tsoar et al, 1979).

If, as we hypothesize, a light-weight fluffy rind is formed on the polar caps (see Stephens et al, "Properties of Filamentary Sublimation Residues from Dispersions of Clay in Ice", this volume) it could provide material easily entrainable by Martian winds, which generally blow equatorward from the poles (Thomas, 1984; Tsoar et al, 1979). These winds would peel the fluffy rind from the surface of the sublimating summer polar caps and from the equatorward slopes of the polar troughs. These pieces of material would then be rolled into lumps (of high sailarea/mass ratio) by the wind (Figure 1). They would become pigmented as they saltate across the surface, perhaps gathering carbonaceous meteoritic dust or other impurities on their surfaces, or through chemical reactions with the ice-free environment away from their point of origin. Once they became trapped in topographic wind "shadows", they would

form dune structures because they are hydraulically equivalent to sand particles (Figure 2).

To experimentally demonstrate that the filamentary sublimate residue could survive the saltation stresses induced by transportation for hundreds of kilometers, two apparatus were constructed. Figure 3 depicts a Mars environment tumbling drum which can make several lumps of sublimate residue saltate "gravitationally" for long distances. The tumbling drum is a glass jar that is coated with a thin coating of montmorillonite clay to simulate a surface composed of compacted sublimate residue. The lumps both roll and slide as the drum rotates. Figure 4 shows a rotary wind tunnel which can also cause the lumps to saltate for long distances. In this apparatus the rotating fan blades produce a cicumferential wind in the bowl that causes the lumps to saltate around and around continuously. The actual distance traveled by the lumps is difficult to determine in this apparatus. These devices were used in a simulated Martian atmosphere to test the durability of the lumps of sublimate residue. The lumps in both cases were capable of surviving for many tens of kilometers without any evidence of deterioration. When a small amount of carbon black was applied to the track of the saltating lumps the lumps became coated with the black material. Another observation was that the larger lumps would cannibalize the smaller lumps after a few hours of tumbling. Once the larger lumps (.5 to 1 cm) had incorporated the smaller lumps they would not aggregate further.

REFERENCES

Arvidson, R., Guinness, E., and Lee, S., "Differential aeolian redistribution rates on Mars." Nature, Vol. 278, 5 April 1979, pp. 533-535.

Thomas, Peter, "Present wind activity on Mars: Relation to large latitudinally zoned sediment deposits." Journ. Geophys. Res., Vol. 87, No. B12, 1982, pp. 9999- 10008.

Thomas, Peter, "Martian intracrater splotches: Occurrence, morphology, and colors." Icarus 57, 1984, pp. 205-227.

Tsoar, Haim, Greely, Ronald, and Peterfreund, Alan R., "Mars: The north polar sand sea and related wind patterns." Journ. Geophys. Res., Vol. 84, No. B14, 1979, pp. 8167-8181.

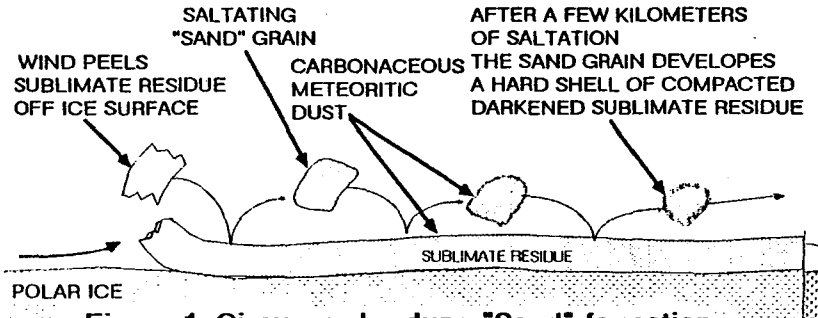

Figure 1. Circum polar dune "Sand" formation

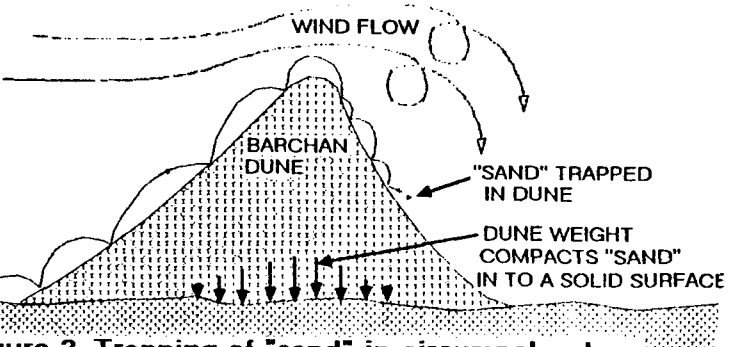

Figure 2. Trapping of "sand" in circumpolar dune

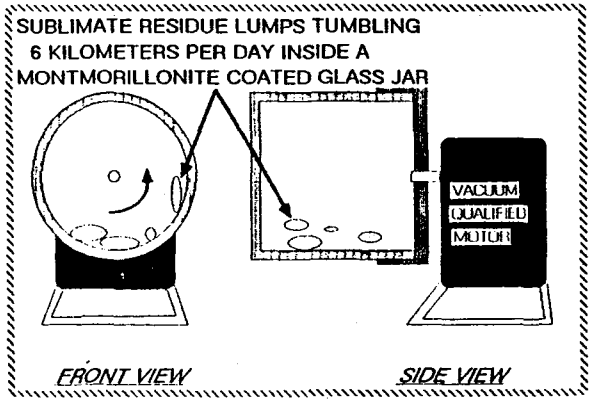

Figure 3. Mars environment saltation simulator

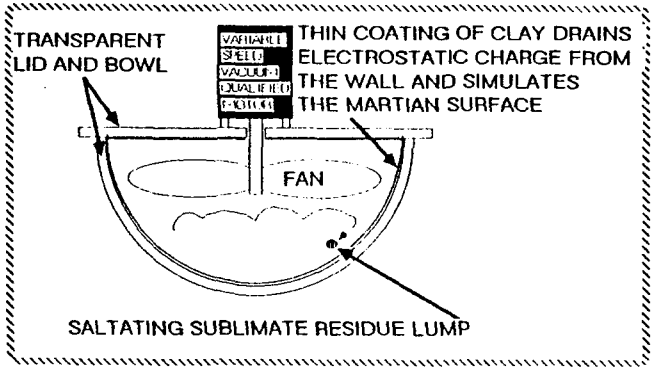

Figure 4. Mars environment wind saltation simulator

THE EFFECT OF PARTICLE DENSITY ON AEOLIAN TRANSPORT

S.H. WILLIAMS and R. GREELEY
Department of Geology, Arizona State University, Tempe, Arizona, 85287

Wind transport by saltation of surficial material is an important planetary geological process. The rate of saltation governs the rate of deposition and erosion on a planetary surface, particularly in the absence of competing processes, such as running water. Hence, the saltation rate affects the development of surface morphology, including the burial and exhumation of impact craters. Saltation flux on Earth has been studied extensively ((1); see (2) for a review). However, transport of particles with unusually high or low densities in atmospheric densities similar to those of other planets have not been investigated as thoroughly. A set of experiments using a wide range of particle densities has been performed in an open-circuit, terrestrial-atmospheric-pressure wind tunnel at Arizona State University. Table 1 shows the materials and size ranges used. The results show that saltation flux equations derived for typical geologic materials overpredict the flux of low-density particles. Walnut shells (ρ~1.1 g/cc) were used in the experiment and would correspond to volcanic ash or ice.

Less mass is transported by the wind in the case of low particle density because the style of transport is different. There is a direct, counter-intuitive relationship between particle density and transport height. Measurements of the vertical distribution of material show that the low-density walnut shells travel in a zone within 10 cm of the surface while high-density (~4.5 g/cc) chromite particles travel as high as 50 cm. Furthermore, the overall saltation rate of the chromite is approximately four times greater than the walnut shells at the same freestream wind speed, even though the wind is much further above threshold for the walnut shells. So many low-density particles move in response to a given wind that they interfere with one another in flight. A particle on the surface cannot move in an unimpeded saltation trajectory without being incorporated into the traction zone. This lowers the overall saltation rate. Only a relatively small number of dense particles will move in response to a given wind. At near-threshold wind speeds, the saltation curtain will tend to be underdeveloped due to the relatively few impact-caused saltation events, resulting in a lower flux than predicted.

Experiments are under way to investigate the saltation of high- and low-density particles at venusian and martian atmospheric densities. It is possible that the parameter controlling the style of transport in the saltation cloud is not the particle density, but is rather a function of the ratio between particle and atmospheric density. If this is true, then equations derived for terrestrial saltation flux may overpredict the venusian saltation flux. This was observed in some preliminary Venus Wind Tunnel (NASA-Ames) runs with 500-600 μm quartz sand (3). Even if particle density alone is the factor controlling saltation style, refinement of the saltation flux equations to be applicable to all particle and atmospheric densities is necessary.

Table 1

MATERIAL	DENSITY g/cm^3	SIZE RANGE μm
Walnut Shell	1.1	170-210, 250-300, 400-500
Quartz	2.6	170-210, 250-300
Olivine	3.5	250-300, 400-500
Chromite	4.5	170-210, 250-300, 400-500

Each material and size range is run at several different freestream wind speeds.

References

(1) Bagnold, R.A., 1941, The Physics of Blown Sand and Desert Dunes, London: Meuthen.

(2) Greeley, R. and J.D. Iversen, Wind as a Geological Process: Earth, Mars, Venus, Titan, Cambridge University Press (in press).

(3) Williams, S. and R. Greeley, 1982, Flux of windblown sand on Venus: Preliminary laboratory results (abs.), NASA TMX-85127, p. 170-172.

A COMPARISON OF TERRESTRIAL SALTATION FLUX IN THE LABORATORY AND THE FIELD

S.H. WILLIAMS and R. GREELEY
Department of Geology, Arizona State University, Tempe, Arizona, 85287

Aeolian transport of surficial material is an important part of the terrestrial geologic cycle. Numerous investigations have attempted to determine saltation rates using theoretical, laboratory, and field investigations. In many areas of geological interest, sand is not transported by the wind at the rate predicted by studies made in idealized conditions. Furthermore, calculated surface-abrasion rates based on laboratory saltation fluxes are often unrealistically high. This work is an attempt to quantify and discuss discrepancies between saltation rates under ideal conditions and in the field under natural conditions.

The saltation-flux data presented by Sharp (1) will be used as the field data for this study. Sharp measured saltation flux during four periods in the early 1950's (Table 1) in the Whitewater River drainage. The site is near Palm Springs, California, and close to the ventifact site at Garnet Hill. The National Weather Service provided weather records from the nearby Palm Springs Airport for Sharp's study periods. Meteorological conditions at the experiment site were extrapolated from the airport records and from wind speeds measured simultaneously by Hunter (2). Wind speeds above threshold were sorted into 4-MPH bins and the frequency of observation over each experimental period was calculated (Table 2). A saltation flux for each bin was calculated and summed to yield a predicted saltation rate for that period. When the predicted fluxes were compared with those measured by Sharp, large discrepancies were found (Table 1).

There are three primary sources for the discrepancy (listed in order of decreasing importance):

1) The surface in Whitewater Wash is not completely covered by sand, as in wind tunnel studies of saltation; therefore, a given wind will move less sand than it is capable of carrying.
2) Spring storms often cause high winds at Whitewater Wash, while rain wets the sand surface and inhibits its free movement. Other impediments to free sand transport (bushes, rocks, etc.) are also common at the site.
3) The sand collectors used by Sharp were not 100% efficient.

Little rain fell during period 2, July 18 to December 11, 1953, so virtually all of the discrepancy between the observed and predicted saltation flux probably is due to sand-supply and mobility problems. Rain is the probable reason for a higher discrepancy in the two springtime periods, 1 and 3. Rain inhibition might offset an increase in sediment supply due to deposition of new sand in the drainage. If this is true, then the effect of rain is much smaller than the effect of a restricted sand supply. It is unclear why the observed flux in period 4 was so low.

The link between the meteorological conditions at Palm Springs Airport and those at the Whitewater Wash site is fairly well established for near-threshold winds. Whether or not it is valid at higher wind speeds has not been determined. The Whitewater Wash site is situated in San Gorgonio Pass, through which strong winds often blow. High-speed winds could occur at Whitewater Wash without a corresponding increase in wind speed at the airport. This error would make the discrepancy between calculated and observed flux rates even larger. Thus, the discrepancies listed in Table 1 could be the lower boundary of the actual discrepancy.

REFERENCES

(1) Sharp, R.P., 1964, Wind-driven sand in Coachella Valley, California, Geol. Soc. Am. Bull., 75, p. 785-804.

(2) Hunter, W.A., 1979, unpublished Master's Thesis, Cal. State Poly. Univ. Pomona, California.

TABLE 1
OBSERVED (1) AND CALCULATED SALTATION FLUX AT WHITEWATER WASH

PERIOD	DATES	OBSERVED FLUX g/cm·sec	CALCULATED FLUX g/cm·sec	DISCREPANCY: $\frac{\text{calculated flux}}{\text{observed flux}}$
(1)	2 Mar-27 May 1955	$9.3 \cdot 10^{-5}$	$1.1 \cdot 10^{-1}$	1200
(2)	18 Jul-11 Dec 1953	$1.5 \cdot 10^{-5}$	$1.5 \cdot 10^{-2}$	1000
(3)	3 Feb-4 Mar 1953	$4.3 \cdot 10^{-5}$	$1.2 \cdot 10^{-1}$	2800
(4)	16 Apr-25 Nov 1954	$2.6 \cdot 10^{-6}$	$1.1 \cdot 10^{-1}$	42000

TABLE 2
FREQUENCY OF WINDS AT WHITEWATER WASH
Inferred from Palm Springs Airport wind data
Listed as percentage of total wind observations

(Wind speeds in MPH)

PERIOD	12-16	16-20	20-24	24-28	28-32	32-36	36-40	40-44	44-48	48-52	52-56
(1)	4.82	3.52	5.60	5.73	1.82	1.56	0.65	0	0.26	0	0.39
(2)	3.17	0.65	1.21	0.37	0.28	0.09	0	0	0.19	0	0
(3)	1.58	1.05	2.11	2.11	0.53	1.05	3.16	0	0	0.53	0.53
(4)	5.56	3.57	3.80	3.38	1.44	1.48	0.83	1.39	0.37	0.09	0

POTENTIAL BEDFORMS ON VENUS: WIND TUNNEL SIMULATIONS

S.J. BOUGAN, J. MARSHALL, and R. GREELEY
Arizona State University, Tempe, Arizona, 85287

Previous studies using the Venus Wind Tunnel (VWT) investigated the behavior of well-sorted unimodal sands and showed that microdunes (approximately 10 cm long, 1 cm high) formed in a limited range of particle sizes (90-250 μm) and windspeeds (0.9-1.5 m/s) (Greeley et al., 1984a). Present studies involving mixtures of particle sizes (bimodal and multimodal distributions) indicate that microdunes and related ridge- and wave-like structures can occur over a wider range of conditions. The results indicate that the bedforms develop as a consequence of the effective sorting capability of the high-density venusian atmosphere.

Four mixtures of different particle-size distributions were investigated. Three of these contained a constant distribution of coarse particles (250 to 700 μm) but varied the distribution of fines (54 to 250 μm). The study of these mixtures was intended to show the importance of fine particles in bedform development. In the fourth mixture, the size of the coarse particles was increased from 250 to 500 μm to study the effects of the coarse fraction on bedform development. Each mixture was tested at five windspeeds in a 30 bar/293 K carbon dioxide atmosphere (duplicating the average atmospheric density at the venusian surface). The saltation threshold velocity for each mixture was equal to the threshold velocity of the most easily moved particle. In the bedform studies the wind velocity was always kept above this threshold velocity. Microdunes and ridges developed in mixed particle sizes for a wide range of velocities. These bedforms also appear to be sorted into distinct coarse and fine layers. Using particles 50 to 700 μm in diameter, for example, the finest material was rapidly winnowed from the coarse particles and both accumulated into well-sorted mounds with the fines overlying the coarse particles--the inverse of ripple sorting (Bagnold, 1941; Sharp, 1963). The mounds evolved into microdunes that migrated across the unsorted substratum. The coarsest grains were entrained in traction by the fines, and consequently were "cycled" through the dunes together with the finer material. The coarse material rolled to the base of the slip face and became buried by the finer particles; the result was distinct coarse and fine layering within the dunes.

The results of these experiments suggest that: 1) small-scale bedforms on Venus may be more common than previously anticipated from simulations involving only unimodal sands (Bougan et al., 1984a); 2) small particles are rapidly sorted on Venus if winds slightly above threshold are available; 3) coarse particles are transported in traction within the bedforms as well as rolled by saltating fines (Greeley et al., 1984b), suggesting that the capacity of wind on Venus to transport material is greater than anticipated from previous flux studies (Bougan et al., 1984b); and 4) microdunes and related ridges and waves with coarse and fine layers can be produced during sorting. This distinctive layering may be related to the ripples and layering reported by Florensky et al. (1983), in the Venera photographs.

REFERENCES

Bagnold, R., 1941. The Physics of Blown Sand and Desert Dunes, Methuen, London.

Bougan, S. et al., 1984a. Parameter controlling aeolian bedform development on Venus, 1984 Geol. Soc. Am. Abstract Pub, in press.

Bougan, S. et al., 1984. Flux and bedforms of windblown material on Venus, Lunar Planet. Sci., 15, p. 80-81.

Florensky, C.P. et al., 1983. A geological-morphological analysis of the Venera 13 and Venera 14 panoramas, Cosmic Res., 21, p. 269-278.

Greeley, R. et al., 1984a. Microdunes and other aeolian bedforms on Venus: Wind tunnel simulations, Icarus, in press.

Greeley, R. et al., 1984b. Rolling "stones" on Venus: An unusual mode of wind transport, submitted for publication.

Sharp, R.P., 1963, Wind ripples, Journal of Geology, 71, p. 621.

MICRODUNES AND OTHER AEOLIAN BEDFORMS ON VENUS: WIND TUNNEL SIMULATIONS

R. GREELEY,*,† J.R. MARSHALL,* and R.N. LEACH†
*Department of Geology, Arizona State University, Tempe, Arizona, 85287
†Department of Physics, University of Santa Clara, Santa Clara, CA, 95053

Previous studies confirm that sand can be entrained at the wind velocities recorded on Venus. Present results describe bedforms produced in the Venus Wind Tunnel (VWT) simulating the average venusian environment. Even at the low wind speeds measured on Venus, dunelike structures form in fine-grained quartz sands (particles 50-200 μm in diameter). The dunelike structures, referred to as microdunes, are considered to be true dunes analogous to those on Earth because they have (1) slip faces, (2) a lack of particle-size sorting, (3) a low ratio of saltation path length to dune length, and (4) internal cross-bedding. The microdunes typically produced in the VWT are 9 cm long and 0.75 cm high. It is proposed that there may be fields of microdunes on Venus that are capable of very fast rates of migration and that they may grow into features much larger than those observed in the VWT. However, neither dunes nor other types of features develop above a wind speed of ~1.5 m/sec; at this wind speed, the bed is flat and featureless. Thus, it is predicted that relatively short periods of higher winds may destroy microdunes and other small bedforms which could account for the sparsity of definitive aeolian features observed in Venera images. Some apparent cross-bedding observed in Venera images, however, could represent preserved aeolian structures.

Page intentionally left blank

CHAPTER 9

FLUVIAL PROCESSES

Page intentionally left blank

PALEOHYDROLOGIC IMPLICATIONS OF VALLEY NETWORKS ON MARS

Victor R. Baker, Department of Geosciences and Department of Planetary Sciences, University of Arizona, Tucson, AZ 85721

Valley networks in the heavily cratered terrains of Mars represent an ancient epoch of hydrologic conditions greatly different from those of today. Available crater counts on the valley networks (1,2,3) indicate formation during the high flux of impacting bodies characterizing the early heavy bombardment phase of Martian history. Crater counting is of limited accuracy in this application because of the limited areal extent of the networks. Difficulties are encountered in distinguishing craters intersected by valley walls from those superimposed on the valleys. Two populations of valleys are recognized in the equatorial regions of Mars: pristine and degraded (3). The latter probably formed at the very end of the heavy bombardment phase, extending into the post-heavy bombardment by formation in the intercrater plains. Pristine valleys generally form segments of larger networks with degraded components. This suggests that valley formation was a prolonged process coeval with the heavy bombardment period and extending just beyond that period in martian history.

Compound networks, containing both pristine and degraded segments, contain an average of 2.5 times more total valley length than the pristine portions of the same networks. Thus, valley formation after the cessation of the heavy bombardment was either slower or of shorter duration than that during the heavy bombardment phase. Drainage densities (summation of valley length divided by basin area) average considerably higher for compound and degraded networks than for pristine ones, perhaps implying a change of process. Unfortunately, morphological attributes of degraded network segments have been obscured by network formation during the period of high cratering rates.

Although drainage density (D) has been recognized to have important terrestrial hydrologic implications (4), interpretation is complicated by variations induced by the scale of investigation and by the geomorphic processes governing channel initiation (5). At the macroscale (relevant for Mars imagery resolution) D on Earth is controlled by climate, measured either as mean annual precipitation (6) or as precipitation intensity (7). Very low D values occur only in arid regions because of lack of runoff. D increases to a maximum in semiarid regions, decreases to a minimum in humid regions, and increases to another maximum in the seasonally superhumid tropics.

For 24 small valley networks in the most dissected portions of the near-equatorial heavily cratered terrains of Mars, drainage densities range from 0.2 to 0.3 km/km^2 (8). Terrestrial macroscale drainage densities vary from approximatley 1 to 100 km/km^2 over the mean annual precipitation range of 1800 mm to 3000 mm (5,6). By analogy, the Mars values, if observed on Earth, would imply extremely arid conditions.

The pristine networks and pristine portions of compound networks show morphological attributes consistent with an origin by headward growth through spring sapping (1,9). On Earth spring sapping occurs where groundwater out-

flow undermines slopes. Where appropriately concentrated, the process contributes to the development of valleys. However, many terrestrial examples are actually relict features because environmental change has been induced by lowered water tables or by desiccating climatic conditions during the Pleistocene. In other cases, the results of spring-sapping processes are obscured through the modification of valley form by non-sapping morphogenic processes.

Valleys formed by spring sapping have been documented in the following regions: the Colorado Plateau (10), dissected volcanoes of Hawaii (11,12) and other oceanic islands, the Gilf Kebir Plateau of Egypt (13,14), and the Arnhemland Plateau of northern Australia (15,16). The valley networks of these regions share the following attributes: theater-like valley heads, structural control of network segments, steep valley sides and flat floors, a low degree of interfluve dissection, short tributaries, relatively constant downstream valley width, irregular junction angle relationships, local hanging valleys, elongate valley shape, and long, narrow interfluves. These properties characterize valley networks in many terrestrial landscapes, implying perhaps that ancient sapping processes may have played a significant role in the early phases of valley development. Unfortunately, because valleys result from the removal of much of the evidence for their antecedent conditions, the precise origins of many terrestrial valleys remain nearly as enigmatic today as they were in the time of James Hutton.

The extrapolation of geomorphic data on terrestrial valleys to the valley networks of Mars has a double jeopardy. First, the origin of the terrestrial valleys is, by no means, well understood. Second, the Martian valleys have unique attributes that may derive from rock types or processes that have no obvious terrestrial analog. The latter include megaregolith materials underlying the heavily cratered plateaus. Ground-water and ground-ice characteristics of the megaregolith may be citical to valley formation aided by ancient ground-water flow. Poleward of the equatorial zone, Martian valleys show evidence of modification by periglacial processes. Periglacial mechanisms of valley formation deserve more attention by Mars investigators.

The German "climatic school" of geomorphology holds that the most rapid process of terrestrial valley formation is the "Eisrinde effect", which occurs in regions of periglacial activity (17). The Eisrinde (ice rind) is the uppermost zone of permafrost which extends beneath braided meltwater channels in subpolar areas such as Svalbard (Spitzbergen). Seasonal melting and freezing beneath the stream bed concentrates mechanical weathering of bedrock at precisely the point where annual melt-season floods can remove the generated detritus. The result can be extremely rapid degradation, as much as 3000 mm/1000 yr. By contrast modern rates of terrestrial landscape degradation range from 50 to 500 mm/1000 yr (18).

If valleys can form on Mars by processes similar to the "Eisrinde effect", then the paleohydrologic implications of the valleys may not be as extreme as implied by models that use rainfall to generate overland flow or recharge aquifers. Nor is it necessary to justify long, continuous flow of surface water (19,20). Instead water can be transported in the frozen state. The phase changes necessary for freeze-thaw activity and/or surface

streamflow can be generated by insolation changes associated with orbital parameters (21) or with geothermal effects, such as might be associated with impact (22) or with the volcanic emplacement of the intercrater plains. Thus, it is appropriate to specify the most conservation deviation from modern hydrologic conditions on Mars that could account for the ancient epoch of valley formation.

The following difficulties must be kept in mind when extrapolating terrestrial experience to paleohydrologic conditions on Mars: 1. Most predictive relationships for terrestrial systems are empirical, ie. derived from correlations of terrestrial morphological variables (responses) to measured hydrologic parameters. The different environmental conditions on Mars preclude a direct transfer of such relationships. 2. The Martian networks are relict valleys. However, most terrestrial studies have been done on channel networks. 3. Model studies on channel network growth, whether by sapping or overland flow, are extrapolated in scale to problems of valley origin on Mars.

REFERENCES

1. D. Pieri, Science **210**, 895-897 (1980).
2. M.H. Carr and G.D. Clow, Icarus **48**, 91-117.
3. V.R. Baker and J.B. Partridge, in Lunar and Planetary Science XV (Lunar and Planetary Inst., Houston, 1984), pp. 25-26.
4. K.J. Gregory and D.E. Walling, Drainage Basin Form and Process (Edward Arnold, London, 1973).
5. A.D. Abrahams, Water Resources Res. **20**, 161-188 (1984).
6. K.J. Gregory and V. Gardiner, Zeitschrift für Geomorphologie **19**, 287-298 (1975).
7. K.J. Gregory, in Geomorphology and Climate, E. Derbyshire, Ed. (John Wiley, New York, 1976), pp. 289-315.
8. V.R. Baker and J.B. Partridge, in Lunar and Planetary Science XV (Lunar and Planetary Inst., Houston, 1984), pp. 23-24.
9. V.R. Baker, The Channels of Mars (University of Texas Press, Austin, 1982).
10. J.E. Laity, Physical Geography **4**, 103-125 (1983).
11. C.K. Wentworth, Journal of Geology **36**, 385-410 (1928).
12. V.R. Baker, N.A.S.A. Tech. Memorandum **82385**, 345-347 (1980).
13. R.F. Peel, Journal of Geomorphology **4**, 3-23 (1941).
14. T.A. Maxwell, in Desert Landforms of Southwest Egypt, F. El-Baz and T.A. Maxwell, Eds. (NASA Contr. Rept. 3611), pp. 281-300 (1982).
15. J.N. Jennings, Geographical Magazine **51**, 822-827.
16. V.R. Baker, N.A.S.A. Tech. Memorandum **81776**, 286-288 (1980).
17. J. Büdel, Climatic Geomorphology (Princeton Univ. Press, Princeton, 1982).
18. C.D. Ollier, Tectonics and Landforms (Longman, London, 1981).
19. D. Wallace and C. Sagan, Icarus **39**, 385-400 (1979).
20. M.H. Carr, Icarus **56**, 476-495 (1983).
21. W.P. Ward, Jour. Geophys. Res. **79**, 3375-3386 (1974).
22. H.E. Newsom, Icarus **44**, 207-216 (1980).

FLUVIAL DRAINAGE BASINS AND VALLEY NETWORKS: EASTERN MARGARITIFER SINUS, MARS

BOOTHROYD, Jon C., and GRANT, John A., Dept. of Geology, University of Rhode Island, Kingston, RI 02881

The fluvial drainage of the eastern Margaritifer Sinus (MC-19NE, SE) and northeastern Argyre (MC-26NE) Quadrangles is dominated by two major longitudinal valley networks (Pieri, 1980; Baker, 1982); the Parana/Loire system on the east, and the Samara Himera system to the west. We believe that both of these drainages are through-going to the northwest and debouch into Margaritifer Chaos (general location: 12S, 22.5W) (Fig. 1).

The Parana/Loire drainage is bounded on the east in part by an ancient multi-ringed impact basin (Schultz et al., 1982) The Parana multi-digitate network drains northwest into a depositional basin, and impact basin floor, characterized by positive relief chaos (pingos?). We believe that Loire Vallis heads in the basin; thus Parana and Loire Valles may be treated as one system. Samara Valles heads in the northeastern Argyre Quadrangle and extends as a major trunk valley to the northwest. Samara Valles cuts through the hills forming one of the concentric rings of the Ladon impact basin (Schultz et al., 1982), and joins the Himera drainage to trend in a more northerly direction to Margaritifer Chaos. We consider the downstream portion of Himera to be part of the Samara system.

Mapping with stereo pairs has allowed not only the delineation of the major drainages, but also the identification of the sub-basins of the two systems, as well as those areas that consist of internal drainage between the two large systems (Fig. 1). Table 1 gives the coordinates of the various sub-basins and initial determinations of drainage basin area. Samara Valles has about one-half the drainage basin area of the Colorado River, USA.

Both valley systems show a pattern of valley cutting followed by mantling of material derived either by eolian or mass-wasting events. There has been either an imcomplete mantling, a later rejuvenation of drainage, or both. Portions of the Samara Valles in particular show up to four stages of downcutting and development of terraces indicating, that the early fluvial history of Mars to be quite complex.

REFERENCES

Baker, V.R., 1982, The Channels of Mars: Austin, TX., University of Texas Press, 198 p.

Pieri, D.C., 1980, Geomorphology of martian valleys: p. 1-160, in Advances in Planetary Geology, NASA Tech. Memo. TM 81979, 326 p.

Schultz, P.H., Schultz, R.A., and Rogers, J., 1982, The structure and evolution of ancient impact basins on Mars: Jour. Geophys. Res., v. 87, No. B12, p. 9803-9820.

TABLE 1

System	Drainage Basin Area
SAMARA	313295 Km^2
LOIRE/PARANA	222255 Km^2
PARANA	40420 Km^2

SAMARA			LOIRE/PARANA		
Sub-basins	Location (degrees)		Sub-basins	Location (degrees)	
	S Lat	W Long		S Lat	W Long
Himera Vallis	21	22	LP1	19.5	16.5
Oltis Valles	23.5	21	LP2	21.5	16
Clota Vallis	26.5	21	LP3	26	13
S1	26.5	19	Parana	23	9
S2	28.5 to 31	18 to 19.5	LP4	18.5	13.5
S3	28.5	18	LP5	18	15
S4	31	16	LP6	16	15
S5	31.5	9	LP7	17.5	16.5
S6	31	11.5			
S7	29	13.5			
S8	28	16			
S9	21	18			

Figure 1. Viking Orbiter mosaic of part of the Margaritifer Sinus (MC-19) and Argyre (MC-26NC, NE) Quadrangles showing area drained by Samara Valles and the Loire/Parana Valles systems. Sub-basins are labelled for both systems (part of Mosaic 211-5821).

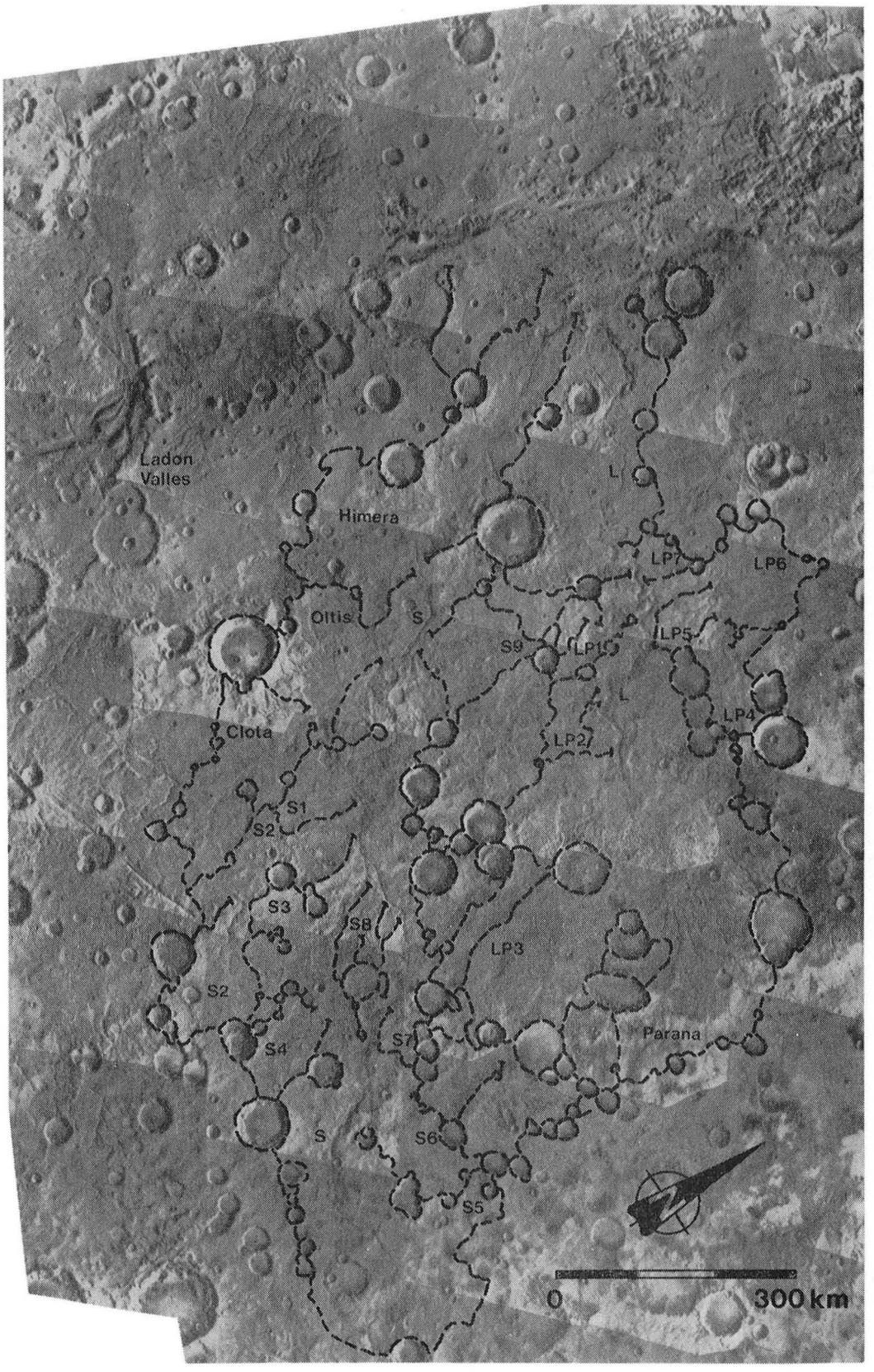
Ladon
Valles
Himera
Oltis
Clota
L
LP7
LP6
S
S9
LP1
LP5
L
LP4
LP2
S1
S2
S3
S8
LP3
S2
S4
S7
Parana
S
S6
S5
0
300 km

CATASTROPHIC-FLOOD FEATURES IN SWEDISH LAPLAND AS A TERRESTRIAL ANALOG FOR MARTIAN CHANNEL FORMS

Lisa A. Rossbacher* and Dallas D. Rhodes, Department of Geology, Whittier College, Whittier, CA 90608
(*Current address: Earth Sciences Department, California State Polytechnic University, Pomona, CA 91768)

Catastrophic flooding associated with deglaciation created unusual landscapes in several areas of northern Sweden (Hoppe, 1969; Daniel, 1975; Ulfstedt, 1979; Elfström, 1983). These areas in Swedish Lapland are distinguished by the large grain-size material that forms them. The presence of boulders at both Viking landing sites suggests the relevance of this analog (Binder et al., 1977; Mutch et al., 1977). The Channeled Scabland of eastern Washington is the most frequently cited analog, but the materials involved there are mostly loess or basalt.

One of these areas in Swedish Lapland was studied in the field in June 1984. The Båldakatj region lies in the upper reaches of the Pite River (Piteälven) at 66°20'N and 18°20'E, about 30 km south of the Arctic Circle. The entire area is underlain by the Precambrian Arvidsjaur granite, with surficial deposits of till and glaciofluvial material (Daniel, 1975). The till has been fluvially eroded into streamlined forms, which were first reported by Elfström (1983). The similar streamlined erosional remnants on Mars have been discussed at length in the literature (see Mars Channel Working Group, 1983, for a summary and review).

Reconstruction of the Båldakatj flood hydrology is difficult, although it has been attempted by Williams (1983). The flood that carved the Båldakatj erosional remnants was probably contained by ice walls, and therefore the upstream width of the delta lobe was assumed to represent water-surface width (Williams, 1983). The streamlined summits of the Båldakatj remnants suggest the water depth may have reached 6 to 10 m, and Williams has estimated the minimum depth around 18 m. Other approaches to reconstructing the paleohydrology indicate depths as much as 200 m. Williams (1983) considers these unrealistically high, but he also notes that Baker (1973) estimated a water depth up to 152 m in the Lake Missoula flood. Estimated peak discharges are $1.3 - 1.8 \times 10^4$ m^3/sec in Båldakatj (Williams, 1983), up to 2.1×10^7 m^3/sec in the Channeled Scabland (Baker, 1971, 1973), and 8.6×10^7 m^3/sec in the Ares Channel on Mars (Masursky et al., 1977).

One contribution of using the Båldakatj area as a terrestrial analog for Mars is the suggestion that other

features associated with the erosional remnants could also be expected on Mars. (1) The possibility of boulder deltas associated with the Martian outflow channels may be worth pursuing. Masursky et al. (1977) have already inferred the presence of boulders up to 2 m in diameter on the channel floor of Ares, similar to the boulders observed at the Viking 1 landing site (Mutch et al., 1977). (2) In addition, the Båldakatj area has a number of large rectangular blocks (2 - 8 m in length) that have been transported and imbricated on smaller, rounded boulders in the delta. Williams (1983) based part of his estimations of flow parameters on these boulders, but the mechanism of transport is not clear. A smaller flow might be capable of moving these large slabs if they can roll across the underlying, rounded boulders, acting as "ball bearings." (3) The meltwater channels between erosional remnants, 2 - 3 km upstream of the boulder delta, include pits up to 2 m deep that are surrounded by boulders on the upstream side. These may be large-scale bedforms created in the boulder-sized material, although Williams (1983) reported seeing no bedforms on the Båldakatj delta itself. Further study may provide additional information on catastrophic flooding in large-grained material. Similar sizes of material are certainly available on the Martian surface, and, if similar conditions and processes prevailed, these types of landforms might also be expected on Mars.

The Båldakatj area of Swedish Lapland offers terrestrial analogs for erosional remnants on Mars. Although the Båldakatj features are an order of magnitude or more smaller than the Martian forms, they were created in boulder-rich till that may be a good approximation of the near-surface material on Mars. The Båldakatj area also includes other landforms that could reasonably be expected to occur with the Martian outflow channels, including boulder deltas, large transported blocks, and large-scale bedforms.

This study has benefited from discussions in the field with Åsa Elfström and from the advice of Prof. Åke Sundborg. The work was supported by NASA grant NAGW-517 and the Faculty of Mathematics and Natural Sciences of the University of Uppsala, Sweden.

REFERENCES CITED

Baker, V.R., 1971, Paleohydrology of catastrophic Pleistocene flooding in eastern Washington: Geological Society of America Abstracts with Programs, v. 3, p. 497.

Baker, V.R., 1973, Paleohydrology and sedimentology of Lake Missoula flooding in eastern Washington: Geological Society of America Special Paper 144, 79 p.

Binder, A.B., and others, 1977, The geology of the Viking Lander 1 site: Journal of Geophysical Research, v. 82, p. 4439-4451.

Daniel, E., 1975, Glacialgeologi inom kartbladet Moskosel in mellersta Lappland: Sveriges Geologiska Undersökning, Ser. Ba, 121 p.

Elfström, Å., 1983, The Båldakatj boulder delta, Lapland, northern Sweden: Geografiska Annaler, v. 65A, p. 201-225.

Hoppe, G., 1969, Norrlandsälven naturvården: Yttande rörande Vindelälvens, Piteälvens, Kalixälvens och Torneälvs betydelse ur naturvårdssynpunkt: Statens Naturvårdsverk, Pub. 13, p. 2-27.

Mars Channel Working Group, 1983, Channels and valleys on Mars: Geological Society of America Bulletin, v. 94, p. 1035-1054.

Masursky, H., J.M. Boyce, A.L. Dial, G.G. Schaber, and M.E. Strobell, 1977, Classification and time of formation of Martian channels based on Viking data: Journal of Geophysical Research, v. 82, p. 4016-4038.

Mutch, T.A., and others, 1977, The geology of the Viking Lander 2 site: Journal of Geophysical Research, v. 82, p. 4452-4467.

Ulfstedt, A.-C., 1979, Geologiska kartbladet 27B Sulitelma: Statens Naturvårdsverk, PM 1230, 52 p.

Williams, G.P., 1983, Paleohydrological methods and some examples from Swedish fluvial environments, I - Cobble and boulder deposits: Geografiska Annaler, v. 65A, p. 227-243.

EXPERIMENTS AND ANALYSES OF THE FORMATION OF EROSIONAL SCOUR MARKS WITH IMPLICATIONS TO THE ORIGIN OF THE MARTIAN OUTFLOW CHANNELS

Paul D. Komar, College of Oceanography, Oregon State University, Corvallis, Oregon 97331.

A number of suggestions have been made concerning the nature of the processes responsible for the primary origin of the Martian outflow channels. These range widely from catastrophic water flows to glaciers. In order to define more precisely the nature of the erosional agent, my research has focused on three channel landforms which hold particular promise in this direction; the streamlined islands, scour marks and longitudinal grooves.

My research into the origin of the streamlined islands has been completed and published (Komar 1983, 1984). Analyses of the shapes of various types of streamlined landforms as well as flume experiments on the development of streamlined islands in water flows led to the conclusion that the streamlined landforms found within the outflow channels on Mars were formed by fully-turbulent flows at very high Reynolds numbers. Those results therefore pointed toward a water-erosion origin, supporting the many previous studies that have argued for such a formation. My present investigation of the erosional scour marks further supports these conclusions.

Erosional scour marks are observed adjacent to many flow obstacles within the outflow channels. These obstacles include bedrock projections, remnants of chaotic terrain blocks, and resistant crater rims, the crescent-shaped scour depressions occurring immediately upchannel from these obstacles (Baker 1978; 1982, p. 44-6). Such scour depressions commonly wrap around the blunt upstream end and sides of streamlined islands.

Baker (1978) has pointed out that the presence of these scour depressions within the Martian outflow channels provides strong evidence for a water-flow origin. Similar scour marks are formed by water flow around obstacles in rivers, and have been preserved in the Channeled Scablands (Baker 1973).

The objectives of the present study of erosional scour marks involve flume experiments to examine the details of scour patterns around a variety of obstacle shapes, and to review the engineering literature on the scour around bridge piers to determine whether those results might provide a quantitative evaluation of the flows which formed the scour marks in the outflow channels.

The flume experiments completed to date have examined the scour which develops around a circular "island" and around a streamlined "island" (having a lemniscate shape with length/width = 3.0). The islands themselves are non-erodable solids, but are surrounded by a fine-grained sediment bed. The scour patterns which occur around the circular island

agree with those produced by prototype bridge piers and by scale-model piers employed in the engineering studies. The scour patterns around the model streamlined islands correspond extremely well with those seen adjacent to the streamlined islands on Mars, providing still more confirmation for a water-flow origin. The scour around the streamlined island in the model tests showed little variation with the flow conditions (depth, velocity, etc.). However, these experiments have been limited to islands which extend above the water surface; different results might be expected in future experiments with a submerged island. Of special interest in the future experiments will be the scour around irregular obstacles, especially cases where the flow strikes an elongated object at an oblique angle. Scour will then be asymmetrical with a more distinctive pattern which changes with variations in flow velocity and depth. It is intended to focus on the modeling of irregular obstacles actually found within the outflow channels in order to determine whether the same scour patterns can be reproduced.

A vast engineering literature exists which reports on studies of scour around bridge piers. For the most part these are flume studies, there still being few prototype measurements. Breusers, Nicollet and Shen (1977) provide a useful review of the studies undertaken to that date, with an assessment of the state of the art. Important subsequent contributions include those by Melville and Raudkivi (1977), Jain and Fischer (1980), Blaisdell et al. (1981) and Raudkivi and Ettema (1983). These studies have examined a variety of pier shapes including circular, rectangular, elliptical and even the streamlined Joukowski Section. For our purposes, however, there are major limitations in the information provided by these studies. Most only report the maximum depth to which the scour extends, this being the main factor in the potential failure of the bridge pier and hence of engineering interest. Such vertical depths cannot be reliably evaluated for our Martian applications, so it is difficult to quantitatively apply most of the engineering results. The engineering studies also do not generally report on the overall pattern of the scour, so comparisons are not possible. Their results, however, do provide a great deal of useful information on the nature of the flow processes which produce the scouring and which flow and obstacle parameters control the amount of scour. These demonstrate that the most important factors are the cross-stream size of the obstacle, the bluntness of the upstream face, the flow depth, and the flow strength (velocity or stress) in comparison with that needed to entrain the channel sediment. Application of these results to the Martian scours indicates that the depth of flow in the outflow channels was small in comparison with the obstacle sizes and that the flow strength greatly exceeded that required for entraining the sediments found in the channel. Although these results offer only limited constraints on the conditions of the flow that formed the Martian channels, it is hoped that further analyses will provide better limits of possible ranges of flow conditions.

REFERENCES:

Baker, V.R. (1973) Paleohydraulogy and sedimentology of Lake Missoula flooding in eastern Washington: Geol. Soc. America Special Paper 144, 79 pp.

Baker, V.R. (1978) A preliminary assessment of the fluid erosional processes that shaped the Martian outflow channels: Proc. Lunar and Planetary Science Conf., 9th, p. 3205-3223.

Baker, V.R. (1982) The Channels of Mars: Univ. of Texas Press, Austin, 198 pp.

Blaisdell, F.W., C.L. Anderson and G.G. Hebaus (1981) Ultimate dimension of local scour: Jour. of the Hydraulics Div., ASCE, v. 107, HY3, p. 327-337.

Breusers, H.N.C., G. Nicollet and H.W. Shen (1977) Local scour around circular piers: Jour. of Hydraulic Research, v. 15, p. 211-251.

Jain, S.C., and E.F. Fisher (1980) Scour and bridge piers at high flow velocities: Jour. of the Hydraulics Div., ASCE, v. 106, HY11, p. 1827-1842.

Komar, P.D. (1983) The shapes of streamlined islands on Earth and Mars: Experiments and analysis of the least-drag form: Geology, v. 11, p. 651-654.

Komar, P.D. (1984) The lemniscate loop — comparisons with the shapes of streamlined landforms: Journal of Geology, v. 92, p. 133-145.

Melville, B.W., and A.J. Raudkivi (1977) Flow characteristics in local scour at bridge piers: Jour. of Hydraulic Research, v. 15, n. 4, p. 373-380.

Raudkivi, A.J., and R. Ettema (1983) Clear-water scour at cylindrical piers: Journal of Hydraulic Engineering, v. 109, n. 3, p. 338-350.

RELATIVE TIME-SCALE FOR CHANNELING EVENTS WITHIN CHAOTIC TERRAINS, MARGARITIFER SINUS, MARS

David Janke, Department of Geology, Arizona State University, Tempe, AZ 85287

A relative time scale for ordering channel and chaos forming events was constructed for areas within the Margaritifer Sinus region of Mars. Transection and superposition relationships of channels, chaotic terrain, and the surfaces surrounding them were used to create the relative time scale; crater density studies were not used.

Channels and chaos in contact with one another were treated as systems. These systems were in turn treated both separately (in order to understand internal relationships) and as members of the suite of martian erosional forms (in order to produce a combined, "master" time scale).

This study suggests that channeling events associated with chaotic terrain development occurred over an extended geomorphic period. The channels can be divided into three convenient groups: those that pre-date intercrater plains development (now seen as "ghosts" or highly segmented remnants); post-plains, pre-chasma systems; and those associated with the development of the Vallis Marineris chasmata. Channels within each group share morphologic characteristics. Post-plains, pre-chasma systems display a complex history of multiple channeling events, though the interval between these may be quite small. Although not all chaotic areas within Margaritifer Sinus are associated with outflow channels, almost all channels formed during the interval represented by the intercrater plains and Vallis Marineris are associated with chaotic areas. These areas show features interpreted to result from the shaping of materials by catastrophic floods.

No correlations with cyclic climatic changes, major geologic events in other regions on Mars, or triggering phenomena (for example, specific impact events) were found.

Page intentionally left blank

CHAPTER 10

PERIGLACIAL AND PERMAFROST PROCESSES

Page intentionally left blank

TERRESTRIAL ANALOG STUDIES FOR MARTIAN PATTERNED GROUND

Lisa A. Rossbacher, Earth Science Department, California State Polytechnic University, Pomona, CA 91768

A group of related studies on patterned ground, including both field work and a method for quantitative analysis, may further understanding of the Martian processes that created these features.

A recurring problem in understanding Martian patterned ground has been explaining its large size. Terrestrial patterned ground in Swedish Lapland offers an analog that may help explain this. In cold, arid regions with strong winds, polygonal features are accentuated parallel to the dominant wind direction (Rapp and Annersten, 1969). Similar effects have also been noted in Spitsbergen (Davies, 1961; Åkerman, 1983). A preferred orientation of polygonal troughs has been noted before on Mars, but the cause was interpreted as tectonic (Pechmann, 1980). Preliminary results of a comparison between Martian polygonal troughs and dominant wind directions (Ward, 1978) suggests a good correlation. This evolutionary model involving aeolian modification of Martian polygonal ground can help explain the large size of the features without requiring multiple, deep freeze-thaw cycles. A single freezing episode with thermal-contraction cracking, followed by strong wind erosion, could explain the development of large-scale Martian polygons. This is especially useful in view of the recent conclusion by Fanale and Clark (1983) that freeze-thaw cycles have not been important in Mars history.

A well-established geographical technique, nearest-neighbor analysis, can be modified and applied to the distribution of patterned ground on Earth and Mars. The procedure determines the R-statistic, which reflects the degree to which an observation departs from an expected random pattern (Clark and Evans, 1954; Vitek, 1973). The R-statistic is independent of scale, and therefore it can be applied to any size of type of pattern; patterns of different scale can not only be described statistically, but they can also be compared with each other. Preliminary results indicate that there may be a correlation between the R-statistic and the process (thermal contraction vs. ice wedging) that created the polygons.

A small lake along the Pite River (Pitedälven) in Swedish Lapland displays extremely well-sorted patterned ground on its floor (Fig. 1). The lake is near the town of Moskosel, and it is located at 65°33'N, 19°50'E. It has previously only been noted in passing in the literature (Daniel, 1975).

Fig. 1. Sorted patterned ground on lake floor in Moskosel area, Swedish Lapland. The polygons average about 2.5 m across; the largest boulders shown here are approximately 1 m in length. The fine-grained material in the center of the photo has cracks intersecting at 120° angles. At the time this photo was taken (June 1984), the water was 0.3 m deep.

The patterns are dominantly sorted circles and range from 1.0 to 4.0 m across. Detailed mapping of the lake floor, including cross sections and augering, indicates an average depth of sorting of about 0.3 m. This corresponds well with the depth of sorting of 0.45 m predicted from the Rayleigh convection model of Ray et al. (1983). Further significance of the development of sorted patterns under conditions other than air-soil interface must still be studied.

These studies have already contributed a new technique for quantitative description of patterned ground and a preliminary model explaining the evolution of Martian patterned ground. Continued work may provide a correlation between polygonal patterns and their origin and a better understanding of sorting processes in a variety of environments.

This work has been funded by NASA Planetary Geology Program grant NAGW-517; it has also been supported by the

Faculty of Mathematics and Natural Sciences of the University of Uppsala, Sweden.

REFERENCES CITED

Åkerman, J., 1983, Notes concerning the vegetation on deflation surfaces, Kapp Linné, Spitsbergen: Polar Research, v. 1, n.s., p. 161-169.

Clark, P.J., and F.C. Evans, 1954, Distance to nearest neighbor as a measure of spatial relationships in populations: Ecology, v. 35, p. 445-452.

Daniel, E., 1975, Glacialgeologi inom kartbladet Moskosel: mellersta Lappland: Sveriges Geologiska Undersökning, Ser. Ba, Nr. 25.

Davies, W.E., 1961, Surface features of permafrost in arid areas: Folia Geographica Danica, v. 9, p. 48-56.

Fanale, F.P., and R.C. Clark, 1983, Solar System ices and Mars permafrost: Proceedings, 4th International Conference on Permafrost.

Pechmann, J.C., 1980, The origin of polygonal troughs on the Northern Plains of Mars: Icarus, v. 42, p. 185-210.

Rapp, A., and L. Annersten, 1969, Permafrost and tundra polygons in northern Sweden, in The Periglacial Environment, T.L. Péwé (ed.), p. 65-91: McGill-Queen's University Press (Montreal).

Ray, R.J., W.B. Krantz, T.N. Caine, and R.D. Gunn, 1983, A model for sorted patterned-ground regularity: Journal of Glaciology, v. 29, p. 317-337.

Vitek, J.D., 1973, Patterned ground: A quantitative analysis of pattern: Proceedings, Association of American Geographers, v. 5, p. 272-275.

Ward, A.W., 1978, Windforms and wind trends on Mars: An evaluation of Martian surficial geology from Mariner 9 and Viking spacecraft television images: Ph.D. dissertation, University of Washington (Seattle), 201 p.

ORIGIN OF MARTIAN POLYGONAL TERRAIN: PRELIMINARY RESULTS

George E. McGill, Department of Geology and Geography,
University of Massachusetts, Amherst, MA 01003

Pechmann (1980) published a review of the morphological characteristics of martian "polygonal terrain", and of the fractures defining the "polygons". He also critically evaluated the several hypotheses proposed by others to explain this terrain, and very effectively eliminated three of these (contraction cracking of cooling lava, contraction cracking of dessicating clay, and frost wedging) as being mechanically unsound processes at the scale necessary to form the martian polygons. The fourth hypothesis, tectonic fracturing, is feasible, but Pechmann found no independent evidence to support or constrain a tectonic model. To my knowledge, no one has improved on this state of affairs since Pechmann's paper. The polygonal terrain discussed by Pechmann and treated in this abstract is specifically limited to those areas in the Acidalia Planitia, Elysium Planitia, and Utopia Planitia regions of the northern plains of Mars. There are other "polygonal terrains" that differ from these and that are very likely due to different processes (e.g., Luccitta, 1983).

My work so far has been limited to the polygonal terrain of Adamas Labyrinthus, found on the MC-6SE, MC-7SW, MC-14NW and MC-14NE subquadrangles. This polygonal terrain was referred to as occurring in the Elysium Planitia region by Pechmann (1980). Two closely related projects are underway simultaneously:

1. Determination of the age relationships between the fractures defining the polygons and the material making up the polygonal terrain. This involves detailed mapping, with the relative ages of key map units and the fractures determined by superposition and crater counts.
2. Development of new or modified genetic hypotheses that are consistent with the mechanical constraints.

As is to be expected, only a fraction of the craters superposed on the material that is fractured are properly located to determine the relative ages of fractures and craters; but in Adamas Labyrinthus, this fraction includes a large number of craters. Almost all of these properly located craters clearly interrupt the continuity of one or more of the fractures bounding polygons. Figure 1 illustrates the typical situation for large craters; these craters obliterate entire portions of the polygonal pattern and thus must be younger than the fractures. Smaller craters (diameters less than about one km) on higher resolution images are less commonly in contact with fractures, but those that are also are younger. A few craters yield ambiguous results because only the thin outer portion of the ejecta blanket intersects a fracture (Fig. 1); in such places, it is not clear if the thin blanket partially fills an older fracture or if the fracture displaces the blanket. There are no unambiguous cases of polygon fractures cutting craters.

The conclusion derived from these crater superposition relationships is that the fractures defining the polygons are the same age as the fractured material. A count of 134 craters between 0.7 and 15 km in diameter superposed on this material yields a cumulative diameter/frequency plot that fits the Neukum and Wise (1976) production curve for craters between 4 and 13 km in diameter. Projecting this portion of the plot along the Neukum and Wise curve yields a crater age for polygonal terrain of 7500 craters $\geq$ 1 km in diameter per 10^6 km^2. This is the best estimate of the age of the fractures as well. A check on this conclusion is provided by the plains materials east of Adamas Labyrinthus; these materials are superposed on the polygonal terrain, clearly truncating the fractures bounding the polygons. Thus both the polygonal terrain and the fractures are older than the plains. A count of 65 craters from 0.9 to 22 km in diameter fits the Neukum and Wise production curve for craters between 4 and 9 km in diameter, and yields a crater age of 5200 for the plains materials. This must be the young limit for the age of the fractures.

If the fractures are the same age as the fractured material, then the fracturing process very likely is genetically related to the deposition of the material. Two existing hypotheses satisfy this constraint--dessication cracking of clays and contraction cracking of cooling lava--but Pechmann demonstrated that the large sizes of the polygons in question render these hypotheses mechanically unsound.

There is, however, a process not considered by earlier workers: compaction. Both water-saturated clays and ignimbrites will compact significantly after deposition. A thick deposit of either of these superposed on a cratered terrain will experience differential compaction producing local stretching and bending over crater rims and central peaks, or over any positive topographic feature for that matter. Preliminary calculations of the tensile stresses that would result from this differential compaction indicate that tensile fracturing of the surface would be expected under almost any reasonable combination of buried topography, thickness of deposit, and degree of compaction. For example, the common occurrence of circular fracture patterns within the polygonal terrain is consistent with differential compaction over crater rims, and is easily accounted for by the tensile stresses that would be reasonably expected to occur in such places.

The crater age of the Adamas Labyrinthus polygonal terrain correlates well with early Tharsis and Elysium volcanism and with at least some outflow channels (e.g., Neukum and Hiller, 1981); consequently, there is a potential source of large volumes of both wet clay and ignimbrite at about the right time.

Future work on these projects will include: 1) extending the mapping to the Acidalia Planitia polygonal terrain, 2) refining the basic differential-compaction model, 3) refining age dates in order to verify correlations with other events, 4) calculating probable volume of the deposits as a check on reasonableness, and 5) attempting

to explain quantitatively why differential compaction over buried topography should produce the pattern of fractures observed.

REFERENCES CITED

Lucchitta, B.K., Permafrost on Mars: polygonally fractured ground. Permafrost: 4th Int. Conf. Proc., 744-749, 1983.

Neukum, G. and Hiller, K., Martian ages. Jour. Geophys. Res., 86, 3097-3121, 1981.

Neukum, G., and Wise, D.U., Mars: a standard crater curve and possible new time scale. Science, 194, 1381-1387, 1976.

Pechmann, J.C., The origin of polygonal troughs on the northern plains of Mars. Icarus, 42, 185-210, 1980.

Fig. 1. Superposition of craters onto fractures bounding polygons. The craters at A and B clearly interrupt the overall pattern of fracturing, and thus must be younger; the crater at C yields an ambiguous result because only the thin periphery of its ejecta blanket intersects a fracture, and the image resolution is not adequate to determine if the blanket is faulted or if it drapes over the wall of the fracture. The large crater at A is 17 km in diameter. Viking image 573A08 (in part).

RADIATION-DOMINATED SNOWMELT ON MARS

Gary D. Clow, U.S. Geological Survey, Menlo Park, CA 94025

The currently favored hypothesis for the formation of the martian valley networks is that they were cut by the action of running water. Carr [1] has shown that liquid water could flow hundreds of kilometers in ice-covered streams and that this result is remarkably insensitive to climate. However, the creation of sufficient volumes of liquid water to initiate streamflow remains a significant problem. Several global-climatic models [2,3,4,5] have shown that greenhouse warming will not lead to surface temperatures near the melting point of water until surface pressures are approximately 1 bar. The existence of the valley networks, coupled with the results of these studies, has been taken as evidence that the climate on Mars was radically different when the valleys formed. A recent study by Postawko [6] appears to make it even more difficult to generate liquid water on Mars through the greenhouse effect. In her latitudinally resolved climatic model, Postawko demonstrates that meridional heat transport will prevent equatorial temperatures from reaching 273 K for pressures as high as 3 bars, unless the planetary albedo was much lower than the present value or gases in addition to CO_2 and H_2O were responsible for the greenhouse effect.

In the present study, a set of microclimatic conditions conducive to the generation of liquid water is being sought to see whether their requirements are any less stringent than those suggested by the global-climatic models. In particular, I am investigating the melting of snow and ice in the equatorial zone (where the valley networks are preferentially situated) with a model that includes detailed infrared radiation transfer between the atmosphere and the snow, penetration of sunlight into the snow, sensible heat transfer to the atmosphere, and water vapor diffusion within the surface boundary layer. IR fluxes are calculated by using pressure and temperature dependent forms for the band absorptances of CO_2 and H_2O in the spectral range 50-2000 cm^{-1}. Sensible heat, water vapor, and momentum are transferred through the surface boundary layer by using a combination of molecular diffusion and stability-dependent eddy diffusion based on the Businger parametrization [7].

Steady-state solutions for the temperature profile within a snowpack reveal that the profile becomes nearly isothermal at depths greater than a few optical pathlengths in snow and that the deep-snow temperature is enhanced above the surface value by an amount dependent on the total solar flux absorbed by the snow and the ratio of the snow's optical pathlength to its thermal conductivity. Under clear skies, the steady-state deep-snow temperature can exceed the surface temperature in the equatorial zone by 35-40 K, assuming an albedo of 0.5, an optical pathlength of 0.1 m, and a thermal conductivity of 0.2 W m^{-1} K^{-1}. Surface temperatures are established by satisfying the energy balance at the snow-atmosphere interface and are expected to remain quite low except at relatively high pressures.

Consider the case of a stable airmass overlying a snowpack and assume that (1) the atmosphere is relatively "clear", (2) the air is nearly saturated with water up to an altitude of several kilometers, and (3) the air is in thermal equilibrium with the surface. The radiation available for snowmelt is maximized under these conditions. Furthermore, assume that the windspeed is approximately 1 m s^{-1} at 50 m above the surface since the rate of energy loss through sublimation and sensible heat transfer to the air is minimized for such winds when using the stability-dependent diffusion rates. Preliminary results, using the mean annual solar flux at the equator, an albedo of 0.5, an optical depth in snow of 0.1 m, and a thermal conductivity of 0.2 W m^{-1} K^{-1}, show that equilibrium surface temperatures remain below 210 K for pressures as high as 100 mb. However, at 300 mb the net radiation flux is so intense that snowmelt is pervasive. Using comparable conditions at 30 mb and latitude 30°S, the mean annual surface temperature is found to be only 189 K, whereas the temperature deep within the snowpack is 223 K. Using the 30 mb mean-annual-temperature profile as a starting point, Mars was allowed to proceed through its orbit, with the result that the 273 K isotherm was reached within the snowpack before midsummer despite the cold temperatures very deep within the profile. Although various aspects of this snowmelt model are not yet complete, results thus far indicate that liquid water can be generated through snowmelt at pressures considerably less than 1 to 3 bars.

References

[1] Carr, M.H., 1983, Stability of streams and lakes on Mars, Icarus, 56, p. 476-495.

[2] Pollack, J.B., 1979, Climatic change on the terrestrial planets, Icarus, 37, p. 479-553.

[3] Cess, R.D., Ramanathan, V., and Owen T., 1980, The martian paleoclimate and enhanced atmospheric carbon dioxide, Icarus, 41, p. 159-165.

[4] Toon, O.B., Pollack, J.B., Ward, W., Burns, J.A., and Bilski, K., 1980, The astronomical theory of climatic change on Mars, Icarus, 44, p. 552-607.

[5] Hoffert, M.I., Callegari, A.J., Hsieh, C.T., and Ziegler, W., 1981, Liquid water on Mars: an energy balance climate model for CO_2/H_2O atmospheres, Icarus, 47, p.112-129.

[6] Postawko, S.E., 1983, Martian paleoclimate, Ph.D. thesis, University of Michigan, 147 pp.

[7] Businger, J.A., Wyngaard, J.C., Izumi, Y., and Bradley, E.F., 1971, Flux-profile relationships in the atmospheric surface layer, J. Atmos. Sci., 28, p.181-189.

MARS: LONG TERM CHANGES IN THE STATE AND DISTRIBUTION OF H_2O

Fraser P. Fanale, James R. Salvail, Aaron P. Zent, and Susan E. Postawko
(Planetary Geosciences Division, Hawaii Inst. of Geophys., Univ. of Hawaii)

A model for H_2O distribution and migration on Mars has been formulated which takes into account: 1) thermal variations at all depths in the regolith due to variations in obliquity, eccentricity and the solar constant; 2) variations in atmospheric PH_2O caused by corresponding changes in polar surface insolation; and 3) the finite kinetics of H_2O migration in both the regolith and atmosphere. Results suggest that regolith H_2O transport rates are more strongly influenced by polar-controlled atmospheric PH_2O variations than variations in pore gas PH_2O brought about by thermal variations at the buried ice interface. The configuration of the ice interface as a function of assumed soil parameters and time is derived. Withdrawal of ice proceeds to various depths at latitudes $< 50°$ and is accompanied by filling of regolith pores at latitudes $> 50°$ and transfer of H_2O to the polar cap. The transfer has a somewhat oscillatory character, but only $< 1 g/cm^2$ is shifted into and out of the regolith during each obliquity cycle. The net irreversible and inexorable transfer of H_2O to higher latitudes involves between 1×10^6 km^3 and 1×10^7 km^3 of H_2O over the history of Mars for most reasonable sets of assumptions. This mass is comparable to the amount of material removed from deflated terrain at mid and low latitudes and to the mass of the polar cap. We conclude that this process combined with periodic thermal cycles played a major role in development of the fretted terrain, deflationary features in general, patterned ground, the north polar cap and the layered terrain.

PERMAFROST AND SUBSURFACE ICE IN THE SOLAR SYSTEM

Duwayne M. Anderson
Department of Geology
Texas A&M University

Atomic hydrogen, oxygen, and the hydroxyl radical are common throughout the universe. Water is known to be abundant in many portions of the solar system. It is known to be a major constituent of comets and it has been seen in the imagery of Mars, Ganymede, Callisto, in the rings of Saturn and on several of the Saturnian satellites. In most instances, sightings have been confirmed by spectroscopic evidence (i.g., Farmer et al., 1977; Farmer and Doms, 1979; Kieffer et al., 1977), or by other direct evidence (e.g., Biemann et al., 1977). In most occurrences, water ice is in close proximity to or in contact with silicate mineral matter. In many occurrences, the mineral matter is very finely divided. Although there are wide variations, maximum temperatures to which the ice is exposed, often are well below the normal freezing point of water. Temperatures on Mars are low enough to yield estimates of permanently frozen ground, ranging from a little more than 3 km at the equator to about 7 or 8 km at the poles. Data presently available, however, are insufficient to support any except general conclusions and hypothetical or speculative discussions (Anderson et al., 1973; Gatto and Anderson, 1975; Coradini and Flamini, 1979; Fanale et al., 1982; etc.). The properties and behavior of permafrost become important considerations when spacecraft landings or construction at desirable locations is contemplated.

When ice contacts silicate mineral surfaces, a liquid-like, transition zone is created. Its thickness ranges from several hundred Angstrom units at temperatures near 0 degrees C to about three Angstrom units at -150 degrees C. When soluble substances are present, the resulting brine enlarges the interfacial zone. When clays are involved, although the interfacial zone may be small, its extent is large. The unfrozen, interfacial water may amount to 100% or more by weight at a temperature of -5 degrees C. Methods are available for determination of the unfrozen water-temperature relationship (Anderson, 1967). When direct measurement is not feasible, unfrozen water contents may be estimated from the relationship

$$\ln w_u = a + b\ln S + cS^d\ln \theta$$

In this equation, S is the specific surface area in square meters per gram, θ is the temperature in degrees below 0 degrees C, and a, b, c and d are 0.2618, 0.5519, -1.449, -0.264, respectively (Anderson et al., 1973). The presence of this interfacial unfrozen water acts to confer plasticity to permafrost, enabling it to exhibit "creep" at all imposed levels of stress. Permafrost, thus, deforms slowly at all temperatures and exhibits different unconfined compressive strengths depending upon the mineral fabric and temperature, as illustrated in Figure 1.

On the microscopic level, the interfacial zone thickens or thins as the temperature changes. Melting and refreezing occur continually. Latent heat effects are, therefore, observed throughout a range of temperatures. Cooling curves for nontronite, the clay mineral cited as the most likely clay mineral on Mars, are shown in Figure 2, with and without the presence of a calcium chloride and sodium sulfate brine (Anderson and Tice, 1980). The curves are interpreted as follows: As the temperature is lowered from 280 degrees K through the normal freezing point of water, to about 266 degrees K, nothing is observed even though the sample has become cooled below its normal freezing point. Spontaneous nucleation occurs at about 265 degrees K in the case of the clay with the highest water content (about 40% water by weight). Nucleation is accompanied by the release of latent heat, registered in arbitrary intensity units by a scanning calorimeter (DSC). As the temperature falls, freezing becomes more complete. In samples at lower water contents, similar results are observed, except that the magnitude of the initial exotherm caused by the release of the latent heat of freezing diminishes with diminishing water content. All the curves exhibit one or more low temperature exotherms at temperatures between 230 degrees K and 240 degrees K. These low temperature exotherms are virtually independent of water content, although they tend to become more complex at the lowest water contents.

Results obtained on the same sample (containing 3% by weight of calcium chloride and 3% by weight of sodium sulfate) at various water contents are shown in Figure 2b. The curves are similar to those of Figure 2a, except that the temperature of initial nucleation is lower because of the brine created by these solutes. A distinct second exotherm is seen to accompany the first but trails it by 12 degrees to 15 degrees K. The low temperature exotherm observed in the case of the salt free clays are not visible. These data illustrate the complex behavior of mixtures of fine grain silicate minerals and water at low temperatures. Deformation due to creep under sustained stress is the

dominant geotechnical feature of permafrost and frozen earth materials. The rate of creep under a given load is dependent upon the unfrozen water and ice contents as well as the mineralogy and physical state of the mineral matter present. Very wide ranges of behavior are observed as these factors are varied.

Very heavy loads can be supported by permafrost as long as it is protected from near melting temperatures. This normally can be insured by thermally isolating load-bearing structures from the permafrost. In addition, the load-bearing capacity of permafrost may be increased by lowering its temperature. Permafrost on Mars generally is colder than -50 degrees C. Consequently, the very high loading densities of Figure 2 may be safely employed in preliminary design considerations. Saline conditions, however, must be anticipated. The influence of soluble substances on liquid content may be estimated by the method described by Banin and Anderson (1974). Methods of predicting the strength and deformation characteristics of saline permafrost from unfrozen water contents are not yet available. This is a subject of continuing investigation.

Experimental outposts will be designed for installation on Mars by the early part of the 21st century. Unlike the moon, the Martian surface contains ice and unfrozen water or brine in varying proportions. The ability of this surface to sustain long term loads depend on the creep characteristics of the Martian permafrost, as they are determined by the characteristics of the mineral fabric, the temperature of the frozen ground, the ice and unfrozen water contents and the presence or absence of soluble materials. Sufficient information on the properties and behavior of terrestrial permafrost is available now for preliminary design purposes. The additional information needed to assure a reliable design can be obtained from experiments and measurements in terrestrial laboratories and from unmanned soft landers, or ballistic bodies instrumented and configured for this purpose.

REFERENCES

Anderson, D. M. (1967). The Interface Between Ice and Silicate Surfaces. Journal of Colloid and Interface Science, v. 25, pp. 174-191.

Anderson, D. M., L. W. Gatto and F. Ugolini (1973). An Examination of Mariner 6 and 7 Imagery for Evidence of Permafrost Terrain on Mars. International

Conference on Permafrost, 2'd Yakutsk, Siberia, N. American Contribution. National Academy of Sciences Pub., pp. 499-508.

Anderson, D. M. and A. R. Tice (1980). Low Temperature Phase Changes in Montmorillonite and Nontronite at High Water Contents and High Salt Contents. Cold Regions Science and Technology, v. 3, pp. 139-144.

Banin, A. and D. M. Anderson (1974). Effects of Salt Concentration Changes During Freezing on the Unfrozen Water Content of Porous Materials. J. Water Resources Research, v. 10, no. 1, pp. 124-128.

Biemann, K., J. Oro, P. Toulmin, III, L. E. Orgel, A.O. Nier, D. M. Anderson, P. G. Simmonds, D. Flory, A. V. Diaz, D.R. Rushneck, J. E. Biller, and A. L. Lafleur (1977). The Search for Organic Substances and Inorganic Volatile Compounds in the Surface of Mars. Journal of Geophysical Research, v. 82, no. 28, pp. 4641-4658.

Coradini, M. and E. Flamini (1979). A Thermodynamical Study of the Martian Permafrost. Journal of Geophysical Research, v. 84, pp. 8115-8130.

Fanale, F. P., J. R. Salvail, W. B. Banerdt and R. J. Saunders (1982). Mars: The Regolith-Atmosphere-Cap System and Climate Change. Icarus, v. 50, pp. 381-407.

Farmer, C. B., D. W. Davis, A. L. Holland, D. D. LaPort and P. E. Doms (1977). Mars: Water Vapor Observations from the Viking Orbiters. Journal of Geophysical Research, pp. 4225-4248.

Farmer, C. B. and P. E. Doms (1979). Global Seasonal Variations of Water Vapor on Mars and the Implications for Permafrost. Journal of Geophysical Research, v. 84, pp. 2881-2888.

Gatto, L. W. and D. M. Anderson (1975). Alaskan Thermokrast Terrain and Possible Martian Analog. Science, v. 188, no. 4185.

Kieffer, H. H., T. Z. Martin, A. R. Peterfreund, B. M. Jakosky, E. D. Miner, F. D. Palluconi (1977). Thermal and Albedo Mapping of Mars During the Viking Primary Mission, Journal of Geophysical Research, v. 84, pp. 4249-4291.

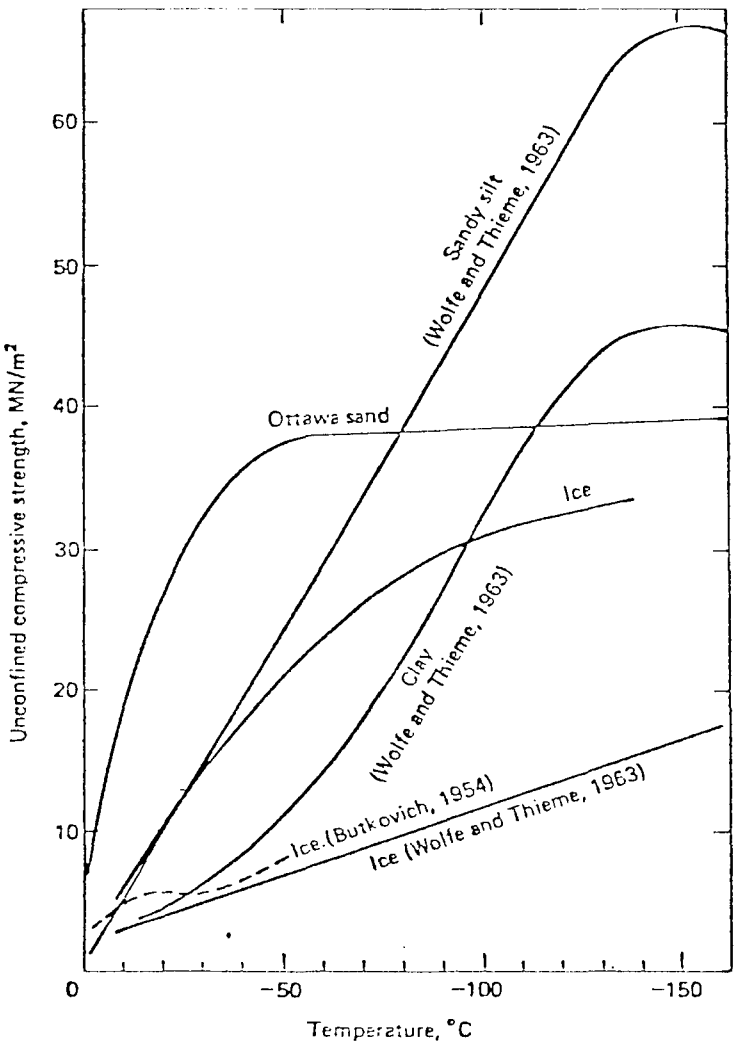

Figure 1. The unconfined compressive strength of several frozen soils and ice as a function of temperature (in Andersland and Anderson, 1978: after Sayles, 1966).

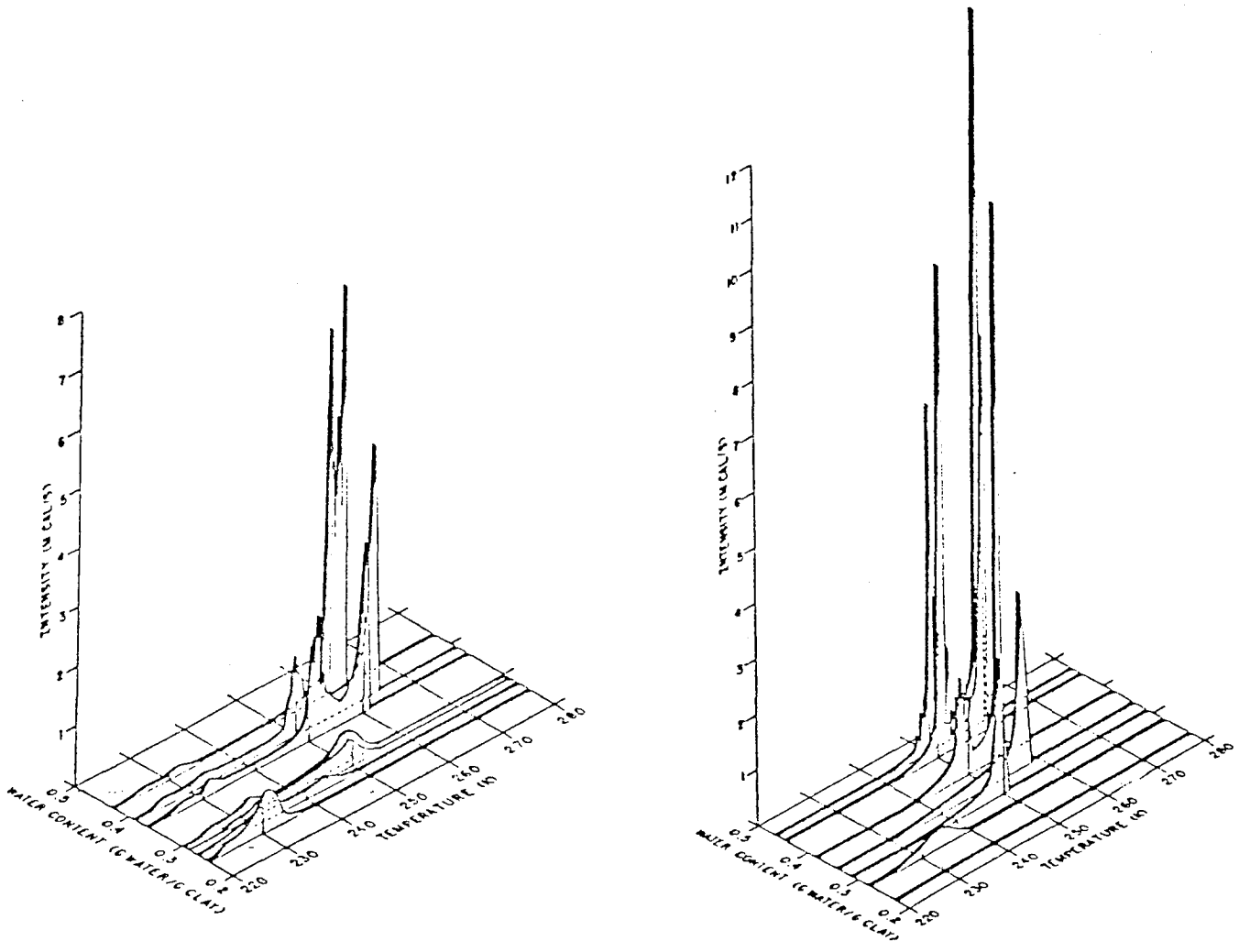

Figure 2. Differential scanning calorimeter cooling curves for nontronite clay at different water contents (a. without salt and, b. with 3% by weight of sodium sulfate and 3% by weight of calcium chloride). (Anderson and Tice, 1980)

Page intentionally left blank

CHAPTER 11

GEOMORPHOLOGY

Page intentionally left blank

MAPPING STRUCTURES CHARACTERISTIC OF THE HIGHLAND BOUNDARY SCARP ON MARS

Herbert Frey and Ann Marie Semeniuk, Geophysics Branch, Goddard Space Flight Center, Greenbelt, MD 20771

In an effort to shed some light on the processes which have produced the highlands/lowlands boundary "scarp" on Mars, we have mapped the global distributions of knobby terrain, detached and separated blocks and mesas, and craters larger than 10 km diameter. We represent these data as fractional areal percentages of the sample box, which is 2.5° high (latitude) by 5.0° wide (longitude) along north-south profiles between +65° and -45° every 5° in longitude. The southern limit of the mapping is dictated by the incompleteness of the 1:2,000,000 controlled photomosaic series which is the source for this work. The fractional area of crater interiors provides a way of quantitatively characterizing the boundary between cratered highlands and relatively uncratered plains. In the vicinity of the nominal "scarp" there is generally good agreement between the drop-off in fractional area of craters and a drop-off in topography. Contoured versions of the fractional area of crater interiors, even at the low resolution imposed by the sample box, show good agreement with the geologic mapping. The 5% contour line closely follows the boundary between the cratered highlands and northern plains as shown on the Geologic Map of Mars. In this mapping only whole crater interiors are counted. Variations in the fractional area which reflect preservation/destruction of the ancient cratered terrain can be quantitatively compared with the distribution of other features, as well as with topography, approach color or other data.

Knobby terrain includes a variety of irregular, positive relief features from large and generally isolated massifs that make up portions of the rims of the Argyre, Hellas and Isidis impact basins to closely spaced hills only 1-2 km wide. We are unable to distinguish at the scale of the controlled photomosaics any difference between the closely spaced irregular hills that make up part of the chaotic terrain and knobby terrain in many other areas. Assuming that chaotic terrain can be described as a combination of broken blocks and knobby terrain, the largest areal percentage of knobby terrain (45% of the sample box) is found in the chaos at the eastern portion of Eos Chasma at 45°W, 15°S. Other major occurances lie at 125°W, 30°N (35%), 25°W, 50°N (20%) and in Elysium-Amazonis at 175 to 185°W between 5 and 25°N. Note that this is southeast of and does not include the prominent Phlegra Montes knobby terrain, which despite its obvious nature is thinly distributed at 5-10% of the sampled area.

The knobby terrain which is mapped along the highland boundary in the Ismenius Lacus-Syrtis Major-Amenthes-Aeolis quadrangles from about 340°W, 45°N to 225°W, 5°S likewise has relatively low spatial density. In Deuteronilus-Protenilus-Nilosyrtis Mensae knobby terrain makes up only 15% of the sampled area. The 5% contour in areal percentage lies north of but immediately adjacent to the 5% contour in crater floor area. The knobby terrain constitutes a band about 8° wide (in latitude) and follows the trend of the cratered highland boundary so closely that there appears to be a clear association between the decrease in crater area

and increase in area of knobby terrain. Scattered occurances of this boundary association also lie at 10°W, 40°N and 25-30°W, 20N. Elsewhere the cratered highland "scarp" lacks the collar of knobby terrain.

Detached plateaus are a subset of separated or isolated blocks which may be detached pieces of the cratered highlands. Large pieces and large areal percentages of these detached pieces are found in the Deuteronilus-Prontenilus-Nilosyrtis Mensae region. Areal percentages reach 30% in the fretted terrain at 25-30°W, 40°N and 40% at 220°W, 5°S. Along the well-defined boundary scarp, detached plateau distributions overlie the knobby terrain distribution only between 275 to 335°W and 215 to 240°W. Here the peaks of the detached plateau distribution lie between the 5% contours in crater area and knobby terrain area and appear to be a transition between the cratered highlands and the adjacent more sparsely cratered knobby terrain. This overlap in the three distinctive types of terrain may be related to the gradual topographic slopes in these regions. Elsewhere where the gradients are steeper or much more gradual this close association of all three types of terrain does not occur.

Detailed comparison of the areal distributions of these features with elevation and topographic gradients is underway.

We have also located the most northerly occurance of detached plateaus and knobby terrain in order to test the plausibility of the hypothesis that much of the present day highland boundary "scarp" is due to southward migration of a former boundary. Significant occurances of both knobby terrain and small, generally isolated but sometimes very numerous detached plateaus do occur well to the north of the nominal highland boundary (as defined, for example, by the fractional area of craters). The northern most detached plateaus between 280 and 360°W lie generally on a line which parallels the cratered highland boundary, knobby terrain and general distribution of detached plateaus, but which lies 10-15° north of the cratered highland boundary. This line extends southeastward to 250°, through the region where the cratered highland boundary is interrupted by the Isidis Basin. Northern-most occurances of knobby terrain in this area have the same overall trend, and lie along or slightly northward of the line of detached plateaus. The pattern is similar to the distribution of the knobby and detached plateaus in the contoured areal percentages. Southward migration of the "scarp" from a line which lies 10-15° north of the present highland boundary seems a very real possibility between 250 and 360°W. However, eastward of 250°W where the cratered highland boundary continues southeastward through Amenthes and Aeolis, the northern most detached plateaus and knobby terrain do not follow the overall areal distribution of these features (which in general follows the cratered boundary). The northern most detached plateaus strike northeast from 250°W, swinging around the Elysium volcanic region to form a band at 50-60°N between 180 and 205°W. In this region the separation of northern most detached plateaus from the cratered highland boundary is over 60°, and simple southward migration from 50-60°N is not likely. The formation of the Elysium volcanic region has probably significantly affected the former and present location of whatever highland boundary scarp existed in this region.

Elsewhere the northern most detached plateaus and knobby terrain form a high latitude band generally between 55 and 65°N. Significant southward

excursions of this general line occur at 220-290°W and 20-60°W. These are regions of broad topographic minima locally and the trend of the lines of northern most features in general follows the contours of the USGS topography. Further study of the relation of the knobby terrain and detached plateaus to topography is underway, as is comparison of the distribution of these features with the approach color data (with T. Maxwell, NASM). We hope to elucidate the varying character of the present day highland boundary, learn something of its former possible location, and investigate the processes responsible for the evolution of this complex but fundamental tectonic feature on Mars.

INVESTIGATIONS OF THE MARS CRATERED TERRAIN - SMOOTH PLAINS BOUNDARY IN THE EASTERN EQUATORIAL REGION. Ted A. Maxwell and Jeffrey D. Corrigan,* Center for Earth and Planetary Studies, National Air and Space Museum, Smithsonian Institution, Washington, D.C. 20560 (*Planetary Geology Intern, present address: Dept. Geosciences, Univ. of Texas, Austin, TX.

As part of an ongoing study to place geologic constraints on, and to interpret the origin of the ancient cratered terrain - smooth plains boundary on Mars, we have been mapping structural features in the eastern hemisphere (Maxwell and Barnett, 1984), looking at wide-scale variations in aereal percentage of crater cover and distinctive landforms (Semeniuk and Frey, 1984a; Maxwell et al., 1984), and most recently, applying Viking 2 approach color data to classify surficial materials in this zone (Corrigan, 1984). Although the hemispheric asymmetry is a global scale characteristic of Mars, we are concentrating in the eastern hemisphere for these analyses to avoid problems of masking of the boundary by the younger volcanic plains of Tharsis, and the lack of a suitable topographic discontinuity due to the Tharsis rise. It is noteworthy, however, that some distinctive landforms associated with the boundary zone in the eastern hemisphere (isolated knobby hills) do occur well to the north of the Tharsis province (Semeniuk and Frey, 1984b).

Maps and a digitized data set for graben, scarps, ridges and elongate plateaus in the eastern hemisphere have been completed for 30° N to 30° S, and we are now extending the analysis into areas covered by Lambert projection orthophoto base mosaics. In the equatorial region, results indicate a marked change from the N oriented ridges north of the boundary to the NW orientations of those in the inter- and intracrater plains south of the boundary. The WNW orientation of the boundary itself is matched by similar orientations of graben and scarps in the southern terrain, and we are presently investigating the extent to which backwasting of the boundary zone may be structurally controlled.

In order to determine whether outlying plateaus and isolated knobby hills found north of the boundary are formed from material of the ancient cratered terrain, we have most recently been using the Viking 2 approach color data to discriminate surface materials in the eastern hemisphere (Corrigan, 1984). Initial data reduction, mosaicking and system corrections applied to the color data are described in Soderblom (1978), as well as observations of the very red ancient terrain and smooth volcanic ridged plains of low reflectance in the red wavelength (0.59 microns). To reduce correlation among the three spectral bands, a principal components analysis was applied to the color data in the manner described by Arvidson and Guiness (1982) and Jacobberger et al. (1983). Although Arvidson and Guiness applied this technique to color, albedo and thermal inertia data, we have concentrated initially on the color data alone for discrimination in response to the Soderblom et al. (1978) suggestion that the ridged plains and the ancient terrain differ in the red wavelengths. After rotating the data back into color coordinates, the resulting images were overlain onto the 1:2M controlled photomosaics, along with a plot of the quality of the original data.

In the southern half of the Amenthes quadrangle (MC-14), several correlations exist among surficial spectral reflectance and observed geologic units. Old terrain on the eastern rim of the Isidis basin is much redder than the smooth volcanic plains on either side of the rim, even though the plains unit east of the rim is located several kilometers higher than the plains on the floor of Isidis. Based on statistics derived from the color data, the plains within Isidis were found to differ (lower violet and green reflectance) from those north of the boundary zone. The color data for two highland areas, two areas containing erosional remnants surrounded by smooth plains, three areas of smooth plains, and two areas of smooth plains with knobby hills were further analyzed by performing basic statistics to

determine both inter- and intra-unit comparisons. The divide between the "pristine" highlands and the smooth plains containing erosional remnants is poorly distinguished in the color data of southeastern Amenthes, although one area of broad, smooth topped plateaus is distinctly blue on the color composites and is under further investigation. We are presently analyzing the relatively low spatial resolution (15-20 km) color data as a function of the percent of terrain type exposed (mapped at a much finer resolution) to determine spectral variations along the boundary zone as well as to determine the optimum spatial resolution needed on future missions to solve such significant geologic problems as the origin of the hemispheric dichotomy on Mars.

References

Arvidson, R.E. and Guiness, E.A., Classification of Surface units in the equatorial region of Mars based on Viking Orbiter color, albedo, and thermal data. Reports of Planetary Geol. Program - 1982, NASA TM-85127, p. 320-321 (1982).

Corrigan, J.D., Inquiries into the nature of the Martian highlands-lowlands boundary. Planetary Geology Summer Intern Report, to be published in Advances in Planetary Geology (1984).

Jacobberger, P.A., Arvidson, R.E., and Rashka, D.L., Applications of Landsat Multispectral scanner data and sediment spectral reflectance measurements to mapping of the Meatiq dome, Egypt. Geology, v. 11, p. 587-591 (1983).

Maxwell, T.A. and Barnett, S.J., Structure and morphology of the ancient cratered terrain-smooth plains boundary zone in the eastern hemisphere of Mars. Lunar and Planetary Science XV, p. 521-522 (1984).

Maxwell, T.A., Frey, H. and Semeniuk, A., Geomorphology and evolution of the ancient cratered terrains - smooth plains boundary of Mars. Geol. Soc. America Abstracts with Programs, in press (1984).

Semeniuk, A. and Frey, H., Distribution of characteristic features across the boundary scarp in Acidalia and Amazonis-Memnonia. Lunar and Planetary Science XV, p. 748-749 (1984a).

Semeniuk, A.M., and Frey, H., Detached plateaus and the highland boundary on Mars. Submitted to AGU Fall Ann. Mtg., (1984b).

Soderblom, L.A., Edwards, K., Eliason, E.A., Sanchez, E.M. and Charette, M.P., Global color variations on the Martian surface. Icarus, v.34, p. 446-464 (1978).

MARTIAN FRETTED TERRAIN MORPHOMETRY INTERPRETED USING PRINCIPAL COMPONENTS ANALYSIS

R. Craig Kochel, Department of Geology, Southern Illinois University, Carbondale, IL 62901

Martian fretted terrain was first described by (1) as an extensive area of complex topography characterized by smooth, flat-floored valleys and mesas separated by abrupt escarpments along the boundary of heavily cratered uplands. Fretted terrain is extensively developed in a 500-km-wide zone along the pronounced planetary dichotomy between 220 degrees W and 30 degrees W longitude (2), separating the sparsely cratered, low-relief, northern plains from the ancient, heavily cratered and hilly terrain to the south (Figure 1).

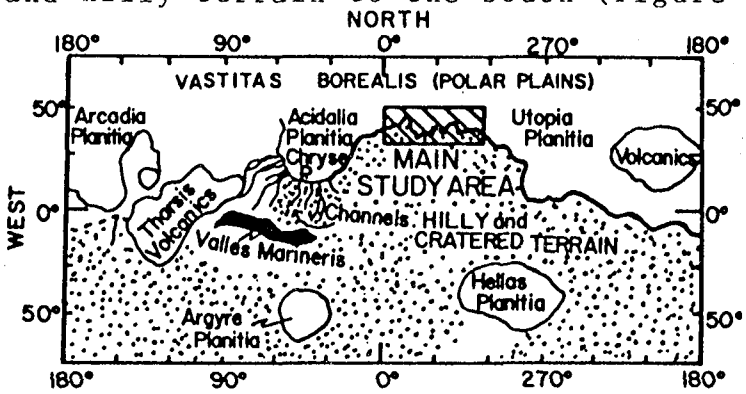

Figure 1. Generalized geomorphic map of mid-latitudes of Mars. The bold line marks the cratered terrain boundary (CTB). The box shows the study area and corresponds to the base maps of data mapped in Figure 2.

Sharp (1) suggested that the fretted terrain developed by degradation of the ancient cratered uplands terrain to the south. Geomorphic mapping of fretted landforms (3) shows an apparent continuum of landforms with increasing degradation away (to the north) from the cratered terrain boundary (CTB).

The Deuteronilus-Protonilus region of the fretted terrain between latitude 35 degrees N and 50 degrees N and between 305 degrees W and 350 degrees W longitude (Figure 1) was selected for quantitative landform study with the use of Principal Components Analysis (PCA). The morphometry of upland mesa remnants and debris aprons was digitized with respect to latitude, longitude, and distance from the CTB to address the following questions: 1) Are there spatial variations in the morphology of the residual mesas and debris aprons?; 2) Are there organized variations in morphology of waste forms with distance from the CTB?; 3) What relationships exist between the morphology of residual mesas and their associated debris aprons? and 4) Is there evidence for structural control in the degraded terrain?

Twenty-eight parameters were digitized for 178 mesa-debris apron assemblages which included: 1) shape and areal extent of the mesas and aprons along eight compass directions spaced 45 degrees apart; 2) distance from the CTB; 3) latitude and longitude of the center of each mesa; 4) trend of the long axis of each mesa; and 5) distance to nearest neighboring mesas along the eight compass directions.

PCA isolates diagnostic, recurrent, and independent modes of covariance into a new set of independent variables. The new independent variables created by PCA are transformed into a new coordinate system where the axes are linear combinations of the original variables and they are mutually orthogonal. The first eigenvector (E_1) explains the largest amount of variance in the system, while subsequent eigenvectors (E_2, E_3, etc.) explain successively smaller amounts. Using PCA in geomorphic studies provides a quantitative description of the major modes of variability in the landforms. Each principal component can be identified with a geomorphic (or geophysical) property of the data set. Spatial variation across the study site is mapped by contouring weightings of the eigenvectors (Figure 2) and summarized in Table 1.

PCA demonstrates that there are definable spatial variations in morphology with respect to longitude and latitude which suggest that the degradation along the CTB proceeded toward the southwest. PCA has also shown that there are organized relationships within the fretted landforms irrespective of their location. PCA runs excluding location parameters will further elucidate these relationships. Finally, PCA has indicated that an orientation of the degraded mesas exists which may be controlled by structure. The northwest trend of mesas agrees with other structural studies done in the region (4,5).

TABLE 1
EXPLANATION OF EIGENVECTORS IN FIGURE 2

Eigenvector	Summary of High (+) Loadings	Geomorphic Interpretation
E1 mesa size	mesa size, apron size, N latitudes, W longtitudes	mesas and aprons become larger toward the SW, degradation proceeded toward the SW
E2 neighbor	distance to neighbor mesas, N latitudes, W longtiudes	distance between mesas increases toward NE, degradation (age) increases toward NE
E3 mesa and apron size	apron size, SE long-axis orientations, smaller mesas	mesa size and apron size are inversely related independent of latitude and longtitude
E4 long axis	distance to neighbor mesa,NW oriented long	mesas are oriented to NW-this is probably controlled by structure

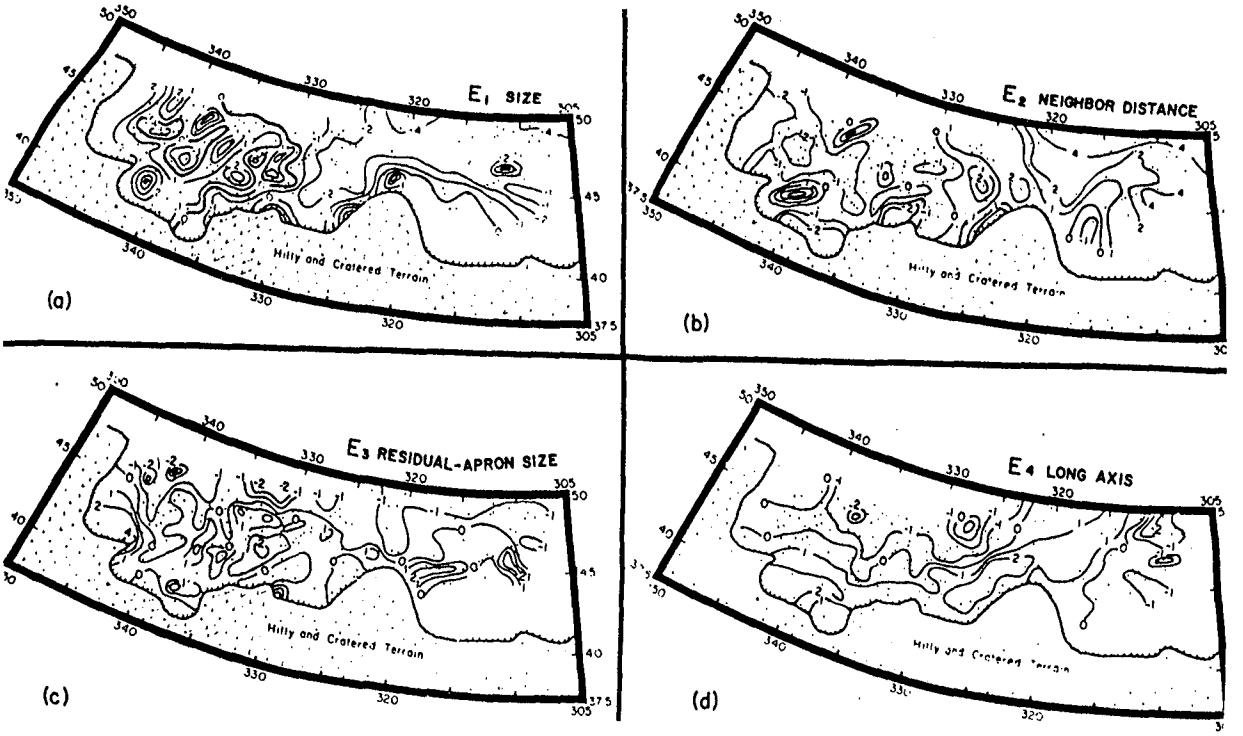

Figure 2. Contours of loadings of first four eigenvectors over the study area. See Table 1 for explanation.

REFERENCES:

(1) Sharp, R.P. (1973) Mars: Fretted and chaotic terrains, J. Geophys. Res., 78, 4073-4083.

(2) Mutch, T.A. Arvidson, R.G. Head, J.W. Jones, K.L. and Saunders, R.S. (1976) The Geology of Mars, Princeton Univ. Press, Princeton, 400.

(3) Kochel, R.C. and Peake, R.T. (1984) in press, Quantification of waste morphology in Martian fretted terrain: J. Geophys. Res.

(4) Chicarro, A.F. and Schultz, P.H. (1984) Global and regional ridge patterns on Mars: in Proc. Abs. Lunar and Planetary Science XV, p. 146-147.

(5) Maxwell, T.A. and Barnett, S.J. (1984) Structure and morphology of the ancient cratered terrain - smooth plains boundary zone in the eastern hemisphere of Mars: in Proc. Abs. Lunar and Planetary Science XV, p. 521-522.

DISTRIBUTION AND PROPERTIES OF LARGE SYMMETRIC KNOBS ON MARS

Herbert Frey, Jennifer Middleton and Ann Marie Semeniuk, Goddard Space Flight Center, Greenbelt, MD 20771

Knobby terrain on Mars exists in a variety of forms from small closely spaced hills to widely separated large massifs. Fractional areal distributions of knobby terrain (discussed in a companion abstract) range from over 40% of the sampled area in regions of chaotic terrain to less than 5% along the cratered highland boundary in Amenthes and Aeolis. Although knobs of all sizes exist, much of the terrain mapped as knobby consists of very small ($\lesssim$ 1 km) or very large (> 10 km) peaks. We have identified, mapped and measured all symmetric knobs with long dimensions greater than or equal to 10 km and classified them by shape. This preliminary report discusses spatial and dimensional distributions and shape characteristics of these features.

Between +65 and -45° latitude we identified 1634 symmetric knobs with long dimension D 10 km, using the 1:2,000,000 controlled photomosaic series. The most common shape is elliptical: 79% of the knobs fall into this category, 11% were circular or round, 6% were triangular or wedge-shaped and the remaining 4% other shapes (e.g., crescent or horseshoe). Figure 1 shows size frequency distributions for the global data set. All types show a roughly similar trend of rapidly decreasing number with increasing size, such that overall less than 10% of the knobs are larger than 20 km in long dimension. Circular knobs show the steepest fall-off in numbers with increasing diameter. Triangular knobs have a broader maximum with more than 65% falling in the 10-14 km range.

For simplicity in this preliminary report the knobs are spatially subdivided by quadrangle. Twelve quads have 50 or more large knobs and another 6 have at least 25 knobs larger than 10 km. Figure 2a shows the relative distributions among the mapped quadrangles. MC-5 (Ismenius Lacus) contains the largest percentage of the symmetric knobs, amounting to about 20% of the total population. These are concentrated along the cratered highland boundary in Deuteronilus-Protonilus Mensae where knobby terrain in general makes up only 10% of the surface (see companion abstract). Although a smaller total number exist in the adjacent quadrangle (MC-6), the large knobs are even more densely grouped in Nilosyrtis Mensae along the highland boundary, where again knobby terrain in general only occupies ~10% of the surface. Note in Figure 2b that elliptical knobs dominate in all quads and typically make up 80-100% of the knobs in a quadrangle. The major exception is MC-5 (which has the largest number of knobs, 306) where elliptical knobs are only 70% of the population. MC-1 and MC-30 were not mapped and MC 24-29 were mapped only to 45°S due to incompleteness of the 1:2,000,000 photomosaic series.

When subdivided by quadrangle, the size distributions for elliptical knobs (the most abundant type) show surprising variation. All but three quads have the principal peak in the 10-12 km, and most show a steep drop in the number of knobs with increasing size such that less than 10% of the knobs are larger than 20 km in the long dimension. But there are exceptions. MC-6, 13, 14 and 21, all of which include knobs along the highland boundary scarp near the Isidis Basin, have about 15% or more of the knobs larger than 20 km. MC-26, which includes knobs making up the

northern rim of the Argyre Basin, has a broad lopsided bell distribution of sizes with ~40% in the range 14-18 km, 15% in the 12-14 km bin and about 10% each in the 10-12 and 18-20 km bins. 25% of the elliptical MC-26 knobs are larger than 20 km. MC-8 and MC-23 have the principle peak in the 12-14 km bin and the secondary peak in the 10-12 km bin. These variations may indicate different populations of elliptical knobs, and require subdividing the knobs on other criteria (such as background geologic unit or terrain type).

There is additional evidence that multiple populations of elliptical knobs may exist. MC-15 (Elysium) and MC-8 (Amazonis) are adjacent quadrangles with a large number of elliptical knobs (108, 56 respectively). Knobby terrain in general is abundant in these quads, reaching 20-25% of the sampled area. MC-15 has a "normal" size distribution like that of the general population (Figure 1) and therefore is different from MC-8. But the elliptical knobs in both quads have similar shape-size characteristics. As shown in Figure 3, when the ratio of long to short dimension is plotted versus the size of the elliptical knob (long dimension), both groups tend toward a rapid increase in the ratio with increasing diameter. Ratios as high as 4.0 to 5.0 occur for diameters of only 18 km. The opposite extreme is shown by the elliptical knobs in MC-13, 14 and 26, which are largely concentrated along the rims of the Isidis and Argyre Basins. Here the knobs reach larger diameters (up to 34 km) but show a flat distribution of long/short diameter ratios which does not exceed about 3.0. Similar data for the other quads in which at least 50 elliptical knobs exist show a mixture of these two extremes. For example, in MC-29, 85% of the elliptical knobs follow the flat distribution and 15% lie in the small diameter (10-16 km), high ratio (2.5 to 4.0) region, and in MC-28, 18% lie in the small diameter (10-18 km), high ratio (2.5 to 4.0) region and 82% fall in the flat distribution (diameters out to 38 km, ratios less than 2.5)

Correlation of these properties of large knobs with background terran, proximity to major structures, topography and surface color data is underway.

FIGURE 1

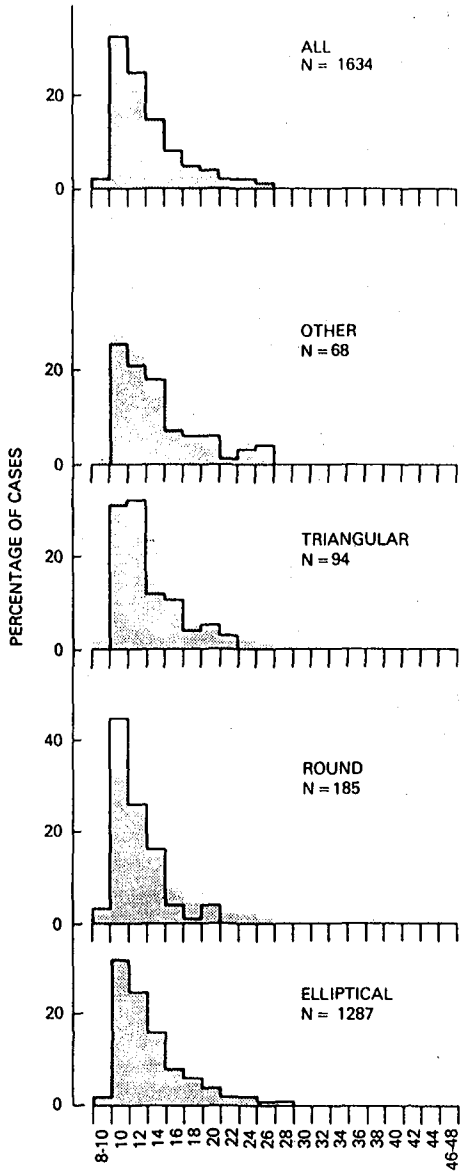

FIGURE 2

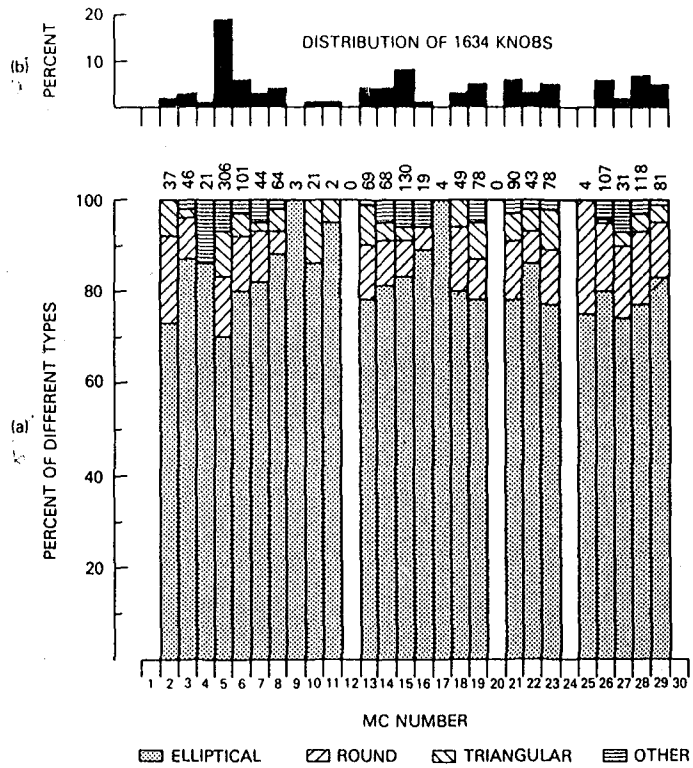

FIGURE 3

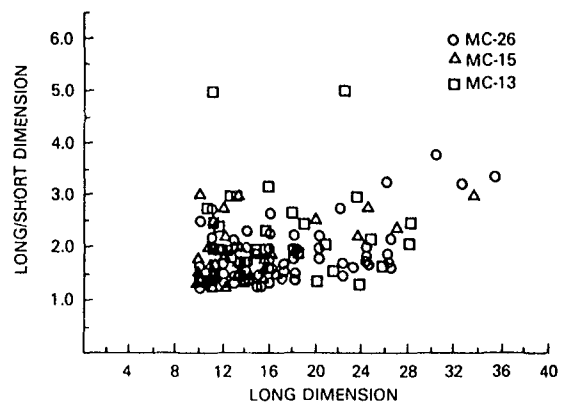

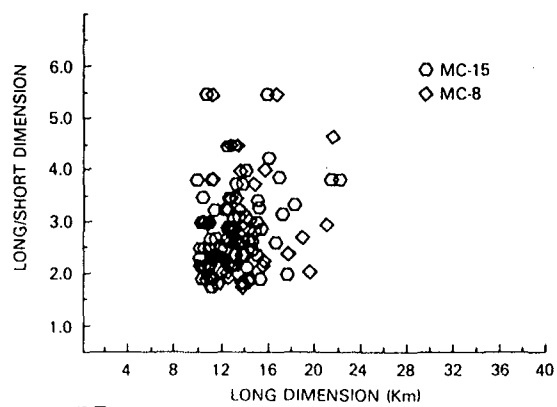

ENIGMATIC HILLS OF THE MOTTLED PLAINS, MARE ACIDALIUM QUADRANGLE (MC-4), MARS.

Nanci E. Witbeck[1] and James R. Underwood, Jr., Department of Geology, Thompson Hall, Kansas State University, Manhattan, KS 66506.

The mottled plains remain one of the most difficult units to define and interpret. Mariner 9 images of the mottled plains in Mare Acidalium quadrangle were blurred and most Viking images are medium or lower, resolution. The Viking images did, however, reveal hitherto unseen geomorphic, textural, and albedo variations within the mottled plains, previously mapped using Mariner 9 images (1). Mapping problems arise with increased resolution and number of morphologic variations (2). Boundaries between sub-units appear in most places, to be gradational. Determining whether textural changes reflect primary or secondary surface land forms characteristically is difficult (2).

These problems were recognized during recent geologic mapping in Mare Acidalium quadrangle (3, 4). Although the boundaries between all the units are gradational, four subdivisions were recognized within the mottled plains region. One of these subdivisions, which occurs between 58° - 65° N, 5° - 60° W, has been designated hummocky mottled plains. The unit is characterized by many small (<1 km), irregularly spaced dark hills surrounded by brighter material (Fig. 1). One very poor-quality, high-resolution Viking strip (528B01-04) indicates that some of these dark hills have circular summit depressions. Possible interpretations of origin of these hills include: cinder cones, volcanic domes, maar volcanoes, pseudocraters, impact craters, or pingos. The uncratered hills or knobs may be igneous plugs, volcanic necks, or the dark remnants of a hummocky, cratered surface protruding through a relatively bright eolian blanket. The presence, however, of the small dark hills on the floor of the large (130 km diameter) C_2 crater Lomonosov (65° N, 10° W), suggests that similar dark hills elsewhere also may be secondary.

Botts (5) designated as "bulbous plains" a unit (type area 72° N, 290° W) that has some similarities to the hummocky mottled plains southward in Mare Acidalium. He interpreted bright material as eolian, the small dark hills as volcanic.

---

[1]Branch of Astrogeology
U. S. Geological Survey
Flagstaff, AZ 86001

Farther north in the polar region, small dark hills are interpreted by Dial (6) to be volcanic but modified by permafrost activity.

On the best of the high-resolution images (528B01,04), very uncertain measurements were made for 14 dark hills of the diameter of the summit depressions and the diameter of the hills. The ratios of the diameters of the summit depression to the diameters of the hills range from 0.19 to 0.39; the arithmetic mean is 0.28.

Wood (7) reported this average ratio for 21 small (most <1 km diameter) martian craters to be 0.41. Frey and Jarosewich (8) reported an average ratio of 0.47 for 1913 small martian cones and suggested, based on an average crater/cone ratio of 0.47 for 87 Icelandic pseudocraters (9), that the martian cones that they had measured might be pseudocraters. The relatively low crater/cone ratio of 0.28 determined for the hummocky mottled plains does not compare well with that of the small features interpreted elsewhere on Mars to be volcanoes or pseudocraters, but does compare well with the average crater/cone ratio of 0.30 for 61 terrestrial cinder cones and a ratio of 0.27 for 19 terrestrial volconic domes reported by Pike and Clow (9). Wood (7) reported a somewhat higher crater/cone ratio of 0.39 for 163 terrestrial cinder cones, but Pike and Clow (9) reported a crater/cone ratio of 0.32 for 61 terrestrial cinder cones.

The few blurred, high-resolution images of the hummocky mottled plains of Mare Acidalium indicate that, although many of the small dark hills have summit depressions, apparently some do not and tend to be much less circular in plan than those with summit depressions. Probably the enigmatic small, dark hills of the hummocky mottled plains are polygenetic; higher resolution images will be required to solve the question of their origin

References

1. Underwood, J. R., Jr., and Trask, N. J., 1978, Geologic map of the Mare Acidalium quadrangle of Mars: U. S. Geol. Survey Misc. Inv. Map I-1048.
2. Scott, D. H., 1979, Geologic problems in the northern plains of Mars: Proc. Lunar Planet. Sci. Conf. 10th p. 3039-3054.
3. Witbeck, N. E., 1982, The geology of Mare Acidalium quadrangle, Mars: M. S. thesis, Kansas State University, 182 p.
4. Witbeck, N. E., 1982, The geology of Mare Acidalium quadrangle, Mars: Advances in Planetary Geology, NASA TM-86247, p. 219-419.
5. Botts, M. E., 1980, The stratigraphic sequence of volcanic and sedimentary units in the north polar region of Mars: NASA TM-81979, p. 265-236.
6. Dial, A. L., 1984, Geologic map of Mare Boreum quadrangle of Mars: U. S. Geol. Survey Misc. Inv. Map I-1640

(in press).
7. Wood, Charles A., 1979, Monogenetic volcanoes of the terrestrial planets: Proc. Lunar Planet. Sci. Conf. 10th, p. 2815-2840.
8. Frey, Herbert and Jarosewich, Martha, 1982, Subkilometer martian volcanoes: Properties and possible terrestrial anologs: Jour. Geophys. Res., v. 87, no. B 12, p. 9867-9879.
9. Pike, R. J. and Clow, G. D., 1981, Revised classification of terrestrial volcanoes and catalog of topographic dimensions, with new results on edifice volume: U. S. Geol. Survey Open File Rep., 81-1039.

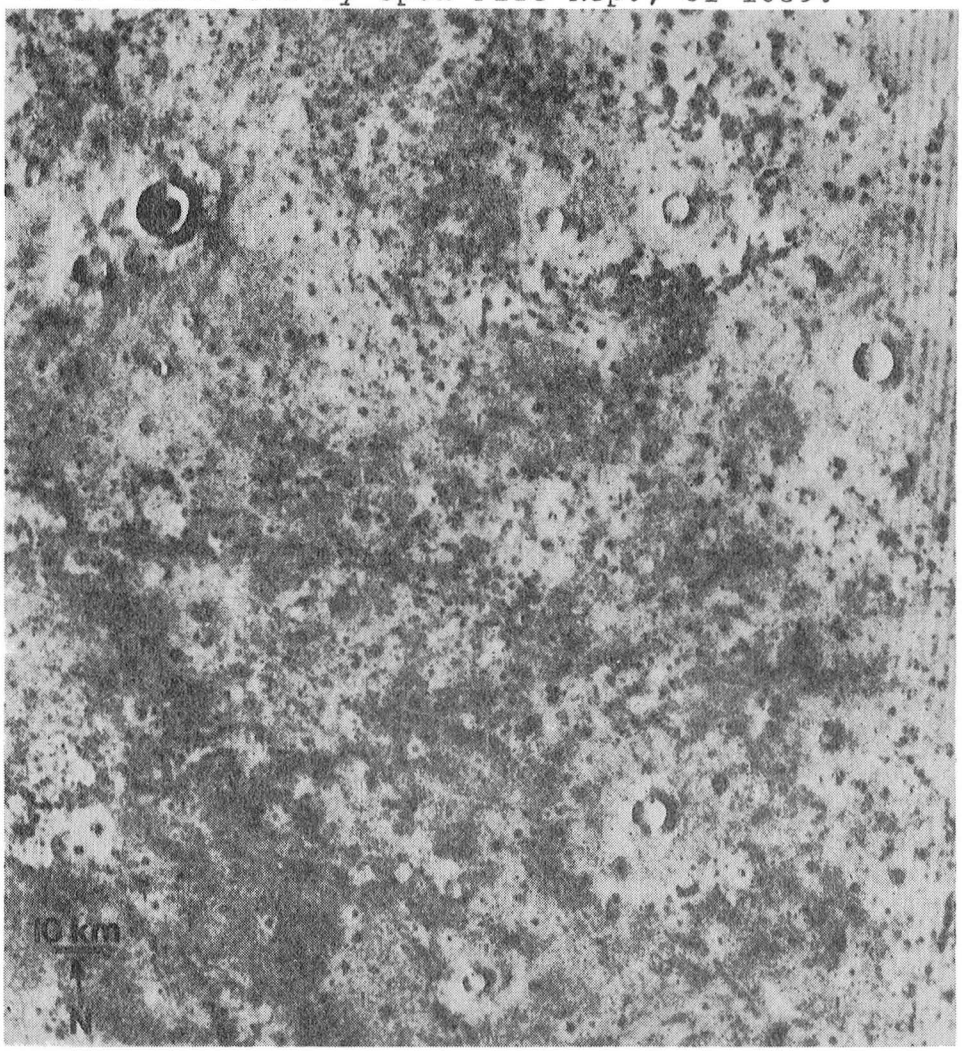

Figure 1. Hummocky mottled plains material. Small (<1 km diameter), dark hills scattered throughout the intercrater areas show no definitive alignments; image artifact along east margin. Viking frame 672B77 (62.7° N, 18.2° W).

GEOMORPHOLOGY AND GEOLOGY OF THE SOUTHWESTERN MARGARITIFER SINUS AND ARGYRE REGIONS OF MARS - I: GEOLOGICAL AND GEOMORPHOLOGICAL OVERVIEW, Timothy J. Parker and David C. Pieri, Jet Propulsion Laboratory, California Institute of Technology, Pasadena, CA 91109.

Based upon Viking Orbiter 1 images of the southwestern portion of the Margaritifer Sinus Quadrangle, the northwestern portion of the Argyre Quadrangle, and a small portion of the southeastern Coprates Quadrangle, three major mountainous or plateau units, seven plains units, and six units related to valley forming processes have been identified (see figure 1). This work is a continuation of previous work we have done with this region (Pieri and Parker, 1981). The photomosaic is oriented such that it provides good areal coverage of the upper Chryse Trough from Argyre Planitia to just above Margaritifer Chaos as well as of plains units on either side of the Trough. The photomosaic was compiled from Viking Orbiter 1 images ranging in resolution from approximately 150 to 300 meters per pixel printed at a scale of about 1:2,000,000. Additional mapping of Argyre Planitia from the extended Viking Orbiter Survey Mission images is currently under way to better understand the relationship between Argyre and the sediments and channel systems associated with it.

Mountain Massifs (M) are probably the oldest features within the map area, and perhaps on Mars itself. They represent remnants of large basin rims and possibly volcanic features which have been largely destroyed by erosion and subsequent impacts. *Hilly to Mountainous material* (Hm) is probably of similar origin to *Mountain Massifs* and ranges from isolated hilly remnants to mountainous terrain (not isolated massifs), which therefore includes some large crater rims such as those of Hale and Holden. Unlike *Mountain Massifs, Hilly to Mountainous material* ranges in age from very ancient to relatively recent. *Cratered Plateau material* (Plc) consists of ancient cratered terrain which, because of local relief, was probably not buried by sedimentary or volcanic deposition and was not removed by valley forming erosional processes. It has a slight hummocky or rolling texture and a somewhat higher albedo than surrounding units. Small valleys and structural lineaments within this unit have a "softened", relatively more degraded appearance than those of surrounding units. This unit may represent one of the earliest surfaces preserved on Mars after the initial heavy bombardment period, perhaps the equivalent of the lunar highlands. *Channeled and Subdued Plains Material* (Pcs) comprises a vast expanse of the northeastern portion of the map, and extends much farther to the northeast of the map area. Small valleys (Pieri, 1980; Mars Channel Working Group, 1983) are clearly the dominant features within this unit. These valleys are generally distinct throughout most of their extent but their terminations at either end are often poorly defined. The unit is also distinguished by its subdued appearance. Lineaments and wrinkle ridges are much less sharply defined here than in the *Smooth Plains material* (Ps, Pd, Pw,- see below), for example. *Grooved Plains material* (Pg) is confined, in the map area, to the region between Nirgal Vallis and Argyre's northern rim. It is characterized by numerous east-west graben and related structural lineaments. It may represent an old volcanic flood unit, similar to the lunar mare, as evidenced by its interaction with the Plc unit to the south, particularly around the large C1 crater which it almost surrounds. The Pg unit can be clearly seen to onlay the Plc unit here, indicating its flow character and younger age. *Grooved and Channeled Plains material* (Pgc), north of Nirgal Vallis, is similar in appearance to the Pg unit except for the presence of several small valleys along its southern and eastern sides. The *Smooth Plains material, Dark Smooth Plains material,* and *Wrinkled Plains material* (Ps, Pd, and Pw, respectively) are the most extensive units in the map area. Most of the extent of these units, from Nirgal Vallis eastward to its onlapping of the Pcs unit just east of Uzboi Vallis probably was formed during one or more mare-flooding events, and thus may be of comparable age. Isolated Ps units within crater floors, however, may be of widely different ages and formed either by interior volcanic flooding of the crater through fractures generated by the impact event, or by regional volcanic flooding of the crater rim. The Ps unit comprising the floor of Ladon Basin into which Ladon Valles and numerous small valleys flow and the Ps unit on the floor of Holden may be composed of channel sediments. The distinctive characteristic of these units is their overall smooth texture. Where wrinkle ridges and structural lineaments are present, they are generally sharp and clearly defined. *Channel Modified material* (Cm) represents previously

existent terrain which has been modified by the formation of major valleys (Uzboi, Ladon, and Nirgal) and their associated tributaries. *Channel Floor material* (Cf) was mapped separately for the large valleys to help distinguish the portion of the valley presumably occupied by flowing water from the remaining valley width. In the case of small valleys, the *Channel Floor material* alone was mapped to indicate their locations within major plains units and their morphology, rather than to classify them as separate from the plains units. In Ladon Valles, the *Channel Floor Material* is of two styles; the main, central floor which is continuous, and isolated terraced channel floors to either side of the main channel floor which were abandoned by down-cutting of the main channel. This latter unit is designated Cfh (for *High Channel Floor material*), represented in this area of the map only. These terraced channel floors represent flow around resistant hills which were streamlined by their activity. At the head of these *Streamlined Hills* (Hs) may be a dike or other resistant structure, as the heads of the hills align roughly with the local structural grain. Northwest of the mouth of Ladon Valles and the small valleys west of Ladon Valles is a relatively light albedo unit which appears to be *Channel Sediments* (Cs) deposited by the small valleys as they entered the lower energy environment of Ladon Basin north of Ladon Valles. The *Chaotic Terrain* (Cht), at the head of Ladon Valles north of Holden, is similar in texture and probably also in origin to that of Margaritifer Chaos to the north but on a much smaller scale. Its formation is believed to represent catastrophic collapse of water-bearing strata with subsequent flow through Ladon Valles. This *Chaotic Terrain* appears to have formed after the Holden impact, prior to which, we believe, Uzboi and Ladon were one continuous system. Within the Nereidum Montes of Argyre is an unusual, light albedo plains unit, *Argyre Plains material* (Pa), comprising the interior floor of the basin in the map area. It resembles terrestrial lacustrine deposits that have been deflated by aeolian activity but at a much larger scale. It may represent sediments left behind when an ancient Argyre sea evaporated. *Debris flows or landslides* (Db) have been identified in a few isolated instances in the map area. These occur within large craters and comprise a portion of the crater's rim. They appear to have been initiated by the impact forming the crater itself upon a weakness in the regional structural grain or by seismic activity along prominent tectonic lineaments. *Dunes* (D) are also found within some large craters in the map area. These dunes represent the youngest, probably presently active unit on Mars.

The most striking structural features are the east-west trending graben, faults, and related tectonic lineaments. These appear to be the result of north-south tensional stresses associated with the rifting of Vallis Marineris to the northwest. They are most numerous west of Uzboi Vallis (closer to the disturbance) but are present nevertheless throughout the map area. Radial and concentric fractures associated with large impacts are not readily apparent, but a few can be seen associated with the "fractured floor craters" within Ladon Basin in the north corner of the map, with the crater Holden, and with Argyre. Interestingly, the east-west lineament trend is still the most prominent trend in the mapped portion of Argyre. This suggests that the crustal shattering associated with the Argyre impact event favored pre-existing structural weaknesses or that the rifting was active after the event, or both. Wrinkle ridges trending primarily north-south (perpendicular to lineament trends), are present more or less throughout the map area but are most common in the volcanic plains units. This may be a result of the buckling of the comparatively thin, rigid volcanic units overlying thick, less competent units (regolith?) such as the *Cratered Plateau material* (Plc).

REFERENCES

Mars Channel Working Group, 1983, Channels and valleys on Mars: Geological Society of America Bulletin, Vol. 94, p. 1035-1054.

Pieri, D. C., 1980, Martian valleys: Morphology, distribution, age, and origin: Science, Vol. 210, p. 895-897.

Pieri, D. C. and Parker, T., 1981, Geologic mapping of martian valley systems I: Nirgal Vallis and vicinity: Reports of the Planetary Geology Program, 1981, NASA Tech. Memo 84211, p. 503.

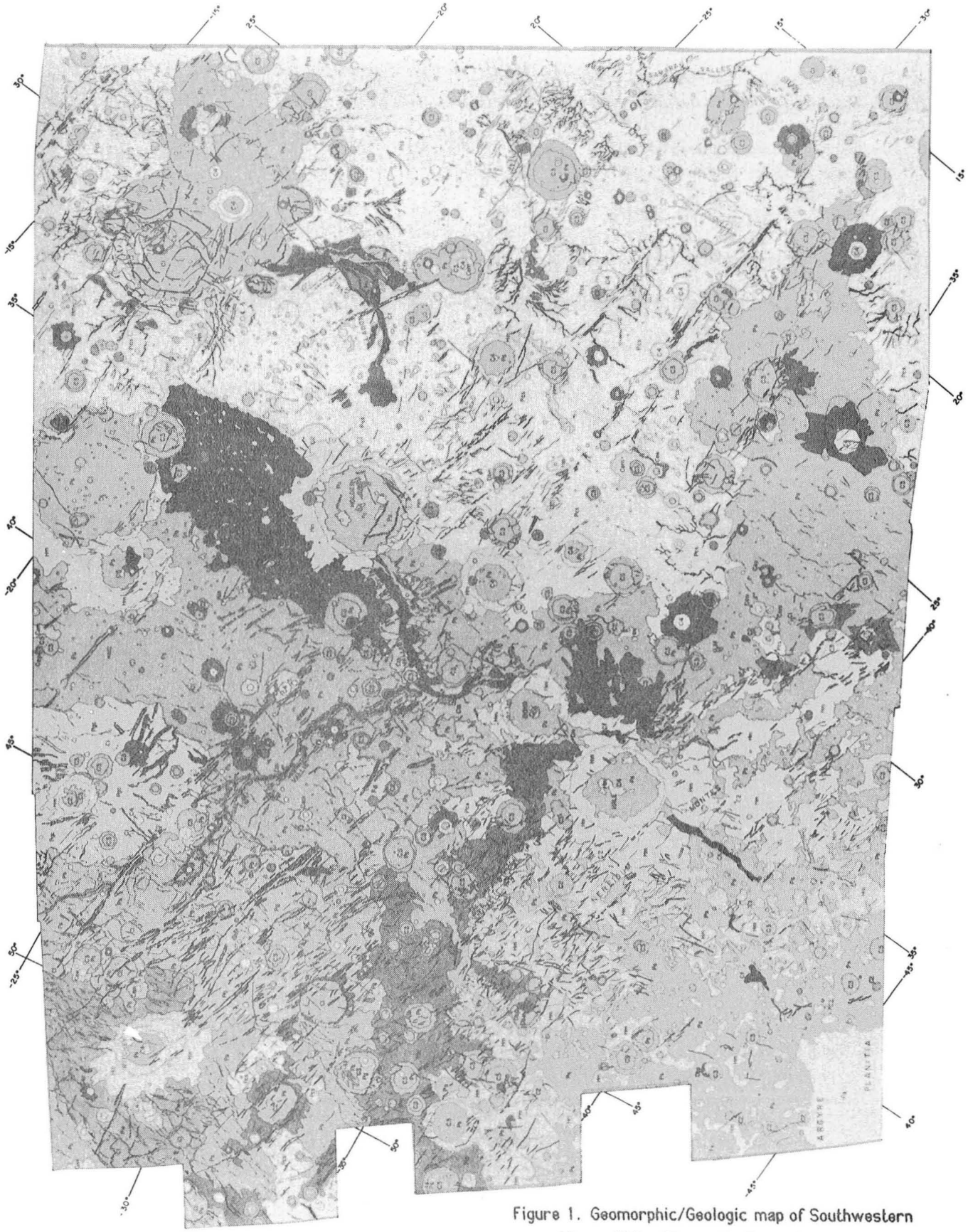

Figure 1. Geomorphic/Geologic map of Southwestern Margaritifer Sinus - Northern Argyre.

GEOMORPHOLOGY AND GEOLOGY OF THE SOUTHWESTERN MARGARITIFER SINUS AND ARGYRE REGIONS OF MARS - II: CRATER SIZE-FREQUENCY DISTRIBUTION CURVES AND GEOMORPHIC UNIT AGES, Timothy J. Parker and David C. Pieri, Jet Propulsion Laboratory, California Institute of Technology, Pasadena, CA 91109.

In assessing the relative ages of the geomorphic/geologic units, crater counts of the entire unit or nearly the entire unit were made and summed in order to get a more accurate value than obtainable by counts of isolated sections of each unit. Cumulative size-frequency counts show some interesting relationships (figure 1). Most of the units show two distinct crater populations with a "flattening out" of the distribution curve at and below 10 km diameter craters. Above this crater size the curves for the different units diverge most notably. In general, the variance may reflect the relative ages of these units as presented in figure 2. At times, however, in the larger crater size range, these curves can overlap and cross one another. Also the error bars (not shown in figure 1 for clarity) at these larger sizes are broader (and thus more suspect), since counts of larger craters show more scatter, whereas the unit areas remain constant. Occasional clusters of relatively large craters within a given unit, particularly one of limited areal extent, can affect the curve so that the unit might seem to be older than units which it overlies or cuts. A clear example of this is the case of Uzboi Vallis and the tributary systems immediately associated with it (Cf and Cm). Uzboi and Ladon are morphologically similar and are probably of the same channel system which has since been separated by the Holden impact. Below the 10 km crater size their crater distribution curves coincide rather well, but above this value they diverge drastically because of the inclusion of two craters (one 20 km and one 55 km in diameter) which are much larger than all the other craters of either valley. This divergence of the Uzboi curve causes it to cross over all but the *Cratered Plateau* and *Grooved and Channeled Plains* curves (the upper error bar does cross these curves and their upper error bars). Another case where this might be a problem is within the *Grooved and Channeled Plains* unit, where a number of large craters form a tight cluster. Unfortunately, a correlation of this unit with other units which might be as helpful as the correlation of Uzboi Vallis with Ladon Valles cannot be easily made. Prior to the crater counts, the unit was thought by the authors to be equivalent in age to the *Grooved Plains* unit, being similar to it in all respects except for the presence of the small valleys. These were thought to have formed on the *Grooved and Channeled Plains* because of their greater topographic slope, relative to the *Grooved Plains*. Crater counts, however, show a greater density of larger (~10 km diameter) craters in the *Grooved and Channeled Plains* unit than in the *Grooved Plains* unit, indicating an apparently older surface. In the approximately 2-10 km range where the curves flatten out somewhat, the *Grooved Plains* unit displays a greater crater density than the *Grooved and Channeled Plains* unit, possibly because of the valley development in the latter unit.

Ignoring for the moment the finer details of the crater count curves, it appears that they fall into three basic groups: those with relatively high crater densities in the 10 km or greater size range and with a pronounced "plateau" between 1-10 km; those with a much lower density in the 10 km or greater size range and a much less pronounced or nonexistent "plateau" in the 1-10 km size range; and those with relatively low overall crater densities. The first group includes the *Cratered Plateau material* (Plc), the *Grooved and Channeled Plains* (Pgc), the *Channeled and Subdued Plains* (Pcs), and the *Grooved Plains* (Pg). The second group includes the *Smooth Plains* (Ps), Argyre's *Hilly to Mountainous material* (Hm) and Argyre's *Smooth Plains* (Ps) (in one curve), Ladon Valles, and Uzboi Vallis (ignoring the anomalous larger craters mentioned above). The third group includes the ejecta and floor of the crater Holden (Hm and Ps on the curve), the possible lacustrine and/or aeolian *Argyre Plains material* (Pa), and the portion of the Argyre Hm and Ps curve below a crater size of about 3 km. The first two groups, although divergent in the larger crater size range, overlap well in the sizes around 1 km (with the exception of the Argyre curve). Presumably a period of removal of craters between about 2-10 km postdates the first group of units but predates the formation of those units in the second group. The third group has a notably lower crater density than the first two groups, indicating probably a much younger age for the units of the group. Most notable of these is the Argyre Hm and Ps curve, which in its larger crater sizes overlaps the *Smooth Plains* curve, but in the smaller sizes drops well below that of

the Holden curve. This curve does not display any of the "plateau" of other units in the 1-10 km size range but instead is gradually "rounded off" from the 10 km crater size downward. This seems to indicate a steady weathering of craters within Argyre from the time of its formation to relatively recent times and perhaps even to the present day. Finally, the *Argyre Plains* unit (Pa) ranks as probably the youngest major unit within the map area - its crater count curve falls well within those of all the other units in crater density.

REFERENCES

Chapman, C. R. and Jones, K. L., 1977, Cratering and obliteration history of Mars, Ann. Rev. Earth Planet. Sci., Vol. 5, p. 515-540.

Neukum, G. and Wise, D. U., 1976, Mars: A standard crater curve and possible new time scale, Science, Vol. 194, p. 1381-1387.

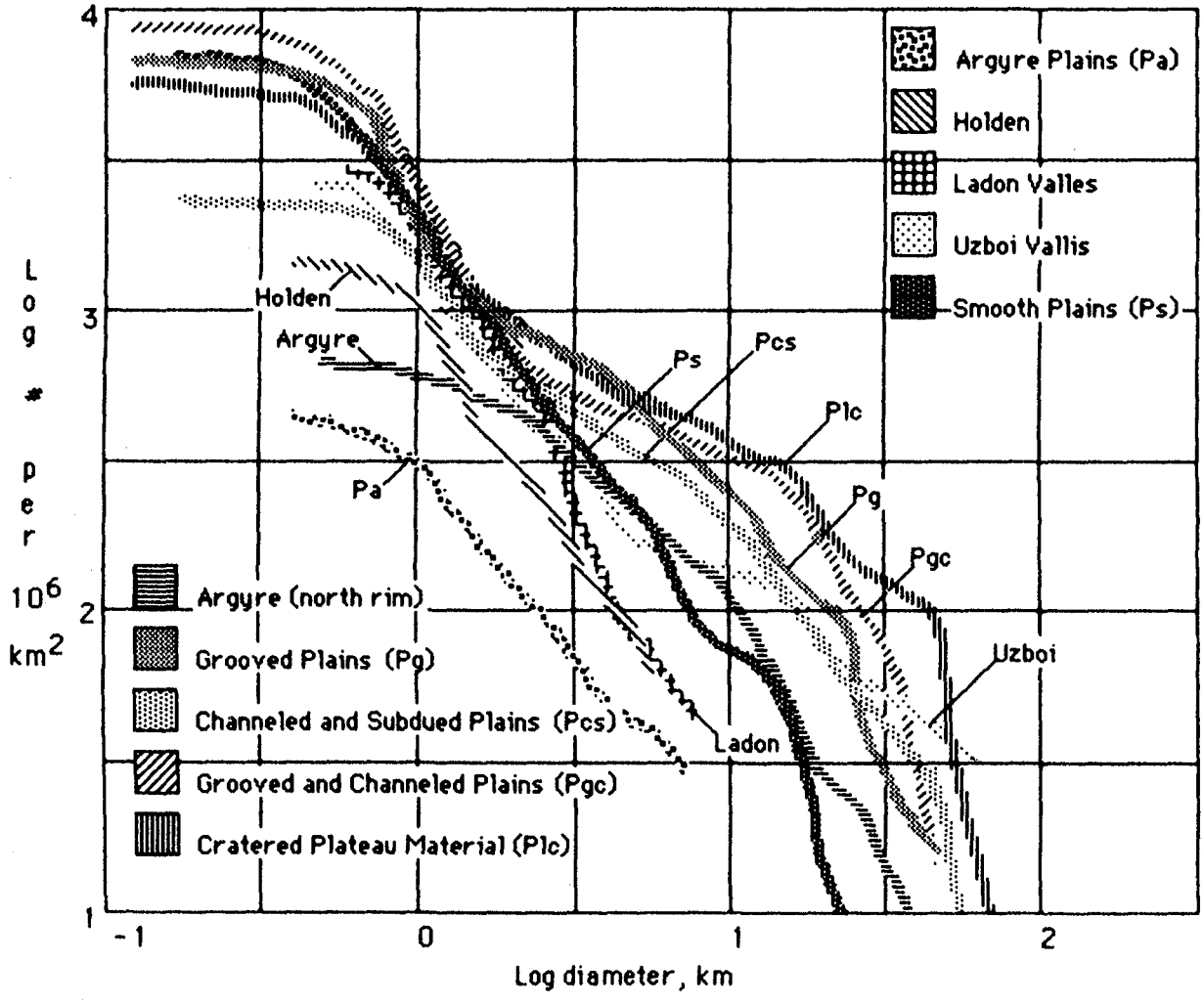

FIGURE 1. CRATER DENSITY COMPARISONS FOR MAJOR UNITS

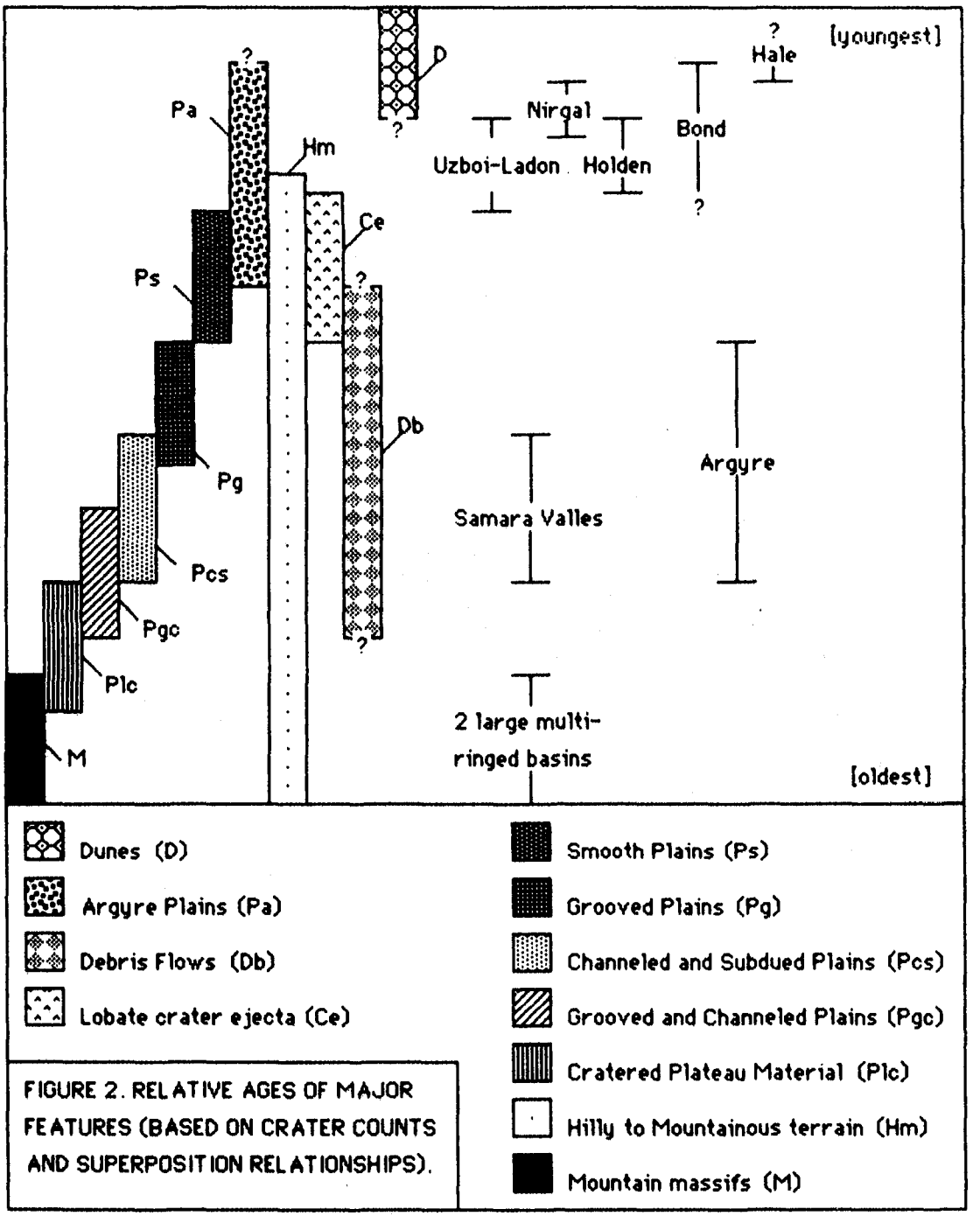

FIGURE 2. RELATIVE AGES OF MAJOR FEATURES (BASED ON CRATER COUNTS AND SUPERPOSITION RELATIONSHIPS).

GEOMORPHOLOGY AND GEOLOGY OF THE SOUTHWESTERN MARGARITIFER SINUS AND ARGYRE REGIONS OF MARS - III: VALLEY TYPES AND DISTRIBUTION, *Timothy J. Parker and David C. Pieri, Jet Propulsion Laboratory, California Institute of Technology, Pasadena, CA 91109.*

Three major valley types have been identified in this region. Two are restricted to specific geologic units while the third is independent of the geology. The first type - the small valley networks (Pieri, 1980; Mars Channel Working Group,1983) - are found within the Channeled and Subdued Plains unit in the eastern half of the map, in the *Grooved and Channeled Plains* unit north of Nirgal Vallis, and in scattered instances in the *Cratered Plateau* unit north of Argyre. The even smaller valleys just inside Argyre's rim and on the inner slopes of many large craters are not directly related to the processes which formed the small valleys but are a result, instead, of post-impact modification of the crater walls. The second type of valley network is represented by Nirgal Vallis and the similar, shorter continuation (?) of it to the west. This type is found only in the *Smooth Plains* material west of Uzboi Vallis in the map area. The third type of valley network is that of the Uzboi-Holden-Ladon Valles system. This system is related to catastrophic outflow from Argyre Basin and is topographically rather than geologically controlled.

The small valleys are shallow, branched and scattered throughout the *Channeled and Subdued Plains* unit. The shallow depth of the small valleys also hints that the surface lithology was either more permeable than the Nirgal-bearing *Smooth Plains* and allowed ground-water to reach the surface through a thermokarst-to-small channel process, or that the surface lithology itself was water rich at the time it was emplaced. As mentioned above, the small valleys are confined to the *Channeled and Subdued Plains*, the *Grooved and Channeled Plains*, and the *Cratered Plateau material*. Comparison of their distribution to superposition and crater count relative age relationships for these and younger units suggests that they postdate the *Channeled and Subdued Plains* but are older than the formation of the *Smooth Plains*, and perhaps older than the *Grooved Plains* (as no small valleys are found within this unit - the reason for this may, however, be due to some lithologic control).

The Uzboi-Holden-Ladon Valles complex is a large, probably originally continuous valley that was formed by the catastrophic release of large amounts of water from Argyre. It is less dependent upon the geology of the terrain through which it cuts than it is upon the topography it encounters downslope. Its first obvious encounter with pre-existing topography is downstream (north) of Uzboi Vallis where the crater Holden now resides. Here it transects a large, very degraded basin (Schultz and Schultz, 1980; Pieri and Parker, 1981; Schultz et al, 1982). The northeast rim of this basin bends the channel from a north-northeast trend to a west-northwest trend in Ladon Valles before Ladon finally debouches through it into Ladon Basin, another large degraded basin to the north (Saunders et al, 1978). Based upon the available regional topography, Argyre is a 2-3 km deep basin which appears to lie on a slight regional slope dipping gently to the north. The head of Uzboi Vallis can be seen just inside Argyre's northern rim (partially obliterated by the crater Hale). Three major valleys enter Argyre from the south. These channels and valleys may be evidence of inflow to Argyre Basin from the south through Charitum Montes (Parker and Pieri, work in progress). The topographic contour data is ambiguous here, however, because the indicated slope may be contrary to indications of a northerly flow direction within the valleys.

Nirgal Vallis is a long, deeply entrenched valley in the *Smooth Plains* unit west of Uzboi Vallis, with fewer branches and much more obvious structural control than the small valleys described above. It probably developed by sapping of a ground-water/ice bearing horizon which was exposed in the wall during the down-cutting of Uzboi Vallis (Mars Channel Working Group, 1983). It clearly postdates the emplacement of Uzboi Vallis and the *Smooth Plains* unit (which overlies the *Channeled and Subdued Plains* unit), making it the youngest valley system in the region.

REFERENCES

Mars Channel Working Group, 1983, Channels and valleys on Mars: Geological Society of America Bulletin, Vol.94, p. 1035-1054.

Pieri, D. C., 1980, Martian valleys: Morphology, distribution, age, and origin: Science, Vol.210, p. 895-897.

Pieri, D. C. and Parker, T., 1981, Geologic mapping of martian valley systems I: Nirgal Vallis and vicinity: Reports of the Planetary Geology Program, 1981, NASA Tech. Memo 84211, p. 503.

Saunders, R. S., Roth, L. E., Elachi, C., and Schubert, G., 1978, Topographic confirmation of 500 km degraded crater north of Ladon Valles, Mars, Reports of the Planetary Geology Program 1977-1978, NASA Tech. Memo. 79729, p. 157-159.

Schultz, P. H. and Schultz, R. A., 1980, Ancient impact basins on Mars, in Papers Presented to the Conference on Multi-Ring Basins: Formation and Evolution, p. 77-79, Lunar and Planetary Institute, Houston, Tex., 1980.

Schultz, P. H., Schultz, R. A. and Rogers, J., 1982, The structure and evolution of ancient impact basins on Mars: Journal of Geophysical Research, Vol.87, No. B 12, p. 9803-9820.

GEOMORPHOLOGY AND GEOLOGY OF THE SOUTHWESTERN MARGARITIFER SINUS AND ARGYRE REGIONS OF MARS - IV: FLOW EJECTA CRATER DISTRIBUTION, Timothy J. Parker and David C. Pieri, Jet Propulsion Laboratory, California Institute of Technology, Pasadena, CA 91109.

Flow ejecta craters - craters surrounded by lobate ejecta blankets - are found throughout the map area. The ratio of the crater's diameter to that of the flow ejecta in this region is approximately 40-45%. Flow ejecta craters are dominantly sharply defined ("fresh") craters, with slightly degraded craters being somewhat less common. This is probably indicative of the ejecta's relatively low resistence to weathering and susceptibility to burial. Hence, only reasonably well expressed flow ejecta craters will have detectable lobate ejecta blankets. Not all well-preserved craters possess lobate ejecta blankets, however. Often a flow ejecta crater can be found adjacent to a non-flow ejecta crater of the same size and degree of preservation and still be within the same geomorphic/geologic unit.

Flow ejecta craters here seem to occur within a narrow range of crater sizes - the smallest being about 4km in diameter and the largest being about 27km in diameter. Although one might assume that ejecta blankets of craters smaller than 4km may not be resolvable due to their thinness, those at 4km are easily seen and those of smaller craters are simply not seen even in images with better than average resolution for the region. This may be due to the depth of excavation of small impacting bodies being insufficient to reach volatile-rich material. Flow ejecta craters above 24km are rare, and those craters above 27km do not display flow ejecta ejecta blankets (with only one possible poor exception in the map area). This may be a result of an excavation depth so great that the volatile content of the ejecta is insufficient to form a fluid ejecta blanket.

The geomorphic/geologic unit appears also to play an important role in the formation of flow ejecta craters. Given the typical size range of 4km - 24km for the occurrence of flow ejecta craters for most units, it can be seen that the percentage of flow ejecta craters to the total number of craters within this size range varies significantly from one unit to the next (see Table 1). The wide variance in flow ejecta crater density over this relatively small geographical area argues strongly for a lithologic control of their distribution. The *Wrinkled Plains* and *Smooth Plains* units are probably young mare-volcanic flood units which could provide a relatively impermeable cap to impede the sublimation of potential ground ice. Their initial high heat content may have mobilized any pre-existing ground-ice or ground-water to concentrate beneath them. The *Grooved Plains* is another probable mare-volcanic unit, but it is older than the *Smooth* and *Wrinkled Plains* and has been subjected to a good deal more faulting and fracturing than the latter units. Its greater time of exposure to the atmosphere coupled with the more intense fracturing might, if this hypothesis is correct, have dessicated the underlying material more than had happened with the *Smooth* or *Wrinkled Plains* units. Or the underlying rock here may simply have contained less water than in the Nirgal Vallis vicinity, or both conditions may have prevailed. (In fact, the Smooth Plains unit appears to have been emplaced within a trough in the region of the headward end of Nirgal Vallis and to the west, which might have concentrated ground-water flow along it). The *Channeled and Subdued Plains* unit, older still, is probably another mare unit. The presence of numerous small valleys here suggests that this unit might be water rich, but the 9% flow ejecta crater value argues against this at the time of flow ejecta crater formation. The style of these small valleys as opposed to that of Nirgal Vallis might be a clue to the relative lack of flow ejecta craters in this unit. The small valleys are shallow, branched and scattered throughout the unit as opposed to Nirgal Vallis, which is deeply entrenched, very long, with few branches and much more obvious structural control. The age of the *Channeled and Subdued Plains* unit and the density of the small valleys argue for a depleted ground-ice or ground-water supply prior to formation of most of the flow ejecta craters (nowhere within this unit can a channel be seen cutting a flow ejecta crater or ejecta blanket). The shallow depth of the small valleys also hints that the surface lithology was either more permeable than the Nirgal-bearing *Smooth Plains* and allowed ground-water to reach the surface through a thermokarst-to-small channel process, or that the surface lithology itself was water rich at the time it was emplaced. The even lower percentage of flow ejecta craters in the *Cratered Plateau material* may also be due to a comparatively high permeability for the unit, particularly if it represents regolith accumulated during the early meteoritic bombardment which was

not buried locally by subsequent depositional events. These percentage values of flow ejecta crater occurrence for the different units are not conclusive however, since higher erosion rates for the Cratered Plateau material and Channeled and Subdued Plains relative to the other units might have been more effective in degrading these ejecta blankets. The presence of flow ejecta craters in all the major units suggests that they formed after emplacement of the units. A relatively large flow ejecta crater (about 27 km in diameter) east-northeast of Hale, has a portion of its ejecta blanket buried by the Smooth Plains unit and hence predates the unit. This is the only such case found in the map area, however. Elsewhere when a flow ejecta crater lies on or near the boundary of two units it clearly superimposes both units.

TABLE 1

Occurrence of flow ejecta Craters as a Function of Geomorphic/Geologic Unit

Geomorphic/Geologic unit	% flow ejecta vs non-flow ejecta craters
Wrinkled Plains	57
Smooth Plains west of Uzboi Vallis	45
Grooved Plains	14
Channeled and Subdued Plains	9
Cratered Plateau Material	8
Argyre (Nereidum Montes and associated Smooth Plains)	<1 (?)

The differences in flow ejecta crater density for different geomorphic/geologic units, we feel, may be related to the water content of the unit at the time of the crater's formation. Thus, although there may be a general latitudinal control for the distribution of flow ejecta craters as has been suggested, there is nevertheless a marked local variation in their distribution.

Another factor affecting their distribution, mentioned above, may be their susceptibility to degradation. In units or regions with on-going erosional processes, such as is likely the case with Argyre, flow ejecta blankets might have relatively short lifetimes. Here, flow ejecta craters may have formed more or less continuously since Argyre's emplacement, but the ejecta blankets have not survived to the present. In units such as the *Channeled and Subdued Plains*, however, we would expect such a relationship to have produced small valleys cutting flow ejecta blankets somewhere within the map area if the flow ejecta craters formed concurrently with emplacement of the unit and development of the small valleys. The lack of any such relationship may point to a lower age limit for the formation of flow ejecta craters.

PLANETARY ANALOGS IN ANTARCTICA: MARS

Michael C. Malin, Department of Geology, Arizona State University, Tempe, AZ 85287

Introduction

A study of chemical and physical weathering rates in Antarctic ice-free areas, sponsored by the National Science Foundation's Antarctic Research Program, permitted observations to be made that also have application other planetary surfaces. Owing to the extremely diverse surface conditions, marked by extreme cold but with different amounts of moisture, observations may be applicable to Mars and the icey satellites of Jupiter and Saturn. This abstract addresses observations pertinent to Mars.

Mars

Four observations are relevent to Mars: the effects of freezing on sand dune morphology (Mars polar dune field), chemical/physical weathering to create pits (Mars pitted rocks, Viking Lander I and II sites), armored surfaces (Mars lander sites), and mass movements (movement of martian debris).

A small dune field in Victoria Valley (Calkin and Rutford, 1974; Selby, et al. 1974; Lindsay, 1973) provides the opportunity to observe sand dune morphology and migration in an area of extreme cold and high winds. The dunes experience wind patterns similar (both in seasonal directivity and nearly in magnitude) to those experienced by the martian polar dunes (Tsoar, et al. 1979). The martian dunes may be currently mobile, although arguments against this possibility have been raised, chiefly on the feeling that the dunes must be frozen. Comparison of the Viking data with field and aerial photographic data from Antarctica and other frozen dune tends to support the notion that the martian dune field is not frozen, and that the sand is free to migrate, possibly even when covered with seasonal or perenial frosts. Among the terrestrial observations are: the general lack of influence on dune morphology of interbedded layers of snow, the strong influence of the permafrost depth within the dunes on morphology, and the response of the dunes to seasonal thermal wave penetration. The influence on dune form of water ice on Mars is probably analogous; the influence of the more volatile carbon dioxide ice will probably be less than that of water.

Pitted stones are abundent in the Antarctic ice-free valleys. Pits form pricipally in finer grained facies of the intrusive dike and sill rocks (dolerite) and in the Beacon Sandstone. Coarser grained materials weather to caverns but rarely pit. Although Whitney and Splettstoesser (1982) have suggested that the pitting in these rocks is eolian, physical and chemical studies as well as field observations suggest that wind

plays a minor role, principally through the removal of granulated material. Rather, moisture permeation, frost action, and salt and oxide precipitation are the principal mechanisms for pit weathering. Evidence includes: gravity normal enlargement of pits, regardless of surface slope; oxide and salt sealed microfractures to depths several millimeters beneath the apparent pit floor; and active moisture pentration and freezing within existing pits. Pits are found on many, including buried, surfaces, but probably form only on those that are near-horizontal, sky-facing. They are rarely found on buried or vertical faces of large boulders, although caverns are found almost exclusively on these faces. Extending these observations to Mars is difficult owing to the poor understanding of martian rock composition. However, the fact that pits are seen on many vertical faces on martian rocks, especially those too large to have moved since their emplacement, suggests that processes similar to those in the Antarctic cannot have created their pits. Primary formation (i.e., vesiculation) remains a more likely mechanism. Continued study of cavernous weathering will address the larger features, and the possibility of their occurring on Mars.

Roughness elements greatly influence the modification of surfaces by eolian processes (Chepil, 1950; Lyles, et al. 1974; Lyles and Allison, 1979). In particular, they inhibit the exportation of fines from an area once a geometric equilibrium (the "Chepil Equilibrium") is reached. Fines may still move through the region, and deposition may occur, but wind erosion cannot proceed beyond the geometric limit. The geometry is related to the impact angle of saltating grains, in turn dependent on the ratio of the horizontal component of wind velocity to the vertical component of velocity (wind plus fall). These velocities are dependent on particle size and atmospheric pressure (White, 1979). Observations in Iceland (Malin and Eppler, 1981) and Antarctica indicate that the terrestrial values for the naturally occuring eolian concentration of stone armors is reproducable over a wide range of wind speeds and roughness element sizes. This results from the extremely effective sorting of materials by wind, thus limiting the size of saltating materials; the atmospheric pressure does not vary significantly on Earth. On Mars the case is more complicated, as atmospheric pressure varies spatially by as much as a factor of 5, seasonally at a given location by as much as 50%, and over periods dictated by astronomical perturbations by factors from 60X lower to 5X higher than presently found. In addition, the effectiveness of wind in sorting materials on Mars may be less than on Earth, leading to possible variations from place to place and/or time to time in the dominent sizes of moving fines. Two sites (VL-I and VL-II) are not sufficient to deconvolve these various possible effects, but preliminary measurements on rectified Viking Lander images differ from predictions made on the basis of terrestrial observations ("corrected" for martian conditions and particle sizes; Greeley, et al. 1982). The apparent discrepencies indicate steeper impact angles. An increase in atmospheric pressure might lead to such steeper angles owing

to lower wind velocities needed to move material; however, higher pressures also reduce vertical velocities (greater "air" resistance). Which effect dominates is still under investigation, but when the dominent effect is deciphered, it is likely that this study will permit past martian eolian transport environments to be examined.

Monitoring of mass movements in Antarctica, in particular those of rock glaciers, may help to address the problems of similarly shaped features on Mars. Hassinger and Mayewski (1983) report movement and stratigraphic observations, based both on geophysical and surface monitoring, that lend credibility to the application of models of dry creep (e.g., Scheidegger, 1970) for surface materials, and alternative models involving deformation for the rock glacier cores. The key factors under given slope and temperature conditions are: the nature of the ice cement (interstitial or segregated), the nature and rate of debris supply (size of particles and rate of movement from source into rock glacier), and the availability of moisture to replenish volatile losses to the atmosphere. Similar factors can be evaluated for Mars, leading to constraints on the formation of martian rock glaciers (e.g., Squyres, 1978). A most promising result is the possibility that only limited amounts of interstial ice, provided constituent materials are moderately fine and repetative thermal cycles of sufficient magnitude occur.

References

Calkin, P. E. and Rutford, R. H. (1974) Geogr. Rev. 64, 189-216.

Chepil, W. S. (1950) Soil Sci. 69, 149-162.

Greeley, R., Leach, R. N., Williams, S. H., White, B. R., Pollack, J. B., Kinsley, D. H., and Marshall, J. R. (1982) J. Geophys. Res. 87, 10009-10024.

Hassinger, J. and Mayewski, P. A. (1983) Arctic Alpine Res. 15, 351-368.

Lindsay, John F. (1973) Geo. Soc. Am. Bull. 84, 1799-1806.

Lyles, L., Schrandt, R. L., and Schmeidler, N. F. (1974) Trans. ASAE 17, 134-139.

Lyles, L. and Allison, B. E. (1979) Trans. ASAE 22, 334.

Malin, M. C. and Eppler, D. B. (1981) NASA Tech. Mem. 84211, 247-248.

Scheidegger, A. (1970) Theoretical Geomorphology. (Prentice-Hall, Englewood Cliffs, NJ). 333 pp.

Selby, M. J., Rains, R. B., and Palmer, R. W. P. (1974) N. Z. J. Geol. Geophys. 17, 543-562.

Squyres, S. W. (1978) Icarus 34, 600-613.

Tsoar, H., Greeley, R. and Peterfreund, A. R. (1979) J. Geophys. Res. 84, 8167-8182.

White, B. R. (1979) J. Geophys. Res. 84, 4643-4651.

Whitney, M. I. and Splettstoesser, J. F. (1982) Catena (Supplement I), 175-194.

PLANETARY ANALOGS IN ANTARCTICA: ICEY SATELLITES

Michael C. Malin, Department of Geology, Arizona State University, Tempe, AZ 85287

Introduction

As part of a study to provide semi-quantitative techniques to date past Antarctic glaciations, sponsored by the NSF Antarctic Research Program, field observations pertinent to other planets were also acquired. The extremely diverse surface conditions, marked by extreme cold and large amounts of ice, provide potential terrain and process analogs to the icey satellites of Jupiter and Saturn.

Icey Satellites

Antarctic ice fields are thought to provide several interesting models for analogy to icey satellite surfaces. These include thin ice tectonic features and explosion craters (on sea ice) and deformation features on thicker ice (glaciers).

Fractures developed in sea ice in many ways resemble lineaments seen on Europa and Ganymede. Straight leads, often dark compared with the surrounding ice and sometimes displaying bright ridges down their centers, are common. However, the comparison with icey satellites may be spurious for several reasons. First, sea ice fractures develop because of movement within a system with a free surface in the plane of movement, and in response to non-steady forces acting over a variety of spatial scales (i.e., response to wind). This is clearly not analogous to forces exerted on a crust over a thermal convective cell (as envisioned for icey satellite tectonics). Second, much of the albedo variation results from silicate materials blown onto the sea ice, from snow drifts and mantles on the ice, and from non-uniform thinning of the ice. Snow mantles, variable thickness crust, and incorporation of silicates may be responsible for the albedo features on Europa and Ganymede, but the scaling relationships make such possibilities improbable. Finally, the sea ice thickness compared to the depth of water beneath the ice does not scale well for comparisons to the icey satellites. Thus, dynamic processes relying on differences in thermal behavior or viscosity between layers in a two layer system probably do not scale either.

Explosion craters on the sea ice may provide a better planetary analog, even though the scaling arguements raised above still hold. Explosives detonated as part of seismic reflection sounding experiments conducted by L. McGinnis (personal communication, 1983) failed to crater the sea ice until certain conditions were met, including changing the depth of the explosion and creating an effective couple between the explosive and the rigid ice crust. However, when craters were created, they strongly resemble "flow-ejecta" craters seen on both Ganymede (Horner and Greeley, 1982) and Mars, and examined at much smaller scale in laboratory experiments (Greeley, et al. 1980). The concern here for the comparison, as with the laboratory studies, is whether the extremely

fluid lower layer (water) is available on the planets as it is in Antarctica. Scaled-depth explosions in thicker ice have not created flow- ejecta craters in Antarctica, and may not be able to do so on other planets.

Finally, thicker ice flows may have some analogy to movements of crustal materials on icey satellites, provided there are variations in topography to which the materials must respond. In these cases, both plateau ice and outlet glacier responses to topography are of interest. Even frozen based glacial ice exhibits a variety of surface forms owing to deformation and structured turbulence in its motion. These forms are most easily studied in aerial photographs, so it is at least possible that they can be found in high resolution images of satellite surfaces. Thus, the Galileo imaging experiment, given its repetative, close encounters with both Ganymede and Europa, has an excellent chance of searching for such features.

References

Greeley, R., Fink, J., Gault, D. E., Snyder, D. B., Guest, J. E., and Schultz, P. E. (1980) Impact cratering into viscous targets: Laboratory experiments: Proc. Lunar Planet. Sci. Conf. 11th, 2075-2097.

Horner, V. M. and Greeley, R. (1982) Pedestal craters on Ganymede: Icarus 51, 549-562.

THE GEOMORPHOLOGY OF RHEA

J.M. MOORE, V.M. HORNER, and R. GREELEY
Department of Geology, Arizona State University, Tempe, AZ 85287

Rhea was imaged to a resolution of ~1 km/lp by the Voyager spacecraft, providing the most detailed view of any saturnian satellite. A preliminary study of Rhea (1) divided the northern hemisphere into population I cratered terrain (between ~0° and 120°W) and population II cratered terrain (between ~300° and 360°W). Population I includes craters that are >40 km and were formed before the termination of population II bombardment, which formed craters primarily <40 km (2). In this study, geomorphic features on Rhea are classified and interpreted.

Physiographic Provinces: Three physiographic provinces are identifed (Figs. 1 and 2). Cratered terrain I undifferentiated (ct_1u) is found in two regions: (a) north of ~60°N between ~0° and 150°W, and (b) south of 0°-20°N between ~0° and 150°W. It is covered with population I craters and morphologically resembles the highlands provinces of the Moon and Mercury (2). An anomalously low density of small craters (<10 km in diameter) and the subdued relief of larger ones is attributed to regional mantling (1). Lineated cratered terrain I (ct_1l), located between 60°N to 0°-20°N and 0°-150°W, is identical to ct_1u except for a pervasive N45°E lineation composed of parallel linear troughs and coalescing pit chains. Cratered terrain II (ct_2) is located between ~0° longitude to at least ~270°W and south from the north polar region to as far as ~60°S. The majority of craters on this terrain are <40 km in diameter (population II) and morphologically fresh. Cratered terrain II is extensively lineated by parallel N30°E trending sharp-crested ridges and scarps.

Multi-ringed Basins: At least three multi-ringed basins are found on Rhea. Basin A, centered at 35°N, 150°W, comprises conspicuous rings (Fig. 3). The outer ring is an inward-facing scarp ~450 km in diameter. The inner ring appears to consist of ridges or hills rather than scarps. The landforms composing the rings of this basin resemble those of Odysseus on Tethys and peak ring basins on the Moon. A second, very degraded multi-ringed basin (B in Fig. 2), centered at ~30°N, 315°W, has rings consisting of broad, low ridges, coalescing pits, and lineaments of an indeterminate nature that rarely extend more than 90° circumferentially about the basin center. Basin-associated lineaments are rarely seen beyond a ~700 km radius. A third, degraded, multi-ringed basin (C in Fig. 2), centered at ~20°S, 315°W, is composed of two essentially continuous rings of broad ridges with diameters of ~350 km and ~700 km. The rings of this basin overlap those of basin B and appear to be slightly better preserved.

Craters: Craters are the dominant landform on Rhea. There is a fairly sharp division between fresh, almost pristine craters and degraded craters which seem texturally indistinguishable from the surrounding terrain (1). Observations of rhean crater morphology include: (a) absence of detectable continuous ejecta deposits, (b) lack of central pits or pitted peaks that are common on Mars and prevalent on the outer Galilean satellites, (c) large central peaks with respect to crater size compared with lunar and mercurian craters, (d) preferred orientations of crater rim segments and (e) lack of palimpsests (2).

Megascarps: Arcuate megascarps and/or ridge-forms with low relief and low slope have been identified. Individual megascarps can be traced through most of the high resolution mosaics.

Ridges and Scarps: Parallel, N30°E striking, sharp-crested ridges or scarps are found on ct_2, especially near the crater Pedn. They are ~5 km wide and up to several hundred kilometers long with relief averaging <0.25 km. Some ~20 km craters are superimposed on the ridges or scarps, whereas ridges transect other craters. The rim of Pedn (E in Fig. 2) shares a common scarp with two lineaments

on its northwest and southeast extensions, implying a common subsurface control of the scarps/ridges and the crater.

Troughs and Coalescing Pit Chains: Parallel linear troughs or coalescing pits oriented at N45°E are found on ct_1l. These features are ~5-10 km wide and up to ~1000 km long. Shadow measurements indicate a depth of <0.5 km. Nearly all troughs and many of the coalescing pits show little or no indication of raised rims. Most troughs and pits are superimposed on the craters. As they cannot be traced on to ct_2, it is inferred that trough and coalescing pit formation continued beyond the end of population I bombardment but ended prior to the resurfacing event which covered the population I craters on ct_2. In a few, small areas of ct_1u (~1% of the total observed unit), there are grooves with spacings of ~2-4 km and low (~0.1-0.25 km) relief. They contain pits or, in places, short chains of pits. A nearby graben that trends in the same direction as the grooves implies a similar tectonic control for both features. Alternatively, these grooves could result from impact sculpture and/or secondary craters. The formation of small grooves must have been comparatively recent, such small landforms probably would have been destroyed if they had formed prior to the conclusion of the major episodes of cratering.

Discussion: The superposition relationships among the landforms and physiographic provinces indicate the sequence of events outlined in Figure 4. Preliminary studies concluded that Rhea had at least one major resurfacing event which emplaced unit ct_2 (1,2), and that a NH_3-H_2O melt may have erupted to cover portions of Rhea (3,4,5). The presence of ct_2 in and around the location of basins B and C might be because the melt moved to the surface through weaknesses in the lithosphere established by basin-forming impacts. Stratigraphic relations indicate that unit ct_2 formed after the development of linear troughs and coalescing pits but before the scarps and ridges formed. Scarps and ridges may be high-angle reverse faults reflecting a period of surface layer compression, as has been suggested for ridge formation on Dione (6). If the resurfacing event responsible for ct_2 was endogenic, it occurred between the initial transition from extensional to compressional tectonics, according to models of rhean thermal-tectonic evolution (4,5).

Rhea's tectonic history was a sequence of extension-compression-extension, provided: a) the troughs and coalescing pit chains developed during an initial era of global surface extension, b) the ridges and scarps formed during a time of global surface compression, and c) small grooves are a consequence of some later period of extensional tectonics. This sequence is consistent with one theoretical model for Rhea's history (5). Alternatively, if small grooves are not tectonic features, then Rhea underwent a simple cycle of expansion followed by contraction (4). If the scarps and ridges are extensional, then there is no evidence for compressional tectonics. This would imply that the compressional phase of tectonics predicted by the models is masked or obscured. Alternatively, the predictions of compressional tectonism may be wrong. Landforms on Rhea do not, however, irrefutably exclude a compressional tectonic phase.

Additional observations and conclusions produced by this study are:

(a) Central peaks are large with respect to crater size as compared with lunar and mercurian craters, possibly reflecting differences in target composition. The lack of central pits within craters is not adequately explained by existing models of central pit formation (7,8,9).

(b) Many craters have preferred rim segment orientations. Crater and noncrater lineament orientations on Rhea do not fit models of global despinning, tidal distortion, or impact basin stresses (10,11,12).

(c) The larger, degraded multi-ringed basins may have played a significant role in the mantling of population I cratered terrains and the resurfacing event responsible for the emplacement of ct_2.

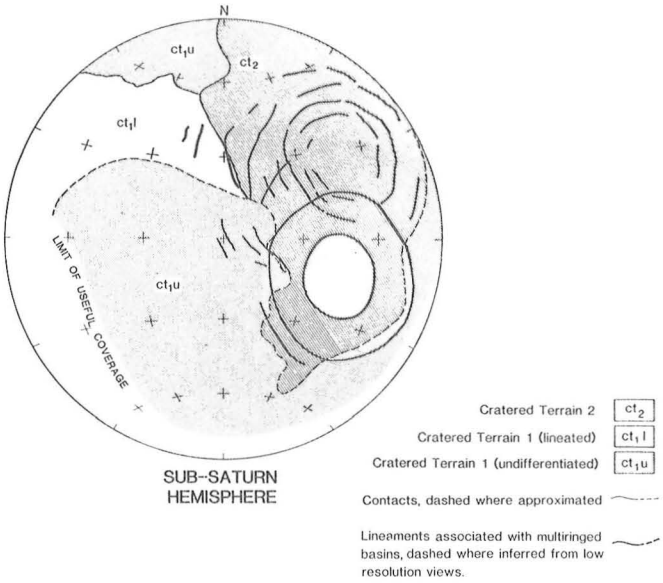

Fig. 1. Major physiographic provinces and multi-ringed basins on the sub-saturnian hemisphere of Rhea.

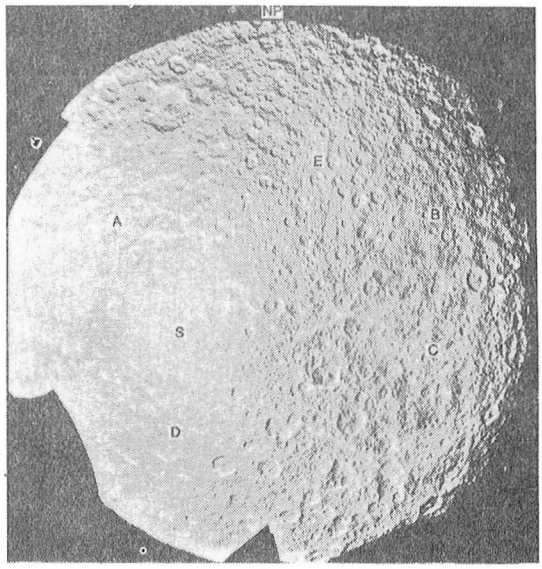

Fig. 2. Rhea's sub-saturnian hemisphere. (A) ct_1l; (B) and (C) centers of multi-ringed basins B and C; (D) ct_1u; (E) ct_2; (S) sub-solar point.

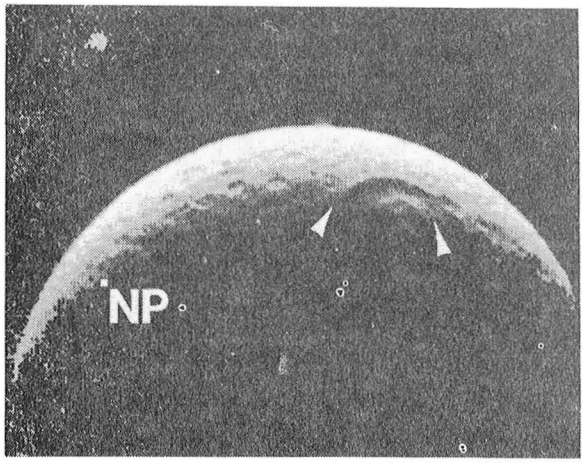

Fig. 3. Multi-ringed basin A.

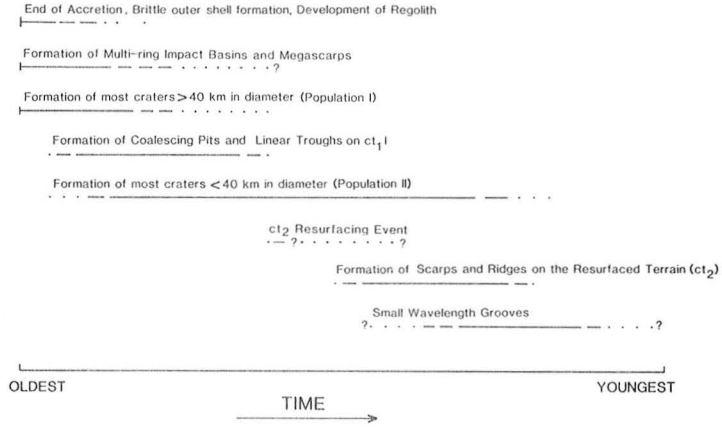

Fig. 4. Generalized chronology for Rhea.

REFERENCES

1. Plescia, J.B. and J.M. Boyce, 1982, Nature, 295, 285-293.
2. Smith et al., 1981, Science, 212, 163-191.
3. Stevenson, D.J., 1982, Nature, 298, 142-144.
4. Ellsworth, K. and G. Schubert, 1983, Icarus, 54, 490-510.
5. Consolmagno, G.J., 1984, submitted to Icarus.
6. Moore, J.M., 1984, Icarus, 59, 205-220.
7. Hodges, C.A., 1978, Lunar Planet. Sci. IX, 521-522.
8. Wood, C.A. et al., 1978, Proc. Lunar Planet. Sci. Conf., 9th, 3691-3709.
9. Passey, Q.R. and E.M. Shoemaker, 1982, Satellites of Jupiter, D. Morrison, ed., University of Arizona Press, 379-434.
10. Melosh, H.J., 1977, Icarus, 31, 221-243.
11. Melosh, H.J., 1980, Icarus, 43, 334-337.
12. Moore, J.M. and J.L. Ahern, 1983, Proc. Lunar Planet. Sci. Conf., 13th (J. Geophys. Res., 88), A577-A584.

CHAPTER 12

REMOTE SENSING AND REGOLITH STUDIES

Page intentionally left blank

MULTISPECTRAL ANALYSIS OF THE KASEI VALLIS - LUNAE PLANUM REGION OF MARS

R.B. Singer, E. Cloutis, T.L. Roush, P.J. Mouginis-Mark, B.R. Hawke, Planet. Geosci. Div., Hi. Inst. of Geophys., Univ. of Hawaii, Honolulu, HI 96822 and P.R. Christensen, Dept. of Geology, Arizona State Univ., Tempe, AZ 85287.

INTRODUCTION - We have investigated the surficial geology of the Kasei Vallis - Lunae Planum region of Mars based largely on 3-color Viking Orbiter I data (663A32,36,38; Fig.1). Spatial resolution is 820m and Ls = 100° , a season of low atmospheric and surface dustiness (1,2). This region was chosen for high-quality color and thermal inertia data as well as for the diversity of volcanic plains and fluvial landforms. The data was reformatted to Mercator projection and calibrated to Normal Reflectance using in-flight calibration parameters (3) and observed photometric properties (4).

COLOR PROPERTIES - Color properties from this image are displayed in two forms: the Red Albedo vs. Violet Albedo 2-dimensional histogram (Fig. 2), and representative 3-point spectra. Virtually the full range of regolith color properties known from prior research is represented, plus some new characteristics. The curve labelled "Bright Red" in Fig. 3 represents the brightest and reddest materials in this scene - most like the heavily weathered (Fe^{3+} -rich) global dust (5). The R/V ratio averages slightly over 3.0, compared to maximum telescopic measurements (convolved to Viking bandpasses) of R/V = 3.0 in 1969 (a relatively dust-free period (6)) and R/V = 3.3 in 1973 (a relatively dusty period (7)). The "Channel Floor" curve represents an average for Kasei Vallis floor, excluding regions of extreme high or low albedo. This material is about 10% lower in Red albedo than the previous example, and has an average R/V = 2.72. These values are consistent with a higher content of less-weathered materials, although other explanations may be possible. This floor material has generally higher thermal inertia than would be expected from the color and albedo values (8,9).

LUNAE PLANUM - The bottom of this scene is dominated by the N. end of the Lunae Planum ridged plains unit, bounded by a substantial scarp (~3 km) down to Kasei Vallis. To the north, surrounded by Kasei channel deposits, are two islands (labelled 'I' in Fig. 1) which were apparently contiguous with the Lunae Planum flows prior to channel formation. The low thermal inertia of these outliers is similar to Lunae Planum (model particle size of ~50μm) (8). The spectral properties, however, differ significantly (Fig. 3). The spectrum for the larger island is very similar in both albedo and color to channel floor materials, while Lunae Planum is slightly redder (R/V = 2.8) but significantly darker. These distinctive characteristics are also visible as a low Violet-albedo cluster (marked 'LP') in Fig. 2. This cluster maps back onto the image as a unit associated uniquely with Lunae Planum. A more hematitic type of oxidation, such as has been suggested for other dark red units (10), is not a viable explanation for Lunae Planum based on its spectral shape (5). We suggest that the ridged plains deposits are physically rougher than other units in the scene and that the effect is due to unresolved shadows cast by the low sun angle (i≈46°) for these images. Computational removal of 12% black shadows from the Lunae Planum data (using a simple "checkerboard" model (11)) brings Lunae Planum into close spectral correspondence with the larger island. Examination of high resolution images indicates some fluvial reworking of the surface of the larger island, and perhaps of the smaller island as well. This reworking apparently eliminated the Lunae Planum-type roughness and accounts for the observed differences between these once connected surfaces. The color and thermal-inertia data indicate that at least the top 5-10 cm of Lunae Planum and the two islands consists of fine-grained weathered soil. This present surface layer must post-date fluvial reworking of the islands, although may have preceeded later stages of channel formation.

LOW-ALBEDO FEATURES - Very dark materials occur both as intra-crater deposits and more extended exposures on the channel floor. They show indications of eolian reworking from east to west, although dune morphology has not been found in higher-resolution images. A spectrum for the darkest, least red material in this scene is shown in Fig. 3 (location indicated by arrow in Fig. 1). R/V for this material is 1.66, considerably less than the minimum of 1.97 ever observed from earth (69-7 (6)). This value falls at the red extreme of the color distribution observed for unaltered terrestrial basalts and indicates that these Kasei exposures have at most only slight coating or mixing with Fe^{3+} -rich weathering products. These darkest deposits have been found to have the highest measured thermal inertias in the region with model grain sizes of 1-4 mm (8,9). The combined interpretation is that these are surficial eolian deposits of coarse sand composed of basalt or basaltic glass, well sorted and probably somewhat mobile. These are the cleanest and least oxidized crustal materials which have been found on Mars and are prime targets for spectroscopic observation and petrologic analysis from the proposed Mars Geosciences/Climatology Orbiter.

REFERENCES - (1) Pollack, J.B., et al., JGR 84, 2929-2945, 1979. (2) Guiness, E.A., et al., JGR 87, 10051-10058, 1982. (3) Klaasen, K., et al., Ap. Optics 16, 3158-3170, 1977; E. Eliason, USGS Flagstaff, pers. comm., 1983. (4) Thorpe, T.E., JGR 82, 4161-4166, 1977. (5) Singer, R.B., JGR 87, 10159-10168, 1982. (6) McCord, T.B. and J.A. Westphal, Ap. J. 168, 141-153, 1971. (7) McCord, T.B., et al., Icarus 31, 293-314, 1977. (8) Christensen, P.R. and H.H. Kieffer, JGR 84, 8233-8238. (9) Christensen, P.R., LPS XIII, 96-97, 1982. (10) McCord, T.B., et al., JGR 87, 10129-10148, 1982. (11) Singer, R.B. and T.B. McCord, PLPSC 10th, 1835-1848, 1979.

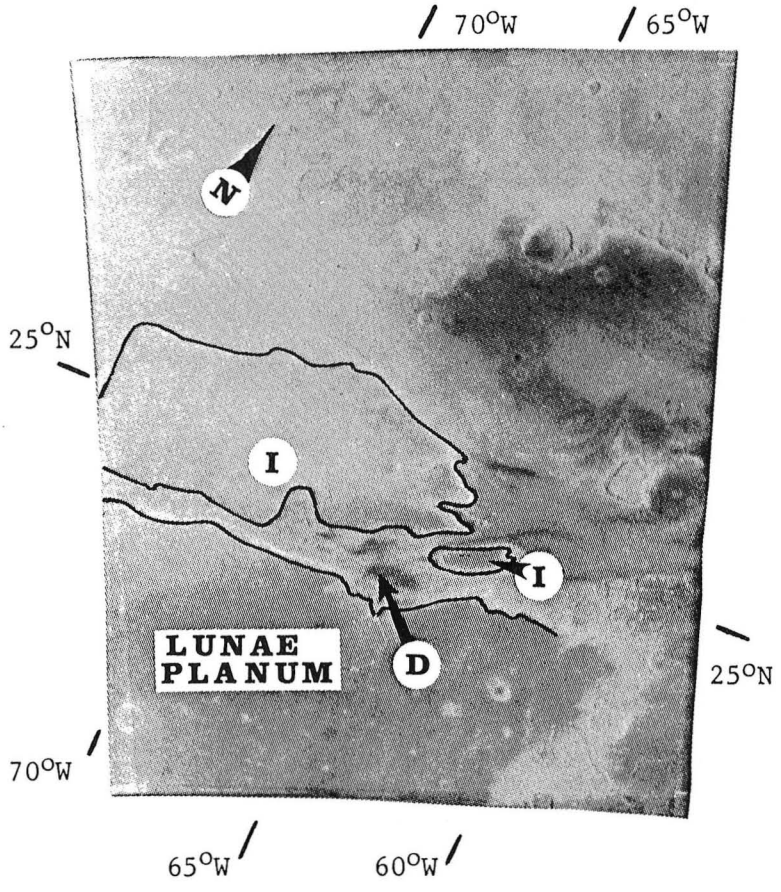

Fig. 1: B/W version of Viking Orbiter color image investigated here. 'I' refers to two islands in Kasei Vallis. Walls of the Vallis have been outlined to aid indentification. Fig. 2(lower left): Red Albedo vs. Violet Albedo histogram for data points contained in analyzed scene. 'LP' is the low violet albedo cluster referred to in the text. Fig. 3 (below): Representative 3-point spectra for color units identified in this analysis.

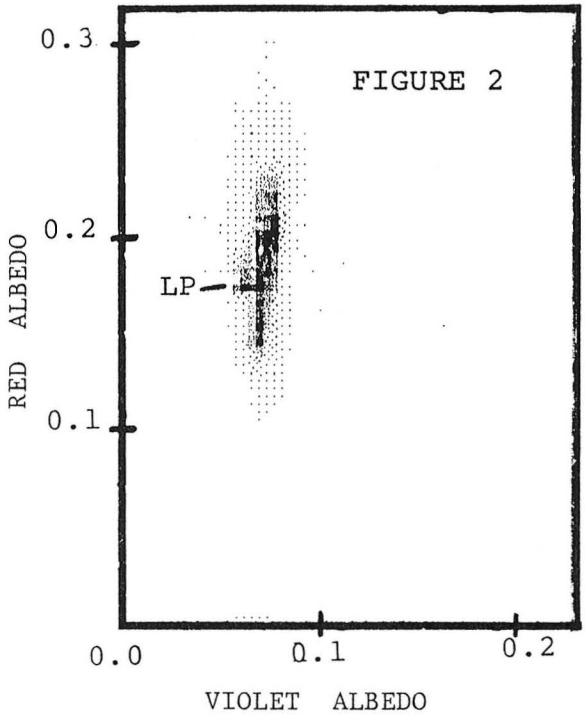

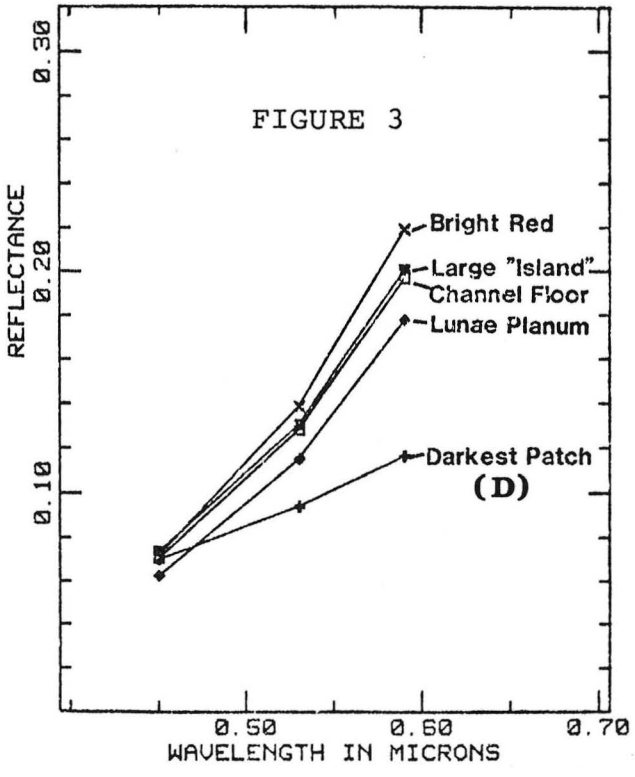

GEOLOGIC INTERPRETATION OF REMOTE SENSING DATA FOR THE MARTIAN VOLCANO, ASCRAEUS MONS

J. ZIMBELMAN and R. GREELEY
Department of Geology, Arizona State University, Tempe, Arizona, 85287

The objective of this work is to relate remotely determined physical properties on Ascraeus Mons to the geologic history of the volcano. Products include a 1:2,000,000-scale photogeologic map of Ascraeus Mons and its environs, a 1:250,000-scale corrected thermal-inertia map of the summit caldera complex (registered with the photogeologic map), four corrected thermal-inertia profiles across the volcano from high-resolution thermal data, fourteen low-resolution thermal sequences providing corrected thermal inertias for the volcano throughout half a martian year, and a calibrated three-color photograph of the volcano. These data were combined with published spectral-reflectance, radar, and atmospheric water-vapor data relating to Ascraeus Mons.

Photogeologic mapping indicates that the sequence of events at Ascraeus Mons is more complex than previously described (1,2). The plains surrounding the volcano include numerous flows, some of which can be traced to the flank of the volcano and some to different locations along the Tharsis Ridge. Surface morphology in the summit area is very distinct for features >100 m in scale, but the surface relief and tonal contrast steadily decrease toward the base of the shield, indicating modification by deposition or erosion.

Reflectance properties of the summit area are very uniform throughout the visible wavelengths when photometric effects due to surface slopes are taken into account. Thermal inertias, corrected for elevation-dependent effects, are very similar for the volcano summit and the surrounding plains; the volcano is not covered by extremely low-thermal-inertia materials as proposed earlier (3). Except for caldera walls, terrain units in the summit area are indistinguishable in thermal inertia. No thermal inertias indicative of extensive bedrock exposures occur anywhere on the volcano, including the caldera walls. The low-albedo "dark collar" surrounding the summit has the same thermal inertia as the summit area, indicating that the albedo change may involve very small quantities of material redistribution. The shield base, below 14 km elevation, has higher thermal inertias representing either increased particle size or increased induration of soil materials. Atmospheric water-vapor abundance is highest over the shield base, consistent with an induration process. Radar signals are strongly scattered by the shield materials, suggesting that the low-thermal-inertia surface materials are at most a few meters thick on the volcano. Ascraeus Mons appears to have an elevation-dependent surface history that is probably related to global climatic conditions.

Future work should include thorough examinations of other major centers of martian volcanism. Photogeologic mapping will be required for locations that have not received detailed post-Viking analysis. Apoapsis color photographs are available for much of the equatorial region of Mars so that spectral reflectance properties can be examined with better than 1-km resolution. High-resolution thermal data cover much of the equatorial latitudes of Mars; most volcanic features should be crossed by at least one

sequence. Radar data will be of limited usefulness due to the strongly scattering surfaces of the youngest volcanics but may be useful for some older features.

REFERENCES

1. Carr, M.H., U.S.G.S. Map I-893, 1975.
2. Scott et al., U.S.G.S. Map I-1269, 1981.
3. Kieffer et al., Science, 194, 1346-1351, 1976.

THE SEARCH FOR IGNEOUS MATERIALS AT THE VIKING LANDING SITES

R. Arvidson, M. Dale-Bannister, E. Guinness, McDonnell Center for the Space Sciences, Department of Earth and Planetary Sciences, Washington University, St. Louis, MO 63130.

The Viking mission to Mars clearly advanced our understanding of the characteristics of the martian surface. On the other hand, not a great deal of information has yet been extracted about the mineralogy of surface materials from Viking data. The Orbiter experiments largely provided information on physical properties; even the Orbiter color imaging data are of use primarily to map variations in color from place to place. The Lander experiments provided information primarily on soil chemistry (x-ray data), together with some information on the reactive characteristics of the soil (biology data) that can be interpreted in terms of models of soil mineralogy. The only experiment designed to detect minerals directly was the magnetic properties experiment. We now know there is a magnetic phase in the soil, but we can only guess as to the mineralogy. The Viking Lander 6 channel (0.4 to 1.1 micrometers) images offer the best data in terms of mapping variations in broad spectral reflectance properties of materials about the landing site. Our recent work suggests that we can also identify igneous materials (i.e. Fe+2 bearing silicates) at the landing sites from the 6 channel data.

We generated cubic spline fits to the 6 channel data by substituting spline basis functions for the spectral reflectance terms inside the integrals describing the Lander camera detector outputs (1). Since the basis function coefficients (e. g. polynomial coefficients) are not wavelength dependent, they can be extracted from the integrals, leaving a vector of known sensor outputs, a matrix of terms involving products of known terms, including solar irradiance, camera transfer functions, and calibration constants, and a vector of unknown coefficients. Simple matrix techniques can then be used to solve for the coefficients. The coefficients can then be used to construct a continuous function describing the spectral reflectance term. The basis function technique takes advantage of both the spectral breadth and pattern of the camera transfer functions, providing more information than can be obtained by 6 point estimates of reflectance. We generated these functions for each pixel for a number of 6 channel scenes for both landing sites. The functions for each pixel were then sampled at regular wavelength intervals and images were generated at each wavelength. Typically 16 to 32 images were generated, making a synthetic "image cube" comparable in volume to what may be generated from the imaging spectrometer that may fly on the MGCO mission.

The 6 channel data and resultant functions cannot, of course, be used to pick out fine spectral detail in the data because of effects related to spectral aliasing. On the other hand, we find that the 16 to 32 synthetic images allow new methodologies of data analysis. In particular, both at the University of Hawaii (with Robert Singer) and at Washington University, the images have been stacked by wavelength and

displayed in movie form, starting with the blue end of the spectrum and moving toward longer wavelengths with subsequent frames. In addition, plots of the data have been generated from given pixels or groups of pixels. Both absolute reflectance image cubes and cubes normalized to the response from various patches of soil were generated and examined.

Movies of the image cubes demonstrate that there are a number of contrast reversals between soils and certain rocks. Typically, large, angular rocks are brighter than the surrounding soils in the shortest wavelengths, and much darker than the soils at longest wavelengths. These results, which seem difficult to explain solely on the basis of photometric effects related to local lighting and viewing, are consistent with the presence of Fe+2 bearing silicates at the rock surfaces, producing relatively moderate absorptions in the blue and green parts of the spectrum, but more significant absorptions near about 1.0 micrometer (e. g. Fe+2 bearing pyroxenes). The soils, on the other hand, have signatures consistent with strong Fe+3 related absorptions at shorter wavelengths (e. g. Fe+3 bearing oxides or hydroxides). While Mariner 9 IRIS data (2) and earth-based spectral reflectance observations (3) confirm the presence of Fe+3 bearing materials on Mars, and Earth-based data (3) suggest that Fe+2 bearing minerals may exist under a patina of weathering products, to our knowledge, this is the first direct evidence for the presence of Fe+2 bearing minerals in rocks on Mars. The tentative correlation between the size and angular character of rocks and the depth of absorption at longer wavelengths is intriguing and suggests that some of the rocks added to the scene are crystalline, igneous materials.

REFERENCES

1. Huck, F. , and others, J. Geophys. Res. , v. 82, p. 4401-4411 (1977)

2. Toon, O. B. , and others, Icarus, v. 30, p. 663-697 (1977)

3. Singer, R. B. , and others, J. Geophys. Res. , v. 84, p. 8415-8426 (1979)

BASALTS OF MARS: CONSTRAINTS ON VOLATILE EVOLUTION

R.L. Huguenin (Remote Sensing Center and Dept. Geology/Geography, Univ. of Massachusetts, Amherst 01003)

The mineralogy of relatively unweathered rocks on Mars place important constraints on models of planetary oxidation state, volcanism and associated outgassing, accretion and associated volatile inventory, and geochemical changes over time. Reflectance spectra (300-2500 nm) provide direct mineralogic information about the surface materials. Spectra measured using earth-based telescopes have been analyzed by a new multiple high-order derivative spectroscopy technique.

The technique, described in an accompanying abstract (Huguenin et al., these abstracts), permits absorption bands to be detected with an accuracy of better than 3% and often better than 1%. Effects of continuum reflections are suppressed. Spectral resolutions as low as 200 cm^{-1} can be analyzed with minimum loss of sensitivity. Noise levels can be at the few percent level with minimum impact on accuracy.

Nine areas, measured during the 1978 opposition, were analyzed by the technique. Each contained suites of well-defined (accuracy probably within a few percent) absorption bands. These bands can be interpreted in terms of constituent mineralogy by the technique of Adams (1975).

Among the features extracted from the spectra were bands attributed to iron oxides, and these are described elsewhere (Huguenin, these abstracts). Other bands can be attributed to silicates within chemically unweathered rocks/fines. These silicate bands are evident in both dark areas and bright areas, with little obvious masking by dust. In the zeroth order spectrum the dust signature dominates bright area spectra, while dark area spectra show absorptions in the silicate absorption band region. With the derivative technique, detection is sensitive to half width more than band height, and the extent of masking depends on how narrow the overlapping bands are, rather than how strong they are (Huguenin et al., these abstracts). For the Mars data, silicate bands are extracted equally well from bright area and dark area spectra, which has significiant implications for analysis of data from future orbiting spectrophotometer instruments.

Absorption features suggest the presence of Mg-olivine. Derivative analyses of laboratory olivine spectra reveal bands in the vicinity of 1260 nm, 1035 nm, and 862 nm, with variations that are a function of the Mg/Fe ratio. Six of these spectra had sets of bands at these three positions, with ranges of 1220-1284 nm, 1019-1040 nm, and 848-868 nm, consistent with relatively magnesian olivines.

Absorption features consistent with the presence of plagioclase feldspar were observed in all nine spectra. Laboratory spectra reveal band positions that range from 1100 nm to 1350 nm, depending on 2V (large 2V corresponds to short wavelength bands, and low 2V corresponds to long wavelength band positions). Band positions in the Mars spectra cluster near 1100 nm and/or at 1226-1347 nm, suggesting a range of plagioclase compositions.

There are also features that are consistent with the presence of Ca-rich pyroxenes. Sets of bands near 756-802 nm, 937-1003 nm, and 1104-1202 nm are similar to laboratory spectra of Fe^{3+} bearing augite-diopsides, and occur in six of the nine areas. Five spectra have bands at 912-937 nm that are consistent with low-Ca pyroxenes being present in those areas. Bands near 2000 nm are consistent with these assignments, but their positions are probably modified by the strong atmospheric CO_2 absorption feature near those bands and their positions may not be accurate.

While the band positions are well defined, assignments are not necessarily unique. Some ambiguity exists in the assignments of isolated bands within individual spectra, but when suites of bands coexist (3 olivine bands, 2-4 pyroxene bands, etc.) within spectra, assignments are strengthened. For the Mars spectra all but the plagioclase bands were assigned based on the presence of suites of bands. The bands attributed to plagioclase were residual after assignments of suites (Fe_2O_3-FeOOH, olivines, pyroxenes). No bands were missing within suites, and no extraneous bands were left unassigned after the plagioclase assignments.

Additional support comes from derivative analysis of spectra of SNC meteorites, which reveal sets of absorption bands that are similar to the Mars bands. The meteorite bands are in the appropriate positions for the known constitutent minerals, and the assemblages are very similar to those derived for the Mars areas.

The derived silicate mineral assemblages suggest that six of the nine areas may contain relatively low silica olivine basalts (or their coarse-grained equivalents). Two spectra show two high-calcium pyroxenes with no evidence for olivine, and one shows a low-Ca pyroxene and high-calcium plagioclase assemblage with no evidence for olivine. The regions are large and the minerals may not coexist within rocks or fines. The spectra may instead represent composits of several rock types, and thus the observed assemblages cannot be classified. The assemblages are, however, similar to the SNC meteorite assemblages.

The assemblages suggest that source magmas may be relatively calcium-rich and iron rich. The mixed oxidation state charge transfer bands suggest possible high oxygen fugacities in the magma source regions, and suggest a high volatile content.

WATER-ICE CLOUDS ON MARS: LOCATION AND SEASONAL VARIATION

P.R. CHRISTENSEN, L. JARAMILLO, and R. GREELEY
Department of Geology, Arizona State University, Tempe, Arizona, 85287

Water-ice clouds have been located on Mars using Viking Infrared Thermal Mapper (IRTM) broadband spectral observations. The IRTM instrument had 5 thermal bands centered at 7, 9, 11, 15, and 20 μm. The 11 μm channel lies entirely within a broad water-ice absorption feature between 10 and 18 μm which was first observed by the Mariner 9 Infrared Spectrometer (IRIS). The 11 μm band is therefore the most sensitive to emission from a cloud, the 20 μm channel is less sensitive, and the 7 and 9 μm channels are nearly transparent. Clouds were detected by comparing the 11 μm brightness temperature (T_{11}) to the brightness temperatures measured at 7, 9, and 20 μm. In daytime measurements, when the cloud is cold relative to the surface, T_{11} is lower than T_{20}. This spectral signature is the reverse of that produced by non-uniform surface temperatures, non-unit thermal emissivity, or atmospheric dust, thus allowing water-ice clouds to be readily detected.

Using this technique clouds and hazes have been detected in several regions on Mars. They are consistently observed in four northern hemisphere regions centered over Tharsis (-10°S to 50°N, 60° to 160°W), Arabia (0° to 20°N, 300° to 360°W), Elysium (20° to 40°N, 190° to 220°W), and along the boundary between the crater uplands and the northern plains (-10°S to 10° N, 210° to 270°W). These clouds were observed at all seasons when the atmosphere had a low enough dust content to permit their spectral signature to be observed; during the global dust storm period (L_s 200° to 300°) clouds are difficult to distinguish from dust.

During the northern spring and summer (L_s 0° to 180°) when the atmosphere is relatively free of dust, there is a distinct difference between the cloud abundance in the northern and southern hemispheres, with clouds and hazes being rare in the south. There are several possible explanations for this difference. First, clouds will be less likely to form in the south due to low, wintertime atmospheric temperatures and high atmospheric stability (Kahn, 1984). A second possibility involves the importance of orographic control of cloud formation, resulting in more clouds centered over topographic highs that are preferentially located in the north. Finally, northern hemisphere clouds appear to occur preferentially over low thermal inertia regions which are primarily located in the northern hemisphere (Palluconi and Kieffer, 1979). Seasonal atmospheric control is difficult to separate from surface control because clouds are difficult to detect during southern summer due to the presence of atmospheric dust. Thus, clouds are much less commonly observed in both the north and the south during southern summer, although their presence within or beneath the dust haze cannot be ruled out on observational grounds.

A second important class of water-ice clouds are those observed along the boundary of the retreating north polar cap (Christensen and Zurek, 1984). These clouds occur at all longitudes around the cap and are generally confined to within ±5° of the cap boundary. After L_s 90° polar water-ice clouds are no longer observed. Similar clouds are not observed along the southern cap during retreat, although observations are again impaired by the presence of atmospheric dust during this season.

The cloud opacities can be estimated using a δ-Eddington radiative transfer model (Christensen and Zurek, 1984) which incorporates Mie scattering and the electrical properties of water-ice. Assuming realistic, but non-unique, values for the ice particle size and cloud temperature, the

derived opacities range from near-zero to 1. In many cases the hazes observed have very low opacities, making them very difficult to detect from images alone. Thermal IR spectral observations therefore provide an excellent means of detecting thin hazes and making quantitative estimates of their water content. These observations are important for determining the saturation state of the lower atmosphere and of determining the total atmospheric water abundance.

REFERENCES

Christensen, P.R. and R.W. Zurek. 1984. Martian north polar hazes and surface ice: Results from the Viking Survey/Completion mission. J. Geophys. Res., 89, 4587-4596.

Kahn, R. 1983. Some observational constraints on the global scale wind systems on Mars. J. Geophys. Res., 88, 10189-10209.

Palluconi, F.D. and H.H. Kieffer. 1981. Thermal inertia mapping of Mars from 60°S to 60°N. Icarus, 45, 415-426.

First Direct Detection of Clay Minerals on Mars

Robert B. Singer, Pamela D. Owensby (Planetary Geosciences, HIG, U. Hawaii), and Roger N. Clark (USGS Geophysics, Denver)

Magnesian clays or clay-type minerals have been conclusively detected in the martian regolith. Near-IR (0.65-2.55μm) spectral observations of Mars using the Mauna Kea 2.2-m telescope in April 1980 show weak but definite absorption bands near 2.35μm. Extreme care was taken in data reduction to insure the validity of these weak absorptions, which have band depths less than about 3%. The absorption band positions and widths match those produced by combined OH stretch and Mg-OH lattice modes and are diagnostic of minerals with structural OH such as clays and amphiboles. Likely candidate minerals include serpentine, talc, hectorite, and saponite. There is no spectral evidence for aluminous hydroxylated minerals such as kaolinite and montmorillonite, which have analogous bands located near 2.2μm. No distinct band occurs at 2.55μm, as would be expected if carbonates were responsible for the 2.35-μm absorption. The 2.15- to 2.55-μm spectral region is free from other potentially complicating absorptions, such as from adsorbed, solid, or gaseous H_2O and CO_2. High-albedo regions such as Elysium and Utopia have the strongest bands near 2.35μm, as would be expected for heavily weathered soils. Low-albedo regions such as Iapygia show weaker but distinct bands, consistent with moderate coatings, streaks, and splotches of bright weathered material. In all areas observed, the 2.35-μm absorption is at least 3 times weaker than would be expected if well-crystallized clay minerals made up the bulk of bright soils on Mars. Two possible explanations are: 1) crystalline clays are a minority phase mixed with other materials (e.g. palagonites), or 2) the bright soils are homogeneous but not fully crystallized into clay minerals. The magnesian composition determined here is fully consistent with the low Al/Mg ratio measured at both Viking landing sites and with the basaltic spectral characteristics observed in martian low-albedo regions (serpentine, for example, is a common alteration product of pyroxene and olivine on Earth). This evidence strongly supports suggestions for a predominantly mafic or ultramafic martian crust.

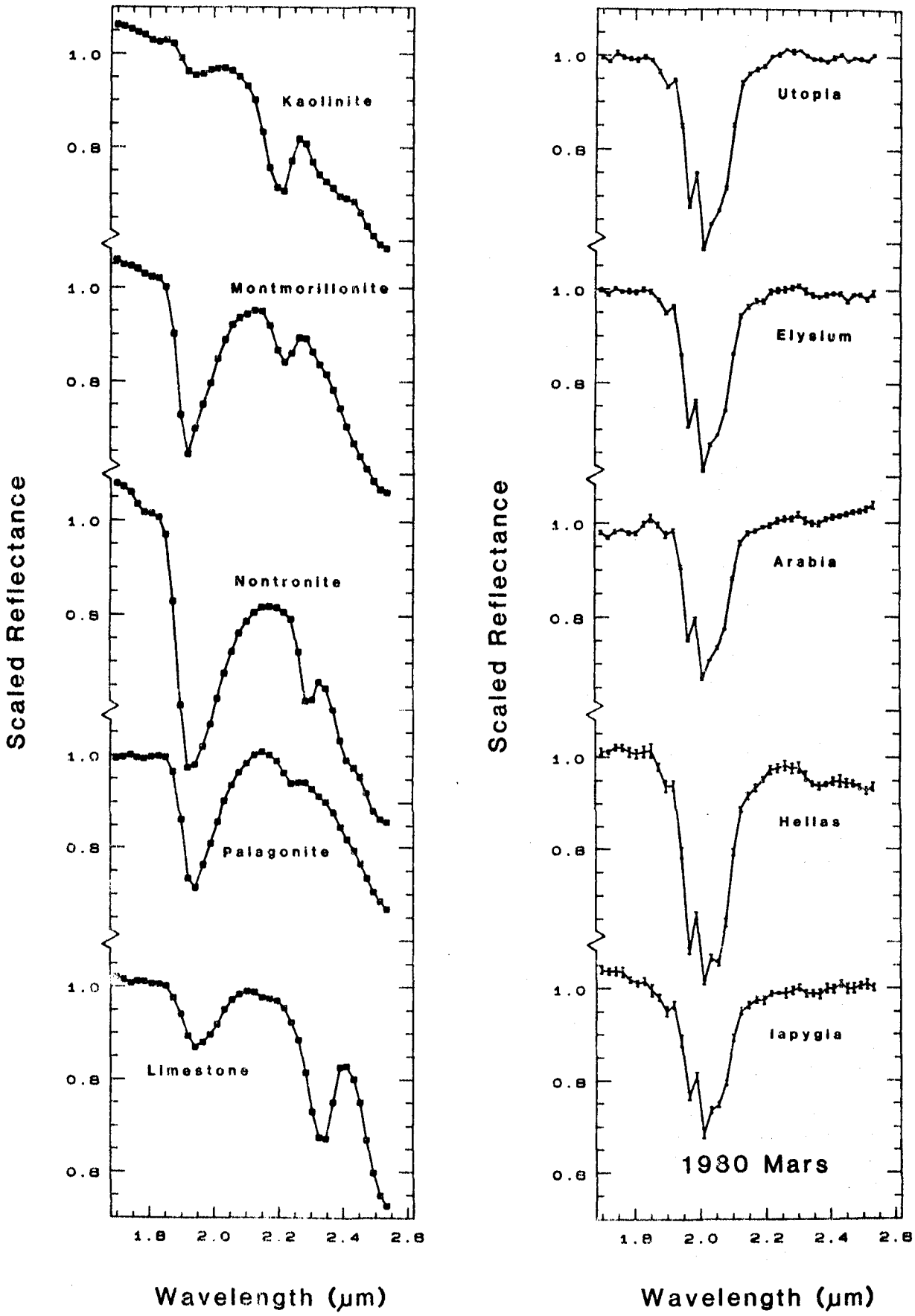
Scaled Reflectance
Kaolinite
Montmorillonite
Nontronite
Palagonite
Limestone
Utopia
Elysium
Arabia
Hellas
Iapygia
1980 Mars
1.0
0.8
1.8
2.0
2.2
2.4
2.6
Wavelength (μm)

IRON OXIDES OF MARS: EVIDENCE FOR CONTEMPORARY WEATHERING

R. L. Huguenin (Remote Sensing Center and Department of Geology/Geography
University of Massachusetts, Amherst 01003

The mineralogy of relatively weathered rocks on Mars place important constraints on models of mechanisms of volatile incorporation, extent of equilibrium with present conditions, and whether alteration processes are contemporary or historical.

Reflectance spectra of Mars measured during 1978 and earlier oppositions have been analyzed using a multiple high order derivative spectroscopy technique. With this technique absorption bands can be extracted from reflectance spectra with accuracies of better than approximately 3% and with high sensitivity. The technique depends on no assumptions about band shape, and continuum contributions are suppressed. Processing is standardized and fully automated. The technique is described by Huguenin et al. (these abstracts).

Among the results of the analysis was the presence of suites of bands in each of the spectra that can be attributed to Fe^{3+} phases. Several of the spectra contained bands that are very close to the band positions in the laboratory spectra of goethite, an hexagonal hydrated ferric oxide. Goethite spectra contains three principal absorption features near 900nm, 670nm, and 530nm. Multiple high order derivative analysis reveals that the 900nm consists of two absorption bands near 850nm and 1090nm that combine to form a composit feature near 900nm. The 670nm feature consists of two bands near 624 and 695nm, while the 530nm feature consists of one band at 531nm. There are additional bands at shorter wavelengths that affect the apparent position of the 530nm feature in the zeroth order reflectance spectrum of goethite. The other iron oxides and Fe^{3+} phases (e.g. silicates with substituted Fe^{3+}) have distinctly different sets of constituent absorption band positions, even though the positions of the composit features are grossly similar for the different phases. The presence of bands in the Mars spectra that are within 0.1 - 3% of the goethite band positions suggest the presence of goethite in those areas.

Spectra of other areas showed absorption bands that were within 3% of the positions for hematite, an hexagonal close packed unhydrated Fe_2O_3. Hematite has a pair of bands at 797nm and 908nm that combine to form an 850nm composit feature. There is a band at 680nm, and one at 567nm, along with shorter wavelength bands. The presence of these "hematite bands" in several of the Mars spectra suggest that hematite may be a principal Fe^{3+} phase in those areas.

Remaining areas showed bands that are intermediate in position to the goethite and hematite bands, suggesting that there may be mixtures of goethite and hematite, and/or intermediate (partially dehydrated goethite) phases present in those areas.

Both bright areas and dark areas showed these suites of "goethite bands" and "hematite bands", and there does not therefore appear to be a correlation

with albedo. The areas that showed the "goethite bands" are, however, within zones of ongoing (1973 spectra) or historically frequent dust cloud activity, and the areas with the "hematite bands" were outside of the zones of frequent dust cloud activity.

This suggests the possibility that the more hydrated phase may occur within a mobile dust component, and that the less hydrated phase may be less mobile. The latter component may correspond to the salt-encrusted duricrust component, and the former may correspond to the unconsolidated drift component that was observed at the Viking Lander sites.

As has been discussed by several investigators, most recently Gooding, goethite is not a stable phase on Mars and should dehydrate over time. Goethite has been proposed to be a primary weathering product by Huguenin, however. The presence of "goethite bands" in the spectra of some areas supports the proposed formation of that phase, and the presence of "hematite bands" and intermediate bands supports the proposed dehydration of that phase. This, combined with proposals that the salt-encrusted component may be an older evolutionary product of the younger unconsolidated component suggests that the goethite may be younger than the hematite. The instability of goethite further suggests that the goethite may be recently formed.

REASSIGNMENT OF THE IRON(III) ABSORPTION BANDS IN THE SPECTRA OF MARS

David M. Sherman, Department of Earth, Atmospheric, and Planetary Sciences, Massachusetts Institute of Technology, Cambridge, Massachusetts 02139

Absorption features in the near-infrared and visible region reflectance spectra of Mars have been assigned to specific Fe^{3+} crystal-field and $O^{2-} \rightarrow Fe^{3+}$ charge transfer transitions [1]. Recently, we have obtained near-ultraviolet absorption spectra of iron oxides [2] and have also determined the energies of $O^{2-} \rightarrow Fe^{3+}$ charge-transfer (LMCT) transitions from accurate SCF-Xα-SW molecular orbital calculations on $(FeO_6)^{9-}$ and $(FeO_4)^{5-}$ clusters [3]. (The new calculations are an improvement over those of [4] insofar as the "overlapping sphere" approach to the molecular potential was used.) Both the theoretical and experimental results, together with existing data in the literature, show that some of the previous Fe^{3+} band assignments in the spectra of Mars need to be revised.

Theory of Fe^{3+} spectra in minerals.

Figure 1 gives the Tanabe-Sugano diagram for the electronic states of Fe^{3+} in either octahedral or tetrahedral coordination. The ground $^6A_1$ state arises from the one-electron orbital configuration $(t_2^{\alpha})^3(e^{\alpha})^2$ where α implies a spin-up orbital. The first two excited states, $^4T_1$ and $^4T_2$, arise from the configuration $(t_2^{\alpha})^3(e^{\alpha})^1(t_2^{\beta})^1$ where β indicates a spin-down orbital. In this configuration, the e^{α} orbital is occupied by only one electron; hence, this configuration will undergo a Jahn-Teller splitting. Although usually not recognized as such, this effect is observed in the spectra of Fe^{3+} minerals as splittings of the $^4T_1$ and $^4T_2$ absorption bands. The rest of the ligand field states in Fig. 1 arise from the "spin-flip" configurations $(t_2^{\alpha})^2(e^{\alpha})^2(t_2^{\beta})^1$ and $(t_2^{\alpha})^3(e^{\alpha})^1(e^{\beta})^1$. Relative to the ground configuration, the energies of these configurations are independant of 10Dq. The states arising from these configurations occur at nearly constant energies in different Fe^{3+} oxides and silicates. (The small dependance of the high r energy $^4T_1$ and $^4T_2$ states on 10Dq is due to configurational interaction.) In these minerals, the $^4E,^4A_1(^4G)$ state occurs at ca. 23 kK (0.43μ) while the $^4E(^4D)$ state occurs at ca. 27 kK (0.37μ).

Fig. 1.

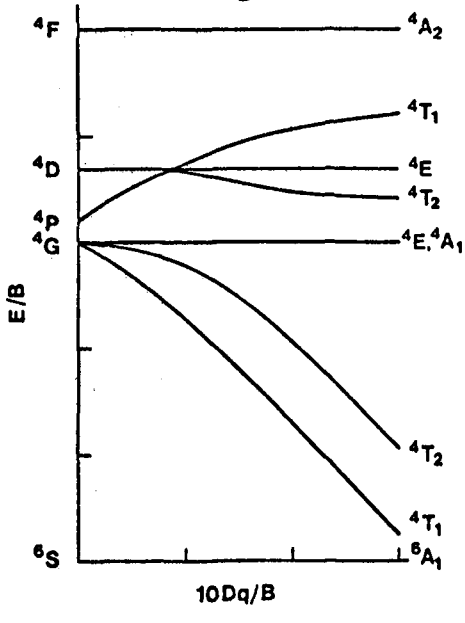

For octahedrally coordinated Fe^{3+}, the lowest energy LMCT transition is from a t_{1u}^{β} O 2p non-bonding orbital to the t_{2g}^{β} Fe^{3+} "crystal field" orbital. From the SCF-Xα-SW molecular orbital calculations, the energy of this transition is estimated to be 37.9 kK (0.26μ) for an $(FeO_6)^{9-}$ cluster with an Fe-O distance of 2.05 A.

The Fe^{3+} ligand field transitions are expected to be both spin- and parity-forbidden. In many systems, however, these transitions become allowed through the coupling of adjacent Fe^{3+} centers by Fe-O-Fe superexchange [5]. In addition to intensifying the Fe^{3+} ligand field transitions, the Fe-O-Fe coupling allows for a new type of electronic transition, namely, the simultaneous excitation of two Fe^{3+} centers by a single photon. These transitions occur at energies given approximately by the sum of two Fe^{3+} ligand field transition energies. At present, these transitions are not fully understood and, in many systems, their identities are uncertain. These phenomena have useful implications for the spectrum of Mars and have been discussed by [6].

Figure 2 shows the near UV to visible region spectrum of goethite and maghemite. These spectra are very similar to those of the other iron oxides and Fe^{3+} smectites [7]. Features corresponding to the $^4A_1$,^4E (^4G) and $^4E(^4D)$ states occur at their expected energies. The energy of the $^4T_1(^4G)$ state is already known (e.g. [8]). From these three state energies, we can calculate the ligand field parameters 10Dq, B and C and use these to estimate the energies of the other ligand field states. These energies can then be used to assign the remaining features in the spectrum. This procedure gives an internally consistent assignment scheme and physically reasonable values for 10Dq, B and C. The values for 10Dq are in good agreement with that estimated from the $(FeO_6)^{9-}$ MO calculation (15.8 kK). The highest energy features are assigned to LMCT transitions. Their energies are in good agreement with those estimated by the MO results. The only feature which cannot be directly explained by either the ligand field theory or the MO calculations is the band at 0.49-0.53 μ. This can be assigned to either a split component (via the dynamic Jahn-Teller effect) of the $^4T_2(^4G)$ band or to the lowest energy Fe-Fe pair transition, $^6A_1+^6A_1 \rightarrow {}^4T_1+{}^4T_1$. Its absence in the spectra of magnetically dilute systems [e.g. 9] suggests that the latter assignment is correct.

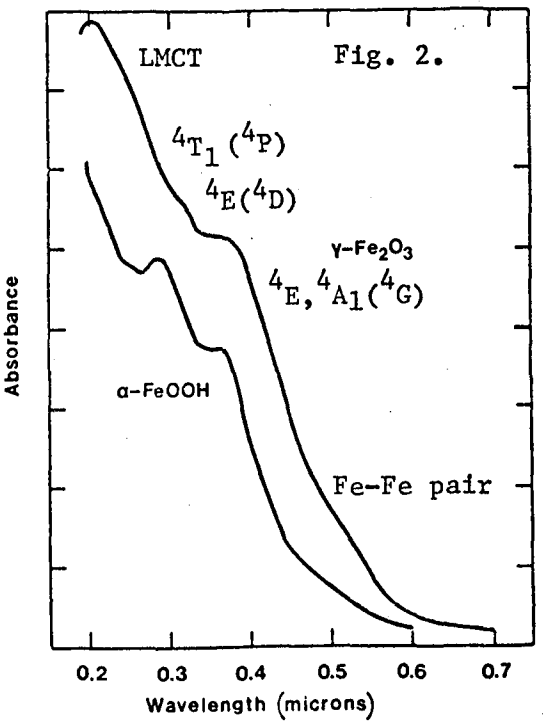

Fig. 2.

Application to the spectrum of Mars.

Table 1 gives the range of energies observed for transitions in different Fe^{3+} oxides and silicates together with a new band assignment scheme for the spectra of Mars. The band positions in the spectrum of Mars are only approximate. In the Martian spectrum, the visible region absorption edge is due mainly to the Fe^{3+} ligand field transitions (intensified by the Fe-O-Fe superexchange interactions) and the Fe-Fe pair excitation. When higher-resolution spectra of Mars become available, these band assignments may allow for an estimate of the ligand field parameters of Fe^{3+} in the Martian mineralogy. It is uncertain, however, whether this would be mineralogicaly diagnostic since these quantities show little variation among iron oxides and silicates [10].

Transition	Range(μ)	Mars
$^4T_1(^4G)$	0.86-0.96	0.87
$^4T_2(^4G)$	0.64-0.66	0.6-0.7
Fe-Fe pair	0.49-0.53	0.5
$^4E,^4A_1(^4G)$	0.42-0.44	0.43
$^4T_2(^4D)$	0.38 (weak)	--
^4E (^4D)	0.36-0.37	0.37
$^4T_1(4P)$	0.29-0.31	--
LMCT	0.24-0.26	--

References. [1] Huguenin, R.L.,et al., LPSC VIII, 478-480 (1977). [2] Sherman, D.M., and D. Waite, Am. Mineral. (submitted). [3] Sherman, D.M., Phys. Chem. Mineral. (submitted).[4] Tossell, J.A., et al., Nature, 244, 42-45, (1973). [5] Lohr, L.L., Coord. Chem. Rev., 8, 24-259 (1972). [6] Sherman, D.M., LPSC XIV, 692-693 (1983). [7] Karickhoff, S.W. and Bailey, G.W., Clays and Clay Min., 21, 59-70 (1973). [8] Mao, H.K. and P.M. Bell, Carnegie Inst. Wash., 73, 502-507 (1974). [9] Lehmann, G., Zeit. Phys. Chem. 72, 279-297 (1970). [10] Work supported by NASA grant NSG-7604 to R.G. Burns.

Zeolites on Mars: Prospects for Remote Sensing

E. S. Gaffney (Los Alamos Nat'l. Lab.), R. B. Singer (U. Hawaii), T. D. Kunkle (Los Alamos Nat'l. Lab.)

Zeolites are hydrous aluminosilicate minerals which are commonly found on earth as alteration products of glass and tuffs, and associated with basic igneous rocks. Their structures have open silicate frameworks with large channels which can accomodate molecules such as water, CO_2 and other volatiles. These molecules are not structural and devolatilization is usually reversible. Weathering in an appropriate alkaline environment alters mafic glass to palagonite and zeolites. Phillipsite, analcime and chabazite are commonly formed, with the palagonite usually depleted in K, Na, Ca, Si, and Al and enriched in Ti relative to the original glass (1). The Martian surface composition measured by Viking can be represented by several combinations of minerals incorporating major fractions of zeolites known to occur in altered mafic rocks and polar soils on earth. The abundant occurence of zeolites on Mars is consistent with what is known about both the physical and chemical environment of that planet. We have measured the laboratory reflectance spectra (0.65 to 2.55μm) of a number of relatively pure zeolite minerals and some naturally occurring zeolite-clay soils. Most published spectra of this mineral group were taken farther in the infrared and are therefore less directly applicable to remote sensing at this time. All of the spectra measured are dominated by strong absorption near 1.4 and 1.9μm and a steep reflectance drop longward of about 2.2μm, all of which are due to abundant H_2O. Weaker water overtone bands are also apparent, and in most cases there is spectral evidence for minor Fe^{3+}. In these features the zeolite spectra are similar to spectra of smectite clays which have abundant interlayer water. The most diagnostic difference between clay and zeolite spectra is the total absence in the zeolites of the weak structural OH absorption which phyllosilicates show in the 2.2 to 2.4-μm region (2). From observations of a number of natural soils containing both smectites and zeolites, we feel that systematics can be developed to permit semi-quantitive differentiation of these species using near-IR spectral reflectance. (1) Hay & Iijima, *GSA Mem. 116*, 331-376. (2) Hunt & Salisbury, *Mod. Geol. 1*, 283-300, 1970.

ELECTRONIC SPECTRA OF MATERIALS SIMULATING PLANETARY SURFACES

Roger G. Burns, Virginia Mee Burns, Melinda Darby Dyar, David M. Sherman, Department of Earth, Atmospheric, and Planetary Sciences, Massachusetts Institute of Technology, Cambridge, Massachusetts 02139

Transition metal-bearing phases in regoliths of the Moon and Mars, and in certain meteorites, contribute to the thermodynamic (redox) stabilities, crystal chemistry, and remote-sensed UV-visible-near IR spectra of these planetary bodies, providing clues to their evolutionary histories. Using a variety of spectroscopic, microanalytical, and diffraction techniques, as well as theoretical modelling by molecular orbital calculations, the MIT group is studying spectral properties of natural and synthetic materials simulating compositions, temperatures, redox conditions, etc., on sunlit surfaces of the Moon and Mars, and refractory phases in meteorites. For example, studies of melts simulating lunar green (15426) and orange (74220) glass spherules, which were rapidly cooled in a variety of quenching media, have revealed different valencies and site occupancies of Fe cations, and produced information on cooling histories of the quenched glasses [Dyar et al., JGR, 88, B221; L&PS, XV, 236; J. Non-Cryst. Sol., in press]; experimental and theoretical studies of numerous Fe^{3+}-bearing phases have demonstrated that mineral structures providing cation disorder and minimal magnetic coupling between adjacent Fe^{3+} ions (e.g. feroxyhyte, ferrihydrite, gels, clays) are likely constituents of the bright areas identified in remote-sensed reflectance spectral profiles of Mars' regolith [Sherman et al., JGR, 87, B10169; L&PS, XV, 764; Phys. Chem. Min., in press]; measurements of refractory corundum and hibonite suggest that their blue colors may originate from $Fe^{2+} \rightarrow Ti^{4+}$ intervalence transitions across face-shared octahedra. Alternatively, observed enrichments of Fe cations in the unusual trigonal bipyramidal site in hibonite suggest that crystal field transitions in V^{3+} and Ti^{3+} located in this 5-fold site could also be responsible for blue and orange colorations of meteoritic hibonites [Burns, Burns, L&PS, XV, 108; Adv. Ceram., in press]. Research is proposed in five tasks: (1) spectra of additional lunar glass compositions quenched in different media; (2) spectra and magnetic properties of other Fe^{3+}-bearing phases relevant to Mars' regolith; (3) low temperature ultraviolet diffuse reflectance spectra of Fe^{2+} silicate and Fe^{3+} oxide minerals; (4) spectral and crystal chemical studies of transition metal-bearing refractory hibonite, rhonite, and melilite minerals found in carbonaceous chondrites; and (5) quantitative molecular orbital energy level calculations for transition metal cation coordination clusters relevant to tasks 1-4.

REMOTE SENSING ANALYSES OF LOCALIZED LUNAR DARK MANTLE DEPOSITS

L. R. Gaddis, P. Lucey, J. Bell, and B.R. Hawke; Planetary Geosciences Division, Hawaii Institute of Geophysics, University of Hawaii, Honolulu, HI 96822

INTRODUCTION

Localized lunar dark mantle deposits are small, low-albedo units of probable pyroclastic origin which are broadly distributed across the nearside of the Moon[1]. These deposits, typified by the Alphonsus dark-halo craters, are generally associated with large highland craters along the perimeters of many of the major lunar maria. Characteristics of the Alphonsus dark-halo craters include: small size (less than 3 km across), noncircular shape, and alignment along crater floor-fractures. They are commonly surrounded by peripheral deposits of low-albedo, generally block-free material[2,3]. Morphometric analyses of these "haloes" have led investigators to suggest an eruption mechanism analogous to that of terrestrial vulcanian explosive eruptions[2]. In this style of eruption, the accumulation of gas in a capped magma chamber leads to explosive decompression, and the subsequent emplacement of a pyroclastic deposit around an endogenic source crater.

Although a possible eruption mechanism has been proposed for the Alphonsus localized dark mantle deposits, a number of questions remain concerning the compositions and modes of emplacement of these and other similar deposits. Do intra- and inter-deposit compositional variations exist? Head and Wilson[2] have presented strong evidence that significant amounts of non-juvenile materials are present in the Alphonsus dark haloes. Remote sensing data for these deposits indicate that they have compositions with mare affinities[2]. Do all localized dark mantle deposits have basaltic compositions? Finally, how do the compositions of localized dark mantle deposits compare to those of the large regional dark mantle deposits such as those near Taurus-Littrow, Aristarchus, and Rima Bode? Remote reflectance spectra for these regional deposits suggest that they have a volcanic glass component[4,5,6]. Do localized dark mantle deposits also contain volcanic glasses? In an effort to address some of these questions, we have obtained near-infrared (0.6 to 2.5 microns) spectral reflectance data (Figure 1) for the following 12 localized lunar dark mantle deposits: Alphonsus CA and R (13° S, 4° W); Archimedes south rim (28° N, 4° W); Aristoteles East 1 (50° N, 35° E) and 2 (50° N, 28° E); Atlas dark-halo craters 1 and 2 (47° N, 45° E); Franklin floor (39° N, 48° E); Grimaldi pyroclastics (1° S, 65° W); J. Herschel (62° N, 41° W); Rima Fresnel (28° 30' N, 4° E); and Vitruvius floor (17° N, 31° E).

PRELIMINARY DATA ANALYSIS AND INTERPRETATIONS

The dominant feature in these data is the Fe^{+2} absorption band in the 1.0 micron wavelength region. In order to emphasize differences in the characteristics of this absorption band, a straight-line continuum has been

removed from these spectra. On the basis of the depth and shape of this "1.0 micron" absorption band, these spectra can be separated into 3 groups. Spectra which can be considered representative of each of these three groups are presented in Figure 1. Group 1 includes spectra from Grimaldi pyroclastics (A in Figure 1), Franklin floor, Atlas dhc 1, and Archimedes south rim. Absorption band centers in this group are located near 0.93-0.95 microns, and depths are approximately 4-5%. The shape of the "1.0 micron" band in these spectra can be described as "check-like", with a straight, steep short-wavelength edge and a straight longer-wavelength edge with a shallower slope. Group 2 is comprised of spectra from Aristoteles East 1 (B in Figure 1) and 2, Rima Fresnel and Atlas dhc 2. As apparent in the spectrum for Aristoteles East 1, these "1.0 micron" bands are centered near 0.96 micron, and are deeper (7%) and more symmetrical than those in Group 1. Spectra in group 3 are represented by that of J. Herschel (C in Figure 1); the two Alphonsus spectra, although noisy, most closely resemble this spectrum. The J. Herschel spectrum has a moderately deep (7%), broad absorption band in the 1.0 micron wavelength region.

Each of the 3 spectra presented in Figure 1, although they were all obtained for localized lunar dark mantle deposits, is spectrally distinct. These spectra therefore reflect marked compositional variations among the localized deposits. Spectra from Group 2 most closely resemble mature mare spectra. The 0.96 micron band centers for this group correspond to those of calcium-rich pyroxenes, the dominant mafic mineral of the lunar mare basalts. Both the spectral features and the geologic relationships exhibited by Group 2 deposits are consistent with an origin as the products of vulcanian eruptions which are dominated by fragmented basaltic plug rock material with much lesser amounts of highlands debris and juvenile material. The relatively broad, shallow "1.0 micron" bands in Group 1 spectra are similar to those exhibited by spectra obtained for many mature highland areas. However, the low albedoes of the deposits which have Group 1 spectra as well as their unusual 0.40/0.56μm ratios suggest the presence of an additional component, probably an Fe-Ti-rich volcanic glass. The spectral characteristics of Group 1 deposits generally fall between those of highlands material and Fe-Ti-rich pyroclastic deposits. These deposits may prove to be composed of highlands-rich wall rock and glass-rich juvenile material with much lesser amounts of basaltic cap rock material. Further analyses of these spectra are required in order to better constrain their compositional affinities. Finally, quantitative analysis of the J. Herschel spectrum of Group 3 has indicated that the "1.0 micron" absorption band is attributable to the presence of a mixture of olivine and pyroxene in the soils of this region.[7]. The other members of this group may also contain material rich in olivine and pyroxene as well as pyroclastic glass. Lesser amounts of fragmental basaltic plug rock/ and highlands-rich wall rock may also be present.

REFERENCES CITED

1) Wilhelms, D. and McCauley, J. (1971). Geologic map of the near side of the Moon. USGS Map I-703.

2) Head, J. and Wilson, L. (1979). Alphonsus-type dark-halo craters: Morphology, morphometry and eruption conditions. PLPSC 10, 2899.
3) Zisk, S., Pettengill, G., and Catuna, G. (1974). High-resolution radar map of the lunar surface at 3.8-cm wavelength. Moon, 10, 17.
4) Pieters, C., McCord, T., Charette, M., and Adams, J. (1974). Lunar surface: Identification of the dark mantling material in the Apollo 17 soil samples. Science, 183, 1191.
5) Hawke, B., Lucey, P., McCord, T., Pieters, C., and Head, J. (1983). Spectral studies of the Aristarchus Region: Implications for the composition of the lunar crust. LPS XIV, 289.
6) Gaddis, L., Adams, J., Hawke, B., Head, J., McCord, T., Pieters, C., and Zisk, S. (1981). Characterization and distribution of pyroclastic units in the Rima Bode region of the Moon. LPS XII, 318.
7) McCord, T., Clark, R., Hawke, B., McFadden, L., Owensby, P., Pieters, C., and Adams, J. (1981). Moon: Near-infrared spectral reflectance, a first good look. JGR, 86, 10883.

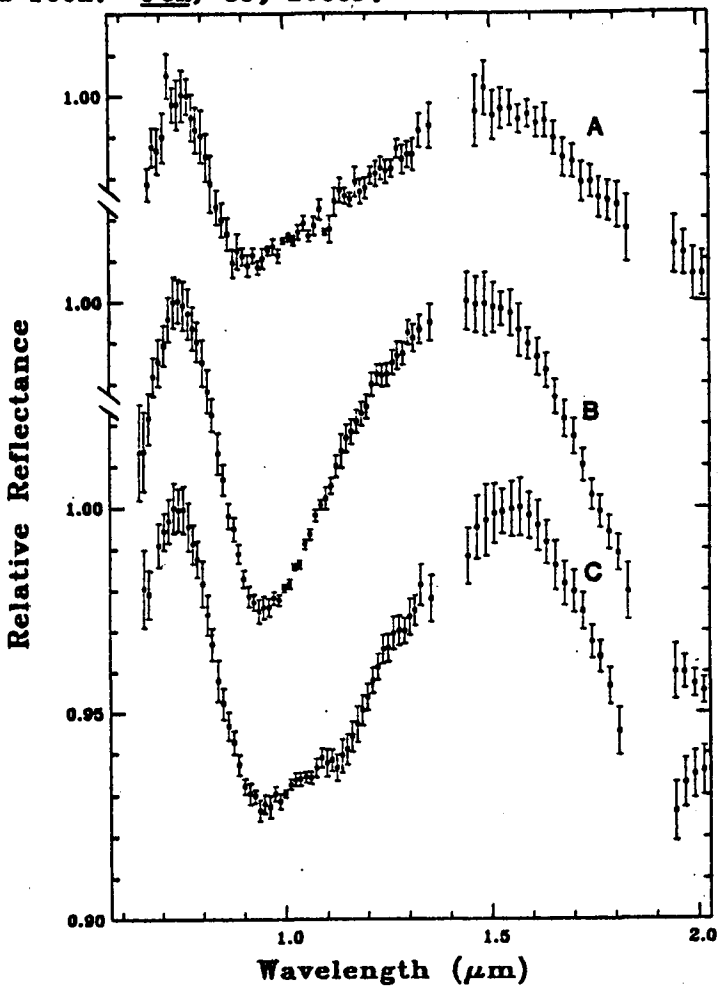

FIGURE 1. Continuum-removed, near-infrared spectra of 3 spectrally distinct localized lunar dark mantle deposits: A) Grimaldi pyroclastics, B) Aristoteles East 1; C) J. Herschel. Each tic-mark on the vertical axis represents a 1% relative reflectance interval.

SPECTRAL REFLECTANCE STUDIES OF THE ORIENTALE BASIN

B. R. Hawke, P. Lucey, and J.F. Bell, Planetary Geosciences Division, Hawaii Institute of Geophysics, University of Hawaii, Honolulu, HI 96822; and P.D. Spudis, Department of Geology, Arizona State Univ., Tempe, AZ 85287.

INTRODUCTION: The Orientale impact occurred in rugged highlands on the southwestern limb of the Moon and was the last of the major basin-forming events. Valuable insight concerning lateral and vertical changes in the composition of the lunar crust can be provided by studies of material exposed by lunar impact basins. These impacts have excavated material from a variety of depths and deposited this ejecta in a systematic manner. Hawke et al. (1) recently presented the results of orbital geochemistry and chemical mixing model studies of the Orientale basin region. It was concluded that the Orientale ejecta north of the basin are dominated by anorthositic material and that only very minor amounts of low-K Fra Mauro basalt are present. In addition, no deposits rich in mafic material of possible mantle origin were identified. Unfortunately, Apollo orbital geochemistry data are available only for terrain north of Orientale. In order to investigate the composition of materials exposed on the interior of Orientale basin, we have collected near-infrared reflectance spectra for units within the Cordillera ring. The purpose of this paper is to present the preliminary results of an analysis of these spectra.

METHOD: Twelve near-infrared spectra (0.6-2.5μm) were recently (October, 1983) obtained at the Mauna Kea Observatory 2.2-m telescope using the Planetary Geosciences Division indium antimonide spectrometer. These include spectra obtained for two fresh surfaces on the inner Rook ring, two fresh craters in the outer Rook Mts. (Eichstadt K, 13-km. in diameter and an unnamed 15-km. crater), and two fresh 11-km. craters (Eichstadt G and H) which are located between the outer Rook ring and the Cordillera ring and expose material from within the knobby facies of the Montes Rook Formation (2) [domical facies of Head (3)]. In addition, spectra were collected for portions of the Maunder Formation (2) which is restricted to the central part of Orientale basin within the Montes Rook ring as well as for portions of Lacus Veris and Lacus Autumni. Extinction corrections were made using the techniques described by McCord and Clark (4). Analyses of absorption bands and continuum slopes were made using the methods presented by McCord et al. (5). The six most relevant spectra are shown in Figure 1 after continuum removal.

RESULTS AND DISCUSSION: Analyses of the spectra obtained for the mare units on the interior of Orientale (Lacus Veris and Lacus Autumni) indicate that these surfaces are contaminated by variable amounts of local highland debris. This is not surprising in light of the limited areal extent of the mare units and the proximity of highland terrain. The presence of a highlands component complicates comparisons with spectra of common nearside mare deposits. The contributions of highlands debris will have to be subtracted by means of newly developed spectral mixing models before additional progress can be made. However, the evidence currently available suggests that the mare deposits within the Orientale basin are similar in composition to nearside mare deposits.

One spectrum was obtained for a portion of the Maunder Formation that

is restricted to the central portion of the Orientale basin within the Montes Rook ring; it has been interpreted to consist largely of Orientale impact melt (2,3). This spectrum exhibits characteristics typical of mature highlands material and is almost identical to spectra obtained for mature units in the vicinity of the Apollo 16 landing site. A similar composition is implied. These results are consistent with those of recent orbital geochemistry studies (6-8).

Special attention was paid to the spectra collected for six immature features within the Cordillera ring, (Figure 1). These fresh features should expose relatively unweathered rock surfaces. Eichstadt G and H (D and C in Figure 1) should be dominated by the material which comprises the knobby facies of the Montes Rook Formation. Eichstadt K and an unnamed crater (E and F in Figure 1) in the outer Rook Mts. should expose the major components of the third Orientale ring. Analyses of the 1-μm band positions and shapes as well as continuum slopes indicate that the spectra for craters in the knobby facies and in the outer Rook Mts., while differing in detail, exhibit many common spectral characteristics. These spectra represent relatively fresh highlands rocks dominated by abundant Fe-bearing plagioclase feldspar and Ca-poor orthopyroxene. Compositions ranging between noritic anorthosite and anorthositic norite are indicated. There is no evidence for the presence of an ultramafic component.

The spectra obtained for the fresh surfaces (a steep massif slope and a small crater on a massif) inthe inner Rock Mts. (A and B in Figure 1) proved to be very different. No well-defined absorption bands are seen. We suggest that at least this portion of the inner Rook Mts. is dominated by plagioclase feldspars which have been subjected to shock pressures of ~200 kb (9,10). There is no evidence for the presence of mantle material in the inner Rook ring.

REFERENCES: 1) B. Hawke et al. (1982) LPS XIII, 306; 2) D. Scott et al. (1977) USGS Map I-1034; 3) J. Head (1974) The Moon, 11, 327; 4) T. McCord and R. Clark (1979) Pub. A.S.P., 91, 571; 5) T. McCord et al. (1981) JGR, 86, 10833; 6) A. Metzger et al. (1981) PLPSC, 12B, 751; 7) C. Andre and F. El-Baz (1981) PLPSC, 12B, 767; 8) P. Spudis (1982) Ph.D. dissertation, Ariz. State Univ.; 9) J. Adams et al. (1979) LPS, X, 1; 10) E. Bruckenthal and C. Pieters (1984) LPS, XV, 96.

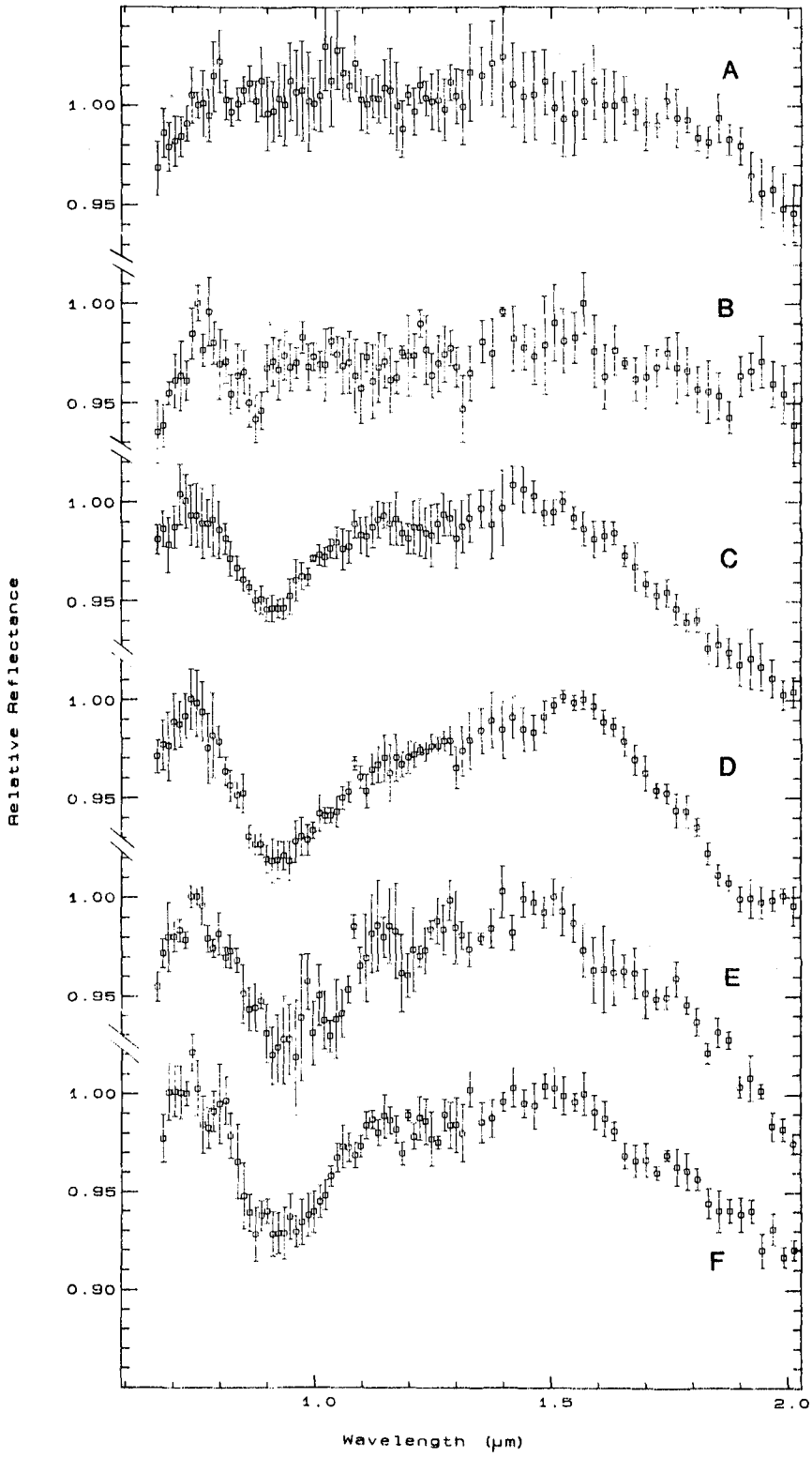
A
B
C
D
E
F
1.00
0.95
0.90
Relative Reflectance
1.0
1.5
2.0
Wavelength (μm)

Figure 1

Accurate Albedos of the Brightest Regions on Io

Damon P. Simonelli and Joseph Veverka, Laboratory for Planetary Studies, Cornell University

The brightest, coldest areas on Io, the "white" regions, may act as cold traps for SO_2 gas, and thus have an important role in governing the pressure, diurnal variation, and flow of the satellite's tenuous SO_2 atmosphere (Matson and Nash, 1983; Ingersoll and Yung, 1984). Therefore, it is essential to derive accurate albedos for the brightest regions, where the necessary "albedos" are those in the energy balance equation of the surface used to compute temperatures (Squyres and Veverka, 1982).

To date, we have studied 41 of the brightest of the white areas (Fig. 1), each 60-120 km on a side. The simplest way to estimate the required energy balance albedo for each region is to determine the Bond albedo of a planet covered with that type of material. This is a three-step process: first, we determine the geometric albedo $p(\lambda)$ for each region. Measurement of I/F from Voyager images at phase angles of less than 6°, combined with information on the limb darkening and opposition surges of white regions (Simonelli and Veverka, 1985) allows us to derive the normal reflectance r_n in the five narrowband Voyager filters. Combination of r_n and limb darkening data then leads to a geometric albedo in each filter. Second, we need to estimate the phase integral $q(\lambda)$ for each region. A first order approximation is to assume that all regions have the disk-integrated phase integrals determined for Io by Simonelli and Veverka (1984). As the bright white regions might be expected to have larger q's than those of Io as a whole, the albedos that will result from this approximation are likely lower limits. Third, we compute the Bond albedo of each region as follows: the product pq in the various filters is averaged over wavelength, with weighting by the solar spectrum. The albedo is further scaled to correct for the excess redness of Voyager spectra (Johnson et al., 1983; Simonelli and Veverka, 1984).

The albedos that result from this procedure are shown in Fig. 2. With the exception of several darker regions on the poorly-resolved post-eclipse face of Io (see the 0-70° W histogram in Fig. 2), typical albedos are 0.6-0.7. The "brightest" areas studied (albedo ~0.7) are located in the cluster of white regions east of Prometheus (longitudes 90-140° W). It is possible using Voyager data and fits to Hapke's equation (Hapke, 1981) to derive albedos for the bright regions without making any assumptions about the phase integrals. Such an analysis is in progress.

This work was supported by NASA's Planetary Geology Program under Grant NSG 7156.

References

Hapke, B. W. (1981). Bidirectional reflectance spectroscopy. I. Theory. J. Geophys. Res. 86, 3039-3054.

Johnson, T. V., L. A. Soderblom, J. A. Mosher, G. E. Danielson, A. F. Cook, and P. Kupferman (1983). Global multispectral mosaics of the icy galilean satellites. J. Geophys. Res. 88, 5789-5085.

Ingersoll, A., and Y. Yung (1984). Supersonic flow on Io. In preparation.

Matson, D. L., and D. B. Nash (1983). Io's atmosphere: Pressure control by regolith cold trapping and surface venting. J. Geophys. Res. 88, 4771-4783.

Simonelli, D. P., and J. Veverka (1984). Voyager disk-integrated photometry of Io. Icarus 59, in press.

Simonelli, D. P., and J. Veverka (1985). Opposition surges and normal reflectances of regions on Io. In preparation.

Squyres, S. W., and J. Veverka (1982). Variation of albedo with solar incidence angle on planetary surfaces. Icarus 50, 115-122.

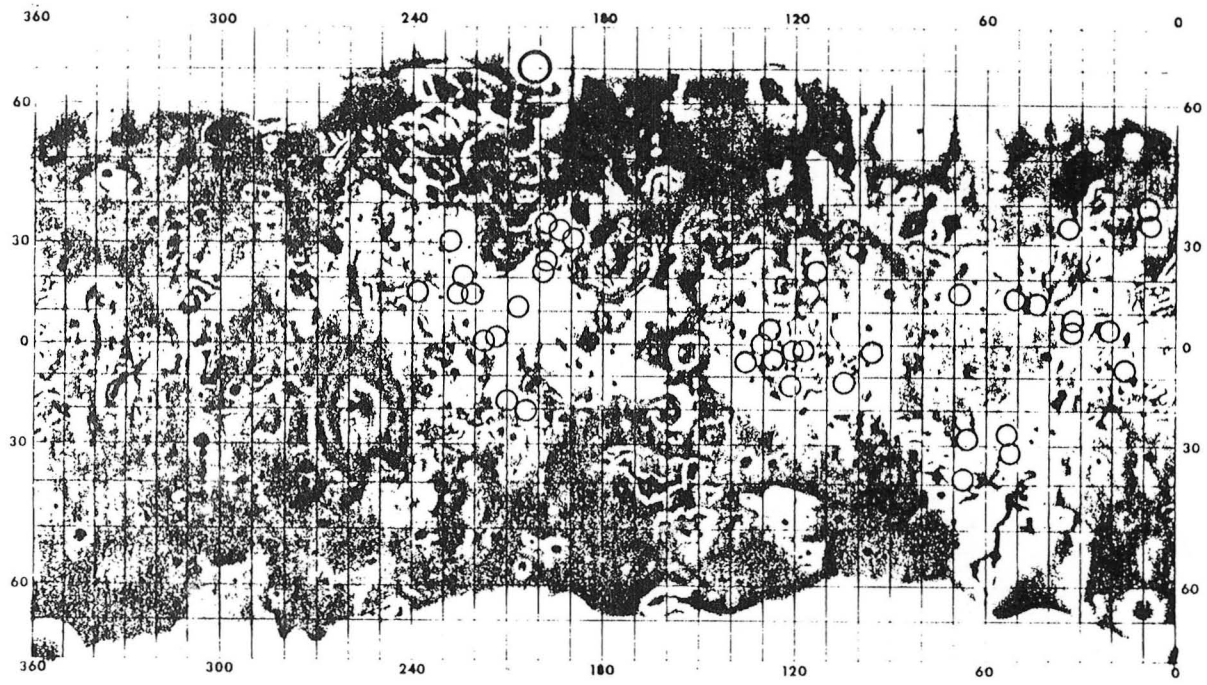

Figure 1. Locations of the forty-one "white" regions under study (solid circles), displayed on a map of Io.

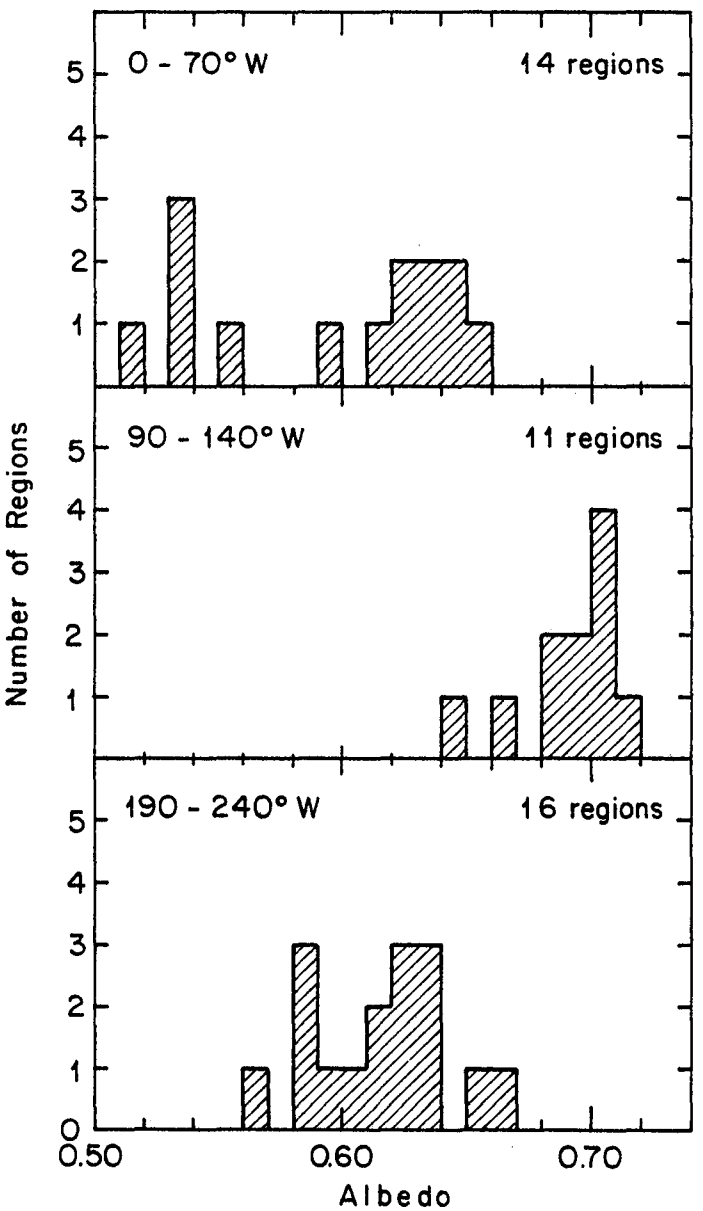

Figure 2. Histograms illustrating the albedos derived for the forty-one regions shown in Fig. 1. For ease of display, the regions have been separated into three groups according to longitude, and a separate histogram has been drawn for each group.

Io: Precise Comparison of Voyager Spectral Curves with Laboratory Measurements

Damon P. Simonelli and Joseph Veverka, Laboratory for Planetary Studies, Cornell University

The most accurate way to compare spacecraft spectra of planetary surface regions with laboratory data on candidate materials is to correct both sets of spectra to the form of a normal reflectance r_n as a function of wavelength, where $r_n = I/F$ ($i = e = \alpha = 0°$). For spacecraft data, this involves correction for limb darkening and accurate extrapolation to zero phase (i.e., including the effect of the opposition surge). In the case of Ionian surface materials, there are previous data on limb darkening (Clancy and Danielson, 1981; McEwen and Soderblom, 1984) but as yet none on phase behavior. In order to derive more accurate normal reflectances for regions on Io, we have thoroughly analyzed the near-opposition ($\alpha < 10°$) photometry of a set of regions on the 20°W face of the satellite, the face with the most complete near-opposition Voyager imaging coverage. Sixty-eight regions were chosen for study, each ~120 km on a side, and divided into three coherent color classes: "white," "orange," and polar "brown" regions. Derivation of normal reflectance spectra of these regions is a three-step process: (1) we make our own determination of the Minneart parameters B_0 and k for each class of regions in each of the twenty images studied; (2) we use these k's to correct for limb darkening, and obtain phase curves for each region in each Voyager filter; and (3) we extrapolate these phase curves to opposition, using a straight-line fit to the opposition surge-dominated section of each curve ($\alpha \lesssim 6°$), to obtain the normal reflectance of each region in each filter.

The derived Minneart parameters (Fig. 1), while generally consistent with previous limb darkening determinations, show a few interesting new trends: (1) for the white regions, k rises linearly with increasing B_0, which is the trend to be expected for normal materials (see the plot for yellow sulfur in Fig. 1); (2) the white regions are slightly limb brightened ($k < 0.5$) at low wavelengths (low values of B_0); and (3) k appears to drop with rising B_0 for the orange regions, contrary to the trend expected for most materials. The most intriguing result of our study of the phase behavior is seen for orange regions in the violet filter: despite similar reflectances, there is one group of orange regions with large opposition surges and a second group showing significantly lower surges, possibly indicating differences in surface texture (porosity and/or particle size). Finally, the normal reflectances derived for the chosen regions on Io are shown in Fig. 2. Included for comparison in Fig. 2 are laboratory spectra of various sulfur samples (Gradie and Veverka, 1984; Gradie et al., 1980; Gradie and Moses, 1983) processed to facilitate direct comparison with the Io data: the lab data have been extrapolated to zero phase where feasible, corrected to a temperature appropriate to the dayside of Io (130° K), and convolved with the spectral response curves of the appropriate Voyager camera/filter combinations. The derived normal reflectance spectra serve to emphasize some features seen in previous studies of disk-resolved Io spectra: (1) as the "white"

region spectra clearly drop towards the ultraviolet, these regions are certainly not white in the spectral sense; and (2) the reflectances of Ionian materials are typically higher in the ultraviolet than those of candidate sulfur samples.

This work was supported by NASA's Planetary Geology Program under Grant NSG 7156.

References

Clancy, R. T., and G. E. Danielson (1981). High resolution albedo measurements on Io from Voyager 1. J. Geophys. Res. 86, 8627-8634.

Gradie, J., and J. Moses (1983). Spectral reflectance of unquenched sulfur. Lunar and Planet. Sci. XIV, 255-256.

Gradie, J., and J. Veverka (1984). Photometric properties of powdered sulfur. Icarus 58, 227-245.

Gradie, J., P. Thomas, and J. Veverka (1980). The surface composition of Amalthea. Icarus 44, 373-387.

McEwen, A. S., and L. A. Soderblom (1984). Multi-image photometric solutions for the galilean satellites. NASA TM 86246, 261-262.

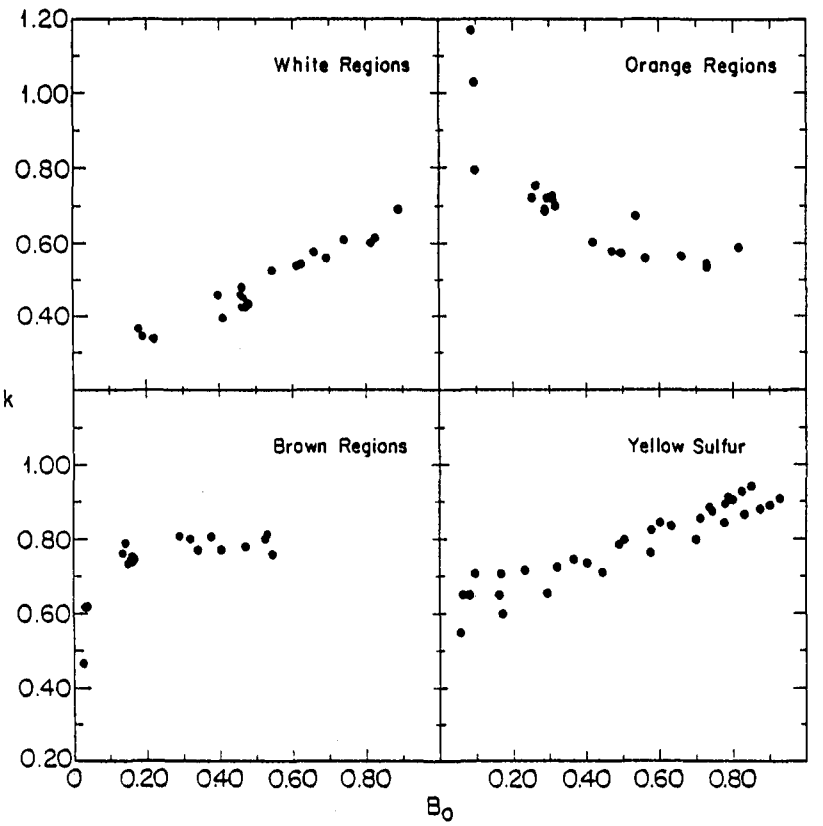

Figure 1. Best-fit Minnaert parameters derived for the regions under study. The limb-darkening parameter k is graphed vs. B_0 for each of the three color classes: "white," "orange," and "brown." Included for comparison is the k vs. B_0 trend measured for powdered yellow sulfur by Gradie and Veverka (1984).

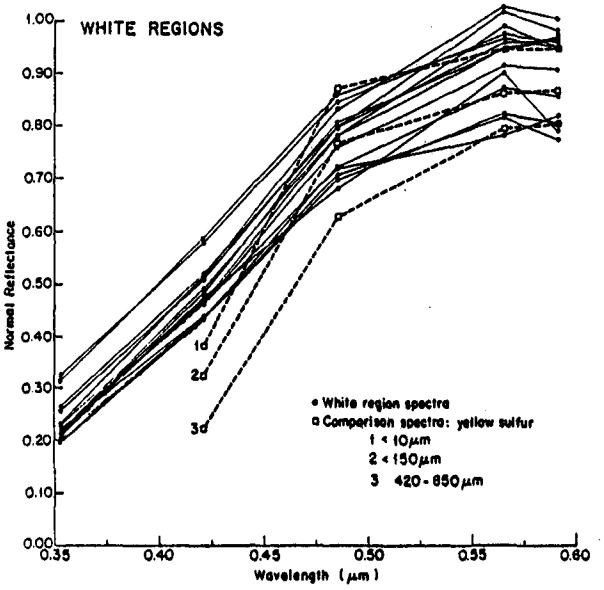

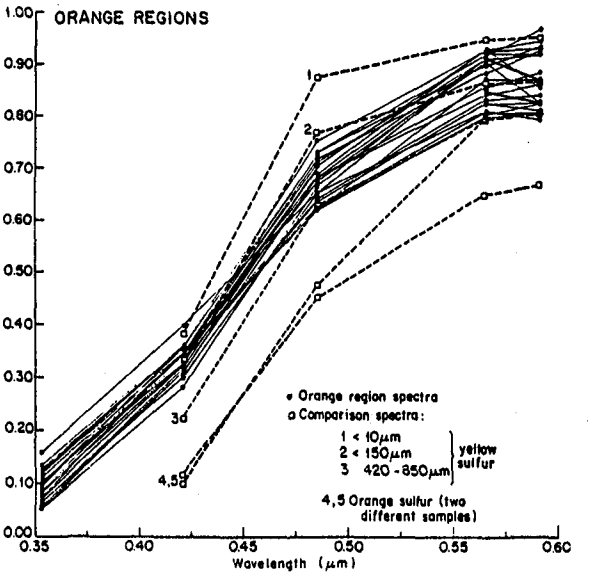

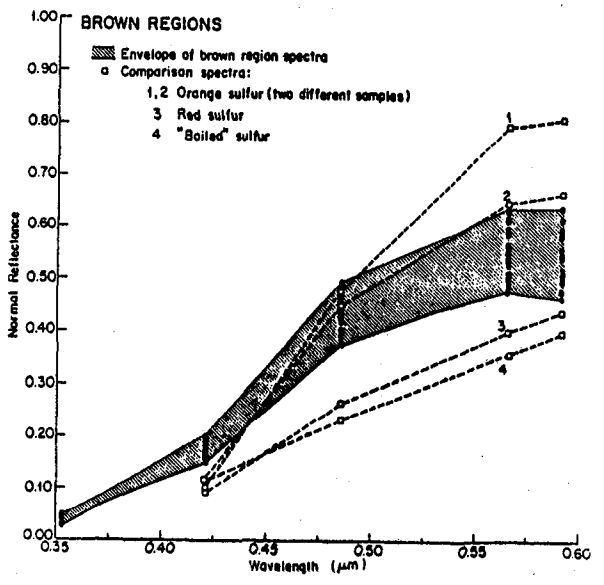

Figure 2. Accurate comparisons of the normal reflectances of areas on Io with laboratory measurements of candidate surface materials. The three color classes studied on Io, the "white," "orange," and "brown" regions, are each displayed separately.

Photometric Analysis of Jupiter-Illuminated Images of Io

B. J. Buratti and R. J. Terrile, Jet Propulsion Laboratory
California Institute of Technology

The surface of Io is believed to consist primarily of elemental sulfur allotropes and sulfur dioxide (Nash and Fanale, 1977; Nelson and Hapke, 1978; Nash et al., 1980). However, the exact nature of these materials, their purity, their fractional surface coverage, and their interaction with a possible SO_2 atmosphere are still uncertain.

During the Voyager 2 encounter several sequences of the dark (Jupiter-illuminated) side of Io were obtained. These images represent a unique opportunity for understanding several problems relating to the surface composition of Io. Since the difference in Ionian surface temperature between noon and early morning is 70 degrees near the equator (Matson and Nash, 1983), the laboratory behavior of various forms of sulfur and SO_2 in different temperature environments can be compared with photometric measurements of the sun-illuminated and Jupiter-illuminated sides of Io.

One problem that has been addressed previously (Terrile and Cook, 1980) is the question of condensation of SO_2 frost on the night side of Io. According to standard vapor pressure curves (Matson and Nash, 1983), the vapor pressure of SO_2 drops more than 10 orders of magnitude between day and night temperatures on Io. The existence or absence of SO_2 condensates on the night side is thus a sensitive indicator of an SO_2 atmosphere. Veverka et. al. (1981) failed to observe post-eclipse brightening as Io emerged from Jupiter's shadow. However, our preliminary analysis of the night side Io images suggests localized brightenings of ~25% may exist.

Another experiment is the comparison of the spectra of day and night sides of Io with laboratory spectra obtained in different temperature environments. Gradie et. al. (1982) found that the 0.45 micron absorption band of "yellow" sulfur shifts at an average rate of 1.6 Å/degree between 80 and 300 degrees (the shift is closer to 1.0 Å/degree near 80 degrees). They conclude that since there is an absence of spectral changes as the dayside solar incidence angle (and thus temperature) changes, pure sulfur does not exist on the surface of Io. Examination of the night side images represents an even more sensitive indicator for pure sulfur.

We calculate that between 60 and 130 degrees (the minimum nighttime and maximum daytime temperatures, respectively), the relative spectral reflectance for "yellow" sulfur observed in the Voyager green and clear filters decreases by 25%. This decrease should be detectable on the night-side images.

A search of the Voyager 2 Jupiter-illuminated images yielded a single pair of green and clear images which are appropriate for this study (green is the only filter other than the clear filter for which observations were obtained on the night side). In these images one hemisphere of Io is sun-illuminated and the other is Jupiter illuminated. Since we cannot use image addition techniques, we are in the process of selecting geologically similar regions of Io to obtain average color ratios of specific geologic units for both day and night sides. We will also compare the color ratios of points on the night side with the ratios for the identical point under solar illumination.

1. Gradie, J., Veverka, J., Thomas, P., Ostro, S. (1982). B.A.A.S. 14, 735.
2. Matson, D., Nash, D. (1983). J.G.R. 88, 4771-4783.
3. Nash, D., and Fanale, F. (1977). Icarus 31, 40-80.
4. Nash, D., Fanale, F., and Nelson, R. (1980). Geophys. Res. Lett. 7, 665-668.
5. Nelson, R., and Hapke, B. (1978). Icarus 36, 304-329.
6. Terrile, R. and Cook, A. (1980). Paper presented at IAU Colloquium 57, Kailua-Kona, HI, May 1980.
7. Veverka, J. Simonelli, D., Thomas, P., Morrison, D., Johnson, T. (1981). Icarus 47, 60-74.

Spectral Units on Europa and Ganymede

Thomas B. McCord, Marcia L. Nelson, Hawaii Institute of Geophysics, University of Hawaii, Honolulu, HI; Roger N. Clark, U.S. Geological Survey, Denver, CO; Torrence V. Johnson, Dennis L. Matson, Jet Propulsion Laboratory, Pasadena, CA; Robert E. Johnson, John Boring, University of Virginia, Charlottesville, VA

Global multispectral unit maps of Ganymede have been created using the techniques developed in creating the multispectral unit map of Europa (Nelson, et al., 1984). Comparisons of the Europa and Ganymede data show that Ganymede is less spectrally variable than Europa. Four major spectral units dominate Ganymede, corresponding to the ancient cratered terrain and the grooved terrain in the leading and trailing hemispheres. A hemispheric asymmetry in UV absorption definitely exists on Ganymede, although it is not as strong as that on Europa. Comparison of normalized spectra for the four major units (Figure 1) shows that the sense of the asymmetry (more absorption toward shorter wavelengths on the trailing hemisphere) is also the same on the two bodies. This hemispheric asymmetry has been interpreted as evidence of alteration of the surface by particle bombardment. Closer examination of the Europa data has shown that the functional form of the exogenic signature (Figure 2) does not completely match the forms to be expected from either magnetospheric bombardment or micrometeorite bombardment. We conclude that the pattern observed on Europa, and presumably on Ganymede, represents a steady state involving both of these exogenic modifying agents (Nelson, et al., 1984). Ganymede, with its different aged units, will be important in discriminating between the effects of the competing processes.

The spectral changes which could be produced by these two processes are grain size alteration and changes in composition. The spectral effects of variation in water ice grain size are fairly well known (Clark, 1981). The laboratory experiments have begun to study the spectral effects of sulfur irradiation on water ice. Six samples have been created in the University of Virginia KeV Ion Accelerator Facility. Five of the samples were irradiated during ice growth with SO_2^+ for varying lengths of time. The sixth sample is a plain ice standard. We have measured visible spectra for two of the irradiated samples, the standard made in Virginia, and one standard made in Hawaii (Figure 3). Until spectra are measured over a broader wavelenth range, it is not possible to determine whether a spectrally detectable amount of sulfur has been implanted in the samples. The positive slope of the Virginia standard and one of the irradiated samples is probably due to gold contamination from the sample holder. This cannot be confirmed until the spectral measurements are completed so that the chemical analysis can be performed.

References:

Clark, R.N. (1981). Water frost and ice: The near-infrared spectral reflectance 0.6-2.5μm. J. Geophys. Res., 86, 3087-3096.

Nelson, M.L., T.B. McCord, R.N. Clark, T.V. Johnson, D.L. Matson, J.A. Mosher, and L.A. Soderblom (1984). Europa: Characterization and interpretation of global spectral surface units. Icarus, submitted.

Nelson, M.L., T.V. Johnson, and D.L. Matson (1984). Exogenic Modification of Europa and Ganymede. BAAS, Vol. 16.

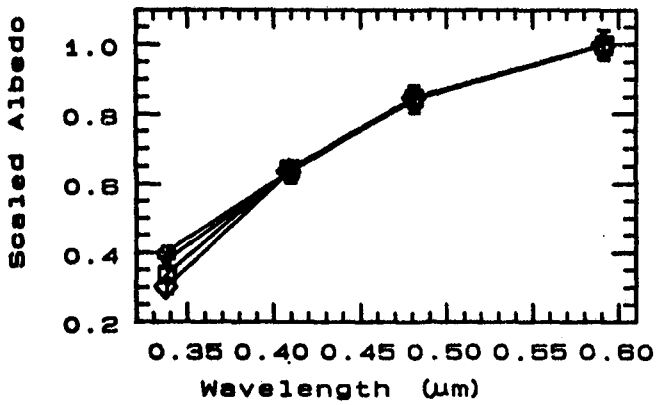

FIGURE 1: NORMALIZED SPECTRA OF THE FOUR MAJOR UNITS ON GANYMEDE. IN ORDER OF DECREASING ULTRAVIOLET ALBEDO, THE UNITS ARE GROOVED TERRAIN ON THE LEADING HEMISPHERE, CRATERED TERRAIN ON THE LEADING HEMISPHERE, GROOVED TERRAIN ON THE TRAILING HEMISPHERE, AND CRATERED TERRAIN ON THE TRAILING HEMISPHERE.

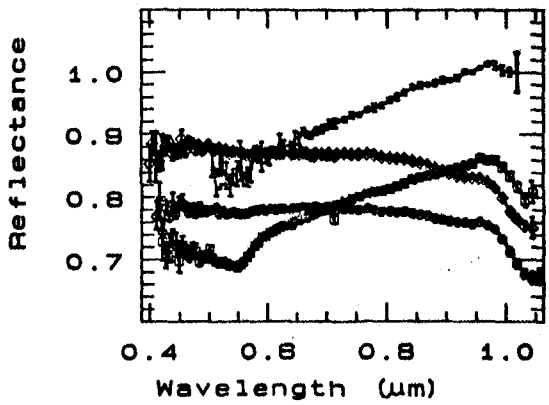

FIGURE 3: REFLECTANCE SPECTRA. IN ORDER OF DECREASING 1.0μm REFLECTANCE, THE SPECIES ARE ICE IRRADIATED WITH SO_2+ FOR 2 HOURS, PLAIN ICE GROWN IN THE VIRGINIA ENVIRONMENT CHAMBER, ICE IRRADIATED WITH SO_2+ FOR 1½ HOURS, AND PLAIN ICE CREATED IN HAWAII.

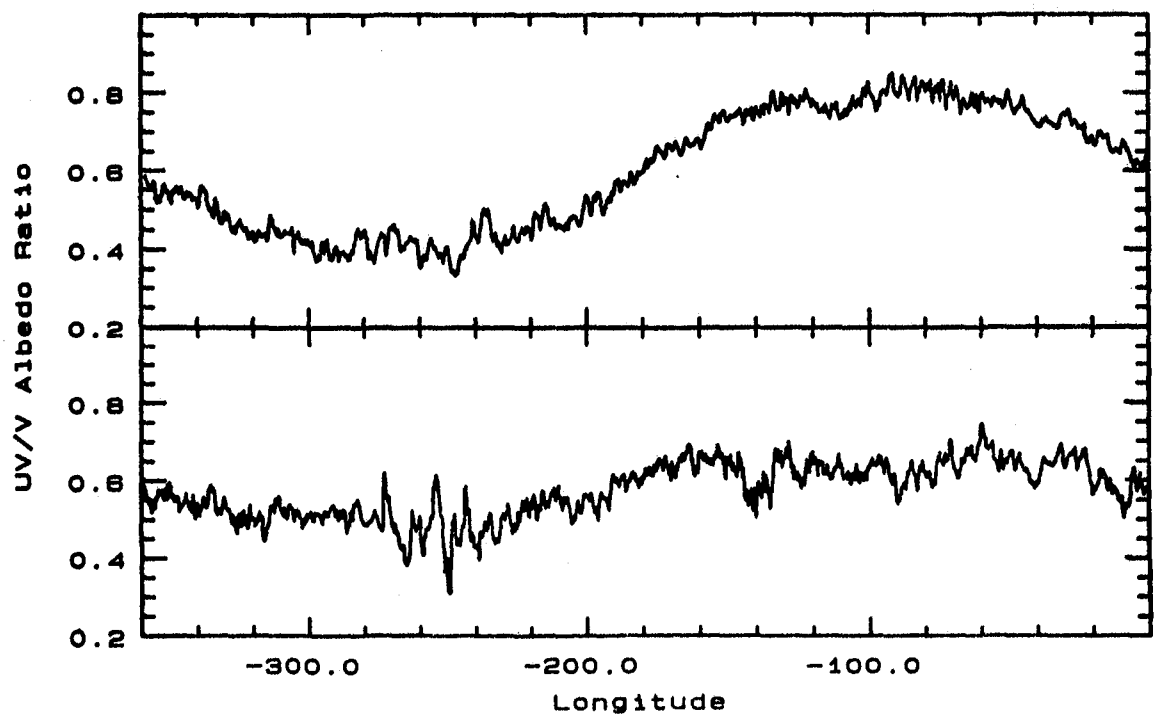

FIGURE 2: EQUATORIAL TRAVERSES ACROSS THE ULTRAVIOLET/VIOLET ALBEDO RATIOS FOR EUROPA (TOP) AND GANYMEDE (BOTTOM). THE TRAVERSES ARE AVERAGES BETWEEN ± 1° LATITUDE.

DETERMINING MINERAL TYPES AND ABUNDANCES FROM REFLECTANCE MEASUREMENTS

Milton O. Smith and John B. Adams
Department of Geological Sciences
University of Washington, Seattle, Wa. 98195

Mineral types and their abundances were quantitatively determined from laboratory reflectance spectra using principal components analysis (PCA). PCA reduced the measured spectral dimensionality and allowed testing the uniqueness and validity of spectral mixing models. In addition to interpreting absorption bands, in this new approach we interpreted variations in the overall spectral curves in terms of physical processes, namely changes in mixtures of minerals, in particle size and in illumination geometry. Application of this approach to reflectances of planetary surfaces allows interpretation to be extended to quantitative determinations of mineral types and abundances.

Two types of spectral mixture models were used. These are referred to as macroscopic spectral mixing (Singer and McCord, 1978) and intimate spectral mixing (Johnson et al. 1983). A macroscopic mixture is characterized by large patches of different mineral types occurring at a spatial resolution smaller than the instrumental field of view. In contrast, intimate spectral mixing results from mixtures of minerals where light is multiply transmitted and scattered by more than a single mineral species. Spectra of macroscopic mixtures are linear combinations of the reflectances of pure mineral endmembers, whereas intimate mixtures are nonlinear combinations. The mixing systematics of reflectance spectra of intimate mixtures can be linearized by conversion of the spectra to single scattering albedos following the method of Johnson et al. (1983).

Reflectances and single scattering albedos have different variances, therefore, their eigenvalues are not directly comparable. Normalizing the spectra following application of each mixture model makes the eigenvalues (variances) comparable so that a best-fit selection is possible. In some cases, the two mixture models may be equally applicable. Such situations may arise when the spectral contrast does not permit differentiation, or when neither model fits exactly, as may occur with some spectra of samples of varied particle size.

Two data sets were used to evaluate the differences between intimate and macroscopic mineral mixtures, and the influences of particle size. The first set of reference spectra was composed of intimate mixtures of olivine, enstatite, and quartz at particle sizes less than 45 um. A second set included these spectra plus spectra consisting of enstatite, olivine, and a 50/50 mixture of enstatite and olivine over a range of 5 sieved particle sizes of < 45, 45 - 63, 63 - 88, 88 - 125, 125 - 250 um.

The magnitude of the secondary eigenvalues resulting from PCA on the spectra of intimate mixtures closely approximated that due to instrumental error (Fig. 1). This criterion described by Malinowski, 1977 forms the basis for determining the number of minerals in a set of mixtures. For the data set with intimate mixtures and particle size variations, it was not possible to assign meaningful interpretation to all principal components of variation which are significantly above the level of error imposed by the spectrophotometer (Fig. 2). As shown by the plot of eigenvalues in Fig. 2, five to six mineral mixtures are indicated for both the intimate and macroscopic models. Thus, indiscriminant use of PCA on a multispectral data set may not provide an accurate estimate of the number of mineral endmembers.

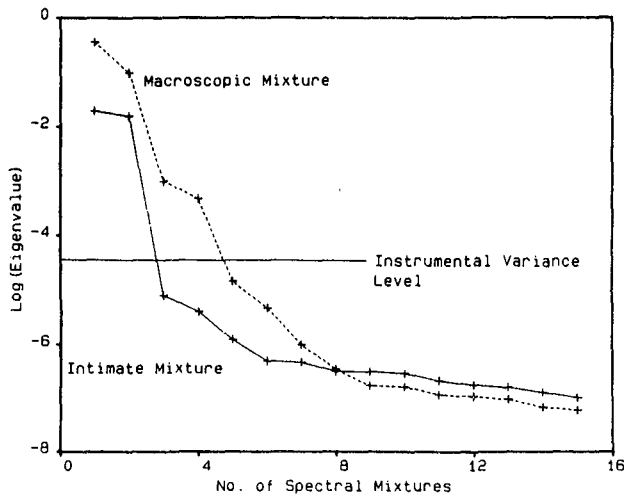

Fig. 1 Eigenvalues from spectra of intimate mixtures of olivine, quartz, and enstatite.

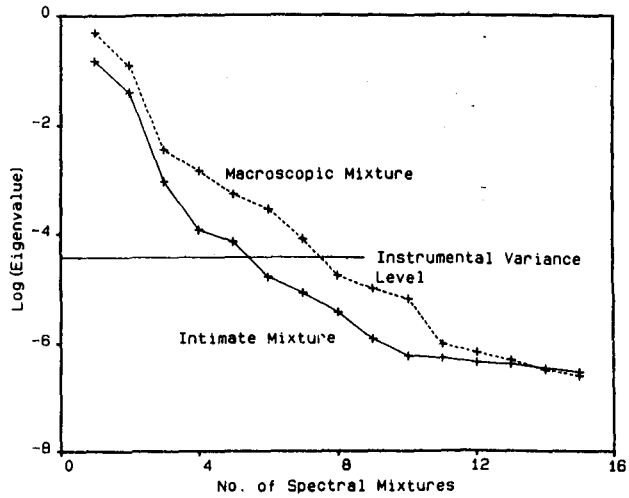

Fig. 2 Eigenvalues from spectra of intimate mixtures of olivine, quartz, and enstatite over 5 particle sizes.

Two methods are proposed for using PCA to quantitatively determine mineral types and their abundances. The first method is useful when a multispectral data set is composed of combinations of spectra some of which fit the macroscopic model and some of which fit the intimate mixture model. The objective is to divide the data into subsets where all spectra fit a single mixture model. Subsets are selected so that the fit of each group of spectra to a mixture model is near the level of instrumental error. For the combined spectral data set the search process is optimized by selecting those spectra with the best fit to the applied mixture model. The best-fit spectra are defined by the cluster of spectra with the lowest rms (root mean square) error, i.e., the square root of the sum of squares of the difference between predicted and measured spectra. Iterating this process by recomputing the PCA on each newly selected subset identifies those spectra which best fit the mixing model. This method allows a precise separation of the spectra of mineral-type mixtures from mixtures of particle sizes.

A second method is useful when the data cannot be fit by either mixing model as is the case with the spectra of varied particle sizes. These spectra were transformed by the eigenvectors defined by only the intimate mixtures of quartz, olivine, and enstatite at a single particle size. Rms errors increased consistently as particle size increased (Table 1), indicating that the intimate model fit gets worse with increasing particle size. This trend in the rms errors suggests that large particles are more linear with the macroscopic model whereas mixtures of smaller particles are linear with the intimate mixture model. Thus, even if neither mixture model fits the data, the trends in spectral fits to each mixture model independently provided a means of isolating the effects of particle size.

Table 1. Comparison of rms errors using the first two eigenvectors determined from the combined spectral data set (intimate mixtures and varying particle size) and spectra consisting of intimate mixtures at a single particle size. The rms errors are lowest using the reference provided by the intimate mixtures alone (single model) and the associated rms errors increase consistently with increases in particle size.

		rms errors determined from the first two eigenvectors of:	
Mineral Type	Size um	Intimate mixture model of olivine and enstatite samples < 45um	Intimate mixture model of olivine and enstatite samples of all particle sizes.
Olivine	<45	4.0e-4	7.1e-4
	45-63	7.4e-4	5.7e-4
	63-88	9.8e-4	5.5e-4
	88-125	1.4e-3	4.3e-4
	125-250	2.7e-3	8.0e-4
Enstatite	<45	8.6e-4	8.6e-4
	45-63	2.4e-3	1.6e-3
	63-88	2.7e-3	8.5e-4
	88-125	3.3e-3	3.1e-4
	125-250	4.6e-3	2.0e-3
50/50 Olivine/ Enstatite	<45	4.1e-4	3.6e-4
	45-63	1.7e-3	9.0e-4
	63-88	2.0e-3	6.5e-4
	88-125	2.3e-3	4.1e-4
	125-250	3.2e-3	1.0e-3

The application of PCA provided a useful framework for determining the interrelation of individual spectra in a data set. The results suggest that analysis of multichannel imaging data should not focus solely on the discrimination of spectral signatures, but also should address the adequacy and uniqueness of quantitative spectral models. As illustrated by our analysis of laboratory spectra such an approach is more likely to produce accurate classifications than a purely statistical analysis which does not incorporate physical models.

References

Johnson, P., Smith, M., Taylor-George, S., and Adams, J. (1983) A semiempirical method for analysis of the reflectance spectra of binary mineral mixtures. J. Geophys. Res., 88, 3557-3561.

Malinowski, E. R. (1977) Determination of the number of factors and the experimental error in a data matrix. Anal. Chem. 49,612-617.

Singer, R. B. and McCord, T. B. (1979) Mars: Large scale mixing of bright and dark surface materials and implications for analysis of spectral reflectance. Proc. Lunar Planet. Sci. Conf. 10th, p. 1835-1848.

Smith, M., Johnson, P., and Adams, J. (1984) Quantitative determination of mineral types and abundances from spectral reflectance measurements using principal components analysis. Submitted to Proc. Lunar Planet. Sci. Conf. 15th.

Determination of Mineral Type, Abundance, and Grain Size with Remotely Obtained Reflectance Spectra

by Roger N. Clark
U.S. Geological Survey, Box 25046 Federal Center, MS964,
Denver, CO 80225.

The goal of many remote sensing studies is to derive information about the minerals present in a study area. The derived results are dependent on knowledge of the optical properties of rocks and minerals: how they scatter, absorb, and emit electromagnetic radiation. In the reflective region of the spectrum, about 0.3 to 4μm, many minerals display diagnostic absorption bands in their reflectance spectrum. The absorptions in a particular mineral are due to a number of causes such as molecular stretching modes, conduction bands, charge transfers, and electronic transitions. Each mineral has unique optical properties (index of refraction and absorption coefficient) as a function of wavelength.

The light reflected from a particulate surface is controlled by two processes: absorption and scattering of photons. It is the scattering of photons in the surface that complicates the determining of mineral abundance from a spectrum of a particulate surface. The reflectance spectrum is affected by the grain size distribution and the abundance of each mineral present. The reflectance spectrum of a surface composed of more than one mineral is a nonlinear combination of the optical properties of the materials in the surface. It is the knowledge of the absorption and scattering within the surface that allows the derivation of mineral type, abundance, and grain size.

The only methods for solving the problem of deriving mineral type and abundance are either by an empirical approach, or by modelling the scattering and absorption using radiative transfer theory. Until recently, radiative transfer theories were not adequate for describing the interactions of photons in complex planetary surfaces. Now, however, there are three theories that have similar solutions to the radiative transfer problem (Hapke, 1981; Gougen, 1981; and Lumme and Bowell, 1981). One of these, presented by Hapke (1981), describes how the spectrum is derived from a surface composed of many materials. In a study of analytical methods using scattering theory, Clark and Roush (1984) showed that it is feasible to invert a reflectance spectrum to derive the abundance and grain size of each mineral in a surface if the optical constants are known. If enough diagnostic wavelengths are measured, the problem is solvable because there are more equations than unknowns.

To derive the abundances of minerals in a surface composed of more than one mineral in an intimate mixture, the bidirectional reflectance spectrum must be measured at several angles of incidence and emission. From these measurements, the scattering parameters may be derived, and the effective single scattering albedo can be computed from the models. If the scattering parameters are not derived, and the particles scatter anisotropically, then the computed effective single scattering albedo will be in error. Once the effective single scattering albedo has been computed, the solution to the model is a non-linear least squares problem with three unknowns per particle type. The solution is feasible when the complex indices of refraction and the densities of each mineral component are known. The unknowns are: the grain size of each particle type, the mass fraction of each particle type, and a grain internal scattering coefficient that

describes grain imperfections. If J wavelengths are measured and there are y mineral components in the surface, then there are 3y unknowns and J equations. It is a simple matter of spectral coverage to have enough data to solve the problem.

Note that in a real surface, the mineral grains are not all one grain size. However, a range of grain sizes may be used in the model by binning the grain size distribution and treating each bin as a separate mineral type.

Unfortunately, there are no reliable published optical constants of minerals that can be used with the theories. Most minerals are optically anisotropic and no theory has yet been published that will derive the average values based on the photon path through the material, so the work on oriented crystals is not appropriate. Some studies have used Kubelka-Munk theory to derive the optical constants of a particulate surface, but Clark and Roush (1984) have shown that Kubelka-Munk theory is not valid for materials that have a reflectance less than about 60% (which includes most geologic materials in at least some part of the spectrum). Fortunately, the same scattering theories can be used to derive the optical constants of minerals. Once an adequate library of optical properties of geologic materials is formed, the models may be used to map mineral abundance and grain size with data from aircraft and spacecraft systems.

In the derivation of the complex indices of refraction, the same models are used and the reflectance measurements are carried out at several angles of incidence and reflection. For this case, the material is of only one type, and the grain size must be well characterized. A reasonable way to characterize the grains is to carefully wet sieve a powdered material, and then examine each sieve fraction with a scanning electron microscope (SEM). SEM photos can then be used to derive the grain size distribution accurately within each sieve fraction. The knowns are the mineral density, grain size, and mass fraction, the remaining unknowns in the problem are: the index of refraction, absorption coefficient, and the grain internal scattering coefficient. Since the index of refraction varies only slowly with wavelength, only the absorption coefficient, k, varies strongly with wavelength. Assuming, for example, that the index of refraction can be described by a 5 term series, and J wavelengths are measured for z sieve fractions, there are k+6 unknowns, and J times z equations. In principle, only 2 sieve fractions need be measured at many wavelengths for the problem to be solvable.

Because the same radiative transfer models are being used for both the derivation of the optical constants as well as in the derivation of mineral abundance, their validity must be tested carefully. Initial tests of the derivation of the absorption coefficient show encouraging results (Hapke and Wells, 1981; Clark and Roush, 1984). Figure 1 shows the absorption coefficient of ordinary water ice (which is optically isotropic) measured by oriented crystal work and from reflectance measurements on a frost. The grain sizes of frosts are difficult to control and measure, so two corning glasses have been selected for future tests. These glasses, Corning #5300 and #5121, have several weak and strong absorption bands for testing the models over the entire range likely to be encountered in geologic remote sensing studies. The glasses were purchased as slabs 5.5 millimeters thick so the transmittance can be measured and the absorption coefficient may be derived to confirm that derived from reflectance measurements. Once the complex indices of refraction have been derived, spectra of mixtures of the two glasses will be constructed, and the model will be tested for inversion

to mineral abundance.

These methods will be invaluable for analysis of imaging spectrometer data if the algorithms prove fast enough for the vast data sets such instruments will generate. Such methods may allow actual mapping of mineral abundances on a planetary surface.

References

Clark, R.N. and P.G. Lucey (1984). Spectral Properties of Ice-Particulate Mixtures and Implications for Remote Sensing 1. Intimate Mixtures. J. Geophys Res. 89, 6341-6348.

Clark, R.N. and T.L. Roush (1984). Reflectance Spectroscopy: Quantitative Analysis Techniques for Remote Sensing Applications. J. Geophys Res. 89, 6329-6340.

Gougen, J.D. (1981). A Theoretical and Experimental Investigation of the Photometric Functions of Particulate Surfaces. Ph.D. Thesis, Cornell Univ., Ithaca, N.Y.

Hapke, B. (1981). Bidirectional Reflectance Spectroscopy, 1: Theory. J. Geophys Res. 86, 3039-3054.

Hapke, B. and E. Wells (1981). Bidirectional Reflectance Spectroscopy, 2, Experiments and Observations. J. Geophys Res. 86, 3055-3060.

Irvine, W.M. and J.B. Pollack (1968). Infrared Optical Properties of Water and Ice Spheres. Icarus, 8, 324-360.

Lumme, K. and E. Bowell (1981). Radiative Transfer in the Surfaces of Atmosphereless Bodies; I; Theory. Astron. J., 87, 1694-1704.

Figure 1
The absorption coefficients from Irvine and Pollack (points) derived from oriented crystal work of several investigators are compared to that derived from a reflectance spectrum (line) of a water frost at 112 degrees Kelvin. The agreement is good and shows that the absorption coefficient, which covers at least three orders of magnitude, can be derived from reflectance spectra. From Clark and Roush (1984).

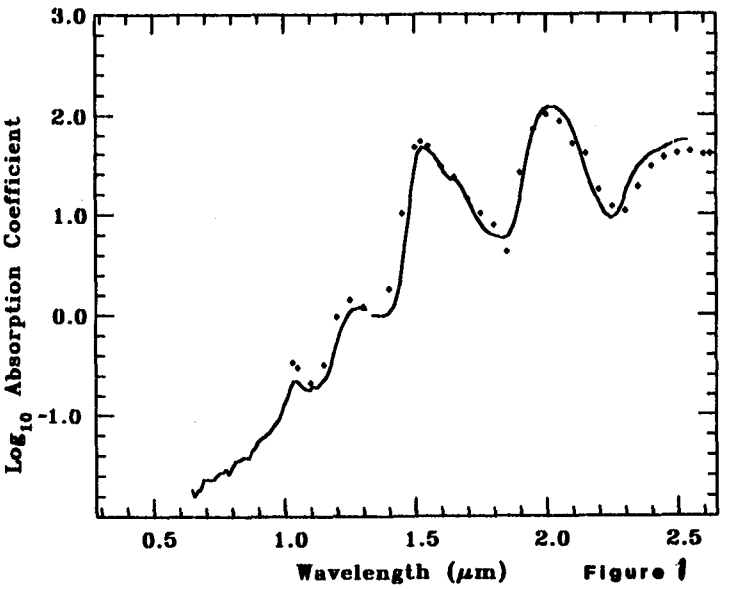

AUTOMATED EXTRACTION OF ABSORPTION BANDS FROM REFLECTANCE SPECTRA

R.L. Huguenin, L. Vale, D. McIntire, and J. Jones (Remote Sensing Center and Dept. Geology/Geography, Univ. of Massachusetts, Amherst 01003

A multiple high order derivative spectroscopy technique has been developed for deriving wavelength positions, half-widths, and heights of absorption bands in reflectance spectra. The technique is applicable to laboratory spectra as well as medium resolution (100-200 cm^{-1}) telescope or spacecraft spectra with moderate (few percent) noise.

The technique permits absorption band positions to be detected with an accuracy of better than 3%, and often better than 1%. The high complexity of radiative transfer processes in diffusely reflected spectra can complicate the determination of absorption band positions. Continuum reflections, random illumination geometries within the material, phase angle effects, composit overlapping bands, and calibration uncertainties can shift apparent band positions by 20% from their actual positions or mask them beyond detection. Using multiple high order derivative analysis, effects of scattering continua, phase angle, and calibration (smooth features) are suppressed. Inflection points that characterize the positions and half-widths of constituent bands are enhanced by the process and directly detected with relatively high sensitivity.

The inflection points are detected using combinations of fifth derivative zero crossings and sixth, fourth, and second derivative magnitudes. Sensitivity of band detection is proportional to A/W^n, where A is band height, W is half-width (FWHM), and n is derivative order. In the original spectrum (n = o) sensitivity is a function of band height, but with our technique (n = 2 - 6) very weak bands (A small) can be detected if they are sufficiently narrow. Extent of band masking thus depends primarily on width rather than height. Overlapping bands that have centers that are closer than W can have errors that exceed 3%; otherwise errors are better than 3%. Accuracy of band center determination is independent of band shape (gaussian, lorentzian, etc.) and requires no assumptions about band characteristics.

The capability to resolve constituent band positions in a complex spectrum is illustrated in Figure 1. Suppression of continuum contributions from scattering reflections, phase effects, and calibration errors is illustrated in Figure 2 and Table 1. In Figure 2 the spectrum shown in Figure 1 is presented along with two straight line continua. In Table 1 are presented the results of the derivative analysis of the spectrum with the continua divided out and subtracted out. The results are virtually indistinguishable from the results in Figure 1. In Figure 3 and Table 2 are presented the results for a complex continuum, and again the results are virtually indistinguishable from the Figure 1 results.

The technqiue is well suited to remote sensing applications, requiring resolutions of only 0.1-0.2 W and tolerating moderate (few percent) noise levels with minimal loss of sensitivity and accuracy. In Figure 4 we reproduce the spectrums of Figures 1-3 in its original high resolution

form, and then show the same spectrum with low (200 cm^{-1}) spectral resolution. Comparison of derived band positions reveal that accuracy is comparable at this low resolution. For mineral bands the required minimum resolution is 200-400 cm^{-1}, but rests suggest that 100 cm^{-1} resolutions provide the most reliable results. At 200 cm^{-1} and lower resolutions neighboring bands frequently remain unresolved and are detected as a single band at an intermediate position. Tests also reveal that noise of a few percent produce minimal effect on accuracy, but that smoothing with a cubic spline increases reliability. Up to n + 1 (n = derivative order) smooths can be applied to a spectrum to produce optimal signal to noise without serious suppression of bands.

The technique is fully automated, standardized, and objective. The technique has been successfully applied to laboratory spectra as well as telescope reflectance spectra. The technique could have potentially significant impact on the analysis of data collected from an orbiting spectrophotometer (resolution of 100 cm^{-1} or better), providing a means for processing large volumes of spectral data into sets of band positions without operator intervention. Onboard processing could substantially reduce transmitter power requirements.

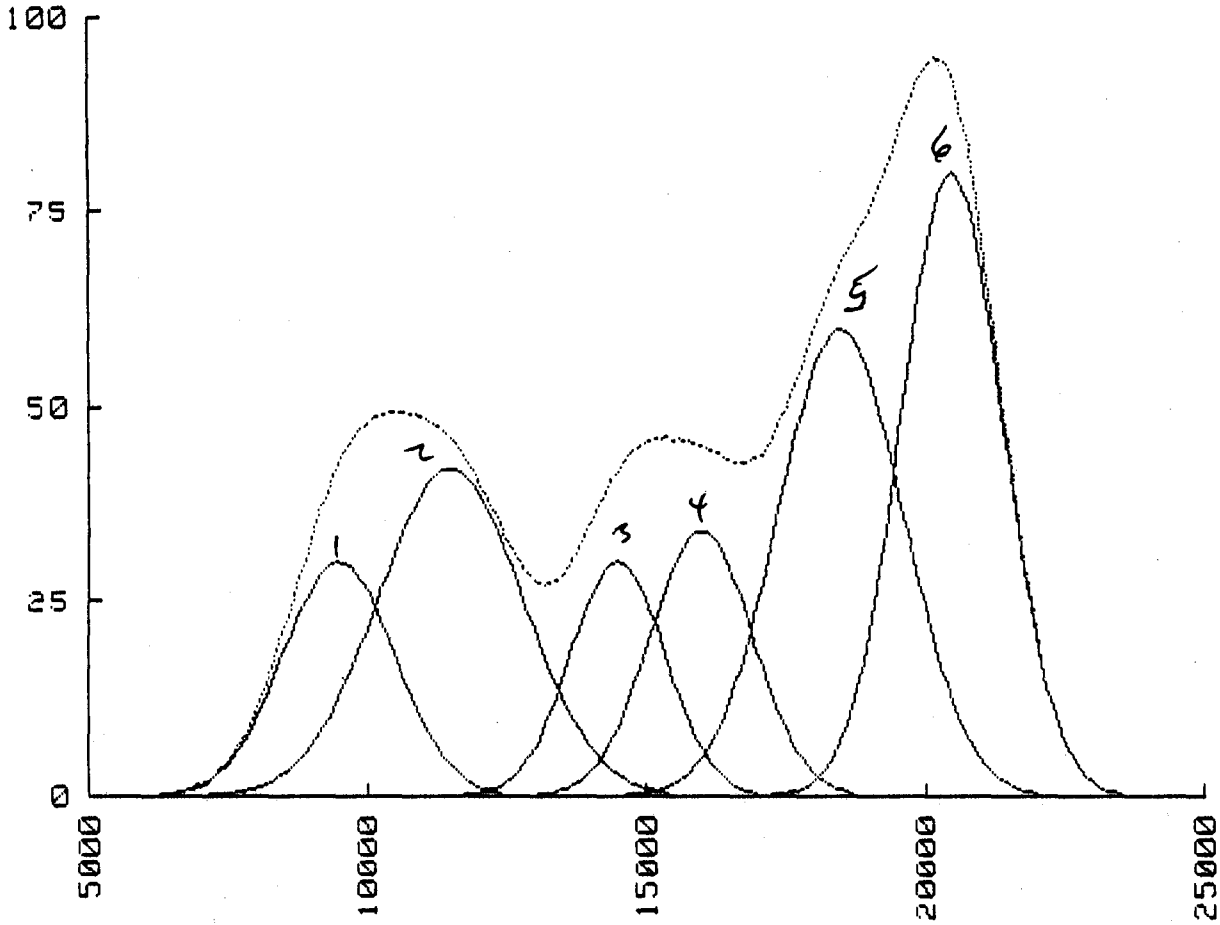

Band	Actual Position	Measured Position	%Error
1	9500cm^{-1}	9468	0.3
2	11500	11895	3.4*
3	14500	14516	0.1
4	16000	16088	0.6
5	18500	18221	1.5
6	20500	20550	0.3

FIGURE 1. Simulated spectrum comprised of 6 bands of various half-widths and heights. The spectrum is very similar to the spectrum of an iron oxide. Note that band 2 and band 1 are separated by less than the half-width of band 2, and the error exceeds the few percent level.

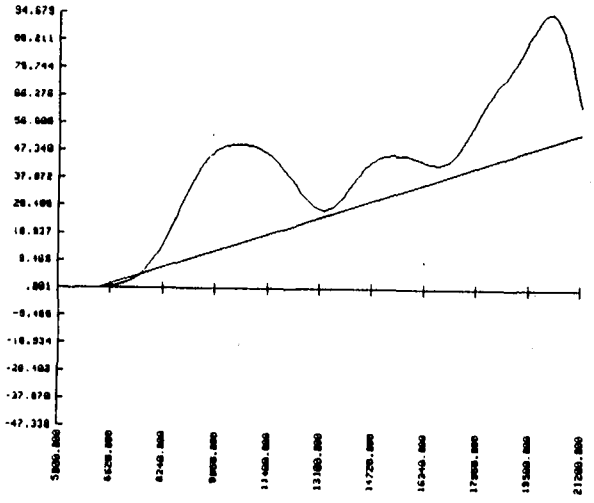

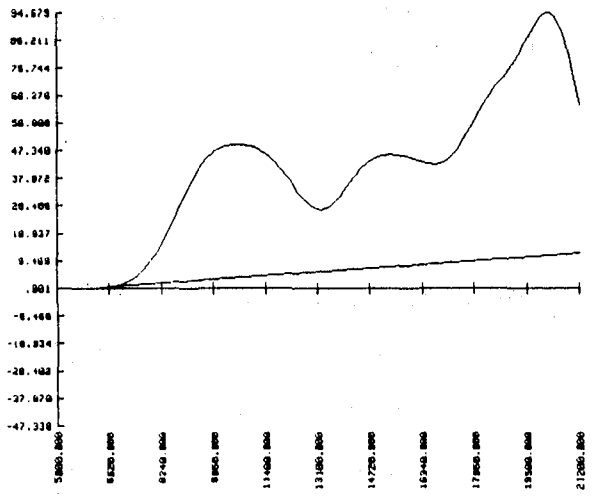

FIGURE 2

TABLE II

Shallow Continuum

Band	Actual Position	Continuum Subtracted Out		Continuum Divided Out	
		Measured Position	% Error	Measured Position	%Error
1	9500 cm^{-1}	9466	0.4%	9226	2.9
2	11500	11884	3.3	11816	2.7
3	14500	14525	0.2	14441	0.4
4	16000	16127	0.8	16080	0.5
5	18500	18210	1.6	18193	1.7
6	20500	20693	0.9	20571	0.3

Steep Continuum

Band	Actual Position	Continuum Subtracted Out		Continuum Divided Out	
		Measured Position	%Error	Measured Position	%Error
1	9500	9468	0.3	9195	3.2
2	11500	11895	3.4	11810	2.7
3	14500	14516	0.1	14437	0.4
4	16000	16088	0.6	16080	0.5
5	18500	18221	1.5	18193	1.7
6	20500	20641	0.7	20569	0.3

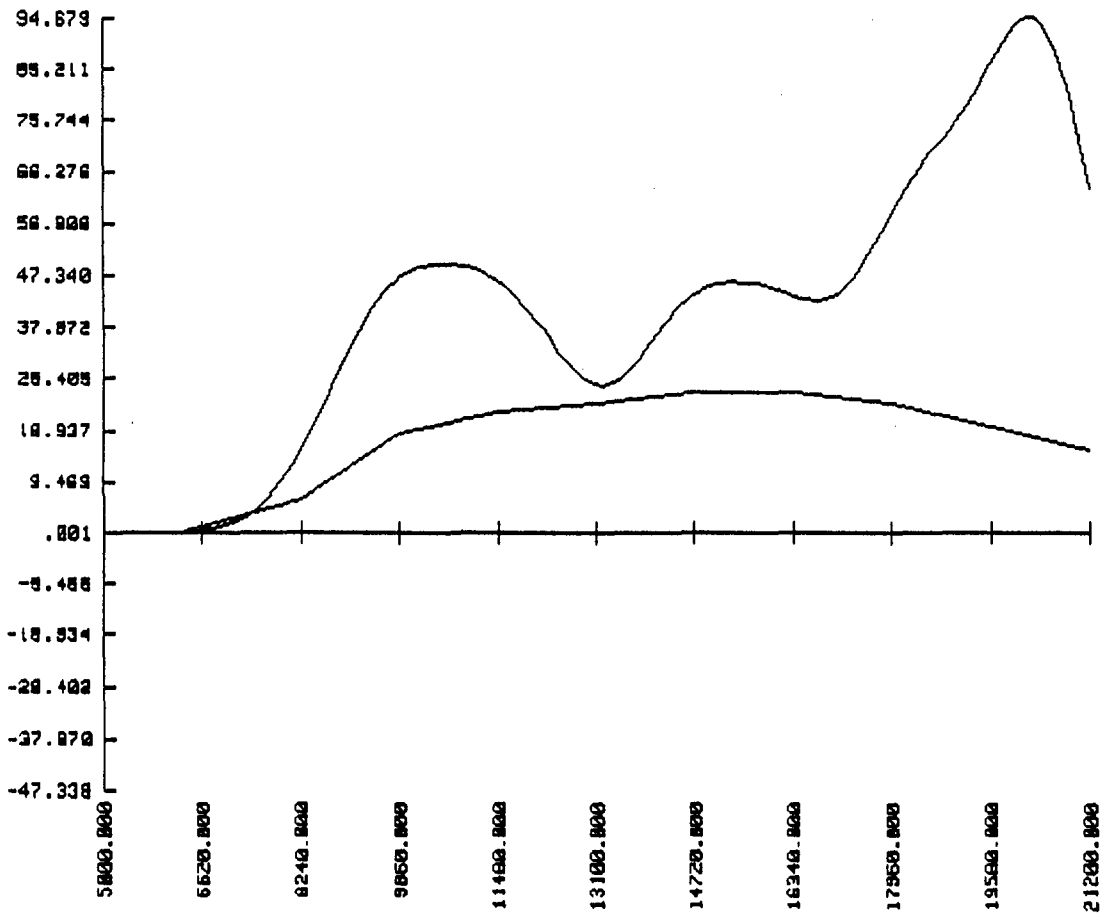
94.679
85.211
75.744
66.276
56.808
47.340
37.872
28.405
18.937
9.469
.001
-9.466
-18.934
-28.402
-37.870
-47.338
5800.000
6620.000
8240.000
9860.000
11480.000
13100.000
14720.000
16340.000
17960.000
19580.000
21200.000

FIGURE 3

TABLE III

COMPLEX CONTINUUM

Band	Actual Position	Continuum Subtracted Out		Continuum Divided Out	
		Measured Position	%Error	Measured Position	%Error
1	$9500cm^{-1}$	9418	0.9	8456	0.5
2	11500	11884	3.3	11889	3.4
3	14500	14513	0.09	14509	0.06
4	16000	16093	0.6	16103	0.6
5	18500	18224	1.5	18240	1.4
6	20500	20642	0.7	20718	1.1

Band	Actual Position	Reduced Resolution (200cm^{-1})		Full Resolution (1cm^{-1})	
		Measured Position	%Error	Measured Position	%Error
1	9500cm^{-1}	9457	0.4	9468	0.3
2	11500	12017	4.5	11895	3.4
3	14500	14398	0.7	14516	0.1
4	16000	16155	0.9	16088	0.6
5	18500	18293	1.1	18221	1.5
6	20500	20548	0.2	20556	0.3

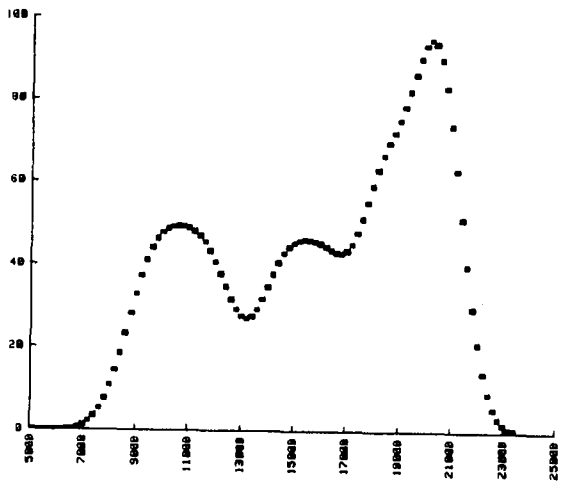

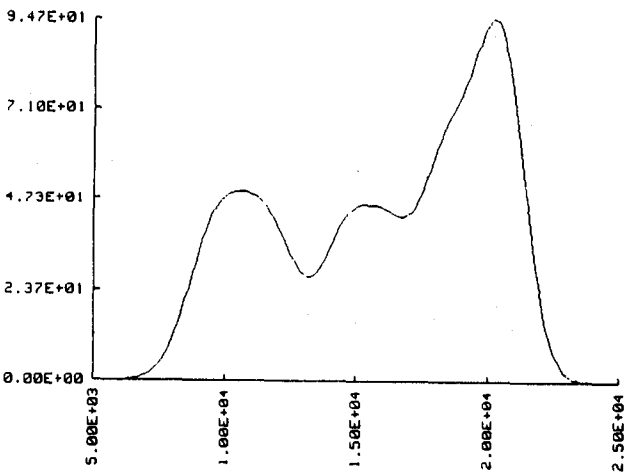

FIGURE 4

QUANTITATIVE ANALYSES OF PLANETARY REFLECTANCE SPECTRA

Paul E. Johnson, University of Wyoming

During the last three years, collaborators (John Adams and Milton Smith of the University of Washington) and I have worked on the development of a set of quantitative models in order to analyse planetary reflectance spectra as a function of microscopic and macroscopic mineral mixtures, particle size, and illumination geometry. Our approach has been to simplify more sophisticated algorithms (such as those found in Hapke, 1981) to include the smallest number of parameters possible, consistent with being able to use them to produce useful results. This means that they should be able to model the data to within the accuracy obtainable by laboratory, telescopic, and space instrumentation (roughly 1%). The algorithms are ideally given in terms of parameters that are directly measureable (such as spectral reflectance or particle size).

During the last two years we have produced a basic non-linear mixing model for predicting the spectral reflectance of binary mineral mixtures (Johnson et al., 1983). This model can also be used to analyse the abundances of components in a binary mixture for which the identity of the two end-members is known. We are now able to accurately model the spectra of binary mineral mixtures from the spectra of end-members, even when the end-members differ widely in albedo. Expansion of the basic model (Johnson et al., 1983) has been along the lines described below (and also found in Johnson et al., 1984a).

Our model consists of a two-stream radiative transfer solution to a semi-infinite medium of isotropic scatterers, as developed by Hapke (1981). We have made the assumption that the particles we are working with are much larger than the wavelength of light under consideration. The algorithms used are simple enough to be useful for handling large data bases, such as those gathered by space missions.

Reflectance spectra of particulate mineral mixtures are a complicated, non-linear function of particle size. We assume that, to first order, the single-scattering albedo of a particle in a particulate surface depends on two effects: 1.) specular reflection from particle surfaces, and 2.) light absorption during transmission through particles. The latter gives rise to mineral absorption bands. We have been able to model particle size effects with the algorithm $w(D) = S + (1. - S) \exp(-\alpha D)$ used by Hapke and Nelson (1975). w is the single-scattering albedo, D the effective particle size for the sample under consideration, α the absorption coefficient,

and S the external scattering coefficient. We solve for S and by fitting the algorithm above to actual data. First a mineral sample is sieved into groups by particle size. Then spectra of the mineral are obtained for several size groups. The reflectances are converted to single-scattering albedos via the method outlined in Johnson et al. (1983). Then the expression above is fit to w at each wavelength using a non-linear least squares fitting routine. This yields values for S and which can be used to predict spectra at a new particle size (or a distribution of particle sizes) or to determine the effective particle size from the spectrum of a sample for which the particle size distribution was not known previously. Results indicate that this technique works reliably (within 1% error) for interpolation.

A basic problem of intercomparing laboratory, field, and telescopic reflectance spectra are the differences in illumination and viewing geometries. It is known that the reflectance spectra of soil samples are sensitive to the illumination/viewing geometry. We have modeled both directional-hemispherical and bidirectional reflectance data with similar, but differing algorithms. Our models fit both data sets to within experimental error.

We are now able to model directional-hemispherical spectra outside the photometric opposition peak with a single-scattering phase function represented by $P(g) = 1 + b\cos(g)$, where g is the scattering phase angle and b is a constant accounting for the anisotropy of the scattering phase function. We in turn model b in terms of the spectrum and optical properties of the sample. This model has been successfully tested directional-hemispherical reflectance spectra of olivine (Johnson et al., 1984a).

We have developed a non-linear least squares fitting code for modeling mixtures with more than two components (Johnson et al., 1984a). These have been tested on 3- and 4-component mixtures, and the results appear to be limited mainly by the errors in the data. Increasing the number of components increases the accumulated error, thus increasing the uncertainty of the results. However, we feel that this is not a serious limitation for many applications. Specifically, the pixel-to-pixel variance in multispectral data can probably be successfully modeled in most cases with a rather small number of components.

For any pair of end-members, one can calculate, for a given uncertainty in the data, the detectability of one component in the presence of another. For example, in laboratory and telescopic spectra of a mature lunar terra soil, obtained with an accuracy of 1%, pyroxene is detected at a threshold of 5%,

whereas green glass must be present at a level of about 20% in order to be detected. This stems from the fact that pyroxene is a more opaque and spectrally dominant mineral phase.

During the last year, we have developed principal components analysis as a technique for quantitatively modeling remotely sensed reflectance spectra of planetary surfaces, the moon in particular, as mixtures of particles on microscopic and macroscopic scales (Smith et al., 1984; Johnson et al., 1984b). Eighteen lunar telescopic reflectance spectra of the Copernicus crater region (obtained by Carle Pieters) were modeled in terms of four likely endmembers: mare basalt, anorthosite, glassy aggluttinates, and clinopyroxene. These endmembers were chosen from a similar analysis of 92 lunar soil and rock samples. The models fit the data to within 2% rms. It was found that the goodness of fit was marginally better for intimate mixing over macroscopic mixing (Pieters et al., 1984). This technique can be used to interactively determine the number of linearly independent sources of variation needed to model the data, identify likely endmembers, and test for the best set of endmembers.

References

Hapke, B. Bidirectional reflectance spectroscopy. I. Theory, J. Geophys. Res., 86, 3039-3054, 1981.

Hapke, B. and Nelson R. Evidence for an elemental sulfur component of the clouds from Venus spectrophotometry. J. Atmos. Sci., 32, 1212-1218, 1975.

Johnson, P.E., Singer, R., Smith, M.O., and Adams, J.B. Quantitative models of planetary reflectance spectra. To be submitted to J. Geophys. Res., 1984a.

Johnson, P.E., Smith M.O., and Adams, J.B. Quantitative analysis of planetary reflectance spectra: Copernicus. Submitted to Proc. Lunar and Planetary Sci. Conf. XV, 1984b.

Johnson, P., Smith, M., Taylor-George, S., and Adams, J. A semiempirical method for analysis of the reflectance spectra of binary mineral mixtures. J. Geophys. Res., 88, 3557-3561, 1983.

Pieters, C.M., Adams, J.B., Smith, M.O., Head, J.W., McCord, T.B., Mouginis-Mark, P., and Zisk, S.H. The nature of crater rays: the Copernicus example. Submitted to J. Geophys. Res., 1984.

Smith, M.O., Johnson, P.E., and Adams, J.B. A strategy for interpretation of multispectral reflectance data from planetary surfaces. Submitted to Proc. Lunar and Planetary Sci. Conf. XV, 1984.

ANALYSIS OF SMIRR DATA FOR VOLCANIC AND SEDIMENTARY TERRAINES OF THE TRANS-PECOS REGION, TEXAS.

H.Grady Blount and James.L.Whitford-Stark, Department of Geology, Sul Ross State University, Alpine, TX 79832.

The Shuttle Multispectral Infrared Radiometer (SMIRR) carried on the second mission of the Space Shuttle produced spectral data for portions of Presidio and Jeff Davis Counties, Texas during the eighteenth orbit of the spacecraft in November of 1981. The data covers an area approximately 100 m in width and 100 km in length (see figure 1) extending from the Rio Grande just north of Candelaria in the southwest to Fort Stockton in the northeast.

The area is part of the Chihuahua Desert ecosystem, with a mean annual rainfall of less than 10 inches. The generally sparse vegetation is represented by drought-tolerant bushes and shrubs, with accumulations of desert grasses on alluvial plains at higher elevations. A conventional black and white calibration film flown alongside the SMIRR scanner shows zero cloud cover over the area during acquisition of the data, although a filter was employed on the camera to reduce atmospheric haze. The purpose of the project is to provide groundtruth for the spectral data produced by the SMIRR scanner. One major problem in West Texas is that the majority of the land is privately owned, so a great deal of time has to be expended in order to gain access.

The ten filters on the SMIRR scanner extend from 0.50 to 2.35 microns. It has been found (e.g., Goetz et al, 1982) that the bands from 2.0 to 2.35 microns are particularly useful for discriminating carbonate and clay minerals. A diversity of rock types lie along the flightpath. The groundtrack commences in the Cretaceous sandstones and claystones of the El Picacho Formation and then crosses the Tertiary Bracks Rhyolite of the Sierra Vieja. It continues across the Tertiary Capote Mountain Tuff and the overlying Mitchell Mesa Welded Tuff. It then crosses the extensive Quaternary alluvial deposits of the Marfa Plain where both varnished and unvarnished varieties of alluvium are found. Continuing northeastwards, the groundtrack passes over the Davis Mountains where a variety of extrusive tuffs and lavas of trachytic, rhyolitic and basaltic composition and intrusives of syenitic composition are exposed (Smith, 1975). Finally, the track extends across Cretaceous limestones and limestone-derived alluvium to the southwest of Fort Stockton.

During the course of its 15 second passage across this portion of Texas, the SMIRR instrument collected some 1,500 spectra. It would be somewhat unproductive to sample each locality so the data are being analyzed to find major spectral changes and the type spectra for the various specific rock units. Field sampling will then be undertaken to ascertain the reasons for the spectral variation.

References:

Goetz,A.F.H.,Rowan,L.C., and Kingston,M.J. 1982 Mineral identification from orbit: initial results from the Shuttle Multispectral Infrared Radiometer. Science 218, 1020-1024.

Smith, M.A. 1975 Geology and Trace Element Geochemistry of the Fort Davis Area, Trans-Pecos, Texas. Ph.D.Thesis, University of Texas, Austin. 231pp.

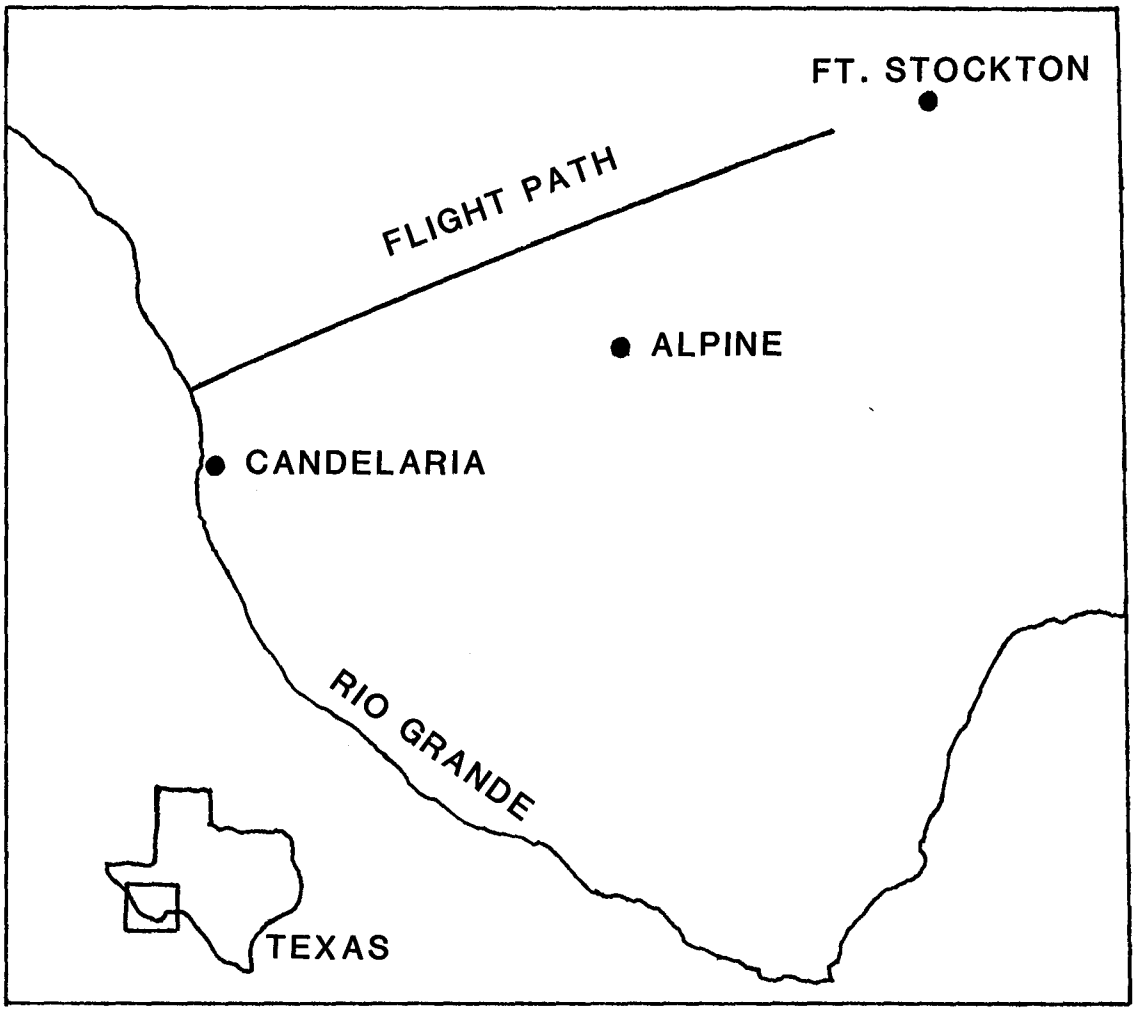

FIGURE 1

MONTE CARLO MODELING OF LUNAR MEGAREGOLITH DEVELOPMENT

Jac Cashore and Alex Woronow, Department of Geosciences, University of Houston, U.P., Houston, Texas 77004.

A new Monte Carlo model of lunar megaregolith development is proposed. Minimum megaregolith depths are obtained in the preliminary model. The new model impacts a gridded, initially flat surface area randomly, with points not constained to grid intersections. Information is recorded at grid points on evolving topography, deepest depth impacted to, and number of hits at that location. Two types of lunar surfaces are simulated, maria and highlands. Crater production functions are after Strom (1977) run to densities that are multiples of observed lunar crater densities for craters of 8 km in diameter and larger. Figure 1 shows the production curves utilized in this model. All craters are considered to have formed in a gravity-scaled regime."Edge effect" problems are corrected in this model by allowing craters forming outside the grid area or along it's edges to affect the gridded area.

Two crater geometries are utilized for each impact, first an excavation bowl and secondly a final relaxed crater. Excavation bowls are composed of spherical caps with depth-to-diameter ratios from Pike (1977). Final crater shapes are for flat-floored craters and various size ranges according to the equations in Table 1 (they are extrapolated from Pike, 1977). Topography retains the final crater shape. For ejecta blanket profiles we used exponentially decaying thickness according to a -3 power. Crater rim thickness is similar to Pike (1977). Ejecta deposits were traced to only 1 crater diameter distance from the crater rim. Further discussion on model assumptions and implementations can be found in Cashore and Woronow (1984).

Preliminary results have given minimum megaregolith thicknesses as shown in Figures 3 and 5. Figures 2 and 3 show the results of highlands simulations. Figures 4 and 5 show the results of maria simulations. The different curves in each figure represent different crater densities. Since the results appear to be dominated by the largest impacts there appears to be only a slight underestimation due to the large minimum crater size. Our results indicate significantly greater megaregolith thicknesses than previous studies (e.g. Horz et al., 1976).This occurs despite the limitation that our thicknesses are only a lower limit of the real regolith thickness. Two reasons may account for the difference: 1) a different production function that correctly produces more large craters than small ones as compared to the Horz model; and 2) we allowed for terrain to develop allowing for the formation of craters in the bottoms of other craters.

References:

Cashore, J. and A. Woronow, 1984, Proc. of the 15th Lunar and Planet. Sci. Conf., JGR, in press.

Horz, F., R.V. Gibbons, R.E. Hill, and D.E. Gault, 1976, Proc. of the Lunar Sci. Conf., 7th, Vol. 3, pp. 2931-2945.

Pike, R.J., 1977, in Impact and Explosion Cratering, pp. 489-509, Pergamon Press:New York.

Strom, R.G., 1977, Phys. Earth & Planet. Int., Vol.15, pp. 156-172.

TABLE 1

Equations Used for Crater and Ejecta Geometries in this Model.

	Diameter Greater Than 15 km	Diameter Less Than 15 km
Excavation Craters	$R_i=0.2D_r$(spherical cap)	
Final Crater Depth	$R_i=0.196D_r^{1.010}$	$R_i=1.044D_r^{0.301}$

	Diameter Greater Than 17 km	Diameter Less Than 17 km
Ejecta Rim Height	$R_e=0.036D_r^{1.014}$	$R_e=0.236D_r^{0.399}$

Final Crater Rimwall Slopes

8-10 km = 29° 10-20 km = 21.5°

20-40 km = 14° 40-125 km = 10°

Greater than 125 km = 7°

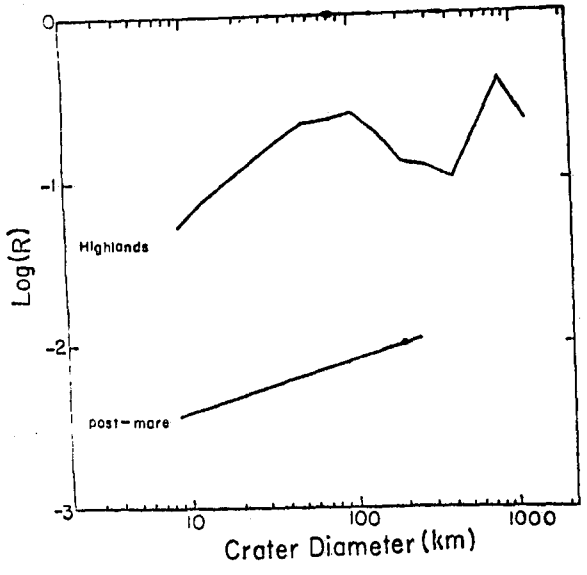

1. Production function used for simulations is identical to the observed size-frequency distribution. (After Strom, 1977)

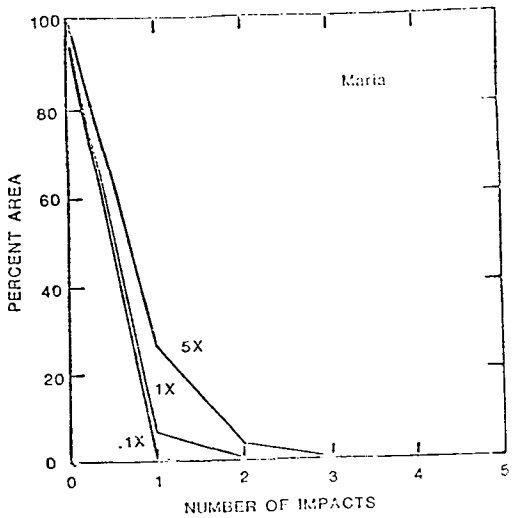

IV. The percentage of lunar maria area affected by a given number, or more, of impacts for four different total fluxes of craters larger than 8km diameter.

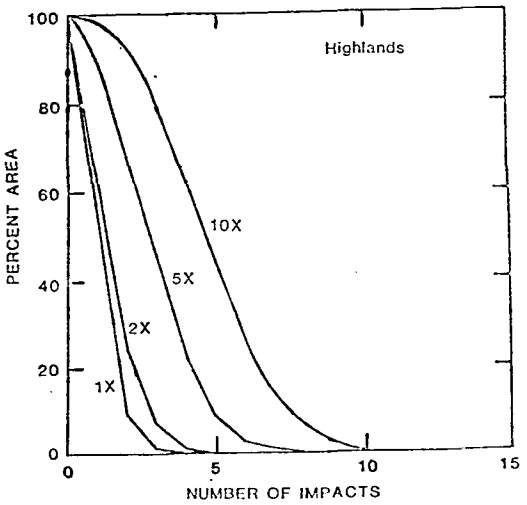

II. The percentage of lunar highlands area affected by a given number, or more, of impacts for four different total fluxes of craters larger than 8km diameter.

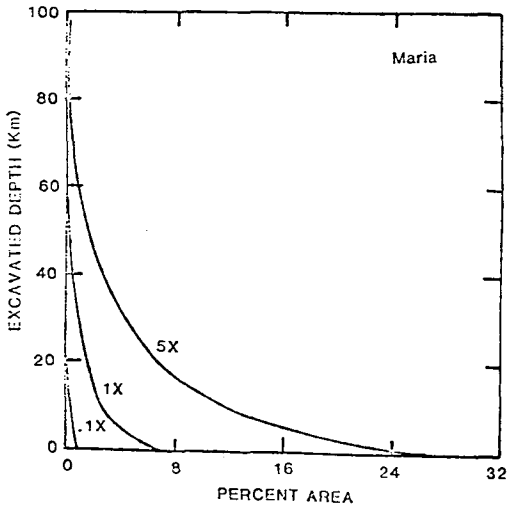

V. The cumulative percent of lunar maria surface excavated beyond a specifed depth for four different total fluxes of craters larger than 8km diameter.

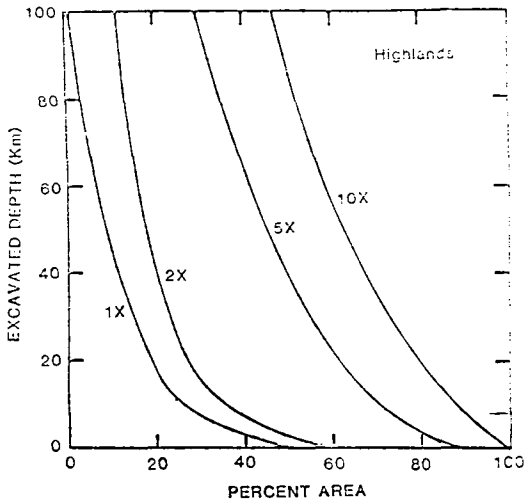

III. The cumulative percent of lunar highlands surface excavated beyond a specifed depth for four different total fluxes of craters larger than 8km diameter.

CHEMICAL WEATHERING OF SOILS FROM THE DRY VALLEYS OF ANTARCTICA: A TERRESTRIAL ANALOG OF MARTIAN WEATHERING PROCESSES

Everett K. Gibson, Jr., SN4, Experimental Planetology Branch, NASA Johnson Space Center, Houston, TX 77058

The nature of the authigenic secondary minerals in soils from the Dry Valleys of Antarctica have been reviewed by Gibson et al. (1983). A summary of these minerals is given in Table 1. In common with soils from other arid parts of the world (El Baz and Prestel, 1980), soluble salt concentrations are characteristic of Dry Valley soils. The origins of the water soluble ions forming the Dry Valley salts is controversial: proposed origins include chemical weathering of rocks, hydrothermal fluids, marine aerosols, and the evaporation of water from marine incursions. Gibson et al. (1983) noted that the molar ratios of the water soluble ions reflect the nature of the secondary minerals present. For example, when the Na^+ and Cl^- molar ratios are equal (i.e. 1:1) the presence of halite is indicated. Similarily, when the Ca^{2+} to Cl^- ratio is 1:2, antarcticite ($CaCl_2 \cdot H_2O$) is present.

Most silicate mineral and lithic fragments in the Dry Valley soils exhibit some degree of alteration. A major problem is in determining which alteration effects are caused by in situ weathering and which are the result of other processes. Some alteration resulted from hydrothermal activity in the source rock- epidote and sericite, for example, are hydrothermal minerals, and some amphiboles have been replaced by biotite. In addition, weathering may have occurred prior to deposition at the soil sites. It is also possible that some of the diagenesis occurred during the subaqueous history of the soils.

There is, however, good evidence for present day weathering in the Dry Valley soils. The sharp increase in iron oxide near the surfaces, especially relative to fresh ferromagnesian minerals, demonstrates increased oxidation towards the surface (Gibson et al., 1983). This phenomenon has been noted previously by Bockheim (1979). Evaporites indicate ionic migration and chemical activity even in the permanently frozen zones. Halite abundances, for example, decrease systematically, closely following an exponential function ($R^2 = 0.97$) from the salt layer near the surface to the bottom of a one meter deep soil pit. Even though halite abundances are very low near the bottom, there is no indication of a break at the boundary of the permanently frozen zone. Secondary calcite abundances increase with depth; the reason for this is not presently understood. The presence of these evaporites also indicates that chemical weathering of rocks and possibly soils has been active within the soil profiles because some of the water soluble ions (Ca^{2+}, Mg^{2+}, K^+, and CO_3^{2-}) in the evaporites originated by rock weathering (Keys and Williams, 1981).

Individual silicate mineral fragments in both the active and the permanently frozen zones show evidence of chemical weathering (Gibson et al., 1983). The characteristic effect of chemical weathering on the surfaces of minerals in temperate climates is dissolution along crystallographically-controlled zones of weakness (Berner et al., 1980). Such dissolution features are common on the surfaces of susceptible silicate fragments (feldspars, amphiboles, and pyroxenes) throughout the Dry Valley soils studied. Differential weathering along exsolution lamellae is present in some pyroxenes. Because such delicate features would probably not survive sedimentary transport, they are evidence for in situ chemical weathering.

The zeolites found in the Dry Valley soils (Gibson et al., 1983) must be authigenic because they were found to be fragile. They were euhedral, unabraded, and unfractured, which strongly suggests in situ formation, so their presence in the Dry Valley soils is another indication that diagenetic processes are active throughout the soils. Pedogenic zeolites are not usually found in Antarctic soils. Chabazite and other zeolites have been identified in Dry Valley Drilling Project (DVDP) rock cores, but their origin is attributed to hydrothermal processes (Berkley and Drake, 1981). Zeolites of sedimentary or pedogenic origin are fairly common in other terrestrial climates. The presence of chabazites in the Dry Valley soils is consistent with other occurrences in that they form in an arid environment under saline, alkaline conditions (Hay, 1977).

Weathering of planetary surface materials results from both chemical and physical interactions of the planet's surface with the atmosphere and, if present, the hydrosphere and biosphere. The net result of weathering is to modify the original surface materials and produce secondary materials that are the products of an approach to equilibrium between the atmosphere and solid body. The detailed study of the soils from the Dry Valleys of Antarctica has produced an idealized soil profile which should be applicable to the Martian regolith. The soil profile would be composed of four basic zones: (1) aeolian zone; (2) salt zone: (active zone; and (4) permanently frozen zone. Processes operating within each of these zones tend to modify the original furface materials. The three zones above the permanently frozen zone are the regions where most of the chemical and physical weathering occurs.

It is known that Martian surface conditions may be favorable for chemical weathering (Gooding, 1978;Booth and Kieffer, 1978). The primary silicates would be expected to be reactive minerals such as pyroxenes, olivines, and feldspars. Because of the possible existence of an extensive subsurface system of water ice or even liquid water (Clifford, 1981), water is probably available to assist in the weathering of the reactive minerals. Such weathering would result in the formation of clays, sulfates, carbonates, hydrates, and zeolites. The formation of pedogenic zeolites under cold, arid Antarctic conditions opens the possibility that zeolites may also form in the Martian regolith. Terrestrial zeolites are especially common in soils derived from volcanic ejecta (Hay, 1977), and such soils may be common on Mars. Zeolites are well known for their volatile exchange and storage properties. Consequently, the possible presence of a significant abundance of zeolites in the Martian regolith may have a profound effect on the volatile budget of Mars. Specifically, zeolites could be a repository of atmospheric gases including CO_2, O_2, and H_2O. Changes in pressure and temperature might induce Martian zeolites to take up or release large quantities of volatiles.

In summary, Martian soil subjected to chemical weathering processes could contain the following likely constituents: (1) fresh primary silicate material; (2) partially altered primary silicates; (3) secondary minerals, possibly including clay minerals, evaporites, carbonates, sulfates, hydrates, and zeolites- and (4) altered volcanic glass or impact glass. The soil may also include palogonite and other alteration products and secondary minerals. It is unlikely therefore that an equilibrium assemblage of minerals would be present. From the detailed study of the soils from the Dry Valleys of

Antarctica, it is obvious that the complex processes in operation produce major changes in the parent materials, depending upon where the constituents reside and the degree to which weathering and diagenesis operates. It is furthermore, clear that natural near-surface environments, even in very cold and dry regions, may produce extremely complex soils. It seems obvious that for any analysis conducted by a remote instrument, extreme caution must be taken when interpreting the results and drawing conclusions, especially about possible processes operating in regoliths in cold, arid environments similar to those of the Dry Valleys or Mars.

References

Berkley J.L. and Drake M.J. (1981) Icarus, 45, 231-249.
Berner R.A. et al. (1980) Science 207, 1205-1206.
Bockheim J.G. (1979) Soil Science 128, 142-152.
Booth M.B. and Kieffer H.H. (1978) J. Geophys. Res. 83, 1809-1815.
Clifford S.M. (1981) Third Intern. Colloq. on Mars, (abstracts),pp.44-45.
El Baz F. and Prestel D. (1980) Lunar and Planet. Sci. XI, 254-256.
Gibson E.K. et al. (1983) Proc. Lunar and Planet Sci. Conf., 13th, J. Geophys. Res., Suppl. A912-A928.
Gooding J.L. (1977) Icarus 33, 483-513.
Hay R.L. (1977) Mineralogy and Geology of Natural Zeolites, pp. 53-64, M.S.A. Publication
Keys J.R. and Williams K (1981) Geochim. Cosmochim. Acta 45, 2299-2309.

Table 1

Authigenic Secondary Minerals in Dry Valley Soils

Wright Valley Soil Pit*		Previously Identified in Dry Valley Soils	
Mineral	*Formula*	*Mineral*	*Formula*
Halite	NaCl	Aragonite	$CaCo_3$
Gypsum	$CaSO_4 \cdot 2H_2O$	Monohydrocalcite	$CaCO_3 \cdot H_2O$
Thenardite	Na_2SO_4	Dolomite	$CaMg(CO_3)_2$
Soda Niter	$NaNO_3$	Trona	$Na_3H(CO_3)_2 \cdot 2H_2O$
Bloedite	$Na_2Mg(SO_4)_2 \cdot 4H_2O$	Thermonatrite	$Na_2CO_3 \cdot H_2O$
Calcite	$CaCO_3$	Burkeite	$Na_6(CO_3)(SO_4)_2$
Limonite	FeOOH	Mirabilite	$Na_2SO_4 \cdot 10H_2O$
Chabazite		Epsomite	$MgSO_4 \cdot 7H_2O$
	$(Ca, Mg, Na_2, K_2)Al_2Si_4O_{12} \cdot 6H_2O$	Darapskite	$Na_3(NO_3)SO_4 \cdot H_2O$
		Sylvite	KCl
		Antarcticite	$CaCl_2 \cdot 6H_2O$
		Tachyhydrite	$CaMg_2Cl_6 \cdot 12H_2O$
		Bischofite	$MgCl_2 \cdot 6H_2O$
		'Clay minerals'	

PROPERTIES OF FILAMENTARY SUBLIMATION RESIDUES FROM DISPERSIONS OF CLAY IN ICE **James B. Stephens, Timothy J. Parker, R. Stephen Saunders, Eric G. Laue,** Jet Propulsion Laboratory; **Fraser P. Fanale,** University of Hawaii.

The properties of sublimate residues are of considerable interest in studies of the thermal modeling of Martian and cometary ice surfaces (Cutts et al, 1979; Fanale & Salvail, 1984). The study of the formation of sand grains from this mantle on Martian polar ice is also supported by these experiments (Squyres, 1979; Tsoar et al, 1979; and see Saunders et al, "Transformations of Polar Ice Sublimate Residue into Martian Circumpolar Sand", this volume).

To understand these properties, a series of low temperature vacuum experiments were run during which dirty ices that might be expected to be found in Martian polar caps and in comet nuclei were made and then freeze dried. In addition to using particulate material of appropriate grain size and minerology, particle nuoleated ices were simulated by dispersing the particulates in the ice so that they did not contact one another. This noncontact dispersion was the most difficult requirement to achieve but the most rewarding in that it produced a new filamentary sublimate residue that was not a relic of the frozen dispersion. If the siliceous particles are allowed to touch one another in the ice the structure of the contacting particles in the ice will remain as a relic after the ice is sublimed away.

Vacuum sublimation of the ice out of a solid dispersion (1:1000) of submicron montmorillonite clay particles (or quartz glass smoke, "Cabosil" particles) in water ice has produced a very low density (0.0009 g/cm^3) filamentary sublimate residue. The fact that the low density structure will, so far, only form with particles that have relatively high solubility parameters with water is also interesting. These constructs (as seen in SEM micrographs and depicted in figure 1) are formed of very long network chains of the clay particles. The material is sufficiently electrically conducting to drain away the SEM charge. The filamentary material is highly resistant (no change in electronic properties are apparent) to SEM electron beam heating for hours in a vacuum. Heating in an oven in air to 350°C also produces little change in the sublimate residue material. The particle bonding forces are strong and produce a mechanically tough and resilient low density material. Lumps of the material will adhere to one another with forces approaching the original tensile strength. The material is porous and will allow vapors to diffuse though it, but the thermal conductivity and the visible light transmissivity are very low. These three features dramatically increase the time it takes to sublime away the ice because the incoming radiant and conducted heat is carried away by the out-flowing water vapor (Scheidegger, 1974). The vapor probably leaves the surface at nearly the temperature of the outer surface.

Two different hydrosols were prepared by mixing distilled water with air classified montmorillonite clay (size <0.2 μm) or Cabosil (quartz glass smoke) in weight ratios of 1000:1. This mixture was sprayed into an open-mouth dewar of liquid nitrogen (LN_2). The sub micron drops froze very quickly upon contact with the LN_2 and trapped the contaminants away from the

surface of the clay or the Cabosil particles. The siliceous particles were sufficiently dispersed that the crystallizing ice could not push the particles ahead of it and agglomerate them. Lower mixing ratios and coarser drops produced sublimate residues that were relics of the particle structure in the ice. The slurry of LN_2 and frozen dirty water ice droplets (while still in the dewar) was placed in the vacuum chamber (capable of reaching pressures below 15 microtorr). The pressure in the vacuum chamber indicated that the water ice was at its lowest temperature (-50°C) at the very end of the sublimation process. The sublimation process takes several days to complete and requires more time (≈ 5 days) with larger quantities (≈ 1 liter) of slurry, and requires even more time if the filamentary residue is particularly light weight (i.e., a good insulator).

Figure 1 provides a microscopic illustrated view of our concept of what takes place as a clean particle of clay is released from the ice and is transported to the filamentary residue forming above. The particle obtains a charge from the ice as it separates from the subliming surface. The particle is electrostatically transported to the residue mantle that is growing above. The contaminating particles and molecules that are much smaller than the siliceous particles are entrained by the water vapor wind before they can recontaminate the siliceous particle surfaces. The charged particle is attracted to the end of a filament chain that is growing as part of the sublimate residue. We believe that, because its surfaces are molecularly clean and electrostatically charged, the siliceous particle makes a molecular bond with the particle at the end of the filamentary chain (van Olphen, 1963). Other materials, that have low solubilities with water, such as rouge (ferric oxide) and carbon black were also used as particulate matter, but no filamentary material was formed. Siliceous particles that previously had been separated by ice are brought together in the presence of water vapor at low pressures (< 0.2 torr) and temperatures (<-25°C), in the absence of liquid water. Therefore, the properties of the sublimate residue could be relevant to the properties of cometary surfaces and Martian polar cap sublimation processes.

REFERENCES

Cutts, James A., Blasius, Karl R., and Roberts, W. James, "Evolution of Martian Polar landscapes: Interplay of long-term variations in perennial ice cover and dust storm intensity." Journ. Geophys. Res., Vol. 84, No. B6, 1979, pp. 2975-2994.

Fanale, F.P., and Salvail, J.R., An idealized short period comet model: Surface insolation, H_2O flux, dust flux and mantle evolution, Submitted to Icarus Aug. 1984.

Squyres, S. W., "The evolution of dust deposits in the Martian north polar region." Icarus 40, 1979, pp. 244-261.

Scheidegger, A.E., The Physics of Flow through Porous Media, 3rd ed., Univ. Toronto Press, p. 243-245. 1974.

Tsoar, Haim, Greely, Ronald, and Peterfreund, Alan R., "Mars: The north polar sand sea and related wind patterns." Journ. Geophys. Res., Vol. 84, No. B14, 1979, pp. 8167-8181.

van Olphen, H., 1963, An Introduction to Clay Colloid Chemistry, Interscience: New York, 301 p.

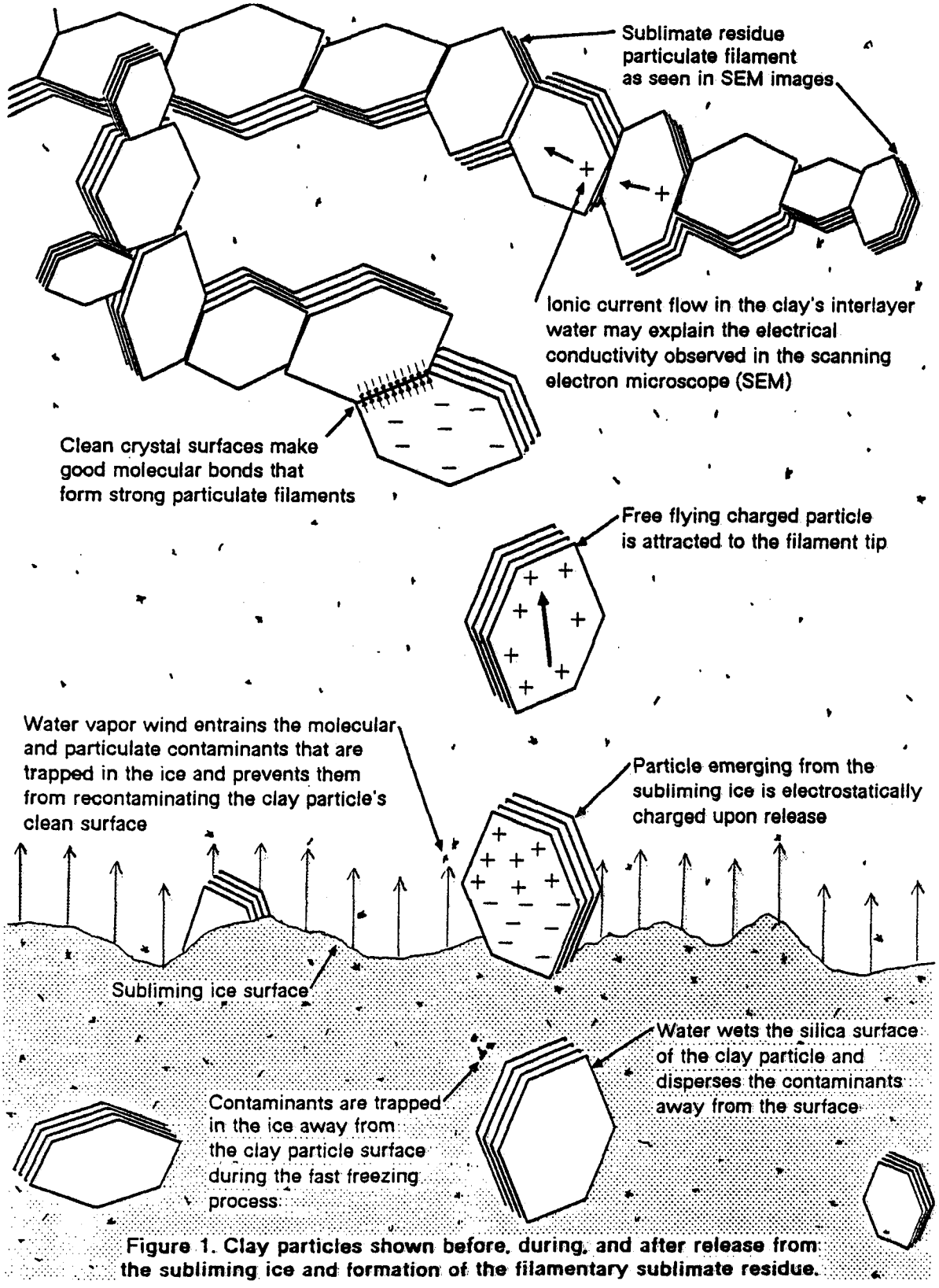

Figure 1. Clay particles shown before, during, and after release from the subliming ice and formation of the filamentary sublimate residue.

CHAPTER 13

RADAR APPLICATIONS

Page intentionally left blank

PROGRESS IN PLANETARY RADARCLINOMETRY

Robert L. Wildey, U.S. Geological Survey, Flagstaff, AZ 86001

Building upon promising initial results [1, 2, 3], efforts have continued to improve radarclinometry in spite of the fact that the theory and algorithms still predate the development of the radiometrically calibrated radar upon which they must depend in order to achieve metric precision. Such efforts help to insure the availability of the technique for data returned by the Venus Radar Mapper. Even now, compensation for layover and production of synthesized stereo enhance geologic interpretability of radar images. The theory of radarclinometry, as previously reported (version 1), utilizes a knowledge of the relation between pixel DN value and terrain surface orientation to produce a topographic map. I showed that the process may be conceived in terms of a surface integral which develops away from a topographic profile as available ground truth. Alternatively, in consideration of the unavailability of ground truth in extraterrestrial applications, radarclinometry may develop as a line integral developing from a single point, providing reasonable assumptions about the mathematical nature of local curvature are made. In verstion 1 it was assumed that the surface was locally cylindrical. Data available in the neighborhood of a pixel renders determinate the magnitude of curvature and the orientation of the cylinder. In version 1 the pixel-energy model was also approximated to depend exclusively on local incidence angle. Finally, in version 1, the line integrals were confined to the ground-range direction with averaging techniques applied to the determination of mean tilt and elevation adjustments within the set of such line integrals, followed by enforcement of a degree of isotropy in the auto-correlation of the topography. The past year's efforts to improve upon version 1 were confined to four main emphases:

(1) Diminished CPU time for the algorithm: The previous program required 20 hours to process an image of approximately 600 x 600 pixel. By a combination of deliberate economy of arithmetic and logic and the adaptation to the VAX 750 system rather than the previous PDP 11/45 system, a reduction by a factor of 5, to 4 hours, has been achieved. This reduction has occurred in spite of two newly incorporated complications: a) a more exact, and therefore more mathematically elaborate model of radar pixel energy has been employed, and b) a more flexible collection of local terrain curvature assumptions has been utilized.

(2) Improved pixel-energy model for a radargram: For a radiometrically calibrated radar, in the limit of many "looks", the pixel DN value is proportional to pixel energy (or, as electric vector amplitude, the square root thereof). Pixel energy is proportional to the product of specific intensity (surface brightness) and a solid-angle of integration. Unlike the case for ordinary images, this solid-angle is not constant. Its boundaries map from those corresponding to the radar pixel dwell in range-time and azimuth. If the directional variability in the forward gain pattern of the antenna is neglected, this variability of solid angle results in a factor of the cotangent of the incidence angle multiplied by the secant of the projected

position angle, as seen from the radar, between the local vertical and the local surface normal, being applied to the radar reflectance function before it becomes a "pseudo-photometric function" applicable to pixel DN values. The dependence on this latter angle, a second-order effect, was neglected in the previous program. Its present incorporation is a severe mathematical complication. The simplicity of a radar image directly convertible to incidence angles as pixel values is lost. The pixel value becomes a function of the two components of slope for which the specification of the strike-line orientation does not yield an explicit analytical solution for the component of slope along the ground-range. An iterative solution, such as given by the Newton-Cotes method, is required. Worse yet, depending on the strike-line orientation, the desired slope is a multiple-valued function of pixel DN value for a fixed strike-line orientation. This non-monotonicity tends to introduce instability in the Newton-Cotes iteration. Additional logic is required both for that reason and for choosing between the three possible roots of the equation. It has been found to be very helpful to process the terrain with a bias-tilt toward the radar, so that the strike-line never makes a very large angle with the azimuthal coordinate axis. This bias-tilt is then removed from the resulting topography with a rotational and scaling transformation.

(3) An increased flexibility of local curvature assumptions: The curvature assumption used in the previous program was that the surface was locally cylindrical in nature, except that low signal-to-noise of the image brightness-gradient resulted in an assumption of local flatness (not local horizontality). In the current program, for the purpose of stepping strike-line orientation in the topographic integration, three curvature hypotheses are available through logical branches based on user-provided tolerances. The first choice is still Local Cylindricity, but if the local curvature of image isophotes is too high, or if the pixel DN value is a relative extremum, or if the ground-range component of image brightness gradient is present at too low a signal-to-noise ratio, this assumption is rejected. If both gradient components, together with other crucial combinations of previously integrated slope-components and brightness-gradient components, prevail over specified thresholds, the terrain curvature assumption is called Local Biaxial Ellipsoidal Hyperbolicity. Herein, the terrain is assumed to be locally a surface of second degree and also a figure of revolution about a vertically aligned axis. Failing all the foregoing criteria, the curvature assumption is called Least-Squared Local Sphericity. As the term implies, this model is overconstrained when the image brightness and both components of the brightness-gradient are available. It is the most stable assumption. The assumption of local flatness (not horizontality) is reserved only as an act of desperation if there is a commencement of numerical divergence in the iterative procedures, or if the difference between (1) the predicted slope at the next integration step, based on the curvature assumptions, and (2) the slope actually calculated from the evolved strike-line orientation and the pixel brightness at the next pixel, is greater than a certain allowed tolerance.

(4) Use of bona fide azimuthal integration: My basic technique involves a line integral rather than a surface integral. In version 1, the method for height-adjusting adjacent line integrals was heavy-handed at best. We have tried to do the cross-range version of the line integral as implied by the theory, which is difficult because that component of slope enters the radarclinomeetry equation only to second order and higher.

Prospectus: The foregoing improvements have been implemented in a working algorithm whose testing continues. It was first found that the tolerance on agreement between a predicted slope at a succeeding step and a calculated slope at that next step, mentioned above, had to be a relatively crude 0.02 in order to keep the incidence of reversion to local flatness below about 6%. In the vast majority of cases, however, the new slope agreed with the prediction much better than with the slope at the previous mesh point. It was discovered that the LBEH assumption always produced overly large curvature in the azimuthal direction. Accordingly, LBEH was disallowed in azimuthal stepping. The incidence of "coarse-mesh abort" then went to virtually zero. The resulting topography is still unnaturally banded. It bodes ill if this is due to the fact that either the curvature assumptions are not always very good or the integration mesh, as implied by the image sampling, is sometimes too coarse for simple forward stepping, or both. The evidence of considerable numerical experimentation suggests that the banding is probably due to nothing more than the current inadequacy of radiometric calibration. These circumstances afford ample opportunity for renewed creativity as our efforts continue.

References:

[1] Wildey, R. L., 1984, Science, 224, 153-156.
[2] Wildey, R. L., 1984, International Archives of Photogrammetry and Remote Sensing, Commission IV, 25, 522-530.
3] Wildey, R. L., 1984, Photogrammetric Engineering and Remote Sensing (in press).

MERCURY RADAR ALTIMETRY: A PRELIMINARY ANALYSIS. J. K. Harmon[1], D. B. Campbell[1], J. W. Head[2], D. L. Bindschadler[2], and I. I. Shapiro[3]. (1) Nat'l Astronomy and Ionosphere Center, Arecibo, PR 00612; (2) Dept. of Geological Sciences, Brown Univ., Providence, RI 02912; (3) Harvard-Smithsonian Center for Astrophysics, Cambridge, MA 02138.

Range-Doppler radar observations have been made of the planet Mercury over the six-year period 1978-1983. Approximately 30 continuous altitude profiles were obtained, each spanning between 20 and 90 degrees of longitude. The profiles are located in the equatorial zone of Mercury between 5^{o}S and 12^{o}N latitude (Figure 1). Approximately 40% of the total coverage is in the unimaged hemisphere.

Data were taken on approximately 130 separate days, with between one and three observations being made each day. Profiles were generated by analyzing the averaged range-Doppler array taken for each run using a technique in which delay templates are fit to each frequency in the array to determine the time delay to the leading edge of each Doppler annulus (1). Subtraction of time delays corresponding to the mean planetary sphere and assignment of latitude and longitude location based on the location of the leading edge of each Doppler annulus results in a single altitude profile. Each profile typically extends 7^{o} from the subradar point in a roughly east-west direction. Because of the rotation of the planet, the Doppler technique yields a much better longitudinal than latitudinal resolution; a typical radar "footprint" is 0.15^{o} in longitude and 2.5^{o} in latitude (corresponding to an area about 6 km by 100 km at the equator). It is important to note that this technique does not yield any kind of average altitude for a given footprint but rather picks out the strongest returned signal with certain Doppler characteristics. For example, a large quasispecular return from a crater floor more than 1.3^{o} to the north or south of the radar ground track could appear as a point in a given profile. However, examination of the profiles has shown this to occur only rarely.

Analysis of altitude profiles is directed toward characterizing the topographic signal of various geologic features in the imaged hemisphere of Mercury and using these models to understand profiles located in the unimaged hemisphere. Using USGS 1:5,000,000 airbrush topo maps and the Atlas of Mercury (2) as references we have attempted to develop criteria that allow for separation of three major surface units based solely on the topographic profiles. Of these units, the smooth plains, intercrater plains, and cratered terrain (as identified by Trask and Guest, 1975) (3) only the smooth plains unit is clearly separable. Tir Planitia, located to the south-southeast of Caloris Basin, is a good example of a smooth plains region that appears to be as much as a kilometer below the surrounding terrain. A similar area appears in profiles taken to the west of Mozart crater, in the unimaged hemisphere of the planet. These observations lend support to the idea that an annular plains region surrounds the Caloris Basin.

In addition, attempts have been made to characterize specific topographic features. Craters and ridges show up distinctly in the profiles, whereas valleys and scarps are less distinctive. Mare-like ridges, such as those identified in Tir Planitia, appear as small disturbances in profile and are typically no more than 300 m high. Ridges as high as 700 m to 1 km are often seen in profiles covering intercrater plains regions. Ridge-like features often occur in intercrater plains and cratered terrain but do not correlate well with any mapped features, particularly in areas that were imaged at high sun-elevation angles. Tir Planitia, which is populated by ridges analogous to lunar mare ridges, is characterized by a broad topographic depression which suggests that the topography and ridges may be a result of lithospheric loading and flexure, analogous to the emplacement and deformation of the lunar mare deposits (4). These similarities in the nature and tectonic deformation of mercurian plains and lunar maria provide additional evidence that the circum-Caloris plains may be of volcanic origin.

We are presently compiling depth-diameter relationships for fresh and degraded craters and extending our analyses to the unimaged part of Mercury.

References: 1) R. Ingalls and L. Rainville (1972) Astron. J., 77, 185. 2) M. Davies et al. (1978) NASA SP-423. 3) N. Trask and J. Guest (1975) JGR, 80, 2461. 4) S. Solomon and J. Head (1980) RGSP, 18, 107.

Figure 1: Map of total Arecibo altimetry coverage of Mercury from 1978-1983. The subradar tracks are denoted by solid lines.

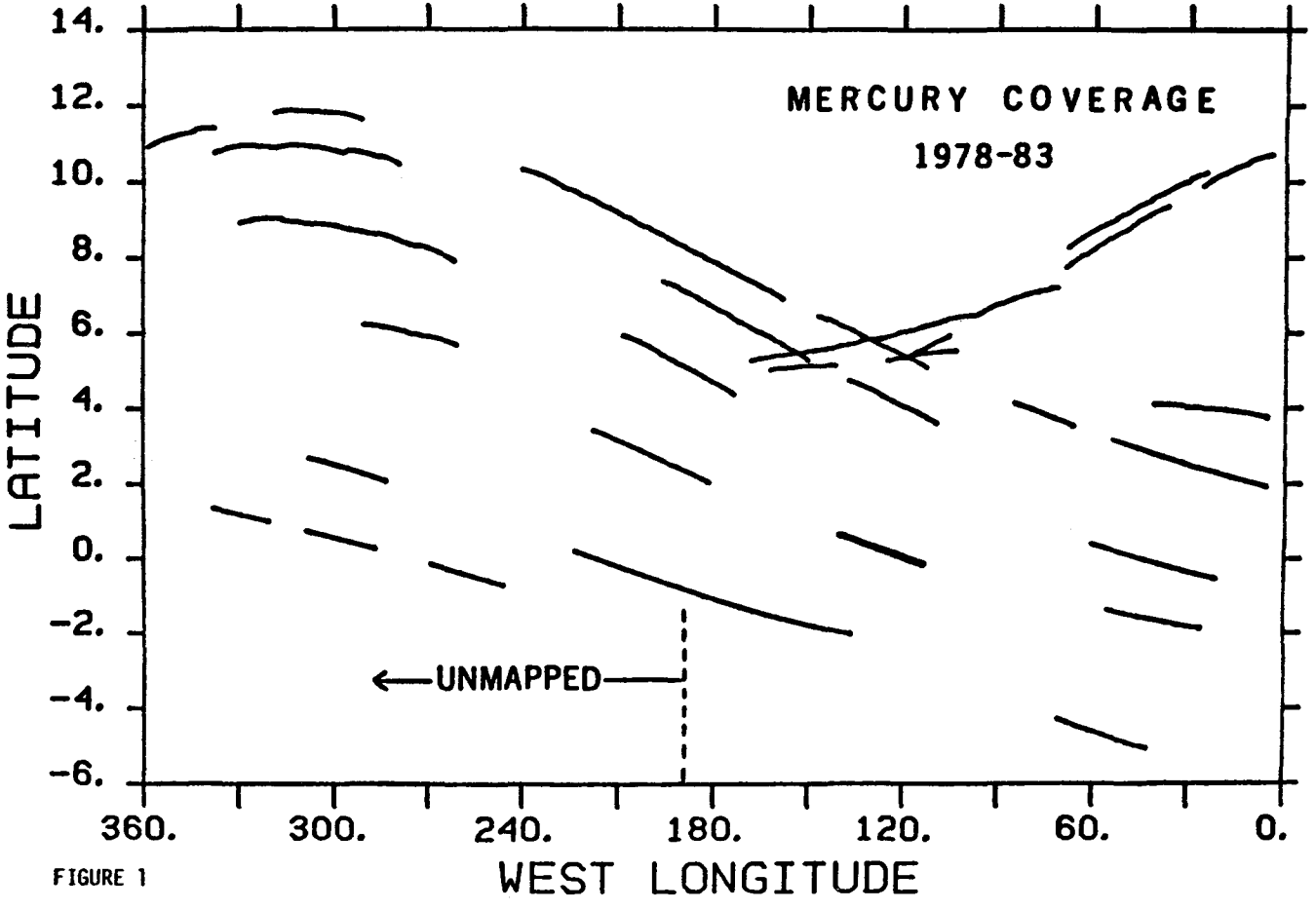
MERCURY COVERAGE
1978-83
LATITUDE
14.
12.
10.
8.
6.
4.
2.
0.
-2.
-4.
-6.
←UNMAPPED
360.
300.
240.
180.
120.
60.
0.
WEST LONGITUDE

FIGURE 1

UNSUPERVISED CLASSIFICATION OF GLOBAL RADAR UNITS ON VENUS

Richard C. Kozak, Philip A. Davis, and Gerald G. Schaber
U.S. Geological Survey, Flagstaff, AZ 86001

Characterization of the Venusian surface in terms of its radar properties was accomplished by application of an unsupervised, linear-discriminant algorithm to two Pioneer-Venus (PV) Orbiter radar data sets: the RMS-slope ("surface roughness") and reflectivity. Both databases were spatially filtered to the same effective resolution of 100 km prior to classification. A recent supervised classification study using these data [1] was based on presupposed morphologic significance of selected data ranges. In our view, the knowledge of both Venusian geology and the geologic significance of the radar data is so limited that the data warrant a more unsupervised approach; for this study a linear-discriminant classifier was chosen. This approach is purely statistical, thereby removing any observer bias. Statistical significance of the resulting clusters was evaluated by an ancillary program in which an F test utilizing the Mahalanobis' distance (a measure of separation of two multivariate means in terms of pooled variance) determined whether clusters were significant at least to the 95% confidence level. Relations between the reflectivity and RMS-slope of the resulting 15 units are shown in Figure 1. In no case do the units' standard deviations exceed actual database errors.

Analysis by breakdown of the units into hypsometric provinces [2] shows some correlation of units with elevation, but indicates that hypsometry alone is not a reliable criterion for quantitative examination of Venusian geology. A classification-unit map was generated [3] to help assess the spatial relations between units and to facilitate comparison of units with other data sets, particularly the Venera lander data, Earth-based radar imagery, and PV altimetry. These data, in addition to a classification-unit encompassment scheme (below), allowed some inferences to be made about composition and physical properties of 10 of our 15 units.

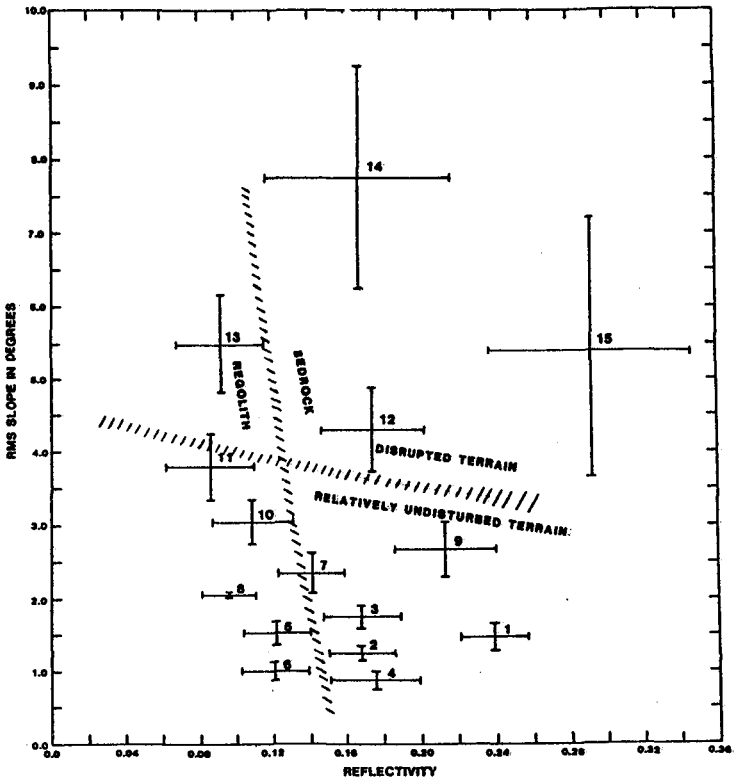

Figure 1. Relations of reflectivity and RMS-slope values between the 15 clusters derived from unsupervised cluster analysis of Pioneer Venus radar data sets. Error bars are +/- one standard deviation. Hatchured lines delineate approximate transitions from dominantly regolith to dominantly bedrock surface (vertical line), and from tectonically disrupted terrain to relatively undisturbed terrain (horizontal line).

Venera lander data provide valuable geochemical ground-truth information for four of the units. Four of the Venera sites (9, 10, 13, and 14, corresponding to units 11, 5, 7, and 7, respectively) have tholeiitic or alkali basalt compositions [4,5]. An index of weathering at these sites, inferred from the "soil"/rock ratios determined from lander images [6] correlates well with the associated units' reflectivity values. This correlation, based on the dominance of bedrock at the Venera 13 and 14 landing sites (unit 7), suggests that the reflectivity value for "fresh" basalt on Venus might approximate 0.14, and that lower values (due to volume scattering and absorption) represent increasing degrees of weathering. This value, however, may represent a lower limit due to: 1) the 100-km resolution of the PV data; 2) reduction of reflectivity by scattering from the rolling topography of unit 7; and 3) smoother, lower elevation terrain (units 1-4) showing higher reflectivity values (0.17 to 0.24). The alkali-syenite/granite-like geochemistry of the Venera 8 site [4,5] is considered to be unrepresentative of the classification unit for that area (unit 10) because of the improbability of such a lithologic unit following a contiguous, peripheral distribution around linear features and basaltic highlands as unit 10 does. This unit's 0.10 reflectivity value is perhaps more suggestive of a weathered basalt. The suggestion of a basaltic composition for unit 10 is reinforced by its occurrence at Colette, a feature whose morphologic and polarization characteristics are indicative of endogenic processes [7], and more recently, by the Venera 15 and 16 radar image data (talks presented at Lunar and Planetary Science Conference, March 1984, by A.T. Basilevsky and V.L. Barsukov). Furthermore, Cleopatra and Sappho Paterae, also within unit 10, show characteristics of volcanic calderas [2].

Alpha Regio, and Akna, Freyja and Maxwell Montes, regions characterized by numerous parallel bands of high backscatter on Arecibo images, have been compared to folded or faulted terrains on Earth [8,9]. Unit 14 is consistently associated with these regions, and we postulate that other occurrences of unit 14 (notably the chasmata of Aphrodite) may also be indicative of faulted terrain.

Unit 15 (generally encompassed by unit 14) is the only unit whose reflectivity and RMS-slope values are higher than those of unit 14. This implies that unit 15 is represents 1) a more disturbed surface zone, perhaps analogous to the continental rift systems of Earth [10], as evidenced by the unit's presence at Atla Regio, which sits on the junction of three global-scale disruption zones [11]; and/or ,2) a lack of finer fill material which is more likely to be found on the lower slopes of unit 14.

Analysis of unit spatial relations was aided by an "encompassment scheme" produced by calculating the percentage of each unit's area that is encompassed by each of the other 14 units [3]. This scheme shows that 92.4% of unit 8 is encompassed by units 5, 7, and 10, -- units which we have determined to most probably represent basaltic surfaces. Therefore, it seems likely that unit 8 is also basaltic, but with a surface roughness between those of units 5 and 7. Unit 13's encompassment (81.6%) by units 11 and 14 suggests that this unit probably represents a transitional surface between the rough, banded terrain of unit 14 and the relatively smooth "soil"-covered basalt of unit 11. Similarly, unit 12 is found dominantly between units 10, 14, and 15, implying a surface that is

dominantly rock (of basaltic composition) with a roughness intermediate to the relatively smooth unit 10 and the folded and/or faulted units 14 and 15. The geologic significance of unit 9 is difficult to infer from this study, because of its isolated occurrence and irregular spatial relations. Unit 6 occurs consistently within unit 5, which is presumed to have a mixed "soil"/basalt bedrock surface. The low reflectivity and RMS-slope values for these two units and their occurrence within the low-lying planitia suggest that the topographic lows are acting as traps for fines, which is corroborated by the smooth, almost featureless appearance of these areas on Arecibo radar imagery. Units 2, 3, and 4 are widely scattered among broad, low-lying areas and along the flanks of promontories, and may represent dominantly bedrock surfaces; varied roughnesses may be responsible for their different RMS-slope values. Unit 1 is perhaps the most anomalous of the fifteen units, as it is very reflective (0.24) for having such a low RMS slope (1.47). This unit occurs mostly around Nightingale and Atalanta Planitia and in the lowlands southwest of Imdr Regio. Absence of ground-truth data or obvious associations with other units makes interpretation of this unit's physical significance difficult.

References

[1] Peterfreund, A.R., Head, J.W., Garvin, J.B., and Zisk, S.H., Venus surface units derived from correlation of Pioneer-Venus altimetry, roughness, and reflectivity measurements, Jour. Geophys. Res., in press.

[2] Masursky, H., Eliason, E.M., Ford, P.G., McGill, G.E., Pettengill, G.H., Schaber, G.G., and Schubert, G., 1980, Pioneer Venus radar results: geology from images and altimetry, Jour. Geophys. Res., v. 85, p. 8232-8260.

[3] Davis, P.A., Kozak, R.C., and Schaber, G.G., Global radar units on Venus derived from statistical analysis of Pioneer Venus orbiter radar data, unpublished ms.

[4] Florensky, C.P., and Nikolayeva, O.V., 1982, Rock types on Venus, Doklady Acad. Nauk SSSR, v. 262, p. 1245-1249.

[5] Surkov, Yu. A., 1983, Studies of Venus by Veneras 8, 9, and 10, in Hunten, D.M., Colin, L., Donahue, T.M., and Moroz, V.I., eds., 1983, Venus, Univ. of Arizona Press, Tucson, p. 154-158.

[6] Garvin, J.B., Head, J.W., Zuber, M.T., and Helfenstein, P., 1984, Venus: The nature of the surface from Venera panoramas, Jour. Geophys. Res., v. 89, p. 3381-3399.

[7] Burns, B.A., and Campbell, D.B., Radar evidence for cratering on Venus, Jour. Geophys. Res., in press.

[8] Pettengill, G.H., Campbell, D.B., and Masursky, H., 1980, The surface of Venus, Scientific American, v. 243, p. 54-65.

[9] Campbell, D.B., Head, J.W., Harmon, J.K., and Hine, A.A., 1983, Venus: Identification of banded terrain in the mountains of Ishtar Terra, Science, v. 221, p. 644-647.

[10] Campbell, D.B., Head, J.W., Harmon, J.K., and Hine, A.A., 1984, Venus: Volcanism and rift formation in Beta Regio, Science, v. 226, p.167-170.

[11] Schaber, G.G., 1982, Venus: Limited extension and volcanism along zones of lithospheric weakness, Geophys. Res. Letters, v. 9, p. 499-502.

Mapping and Geological Analysis of Mercury and Venus Radar Ranging Data

P. E. Clark, R. F. Jurgens and G. S. Downs (JPL) and M. E. Strobell and G. G. Schaber (USGS)

Although many radar profiles and images of the areas within 20^{o} of Mercury's equator had been obtained from 1971 to 1981, at both Goldstone and Arecibo radar facilities, surprisingly little geological analysis had been done with these data until recently (1,2,3). Topographic profiles and radar roughness reflectivity images which can be derived from these data will be crucial in completing the geological mapping of Mercury now underway at the U.S. Geological Survey (4,5,6,7). Earth-based radar observations of Mercury and the other terrestrial planets as well are a potentially very valuable tool in the determination of the physical nature of their surfaces. Processing of available radar data must be completed to establish any systematic relationship between radar reflectivities and roughness, density, dielectric constant, and other related geological parameters. Specific tasks accomplished for these purposes include the following:

(1) Documentation was located and searched to establish the type and quantity of Goldstone 12.5 cm radar observations which were available from Mercury. Data has been collected during approximately 50 observation periods from 1971 to 1981. Each observation period consists of large numbers of collected spectra. About half of the data, collected during 1972 and 1973, have been processed, but without adequate documentation.

(2) We attempted to establish a standarized, well-documented procedure for processing and analysis for all Goldstone Earth-based radar imaging observations of Mercury and Venus by starting this effort with the relatively well-documented, high-quality radar observations of 1974. Steps included:

   (a) Preliminary processing -- tape conversion and data translation;
   (b) Ephemerides determination -- location of area of detection on planet from celestial mechanics considerations, incorporating standard set of ephemeris programs;
   (c) Display of measured reflectivities in delay and frequency coordinates as received by the instrument;
   (d) Mapping and display of reflectivities in planetary coordinates (longitude, latitude);
   (e) Correction -- removal of noise and normal scattering function from data;
   (f) Calibration, registration, and combining of individual data runs with overlapping coverage for image enhancement;
   (g) Production of topographic (reflectivity) profiles along doppler equator;
   (h) Removal of twofold ambiguity from reflectivity maps; and
   (i) Accurate determination of Mercury's spin axis.

Work on items (a) through (g) has been completed. We have now produced hardcopy of all images and profiles from 1974. The signal-to-noise ratio of data was noticeably enhanced when frames from an entire observation period were normalized, calibrated and averaged. The portion of each image immediately adjacent to the Doppler equator was removed due to its large specular reflection and poor spatial resolution, which significantly improved the contrast, and thus the detectability, of most features in the image. Work has been initiated on the following: the removal of twofold ambiguity from the reflectivity maps, and the determination of Mercury's spin axis (and hence exact longitudinal and latitudinal coordinates). On the basis of our preliminary calculations and our ability to match features on derived radar reflectivity maps with known geological features, the spin axis has already been determined surprisingly accurately at the level of the spatial resolution of the Mercury radar data.

(3) In collaboration with colleagues at the U.S. Geological Survey (4,5,6,7), and on the basis of analysis of available, newly-devised profiles and reflectivity maps, we have made the following determinations:

(a) Correlation between radar and geological features on the 1:5 million Mercury maps, H-6, H-7 and H-8, and on the 1:15 million map are generally quite good. Overlapping portions of Goldstone radar profiles and the one Arecibo radar profile which we managed to obtain agree well (8). On both radar reflectivity maps and profiles (from H-7 particularly) many curvilinear or linear features (scarps, troughs, runs), which are barely visible in Mariner 10 visual imagery, are clearly depicted.

(b) Systematic elevation and roughness differences (as indicated by the Hagfors C parameter) between major terranes are quite noticeable on Mercury, though smaller in magnitude than analogous differences on the Moon. Extensive mare-like smooth plains units are low in elevation; smooth plains around Caloris Basin are more than 2 km lower than adjacent material. A volcanic origin is inferred for the unit. Bright curvilinear features which appear on some of the smooth plains (Budh and Tir Planetia) may indicate the presence of subdued basins, perhaps buried by extensive volcanic deposits. Distinctive rim-like boundaries appear to enclose regions of smooth terrane.

(c) Craters, ridges and scarps along the radar track have distinctive signatures. Ridges and scarps reach heights of almost 1 km. Carter depth-to-diameter ratios appear to be much lower on Mercury than on the Moon; depth-to-diameter ratios are approximately 1:100 for the fresh basin Mozart (280 km diameter), the crater Titan (185 km diameter), and the crater Wang Meng (250 km diameter).

(d) Radar profiles of the unimaged region southwest of Caloris basin reveal high areas which may be structural rings, and a low area which may be another basin.

(e) It appears that early extensive surface heating of Mercury may be responsible for the relatively subdued topography of Mercury, due to extensive plastic deformation. There are indications of large, subdued double ring basins in many locations.

From these results we conclude that Earth-based radar data of Mercury are an important and effective tool for geological interpretation of this planet's superficial geology and tectonic history. Active collaboration by our interdisciplinary team will continue to provide more details on the nature and origin of Mercury's surface and the relationship between the surface of Mercury and the other terrestrial planets.

Work on additional Mercury radar data and the plethora of Venus radar ranging observations is being initiated now that a standardized, documented work set of data reduction and analysis software exists.

REFERENCES

(1) S. Zohar and R.M. Goldstein, 1974, Astron J, 79, pp. 85-91.

(2) R.F. Jurgens, 1980, personal communication from S. Zohar unpublished report of 1974.

(3) P.E. Clark, 1983, Lunar and Planetary Science XIV, pp. 119-120.

(4) P.E. Clark, G.G. Schaber, M.E. Strobell, R.F. Jurgens and G.S. Downs, 1983, Amer. Astron. Soc., 15, p. 838.

(5) M.E. Strobell, P.E. Strobell, G.G. Schaber and R.F. Jurgens, 1983, GSA Abstracts, 15, p. 700.

(6) P.E. Clark, M.E. Strobell, G.G. Schaber, R.F. Jurgens and G.S. Downs, 1984, in publication.

(7) P.E. Clark, M.E. Strobell, G.G. Schaber, R.F. Jurgens and G.S. Downs, Lunar and Planetary Science XV, pp. 166-167.

(8) D.E. Campbell, 1982, personal communication.

(9) P.E. Clark and R.F. Jurgens, 1984, Amer. Astron. Soc. (in press).

Correction and Geological Analysis of Lunar 3.8 cm Radar Data

P.E. Clark and T. W. Thompson (JPL)

Earth-based radar observations of the Moon have been taken at many wavelengths during the last ten years -- at 3.8 cm (1), 70 cm (2), and most recently, 7.5 cm (3). Radar returns have been collected in both polarized and depolarized form so that it is possible to derive both topographic and local surface roughness from the data.

Until recently, work with 3.8 cm radar data had consisted of qualitative correlation of photographic and thermal IR data (4) with individual depolarized radar data frames (local surface roughness) at different wavelengths (5,6,7). These studies provided results which demonstrated that the relationship between surface roughness (measured by either thermal emission or radar reflectivity) at different wavelengths can be used as an index of a crater's state of degradation (age). However, systematic studies of craters, or other local terrane features, as well as regional or global studies of major terranes (involving a number of data frames), cannot be done until individual frames are calibrated, geometric distortion is removed, and corrected frames are mosaicked.

At this point, a number of 3.8 cm radar frames have been calibrated and corrected for geometric distortion. Calibration was accomplished empirically by histogram fitting, because no instrument background data is available. Then data were corrected for geometric distortion by: (1) redetermining position of individual frames using most accurate recent lunar ephemerides; (2) reprojecting frames into simple cylindrical standard map projection; and (3) using most recent catalogue of lunar craters (8) to determine the exact positions of features identifiably on radar frames, and then correcting for apparent distortion (misplacement of features in frames) by resampling using a different bilinear interpolation derived for each of the parallelopideds of the set defined for each frame. A hardcopy set of corrected frames has now been produced. We are presently attempting to produce a mosaic of such corrected frames. The resulting mosaic will be used to show the systematic wavelengths in a region dominated by both mare and highland terrain. Global mosaics of appropriate lunar data (other radar data, thermal IR, and visual albedo data) have been obtained for correlation.

REFERENCES

(1) S.H. Zisk, G.H. Pettengill and G.W. Catuna, 1974, The Moon 10, pp. 17-50.

(2) T.W. Thompson, 1974, The Moon 10, pp. 51-85.

(3) T.W. Thompson, 1978, Icarus 36, pp. 174-188.

(4) R.W. Shorthill, 1973, The Moon 7, pp. 22-45.

REFERENCES (Cont.)

(5) S.H. Zisk, M.H. Carr, H. Masursky, R.W. Shorthill and T.W. Thompson, 1971, Science, 173, pp. 808-812.

(6) T.W. Thompson, H. Masursky, R.W. Shorthill, G.L. Tyler and S.H. Zisk, 1974, The Moon 10, pp. 87-117.

(7) S.H. Zisk, C.A. Hodges, H.J. Moore, R.W. Shorthill, T.W. Thompson, E.A. Whitaker and E.E. Wilhelms, 1977, The Moon 17, pp. 59-99.

(8) C.A. Wood, C.E. Anderson, D.W.G. Arthur, R.G. Strom and E.A. Whitaker, 1979, Catalogue of Lunar Craters, The Lunar Planetary Laboratory.

LANDFORM IDENTIFICATION ON RADAR IMAGES

Henry J. Moore, U.S. Geological Survey, Menlo Park, CA 94025
T. W. Thompson, Jet Propulsion Laboratory, Pasadena, CA 91109

Polarized radar echo images of the Moon acquired using 3.8 and 70 cm wavelengths (1, 2) are being examined to learn more about (a) the relationships between theoretical resolutions of the radars and the sizes of landforms that can be identified and (b) the factors that affect landform identification.

The radar images are interpreted and apparent landforms identified. These results are, then, compared with landforms portrayed on lunar maps and photographs. This comparison leads to the following classification of the radar portrayal of the lunar landforms: (1) resolved and clearly identified; (2) resolved and would probably be correctly identified; (3) resolved but interpretation uncertain; (4) detected, but elements not resolved; (5) not detected; (6) array of landforms resolved, but interpretation of array is ambiguous, and (7) fictitious. About 370 landforms portrayed by the 3.8 cm radar (resolution: 1-2 km) and 265 by the 70 cm radar (resolution: 10-20 km) have been classified in this way. Recent 70 cm radar images with a resolution of 2.5-5 km have not yet been examined.

A computer program sorts and orders the data, computes the fraction of each class in frequency bins of 100, and computes the geometric mean of the landform diameter for each frequency bin. Calculations are made in frequency steps of 10.

Preliminary results reveal the following: (a) the percentage of landforms that can be identified increases with increasing size, (b) the percentage of landforms that are detected tends to decrease with increasing size, (c) undetected, ambiguous and fictitious landforms occur at all sizes, (d) some landforms cannot be identified regardless of size, and (e) landform identification is strongly dependent on the theoretical radar resolution. Some results are shown in figures 1 and 2.

References

(1) Zisk, S. H., Pettengill, G. W., and Catuna, G. W., 1974, High-resolution radar maps of the lunar surface at 3.8-cm wavelength: The Moon, v.10, p. 17-50.

(2) Thompson, T. W., 1974, Atlas of lunar radar maps at 70 cm wavelength: The Moon, v.10, p. 51-85.

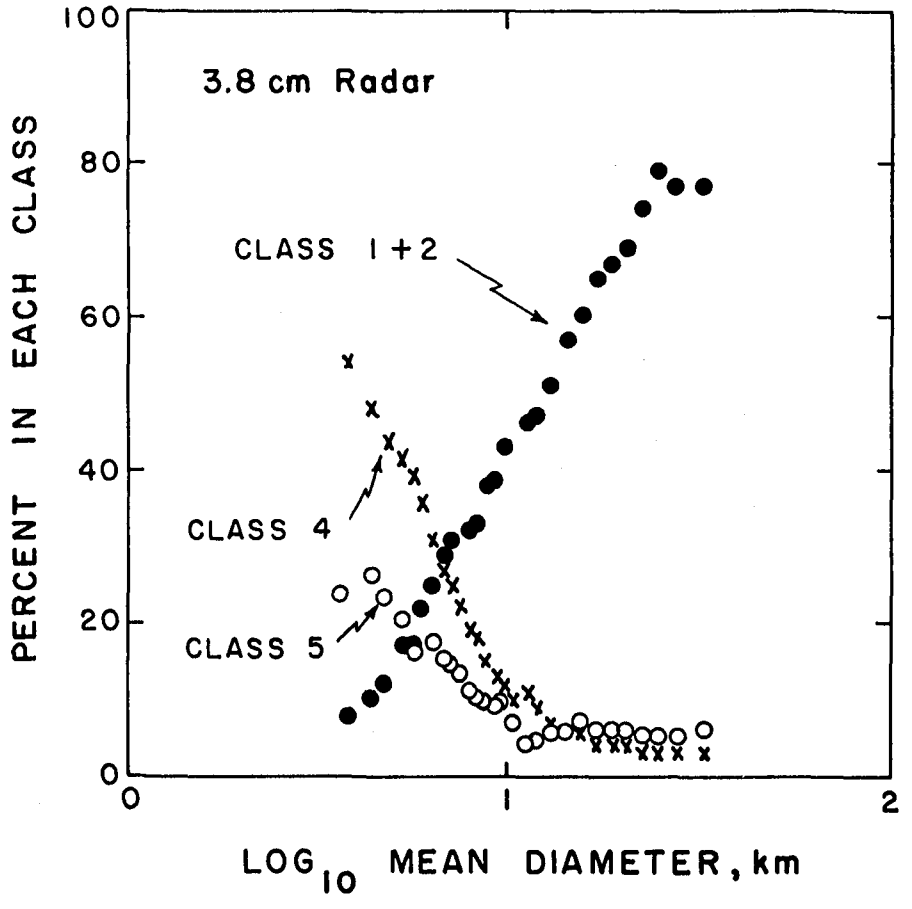

Figure 1. Percent of identified and probably correctly identified (class 1 + class 2), detected (class 4), and undetected (class 5) landforms portrayed and not portrayed by 3.8 cm radar images of the Moon. Note that about 77% of the landforms with diameters between 18 and 153 km (mean 32.4 km) and 8% of the landforms with diameters between 1 and 6 km (mean 3.8 km) would or probably would be correctly identified on the radar images.

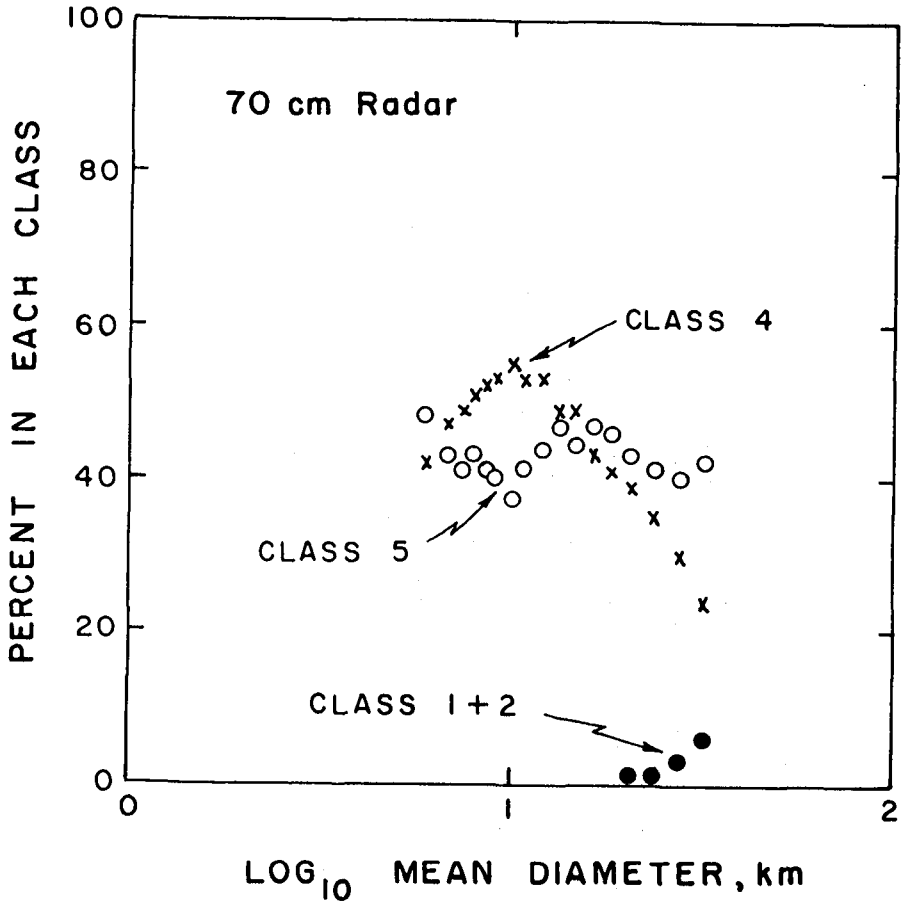

Figure 2. Percent of identified and probably correctly identified (class 1 + class 2), detected (class 4), and undetected (class 5) landforms portrayed and not portrayed by low resolution 70 cm radar images of the Moon. Note that about 6% of the landforms with diameters between 15 and 153 km (mean 31.6 km) would or probably would be correctly identified on the radar images. Landforms below 33 km could not be identified.

MARS RADAR CATALOG

Richard A. Simpson and G. Leonard Tyler
Center for Radar Astronomy, Stanford, CA 94305

Radar observations of Mars have been conducted since 1963 using four earth-based facilities: Goldstone Tracking Station (California), Arecibo Observatory (Puerto Rico), Haystack Observatory (Massachusetts), and the Canberra Deep Space Communication Complex (Australia). Wavelengths have ranged from about 3 to about 70 cm. Experiments have been conducted in ranging, spectral, and mixed modes. Results include topographic profiles, estimates of dielectric constant and meter-scale surface roughness, and qualitative determinations of centimeter-scale structure.

The data remain scattered but are generally in the possession of the investigators who acquired them. We have compiled a listing of these potentially accessible data sets and have constructed map overlays at 1:25M scale showing ground coverage through the 1982 observations. A summary is given in Table I.

The catalog data have been forwarded to the U.S. Geological Survey for possible publication as a special series of 1:25M scale maps. Investigators having immediate need of this information can request copies of the catalog and/or overlays from the authors.

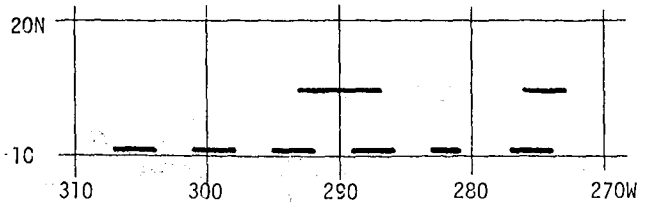

Fig. 1 -- Portion of overlay showing 1978 Arecibo coverage in the Syrtis Major area (reduced from original 1:25M scale).

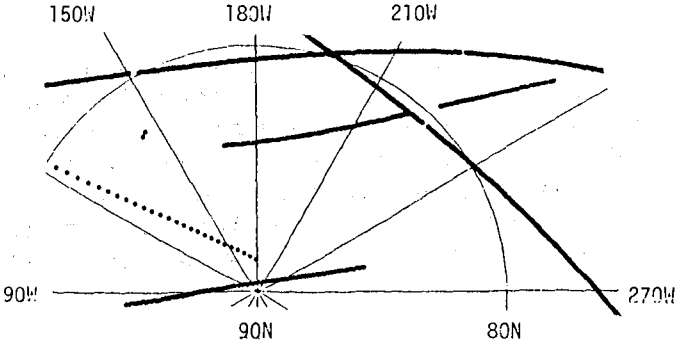

Fig. 2 -- Portion of overlay showing 1977-78 Viking bistatic radar coverage near Mars' north pole (reduced from original 1:25M scale).

TABLE I

Mars Radar Coverage

Opposition Year	Observatory	Wavelength (cm)	Coverage Type*
1963	Goldstone	12.6	1
1965	Arecibo	70.	1
1965	Goldstone	12.6	1
1967	Goldstone	12.6	2
1967	Haystack	3.8	2
1969	Goldstone	12.6	1
1969	Haystack	3.8	1
1971	Goldstone	12.6	3
1971	Haystack	12.6	1
1973	Arecibo	70.	3
1973	Goldstone	12.6	3
1975	Arecibo	12.6	3
1975	Arecibo	70.	2
1975	Goldstone	3.5, 12.6	2
1978	Arecibo	12.6	2
1978	Bistatic#	3.6, 13.1	3
1978	Goldstone	3.5	1
1980	Arecibo	12.6	2
1980	Goldstone	3.5, 12.6	1
1982	Arecibo	12.6	2
1982	Goldstone	12.6	2

Bistatic data were acquired at both the Goldstone Tracking Station (California) and the Canberra Deep Space Communication Complex (Australia).

* Ground coverage is known with the following levels of certainty:
Type 1: Only general area covered is known.
Type 2: Latitude is known, but not exact longitudes.
Type 3: Latitudes and longitudes are known.

STATISTICS OF AEOLIAN SURFACES ON MARS

Richard A. Simpson, Frank Webb, and G. Leonard Tyler
Center for Radar Astronomy, Stanford, CA 94305

Aeolian control of large-scale surface texture is apparent in orbiter images from selected regions of Mars -- the polar areas, equatorial canyons, and some craters. At other locations on Mars there is evidence suggesting aeolian control on meter scales within a context provided by larger landforms (Simpson **et al., Icarus, 49,** 258-283, 1982).

Quantitative descriptions of such surfaces can be obtained in a number of ways. Breed **et al. (J. Geophys. Res., 84,** 8183-8294, 1979) have examined Viking images and drawn conclusions using earth analogs; Thomas (**J. Geophys. Res., 87,** 9999-10008, 1982) has considered wind patterns. In both bases numerical estimates of dune dimensions have been obtained, but the analysis has been largely qualitative. Howard **et al.** (**Icarus, 50,** 245-258, 1982) and Davis and Soderblom (NASA TM-86246, 263-265, 1984) have developed photoclinometric techniques which give more quantitative descriptions of aeolian surfaces. All of these methods, however, use images and, as a result, the smallest textural components measured are on the order of 1 km. Radar scattering, on the other hand, is inherently a statistical tool. Roughness estimates usually apply to scattering areas of several hundred square kilometers, but the values represent an average over horizontal scales considerably smaller than those seen in images (a few centimeters to several tens of meters).

In the past few months we have begun a small effort to determine more accurately the roughness scales being sensed in bistatic radar scattering experiments conducted on Mars. Dune fields were the roughest of three major terrain types observed in the north polar region (see Fig. 1, Simpson and Tyler, NASA-TM 86246, 273-275, 1984). Roughness estimates of 5° rms were derived from the radar data. Comparable slopes have also been measured photoclinometrically from images in some areas (Breed **et al., J. Geophys. Res., 84,** 8183-8204, 1979). If both values apply to the same surfaces, then only kilometer scale texture is present; there can be no ripples on smaller scales -- otherwise the roughness measured by the radar would have been larger. The measurements, however, are very limited and one must exercise care in making these comparisons.

Our work to date has centered on identifying possible terrestrial analog dune fields and attempting to relate large- and small-scale texture. Slope estimates from (stereo-photogrammetric) digital elevation measurements provided by the U.S. Geological Survey in the Algodores Dunes near Yuma, AZ, were computed over horizontal scales in the range 50-100 m -- still large compared to the 0.13 m wavelength used in the Mars radar experiments. RMS roughness of a few degrees was found in directions parallel to the dune crests; perpendicular to the dune crests rms slopes were sometimes greater than 20°. Measurements at smaller horizontal scales are not available in the Algodones Dunes, and coverage elsewhere (even at 50-100 m sampling intervals) is still very limited. Schaber **et al.** (NASA TM 86246, 268-269, 1984) have obtained more closely spaced terrain samples in Death Valley, but these are only along one-dimensional profiles. Additional measurements of terrestrial aeolian features (on a wide range of scales) are being sought in hopes of better understanding scale-dependent phenomena on Mars through analog studies.

RADAR AND THE DETECTION OF LIQUID WATER ON MARS

L. E. Roth and R. S. Saunders, Jet Propulsion Laboratory, California Institute of Technology, Pasadena, California 91109.

Detection (1) of the seasonally variable radar reflectivity in the Goldstone Mars data (2) (the 'Solis Lacus radar anomaly'(1)) and the proposed interpretation in terms of the near-surface presence of liquid water (1) created a controversy in the planetary science community. Over the past year a number of investigators voiced, in private conversations, skepticism about the reality of the phenomenon of a seasonally variable radar reflectivity anywhere on Mars. To counter this skepticism we (again) discuss the necessary background information and we display the pertinent data in a format perhaps more convincing than that employed in the original presentation (1) of the discovery. We conclude with a summary of the results of our investigation and with recommendations for future work.

In the course of the 1971 and 1973 oppositions the Goldstone radar scanned Mars along (constant-latitude) tracks within the -14^{o} to -22^{o} lat. band. By coincidence, a few scans were taken along almost identical latitudes during both the 1971 and 1973 experiments. Detailed analysis (1) showed that there are significant differences between the two data sets, particularly in the general location of the Sinai Planum. The data exhibiting these differences are presented in Figs. 1(a) through (c). The graphs show smoothed radar reflectivity vs. longitude for pairs of scans along almost identical latitudes. The pairs are arranged in the order of the increasing difference ΔL_s, i.e. in the order of the increasing difference in areocentric solar longitude, L_s, of the two scans forming a pair. In this context, ΔL_s is a measure of the time interval separating the scans of each pair. It is seen that reflectivity in all three plots follows the same trend, viz., it is low in the S hemisphere spring (lower L_s), high in the S hemisphere summer (higher L_s). In Fig. 1(a) (1971/1973, $\Delta L_s = 15.80^{o}$) this trend is not pronounced or may even reverse itself. However, the data in Fig 1(c) (1971/1973, $\Delta L_s = 47.48^{o}$) leave no doubt and should convert the skeptics. In the area of Sinai Planum higher radar reflectivity has been recorded deeper into the S hemisphere summer. It is this phenomenon, the seasonally variable radar reflectivity over Sinai Planum, that was termed the Solis Lacus radar anomaly (1). The data in Fig. 1(b) (1973/1973, $\Delta L_s = 23.50^{o}$) are even more tantalizing since they hint at a possible reflectivity increase taking place during the same opposition. Unfortunately, the coverage is incomplete.

In our attempt (3,4) to interprete the Solis Lacus anomaly we have approximated the Martian surface with a stack of layers (dust, duricrust, thawed permafrost) resting on a half-space (frozen permafrost). The goal was to match the model reflectivities of various multi-layer configurations to the data in Fig. 1(c). It should be pointed out that the question of applicability of the idealized, planar models to the real-world geologic surfaces still remains unresolved (5,6). There is some evidence from both the passive- and active-microwave experiments (7,8,9,10) that the interference effects predicted by the planar models have been observed. This raises the possibilty that the planar models have at least a limited applicability to the bland topographies in which the dominant morphogenic processes have been the eolian/fluvial erosion/deposition.

Of all the multiple-layer models tested the one-layer models match (at λ12.6 cm) the data in Fig.1(c) with the greatest ease. The models with three and more layers cannot be made to match the data at all. The anticipated 'paradoxical situation...when each improvement in the model [i.e., inclusion of larger number of layers] will introduce additional ambiguities in the data interpretation' (4) has not been reached. One-layer models approximate the following situations: Thawing of permafrost under a layer of overburden (variable dielectric constant of the half-space) or redistribution of dust over a homogeneous half-space (variable depth of the layer). Removal or deposition of a uniform layer of dust, $\sim 1.x10^{-1}$ cm to $\sim 1.5x10^{-1}$ cm in depth, can arbitrarily closely mimic the data in Fig.1(c) (4). The Viking Landers observations (11,12,13) indicate that deposits of 'up to hundreds of micrometer' ($\sim 10^{-2}$ cm) might be associated with a global dust storm. The polar dust deposition rates have been estimated at $4.x10^{-2}$ cm/yr (14). In the absence of reliable data it is a matter of opinion whether the required rates of $\sim 10^{-1}$ cm/yr fall short of the estimated rates of $\sim 10^{-2}$ cm/yr. However, a more serious objection can be raised against the layered-surface model of the Solis Lacus anomaly. The 1971 data in Figs.1(a) and (c) were taken on 20 Sept 71 and 24 Sept 71, respectively. The 1973 data were taken on 10 Sept 73 and 6 Oct 73. The 1971 global dust storm started 22 Sept 71 (15). Thus there is one major dust-depositing event, the 1971 storm, between the two scans in each pair, Figs. 1(a),(c). It is reasonable to expect that a global storm would have associated with it a regionally uniform dust deposition rate and that this uniform rate would, in turn, produce deposits causing reflectivity changes uniform over the entire region. Figs.1(a) and (c) indicate that this is not so. Furthermore, between the times the scans in Fig. 1(b) were taken, 18 Aug 73 and 5 Oct 73, there has been no major storm reported; the 1973 global storm commenced 13 Oct 73. Yet there is a suggestion in the data (Fig. 1(b)) that reflectivity changes were about to take place. Thus it appears that the radar reflectivity variations observed over Sinai Planum had to be caused by a subsurface agent. Thawing of permafrost at very shallow depths (perhaps as shallow as 10 cm below the surface) is the only candidate. Eolian effects cannot be ruled out entirely, but their contribution was not decisive.

Conclusions: (a) In theory, both the liquid-water model (1) and the layered-surface model (3) are equally likely to account for the Sinus Lacus anomaly. The presently available Mars S-band radar data may not be sufficient to decide with finality in favor of either of the proposed interpretations. The circumstantial evidence, particularly the incomplete scans in Fig. 1(b), favor the liquid-water hypothesis. (b) Since the evidence is incomplete the results reported here do not make the case for a program of multi-frequency radar observations of Mars any less compelling. If the reflectivity at lower frequencies (S-,L-bands) displays the familiar seasonal pattern the planet behaves as a homogeneous half-space; liquid water is present. In the frequency interval from $\sim$2 GHz to $\sim$20 GHz the magnitude of the dielectric constant of liquid water drops from $\sim$80 to $\sim$3 (16), the same as that for many common rocks. If the reflectivity at shorter frequencies (S-,X-,K-bands) displays a seasonal pattern the planet behaves as a layered half-space; the reflectivity variations are due to redistribution of dust. (c) To test the validity of the multi-layer models for planetary surfaces in general it would be advisable to carry out scatterometer experiments over the variable-roughness testbeds on Earth.

Fig. 1
Light lines: 1971 data
Heavy lines: 1973 data
(a) 1971: -15.47° lat.
1973: -15.42°
(b) 1973: -15.75°
1973: -15.84°
(c) 1971: -15.93°
1973: -15.94°

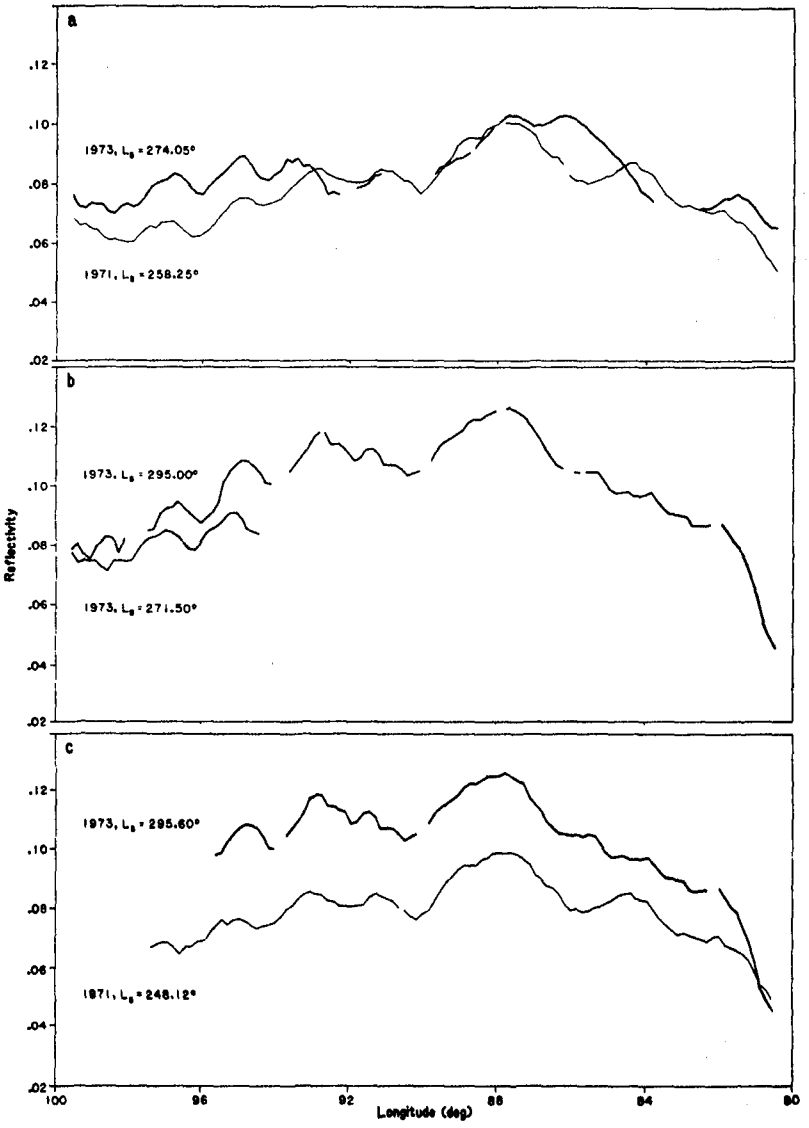

References: (1) Zisk, S. H., Mouginis-Mark, P. J. (1980). Nature 288, 735. (2) Downs, G. S., Reichley, P. E., Green, R. R. (1975). Icarus 26, 273. (3) Roth, L. E., Saunders, R. S., (1984). Lunar Planet. Sci. XV, 693. (4) Roth, L. E. (1984). NASA TM 86246, 274. (5) Zisk, S. H., Mouginis-Mark, P. J. (1981). Papers 3rd Int'l Colloq. Mars, 294. (6) England, A. W., Johnson, G. R. (1977). Geophysics 42, 514. (7) Blinn,J. C., Conel, J. E., Quade, J. G. (1972). J. Geophys. Res. 77, 4366. (8) anna,A. P., Waller, W. M., Strangway, D. W., Rossiter, J. R., Redman, J. D., Watts, R. D. (1975). Geophysiscs 40, 285. (9) Rossiter, J. R., Strangway, D. W., Annan, A. P., Watts, R. D., Redman, J. D. (1975). Geophysics 40, 299. (10) Sadeghi, A. M., Hancock, G. D., Waite, W. P., Scott, H. D., Rand, J. A. (1984). Water Resources Res. 20, 927. (11) Jones, K. L., Arvidson, R. E., Guinnes, E. A., Bragg, S. L., Wall, S. D. (1979). Science 204, 799. (12) Guinness, E. A., Leff, C. E., Arvidson, R. E., (1982). J. Geophys. Res. 87, 10051. (13) Arvidson, R. E., Guinness, E. A., Moore, H. J., Tilman, J., Wall, S. D. (1983). Science 222, 463. (14) Pollack, J. B., Colburn, D. S., Flasar, M., Kahn, R., Carlston, C. E., Pidek, D. (1979). J. Geophys. Res. 84, 2929. (15) Martin, L. J. (1974). Icarus 22, 175. (16) Hoekstra, P., Delaney, A. (1974). J. Geophys. Res. 79, 1699.

Intra-Eruption Geologic Map from an X-Band Radar Image During the May 18, 1980 Eruption of Mount St. Helens, Washington

Criswell, C.W. and Elston, W.E., Dept. of Geology, University of New Mexico, Albuquerque, NM 87131

The use of side-looking airborne radar images for geologic interpretations has increased with the Vesuvian exploration projects, both in the United States and USSR. Interpretation of images without ground truth relies on examples in terrestrial environments for which geologic data are available.

During the afternoon of May 18, 1980 the Oregon Army National Guard obtained several real-aperture, x-band radar images (1) of Mount St. Helens (MSH) and surrounding area, including the North Fork Toutle Valley (NFTV). Hours earlier MSH experienced major sector collapse resulting in a massive debris-avalanche (2) quickly followed by devastating lithic pyroclastic surges, flows and lahars (3, 4), pumiceous plinian tephra (5, 6) and ignimbrite-forming pyroclastic flows (7, 8). A high resolution image (Fig. 1) was obtained during the early-afternoon ignimbrite-forming eruptions at 1350 hrs PDT; mass flux of pyroclastic flows peaked about 1600 hrs PDT (4, 9). Although the image is small scale (1:500,000) 1 volcaniclastic and 2 pyroclastic stratigraphic units are resolvable and show distribution patterns that were covered by later ignimbrite deposits (dotted line of Fig. 2).

Figure 2 is an interpretive geologic map; emplacement times, signal return (S) and field (F) characteristics of deposits are described below. Pyroclastic-flow deposits are interpreted as having been emplaced as semi-fluidized, fragmental mixtures in which gases, possibly steam, acted as the continuous phase. Lithic pyroclastic deposits correlate with deposits of the directed blast (3, 4) and contain poorly-vesiculated, microcrystalline dacite of 62-63% SiO_2. Ignimbrite deposits correlate with tephra deposits (4, 5, 6) and contain pumiceous microlite-free dacite of 64-65% SiO_2. Dacites are porphyritic, with up to 35% phenocrysts of hornblende, hypersthene, lesser plagioclase and iron-titanium oxides, and rare augite (10).

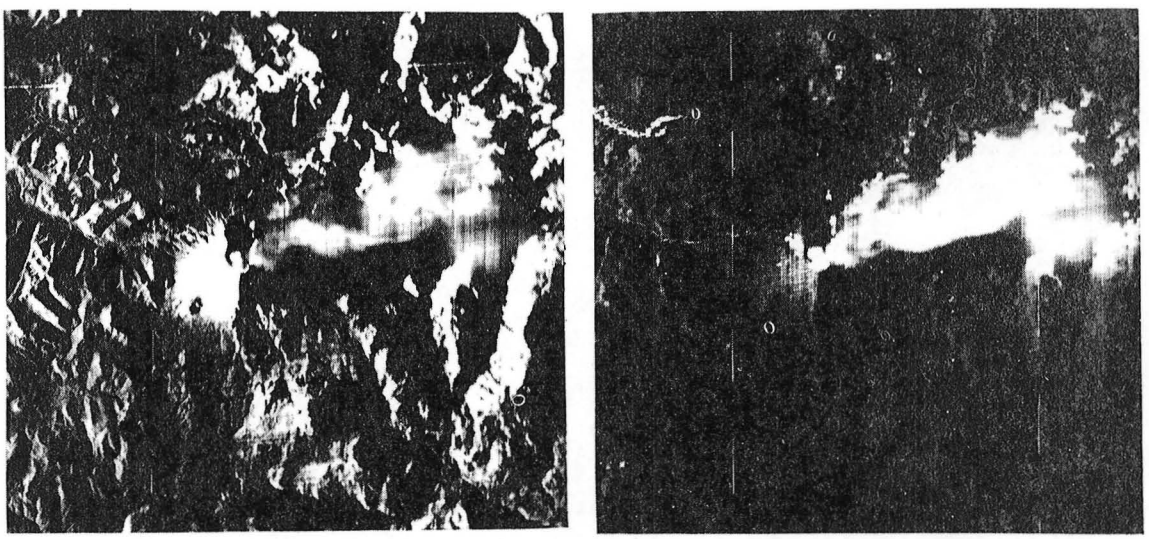

Figure 1. Fixed (left) and moving target (right) modes of real-aperture, x-band radar image of 1350 hrs PDT, May 18, 1980 (1). Ground resolution is about 1 m, data (film) storage about 10 m. Distance between dashed lines is 20 km.

P LOWER IGNIMBRITE DEPOSITS (1217 to image time 1350 hrs PDT)
S: moderately strong, diffuse reflector with longitudinal ridges and lobate outline form; m-moving pyroclastic flows.
F: sequence of unconsolidated deposits of graded pumiceous lapilli and lesser blocks in a poorly sorted pumiceous ash matrix; reversely graded pumice clasts <25 cm and normally graded accessory lithic fragments <15 cm, most <5 cm. Surfaces of pumice lapilli and rare blocks in low relief (<<1 m) longitudinal and transverse ridges, locally grading to small flow lobes (<1 m high, 1-2 m wide and <10 m long) of fines-poor pumice clasts. Exposed in deep gullys of Spirit Lake pumping outlet channel along the former course of the North Fork Toutle river.

L LITHIC PYROCLASTIC-FLOW DEPOSITS (0833 to 0842 hrs PDT)
S: dark, nearly specular reflector; grades to isolated specular reflectors with concave and convex margins (w).
F: composite stratigraphic unit of (i) unconsolidated deposits of normally graded lapilli- to block-sized clasts of lithic dacite, accessory fragments and incipiently charred wood in a poorly sorted non-pumiceous ash matrix; accessory fragments originated in the reducing provenance of the MSH hydrothermal system; upper portions are ash and fine ash, locally cross-bedded and locally containing accretionary lapilli; surfaces are relatively smooth and flat with local transverse ridges (1-2 m amplitudes and 5-10 m wavelengths); widely exposed in the NFTV; and (ii) pyroclastic lahar deposits (w) of non-graded, lithic dacite blocks supported by a slightly indurated, poorly sorted matrix with abundant fine sand and "open-work" vesicle textures, indicating water saturation; surfaces are block strewn with local fluvial channels and reworked, clay-rich deposits; locally exposed and associated with phreatic explosion craters and stratified ejecta deposits.

D DEBRIS-AVALANCHE DEPOSITS (0832-0833 hrs PDT)
S: mottled, variable-strength, generally weak diffuse reflector dominating NFTV.
F: unconsolidated deposits of poorly sorted, partly hydrothermally altered volcaniclastic cobbles and blocks in a silty sand matrix; blocks in map area locally >100 m, preserve original volcanic stratigraphy; further down valley, smaller blocks are lithologically mixed; surfaces are extremely irregular and hummocky with non-integrated drainage. Relief is typically 20-30 m, locally >50 m in north-central map area. h-locations and relative sizes of hummocks on image, locally field checked.

F Floating logs on Spirit Lake: diffuse reflector.

C Crater wall: saturated return.

R/S Ridges and slopes of pre-eruption rocks, some slopes have thin mantle of blast deposits: facing ridges saturated return.

N No signal return: ridges facing away from aircraft.

REFERENCES: (1) Rosenfeld, 1980, Am. Sci., 68, 5, p.494 (2) Voight et al., 1981, USGS PP 1250, p.347 (3) Hoblitt et al., ibid, p.401 (4) Criswell et al., in prep. (5) Sarna-Wojcicki et al., 1981, USGS PP 1250, p.577 (6) Waitt and Dzurisin, ibid, p.601 (7) Rowley et al., ibid, p.489 (8) Criswell and Elston, 1982, NASA TM 85127, p.143 (9) Criswell and Elston, 1983, NASA TM 86246, p.125 (10) Kuntz et al., 1981, USGS PP 1250, p.525.

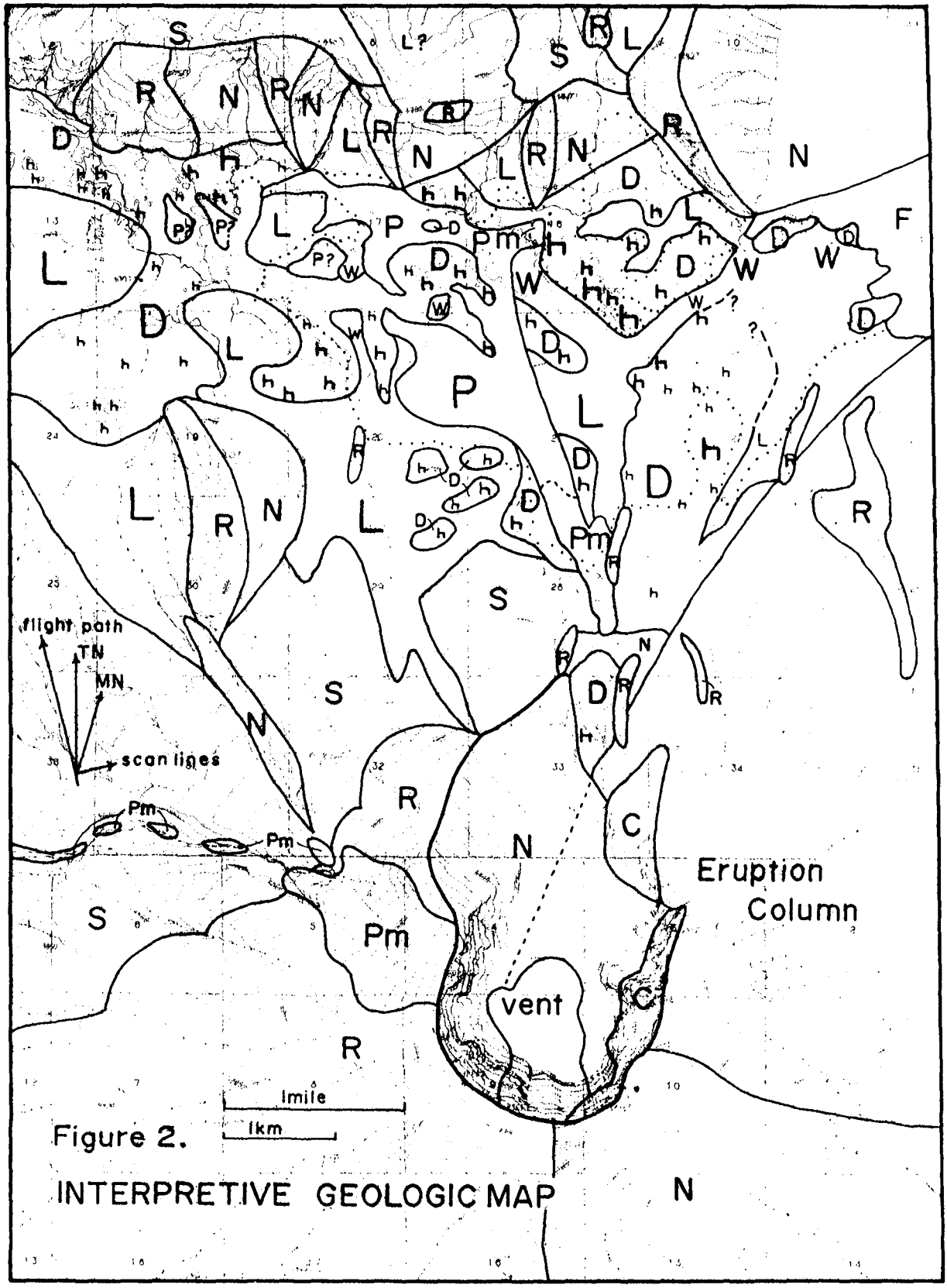

Figure 2.

INTERPRETIVE GEOLOGIC MAP

RADAR OBSERVATIONS OF FISSURE-FED BASALTIC LAVA FLOWS, CRATERS OF THE MOON, IDAHO

L. MARTEL and R. GREELEY
Department of Geology, Arizona State University, Tempe, Arizona, 85287

Changes in surface roughness of lava flows, estimated from dual polarization, synthetic aperture, X and L band side-looking airborne radar images, were tested as a means of locating fissure vent areas. If lava textures progress from smooth, near-vent shelly pahoehoe to hummocky pahoehoe to aa with distance from fissure vents, then radar images of the lava flows would show a progression from dark to brighter tones due to the flows' increasing radar back-scatter. Flows chosen for this study, in the Craters of the Moon lava field, were erupted from fissure vents along the Great Rift of Idaho. The resolution cells (azimuth x range) of the X band and L band images are 15 x 15 m and 30 x 10 m, respectively.

Some, but not all, smooth pahoehoe flows, which have dark tones in the radar images, are adjacent to fissure vents. Therefore, their dark image tones are not diagnostic of proximity to a vent.

Tonal changes within a flow are not easily identified in the radar images. Rather, changes in tone correspond to contacts between flows. The complex stratigraphy of the lava field and the resolution limits of the radar systems hinder the tracing of textural changes along the lengths of flows and the locating of fissure vent areas.

Fissure vent areas are detected on X band images because spatter ramparts bordering the vents appear as bright lines. Spatter ramparts are not detectable in L band images at the resolution used in this study.

LATE TERTIARY AND QUATERNARY RIVER SYSTEMS OF THE EASTERN SAHARA AS MAPPED ON SHUTTLE RADAR AND LANDSAT IMAGES

John F. McCauley, Carol S. Breed, and Gerald G. Schaber; U.S. Geological Survey, 2255 No. Gemini, Dr., Flagstaff, AZ 86001

SIR-A pictures of the Eastern Sahara show segments of what are interpreted as relics of once major Tertiary and Quaternary stream valleys. These previously unmapped features have a dark to very dark radar response and are generally concealed below a thin cover of flat to slightly undulating deposits, mostly of eolian origin. In most of the 150 pits and trenches we have studied to date, unconsolidated surface deposits range from a few centimeters to about a meter thick. The SIR-A system was able to "see through" this loose, dry material, to a depth of about a meter or two.

Aggradation of the valleys and eolian modification of the divides make recognition of the former fluvial imprint in this region very difficult. Many previous workers had suspected the presence of large stream systems, evidenced by scattered lag patches of gravels and cobbles. Attempts to reconstruct drainages around the Gilf Kebir Plateau using Landsat data led to the recognition of the south-flowing Wadi Eight Bells drainage system that emanates from the Gilf and then disappears beneath the active sand cover of the surrounding pediplane. Other discoveries of desert channels have been made in Libya by various workers primarily using geophysical methods.

The 50-km-wide SIR-A radar swath across Sudan and Egypt reveals three basic types of riverine patterns. The first type consists of broad, dark, sinuous features, 10 to 30 km wide and hundreds of kilometers long, with very poorly expressed broad, open, stubby tributary systems. Though only very vaguely expressed on Landsat in south-central Egypt, these "radar valleys" can be connected with segments of valley systems evident on Landsat in northwestern Sudan. They are interpreted as alluvial valleys, comparable in size to the Nile Valley, incised into the regional bedrock surface during late Tertiary(?) time. The second type is generally of very dark radar reflectivity, long but narrow (30 to 40 km long and 1-3 km wide) and locally controlled by underlying structure. These well-defined channels are underfit with respect to the major alluvial valleys into which they appear to discharge or to fan upon. Some of these channels are expressed on Landsat and at least one contains non-diagnostic rolled artifacts in a 1-m-deep gravel lens. These channels are considered to be generally younger than the great alluvial valleys and probably were rejuvenated from time to time during the Quaternary pluvials that affected the Eastern Sahara. The third type of riverine pattern consists of groups of narrow (1/2-2 km wide), anastamosing, radar-dark to very dark channels that separate islands of intermediate radar response within the large valleys. The islands are thinly veneered with sand sheets and are composed of consolidated alluvium with well-developed petrocalcic layers in the upper few meters. Abundant rhizoliths of reed-like plants occur, many of which are still upright and project above the present deflated kunkur surface. The channel and island complexes, such as those near Bir Safsaf, have little or no surface expression and appear to be confined to the broadest and least defined reaches of the large valleys. Geoarchaeologic evidence indicates that stream flow in these anastomosing channels is post-late Pleistocene (post-Acheulean) in age.

Field investigations of the radar swaths in south central Egypt and north central Sudan (the region around Egyptian Petroleum Company Water Well #1 Uweinat East and Bir Safsaf) confirm the presence of clay-poor desertic alluvial sediment at depths of several meters in the large valleys. Deposits consist of fine, well-sorted, poorly bedded, quartzitic gravels generally overlying but also interbedded with white, clean fluvial sands. Current bedding is not well developed but unambiguous cut-and-fill structure is present locally. Calichification is extensive in the alluvial deposits except where the calcic horizon is incised by the radar-dark anastomosing channels, which contain loose graveliferous sands, rolled caliche fragments and rhizoliths from the surrounding islands (see Schaber et al., this volume). Acheulean handaxes, found in calichified overbank deposits on discontinuous bedrock terraces marginal to the large alluvial valleys, are useful new indices to events in the Western Desert. Their setting indicates that the valleys were cut into bedrock and then aggraded prior to late Pleistocene Acheulean occupation of the river banks and terraces. Overbank flooding in the valleys occurred during or after Acheulean time, when the artifacts were buried in deposits of pea gravel and sand that were later extensively calichified.

Recent field work was concentrated within the radar swath in order to better define specific radar responses, but was extended in a reconnaissance mode outside the area of radar coverage in order to trace individual fluvial features. Mapping of major valleys, divides and terraces identified on SIR-A pictures was extended to contiguous areas on Landsat RBV and MSS frames centered about lat 23°30'N. long 29°00'E. The map of reconstructed drainage patterns shows several major but ill-defined, southwest-trending alluvial valleys. The depressions at Bir Terfawi and Terfawi West appear to be remnants of aggraded alluvial valleys that were once tributary to a south-flowing drainage network that discharged into larger valleys in and near the Sudanese border. Reentrant trends along the western edge of the Limestone Plateau in Egypt are consistent with the presence of now-defunct westward flowing streams, the higher order trunks of which we may be seeing on the SIR-A swath. The post-Acheulean anastomosing channels that are inset into the valley south of Safsaf oasis may trend to the northeast, suggesting drainage reversals during late Quaternary time. Although most constituents in the alluvial samples studied so far can be explained as derivatives of the Nubia Sandstone, systematic petrologic studies of shallow alluvium from our early hand-dug pits show that golden biotite occurs consistently in the fine size fraction, either as a trace or in amounts as much as 1%, in "radar valleys" far to the southwest in north-central Sudan. A saprolitic, migmatized biotite schist discovered in one of our backhoe trenches at Bir Safsaf could be the source area. Further evidences of east-to-west fluvial transport in south-central Egypt are scattered cobbles of silicified Garra and Kurkur Limestones along with pebbles and scattered artifacts of Eocene fossiliferous chert near the Sudanese border, about 150 km southwest of the nearest outcrops. Until recent more extensive coverage of the Eastern Sahara by SIR-B is analyzed, regional drainage directions of Tertiary to Holocene age remain uncertain.

The discovery of these extensive networks of large, partly or completely buried river valleys in the hyperarid Eastern Sahara now prompt comparisons of these features to the channels of Mars, particularly those of the Mangala Valles system. Many similarities of pattern and scale

exist. It is probable that the rivers on both planets were mainly exogenous on the basis of their lack of well-developed, orderly tributary systems. Both show a high degree of structural control, have discontinuous terraces, and are frequently deranged by later fluvial pulses. Both also have smaller underfit channels locally superposed on their floodplains. Recent geologic mapping of Mars reveals segments of what appear to be relict drainage systems (near long 40°, lat 30° N. and long 185°, lat 40° N.) that have been dismembered by later blanketing materials. The Saharan channels are now masked over much of their extent by an eolian veneer of tabular sand sheets that began forming with the onset of aridity in the early Pleistocene. Such common characteristics suggest that these terrestrial and Martian drainages have had somewhat similar origins and histories. In the last 3 X 10^6 years the Eastern Sahara has undergone progressive dessication punctuated by generally more feeble pluvial episodes. A similar pattern of climatic fluctuation over a 3 X 10^8 time scale has been inferred for Mars.

ANALYSES OF RADAR IMAGES OF SMALL CRATERS

R. GREELEY, P.R. CHRISTENSEN, and J.F. McHONE
Department of Geology, Arizona State University, Tempe, AZ, 85287

Spacecraft exploration of the Solar System frequently involves the return of images. Clouds hide the surface of Venus from all but radar imaging systems, supplemented by limited views from land spacecraft. Among the surfaces features likely to be observed by radar are craters that have formed by a variety of processes. In order to assess the radar characteristics of craters, this report describes volcanic craters and impact structures on Earth imaged by the Shuttle Imaging Radar (SIR-A) experiment. Although most of the craters are small, this analysis provides insight into the ability to discriminate craters of various origins and provides some basis for interpreting radar images returned from Venus.

Four sites were analyzed: (a) a volcanic-aeolian terrain in northern Mexico (Pinacate), which includes 9 volcanic craters; (b) a caldera on Cerro Volcan Quemadeo, a silicic shield volcano in the Andes of Bolivia; (c) Talemzane impact crater, Algeria; and (d) Al Umchaimin, a possible impact structure in Iraq.

Definitive identification of impact craters using remote sensing is, at best, difficult. As assessed from aerial photographs, fresh impact craters tend to: (1) be circular in plan-form, (2) have rims that are raised above surrounding surfaces and that may be composed of overturned strata, 3) have floors lower than the surrounding surface, and 4) have fields of blocky ejecta and possibly secondary craters extending outward from the crater rim. Many of these criteria can be evaluated on radar images, although there are some important differences when compared with conventional images. Radar images are typically of lower resolution and features such as overturned strata may not be visible; blocky ejecta, however, may be enhanced on a radar image due to backscattering.

Impact craters tend to be more circular in plan-form than other craters. Murray and Guest (1970) and Oberbeck et al. (1972) reviewed various methods to determine circularities and applied the results to planetary features; these techniques may be important in analyzing radar images of Venus. To assess the potential for deriving circularity values from radar images, circularities were determined from both conventional and radar images for the craters studied here, using the equation

$$C = 1 + \frac{\sum_{i=1}^{N} | \bar{r} - r_i |}{N \bar{r}}$$

where C = circularity, r_i is the dimension of the ith crater radius measured from crater rim to crater center, and N is the number of measurements. Thus, for a perfectly circular crater, C = 1.0; with decreasing circularity, the value of C increases. We found that the radar values are within 5% of the values derived from conventional photographs, and we conclude that the

circularity of craters derived from radar images should be as valid as those derived from conventional photographs.

Of the various non-impact craters, maars are most likely to be confused with impact structures. Because both maars and impact craters result from violent point-source releases of energy, the geometries of both are nearly the same. However, in the Pinacate field all of the maar craters involved multiple eruptions which led to asymmetries in plan-form. Many of the maar craters at Pinacate (and other types of volcanic craters elsewhere) have wall sections that are nearly vertical. Steep wall segments are visible as radar shadows on some of the craters, such as Crater Grande and Elegante, but the ability to detect steep walls on radar is a function of viewing geometry, incidence angle of the radar beam, and reflectivity of wall material. Many Pinacate maar craters display radar-dark floors with central bright spots; in one case, Moon Crater, this bright spot results from the presence of a spatter cone which could be misinterpreted as a central peak typical of impact craters. In most cases, the central bright spots correspond to playa deposits and vegetation which evidently are excellent radar-reflective surfaces.

In general, it does not appear possible to distinguish the elevation of the crater rim and floor in relation to the surrounding plain using SIR-A images. Thus, important geometric criteria for the identification of impact craters cannot be used, at least in non-quantitative analyses of radar images. The rim crests and outer flanks of the impact structures and several of the volcanic craters are radar-bright because of blocks. The blocks range in size from tens of centimeters to larger than 2 m across; both the block size and the frequency decrease with radial distance from the rim. On radar images, the brightness also decreases from intense at the rim crest to mottled with radial distance. Some of the craters, however, have been weathered and eroded (e.g., Al Umchaimin) or mantled by younger deposits (e.g., Moon Crater) and do not show this radar pattern. In other cases, (e.g., Elegante), the flank is radar-bright mottled, not from blocks, but from erosional gullies that serve as radar-scatterers. Thus it would be very difficult to separate impact craters from certain volcanic craters solely on patterns of radar brightness on crater flanks, especially if the surface had been weathered and eroded or partly mantled.

REFERENCES

Murray, J.B. and J.E. Guest, 1970, Circularities of craters and related structures on Earth and Moon, Modern Geology, 1, 149-159.

Oberbeck, V.R., M. Aoyagi, and J.B. Murray, 1972, Circularity of martian craters, Modern Geology, 3, 195-199.

Page intentionally left blank

CHAPTER 14

STRUCTURE, TECTONICS AND STRATIGRAPHY

Page intentionally left blank

MECHANISMS OF BASALT-PLAINS RIDGE FORMATION

Thomas R. Watters and Ted A. Maxwell, Center for Earth & Planetary Studies, National Air & Space Museum, Smithsonian Institution, Washington, D.C.

Ridges are morphologically unique features that have been observed on all the terrestrial planets including Venus (observed in radar images by Venera radar mapping satellites). The common denominator in the occurrence of these ridges is that they are found on the relatively smooth-plains basalt or basalt-like units. The morphologic similarity between ridges on the Moon, Mercury, Mars and the Earth is striking, but the mechanical origin is a matter of speculation. In order to examine the phenomenon of folding of flood basalt layers, we are examining the morphology of the ridges in detail, and plan future investigations to determine their fold geometry. The consistent occurrence of ridges on mare basalts on the Moon and basalt-like units on Mercury and Mars has led to many attempts to locate terrestrial analogs to these ridges. Bryan (1973) and Hodges (1973) described small-scale ridges formed by buckling of the crust on terrestrial lava lakes and proposed these as analogs. Greeley and Spudis (1977) first suggested that the best terrestrial analogs for the ridges on the Moon, Mercury and Mars might occur on the western Columbia Plateau. The Columbia Plateau represents one of the largest flood basalt regions in the world, with a total areal extent on the order of 2×10^5 km^2. The plateau ridges are sinuous, with an overall E-W trend (figure 1). Most of these ridges abut against the Cascade Range to the west of the plateau. Like the ridges on the volcanic plains of the Tharsis region of Mars, ridges on the Columbia Plateau are roughly parallel trending and somewhat regularly spaced (figure 1). The similarities between the mean dimensions of the ridges on the Earth and Moon and basalt-like units on Mercury and Mars, suggest that these ridges represent a phenomenon unique to basaltic-plains deformation. Perhaps the clearest insight into the structural nature of basalt-plains ridges may be obtained by studying the Columbia Plateau ridges. In one of the earliest geologic studies of the region, Smith (1903) described five ridges, as observed in cross-section at water gaps, as anticlinal structures. The only evidence for faulting was observed in the displacement on the plain between two basalt sheets. Waters (1955) expanded Smith's study area eastward and confirmed his conclusions that the ridges were anticlines and not the result of block faulting. Waters suggested that the anticlines had developed in a single period of deformation rather than two orogenic episodes separated by a period of peneplanation as proposed by Smith (1903). Swanson (1967) studied the Yakima basalt in the Tieton River area and described five nearly E-W trending folds. He concluded that these folds fit into the regional structural pattern of the Columbia Plateau described by Waters (1955), just east of his study area. Bentley (1977) noted that the basalt units of the plateau were folded as well as faulted into anticlinal ridges. He concluded the ridges were drape folds generated by vertical movement of basement blocks on high angle reverse faults.

In a recent study of the Umtanum ridge on the Columbia Plateau, Price (1982) proposed a mechanical model for the formation of the anticlinal ridges which suggests that the reverse faults associated with the ridges formed after the development of the folds. In his model, deformation goes from folding to faulting after the folds begin to "lock up". The suggestion by Price (1982) that faulting is confined to the basalt sequence is supported by geophysical data from Mitchell and Bergstrom (1983). They conclude that with the present data there is no dominant structural trend in the basement that corresponds to the dominant surface structure. They suggest a regional change in deformational character between the development of the pre-Columbia River basalt group structures and the formation of the anticlinal ridges. Studies on the origin of the N-S compression responsible for the formation of the ridges support models which predict a clockwise rotation through localized dextral shear of a closely spaced N-NW trending shear system as opposed to rotation of a rigid block or

microplate (Reidel et al., 1984). Reidel (1984) has proposed a similar mechanism to the model of Price (1982) for the development of the anticlinal ridges. Independent of the origin of compressional stresses, observations of the structure of the ridges on the Columbia plateau suggest the possibility that both folding and thrust faulting play a role in the formation of the ridges on Mars as well as the Moon and Mercury.

The morphologic similarities between the Columbia Plateau ridges and ridges on the Moon, Mercury and Mars form a strong basis for the interpretation of basalt-plains ridges as compressional folds. The basalt-plains ridges appear to have formed on competent flood basalt units deformed at the surface with essentially no confining pressure. Estimates of compressive strain for planetary ridges range from a few tenths of a percent on the Moon (Maxwell et al., 1975) to up to. 0.4% on Mars (current studies), to as high as 35% for Columbia Plateau folds with associated thrust faults (Reidel, 1984). Such values have strong implications for both deformational mechanisms as well as for the source of stress. Deformational mechanisms that will attempt to account for the morphology, fold geometry, possible associated thrust faulting and regular spacing of the basalt-plains ridges on the terrestrial planets are under investigation.

References

Bentley, R.D., 1977, Geol. Soc. of Am. p. 339-389

Bryan, W.B., 1973, Geochim et Cosmochim. Acta suppl. 4, p. 93-106.

Greeley, R., and Spudis, P.D., 1978, Lunar and Planetary Science IX, p. 411-412.

Hodges, C.A., 1973, NASA Special Publication 330, p. 31-1—31-21.

Mitchell, T.H., and Bergstrom, K.A., 1983, Rep. RHO-BW-ST-19P: Rockwell Hanford Operations, Richland, WA, p. 4-1—4-18

Maxwell, T.A., El-Baz, F., and Ward, S.W., 1975, Geol Soc. of Am. Bull., v. 86, p. 1273-1278.

Price, E.H., 1982, Rep. RHO-BWI-SA-138, Rockwell Hanford Operations, Richland, Washington.

Reidel, P.S., 1984, American Journal of Science (in press).

Reidel, P.S., Scott, G.R., Bazard, D.R., Cross, R.W., and Dick, B., 1984, Tectonics, AGU, v. 3 p 251-273,

Smith, G.O., 1903, Journal of Geology, v.11, p. 166-177.

Swanson, D.A., 1967, Geol. Soc. of Am. Bull., v. 78. p. 1077-1110.

Waters, A.C., 1955, Geol. Soc. of Am. Bull. v. 66, p. 663-624.

A

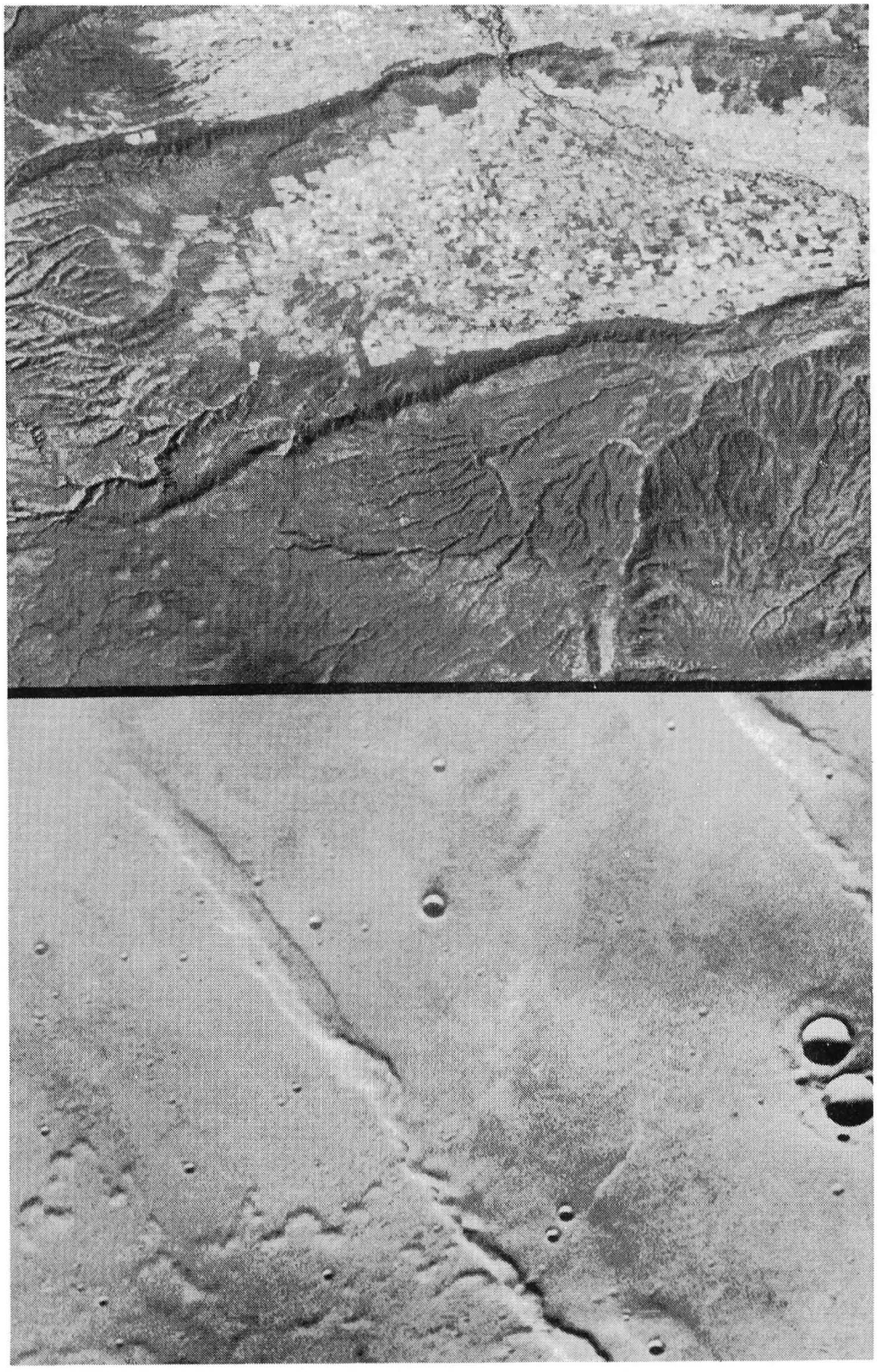

B

Figure 1. SW Columbia Plateau, Earth (A) and SE Tharsis Plateau, Mars (B). Images are at the same approximate resolution (160 m). Scale: 1 cm = 8.6 km. Images processed at C.E.P.S. using ELAS image processing software.

TERRESTRIAL ANALOGS FOR PLANETARY WRINKLE RIDGES J.B. Plescia[1] and M. Golomobek[2]. [1] U.S.Geological Survey, Flagstaff, AZ 86001, [2] Jet Propulsion Laboratory, Pasadena, CA 91109.

Wrinkle ridges are common physiographic features on the terrestrial planets. Their origin has remained enigmatic, although two different types of models, volcanic and tectonic, have been proposed. The major impediment to deciphering the origin of wrinkle ridges has been the lack of a terrestrial analog. We note here seven terrestrial analogs and describe two in detail. We then discuss their implications for the origin for planetary wrinkle ridges. All of the terrestrial analogs formed in compressional environments and are the surface breaks of thrust faults.

The volcanic models suggest uplift over linear laccoliths (1); constructional features built by extrusion of viscous lavas along fissures (2,3); and the intrusion and extrusion of lava associated with buckling of a solid crust over liquid magma (4). The tectonic models include draping of surficial deposits over bedrock topographic highs (5,6); folding (7); strike-slip faulting (8,9); vertical tectonism (10); and thrust faulting (11,12,13).

On the terrestrial planets, wrinkle ridges occur primarily on plains units, although they are known to extend into ancient highlands as well. Morphologically, the ridges occur as either 1) long, linear to sinuous, broad topographic highs that may branch and rejoin along strike; or 2) circular topographic highs (1). Both forms may have a few hundred meters of relief and profiles that are commonly asymmetric, with slopes of less than 10^{0} (14).

On Earth, features that are morphologically similiar to planetary wrinkle ridges occur along thrust faults. Known examples include features formed during 1) the 1931 Hawkes Bay earthquakes in northern New Zealand (15); 2) the 1968 Meckering earthquake in Western Australia (16,17); 3) the 1969 Pariahuanca earthquakes in central Peru (18); 4) the 1978 Tabas-e-Golshan earthquake in east-central Iran (19); and 5) the 1980 El Asnam earthquake in northern Algeria (20,21,22,23). Structures similar to wrinkle ridges have also developed on the Abalone Cove landslide in Palos Verdes Hills of California and in the basalts of the Columbia Plateau (24). Two of these examples, the Meckering earthquake and the Abalone Cove landslide, are described below.

The 1968 Meckering earthquake produced a 37-km-long fault scarp (16,17) morphologically similar to a wrinkle ridge (Figure 1, from 17). The scarp formed in layers, 1-60 m thick, of sandy lateritic soil and sand overlying granitic bedrock. The surface layers were deformed into asymmetric compressional anticlines 1-2 m high and tens of meters wide; the steeper sides have fault breaks at their bases. Behind and parallel to the anticline, a series of tension cracks were formed. Along strike, the fault break is discontinuous and is offset up to 2.4 km by zones of lateral shearing that exhibit either a single fault break or en echelon fractures. The surface dip of the fault is shallow and reverses along strike; each section of opposing dip direction is connected by lateral shear zones.

Within the Abalone Cove landslide, a paved paddle tennis court has been compressed above the toe of the landslide. A series of thrust faults has produced surface features similar to wrinkle ridges (Figure 2). The faults have reverse and strike-slip displacements. The pavement is deformed into a series of asymmetric anticlinal ridges with faults that surface at the base of the steeper sides. Tension gashes occur behind the anticlines. The near-surface vergence of the fault reverses along the ridges and each section is

separated from the next by a shear zone.

The morphologic details of the anticlinal ridges at Meckering depend upon the strength and thickness of the surface material. Three forms were produced: unfaulted anticlinal ridges, asymmetric anticlines broken by a fault, and reverse faults. In areas of thick, competent soil, anticlinal ridges formed, whereas in areas of thin, incompetent soil, simple breaks developed. At the paddle tennis court, only pavement was involved, hence the morphology is similar throughout. Experimental studies (25) have shown that compressing loose sand produces features similar to wrinkle ridges. The different competencies of the units involved in the terrestrial examples indicate that wrinkle ridges can form in varied materials. Caution should be exercised when interpreting the lithology of a planetary unit based solely on the presence of wrinkle ridges.

These examples illustrate that thrust faults reaching the surface can deform the surface layers into structures identical to wrinkle ridges. Morphologic features common to both the terrestrial analogs and planetary ridges are: 1) linear to sinuous features with asymmetric profiles, 2) reversals in the sense of asymmetry and fault vergence along strike, and 3) en echelon, overlapping, steep-sided lobes. In addition, both planetary and terrestrial examples occur in compressional environments. These morphologic similarities suggest that planetary wrinkle ridges have an origin similar to the examples on Earth, that is, they are tectonic features formed by thrust faulting.

REFERENCES: (1) Strom, R., 1972, The Moon, I.A.U. Symp. 47, 187-215. (2) Quaide, W., 1965, Icarus, 4, 374-389. (3) Baldwin, R., 1963, The Measure of the Moon, Univ. Chicago Press. (4) Hodges, C., 1973, Apollo 17 Pre. Sci. Rept. NASA SP-330, 31/12-31/21. (5) Phillips, R., and Maxwell, T., 1978, Lunar Planet. Sci. Conf. Abs. 9, 890-892. (6) Sharpton, V., and Head, J., 1982, J. Geophys. Res., 87, 10983-10998. (7) Muehlberger, W.R., 1974, Proc. Lunar Planet. Sci. Conf. 5, 101-110. (8) Tija, H., 1970, Geol. Soc. Amer. Bull., 81, 3095-3100. (9) Tija, H., 1976, Earth Planet. Sci. Let., 11, 207-215. (10) Lucchitta, B., 1976, Proc. Lunar Planet. Sci. Conf. 7, 2761-2782. (11) Howard, K., and Muehlberger, W., 1973, Apollo 17 Pre. Sci. Rept., NASA SP-330, 31/22-31/35. (12) Bryan, W., 1973, Proc. Lunar Planet. Sci. Conf. 4, 93-106. (13) Lucchitta, B., 1977, Proc. Lunar Planet. Sci. Conf. 13, 2691-2703. (14) Maxwell, T., et al., 1975, Geol. Soc. Amer. Bull, 86, 1273-1278. (15) Henderson, J., 1931, New Zealand J. Sci. Tech., 15, 38-75. (16) Everingham, J., et al., 1969, Nature, 223, 701-703. (17) Gordon F., and Lewis, J., 1980, Geol. Sur. W. Aust. Bull. 126, 229 pp. (18) Philip, H., and Megard, F., 1977, Tectonophysics, 38, 259-278. (19) Berberian, M., 1979, Bull. Seis. Soc. Amer., 69, 1861-1887, (20) Philip, H., and Meghraoui, A., 1983, Tectonics, 2, 17-49. (21) King, G., and Vita-Finzi, C., 1981, Nature, 292, 22-26. (22) Ouyed, M., et al., 1981, Nature, 292, 26-31. (23) Yielding, G., et al., 1981, Earth Planet. Sci. Let., 56, 287-304. (24) Waitt, R., 1979, U.S.G.S. Prof. Paper 1125, 18 pp. (25) Hubbert, M.K., 1951, Geol. Soc. Amer. Bull., 62, 355-372.

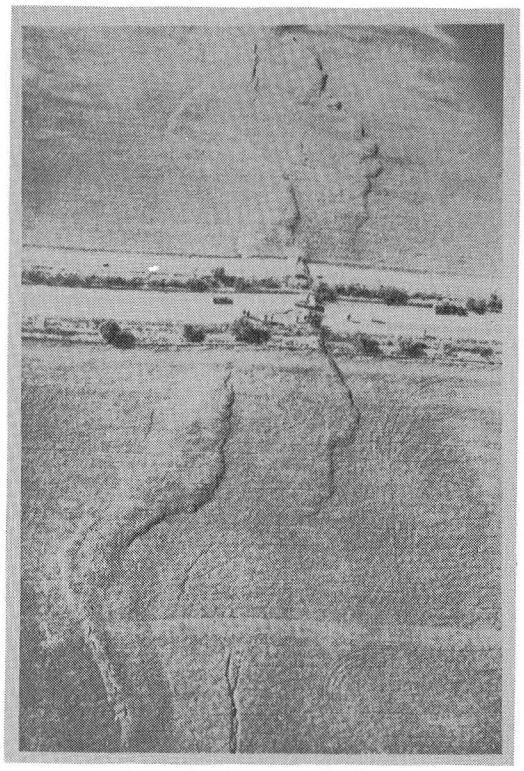

Fig. 1. Aerial view of a section of fault scarps formed during the 1968 earthquake near Meckering, Western Australia, from (17)

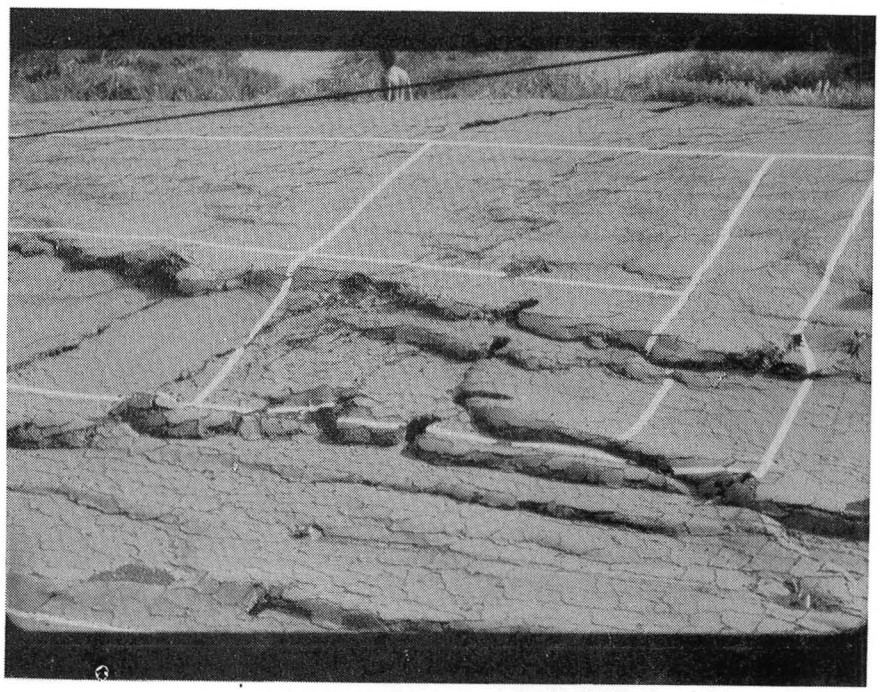

Fig. 2. Deformation features formed in paved paddle tennis court in Abalone Cove, Palos Verdes Hills, California

ON THE ABSENCE OF STRIKE-SLIP FAULTS FROM THE PLANETS AND SATELLITES

Matthew P. Golombek, Jet Propulsion Laboratory, California Institute of Technology, MS 183-501, 4800 Oak Grove Drive, Pasadena, CA 91109

Strike-slip faults are conspicuously absent from the surfaces of almost all of the hitherto imaged planets and satellites. Nevertheless, geophysical models that calculate stresses on the planetary surface from idealized lithospheric deformation models typically predict the formation of strike-slip faults. How then, can this apparent paradox be explained? One possibility, of course, is simply that strike-slip faults have formed but that they are all very small and have experienced undetectable displacements. (Clearly, the near ubiquity of circular craters on planet and satellite surfaces limits strike-slip displacements to trivial amounts.) This explanation, although possible, is scientifically unsatisfying (equivalent to "swepping them under the rug"), is not particularly well suited to testing, and must be substantiated in other ways before it is accepted. In this abstract, I review the most common tectonic features observed on planet and satellite surfaces and their origins, briefly discuss the models that predict strike-slip faults, and describe a reasonable hypothesis that is capable of explaining their apparent absence.

Grabens, wrinkle ridges, and ridges are the dominant tectonic features on the surface of planets and satellites. Grabens and analogous extensional structures have been found on the moon, Mars, Ganymede, Io, Callisto, and some of the Saturnian satellites while wrinkle ridges, lobate scarps and tectonic ridges have been reported on the moon, Mercury, Mars, Europa and some of the Saturnian satellites. Grabens have been ascribed to normal faulting resulting from extensional stresses whereas wrinkle ridges, lobate scarps, and tectonic ridges are mostly thought to result from thrust faulting or folding due to compressional stresses.

Analysis of lunar grabens and wrinkle ridges has resulted in the most complete understanding of these structures. Lunar grabens are bounded by two downward converging 60^{o} dipping normal faults (1). These faults intersect below the surface at a major mechanical discontinuity in the shallow crust between the megaregolith (total ejecta built up by repeated cratering) and the underlying in situ fractured rock. The symmetry and simplicity of lunar grabens demands that the bounding faults initiate at this mechanical discontinuity and propagate up (2). Most workers believe wrinkle ridges result from thrust faulting or compressinal folding of mare basalts (3,4,5). The recent identification and analysis of a number of terrestrial analogs that are morphologically similar to lunar and martian examples indicates that wrinkle ridges result from thrust faulting (6). The location of wrinkle ridges above suggested subsurface basin structures indicates that the trend and location of many wrinkle ridges are inherited from these pre-existing basin structures (4,5). This implies that the thrust faults responsible for wrinkle ridges initiate at the base of the basalt-basin floor contact. This contact almost certainly represents a mechanical discontinuity in the shallow lunar crust because mare basalts are undoubtedly stronger than the underlying fall-back ejecta of the basin floor.

The morphologic similarity of lunar grabens and wrinkle ridges with the structures observed on the surfaces of the other planets and satellites implies similar controls on the origin of these structures. For example,

grabens that are very similar to those on the moon also exist on Mars and Ganymede; broadly analogous structures may also exist on Io, Callisto, and some of the Saturnian satellites. Analysis of the grabens on Mars (7), Ganymede (8,9), and Callisto (8) also suggests that these structures initiate at particular mechanical discontinuities in the outer layers of these bodies. The exact nature of the mechanical discontinuity does not appear to be important in controlling the initiation of faults bounding grabens (i.e., the discontinuity may result from the following superposition of material units - strong over weak, weak over strong, brittle over ductile), only a significant change in mechanical properties is required (2). Although no detailed study of wrinkle ridges and tectonic ridges on other planets and satellites has been made, morphologic similarities with those on the moon implies a similar origin. Thus, the initiation of the faults responsible for both grabens and wrinkle ridges are controlled by mechanical discontinuities in the shallow crusts of planets and satellites. This implies that these mechanical discontinuities act as stress guides that concentrate stresses at particular levels that may be controlled by, for example, variations in strength of the material, layer thickness, or substrate structure.

Numerous geophysical models that calculate stresses at planetary surfaces have been developed to explain a variety of tectonic patterns that probably are related to lithospheric deformation. These models include adjustment of the lithosphere following the formation of a basin (10), loading of the lithosphere (11,12,13), despinning (14), tidal stressing, planetary expansion (15), and stresses associated with large topographic uplifts (16) on a variety of planets and satellites that include Mercury, the moon, Mars, Europa, and Ganymede. Unfortunately however, most of these models show stresses that predict the formation of strike-slip faults, yet definitive examples of these structures are notably absent from almost all planetary surfaces except perhaps two. Some evidence on Europa suggests transform faulting in conjunction with minor rotation of ice blocks (17). In addition, strike-slip faults have been suggested to occur on Ganymede but most or all of these can be explained as a hierarchy of normal faults (18).

The reason strike-slip faults are not found on most planetary surfaces may be analogous to the reason they are not found on the moon (discussed and developed fully by Golombek (19). Although lithospheric deformation models predict one horizontal stress compressive and the other tensile at the surface (the stress distribution for strike-slip faults i.e., intermediate compressive stress vertical), strike-slip faults may not form because at a few km depth there exists a mechanical discontinuity along which the maximum compressive stress due to overburden is vertical. Thus normal faults or grabens would be expected instead of strike-slip faults. Clearly for those places where this can occur, the horizontal compressive stress in the outer few km of the planet or satellite derived from the deformation models must be less than the stress due to overburden. Nevertheless, the rotation of the maximum compressive stress from horizontal at shallow depths to vertical at deeper levels due to increasing overburden pressure is supported by observed earthquake focal mechanisms on the earth (Iceland and Basin and Range Province) where strike-slip motions occur at shallow depths and normal slip occurs at deeper levels (20,21). If this

explanation is correct, mechanical discontinuities in the shallow crusts of planets and satellites exert extremely important controls on the structures that develop and are seen on their surfaces.

This hypothesis suggests the following possible corollaries. First, horizontally oriented mechanical discontinuities are of greater relative magnitude and importance in determining the type of structures that form than vertically oriented anisotropies. It is well known that the strength of geologic materials and the limiting stress levels in the earth's crust are controlled by the ubiquitous presence of all sizes of joints, cracks and fractures (Byerlee's law, 22). The absence of strike-slip faults on the surfaces of planets implies that these anisotropies, many of which are oriented vertically, are less important in localizing stress than horizontal mechanical discontinuities that result from bulk changes in material properties. Third, if this hypothesis is correct and if the satellites of Uranus and Neptune fit within the tectonic-geologic evolutionary range of the satellites of Jupiter and Saturn, strike-slip faults should not be expected on their surfaces.

In conclusion, the conspicuous absence of strike-slip faults on the surfaces of planets and satellites may be due to the widespread presence of subsurface mechanical discontinuities that effectively concentrate stress at particular levels in the crust. This results in a vertical maximum compressive stress due to overburden and thus the preferential development of normal faults or grabens. Consequently, mechanical discontinuities in the shallow crusts of planets and satellites play an extremely important and hitherto unrecognized role in the formation of structures observed on their surfaces.

References (1) Golombek, M. P. (1979) J. Geophys. Res., 84, 4657-4666. (2) Golombek, M. P., and G. E. McGill (1983) J. Geophys. Res., 88, 3563-3578. (3) Howard, K. A., and W. R. Muehlberger (1973) Ap. 17 Sci. Rep., NASA SP-330, 31-22 to 31-35. (4) Maxwell, T. A., F. El-Baz, and S. H. Ward (1975) Geol. Soc. Am. Bull., 86, 1273-1278. (5) Sharpton, V. L., and J.W. Head (1982) J. Geophys. Res., 87, 10983-10998. (6) Plescia, J., and M. Golombek (1984) Bull. Am. Ast. Soc., DPS Meeting. (7) Runyon, C. J., and M. P. Golombek (1983) Lunar Planet. Sci. XIV, 660-661. (8) McKinnon, W. B., and H. J. Melosh (1980) Icarus, 44, 454-471. (9) Golombek, M. P. (1982) Lunar Planet. Sci. Conf., 13th, J. Geophys. Res., 87, A77-A83. (10) Melosh, H. J. (1976) Proc. Lunar Sci. Conf. 7th, 2967-2982. (11) Melosh, H. J. (1978) Proc. Lunar Sci. Conf. 9th, 3513-3525. (12) Solomon, S. C., and J. W. Head (1979) J. Geophys. Res., 87, 1667-1682; (1980) Rev. Geophys. Space Phys., 18, 107-141. (13) Pullan, S., and K. Lambeck (1981) Proc. Lunar Planet. Sci. 12B, 853-865. (14) Melosh, H. J. (1977) Icarus, 31, 221-234. (15) McKinnon, W. B. (1981) Proc. Lunar Planet. Sci. 12B, 1585-1597. (16) Banerdt, W. B., R. J. Phillips, N. H. Sleep, and R. S. Saunders (1982) J. Geophys. Res., 87, 9723-9733. (17) Schenk, P. (1984) NASA Tech. Mem. 86247, 3-111. (18) Golombek, M. P., and M. L. Allison (1981) Geophys. Res. Lett., 8, 1139-1142. (19) Golombek, M. P. (1983) Lunar Planet Sci. XIV, 249-250. (20) Klein, F., P. Einarsson, and M. Wyss (1977) J. Geophys. Res., 865-888. (21) Vetter, U., and A. Ryall (1983) J. Geophys. Res., 88, 8237-8250. (22) Brace, W., and D. Kohlsted (1980), J. Geophys. Res., 85, 6248-6252.

LUNAR MASCON LOADING: AN EXAMPLE OF THE IMPORTANCE OF FAULT INITIATION DEPTH ON FAULT TYPE PREDICTIONS FROM STRESSES ON PLANETARY SURFACES

Matthew P. Golombek, Jet Propulsion Laboratory, California Institute of Technology, MS 183-501, 4800 Oak Grove Drive, Pasadena, CA 91019

Geophysical models that predict fault type from stresses calculated at the planetary surface (zero depth) can be misleading because faults generally initiate at depth under a different stress regime and propagate to the surface. This abstract briefly reviews the generally accepted and most commonly employed criteria for fault prediction from calculated stresses on planetary surfaces (Anderson's, 1) points out problems in neglecting the effects of non-isotropic overburden stresses and the use of realistic material constants and shows a well known example (mascon loading on the moon) where neglecting this effect predicts a different type of fault than is actually observed.

Anderson (1) deduced that the three types of shear faults commonly seen at the surface of the earth are formed under three distinct stress states. He surmised that at or near the surface of the earth one principal stress direction is vertical and two are oriented horizontally, parallel to the surface, except in areas of extreme relief. Because the surface of a planet is a free boundary, there can be no vertical stress across it and so the vertical stress at the surface must be zero. As a result, the magnitude and signs of the horizontal principal stresses will determine the type of fault. If both horizontal principal stresses are tensile, then the maximum compressive stress is vertical (and equal to zero by definition) and normal faults or grabens are expected. If both horizontal principal stresses are compressive, then the minimum compressive stress is vertical and reverse or thrust faults (evidenced by wrinkle ridges) are expected. Finally, if one horizontal principal stress is tensile and the other is compressive, then the intermediate principal stress is vertical and strike-slip faults are expected.

Faults seen on planetary surfaces, however, initiate at some non-negligible depth and propagate to the surface. As a result, the critical stresses necessary to predict fault type must be calculated at the depth where faults initiate. Structures seen on most planetary surfaces (other than the earth) probably initiate at fairly shallow depths (i.e., grabens and wrinkle ridges), so that the orientations of the principal stresses are most likely still horizontal and vertical (1). Nevertheless, the vertical stress is non-zero at depth, due to overburden and the confined nature of the subsurface results in a horizontal stress as well. This alters the stress conditions necessary for the prediction of each type of fault in that the relative magnitude of the vertical principal stress alone determines the type of fault expected and there is no need for horizontal tensile stresses to produce normal faults or strike-slip faults. Thus, to predict the type of fault most likely to form, theoretical model stresses must be calculated at the probable depth of fault initiation and then superposed with overburden stresses due to gravity. To illustrate this method to predict fault type from calculated stresses, a geometrically simple and reasonably well understood example will be investigated; modifying these stress calculations by using realistic material constants at the depth of fault initiation and superposing overburden stresses correctly predicts the observed structures.

Lunar mason basins are typically surrounded by concentric grabens while the basalts in the basin interior are deformed by wrinkle ridges. This led a number of workers to calculate bending stresses from simple axisymmetric elastic plate flexure models to explain the location and type of fault (2,3,4). Unfortunately, as Melosh (2) originally pointed out, calculations of stresses at the surface predict a central zone of reverse or thrust faults, surrounded by an annulus of strike-slip faults, surrounded by a still larger zone of normal faults. Little or no evidence exists for strike-slip faults on the moon, and although wrinkle ridges are found in the interiors of basins and grabens occur on the edges, basin flexure models predict the largest stress difference, and thus the most likely place for faulting to occur, in the strike-slip zone at about the distance at which grabens are found. This problem has been circumvented by superposing fairly large stresses due to global expansion and contraction to yield the correct stresses for graben formation followed by wrinkle ridge formation (3); however, there is no geologic evidence for, and considerable evidence against global expansion on the moon (5). Thus, simple flexure models alone do a poor job predicting the correct faults from stresses calculated at the surface. Nonetheless, using these same models to calculate stresses at the depth where faults initiate using realistic material constants and superposing non-isotropic overburden stresses yields the appropriate stress state for the prediction of grabens and wrinkle ridges where they are found without a zone of strike-slip faults (and without the need for an apparently ad hoc global stress).

Faults bounding lunar grabens initiate at the base of the megaregolith (cummulative crater ejecta) 1-3 km thick (6). Although the depth at which the thrust faults responsible for wrinkle ridges (7) initiate has not been investigated, lunar sounder data (8) imply a depth of about 1 km. Seismic velocities in the outer few kilometers of the moon (9) indicate Young's modulus is at least an order of magnitude less than generally assumed in plate flexure calculations (most use 10^{12} dyne/cm^2). Because the calculated stresses are critically dependent on the value of this assumed parameter, stresses in the outer few kilometers of the moon are correspondingly lower by an order of magnitude (tens of bars as opposed to hundreds of bars). This follows directly from making the reasonable assumption of continuity of displacement; that is, all the strain experienced at the top of the lithosphere is imposed on the overlying megaregolith (in the laminated plate model (4), stresses are continuous at an elastic boundary and their magnitudes are a function of the respective elastic constant). The weight of overburden results in a compressive vertical stress that equals the thickness times the density of the overlying rock times the acceleration due to gravity (10). Because the megaregolith and the basalt were deposited incrementally (megaregolith - superposition of impact ejecta sheets, basalts - very thin flows that cooled very quickly) and both were laterally constrained, the horizontal stress after the addition of overburden was complete equals Poisson's ratio divided by one minus Poisson's ratio, all times the vertical overburden stress (11). This results in vertical and horizontal stresses due to the weight of the overburden that are ~33 bars/km of depth and ~10 bars/km of depth, respectively.

Superposing these stresses on the theoretical stresses due to the load using the lower Young's modulus yields the appropriate stress state for the prediction of grabens and wrinkle ridges where they are found. At the edges of mare basins concentric grabens are observed because the maximum compressive stress is vertical and roughly 30-100 bars for 1-3 km depth and the minimum compressive stress is horizontal and radial to the basin center and roughly 0-50 bars tensional. Furthermore, a maximum stress difference and thus the most likely place for faulting, occurs in this distance range where the grabens are found. Within the interiors of mare basins wrinkle ridges are predicted (as observed) because the minimum compressive stress is vertical and the maximum compressive stress is horizontal and roughly 50-100 bars. In general, the hoop stress is larger than the radial stress and thus predict radially oriented wrinkle ridges. Nevertheless, the two horizontal stresses are very close in magnitude and so do not preclude the possibility that the location and trend of some wrinkle ridges could be inherited from underlying structures. In addition, the central part of the basin is the site of another maximum stress difference and thus a likely location for faulting. Although this model also predicts the stresses appropriate for strike-slip faults in a narrow zone around the basin edge, this zone has a minimum stress difference and thus the least likely place for faulting to occur (in agreement with the lack of strike-slip faults around mascon basins).

Note that even though the stress levels in this model are low (tens of bars), they do predict failure when overburden and bending stresses are superposed. Maximum stress levels in the earth's crust are accurately predicted by a simple relationship with the frictional resistance to sliding on ubiquitous pre-existing fractures (Byerlee's law (12); maximum principal stress <5 times the minimum principal stress). For overburden stresses alone, maximum (~33 bars/km) and minimum (~10 bars/km) are below the maximum allowable and so will not fail. Superposing the stresses due to plate flexure in the graben zone (e.g., at 1.5 km depth) results in maximum (50 bars compressive) and minimum (16 bars tensional) principal stresses that exceed the limiting level and so will fail, in accord with the formation of grabens around mascon basins.

References: (1) Anderson, E.M., 1951, The dynamics of faulting, 2nd Ed., 106 pp. Oliver and Boyd, London. (2) Melosh, H.J., 1978, Proc. Lunar Planet. Sci. Conf. 9th, 3513-3525. (3) Solomon, S.C., and J.W. Head, 1979, J. Geophys. Res. 84, 16678-1682 and 1980, Rev. Geophys. Space Phys. 18, 107-141. (4) Pullan, S., and K. Lambeck, 1981, Proc. Lunar Planet. Sci. 12B, 853-865. (5) Golombek, M.P., and G.E. McGill, 1983, J. Geophys. Res. 88, 3563-3578. (6) Golombek, M.P., 1979, J. Geophys. Res. 84, 4657-4666. (7) Plescia, J.B., and M.P. Golombek, 1984, Bull. Amer. Ast. Soc., DPS Meeting. (8) Phillips, R.J., and T.A. Maxwell, 1978, Lunar Planet. Sci. IX, 890-892. (9) Cooper, M.R., R.L. Kovach, and J.S. Watkins, 1974, Rev. Phys. Space Phys. 12, 291-308. (10) McGarr, A., and N. C. Gay, 1978, Ann. Rev. Earth Planet. Sci. 6, 405-436. (11) Voight, B., and B.H.P., St. Pierri, 1974, Proc. 3rd Congr. Int. Soc. Rock Mech. IIA, 580-582. (12) Brace, W.F., and D.L. Kohlstedt, 1980, J. Geophys. Res. 85, 6248-6252.

THE DEEP STRUCTURE OF LUNAR BASINS: CLUES TO THE UNDERSTANDING OF BASIN FORMATION AND MODIFICATION. Steven R. Bratt and Sean C. Solomon, Dept. of Earth, Atmospheric, and Planetary Sciences, Massachusetts Institute of Technology, Cambridge, MA 02139; James W. Head, Dept. of Geological Sciences, Brown University, Providence, RI 02912; and Clifford H. Thurber, Dept. of Earth and Space Sciences, State University of New York, Stony Brook, NY 11794.

Introduction. Basin excavation has played a major role in shaping the surface and subsurface of the Moon. Though photogeologic observations provide estimates for the present volumes of lunar impact basins and their ejecta deposits [1,2], there is not sufficient information to describe completely either the geometry of the basins at the time of impact or their modification with time. Determination of the structure of the crust and upper mantle beneath large basins can provide important insight into the thermal and mechanical processes associated with basin formation and modification as well as the differences in these processes as functions of basin age and size [3]. Using observed gravity and topography together with the seismically determined crustal thickness of the central nearside, we present a model for the structure of the crust and upper mantle of the nearside of the Moon. With this model we compare the deep structure of the largest lunar basins, and we explore the implications for the processes of basin formation and modification at different stages in lunar history.

Sub-basin Structure. We compute the crustal and upper mantle structure of the lunar near-side from an inversion of gravity data in the manner of Thurber and Solomon [4]. Gravity anomalies are calculated from the mass disk model of Wong el al. [5]; and topographic corrections are made using 5° x 5° averages of the 15887 nearside topographic measurements compiled by Bills and Ferrari [6]. We assume that the Bouguer anomaly arises from density contrasts between average crustal material (2.9 g/cm^3) and either mantle material (3.4 g/cm^3) at the lunar Moho or mare basalt (3.4 g/cm^3) at the base of the mare units. At the time of basin formation, the thin lunar lithosphere, coupled with the conversion of impact kinetic energy to buried heat, should permit rapid and nearly complete isostatic compensation of a large basin [4,7,8]. Models in which the pre-mare compensation is significantly less than complete require unreasonably large thicknesses of mare basalt to fit the gravity and topographic data [4]. We therefore assume that pre-mare isostatic compensation was complete and that no compensation of mare units has occurred since their emplacement [4]. A final constraint on the structure is provided by the seismic measurement of the crustal thickness (~55 km) in the area of the Apollo 12 and 14 landing sites [9]. The resulting structural model for the lunar nearside indicates that the Moho has been uplifted by tens of kilometers beneath the youngest mare basins (Figure 1). Table 1 lists the magnitude of uplift, relative to the ambient Moho depth, together with the volume V_u of uplifted mantle beneath the centers of major basins well covered by the gravity and topographic data. Basins are listed in order of increasing age [10].

Implications. One observation evident from the results listed in Table 1 is that the extent of present mantle uplift beneath basins of a given size is generally less for older basins. The extent of mantle uplift beneath the three oldest basins (Nubium, Fecunditatis, and Tranquillitatis) is much less pronounced than that beneath any of the younger structures. We attribute this result primarily to enhanced rates of lateral flow of crustal material early in lunar history when crustal temperatures were relatively high and the elastic lithosphere comparatively thin [7]. Non-mare volcanic activity may

also have contributed to the greater extent of modification of older basins. The relaxed topographic and Moho relief for older basins on the central nearside, in particular, may be at least partly a consequence of the extensive crustal and subcrustal heating associated with the formation of the large Procellarum basin [11, 12].

The total volume V_e of pre-basin crustal material now external to the basin rim can be equated to the sum of the volume V_b of the present basin (topographic depression plus mare fill) and the volume V_u of uplifted mantle material [13]. The quantity V_e provides only a lower bound on the volume of crustal material originally transported beyond the rim (V_p), because lateral transport of crustal material during cavity collapse and basin modification as well as deposition of non-mare volcanic material will act to reduce V_b, V_u, or both. For the youngest basins formed at a time when the elastic lithosphere was relatively thick, V_e may approach V_p. Values for V_e derived from the structural model of this paper are given in Table 1. Previous estimates of V_e for basins the size of Serenitatis or Orientale range from 0.4×10^6 km^3 [1] to 12×10^6 km^3 [14]. The estimates in Table 1 fall within this range. The largest V_e value, 9×10^6 km^3 for Serenitatis, falls toward the upper end of this range. This volume, spread evenly around the Moon, would constitute a layer 230 m thick. Considering the 30 or more impact basins preserved on the Moon [10], such large ejecta volumes suggest that the accumulated thickness of ejecta deposits on the lunar surface may, on average, be several kilometers.

If basin excavation did not extend at least to the base of the crust, then the thickness t_c of preserved non-mare crustal material beneath basins should increase with increasing pre-impact crustal thickness for basins of a given diameter (compare Orientale and Serenitatis, Table 1). By the same reasoning, t_c should decrease with increasing basin diameter for basins formed in crust of a given thickness (Serenitatis and Humorum). However, the quantity t_c beneath the central regions of the 6 youngest basins from Table 1 is remarkably uniform (20 to 30 km), despite large differences in basin size and in the pre-impact thickness of the crust. These results suggest that basin excavation extended in depth at least to the lowermost crust for these impacts, and that significant deepening of cavity excavation for the largest basins may have been impeded by an abrupt increase in strength at the crust-mantle boundary [15]. The preserved layer of non-mare crust beneath the basin centers, by this view, may be some combination of fallback and crustal material transported laterally during cavity collapse.

Conclusions. Lunar gravity and topographic data provide valuable constraints on the process of basin formation and modification. A general trend toward a decreasing extent of preserved Moho relief with increasing basin age suggests that processes acting to reduce topographic and Moho relief (viscous relaxation, volcanic deposition) were more important early in lunar history than later. The extent of mantle uplift beneath major basins on the lunar nearside indicates that the net volume of crustal material transported beyond the basin rim during basin formation was on the order of 10^7 km^3. In addition, the nearly constant thickness of non-mare crust preserved beneath the central regions of the youngest nearside basins suggests that the mantle may have acted as a barrier to the penetration of large impact cavities on the Moon.

References: [1] J.W. Head et al., PLSC 6th, 2805, 1975; [2] R.S. Pike, GRL, 7, 291, 1974; [3] S.R. Bratt et al., LPS, 12, 109, 1981; [4] C.H. Thurber and S.C. Solomon, PLPSC 9th, 3481, 1978; [5] L. Wong et al., Jet Propulsion Lab., 1975; [6] B.G. Bills and A.J. Ferrari, Icarus, 31, 244, 1977; [7] S.C. Solomon et al., JGR, 87, 3975, 1982; [8] J.W. Head, Moon, 11, 327, 1974; [9]

M.N. Toksoz et al., RGSP, 12, 539, 1974; [10] D. Wilhelms, NASA TM-84211, 405, 1981; [11] D.E. Wilhelms, LPS, 14, 845, 1983; [12] E.A. Whitaker, PLPS, 12A, 105, 1981; [13] S.R. Bratt et al., LPS, 13, 67, 1982; [14] W.M. Kaula, PLSC 5th, 3049, 1974; [15] W.F. Brace and D.L. Kohlstedt, JGR, 85, 6248, 1980.

Basin	Radius, km	Moho relief, km	Ambient crustal thickness, km	V_u, 10^6 km^3	V_b, 10^6 km^3	V_e, 10^6 km^3
Orientale	310	66	85	6	0.7	7
Serenitatis	305	30	60	8	1	9
Crisium	225	31	55	6	1	7
Humorum	205	27	60	3	0.5	4
Nectaris	300	28	60	4	0.7	5
Smythii	300	33	65	4	0.6	5
Nubium	340	10	60	2	0.3	2
Fecunditatis	345	14	60	2	0.2	2
Tranquillitatis	340	12	60	2	0.2	2

Table 1. Estimates of the magnitude of Moho relief, volume (V_u) of uplifted mantle material, basin volume (V_b), and volume (V_e) of crustal material residing outside the basin rim for major nearside basins.

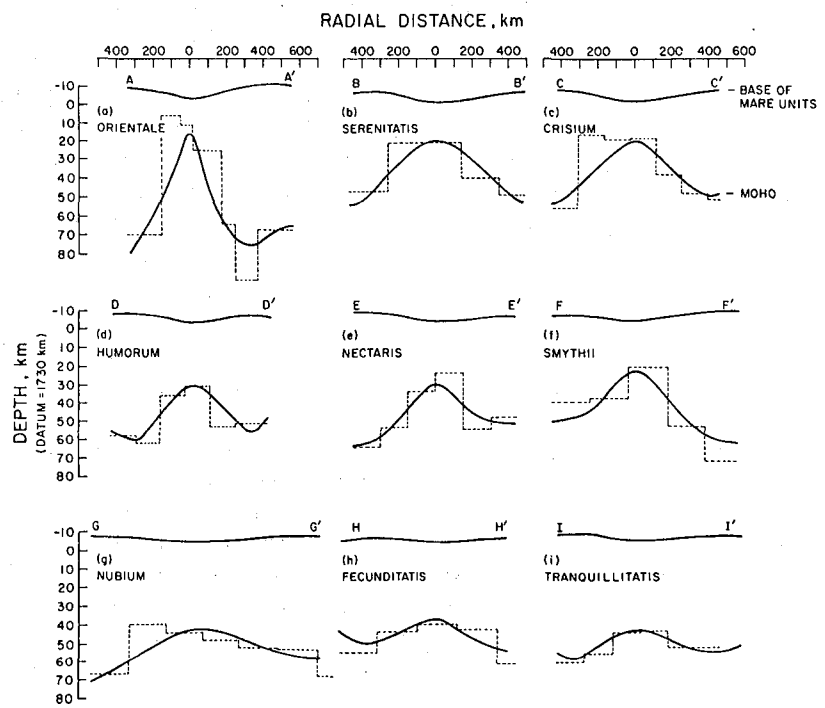

Figure 1. Cross-sections of crustal structure for basins on the lunar nearside. Dashed lines indicate the Moho depth along profiles through the center of each basin as determined from the 5° x 5° block model presented here. Solid curves represent azimuthally averaged profiles of the lunar Moho and the basin topography at the base of the mare basalts. Depths are relative to a datum at 1730 km radius.

BOUGUER IMAGES OF THE NORTH AMERICAN CRATON

R.E. Arvidson, D. Bindschadler*, S. Bowring, M. Eddy, E. Guinness, and C. Leff, McDonnell Center for the Space Sciences, Dept. of Earth and Planetary Sciences, Washington Univ., St. Louis, MO 63130 *Present address: Dept. of Geological Sciences, Brown University, Providence, RI

Technologies developed as part of the planetary program have much to offer the earth sciences. In this abstract, we report on work where we applied image processing techniques to Bouguer data. Results are directly relevant to, for example, NASA's Early Crustal Genesis Program.

Processing of existing gravity and aeromagnetic data with modern methods is providing new insights into crustal and mantle structures for large parts of the United States and Canada (1-3). More than three-quarters of a million ground station readings of gravity are now available for this region. These data offer a wealth of information on crustal and mantle structures when reduced and displayed as Bouguer anomalies, where lateral variations are controlled by the size, shape and densities of underlying materials. We have used digital image processing techniques to generate Bouguer images that display more of the granularity inherent in the data as compared with existing contour maps. A dominant NW-SE linear trend of highs and lows can be seen extending from South Dakota, through Nebraska, and into Missouri. The structural trend cuts across the major Precambrian boundary in Missouri, separating younger granites and rhyolites from older sheared granites and gneisses. This trend is probably related to features created during an early and perhaps initial episode of crustal assembly by collisional processes. The younger granitic materials are probably a thin cover over an older crust.

Our processing technique, which is based on local arithmetic averages of Bouguer values, was chosen specifically to preserve local details (4), thus enhancing short wavelength anomalies of probable crustal origin. The data were reduced to Bouguer anomalies using the 1967 International Gravity Formula and a slab density of 2.67 g/cm^3. We concentrated on delineating and interpreting NW-SE trending features in the midcontinent, covering the Dakotas, Nebraska, and Missouri. This area is one where gravity and magnetic data can provide considerable information on crustal structure as much of the region is covered by Phanerozoic sedimentary rocks.

The examined area includes the Superior Province (2,500-2,700 Myr (ref. 5)), the Churchill Province (1,800-1,900 Myr, with residual Superior ages (5)), and areas to the south. We have included part of Canada because large parts of the Superior and Churchill Provinces are exposed, thereby allowing the Bouguer trends to be interpreted in concert with extensive geological data. Trends within the Superior Province are largely NE-SW, reflecting the presence of belts of mafic metavolcanic rocks (6). The western boundary between the Superior Province and the younger Churchill Province shows up clearly in the images, partly because the structural fabric has very different wavelengths and trends in the two provinces. The Churchill Province exhibits structures that trend in N-NW directions. These structures

consist of curvilinear belts of metamorphic and igneous rocks that are thought to have formed in a series of collisional events associated with convergent plate margins (7-8).

The Churchill trend appears to be truncated along a linear zone extending NE-SW from Minnesota, through South Dakota, and into Wyoming. This zone corresponds to the Great Lakes Tectonic Zone in Minnesota and to the Wyoming Shear Zone in Wyoming (9,10). The structures to the south of the zone strike more towards the NW and have a finer texture than do the structures in the Churchill Province. Our presentations show that this NW-SE trending fabric extends from South Dakota to the southeastern section of Missouri. The NW-SE trending fabric extending into Missouri has clearly been cut by the younger 1,100 Myr basalts emplaced during the Keweenawan rifting event (11). Within the zone of NW-SE trending fabric, the Precambrian terranes consist of igneous and metamorphic rocks that range in age from 1,600 to 1,700 Myr in South Dakota and Nebraska, to undeformed granitic rocks 1,300-1,400 Myr in age in asouthern Missouri (12). The northern boundary of the younger granitic rocks runs in an E-W to NE-SW direction, roughly perpendicular to the NW-SE trending fabric.

The dominant NW-SE trending feature in Missouri, the "Missouri Gravity Low" (MGL) (13,14), is 700 km long, 120 km wide, and has a maximum amplitude of -40 mGal. It is best modelled as a 4-6 km crustal excess at the Moho (15). The gravity signature of the Missouri feature is similar to those for modern rift valleys. On the other hand, negative Bouguer rift signatures arise because of sediment fill or because of low-density magma ponded at the base of the crust (16). Neither hypothesis seems valid for the Missouri feature, since: (1) no Precambrian sediments are associated with the gravity low, and (2) the last major magmatic activity was associated with mafic dykes and sills that are unconformably overlain by Cambrian sediments (15). It is equally difficult to explain the Missouri feature as a shear zone, given the amplitude of the low (15). The most plausible origin is one involving crustal thickening due to events associated with convergent plate margins (17). In fact, the signature is not unlike the pattern found in selected regions within the Churchill and Superior Provinces (7,8).

The preservation of the deep-seated MGL beneath the granitic basement of southern Missouri is consistent with the younger granitic rocks being a veneer emplaced over an older igneous and metamorphic crust. Neodymium-Samarium data imply that the Missouri granites and rhyolites formed by partial melting of crustal rocks that have a mantle separation age of 1,800-1,900 Myr (ref. 18). The mantle separation age is similar to the age of the hypothesized collisional events to the north that produced the Penokean, Trans-Hudson and Wopmay Orogens (5). Given the cumulative evidence, it is not inconceivable that the NW-SE trends in South Dakota, Nebraska, and Missouri formed by collisional processes similar to those that occurred to the north, during approximately the same time period. We treat such a hypothesis as intriguing and one deserving further scrutiny and evaluation. If true, much of the original Proterozoic craton was assembled in a similar manner over a relatively brief interval.

1) Arvidson, R.E., Guinness, E.A., Strebeck, J., Davies, G., and Schulz, K. EOS 18, 261-265 (1982).

2) Hildenbrand, T.G., Simpson, R.W., Godson, R.H. and Kane, M.F. U.S. geol. Surv., Geophys. Inves. Map GP-953-A (1982).

3) Arvidson, R.E., D. Bindschadler, S. Bowring, M. Eddy, E. Guinness, C. Leff, Nature, 311, 241-243 (1984).

4) Eliason, E. and Soderblom, L. Proc. 8th Lunar Planet. Sci. Conf. 1163-1170 (1977).

5) McCullogh, T. and Wasserburg, C. Science 200, 1003-1011 (1976).

6) Morey, C. and Sims, P. Bull. Geol. Soc. am. 87, 141-152 (1976).

7) Gibb, R.A. and Thomas, M.D. Nature 262, 199-200 (1976).

8) Lewry, J.F. Nature 294, 69-72 (1981).

9) Sims, P.K., Card, K.D., Morey, G.B. and Peterman, Z.E. Bull. geol. Soc. Am. 91, 690-698 (1980).

10) Warner, L.A. Bull. Geol. Soc. Am. 89, 161-171 (1978).

11) Green, J.C. Geol. Ass. Can. Spec. Pap. 16, 407-422 (1977).

12) Van Schmus, W. and Bickford, M. Precambrian Plate Tectonics (ed. Kroner, A.), 261-296 (Elsevier, 1981).

13) Guinness, E.A. et al. J. Geophys. Res. 87, 8529-8545 (1982).

14) Guinness, E.A., Arvidson, R.E., Leff, C., Edwards, M. and Bindschadler, D. Econ. Geol. 78, 654-663 (1983).

15) Eddy, M.S. Thesis, Wash. Univ. (1984).

16) Burke, K. and Whiteman, A.J. in Implications of Continental Drift to the Earth Sciences (eds. Tarling, D.H. and Runcorn, S.K.) 735-755 (Academic, 1973).

17) Dutch, S.I. Geology 11, 478-481 (1981).

18) Nelson, B. and DePaolo, D. Geol. Soc. Am. Abstr. 14, 575 (1982).

PLANETARY INTERIOR MODELING AND TECTONIC IMPLICATIONS

R. J. Phillips, Dept. of Geological Sciences, S.M.U., Dallas, TX 75275

Line-of-sight Admittance Estimates for Venus: We have developed a technique to estimate spectral admittance functions using Pioneer Venus gravity and topography data. These admittance functions provide a convenient means to carry out systematic geophysical studies over much of the surface of Venus with a variety of interior density models. The admittance functions are calculated in the observation space of line-of-sight (LOS) gravity, obviating the need for long complex computer runs associated with the dynamic inversion of Doppler gravity data.

The topography of a given region (say a 30 deg by 30 deg block) is Fourier transformed and the resulting spectrum operated on with a dimensionless transfer function that describes a geophysical model (e.g., isostasy, flexure, convection) with a specific set of parameter values. The inverse transform of this result describes the "theoretically equivalent topography" that would give rise to the same gravity signal as the real topography and its associated model of subsurface density distribution. The gravity vectors from both the actual and theoretical topography are calculated at Pioneer Venus spacecraft positions for a particular orbit passing over the designated topographic block. The two vector sets are separately supplied to an orbit simulation program [1] to yield estimates of the LOS gravity. The three data sets of observed LOS gravity, LOS gravity due to actual topography, and LOS gravity due to theoretical topography are treated as one-dimensional data along the orbital track and Fourier transformed to yield power spectral, cross spectral, and coherence functions from which estimates of the observed and theoretical dimensionless admittance spectra are derived.

The results of the admittance studies allow a systematic comparison of interior models [2,3,4,5,6] for various regions of Venus as well as tests of the uniqueness of specific models within a given area.

Petrological and Mechanical Models for Tharsis: A series of petrological and mechanical models for the Tharsis region of Mars have been analyzed in an effort to understand better the tectonic history of this region [7,8].

We consider both closed and open system petrological models [9, 10]. In a closed system model, the great height of Tharsis is achieved by partial melting of a peridotite mantle source region and conversion to lower density crustal mineralogy. The magmas that are evolved are more Fe-rich than the initial rock, and the residuum is correspondingly Fe-poor and therefore of lower than original density. The magma ascends to the surface because despite Fe-enrichment, the liquid is of lower density than the surrounding rock. Upon extrusion, the magma freezes to a lower pressure mineral assemblage and/or glass, having a lower density

than the rock that would form from the same composition at depth. The area above the source region may subside as magma is removed, but the net height of the rock column including source region, upper mantle, crust and extrusive rock must increase because mass is conserved while density is becoming lower. The closed system by definition conserves mass but is not isostatic because of the variation of planetary gravity and membrane stress with planetary radius. The amount of material moved towards the surface is on the order of 10% in excess of that required for isostasy, and there must be downward adjustment of the column to achieve isostatic balance.

In open system models part of the mantle melt migrates laterally outward from Tharsis, say, by fractures, by extrusion, and by ponding of melt at the base of the crust. The consequence of lateral melt migration would be the buoyant uplift of the Tharsis region (an isostatic process). Only a small fraction of the melt needs to migrate in order for most of the elevation of Tharsis to be caused by isostatic uplift.

For Mars we have applied an analytic theory for isostatic compensation on one-plate planets, including membrane stresses in the lithosphere, self gravitation, and rotational ellipticity. Crucial to this stress modeling and also to the petrological modeling is the observation that the earliest fracturing seen in the Tharsis region is associated with isostatic stresses [11,12,13]. The radial fractures that extend far from Tharsis are associated with an additional and/or a completely different mechanism.

The results of applying the isostatic theory are similar in crust-mantle configuration to the model proposed by Sleep and Phillips [14], but allow for a much more rigorous calculation of stress distribution. The sign, relative magnitude, and orientation of the stresses agree with the isostatic calculation of Banerdt et al. [11] in that isostatic stresses are orthogonal to old graben in the Tharsis region, but do not match the radial fractures extending far from Tharsis. The present theory can be perturbed, however, to allow for a flexural load, and it can be shown that only a few kilometers thickness of volcanics are required to modify the stresses to produce these outlying radial fractures. The amount of this proposed late accumulation of volcanics may be consistent with geological observations [15]. An alternative mechanism to create these features is planetary expansion, which adds extension to the strains produced by the isostatic stresses. Conversely, later planetary contraction superimposed on the isostatic regime could account for the (presumably compressive) wrinkle ridges in Lunae Planum. This hypothesis, if correct, strongly ties the tectonic observations on the surface to the thermal history of the planet [16]. It also implies a lithospheric viscosity of about 10^{28} poise. At present we are testing both the flexure and the thermal expansion hypotheses.

References:

[1] Phillips, R.J., W.L. Sjogren, E.A. Abbott & S.H. Zisk, in J. Geophys. Res., 83, 5455, 1978.

[2] Phillips, R.J., in Nature, 302, 655, 1983.

[3] Phillips, R.J., & M.C. Malin, in Venus, University of Arizona Press, Tucson, 159, 1983.

[4] Phillips, R.J., & M.C. Malin, in Ann. Rev. Earth Planet. Sci., 12, 411, 1984.

[5] Morgan, P., & R.J. Phillips, in J. Geophys. Res., 88, 8305, 1983.

[6] Solomon, S.C., & J.W. Head, in J. Geophys. Res. ,87, 9236, 1982.

[7] Sleep, N. H., & R.J. Phillips, in press, J. Geophys. Res., 1984.

[8] Finnerty, A.A., R.J. Phillips & W.B. Banerdt, submitted to J. Geophys. Res., 1984.

[9] Finnerty, A.A. & R.J. Phillips, in Third International Colloquium on Mars, LPI, Houston, 77, 1981.

[10] Phillips, R.J., N.H. Sleep, W.B. Banerdt & R.S. Saunders, in Third International Colloquium on Mars, LPI, Houston, 191, 1981.

[11] Banerdt, W.B., R.J. Phillips, N.H. Sleep & R.S. Saunders, in J. Geophys. Res., 87, 9723, 1982.

[12] Golombek, M.P., & R.J. Phillips, in Lunar & Planetary Science XIV, LPI, Houston, 253, 1983.

[13] Phillips, R.J., & M.P. Golombek, in Lunar & Planetary Science XIV, LPI, Houston, 604, 1983.

[14] Sleep, N.H., and R.J. Phillips, in Geophys. Res. Lett., 6, 803, 1979.

[15] Plescia, J.B., & R.S. Saunders, in J. Geophys. Res., 87, 9775, 1982.

[16] Solomon, S.C., & J. Chaiken, in Proc. Lunar Sci. Conf., 7, 3229, 1976.

ELYSIUM REGION, MARS: TESTS OF LITHOSPHERIC LOADING MODELS FOR THE FORMATION OF TECTONIC FEATURES. J. Lynn Hall and Sean C. Solomon, Dept. of Earth, Atmospheric, and Planetary Sciences, Massachusetts Institute of Technology, Cambridge, MA 02139; and James W. Head, Dept. of Geological Sciences, Brown University, Providence, RI 02912.

Introduction. The Elysium region is the second largest volcanic province on Mars [1,2]. It consists of a broad topographic rise, 2400 by 1700 km in extent, on top of which sit the three volcanoes Elysium Mons, Hecates Tholus and Albor Tholus. The region is also the site of a broad positive free-air gravity anomaly [3,4]. On the basis of crater densities, the surfaces of both the plains and the shields of Elysium are older than their Tharsis counterparts [2,5]. In an effort to constrain the tectonic history and mechanical properties of the lithosphere in the Elysium province, we have compared the stress fields predicted by different models to the observed tectonic features of the region. The stress models we have treated are all products of volcanic loading of the Martian lithosphere, but at three different scales: global (Tharsis), regional (Elysium Planitia), and local (individual shields).

Tectonic Features. The tectonic and tectonically controlled features of the Elysium region have been defined from Viking Orbiter images [6,7]. A number of linear depressions, including both extensional fractures and volcanic vents, have a predominantly NW-SE trend, indicating a regional stress field with least compressive horizontal stress oriented NE-SW. There are also prominent sets of graben circumferential to Elysium Mons; these features are best developed in locations where the local stress field adds constructively to the regional field. No comparable graben surround the other two major volcanoes, but these constructs have been partially buried by extensive lava flows from the vicinity of Elysium Mons [7].

Stress Models. Our working hypothesis is that volcanic loading of the Martian lithosphere has led to the formation of the tectonic features of the Elysium region. We consider as specific models the local loading by individual volcanoes, the regional-scale loading of Elysium Planitia, and the quasi-global loading of Tharsis. For the loads of individual volcanoes, we use the theory for flexure of a thin elastic shell, and we match the locations of concentric fractures to radial stress profiles predicted by circularly symmetric load models to obtain estimates of the local thickness of the elastic lithosphere at the time of failure [8].

Because the equation for flexure is linear, the stresses due to any distributed load can be represented by the superimposed stresses due to an equivalent distribution of cylindrical loads. We use this Green's function approach to determine the stress distribution predicted by the regional loading model proposed by Janle and Ropers [4] to fit line-of-sight gravity data.

For the Tharsis load, we use the spherical harmonic solution of Banerdt et al. [9] for displacement and stress in a self-gravitating elastic sphere given the topography and gravity. We have calculated the stresses in the Elysium region predicted by two of the Banerdt et al. models for Tharsis: their isostatic model, and their flexural loading model.

Elysium Mons Loading. By comparing the stresses predicted by a 20-disk Elysium Mons load model to the observed distribution of concentric graben,

Comer et al. [10] estimate the thickness of the elastic lithosphere beneath Elysium Mons at the time of graben formation to be 54±6 km, similar to values determined for the Tharsis Montes shields [11]. We have calculated the stresses due to an Elysium Mons load model whose mass distribution more closely matches that of the actual shield, and find no significant difference in predicted lithospheric thickness from that of Comer et al. [10].

Regional-scale Loading. We have examined several different models for loading by Elysium Planitia volcanic units. The load models are based on the gravity models of Janle and Ropers [4] and consist of combinations of tapered disk loads ranging in size from individual shields to regional volcanic units. We treat the degrees of local compensation of the various disk loads as adjustable parameters. All sets of models predict a greatest extensional stress that is approximately radial to the center of mass of the total load (a point lying between Elysium Mons and Hecates Tholus). Such a stress field cannot explain the linear tectonic features which have pronounced NW-SE trends.

Tharsis Loading. The Banerdt et al. [9] isostatic model predicts compressive principal stresses in the vicinity of Elysium; the direction of the least compressive stress is inconsistent with the NW-SE trending features found throughout Elysium, although it is generally consistent with the N-S trending ridges found in eastern Elysium.

The flexural loading model, held by Banerdt et al. [9] to represent a later stage in Tharsis evolution, predicts extensional principal stresses in eastern Elysium. The orientation of the maximum extensional stress is consistent with the major extensional features of eastern Elysium Fossae and with the scarp system Cerberus Rupes. In the Cerberus Rupes region, the magnitudes of greatest extensional stress range from approximtely 300 to 600 bars, suggesting that these features may be predominantly the result of Tharsis loading. The principal stresses predicted by the Tharsis flexural model are compressive in western and southern Elysium, with the axis of least compressive stress oriented NE-SW. Such a stress field, if combined with a horizontally isotropic extensional stress (such as one due to planetary thermal expansion [12]), could produce NW-SE trending linear extensional features (e.g., Elysium Fossae), but it then becomes difficult to explain why there are relatively fewer extensional features in eastern Elysium.

Combination Models. We have calculated the stresses due to various linear combinations of regional loading models, the Banerdt et al. [9] Tharsis models, and a globally uniform and horizontally isotropic stress field. In general the combined stress field is dominated by Tharsis-related stresses except in the immediate vicinity of the volcanic loads. No single combination model can account for both the NW-SE trending linear extensional features found in western and central Elysium and the N-S trending ridges in eastern Elysium.

Conclusions. The concentric graben surrounding Elysium Mons can be ascribed to the flexural response of an approximately 50-km-thick elastic lithosphere to loading by the volcano. We find no tectonic evidence for the support of larger-scale Elysium Planitia volcanic units by lithospheric flexure; either such flexural stresses are small or the major volcanic plains units of Elysium are locally and essentially fully compensated [4]. The

quasi-global loading of the Tharsis rise appears to have produced identifiable tectonic effects in the Elysium region; both the isostatic and flexural Tharsis models of Banderdt et al. [9] are consistent with subsets of the Elysium tectonic features.

References: [1] M.H. Carr (1973) JGR, 78, 4049; [2] M.C. Malin (1977) BGSA, 88, 908; [3] W.L. Sjogren (1979) Science, 203, 1006; [4] P. Janle and J. Ropers (1983) PEPI, 32, 132; [5] J.B. Plescia and R.S. Saunders (1979) PLPS10, 2841; [6] J.L. Hall et al. (1983) Lunar Planet Sci. XIV, 275; [7] P.J. Mouginis-Mark et al. (1984), Earth Moon Planets, 30, 149; [8] S.C. Solomon and J.W. Head (1979) JGR, 84, 1667; [9] W.B. Banerdt et al. (1982) JGR, 87, 9723; [10] R.P. Comer et al. (1984) RGSP, submitted; [11] R.P. Comer et al. (1980) Lunar Planet Sci. XI, 171; [12] S.C. Solomon (1978) GRL, 5, 461.

LITHOLOGIC AND STRUCTURAL CONTROL ON SLOPE MORPHOLOGY IN THE VALLES MARINERIS

Peter C. Patton, Department of Earth and Environmental Sciences
Wesleyan University, Middletown, CT 06457

Throughout the Valles Marineris scarp morphology varies as a function of lithology, structure and scarp height. In addition lithology is an important control on permeability and the relative importance of spring sapping processes. Geomorphic mapping of distinct subareas can be used to define the characteristic scarp forms. Distinct morphologic zones can be defined on the basis of regional variations in lithology, but these broad generalizations must be locally modified because of the influence of scarp height and structure. The general morphologic regions consist of Noctis Labyrinthus and the westen end of Ius Chasma, west of approximately 90° west longitude; the large chasmata, Ius, Melas, Candor and Coprates to about 55° west longitude; and the eastern chasmata of Eos, Capri and Gangis. While the morphologic boundaries are close to the boundaries between the three major stratigraphic units; cratered plains, ridged plains and cratered plateau, respectively; they do not coincide.

Scarp forms within Noctis Labyrinthus are developed on mesas formed along three intersecting fracture systems (Plescia and Saunders, 1982). The troughs have evolved through the coalesence of discrete centers of subsidence and the size of the residual plateau is inversely proportional to the fracture density. Slopes are completely mantled with talus, merge gradually with the canyon floor and have a nearly ubiquitous cap rock. In places this cap rock corresponds to the Syria Planum Flow Unit 2 but is usually mapped as undivided Terra Material (Scott and Tanaka, 1981). Where the plateau has been eroded to a single ridge this resistant strata caps the spurs of the residual hillslope. Slope retreat is caused by small scale slumping along preexisting fractures at the plateau margins. The lack of large slumps in contrast to those observed in the eastern chasmata implies that the critical height for instability processes has not been reached in these canyons and/or that talus accumulation has had a buttressing effect on these slopes. No fault scarps are evident along the base of the slopes indicating that deposition following subsidence has buried these stuctures. As a result well developed spur and gully topography is absent from this segment of Valles Marineris.

In central Valles Marineris sub-parallel chasmata are developed along predominantly east-west fractures and scarp walls reach their greatest relief. Large segments of the chasmata slopes are bounded by fault scarps at their base and these slope segments have the best defined spur and gully

topography (Patton, 1981, 1982). The abrupt contact between the chasmata floor and slope base implies motion on these bounding faults after the original period of subsidence and sedimentation. This renewed tectonic activity which lowered the base level of the slopes and increased scarp height is probably the most critical factor in the development of the spur and gully topography (Patton, 1984). By contrast, in Tithonium Chasma and other small parallel grabens there is no evidence of renewed faulting and scarps in these canyons have lower relief, are generally mantled with talus and are more similar to those in Noctis Labyrinthus. The correlation between the presence of fault scarps and the development of spur and gully topography emphasizes the importance of the structural history in the development of scarp forms. Large landslides in these canyons are probably related to greater height of the scarps and perhaps the exposure of less competent cratered plateau material at the base of the scarp beneath the ridged plains unit (De Hon, 1982). Large landslide deposits in Coprates Chasma which originate in the central portion of the scarp have a fluidized appearance (Lucchitta, 1979) which suggests the presence of a highly brecciated lithology within the lower part of these slopes. Well documented large spring sapping channels on the southern margin of Ius demonstrate that subsurface water must have been an important erosional agent (Laity and Saunders, 1981; Kochel and Capar, 1982). One explanation for their preferential location in this region of Valles Marineris may be related to a contact between more permeable and less competent cratered plateau material beneath more resistant ridged plains lithologies.

Finally, the eastern chasmata have irregular embayed slopes characterized by large areas of chaotic terrain at their base. In contrast to the canyons to the west, this segment of the Valles Marineris is exceedingly wide, the result of greater rates of scarp retreat in the less resistant cratered plateau material. The presence of debris fans, streamlined channels on the margins of the chasmata and the direct association with the outflow channels demonstrate the importance of both subsurface and surface water in eroding the scarps in this segment of the Valles Marineris.

In the Valles Marineris lithology and tectonic history are the two most important factors controlling slope development. Regional variation in scarp morphology can be correlated with the orientation and density of fracture systems; scarp height and the presence of rejuvenated fault scarps; and the thickness and degree of exposure of presumably less competent, more permeable, water saturated crated plateau material in the chasmata scarps.

References Cited

De Hon, R. A., 1982, Martian volcanic materials: preliminary thickness estimates in the eastern Tharsis region. J. Geophys. Res. 87, p. 9821-9828.

Kochel, R. C. and A. P. Capar, 1982, Structural control of sapping networks along Valles Marineris, Mars: NASA Tech. Memo. 85127, p. 297-299.

Laity, J. E. and R. S. Saunders, 1981, Sapping processes and the development of theatre-headed valleys: NASA Tech. Memo. 84211, p. 280-282.

Lucchitta, B. K., 1979, Landslides in Valles Marineris, Mars: J. Geophys. Res. 84, p. 8097-8113.

Patton, P. C., 1981, Evolution of the spur and gully topography on the Valles Marineris wall scarps: NASA Tech. Memo. 84211, p. 324-325.

Patton, P. C., 1982, Quantitative morphology of the Valles Marineris Scarps: NASA Tech. Memo. 85127, p. 242-243.

Patton, P. C., 1984, Comparative morphology of large tectonically formed escarpments on Earth and Mars: Geol. Soc. Am. Abstracts with Programs, v. 16, n. 6, p. 620.

Plescia, J. B. and R. S. Saunders, 1982, Tectonic history of the Tharsis Region, Mars: J. of Geophys. Res., 87, p. 9775-9791.

Scott, D. H. and K. L. Tanaka, 1981, Map showing lava flows in the northeast part of the Phoenicis Lacus Quadrangle of Mars: U. S. Geological Survey, Atlas of Mars, Map I-1277 (MC-17NE), scale 1:2,000,000.

VALLES MARINERIS BASIN BEDS: A COMPLEX STORY

B. K. Lucchitta, U.S. Geological Survey, Flagstaff, AZ 86001

High-resolution stereoimages of the central Valles Marineris have enabled detailed geologic mapping in Ophir and Candor Chasmata (quadrangle MTM-05072, scale 1:500,000). The area is covered by Viking Orbiter 1 images of orbits 912 to 917 (resolution about 60 m/pixel), and a narrow strip of Viking Orbiter 1 images of orbit 815 (resolution 25 to 30 m/pixel). Abundant light-colored deposits, both layered and massive, fill the chasmata in this region. Units within these deposits were identified by their erosional characteristics and superposition and cross-cutting relations. Results show that the deposits inside the Valles Marineris are more complex than previously recognized [1,2,3,4]. The beds reflect a history of repeated faulting, volcanic eruptions, and deposition and erosion, resulting in stratigraphic sequences with several unconformities. Because of the preponderance of apparent volcanic deposits inside the troughs, the chasmata may not be simple grabens, but rather giant volcano-tectonic depressions. Major events in chasmata development are as follows:

1) Faulting dropped the trough floors to near their present levels. Trough walls were dissected by erosion into spurs and gullies. Ancient landslides, if they existed, were largely obliterated by spur-and-gully erosion and by burial.

2) The troughs were filled with basin beds to about 1000 m below their present rims. The beds were deposited in reentrants and gullies in the Valles Marineris walls, and locally overtopped eroded wall-rock spurs. Their deposition against eroded walls indicates that it was concurrent with or subsequent to the faults that formed the troughs and erosion that formed the spurs and gullies. The basin deposits, from oldest to youngest, can be described as follows:

a. A sequence of beds of two types: (1) Prominent, dark, even, smooth layers that are resistant to all forms of erosion. The layers form ledges near the base of slopes or form mesas on the trough floors. (2) Less resistant interbeds that are light colored, massive, and smooth in southwest Ophir Chasma; and light colored, even bedded and thin bedded with local wind fluting in west Ophir and west-central Candor Chasmata and perhaps in east-central Candor Chasma. In southwest Ophir Chasma, an erosional unconformity occurs above the basal bed, which is light colored and massive. The dark, ledge-forming layers are interpreted to be mafic volcanic flows because of their dark color and resistant appearance; the lighter layers may be mixtures of more felsic volcanic and air-fall or water-laid materials.

b. A very light colored, massive, thick-bedded deposit. This unit yields readily to wind erosion and is conspicuously fluted in exposures facing all compass directions except east. The unit occurs in Ophir Chasma and east-central and central Candor Chasma, but is

either absent or has changed facies and is more thinly bedded in west-central Candor Chasma. The unit is interpreted to be composed of thick sequences of ash-flow tuffs because of its light color, thick bedding, susceptibility to erosion by wind and surficial resemblance to terrestrial ash flows.

c. A unit of even, alternating thin and thick beds. This unit is deposited on an uneven surface formed by either depositional irregularities or a minor interval of erosion. The unit forms steeper slopes than the underlying massive unit; it is little affected by wind erosion and appears generally more resistant than other units (except for the dark ledges in the basal part of the entire sequence). The layered unit is well exposed in east-central Candor Chasma, may be present in west-central Candor, but appears largely absent in Ophir Chasma. The unit may be composed of air-fall or reworked tuffs and volcanic flows, perhaps intermixed with fluvial deposits.

3. Episodes of tectonism and major erosion ensued. The basin beds were faulted; a few were thrust faulted, folded or tilted. They were also deeply dissected, so that they form interior mesas standing as much as 6 km above the trough floors. A large "moat" formed in many places between the interior mesas and the walls of the troughs. Only small remnants of basin beds were left in protected niches in wall-rock gullies bordering the moat. Huge landslides fell into the newly formed low areas.

4. A second sequence of deposits was emplaced. These beds have varied and contrasting albedos, which locally give the sequence a mottled appearance. Their texture is also highly varied: locally surfaces are rugged with irregular or linear patterns, in places beds are thin but irregularly layered, and elsewhere they may be fluted by wind erosion. The sequence has bright, steep, slightly sinuous fronts in east-central and west-central Candor Chasma. It also contains dark and light patches and stubby dark flows along faults. In places, it has associated dark knobs, sharp linear ridges, volcanic cones, and lobate flows. The rugged materials are interlayered with light-colored, thick, soft-appearing, smooth material that forms gently rolling topography and displays fine incipient wind-erosion flutes. This interlayered material is thick bedded but does not form ledges. It is associated with at least two large (5- to 7-km diameter) volcanic craters and several caldera-like depressions.

Deposits of episode 4 are highly unconformable with all other units in the troughs and occur at different elevations, ranging from near the top of interior mesas to the floors of the troughs. The deposits overlap erosional surfaces on all older units including folded and tilted basin beds and a landslide-debris blanket. The sequence has few superposed impact craters. By all indications, it is young. The association with volcanic flows, cones, and volcanic craters suggests that the sequence is of volcanic origin; its morphology and albedo suggest that it is composed of felsic and mafic rocks.

Overall, the history of the Valles Marineris is complex. An early episode of infilling of the troughs with layered beds and volcanic flows, interrupted by minor erosional intervals, occurred during or shortly after the time of spur-and-gully development. This episode was followed by structural deformation, extensive erosion, and renewed volcanic infilling in relatively recent time.

References

[1] McCauley, J.F., 1978, Geologic map of the Coprates quadrangle of Mars: U.S. Geol. Survey Misc. Inv. Ser. Map I-897.

[2] Blasius, K.R., Cutts, J.A., Guest, J.E., and Masursky, H., 1977, Geology of the Valles Marineris: First Analysis of imaging from the Viking 1 Orbiter Primary Mission: Jour. Geophys. Res., v. 82, no. 28, p. 4067-4091.

[3] Peterson, C., 1981, A secondary origin for the central plateau of Hebes Chasma: Proc. Lunar Planet. Sci. Conf. 12th, p. 1459-1471.

[4] Lucchitta, B.K., 1982, Lakes or playas in Valles Marineris (abstract). In Reports of Planetary Geology Program 1982, NASA TM 85127, p. 233-234.

MARS: STRATIGRAPHY OF WESTERN HIGHLANDS AND POLAR REGIONS

Kenneth L. Tanaka, David H. Scott, and Marlene F. Tuesink, U. S. Geological Survey, Flagstaff, Arizona 86001

Recent geologic mapping and stratigraphic studies of Mars based on Viking images have improved our knowledge of the relative age and occurrence of geologic units on a global scale. A partial stratigraphy of the western highlands and polar regions is presented here (Table 1).

Western highlands: Most of the heavily cratered plateau terrain in the western highlands of Mars is situated peripheral to Tharsis volcanic rocks and ridged plains deposits surrounding Valles Marineris (Fig. 1). We have obtained cumulative counts of crater-size frequencies for craters larger than 2 km in diameter on plateau units mapped in the western region of Mars [1], using the technique of distinguishing superposed from partly buried craters [2]. These counts indicate that the plateau terrain as a whole was thinly resurfaced during the Hesperian Period, and a large proportion of pre-existing craters less than 10 to 15 km in diameter was buried. Regional deficiencies in large-crater populations suggest thicker and more extensive resurfacing events. These regional variations shown in Fig. 1 apparently were caused by a pulse of intercrater volcanism within about 2000 km of the Argyre Basin mountain terrain. The pulse was stimulated by the Argyre impact. Another episode of pervasive intercrater volcanism occurred during Hesperian to early Amazonian time between long 60° and 180° W. The densities for early Noachian large craters in the western part of Mars match or exceed those for some of the heavily cratered terrain in the eastern part [3].

North polar and northern plains regions: Recent mapping of the north polar and northern plains regions of Mars [1; work in progress] has added to our knowledge of the history of this one-fourth of the planet's surface. Knobby terrain that appears to be a degraded form of highland terrain extends from the highland-lowlands scarp as far north as lat 70° N. Its recognition so far north suggests that most, if not all, of the northern lowlands formed by degradation of former highland terrain. Such degradation may have been due to periglacial, mass-wasting, fluvial, and eolian processes. The formation of these lowlands presumably began in the polar latitudes, where highland terrain is virtually absent, and expanded into present areas due to one or more of the following processes: alluvial flooding (as in Chryse Basin) [4]; possible deposition of ground ice and its later release due to extensive, voluminous, and long-lived volcanism (as in the Tharsis and Elysium regions) [5]; and ice sapping (as at Deuteronilus Mensae). These processes were most active during Hesperian time and continued in places into late Amazonian time. Lowland surfaces north of about lat 55° N. that underlie uncratered polar layered material are mostly early Amazonian in age according to crater density stratigraphy [1]; however, widespread small knobs and pedestal craters and terraced remnants of patterned plains and mantled patterned plains in Borealis Chasma (lat 81° N., long 59° W.) suggest that the subpolar mottled and knobby plains have been stripped of a thin layer of early to middle Amazonian-age deposits.

South polar region and subpolar highlands: In contrast to the relatively young northern plains where older highland materials have nearly disappeared, the south polar region of Mars is dominated by Noachian highlands and Hesperian intercrater plains material and volcanic fields (Table 1) [4; work

in progress]. The character of the highland terrain is similar to that found in equatorial regions [1]. The oldest rocks exposed are rugged basement material along impact-basin rims at Hellas, Argyre, and Promethei Rupes. Noachian fluvial dissection occurred on rugged heavily cratered terrain, and Hesperian channels and furrows cut ridged plains along the southern rim scarp of Hellas Basin. Etching of the plateau materials occurred mostly during the Hesperian Period and was associated with local volcanism, forming Cavi Angusti and Sisyphi. This etching is deeper than found elsewhere on Mars and may be caused by eolian deflation of a deep, ice-rich zone. In the south polar region overall, volcanic activity was sporadic in Hesperian time and virtually nonexistent during Amazonian time. This near absence of volcanism may help to explain why degradation of the south polar highlands was limited to formation of local cavi and channels, in contrast to the widespread disappearance of the northern highlands where volcanism was more prevalent. The south polar layered deposits appear to be poorly consolidated, have very few superposed craters [4], and overlie Hesperian- and Noachian-age materials.

References: [1] Scott, D. H., and Tanaka, K. L., 1984, U. S. G. S. Open-File Report 84-659-A. [2] Scott, D. H., and Tanaka, K. L., 1981, Icarus, v. 45, p. 304-319. [3] Gurnis, M., 1981, Icarus, v. 48, p. 62-75. [4] Scott, D. H., and Tanaka, K. L., this publication. [5] Soderblom, L. A., and Wenner, D. B., 1978, Icarus, v. 34, p. 622-637.

TABLE 1. GENERALIZED STRATIGRAPHY OF MARS BY REGION

Geologic unit or feature	Equatorial region[a]	North Pole region (lat >55°N.)	South Pole region (lat <-55°N.)	
Polar ice		XXXXX[b]	X	Amazonian
Polar layered material		XXX	XXXXX	
Dune deposits	X	XXXXX	X	
Mottled/knobby plains material	XX	XXXXX		
Channel material	XXXXX			
Volcanic fields	XXXXX			
Channels/chaotic terrain	XXXXX			Hesperian
Knobby terrain	XXXXX	XX	X	
Volcanic fields	XXXXX		XX	
Ridged plains	XXXXX		XXXXX	
Deeply etched terrain			XXXXX	
Plateau material	XXXXX		XXXXX	
Fractured terrain	XXXXX			
Cratered plateau material	XXXXX		XXXXX	Noach.
Ridged plateau deposits	XXXX		XXXXX	
Impact basin rims	XXXXX		XXXXX	
Basement/fractured terrain	XXXXX			

[a]Includes western highlands (described in text).
[b]Number of X's denotes relative proportion compared with other regions.

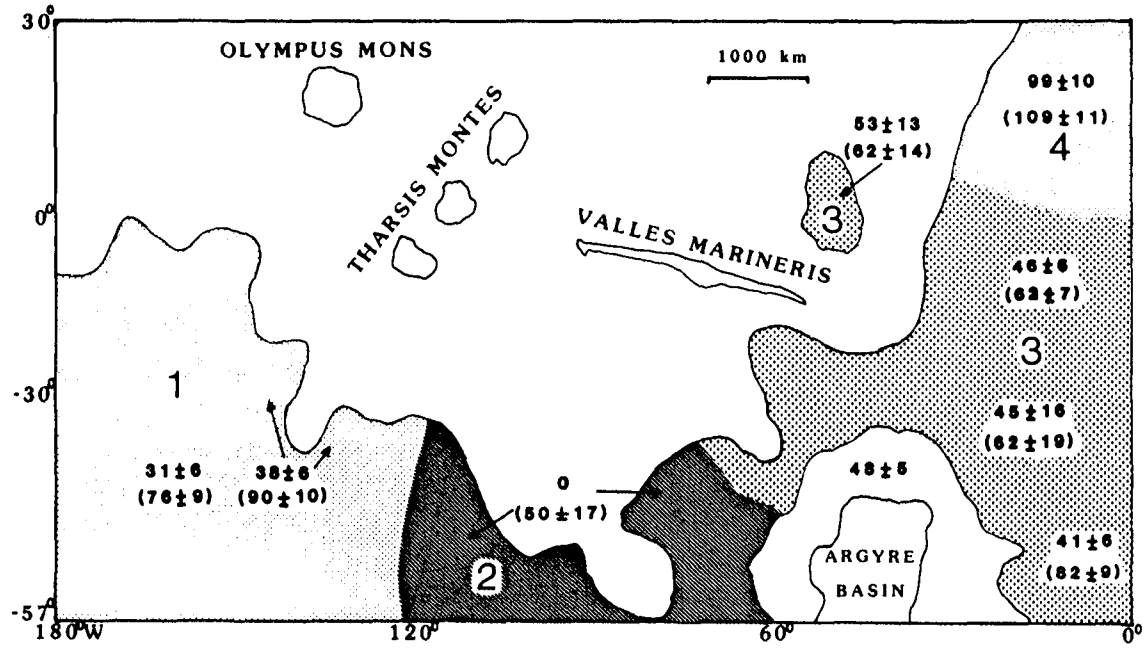

Figure 1. Map of western highlands of Mars generalized from [1] showing occurrence of heavily cratered plateau rocks of Noachian age (stippled patterns) and degree of resurfacing stimulated by the Argyre Basin impact. Heavy stipple indicates complete burial of pre-Argyre craters <45 km in diameter; medium stipple, partial burial of pre-Argyre craters >16 km in diameter; light stipple, Argyre-age resurfacing not detected. Unstippled area around Argyre Basin indicates Argyre Basin mountain material of late Noachian age; remainder of unstippled area represents post-Noachian materials. Large numbers indicate four areas of plateau terrain distinguished on the basis of populations of craters 16 km in diameter and larger. These areas are characterized by: (1) Population of large craters that dates back to early Noachian; extensively resurfaced during early Hesperian. (2) Craters 16 to 45 km in diameter having Argyre-age density; most are embayed by pervasive Hesperian and Amazonian deposits. (3) Population of early- to mid-Noachian craters larger than 16 km embayed by Argyre-age deposits. (4) Very early Noachian age; only minor resurfacing and embayment of craters larger than 16 km diameter. Small numbers indicate cumulative density of superposed craters larger than 32 km in diameter per 10^6 km^2; numbers in parentheses indicate cumulative density of all craters larger than 32 km in diameter per 10^6 km^2.

KASEI VALLIS OF MARS: DATING THE INTERPLAY OF TECTONICS AND GEOMORPHOLOGY

WISE, Donald U., Dept. Geology/Geography
University of Massachusetts, Amherst, MA 01003

Crater density age dates on more than 250 small geomorphic surfaces (terraces, fans, islands, etc.) in the Kasei Region of Mars show clusterings indicative of times of peak geomorphic and tectonic activity. All dates are given as crater numbers (number of craters > 1 km/10^6km^2) as derived by projection using the standard curve of Neukum and Wise (1976). Kasei Vallis is part of a 300 km wide channel system breaching a N-S trending ancient basement high (+50,000 crater age) separating the Chryse Basin from the Tharsis Volcanic Province of Mars. The basement high was covered by a least 3 groups of probable volcanic deposits, commonly lumped under the term Lunae Planum (20,000, 10,000 and 5,000 ages). Major regional fracturing took place at age 4,000-5,000 and was immediately followed by deposition of regional volcanics of the Fesenkov Plains (age 3,000-4,200). The only major younger fracture system (N50E) cutting the Fesenkov units also controls much of the structural grain of the Kasei erosion in the time span 2,000-2,500. These dates are widespread in the Kasei Gap and the fans on Chryse at its mouth. Younger clusterings of dates in the 900-1,500 and 500-700 range represent only minor modification of the basic tectonic-geomorphic landform. The main Kasei 2,000-2,500 date is approximately 3 b.y. by analogy with lunar crater data. The dating technique also yields minimum size craters consistently preserved from differing age surfaces: +5 km for 100,000 ages; + 1 km for 13,000 ages and +.25 km for 2,000 ages. These values suggest rates of erosion about 10^{-3} that of terrestrial ones. The data suggest that Kasei gap is a structurally controlled breach of a buried ridge by a rather brief episode of fluvial activity.

CREEP OF ICE: FURTHER STUDIES

H. C. Heard[1], W. B. Durham[1], and S. H. Kirby[2]
[1]UCLLNL, Livermore, CA 94550; [2]USGS, Menlo Park, CA 94025

In the past year our research into the flow and fracture of ice has branched into several areas and we have continued to upgrade the experimental apparatus in order to expand our capabilities. In the ice I_h (i.e. ordinary ice) stability field we have begun doing frictional sliding experiments to study crustal behavior on the icy Galilean satellites, and we are pursuing in detail the microstructural aspects of flow. With the help of a greatly improved heat exchanger and computer control of temperature we have begun exploring the lower regimes of strain rate. We have also achieved a preliminary measurement of the strengths of some of the higher pressure polymorphs of ice. The following paragraphs summarize the results of three studies carried out in the past year.

Frictional Sliding of Ice: We have performed a number of experiments exploring the characteristics of frictional sliding in water ice in its ordinary I_h phase, with application to Ganymede and Callisto. Earlier tests have established the brittle and ductile strength of intact ice under conditions appropriate to the icy moons. However, Voyager photographs indicate that fractures (normal faults expecially) are an important tectonic feature on Ganymede and Callisto. The strength of existing faults has an effect on the shape of local features (depth of graben, for example) and may have an important influence on the overall strength of the near surface layers of those bodies.

The test samples were cylinders of laboratory-made polycrystalline ice 25.4 mm in diameter and 63.5 mm long in which a sawcut was made at 45° to the loading axis. The sawcut surfaces were shaved flat and ground with a fine wire screen. Samples were jacketed in 0.5 mm-thick indium. Testing was done at a constant (longitudinal) displacement rate of 2×10^{-3} mm/s, T = 77 K, and confining pressure P = 10 to 150 MPa. The frictional behavior of the samples was without exception stick slip, and in most cases strength increased after each stick slip event in a given sample, perhaps because of improved surface-to-surface contact as sliding proceeded. For first events only, the relation between shear stress (τ) and normal stress (σ_n) was $\tau = 3 + 0.2\sigma_n$ (in MPa). For maximum strength events it was approximately $\tau = 10 + 0.2\sigma_n$. We note that the coefficients of friction are considerably less than for most other rocks.

Thin Section Studies: We have conducted petrographic studies of optical scale structures and textures for three suites of experimentally deformed ice in an effort 1) to understand the yield point behavior observed in stress-strain curves, 2) to suggest mechanisms for the three temperature regimes of steady-state flow reported in Durham et al. [1], and 3) to examine grain textures in samples that have undergone phase changes during experiments. To investigate yield point behavior, we performed constant-strain-rate tests at $\dot{\varepsilon} = 3.5 \times 10^{-4} s^{-1}$, T = 213 K, and P = 50 MPa to four different strains. At strains less than where the ultimate strength, σ_{max}, was reached, grains are deformed but not recrystallized, whereas at strains beyond the point of σ_{max},

recrystallization is responsible for the strain weakening. To investigate the three temperature regimes of steady state flow reported in Durham et al. [1], we studied samples deformed to steady-state at $\dot{\varepsilon} = 3.5 \times 10^{-5}$ s^{-1} and 3.5×10^{-4} s^{-1}, and P = 50 MPa, at temperatures of 183, 195, 213 and 244 K. Variations in grain size, grain shape and the degree of undulatory extinction seen in the samples suggest that deformation at T > 243 K is rate-controlled by grain boundary mobility facilitated by grain boundary melting, deformation at intermediate temperatures (195-243 K) is rate-controlled by recrystallization, and deformation at T < 195 K is rate-controlled by intragranular recovery mechanisms although recrystallization occurs in this temperature regime as well. A phase-change sample reverted from ice II to ice I_h and one reverted from ice III to ice I_h were both recrystallized; the grain size in the ice III-reverted samples was reduced by 50%.

Flow of Ices II and III: We have performed exploratory constant strain rate tests at $\dot{\varepsilon} \simeq 4 \times 10^{-4}$ s^{-1} on polycrystalline ice II and III samples produced by pressurizing ice I into the stability fields of ice II and ice III. The onset of transformation was recognized by rapid

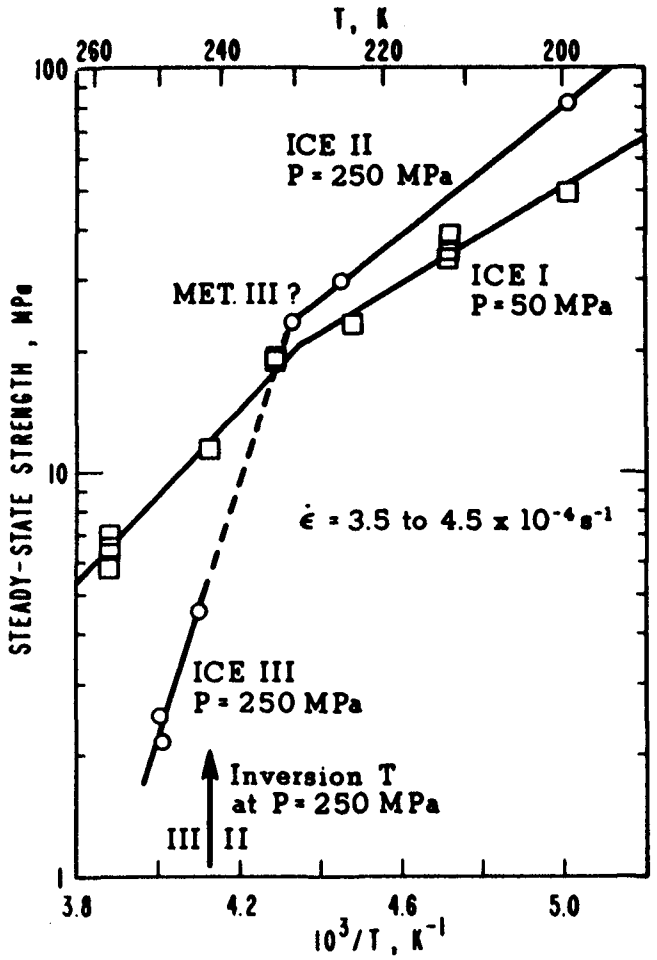

Figure 1. Ductile flow of ices II and III at P=250 MPa compared to the flow of ice I_h at P=50 MPa, all at $\dot{\varepsilon} \sim 4 \times 10^{-4}$ s^{-1}. Circles represent experimental data on ices II and III and the squares represent data on ice I_h. Phase identification is inferred from position in the phase field and metastability information from Bridgman [2]. The data point at T = 230 K is suspected to pertain to ice III existing metastably in the ice II field. At P = 250 MPa the ice II-III boundary occurs at T ~ 240 K.

pressure drops due to the volume reduction to the denser phase, by the measured reduction in sample length, and by the opposite changes during depressurization. The phases were identified by these volume changes, the known phase diagram for H_2O, and recognition of the known conditions of metastability in this system.

The flow of ices II and III at $\dot{\varepsilon} \sim 4 \times 10^{-4}$ s^{-1} is compared to that of ice I_h in Figure 1. The rheologies of ices II and III are distinctly different, with III being more temperature sensitive than either I_h or II. We have made measurements at $\dot{\varepsilon} \sim 4 \times 10^{-4}$ s^{-1} comparing strengths of the phases at common pressures (i.e. transition pressures) and found that ice II is roughly 30% stronger than ice I_h, with the difference not strongly dependent on temperature. The relative strengths of ices I_h and III are very temperature sensitive, as can be inferred from Figure 1. At 244 K, ice III has 40% the strength of ice I_h; at 248 K, ice III has barely 20% the strength of ice I_h. The pressure and stress sensitivity of flow rate of ices II and III are currently under investigation.

References: [1]W. B. Durham, H. C. Heard, and S. H. Kirby (1983), Experimental deformation of polycrystalline H_2O ice at higher pressure and low temperature: preliminary results J. Geophys. Res., 88, B377-B392; [2]P. W. Bridgman (1911), Water, in the liquid and five solid forms, under pressure, Proc. Am. Acad. Arts Sci., 47, 347-438.

FAULT OFFSETS AND LATERAL CRUSTAL MOVEMENT ON EUROPA

Paul M. Schenk, Dept. Earth and Planetary Sciences and McDonnell Center for the Space Sciences, Washington University, Saint Louis, MO 63130

The surface features of the bright ice covered Galilean satellite Europa are dominated by abundant long narrow brownish lineaments and irregular brownish terrain units subdivided on the basis of morphology and color (Smith et al., 1979; Pieri, 1981; Lucchitta and Soderblom, 1982). A fracture origin for many of these lineaments has been proposed by these authors. Here I present structural evidence for tension cracking associated with strike-slip faulting and crustal movement.

The most ubiquitous lineament type is the "simple" lineament (equivalent to Types 4 and 5 of Pieri, 1981), so called because they consist of single, long, narrow, (~8 km) dark bands. There are two sub-types of simple lineaments; straight northeast-southwest trending lineaments usually less than 200 km long concentrated southwest of the anti-jove point (Type 5; Pieri, 1981), and longer (up to several 1000 km), more arcuate lineaments found to the north and east (Type 4). Brown wedge-shaped bands are associated with and very similar to the short Type 5 simple lineaments near the anti-jove point except that they are wider (up to 40 km wide and 200 km long) and generally wedge-shaped. The edges of the wedge-shaped bands fit tightly together when the sides are rejoined, much like jigsaw puzzle pieces, indicating the edges of the bands were once together. A pair of older simple lineaments (C) (Fig. 1) and a triple band (D), each on the north side of northwest trending lineament (H), can be realigned with counterparts on the south side of (H) when the crustal blocks on either side of (H) are moved such that the sides of wedge-shaped bands (A), (B) and (L) are brought together, as in the reconstruction in Fig. 1. The width, morphology and direction of the older lineaments (C) and (D) become continuous across lineament (H) when reconstructed. Both (C) and (D) have been offset by right-lateral movement along lineament (H). These offsets appear to result from rifting and rotational separation of crustal elements due to the opening of fractures (A), (B) and (L). Additional unlabeled lineaments (Fig. 1) also appear to have been offset. The amount of lateral displacement of (C) and (D) is consistent and matches the maximum width of bands (A) and (B), at 25 +/- 3 km.

Graben formation is probably not involved in the formation of these features as the measured offsets of lineaments along (H) would be significantly less than the width of band (A) if a down-dropped block were buried under band (A), as much less extension is required to produce graben or normal faulting, then to dilate a simple fracture. Lineaments (F) and (G) strongly resemble transform-type faults in that they appear to offset the three wedge-shaped bands (B), (J) and (K) in the same direction and approximately the same amount (~25 km). Both (J) and (K) are thus interpreted as offset extensions of the wedge-shaped band, or fracture (B). Numerous additional wedge-shaped bands up to 20 km wide, oriented dominantly northwest-southeast, are distributed in a northwest-southeast

trending belt ~1300 km long and less than 500 km wide, southwest of the anti-jove point. The demonstrated offsets, opening of fractures, rotation of crustal blocks and restricted belt-like distribution of the subparallel wedge-shaped bands indicate that these lineaments mark a major fracture zone in Europa's crust (Fig. 2). Perpendiculars to inferred transform faults (i.e. simple lineaments) near the anti-jove point converge in a region north of Thrace Macula at approximately 38° S, 160° W, +/-10°. The convergence of most of the perpendiculars is consistent with a crustal rift zone model and suggests that most of the icy crustal blocks, with few exceptions, have probably moved with a common sense of motion. Several lines of evidence suggest that the bright band Agenor Linea may be a compressional feature related to this rift zone. Its lobate pattern is loosely reminiscent of some terrestrial subduction zones (e.g. Marianas and Peru-Chile trenches), wrinkle ridges, and lobate scarps on Mercury, which are most likely of compressional origin. Agenor Linea is subparallel to and approximately the same length as the wedge-shaped band rift zone and is approximately radial to the proposed pole of rotation. Rotation arcs concentric about the proposed rotation pole and drawn through the rift zone intersect Agenor Linea along its length (Fig. 2). An association between the two features, although speculative, is plausible.

The structure and morphology of wedge-shaped bands argues that they formed as a result of the rotation and lateral displacement of crustal units bounded by near-vertical faults penetrating through the brittle crustal layer. The significant rotation and lateral motion of crustal blocks near the anti-jove point on Europa, withouth graben formation, also argues that the lithosphere in the fractured area is mechanically decoupled from the 'solid' silicate interior, by either warm ice at depth or liquid water. Ice at depth and at a large fraction of its melting temperature is expected to behave as a fluid over geologically short time intervals due to its extremely low viscosity relative to the cold, brittle ice near the surface. One proposed convection mechanism (Finnerty et al., 1981) is thus considered unlikely as it would be difficult to transmit internal stress through a decoupling layer to the surface. An alternative to silicate convection is convection in a warm, low viscosity layer at depth within the icy crust (Cassen et al., 1982).

This research was partially supported by NASA grant NAGW-432.

REFERENCES

Cassen, P., et al., in Satellites of Jupiter, pp. 93-128, 1982; Finnerty, D., et al., Nature 289, 24-27, 1981; Lucchitta, B., and Soderblom, L., in Satellites of Jupiter, pp. 521-555, 1982; Pieri, D., Nature 289, 17-21, 1981; Smith, B., et al., Science 206, 927-950, 1979.

Figure 1

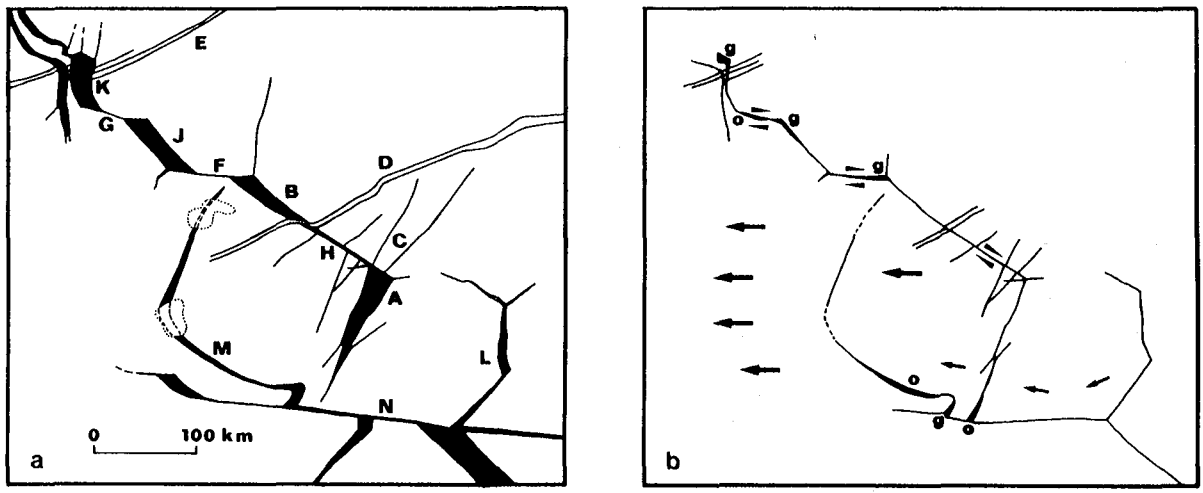

Figure 2

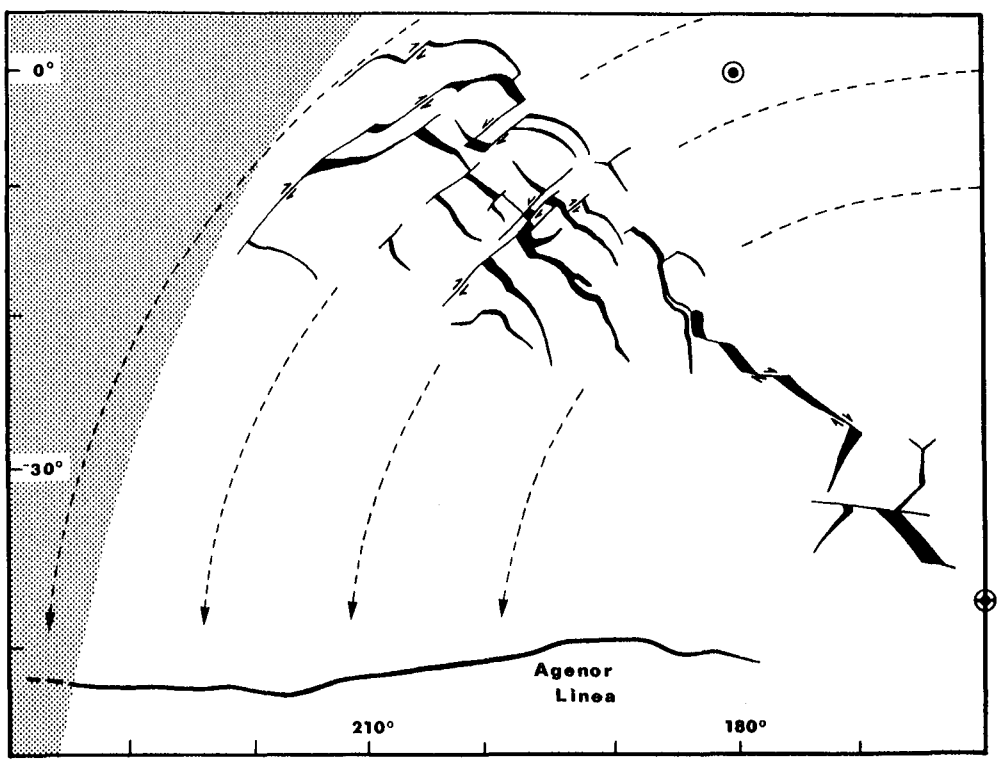

THREE-LAYER GENERIC GANYMEDES: STRUCTURE AND EVOLUTION

S.W. Mueller and W.B. McKinnon, Dept. Earth and Planetary Sciences and McDonnell Center for the Space Sciences, Washington Univ., Saint Louis, MO 63130.

Accurate, three-layered structural models were generated for Ganymede and Callisto. Three-layered satellites consist of a rock core, a region of mixed rock and ice, and an outer shell of pure ice. This structure would result from either accretional melting of the outermost region of the satellite or differentiation subsequent to localized melting. Thus, the three-layered approach may shed some light on the evolution of ice-rock satellites.

Considerable attention was given to evaluating various alternatives for the rock component. Our first, and wettest, choice was C1 carbonaceous chondrite, a popular candidate for a primordial rock type. Our second choice was a mineral assemblage predicted by Prinn and Fegley (1) to have condensed from a Jovian nebula and possesses a water content intermediate between C1 carbonaceous chondrite and a completely anhydrous assemblage which represents our third choice - called pre-tremolite condensate (PTC) because it is based on the important rock-forming minerals that occur in the condensation sequence prior to tremolite, the first water-bearing phase. Condensation considerations suggest that PTC is an unreasonable choice for a primordial rock type; therefore, we only consider PTC as a core alternative. All three of our rock types are based on solar elemental abundances; thus, it seems plausible that the drier assemblages could be produced from the wetter assemblages after incorporation into a warm rock core. Also, free energy calculations indicate that C1 rock would not be stable at the pressures encountered in the Galilean cores due to dehydration of epsomite and gypsum. For these reasons, we generate no models with PTC in the mix or C1 in the core. Effective whole-rock equations of state are constructed from the physical properties of the component minerals.

Satellite structures (Figs. 1 and 2 are examples) are determined on the basis of a 250 K isotherm, which is a reasonable approximation to the gentle adiabats expected to occur in icy satellites. Differentiation, as the result of localized (non- accretional) melting, requires the existence of a transient liquid-water region which cannot be incorporated into our sub-liquidus, isothermal models; therefore, we can only generate "pseudo-evolutions". However, refreezing of even an extensive liquid-water region would result in very little change in satellite radius (2) and our "pseudo-evolutions" should provide good approximations to reality. Differentiation of an ice-rock satellite generally involves an increase in satellite radius; our three-layered approach allows us to look at this behavior in some detail. As differentiation proceeds, and more rock migrates downward, the average pressure to which ice is subjected to is reduced. Just as importantly, the difference in average ice pressure

between two neighboring differentiation states decreases - the result is initially rapid satellite expansion followed by a period of less vigorous expansion (Figure 3). This "plateau effect" is important because it indicates the difficulty in distinguishing, on the basis of surface inferences alone, between a completely differentiated Ganymede (for example) and a Ganymede that is only partially differentiated. Useful quantities such as J_2, binding energy, and heat flow (both present-day and 4by ago) were calculated on the basis of the structural models.

Finally, we evaluated the relative likelihood of melting of the various models. Our approach was to assign the same Rayleigh number to each convective boundary layer and then determine the minimum Rayleigh number required for melting (i.e., the thermal profile that barely intersects the melting curve). This method does not require that the top and bottom boundary layers of a given cell be identical and allows each individual boundary layer to adjust to the local viscosity (which can vary considerably throughout the satellite). The result was a bimodal distribution of minimum Rayleigh numbers. Models with small degrees of differentiation ($\lesssim$35% of silicates reside in core) require Rayleigh numbers of 25 to 50 for melting; more differentiated structures require Rayleigh numbers of at least 800. This is because the position of the 2nd and 3rd boundary layers is determined by the position of the mix-pure ice interface. For small degrees of differentiation this interface remains near the surface and in the vicinity of the triple-point of ice (the minimum melting temperature); thus, there are three boundary layers available to reach this minimum melting point and only small Rayleigh numbers are necessary. For larger degrees of differentiation the interface is located a safe distance below the triple-point and a single (top) boundary layer must provide the necessary temperature increase to reach the minimum melting temperature and this requires a significantly higher Rayleigh number. A completely undifferentiated ice-rock satellite possesses only the single, top boundary layer and, in this case, melting is also relatively difficult to initiate; this suggests that, if accretional melting results in a small degree of differentiation initially, subsequent melting may readily occur as the satellite warms due to radiogenic heating. Alternatively, if accretion is not accompanied by a small degree of differentiation, it may prove too difficult to initiate non-accretional melting and the satellite might remain undifferentiated indefinitely.

This research was supported by NASA Grant NAGW-432.

REFERENCES

(1) Prinn, R.G., and Fegley, B. Jr. Astrophys. J. 249, 308-317 (1981).
(2) Squyres, S.W. Geophys. Res. Lett. 7, 593-596 (1980).

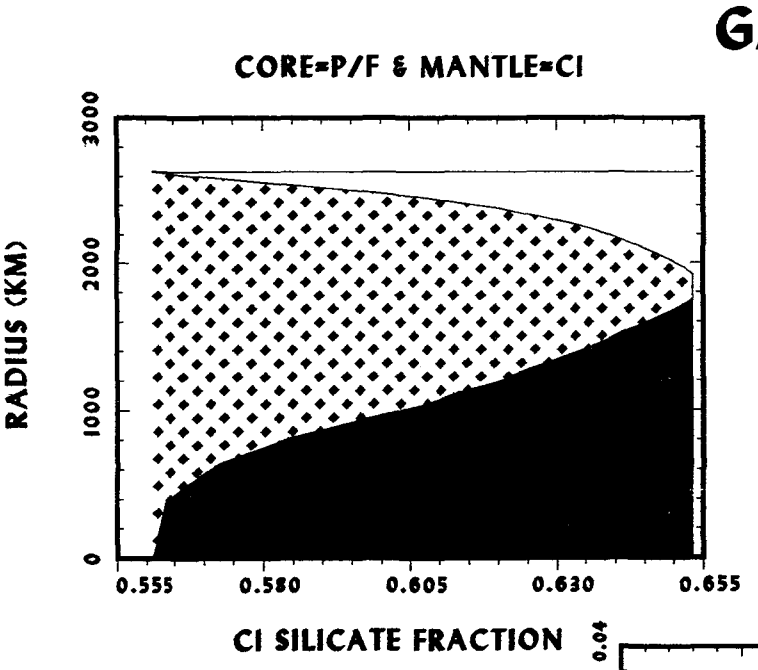

Figure 1.

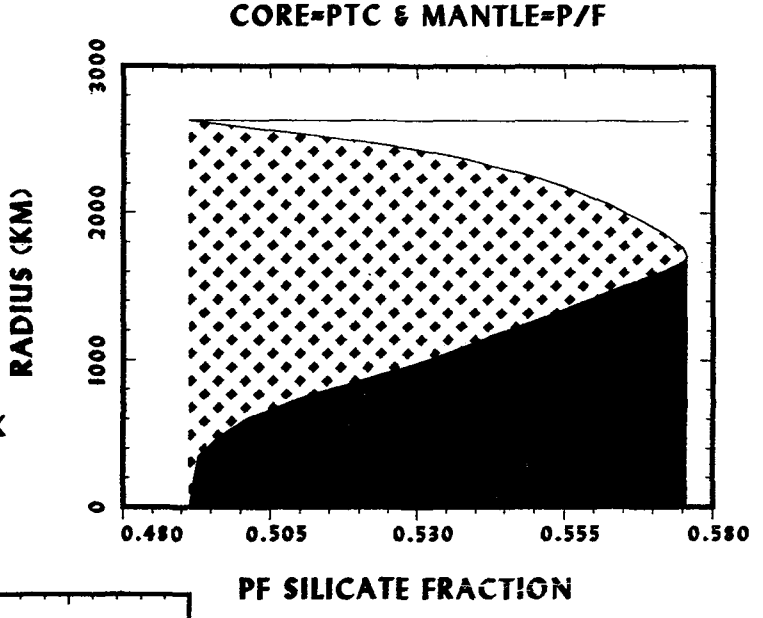

Figure 2.

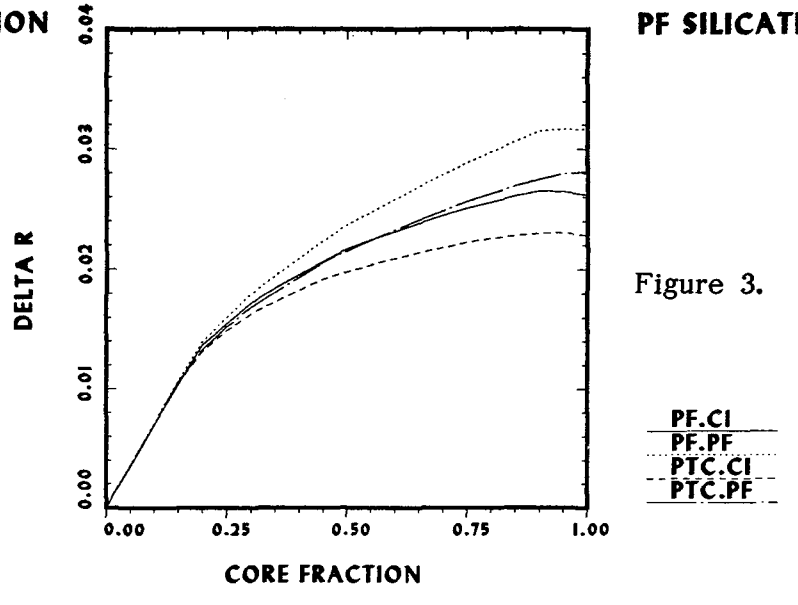

Figure 3.

Lineaments on Ganymede: New Evidence for Late Tectonic Activity

Steven K. Croft, Lunar and Planetary Laboratory
University of Arizona, Tucson, Arizona 85721

Tectonic and volcanic features on a planet's surface provide important constraints on the inferred geologic and thermal history. Observed systems of furrows and grooves (e.g., 1-5), and inferred episodes of resurfacing based on low crater counts compared to neighboring Callisto (4, 6) have been discussed relative to the thermal history of the icy jovian satellite Ganymede. In the course of a structural study of impact basins on Ganymede (7), an additional class of tectonic features - lineaments - was recognized.

Description. Figures 1a, b show, respectively, a photomosaic and geologic sketch map (from 7) of the Gilgamesh basin and environs. Two directional families of lineaments are indicated (though not all individual lineaments are drawn) on the map: a NE trending family both to the north and south of the basin center, and a less numerous NE trending family south of basin center. Both sets of lineaments consist of parallel depressions, scarp faces, and flat faces of massifs that frequently occur in sets of three or more, reminiscent of what might be obtained by dragging an enormous 3- or 4-prong rake across the uneven basin floor. Note in particular the gently curving triplet trending NW radial to the basin center. Figure 2 is an image (FDS 20638.39) of the Ninki basin (the Western Equatorial basin of Ref. 5). The arrows indicate a family of ENE trending lineaments that cut across the southern rim and floor of this basin. A parallel family of lineaments is visible beyond the basin rim on the NE quadrant of the basin's ejecta. Lastly, figure 3 (FDS 20638.59) shows a rayed 83 km diameter crater north of Gilgamesh whose rim is cut by a NE trending lineament pair (arrow). The pair cuts sharply NNE, tangent to the large central pit, becoming quite deep and intersecting several of the small depressions surrounding the pit before ending in the deposits at the base of the crater's primary scarp. In all three impact structures, the lineaments follow prominent trends of grooves beyond the ejecta blanket: 1) the NW trending lineaments in Gilgamesh follow groove trends to the north and south of the basin while the NE trending lineaments parallel a prominent neighboring set of grooves in the south; 2) the lineaments in Ninki parallel grooves to the north of the basin but angle ~50^{o} away from a prominent nearby set of grooves to the SW; 3) the lineament pair in the rayed crater parallel, and appear almost contiguous with, a groove set to the SE. The spacing of the lineaments is close to 3 km in all three cases, significantly less than the typical 5-6 km spacing of the grooves (8). The vertical topography is only on the order of 100 m, again significantly less than the 300-400 m topography of the grooves (8). The global distribution of lineaments is unknown at this point: the features are topographically subtle and show up in figures 1-3 because of the high resolution of these frames (1-2 km per pixel) and the near-terminator lighting conditions.

Discussion. 1) Age Relations: Portions of Gilgamesh's primary rim

(feature 4 in fig. 1b) and secondary concentric rings (features 6) show evidence of pre-impact structural control, and none of the lineaments unabiguously cut the primary rim, hence the lineaments might be considered an expression of pre-impact structures (9). However, the lineament triplet radial to basin center is virtually continuous with ridges and possible flow features superposed on Gilgamesh's central plain, which plains are prominent impact deposits in virtually all basins on Ganymede. This association implies the lineaments represent post-impact tectonic activity. Further, lineaments unambiguously cut the rims of both the Ninki basin and the rayed crater. The cutting of rims and floors in lunar craters by grabens, which closely resemble the lineaments on Ganymede, is evident only in post-impact movements; the rims and floors of craters forming on pre-existent grabens (such as Rima Sirsalis) are not broken. Hence the lineaments are inferred to be primarily post-impact. This inferred age relation has significant consequences. The grooves, previously considered the youngest tectonic features, are estimated to have formed between 3.8 and 3.1 Gyr ago (5). Gilgamesh and Ninki date to the same period. The rayed crater in figure 3, however, is probably less than 1 Gyr old (see 5), implying tectonic activity on Ganymede has extended nearly to the present. 2) Structure & Source: like the grooves, the lineaments appear to be extensional. The parallel trends and nearly contiguous associations of the lineaments with the grooves imply that both are products of the same stress systems. The young inferred age of the lineaments implies that they (and presumably also the grooves) are not associated with stresses in the cooling of fresh deposits of bright terrain, but are probably associated with underlying convective stress patterns (4). Also, the long implied duration of an extensional stress regime in Ganymede's lithosphere is consistent with the stress models of (10) derived assuming a differentiated interior. Thus the existence of lineaments on Ganymede provides new constraints on its thermal history and interior structure.

References. 1) Smith B.A. et al., Science 204, 951-972, 1979. 2) Smith B.A. et al., Science 206, 927-950, 1979. 3) Luchitta B.K., Icarus 44, 481-502, 1980. 4) Squyres S.W. and S.K. Croft, in Natural Satellites, in press, 1984. 5) Shoemaker E.M. et al., in Satellites of Jupiter, p. 435-520, 1982. 6) Strom R., et al., J. Geophys. Res. 86, 8659-8674, 1981. 7) Croft. S.K., Icarus, in press, 1984. 8) Squyres S.W., Icarus 46, 156-168, 1981. 9) Schultz R.A., Icarus, submitted, 1984. 10) Zuber M.T. and E.M. Parmentier, J. Geophys. Res. 89, B429-B437, 1984.

Figure 1a. Gilgamesh Basin.

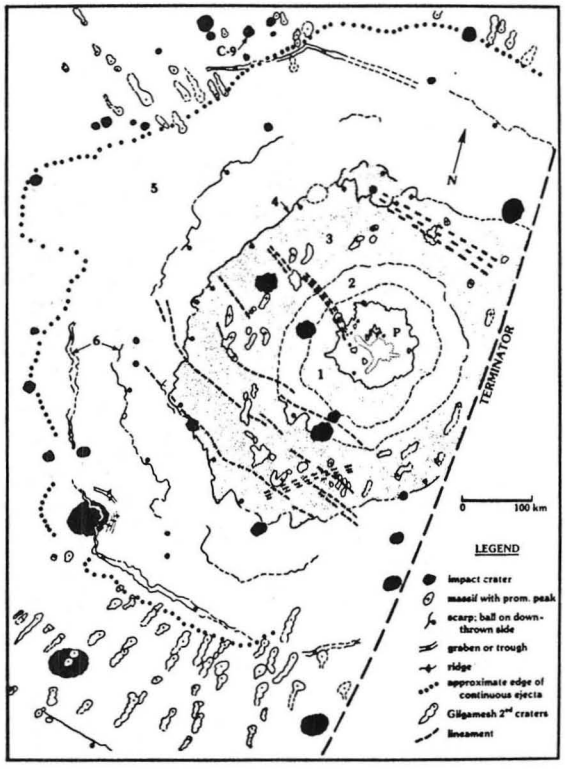

Figure 1b. Gilgamesh Sketch Map.

Figure 2. Ninki Basin.

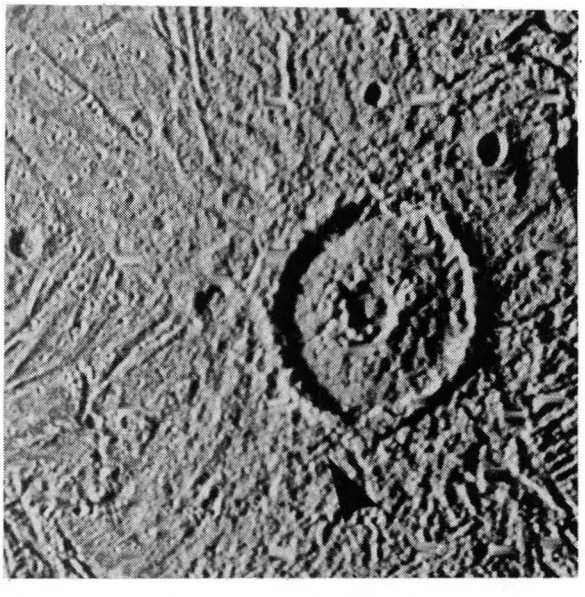

Figure 3. A rayed crater N. of Gilgamesh

GLOBAL TECTONICS ON GANYMEDE

Pierre G. THOMAS, Olivier P. FORNI, and Philippe L. MASSON,
Lab. Geol. Dyn. Int. bat. 509, UA 730, Université PARIS XI,
91405 ORSAY cedex, FRANCE

The surroundings of Orientale on the Moon (Scott, 1977), Caloris on Mercury (Thomas and Masson, 1984 a) and Argyre on Mars (Thomas and Masson, 1984 b) show structural directions that appear to be largely controlled by regional structures. We undertook (Thomas et al, 1984) the study of three large basin surroundings on Ganymede. These three basins are located on grooved terrains, which are supposed to be intensely tectonized areas (Smith et al, 1979). The blocky and mountainous terrains around Gilgamesh, the largest fresh impact basin on Ganymede, exhibit ridges, crests and troughs with somewhere rectilinear or angular appearances. Some of these rectilinear elements - but not all of them - are radial or tangential to the basin. Some rectilinear elements exist also around Western Equatorial and Eastern Hathor basins, two other relatively fresh large impact basins. Looking for an eventual structural control of these ridges and blocks, we have undertaken the mapping of all rectilinear morphologic elements (named "lineaments" in the following) around the 3 basins such as ridges, block edges, rectilinear parts of scarps, ... (fig. 1).

The figure 1 shows the cumulative length of all these lineaments for each basin with respect to the N/S system and also the cumulative length of the Galileo Regio furrow systems (this fourth azimuth rosette is very similar to that of Casacchia and Strom, 1984). Five geometric properties of these lineaments are immediately apparent on this figure:

1) The azimuthal repartition of the lineaments around the 3 basins is absolutely not homogeneous, with significant maxima: N-S, NE-SW and NW-SE for Gilgamesh and Western Equatorial, and only NE-SW and NW-SE for Eastern Hathor. Such a disposition cannot be only due to the impact alone, which would produce an equal repartition of the structures without any preferential azimuthal direction. Thus, though the formation of the crests, ridges and troughs is the consequence of the impacts (they only occurred around the basins), their directions appear to be largely controlled by non basin related structural patterns which predate the impacts.

2)The directions of these preexisting structural patterns do not exhibit any geometric relation with the groove pattern of each basin basement.

3) The directions of these preexisting structural patterns are relatively similar for the 3 studied basins, implying the presence of a "ganymedean grid", at least in the 3 basins areas.

4) The directions of this grid are symmetrical with regard to the actual N/S system.

5)The directions of this grid are the same as the directions of the Galileo Regio furrow systems (Casacchia and Strom, 1984).

Such a pattern, named "grid pattern" characterizes almost all silicated and icy bodies observed so far in the Solar System. Several interpretations were proposed for the origin of these grids; they all

imply tidal forces: tidal deformations (Melosh, 1980) or tidal despinning (Pechmann and Melosh, 1979). The first model produces a fracture pattern symmetrical with respect to the sub-Jupiter point and its antipode. That is not the case of the ganymedean pattern. The second model predicts NE-SW and NW-SE strike slip faults associated with N-S thrust faults pattern, whatever the longitude. The directions of this second theoritical pattern correspond to the directions observed on Ganymede. But the nature of the tectonic elements (furrows in Galileo Regio and uplifted blocks around basins) does not correspond to the theoritical motions along this pattern (thrusts or strike slip faults). That would indicate that the present morphologies are not due to the primitive motions, but to post grid motions re-using the old directions. Thus, whatever the origin of the grid pattern, we propose the following history for Ganymede:

After the grid was generated, the furrows were formed (by an unknown process, Thomas and Masson, this issue) and they partially re-used the directions of the preexisting grid pattern. Then the grooved terrains were formed (also by an unknown process). But, whatever the origin of the grooved terrains, their formation does not seem to be influenced by the preexisting pattern (the groove patterns do not bear any geometrical relation to the grid pattern). But their formation does not distroy or disturb the grid pattern which is still present under the grooved terrains as shown by its influence on the direction of the fractures around the post-grooved terrain impacts; their formation does not rotate the preexisting grid pattern which everywhere exhibits the same directions. Then occurred the impacts of the three studied basins, which induced tectonic motions occurring preferentially along the still present grid pattern, without any preferential motion along the groove pattern' directions. All this would indicate that the grooved terrains are very surficial layers, and that their formation does not significantly affect, disturb or rotate the basement. This is in agreement with the conclusion obtained by Forni et al (this issue) from completely different data (crosscutting relationships between groove sets and their basements).

REFERENCES

Casacchia, R. and Strom, R.G., 1984, J. Geophys. Res. 89 supple. B419.
Melosh, H.J., 1980, Icarus 43, 334.
Pechmann, J.B. and Melosh, H.J., 1979, Icarus 38, 243.
Scott, D.H., Mc Cauley, J.F. and West, M.N., 1977, USGS Misc. Inv. Series, Map I-1034;
Smith, B.A. and the Voyager Imaging Time, 1979, Sciences 204, 951.
Thomas, P.G. and Masson, P., 1984 a, Icarus 58, 396.
Thomas, P.G. and Masson, P., 1984 b, Earth, Moon and Planets 31, 25.
Thomas, P.G., Forni, O.P. and Masson, P., 1984, submitted to Earth, Moon and Planets.

AKNOWLEDGMENTS

This work was supported by Institut National D'astronomie et de Géophysique du CNRS (ATP de planétologie).

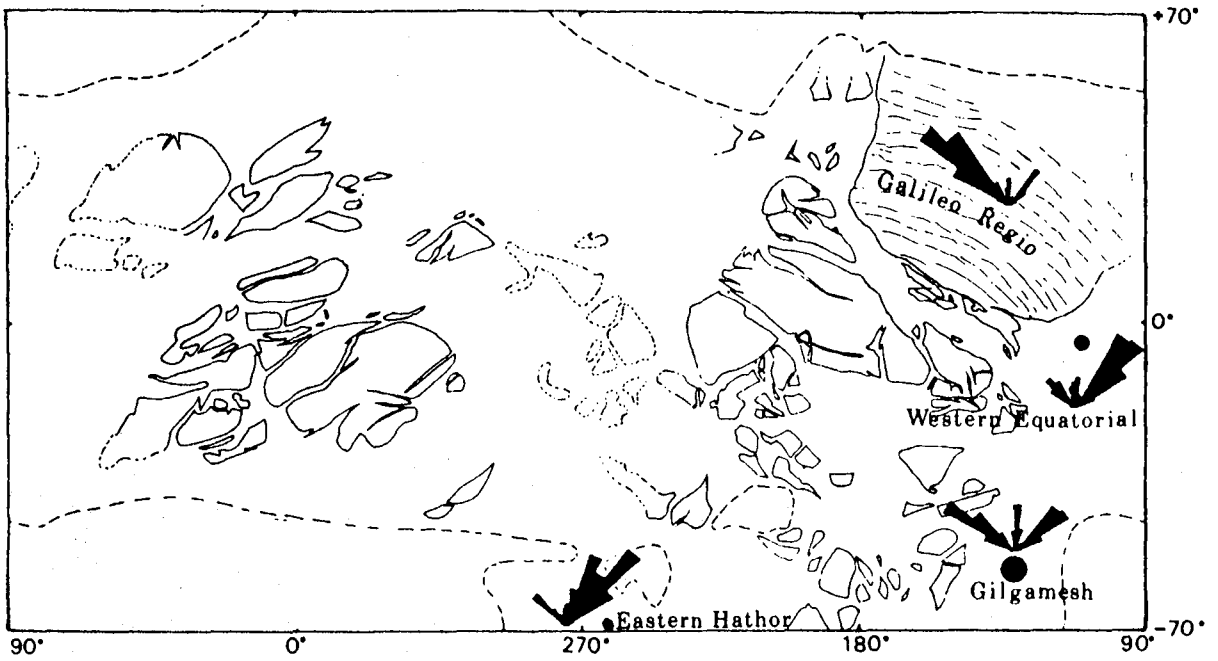

Fig 1 General map of Ganymede showing the relationships between the tectonic azimuth rosettes of Gilgamesh, Western Equatorial, Eastern Hathor, and Galileo Regio. The azimuthal similarity of the mains directions of these rosettes are immediately apparent on this figure.

• studied crater ⬭ polygone of dark and cratered terrains

limit of the known surface

TECTONICS OF THE GALILEO REGIO ON GANYMEDE

Pierre G. THOMAS and Philippe MASSON,
Lab. Geol. Dyn. Int., bat.509, UA 730, Université PARIS XI,
91405 ORSAY cedex, FRANCE.

The surface of Ganymede consists of two major units (Smith et al 1979): the dark cratered terrain, and the grooved terrain. The dark cratered terrains forms polygonal units. The largest one is named Galileo Regio. The surface of Galileo Regio is transected by furrows, which are smooth floored valleys bounded by relatively sharp parallel ridges. Their lengths vary from about 50 km to several hundreds of kilometers, their widths range from 6 to 20 km (Shoemaker et al, 1982). The most apparent of them are grouped together and form an apparently "arcuate" system of subparallel furrows. This system has been interpreted to be the remnants of concentric fractures surrounding a large impact basin, similar to those surrounding the Valhalla basin on Callisto (Smith et al, 1979). The center of this impact would be localized at -20°, 165° (Passey and Shoemaker, 1982). Mc Kinnon and Melosh (1980) explain these numerous rings by the thinness of the lithosphere at the time of the "supposed impact". Casacchia and Strom (1984) suggest that this system of "arcuate" furrows is not of impact origin because of its detailed morphology, the absence of variation in furrows' spacing, and the existance of others crosscutting furrow systems. The global azimuthal distribution of these furrows (Casacchia and Strom, 1984) shows two secondary trends (N-S and NE-SW), and one main trend: NW-SE, with a variation in direction of about 40°, that would reflect the broadly "arcuate" trend of this system. Casacchia and Strom (1984) explained this "arcuate" pattern by a possible plume-like cell in a fluid mantle underlying a thin lithosphere.

Using the Voyager pictures, we undertook (Thomas et al, 1984) the mapping of the "arcuate" furrow system (fig 1). Then these furrows were plotted on a map using a stereographic projection centered on +30°, 145°, the center of the known Galileo Regio (fig 2). On the same map, we reported 4 small circles (with angles of aperture equal respectively to 40, 55, 70 and 85 degrees centered at -20°, 165°, the theoritical center of the hypothetical basin supposed to have induced the furrows formation. Two geometric properties of these furrows are immediately apparent on this map:

-with this kind of projection, the main furrow system is not arcuate, but rectilinear. The difference in the azimuthal directions of this system is due to the convergence of the meridians in the high latitudes and not to an arcuate shape.

-the main furrow system is not concentric to the center proposed by Passey and Shoemaker (1982).

Since it is rectilinear in this kind of projection, the furrow that passes at the center of the projection (+30°, 145°) is a great circle, with geometrically determined poles located near -45°, 200° and +45°, 20°. One of these points would be the center of the impact, if the furrows were due to an impact, or the center of a plume-like cell. None of these 2 points seems to be an impact or a plume-like cell center's for the following reasons:

-in that case, the impact or the cell would affect more than one half of the satellite, that is not the situation of many polygones of dark terrains located in the same hemisphere than a part of Galileo Regio;

-the furrows of Marius Regio are not concentric to any of these points;
-no large crater could be seen at these points.

Moreover, all the furrows seem to follow great circles which are crosscutting near -30°, 60° and +30°, 240°, although it is difficult to tell the difference between a great circle and a small circle of 80° of aperture. And, as noted by Casacchia and Strom (1984), the impact origin hypothesis does not account for the other systems of furrows.

All these observations strongly suggest that the Galileo Regio furrow systems are not of impact origin. Consequently, the furrow systems of Galileo Regio appear to be irrelevant to discussions about the basins' morphology or evolution of planetary lithosphere determined from multi-ring structures. Because the main furrow system does not seem to follow little circles concentric to a single point, it seems difficult to explain this pattern by a single plume-like convection cell. Thus, the origin of the motions inducing the furrow systems remains unknown, but they are not due to external origin (impact). These motions must be taken into account in discussions about internal geological evolution of Ganymede.

REFERENCES

Casacchia, R. and Strom, R.G., 1984, J. Geophys. Res. 89 supple. B419.

Mc Kinnon, W.B., and Melosh, H.J., 1980, Icarus 44, 454.

Passey, Q. R., and Shoemaker, E. M., 1982, The Satellites of Jupiter, D. Morisson Ed., 379.

Smith, B.A., and the Voyager Imaging Team, 1979, Sciences 204, 951, and Sciences 206, 907.

Thomas, P.G., Forni, O.P. and Masson, P.L., 1984, submitted to Earth, Moon, and planets.

AKNOWLEDGMENTS

This work was suported by Institut National d'Astronomie et de Géophysique du CNRS (ATP de Planétologie).

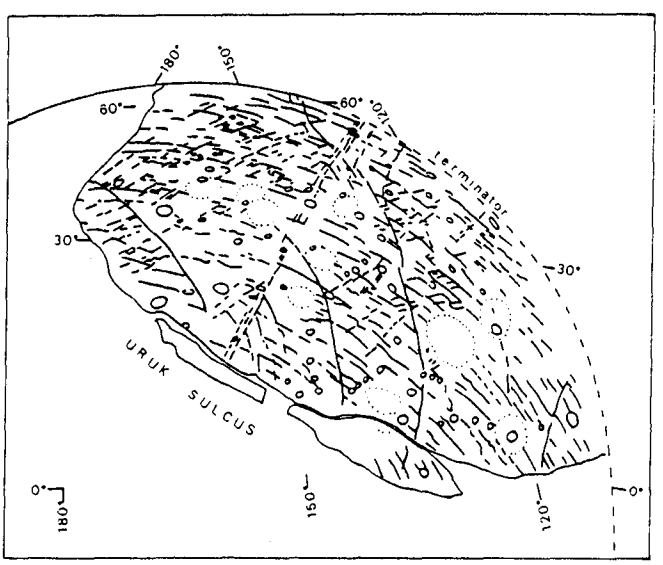

Fig 1 Non rectified tectonic map of Galileo Regio. Note the apparently arcuate furrows and the two other poorly represented furrows systems.
O impact craters palimpsets furrows

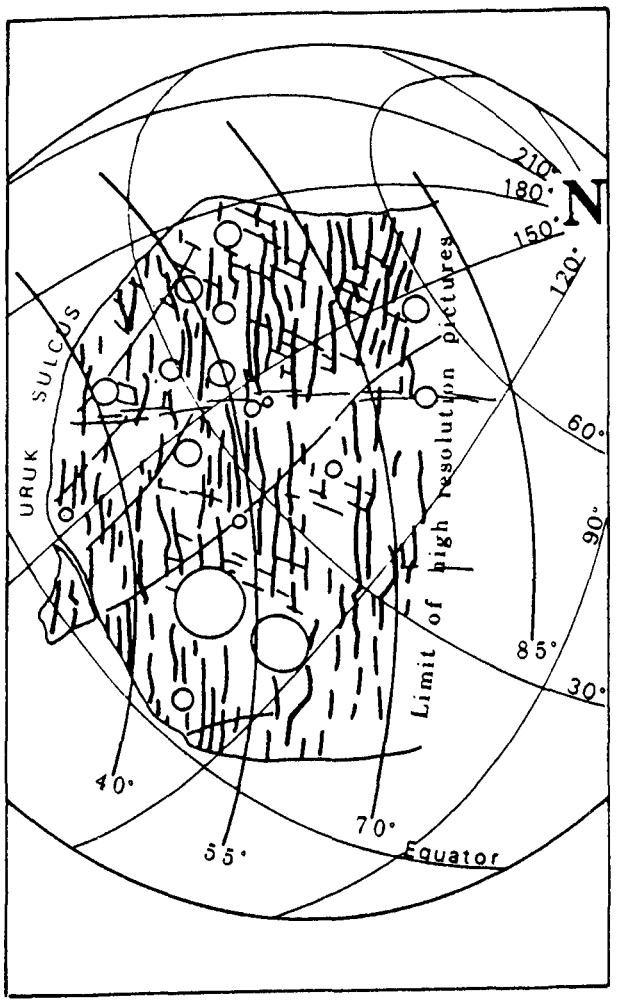

Fig 2 Shematic tectonic map of Galileo Regio, with a stereographic projection centered on +30°, 145°. Note that the prominent furrow system is rectilinear and different from the circular arcs centered on +30°, 145°, the proposed center of the supposed impact which generated the furrows.

— main furrow system
○ craters and palimpsests
/ other furrow systems
| circular arcs centered on +30°, 45°.

IMPORTANCE OF THE TECTONIC MOTIONS ON GANYMEDE

O.P. FORNI, P.G. THOMAS, P.L. MASSON
Laboratoire de Géologie Dynamique Interne
UA 730. Bat 509. Université Paris XI. 91405 Orsay Cédex. France.

Ganymede is the largest Galilean satellite (5,270 km in diameter). Voyager close-up views reveal some provinces of old, cratered, dark terrains that are broken into polygons and cut through by light stripes of grooved terrains (Smith et al., 1979).

It has been proposed that the grooves may have been formed by normal faulting that was produced by extensional tectonics followed by resurfacing processes (Parmentier et al., 1982 ; Squyres et al., 1981 ; Shoemaker et al., 1982).

However, the origin and the significance of groove formation remain unclear and controversial. In order to contribute to a better knowledge of these structures, a detailed study of this terrain unit and of its relationships with the other units was undertaken. This study was performed at various scales because these features seem to relate at least to two main scales of processes :

- Minor displacements concerning only local features i.e., large scale processes.
- Major displacements concerning usually the major evolution of the surface i.e., small scale processes.

1. Large scale observations.

The feature centered at Lat. -16° Long. 172° (Fig. 1a) was interpreped as a crater truncated by a furrow and spread apart (Lucchitta. 1980). It was therefore presented as one of the best evidence of extensional tectonics on Ganymede. However, our study of this feature allows us to propose another interpretation based on the following observations.

First, it is noticed that the northern part of the crater's rim crosscuts the limits of the furrow, meanwhile the southern part does not transsect this limit (Fig. 1b). In addition, the two parts of the crater do not have the same curvature radius : the smallest would have a 20 km radius and the largest would have a 27 km radius (Fig. 1c).

According to these observations, it seems that these two crater parts do not belong to the same crater. On the contrary, they should belong to two different craters. The smallest part should belong to the oldest crater because its rim do not appear inside the limits of the largest crater, as it should be if it has been formed later on.

Consequently, it seem unlikely that the furrow formation could be interpreted as the result of important extensional process. Moreover, in its northern limit, the crosscutting relations of the furrow with the crater's rim seem to indicate that the furrow is only a superficial feature. Additional argument against important extensional movement is provided by the virtual part of the largest crater's rim. This virtual rim appears to be tangent to the furrow's northern limit (Fig. 1b). Taking into account the hypothesis of spreading mechanism, this virtual rim should not be tangent to the furrow's northern limit, which is not the case. Nevertheless, a limited extension that may have produced a graben like feature, may have played a role. However, according to our observations, the effect of such extensional process should be smaller than the Voyager image resolution (i.e. below 1.4 km per pixel).

Consequently the spreading mechanism, which should have produced the furrow, seems very unlikely. The furrow cannot be taken therefore as an argument to demonstrate that important extensional tectonics did exist, at least in this region of Ganymede.

2. Small scale observations.

The relations between the furrows of Galileo Regio and the grooved terrains that are observed in its immediate vicinity, are presented. For the purpose of this study, image centered at Lat.-3°, Long. 130° (Fig. 2a) was processed with an image color enhancement system (Fig. 2b) that was used for directional filtering).

Filtering based on a convolution matrix $\begin{matrix} 0 & 1 & 2 \\ -1 & 0 & 1 \\ -2 & -1 & 0 \end{matrix}$ enhanced the features oriented NW-SE. This image processing shows that most of the furrows in this area seem to extend through the grooved terrains (Fig. 2b, 2c). It was noticed additionally that none of the other bi-dimensional analyses showed any other preferential orientation which seems to indicate that the structures observed through the grooves are neither random features nor artefacts. Moreover, because of their orientation and of their apparent continuity with the furrow system of Galileo Regio, it is deduced that these stuctures are furrows overlaid by the grooved terrains. This implies that the grooves did not affect significantly the underlying furrows. Consequently the grooved terrains in this area appear to be superficial features, else the underlying stuctures should not be apparent. Moreover, if the grooves were related to tectonic processes, these processes should have limited geometric effects i.e., relative displacements, because the underlying formations do not seem to be affected by these processes at the image resolution (800 meters per pixel).

This example leads to the preliminary conclusion that very limited extensional tectonics followed by limited overflooding processes could be accounted for the formation of the grooved terrains : the superficial cover produced by the overflooding processes should have a relatively limited thickness (the superficial grooved terrains apparently preserve the underlying features) and the tectonic processes should have a relatively limited importance (the superficial grooved terrains do not seem to affect the underlying features).

It appears that tectonic processes, at least in the studied areas, if playing a role in the formation of local or regional features, are very limited. If these observations and interpretations were to be confirmed by extensive studies conducted on a more global scale, they would constrain the hypotheses of important extension on Ganymede's surface. These conclusions agree with those of Thomas et al. (this issue) who show that post grooves basins reveal the presence of a primitive "grid" that is not disturbed by the grooved terrains.

Aknowledgments.

We are grateful to S. Equilbey from the C.D.S.I. for his help. This work was supported by Institut National d'Astronomie et de Géophysique du CNRS (ATP de planétologie) under research contract No 47.24.

References.
LUCCHITTA, B. K. (1980) : Icarus 44, pp 481-501.
PARMENTIER, E. M., SQUYRES, S. W., HEAD, J. W. and ALLISON, M. L. (1982): Nature 295, pp 290-293.
SHOEMAKER, E. M., LUCCITTA, B. K., WILHELMS, D. E., SQUYRES, S. W. and PLESCIA, J. D. (1982) : In The Satellites of Jupiter. (D. Morrison Ed.). University of Arizona Press. Tucson. pp 435-520.
SMITH, B. A. AND THE VOYAGER IMAGING TEAM. (1979) : Science 206, pp 927-950.
SQUYRES, S. W., PARMENTIER, E. M. and HEAD, J. W. (1981) : Lunar and Planet. Science XII, pp 1031-1033.

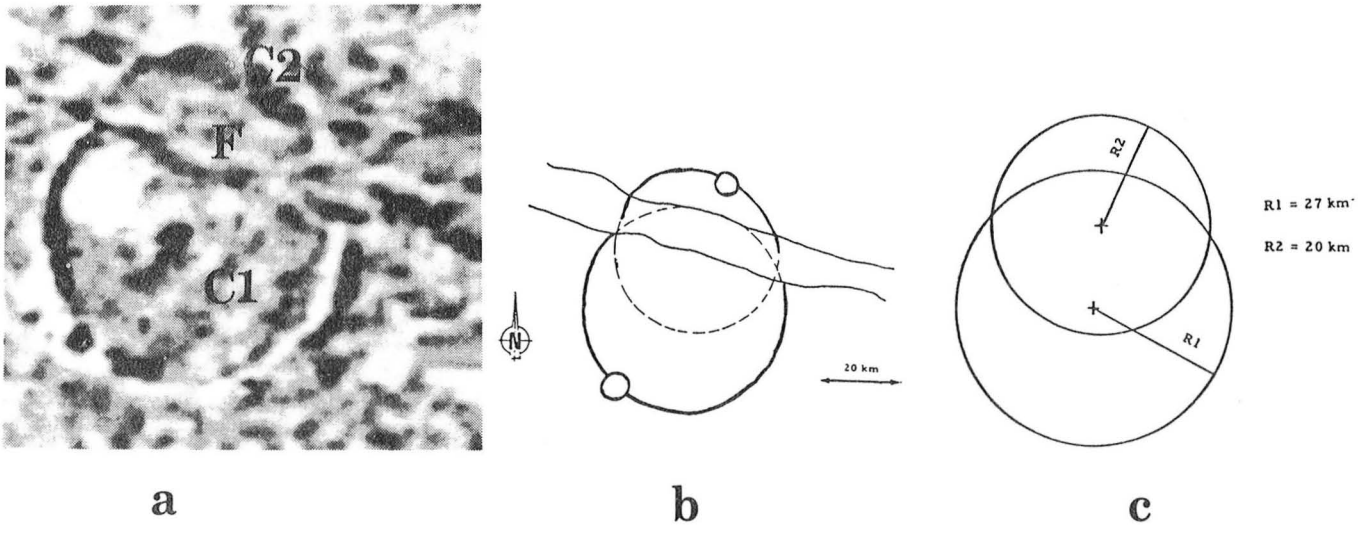

Fig. 1 : (a) Detail of image 395J2-001 (Filtered) showing two parts of craters (C1, C2) truncated by a furrow (F). (b) Sketch map illustrating the crosscutting of the furrow by the crater's rim (In full line are drawn the observations, in dashed line the virtual rims). (c) Interpretation in terms of two distinct craters.

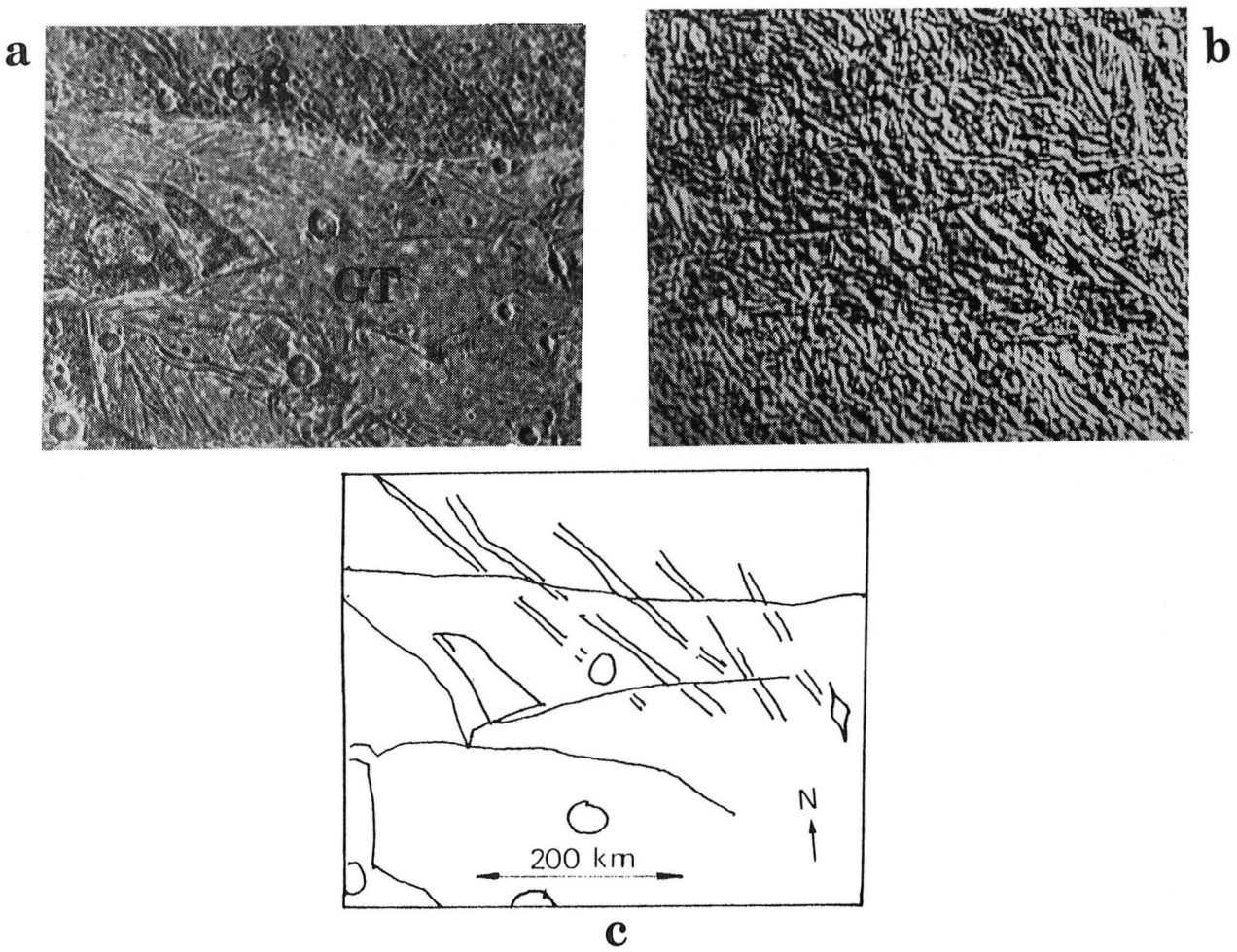

Fig. 2 : (a) Detail of image 550J2-001 (Filtered) showing the cratered terrains of Galileo Regio with its furrow system (GR) and the grooved terrains in its vicinity (GT). (b) Processed image. (c) Sketch map illustrating the observations of the processed image and showing the furrows extending through the grooved terrains.

TECTONICS OF THE VALHALLA STRUCTURE ON CALLISTO

Pierre G. THOMAS and Philippe MASSON,
Lab. Geol. Dyn. Int., UA 730, Université Paris XI,
91405 ORSAY cedex, FRANCE.

The surficial morphology of Callisto is dominated by two large concentric patterns of ridges, scarps, and furrows named Asgard and Valhalla . The largest one, Valhalla, shows a smooth central area 350 km in radius, surrounded by concentric sinuous ridges which extend as far as 600 km from the center. Beyond the ridged area, scarps and furrows are observed as far as 2000 km. This structure is usually interpreted as an impact structure (Smith et al, 1979). The numerous rings would be probably due to the thinness of the callistean lithosphere in regard to the impact crater's primitive depth (Mc Kinnon and Melosh, 1980). Another explanation was proposed by Wood (1981): a diapiric instability of a thick and dense lithosphere into a water mantle.

We undertook (Thomas and Masson, 1984) the study of the outer rings beyond 700 km from the center. These scarps and furrows are approximatively concentric, but they are discontinuous and irregular in plan. They somewhere exhibit a broken line morphology, with generally two by two paralell rectilinear fragments. Somewhere else, the rectilinear fragments continue as faint but distinguishable lineaments, that extend beyond one or both of their ends.

Such a broken line pattern may be interpreted in term of inherited structures: the radial stresses due to the formation of the Valhalla structure induced motions which occurred preferentially along preexisting discontinuities where they are oriented approximately tangentially to the structure.

Because these local geometric patterns seems to indicate local preexisting pattern, we undertook an azimuthal study of these scarps and furrows, only for the eastern half of the structure because of the low resolution of the western part (fig 1). For each angular sector, the concentric orientation is largely the most expressed. But some non concentric directions exist. For example the NW-SE direction exists in the northeastern area, where it corresponds to the concentric direction. But this NW-SE direction exists also in the NNE and ENE areas, where it makes a more than 22.5° angle with the concentric direction.

The global azimuthal distribution of these scarps and furrows (fig 2) reflects the presence of largely expressed directions. This global distribution exhibits a bimodal distribution with two maxima: NW-SE and NE-SW.

It seems unlikely that such an unequal distribution could be only the result of an impact mechanism, which would have produced an approximately circular pattern without any preferential trend dominance. It is proposed therefore that the local geometry and the global distribution of scarps and furrows around Valhalla are the results of the reactivation of an old pattern by the Valhalla event. The coincidence of these local directions of a preexisting pattern (NW-SE and NE-SW) with the directions of the grids observed on almost bodies observed so far in the solar system would indicate that this local pattern is a part of a global callistean grid.

These observations and their interpretation have two important implications on Callisto's history:

-Callisto is not a "tectonic-free" planetary body, as usually though, but, as most of the bodies observed so far in the solar system, it exhibits a planetary wide grid pattern, that probably results from tidal flexing or despinning;

-At the time of the Valhalla event, the icy lithosphere of Callisto was thick and strong enough to preserve the existance of a fracture pattern during the time interval between the despinning or flexing and the Valhalla event. This result should be taken in account in further thermal and rheological model of Callisto.

REFERENCES

Mc Kinnon, W.B and Melosh, H.J., 1980, Icarus 44, 454.
Smith, B.A. and the Voyager Imaging Team, 1979, Sciences 204, 951.
Thomas, P.G. and Masson, P, 1984, submitted to" Ice in the solar system", NATO Adv. Study Institute Series.
Wood, C.A., 1981, Proc. of Lunar and Plan. Sci. 12 A, 173.

AKNOWLEDGMENTS
This work was supported by Institut National d'Astronomie et de Geophysique du CNRS (ATP de Planétologie)

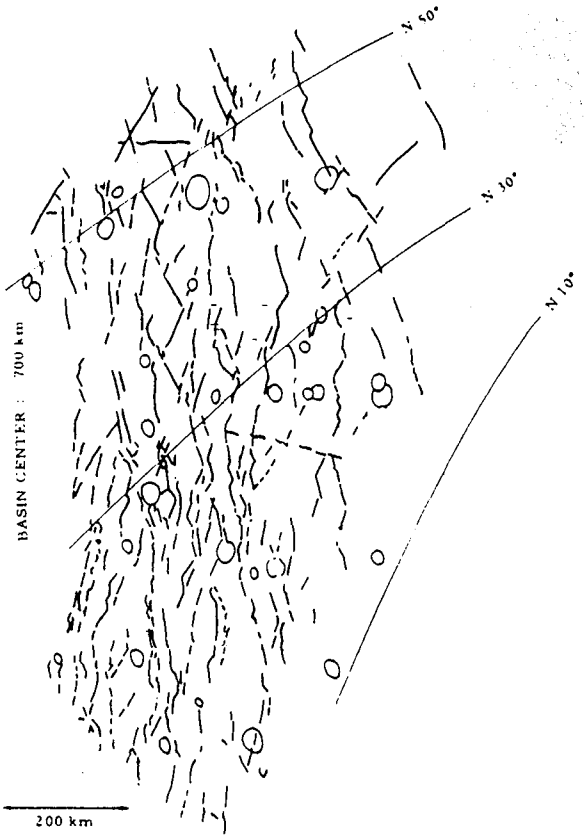

Fig 1 Non rectified structural map of the northeastern outer part of the Valhalla structure. One can note the broken line geometry of the scarps and furrows (full line).

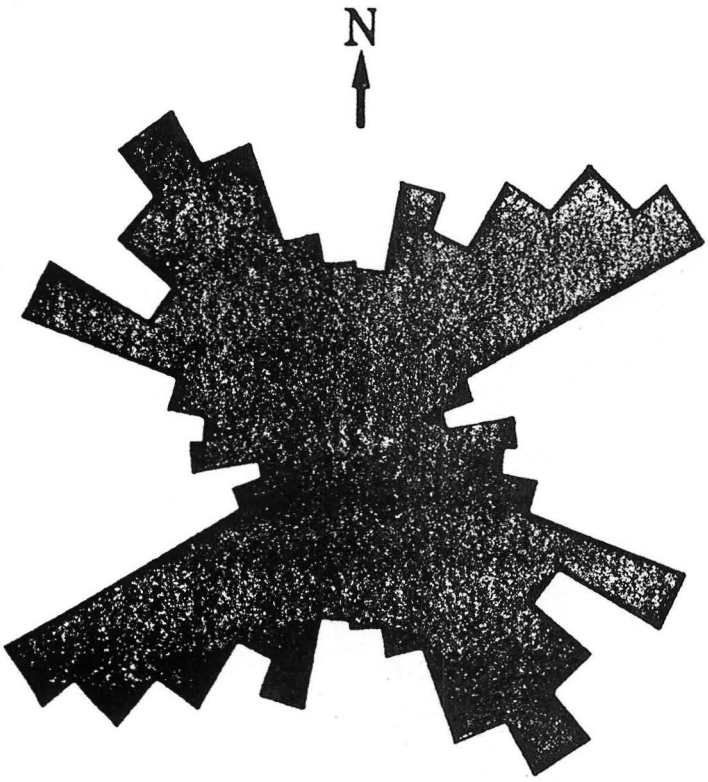

Fig 2 Global tectonic azimuth rosette of the eastern Valhalla scarps and furrows. Length of histogram is given as percent of total length of scarps and furrows. One can note the bimodal distribution of these structures and the dominent NE-SW and NW-SE trends.

Page intentionally left blank

CHAPTER 15

GEOLOGICAL MAPPING, CARTOGRAPHY AND GEODESY

Page intentionally left blank

MARS GEOLOGIC MAPPING: A REVIEW AND NEW CONCEPTS

David H. Scott and Kenneth L. Tanaka, U.S. Geological Survey, Flagstaff, Arizona 86001

The new geologic map of the western equatorial region of Mars at 1:15 M scale [1] has been completed in open-file format. It is thus available for public consultation and may be cited as a source of information. The final version of this map and accompanying information are currently in review prior to submittal for publication. The map is the first in a series of three sheets showing the global geology of Mars. Based on Viking pictures, the series shows greater detail than does the previously published map [2] based on Mariner pictures. Geologic maps of the north and south polar regions (to be published as one sheet) have been completed in provisional form; the third sheet, a map of the eastern equatorial region, is in compilation. Some results of this mapping project have been reported previously [3]. The following are new developments.

Western Equatorial Region: The oldest rocks on Mars identifiable as in situ occur in this region and have been grouped as basement complex [4]. They consist of undifferentiated materials of probably diverse types having highly complicated structure. Stratigraphically they underlie all other map units. Largest exposures are in the Phoenicis Lacus (MC-17) and Thaumasia (MC-25) quadrangles where they appear to be of tectonic origin, but in places they represent erosional remnants of an irregular basement surface that project as "islands" above more recent lava flows.

The question of the extent of fluvial processes on Mars has been partly answered by the recognition of meander channels extending far into the northern plains [5,6]. Within the Kasei Vallis and Ares Vallis drainage systems, crater counts suggest that the earliest water flooding occurred at about the same time as volcanism began at Tharsis Montes. Farther north in Chryse Basin the relics of meander channels are partly buried by the basal member of the Arcadia Formation of early Amazonian age.

North and South Polar Regions: The youngest areally extensive group of map units on Mars, aside from the ice caps, consists of vast dune fields in the north polar region and layered plains deposits surrounding both poles. The north polar dunes appear to be of two morphologic types: crescentic or barchanoid ridges [7] oriented mostly normal to wind directions, and long, linear dunes parallel to prevailing winds; the two dune types are intergradational. The close association of dunes, especially near the north pole, with layered plains deposits suggests that these plains are their major source [7,8]. The northern layered plains are much less extensive than their southern counterparts, but the northern dune fields are very much larger. The relative absence of dune sheets in the south polar region may result from differences in erosional-depositional activity between the two poles. Geologic mapping shows large areas around the south pole to be deeply eroded and older rocks to be exhumed. Some of this eroded material may be incorporated in the layered plains material, but this material also is being eroded [8]. Deep erosion has not been observed around the north pole, except locally in some troughs and valleys. Unlike the situation in the south polar region, the erosion of layered plains to

form large dune fields requires no net transport of material from the north polar region. Thus the theory of entrainment and transportation of wind-eroded particles from the etched terrains and southern layered plains into higher latitudes is supported by the mapping. With time, the northern layered plains might grow by this process at the expense of the south polar plains. Long-term periodic changes in the orbital dynamics of Mars and associated climate cycles may account for the shifting of dune and layered plains deposits between the two polar regions.

The large asymmetry of the south polar ice cap with respect to the pole position may be explained in part by the presence of the great impact basin centered near 83° S., 270° W. (Fig. 1). The basin is generally opposed to the present offset position of the ice cap and is filled largely by layered plains deposits. Active erosion of the plains material by downslope winds from the pole into this depression could account for the stripping of a CO_2 frost cap within the confines of the basin. Small patches of layered plains material occur in places along the scarp base of Promethei Rupes. Their presence here indicates that the impact basin may have been more completely filled with these deposits in the past. Erosion of this material from part of the basin floor is apparently due to strong latitudinally directed winds, as is shown by scouring of the older rocks. These winds have removed material from the encroaching front of plains deposits transported into the basin by winds from the pole. The exhumation of older primary craters [8] and satellitic craters is clear on the Viking images. The large lobe of layered plains deposits extending northward between a remnant of the basin rim and the 180° W. meridian may have grown by the addition of plains material eroded from within the basin.

References

[1] Scott, D. H., and Tanaka, K. L., 1984, Geologic map of the Western Equatorial Region of Mars: U.S. Geological Survey, Open-file Report 84-659-A.

[2] Scott, D. H., and Carr, M. H., 1978, Geologic map of Mars: U.S. Geological Survey, Miscellaneous Investigations Series Map I-1083, scale 1:25,000,000.

[3] Scott, D. H., 1983, Geologic mapping, Mars: Progress and highlights (abs.): Reports of Planetary Geology Program, NASA Tech. Memo. 86246, p. 321-323.

[4] Scott, D. H., and King, J. S., 1984, Ancient surfaces of Mars: The basement complex (abs.): Lunar and Planetary Conference 15, p. 736-37.

[5] Tanaka, K. L., and Scott, D. H., 1980, Channeling and flooding on Mars (abs.): Proceedings Third Colloquium on Planetary Water, p. 76-79.

[6] Scott, D. H., 1983, Meander relics: Direct evidence of extensive flooding on Mars: Conference on Planetary Volatiles, Lunar and Planetary Institute Tech. Report 83-01, p. 157-165.

[7] Breed, C. S., Grolier, M. J., and McCauley, J. F., 1979, Morphology and distribution of common "sand" dunes on Mars: Comparison with the Earth: Journal Geophysical Research, v. 84, no. B14, p. 8183-8204.

[8] Thomas, P., 1982, Present wind activity on Mars: Relation to large latitudinally zoned sediment deposits: Journal Geophysical Research, v. 87, no. B12, p. 9999-10,008.

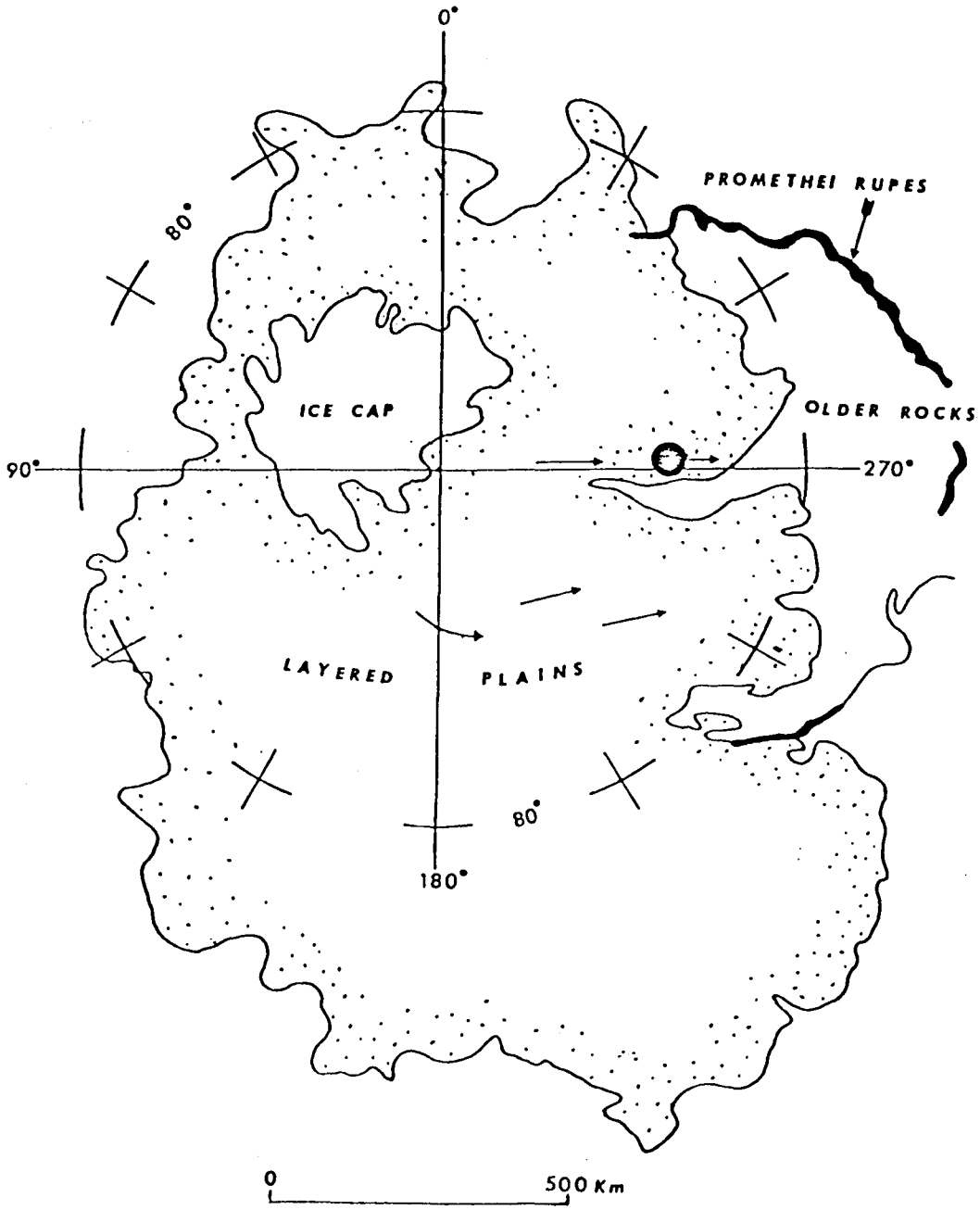

Fig. 1. Disposition of layered plains deposits around south polar ice cap. Plains partly fill large impact basin whose rim is marked by Promethei Rupes. Approximate basin center shown by black dot. Small arrows show inferred wind direction.

THE GALILEAN SATELLITE GEOLOGICAL MAPPING PROGRAM, 1984

B.K. Lucchitta, U.S. Geological Survey, Flagstaff, AZ 86001

The Galilean Satellite Geological Mapping Program was established to illuminate detailed geologic relations on the four large satellites of Jupiter. The program involves about 40 investigators from various universities, research institutes, and government offices in the United States, England, Germany, and Italy. A total of 24 researchers has been assigned to map 10 quadrangles on Ganymede, 15 to map 6 quadrangles on Io, and 3 to map 2 quadrangles on Europa. All maps are at a scale of 1:5 million except for three of the Io maps, where high-resolution pictures permit compilation of selected areas at larger scales.

During 1984, preliminary base materials were sent to the mappers of Jg (Ganymede) 9 and 10, and final cronaflex brownlines and other base materials to the mappers of Jg7, 8, and 9, and Ji (Io) 2, 3, and 4. Deadlines for the compilation of these maps were set. Ji2c (Maasaw Patera) has gone through review and is undergoing author's revision. Ji2a (Ra Patera) and Jg7 have been submitted for review. A meeting was convened in March 1984, in Houston, Texas, and guidelines for the mapping of Ganymede were established. Reports detailing mapping guidelines for Io, Europa, and Ganymede were compiled and distributed.

For mapping Ganymede, it was decided that the major division would be between light and dark materials, because albedo differences are conspicuous and recognized easily. Subdivisions within albedo units will be based on morphology: for instance, grooved and smooth units in the light materials, and lineated and hummocky units in the dark materials. Transitional units will be grouped with light or dark materials depending on the albedo they approximate.

Within the light materials, groove sets will be outlined by a structural symbol. Different types of grooved materials may be defined as different material subunits and given different letter symbols, but they will be given similar colors to emphasize the continuity of grooved terrain. Alternatively, different types of grooved material may be shown by location, trend, and spacing of symbols, or by a combination of subunits and symbols. Similarly, different types of dark materials may be divided into subunits or shown by symbols. Furrowed dark materials are to be mapped as material units where wide, and by symbols where narrow. Pervasively furrowed materials may be mapped as separate material units, and the location, trend, and spacing of furrows shown by symbols.

Most craters on Ganymede have shallow flat floors and narrow rims, and will be lumped into a unit that probably spanned most of Ganymede's history. Crater remnants will be mapped separately, as will fresh-looking rayed and deep bowl-shaped craters. Central pits, peaks and domes will be indicated by symbols. Secondary craters will be mapped individually where they occur in distinct clusters, or with an overlay pattern where widely dispersed.

All crater palimpsests (scars of craters whose topography has nearly disappeared) will be combined into one unit; individual morphologic differences will be shown by ridge, scarp, or ring symbols. To distinguish between palimpsests and craters the following criteria were established: palimpsests are defined by smooth centers, very subdued or discontinuous rings, ejecta blankets that have little texture, a relatively circular outline, and no rays. Craters or basins, by contrast, commonly have floor structures, rugged rings or rims, ejecta with radial patterns, a more rugged outline, and may have rays.

Even though units can be crudely positioned in time (dark materials tend to be older than light materials, grooved materials older than some smooth materials, and palimpsests older than craters), ages of units overlap to the extent that the correlation chart will show most units as virtually the same age.

GEOLOGY OF THE GANYMEDE QUADRANGLE Jg7

B. K. Lucchitta, U.S. Geological Survey, Flagstaff, AZ 86001

The western half of Ganymede quadrangle Jg7 is covered by Voyager 2 images with resolution of .5 to 5 km/pixel. The imaged area includes dark terrain in the north underlying the southeastern part of Galileo Regio, and light terrain in the south underlying the southeastern extension of Uruk Sulcus. Several slivers and wedges of dark terrain occur within the light areas. Numerous craters are present, as well as three large palimpsests (crater scars with little topographic expression) in the dark terrain and a basin in the light terrain.

Dark materials in Galileo Regio have irregularly textured surfaces. In places, especially near furrows, these rugged dark materials are smoothed by additional dark material. Dark materials in slivers and wedges are ridged, grooved, or hummocky, suggesting that they were structurally disrupted. Conspicuous furrow sets traverse the dark material; a north-northwest-trending set is superposed on a northwest-trending set. A third set trends northeast and occurs between the northwest-trending furrows. Large furrows are bounded by fields of hummocks or ridges with irregular, knobby crests. The knobs and hummocks have a higher albedo than the surrounding dark material; the lighter tone suggests that they are composed of different materials than the background unit. Furrow development predated all crater and palimpsest emplacement.

Grooved materials in the light terrain form parallel to subparallel sets; some sets, however, are irregular, and some grooves are single. Groove sets may become subdued and fade out. Large, throughgoing and slightly sinuous grooves in places form boundaries of groove sets or of slivers of dark terrain. Light smooth materials merge with, overlap, or embay grooved material. Smooth materials that overlap dark terrain have either diffuse or sharp boundaries. These relations indicate that smooth materials are of about the same age or younger than grooved materials, and that smooth materials may have been emplaced as liquids or precipitates.

The boundary between dark and light materials on the south side of Galileo Regio is locally marked by a scarp that faces the light terrain. The scarp truncates several craters. Furrows in the dark terrain generally terminate at the boundary, but a few extend into separated slivers of dark material and show a slight rotation. South of Galileo Regio, a vestige of the conspicuous northwest-trending set of furrows can be recognized in an area of dark terrain surrounded by light material. The furrow vestiges consist of aligned fields of hummocks, and the trend of the vestiges is also slightly rotated with respect to the trend of the furrows in Galileo Regio. The truncation and rotation of structures suggest that light material grew at the expense of dark material, and that the destruction, except for minor pivoting, was essentially in situ.

Palimpsests in the dark terrain have light interiors that contain locally dark patches near their rims. Some of the dark patches may be ejecta from adjacent or superposed craters. Ejecta blankets from craters on the dark

terrain or on palimpsest rims appear to darken with age. By contrast, ejecta from craters superposed near the center of palimpsests remain light in tone. This observation suggests that the central material, because it does not darken with age, is different from material excavated near the rims. Small palimpsests are also composed of material that remained light upon aging, whereas craters of similar size darken with age; apparently the palimpsests excavated different material than later craters. Perhaps the light material was nearer the surface when palimpsests were emplaced than it was later, when craters were emplaced. Some palimpsests have depressions around their outside edges; these troughs suggest that the weight of the ejecta blankets may have caused isostatic sinking.

Most craters within the quadrangle have narrow rims and shallow floors. A few craters are more degraded and may be older; a few have deep bowls with rays and may be younger. With increasing size, craters display more flat floors, peaks, central pits and central domes with pits. Most pit craters near the terminator also have shallow central domes; others farther from the terminator may have domes as well, but they cannot be seen on the images. The transition from flat-floored to peak and pit craters takes place at larger crater diameters in the grooved terrain than in the cratered terrain. Some craters have ejecta with indistinct flow lobes at their margins; others have central domes or platforms surrounded by conspicuous depressions. These "moat" craters appear in all stages of degradation but are common as transitional forms between craters and palimpsests. They appear to be a form unique to the icy satellites of Jupiter.

MARS PLANIMETRIC MAPPING

R. M. Batson, P. M. Bridges, and E. M. Lee, U.S. Geological Survey, Flagstaff, AZ 86001

Revisions of 1:5,000,000-scale shaded relief maps: The 1:5,000,000-scale shaded relief maps of Mars originally compiled from Mariner 9 pictures are being upgraded by adding details visible on Viking Orbiter images. This work is done by modifying the original airbrush drawings; no attempt is made to reposition features according to the latest control nets. Thirteen of these maps have been published to date, two are in compilation, and two are in press.

Atlas of Mars: A hard-cover atlas containing reduced-scale versions of all Mars cartographic products will be published upon completion of the revisions of the 1:5,000,000-scale maps, the 1:2000,000-scale photomosaics, and the Mars color albedo mapping tasks defined below. This atlas will supersede the existing Atlas of Mars prepared by Batson and others [1]. Although full-scale efforts to compile the atlas will not begin until all of the component products are essentially complete, preliminary experiments with formats and map presentation style are in progress. This work includes making composite images of comparatively low resolution digital color mosaics and high-resolution shaded-relief maps and/or photomosaics, and also defining scales and formats for the presentation of the maps. In addition to these experiments, a new small-scale index map of Mars has been prepared that shows relief and albedo at resolution suitable for page-size publication.

Mars color albedo mapping: Viking Orbiter pictures of Mars taken from near apoapsis with small phase angles are being used to compile a visual albedo map of Mars in three colors. Four products are planned: 1) a preliminary 1:15,000,000-scale airbrush map of a large area between the fiftieth parallels, made with pictures taken through the red filter at an Ls of 52 through 87 degrees [2]; 2) a controlled computer mosaic of the equatorial zone consisting of pictures taken through three color filters during Viking 1 orbital revolutions 614 through 699; 3) a final airbrush map of the entire planet compiled at 1:15,000,000-scale, made with pictures taken through the red or clear filters; and 4) a controlled computer mosaic of the best available color pictures that show as much of the planet as possible.

The preliminary 1:15,000,000-scale airbrush map is in press [3], but publication has been delayed pending resolution of nomenclature problems. Color images taken during revolutions 583 through 699 have been processed and projected [4]. Controlled color mosaics for revolutions 583, 586, 593, and 614 are complete. Uncontrolled mosaics of revolutions 663, 666, 669, 672, 681, 684, and 687 have been completed and are being modified to fit map control. Experimental hybrid mosaics of a digitized airbrush map of MC-19 and part of rev 586 have been made, with the color "painted" digitally onto the shaded relief. Similar hybrid composites have been made with the 1:2000,000-scale controlled mosaics of MC-17NE and rev 583, and MC-17NW and revs 583 and 614. No decision has yet been made as to the appropriate form of publication of these products.

References

[1] Batson, R. M., Bridges, P. M., and Inge, J. L., 1979, Atlas of Mars: The 1:5000,000-scale map series: NASA SP 438, 146.

[2] Batson, R. M., and Davis, S. L., 1982, Albedo map of Mars: in Reports of the Planetary Geology Program, 1982, NASA TM 85127, 359.

[3] U.S.G.S., Shaded relief and surface markings of Mars, western region (sheet 1) and eastern region (sheet 2), U.S. Geol. Survey Misc. Inv. Ser. Map I-1535, in press.

[4] Batson, R. M., Hall, D. G., and Jordan, JoAnne, 1979, Color pictures of Mars: in Reports of the Planetary Geology Program, 1978-1979, NASA TM 80339, 439.

CONTROLLED PHOTOMOSAICS OF VIKING ORBITER IMAGES OF MARS

R. M. Batson and J. L. Inge, U.S. Geological Survey, Flagstaff, AZ 86001

1:2,000,000-scale mosaics: A series of 1:2,000,000-scale controlled photomosaics of Viking Orbiter pictures of Mars has been completed. The series was started in 1979, and consists of 140 quadrangles. Pictures taken with morning or afternoon illumination (average solar zenith angle of 70 degrees) and resolutions of 135 to 200 m/pixel were selected for the mosaics. A second edition was published for 20 of the mosaics that have been revised with images that were not available at the time of the original compilation.

1:500,000-scale mosaics: Controlled photomosaics of areas of special scientific interest on Mars are being compiled from high-resolution Viking Orbiter pictures at a scale of 1:500,000. Compilation is on a Mars Transverse Mercator (MTM) system consisting of 18 zones with 20-degree longitudinal dimensions. The quadrangles cover five degrees in latitude and five degrees in longitude in the intermediate and equatorial latitudes of the planet.

Most of the pictures used in these photomosaics have resolutions of 100 m/pixel or better, but image resolutions of 200 or even 300 m/pixel are used where no other coverage is available. The highest available resolution is always used, with no attempt to retain uniformity of resolution or illumination across the mosaic. Much of the available planimetric control for Mars is not sufficiently precise for mapping at a scale of 1:500,000, where 1mm = 500m, because published standard errors of the control nets are as large as ten times that value [1,2]. Where no other control is available, image points are identified on the 1:2,000,000-scale controlled mosaics and transferred to the MTM projection. In some cases, a new and more precise control net has become available for a particular area after several mosaics have been completed on an older net. Subsequent adjacent compilations are always tied to the best available control, even if this results in edge mismatch with earlier compilations.

Status of the 1:500,000-scale mosaicking is as follows:

AREA	TOTAL NUMBER OF QUADRANGLES	NUMBER IN PROGRESS	COMPILATION COMPLETE	NUMBER PUBLISHED
V. Marineris/ Candor Mensae	8	-	8	6
Maja Valles	16	-	16	-
Kasei Valles	9	-	2	2
Mangala Valles	8	-	8	-
Alba Patera	12	11	1	-
Elysium Mons	20	12	-	-
Boreale Chasma	5	-	-	-
Australe Planum	10	-	-	-
Albor Tholus	4	-	-	-
Nylosyrtis Mensae	6	-	-	-
TOTALS	98	23	35	8

References

References

[1] Davies, M. E., Katayama, F. Y., and Roth, J. A., 1978, Control net of Mars: February, 1978: The Rand Corporation, R-2309-NASA, 91 p.

[2] Wu, S. S. C., and Schafer, F. J., 1984, The Mars control network: American Society of Photogrammetry, in Technical papers of the 50th annual meeting of the American Society of Photogrammetry, v. 2, Washington, D. C., March 11-16, 1984, p. 456-463.

VIKING LANDER MOSAICS OF MARS

E.C. Morris

The Viking Lander 1 and 2 cameras acquired many high-resolution pictures of the Chryse Planitia and Utopia Planitia landing sites. Based on computer-processed data of a selected number of these pictures, eight high-resolution mosaics have been published by the U.S. Geological Survey. The mosaics were formatted at the Image Processing Laboratories of the Jet Propulsion Laboratory of the California Institute of Technology, Pasadena, Calif., under the general supervision of Elliot C. Levinthal of the Department of Genetics, Stanford University, who represented the Viking Lander Imaging Team. The mosaics are composites of the best picture elements (pixels) of all the Lander pictures used. In the computer-mosaicking process, the data derived from the images were assigned priorities on the basis of quality or detail. These data were examined by the computer in sequence according to the priorities, and the best pixels of each data set were used for the mosaic. Mosaics from Lander 1 data consist of one mosaic from each camera, forming a pair; one pair was made from data taken in the morning (0700-0800 hours) and the other from data acquired in midafternoon (1400-1530 hours). Similarly, three pairs of mosaics of the Lander 2 site consist of one pair acquired between 0700 and 0800 hours, one pair at noon, and one pair between 1700 and 1800 hours.

Each complete mosaic extends 342.5° in azimuth, from approximately 5° above the horizon to 60° below, and incorporates approximately 15 million pixels. The procedures used for processing the Viking Lander Camera data were described by Levinthal and others (1977). A detailed description of the multiple steps involved in the construction of the Viking Lander mosaics was given by Levinthal and Jones (1980).

The mosaics were published as part of the Atlas of Mars, Miscellaneous Investigations Series. Each mosaic is shown in a set of five sheets. One sheet contains the full panorama from one camera taken in either morning or evening. The other four sheets show sectors of the panorama at an enlarged scale; when joined together they make a panorama approximately 2' X 9'.

The Viking Lander 1 mosaics were published in 1982 and the Viking Lander 2 mosaics in late 1984. They will be distributed to all Regional Planetary Imaging facilities and will be available from the U.S. Geological Survey Map Distribution Centers.

The mosaics are identified as follows:

U.S. Geological Survey, 1982, Viking Lander 1 Rectified Photomosaics - Morning Scene - Camera 1, Miscellaneous Investigations Series Map I-1366

U.S. Geological Survey, 1980, Viking Lander 1 Rectified Photomosaics - Morning Scene - Camera 2, Miscellaneous Investigations Series Map I-1243

U.S. Geological Survey, 1982, Viking Lander 1 Rectified Photomosaics - Evening Scene - Camera 1, Miscellaneous Investigations Series Map I-1368

U.S. Geological Survey, 1982, Viking Lander 1 Rectified Photomosaics - Evening Scene - Camera 2, Miscellaneous Investigations Series Map I-1367

U.S. Geological Survey, 1984, Viking Lander 2 Rectified Photomosaics - Morning Scene - Camera 1, Miscellaneous Investigations Series Map I-1515

U.S. Geological Survey, 1984, Viking Lander 2 Rectified Photomosaics - Morning Scene - Camera 2, Miscellaneous Investigations Series Map I-1516

U.S. Geological Survey, 1984, Viking Lander 2 Rectified Photomosaics - Evening Scene - Camera 1, Miscellaneous Investigations Series Map I-1517

U.S. Geological Survey, 1984, Viking Lander 2 Rectified Photomosaics - Evening Scene - Camera 2, Miscellaneous Investigations Series Map I-1518

References Cited

Levinthal, E. C., Green, William, Jones, K. L., and Tucker, Robert, 1977, Processing the Viking Lander camera data: Journal of Geophysical Research, v. 82, no. 28, p. 4412-4420.

Levinthal, E. C., and Jones, K. L., 1980, The mosaics of Mars as seen by the Viking Lander cameras: NASA Contractors Report 3326.

VOYAGER CARTOGRAPHY

R. M. Batson, P. M. Bridges, and K. F. Mullins, U.S.Geological Survey, Flagstaff, AZ 86001

The Jovian and Saturnian satellites are being mapped at several scales from Voyager 1 and 2 data [1,2,3]. The maps include specially formatted color mosaics [4], controlled photomosaics, and airbrush maps.

More than 500 Voyager images of the Jovian and Saturnian satellites have been radiometrically processed in preparation for cartographic processing. Of these images, 235 have been geometrically transformed to map projections for base mosaic compilations. Film and magnetic tape copies of the images have been distributed to the Regional Planetary Image Facilities.

Special techniques for producing hybrid photomosaic/airbrush maps of Callisto are currently under investigation. The techniques involve making controlled computer mosaics of all available images with highest resolution images superimposed on lowest resolution images. The mosaics are then improved by airbrushing: seams and artifacts are removed, and image details enhanced that had been lost by saturation in some images. If these techniques result in maps of publication quality, they will be used to compile the 1:5,000,000-scale series of relief and albedo maps of Callisto.

A controlled mosaic of the northern hemisphere of Rhea is complete, as is all processing for a similar mosaic of the equatorial region. Work on the equatorial section has been suspended pending resolution of severe control problems.

Current plans and status of the various series are shown in the following table:

SERIES	TOTAL NUMBER OF QUADRANGLES	NUMBER IN PROGRESS	COMPILATION COMPLETE	NUMBER PUBLISHED
Galilean Satellites:				
Preliminary Voyager maps	4	-	4	4
Io 1:15M color mosaics+	2	-	2	-
1:15M relief only	1	-	1	-
1:15M relief & albedo*	1	-	1	-
1:5M relief & albedo*	3	-	3	-
special B&W mosaics#	1	-	1	1
Europa 1:15M color mos	1	-	1	-
1:15M rel & alb*	1	-	1	-
1:5M rel & alb*	2	-	2	2
Ganymede 1:25M rel & alb*	1	-	-	-
1:15M relief & albedo*	3	-	-	-
1:5M relief & albedo*	15	4	6	3
Callisto 1:25M rel & alb*	1	-	-	-
1:15M rel & alb*	3	-	-	-
1:5M rel & alb*	15	3	-	-

SERIES	TOTAL NUMBER OF QUADRANGLES	NUMBER IN PROGRESS	COMPILATION COMPLETE	NUMBER PUBLISHED
Saturnian Satellites:				
Preliminary Voyager maps	10	-	10	10
Mimas 1:2M rel & alb*	1	-	-	-
1:2M rel only	1	-	-	-
Enceladus 1:2M rel & alb*	1	-	-	-
1:2M rel only	1	-	-	-
Dione 1:5M rel & alb*	1	-	-	-
1:5M rel only	1	-	-	-
Tethys 1:5M rel & alb*	1	-	-	-
1:5M rel only	1	-	-	-
Rhea 1:10M rel & alb*	1	-	-	-
1:10M rel only	1	-	-	-
1:5M mosaics	1	1	-	-
Iapetus 1:10M rel & alb*	1	-	-	-

+separate mosaics for Voyager 1 and Voyager 2 images.

*includes 1 version with names and graticule, and a second version with image base only.

#three maps on one sheet

References

[1] Batson, R. M., Bridges, P. M., Inge, J. L., Isbell, C. E., Masursky, Harold, Strobell, M. E., and Tyner, R. L., 1980, Mapping the Galilean satellites of Jupiter with Voyager data: Photogrammetric Engineering and Remote Sensing, 46, 10, 1303-1312.

[2] Batson, R. M., Bridges, P. M., and Mullins, K. F., 1981, Voyager cartography: in Reports of the Planetary Geology Program, NASA TM 84211, 484-485.

[3] Batson, R. M., Bridges, P. M., Inge, J. L., Lee, E. M., Masursky, Harold, Mullins, K. F., Skiff, B. A., and Strobell, M. E., 1984, Voyager 1 and 2 atlas of six Saturnian satellites: NASA Spec. Pub. SP 474.

[4] McEwen, A. F., and Soderblom, L. A., 1984, High-resolution color images of Io: in Reports of the Planetary Geology Program, NASA TM 86246, 38.

A UNIFIED LUNAR CONTROL NETWORK

Merton E. Davies, The Rand Corporation, Santa Monica, California 90406

At this time, control on the Moon is composed of a number of independent regional networks; these networks frequently have different origins and never have common ties even in overlapping areas. The objective of the unified network program is to tie the regional networks into a single consistent planetwide control network. The plan is to start with the best defined regions, create common ties with neighboring data sets, and then expand into poorly defined regions.

The most accurately defined points on the Moon are locations of the laser ranging retroflectors (Ferrari et al., 1980) and the VLBI measurements of the locations of the ALSEP stations (King et al., 1976). The accuracy of these locations is about 30 m and their locations are used to define the center-of-mass and hence the origin of the unified lunar coordinate system.

The Apollo 15, 16, and 17 ALSEP stations have been identified on Apollo panoramic photography and their locations transferred to Apollo mapping frames. Thus their coordinates are available in the control network computations.

Two primary control networks have been computed based on the Apollo mapping pictures; they are the DMAAC/A15 system (Schimerman, 1976) and the NOS/USGS system (Doyle et al., 1977). Although these systems were computed relative to the center-of-mass it was necessary to translate their origins to best-fit the ALSEP locations. The DMAAC/A15 system was translated 299±165 m and the NOS/USGS system was translated 2033±575 m.

Many control networks have been computed based on pictures of the Moon taken through telescopes; these cover the Earth-facing region. Probably the most carefully prepared network is that published by Meyer, 1980, and this is the one incorporated in the present program. Points common to the Apollo networks and the telescopic network have been selected. Using these points in the overlapping region of the two networks, best-fit translation, rotation, and scale parameters are computed to adjust the telescopic net to the Apollo net. As a start, ten well distributed points have been selected and parameters determined to adjust the telescopic network to the translated DMAAC/A15 system and the NOS/USGS system. The goodness of fit has not yet been examined.

References

Doyle, Frederick J., Atef A. Elassal, and James R. Lucas, *Selenocentric Geodetic Reference System*, National Oceanic and Atmospheric Administration, Technical Report NOS70NGS5, February 1977.

Ferrari, A. J., W. S. Sinclair, W. L. Sjogren, J. G. Williams, and C. F. Yoder, "Geophysical Parameters of the Earth-Moon System," *J. Geophys. Res.*, Vol. 85, No. B7, July 10, 1980, pp. 3939-3951.

King, R. W., C. C. Counselman III, I. I. Shapiro, "Lunar Dynamics and Selenodesy: Results From Analysis of VLBI and Laser Data," *J. Geophys. Res.*, Vol. 81, No. 35, December 10, 1976, pp. 6251-6256.

Meyer, Donald L., *Selenocentric Control System (1979)*, Defense Mapping Agency, DMA TR 80-001, April 1980.

Schimerman, Lawrence A., *The Expanding Apollo Control System*, Defense Mapping Agency Aerospace Center, August 1976.

THE CONTROL NETWORK OF MARS: OCTOBER 1984

Merton E. Davies, The Rand Corporation, Santa Monica, California 90406

Strips of Viking mapping pictures are being added to the planetwide control network of Mars. These high resolution strips run from the Viking 1 lander site east to Airy-0, north along the 0° meridian to 60° latitude, southwest through the Viking 1 lander site to the equator, and along the equator encircling the planet. Everywhere along these strips, old points are incorporated in the measurements, thus assuring that the strips and planetwide net make a single large data set. The control points are much denser in the areas covered by the strips than in those regions not covered by strips and as they are usually associated with smaller craters their coordinates will be more accurate. Within the strips the standard error of the coordinates of the control points is estimated to be less than 3 km and the error in longitude of a few points near Airy-0 is less than 40 m.

The horizontal coordinates of the control points on Mars have been updated with a single-block planetwide analytical triangulation computed in September 1982 (Davies and Katayama, 1983). The computation contained 47,524 measurements of 6,853 points on 1811 pictures. These comprised 1054 Mariner 9 and 757 Viking frames. The overdetermination factor was 2.48 and 19,139 normal equations were solved. The standard error of measurement was 18.06 μm. The longitude of the Viking 1 lander site was 47°.962 and the latitude 22°.480. The latitude of Airy-0 was -5°.152.

The Mars data set now contains 7,294 points, 50,168 measurements on 1054 Mariner 9 and 887 Viking Orbiter pictures, 20,411 normal equations, and a 2.46 overdetermination factor.

References

Davies, M.E., and F. Y. Katayama, "The 1982 Control Network of Mars," *J. Geophys. Res.*, Vol. 88, No. 89, September 10, 1983, pp. 7503-7504.

THE CONTROL NETWORKS OF THE SATELLITES OF JUPITER AND SATURN

Merton E. Davies, The Rand Corporation, Santa Monica, California 90406

Geodetic control networks are being computed photogrammetrically for the large satellites of Jupiter and many of the satellites of Saturn using pictures from the Voyager 1 and 2 encounters. Control points have been identified on the satellites and their coordinates computed by single-block analytical triangulations.

Coordinates for the control points on the Galilean satellites have been published in Davies and Katayama, 1981. Since that time additional points and pictures have been added to the data sets. Currently, the Io control net contains 644 points, with 11,100 measurements of these points on 205 Voyager 1 and 43 Voyager 2 pictures. This system contains 2,032 normal equations with 5.46 overdetermination. The Europa control network now contains 181 points, with 3,804 measurements of these points on 53 Voyager 1 and 67 Voyager 2 pictures. The network computations required solving 722 normal equations and the system had an overdetermination of 5.27. The Ganymede data set is very large, containing 1,825 points and 18,148 measurements of these points on 145 Voyager 1 and 155 Voyager 2 pictures. The system has 4,550 normal equations and an overdetermination of 3.99. The Callisto control network has been expanded and contains 944 control points and 14,060 measurements on 159 Voyager 1 and 99 Voyager 2 pictures. The overdetermination is 5.28 with 2,662 normal equations.

The control networks of the Saturnian satellites Mimas, Enceladus, Tethys, Dione, Rhea, and Iapetus have been published (Davies and Katayama, 1983a,b,c, 1984). The Rhea data set has been increased and now contains 418 control points, 4,343 measurements on 83 Voyager 1 and 3 Voyager 2 pictures, 1,094 normal equations, and an overdetermination of 3.97.

References

Davies, M. E., and F. Y. Katayama, "Coordinates of Features on the Galilean Satellites," *J. Geophys. Res.*, Vol. 86, A10, September 30, 1981, pp. 8635-8657.

Davies, M. E., and F. Y. Katayama, "The Control Networks of Mimas and Enceladus," *Icarus*, Vol. 53, No. 2, February 1983a, pp. 332-340.

Davies, M. E., and F. Y. Katayama, "The Control Networks of Tethys and Dione," *J. Geophys. Res.*, Vol. 88, A11, November 1, 1983b, pp. 8729-8735.

Davies, M. E., and F. Y. Katayama, "The Control Network of Rhea," *Icarus*, Vol. 56, No. 3, December 1983c, pp. 603-610.

Davies, M. E., and F. Y. Katayama, "The Control Network of Iapetus," *Icarus*, Vol. 59, No. 2, August 1984, pp. 199-204.

SHAPE OF IO

S.P. Synnott, J.E. Reidel, J.C. Callahan, A.J. Donegan

Jet Propulsion Laboratory, California Institute of Technology,
Pasadena, California 91109

Abstract

The primary purpose of the work described here is to measure the triaxial shape of Io from Voyager images.

The shape of Io has been of considerable interest since Voyager images revealed Io's volcanism. The tidal flexing of Io due to its eccentric motion around Jupiter has been identified as the liekly energy source for the volcanism, and Io is expected to be largely molten. It would therefore be expected to be very nearly in hydrostatic equilibrium. Under these conditions Dermott (1979) computes the semi axes differences to be (a-c) = 15.6 km, (b-c) = 3.9 km, where a > b > c, a points along the direction to the planet center and c is normal to the orbit plane. Since the resolution of the Voyager narrow angle camera is ~ 10^{-5} radians, and at ~ 5 x 10^5 km Io fills the field-of-view, we might expect the Voyager images to allow ~ 5 km measurement of Io's figure. We should then easily be able to see the (a-c) = 15 km presuming the viewing geometry allowed us to observe (a-c).

Two different approaches have been taken in the past to exploit the accuracy of the Voyager images and measure the triaxial shape of Io. Davies (1981) establishes a large grid of landmarks over the surface of the satellite, and observes the location of those features in many different frames which view the satellite from many different directions. The latitude and longitude of each grid point can then be determined, along with the global shape of the body. In the reference, only the mean radius of the body is mentioned, but Davies (private communication) has indicated that he obtained a solution of (a-c) ~ = 8 km, although he believes his error also is ~ 6 km, so his result may be only marginally inconsistent with a hydrostatic shape.

The second method, which is described here, determines the triaxial shape of a satellite by comparing the theoretical shape and location of the body's limb and terminator curves with the actual curves observed in the two dimensional images. In the coordinate system in which the principle axis of a triaxial ellipsoid are aligned along the system axis, $\xi\eta\zeta$, the equation of the figure is simple and well known.

$$\frac{\xi^2}{a^2} + \frac{\eta^2}{b^2} + \frac{\zeta^2}{c^2} = 1$$

The ξ axis points from the satellite center to planet center and the ζ axis is aligned essentially along the planet north pole vector. This system rotates with the period of the satellite, Conditions describing the limb or terminator can be written as $N \cdot L = o$ or $N \cdot S = o$, where N is the surface normal, L is the spacecraft-limb line of sight vector and S

is the Sun-object vector. These curves can then be projected into image space, and partials taken with respect to the three axes dimensions a,b,c.

Limb or terminator points are found by matching a model for the limb profile with the actual appearance of the limb in the digital data. The theoretical model for the limb model depends on the viewing and illumination geometry, the satellite reflection characteristicss and the camera 'point spread function'.

We will concentrate on imaging data taken of Io in the last 25 hours before Voyager 1's closest approach to the satellite. In Figure (1) the positions of Io and the spacecraft at the data times are marked by corresponding letters. The Voyager camera captures (a-c) very nearly directly at A, F and G, and (b-c) at C. Combinations of (a-c) and (b-c) are observed at the other times.

The data is of various types. At positions A and B, Io's full figure is captured in a single narrow angle frame. The distances at these positions range from 1.4×10^6 down to 0.9×10^6 km, so that a 1 pixel measurement amounts to ~ 14 to 9 km. However, with averaging over a large number of limb points the actual size estimation capability is significantly smaller.

At positions C, D, E, F, 2 x 2 mosaics of Io are shuttered at distances ranging from 6×10^5 to 3.7×10^5 km and so the potential accuracy of measuring the projected dimensions is a few kilometers. In this time our view of Io changes from seeing (b-c) directly to seeing (a-c) directly. A scene is shown in Figure (2). There is considerable overlap (~ 1/3 field-of-view) between frames so that some landmarks will appear in these common areas. The relative inertial pointing directions of each frame can therefore be estimated to an accuracy limited by our ability to choose repeatedly the same point on an extended landmark image. Using a number of such landmarks, the relative picture pointing is determinable to sub-pixel accuracy. The position of a landmark in a picture is predicted by transforming it's known angular and radial position from the satellite fixed to the camera system in a manner similar to that described above. The landmark latitudes and longitudes of Davies (1981) serve as our a priori.

At H, several wide angle frames capture the whole disk of Io and at J 2 x 2 wide angle mosaics are needed to cover the satellite. Here again, resolutions is of the order of a few kilometers.

After we have determined the relative pointing of mosaic frames, and chosen limb points, we then compute differences between the observed and theoretically predicted limb points to form residuals, and take partials of these points with respect to the satellite dimensions a, b, c. We then solve for these dimensions in a least squares fit.

To date, 12 frames have been processed. The frames were selected so that a complete 2 x 2 mosaic from each of the data sets C, E, F would be analyzed. With a data weighting of 1 pixel, the formal errors on the three semi-axis dimensions a, b, c are less than 1 kilometer. Because we have not yet been able to accomplish all the desired testing of the sensitivity of the solution with respect to error sources such as the

extensive albedo variations on Io we currently set more realistic uncertainties on the axis estimates as follows

a = 1830 ± 5 km
b = 1822 ± 5 km
c = 1814 ± 5 km

The root-mean-square of the postfit residuals is ~ 0.6 pixels.

In the next six months to a year we expect to test the solution sensitivity to various limb detection algorithms and to include all the useful Io data in one fit. We then expect to apply the technique to other satellites which may have appreciable oblateness such as Mimas, Enceladus and Tethys.

References:

S.F. Dermott (1979) ICARUS 37 575-586
M. E.Davies (1981) JGR 86 8635

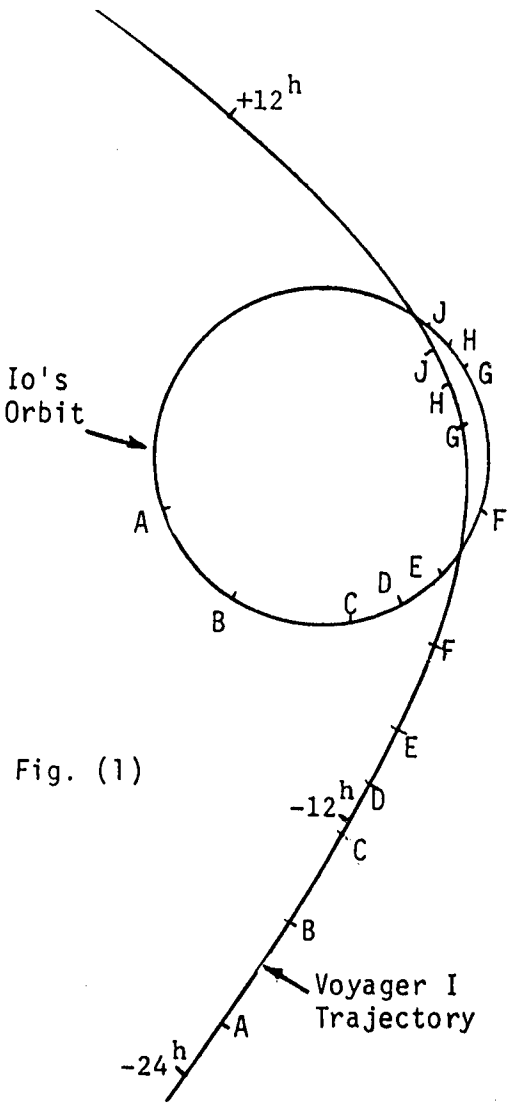

Fig. (1)

2x2 MOSAIC OF IO

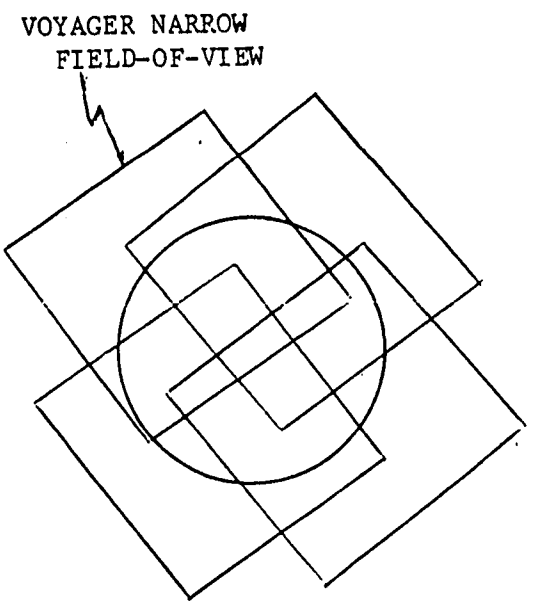

Fig. (2)

CHAPTER 16

SPECIAL PROGRAMS

Page intentionally left blank

WASHINGTON UNIVERSITY'S EARTH AND PLANETARY REMOTE SENSING LABORATORY IMAGE PROCESSING SYSTEM

L. Bolef, E. Guinness, S. Slavney, R. Arvidson, McDonnell Center for the Space Sciences, Department of Earth and Planetary Sciences, Washington University, St. Louis, MO 63130

In this abstract we describe the capabilities of our digital image processing system and the philosophy that we used in its assembly. The capabilities should be of interest to the planetary science community and we hope that our experiences in system design might be of use to those researchers about to put together their own systems. The system configuration is shown in Figure 1.

Our design goals included: (a) assembling an easily used, interactive system flexible enough to handle vector and array data, independent of specific data types (e.g. Landsat TM vs. Viking Lander images vs. aeromagnetic anomalies); (b) using commercial hardware; (c) taking advantage of wide band, consumer technologies such as videodisks, which offer large ratios of data volume to hardware cost; (d) developing as little in-house software as possible. The last goal was a major constraint, driven by the fact that we have a small research group and cannot afford major software development efforts. Thus, in designing the system, the hardware choices were governed to some extent on the basis of availability of and compatibility with free or inexpensive software packages.

Our hardware consists of a Digital Equipment Corporation VAX 11/750 minicomputer and peripherals. The system has four megabytes of physical memory plus a floating point processor for fast execution of complex image analysis operations. Three 405-megabyte hard disks are used for digital data storage. Long-term storage on magnetic tape is accomodated by two tape drives capable of handling densities of 800, 1600, and 6250 bpi. We also have high-density analog storage on three-quarter-inch videotape. The videotape system also has an animation capability that uses one of the few in-house developed interfaces. A videodisk player is used with our BIRP programs to do image SEDR searches and interactive browsing through images.

Two workstations provide interactive image processing. The first is a Ramtek system that supports a 1024x1280 pixel monochrome display. The second is a color display built by Computer Design and Applications, Inc. The color display occupies 512x480 16-bit pixels. The color display is part of a CDA MSP-3000 array processor with 2 megabytes of memory. This combination display/processor workstation allows us to transfer data from the VAX and to work with it at about 5 to 10 times VAX speed, thereby both increasing speed and offloading CPU-intensive work from the VAX. Hard copies are generated from a Matrix 1024x1280 color camera. For graphics displays, we have four terminals which operate in either alphanumeric or graphics mode, and a low-cost printer/plotter that can produce graphs, maps, etc., in addition to draft- and letter-quality printouts.

We based our software on TAE, the Transportable Applications Executive developed at Goddard Space Flight Center (Table 1). This package acts as the interface between the user and the application programs. It provides a menu system and online help for novice users, and terse command-line entry for users familiar with the system. The use of TAE is especially important to us because of the relatively large number of novices (students) being trained in image processing. Because of the extensive self-tutoring modes, TAE significantly reduces the amount of formal training. Our image processing software is based on the Landsat Assessment System (LAS), which was designed to use TAE. LAS includes application programs and a special set of subroutines for doing image disk I/O. Both TAE and LAS are supported by outside organizations, relieving us of the need to spend a lot of time maintaining them. In addition to TAE and LAS, we have miscellaneous image processing programs from JPL's Mini-VICAR system and USGS Flagstaff's IPSYS system. We expect to receive the new MIPL image processing software from JPL in 1985, which also runs under TAE. Our graphics software, which was developed by the National Center for Atmospheric Research (NCAR), was integrated by us into the TAE environment. The graphics software can plot two- and three-dimensional graphs and contour maps, and provides a set of basic subroutines for creating custom-designed graphics programs.

The system, which has been operational for a number of months, supports some twenty researchers in planetary sciences, earth sciences, and marine geology. Currently, through the Pilot Planetary Data System efforts, we are adding a 9600 baud synchronous dial-up capability for communications with JPL, U. S. Geological Survey, Flagstaff, and the University of Hawaii. The intent of the activity is to initiate experiments in distributed computation and data management. It is hoped that during the Mars Geoscience Climatology Observor mission, for example, a distributed system will be in place to allow researchers to work on various data sets at their home institutions.

Table 1. Software Components

Function	Component	Source
Operating system	VMS	Digital Equipment Corporation
Manager	TAE	Goddard Space Flight Center
Graphics	NCAR	National Center for Atmospheric Research
Image processing	LAS	Goddard Space Flight Center
	VICAR	Jet Propulsion Laboratory
	IPSYS	U.S. Geological Survey
	WU	Washington University EPRSL
	SPAM	Jet Propulsion Laboratory
Array processor	DeltaPro	Computer Design and Applications
Data base management	BIRP	Washington University EPRSL
	RIM	NASA
	RDB	Digital Equipment Corporation

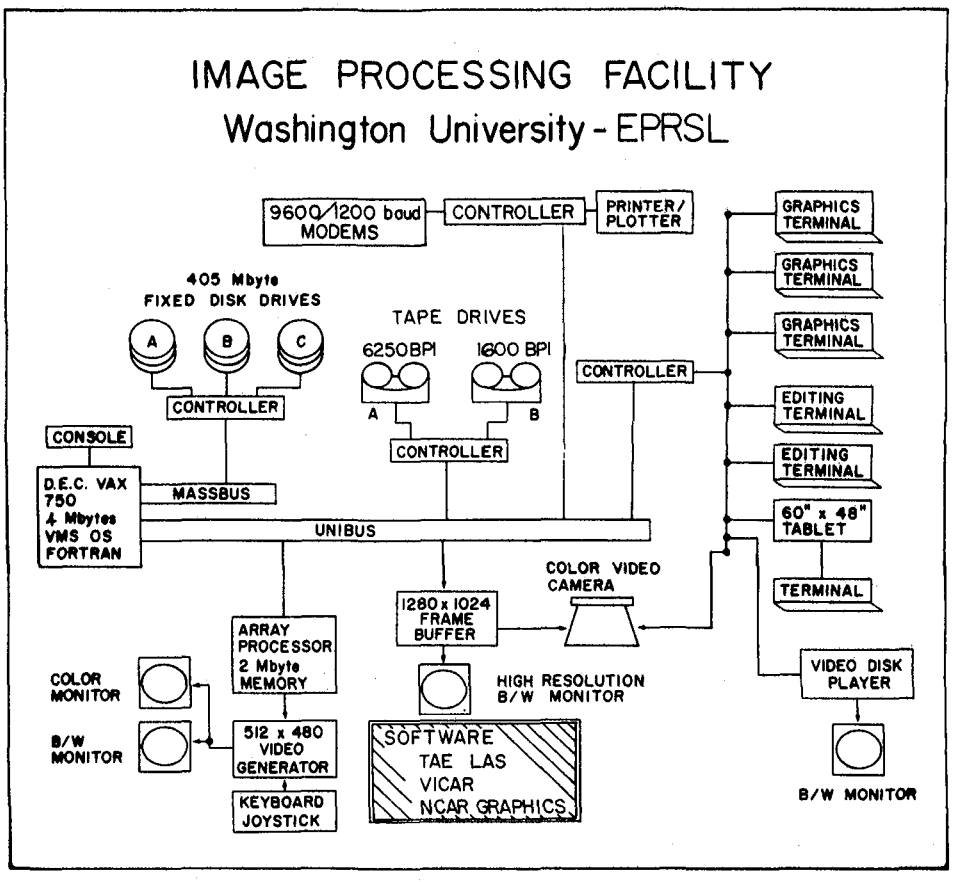

Figure 1

EXPERIMENTS IN DISTRIBUTED COMPUTATION AND DATA MANAGEMENT USING PROTO-TYPE MGCO DATA

R. Arvidson, M. Presley, McDonnell Center for the Space Sciences, Department of Earth and Planetary Sciences, Washington University, St. Louis, MO 63130

It is clear that in many cases the best science data are those that are kept under the control of the science community, since that community has a vested interest in producing calibrated, high quality data for use in their research (1). Given the wide geographic distribution of researchers interested in Mars, together with the rapid increase in computation and data management capabilities (even at constant cost) (2), it also is clear that the trend is toward production and maintenance of data sets at different geographic locations. On the other hand, in certain circumstances the real scientific "payoff" comes from analyses of a variety of data. For instance, comparison of Viking images and IRTM data with MGCO imaging spectrometer, gamma ray, and altimetry data will probably produce the most significant scientific returns of the MGCO mission. No one research group has the expertise to understand all these data sets at the appropriate level to conduct quantitative science with them. Thus, teams or consortia of investigators are needed. In the past, detailed comparison of data from different missions or even from different sensors on the same scan platforms have usually been done long after the data were acquired. In addition, the comparisons have necessarily been part of a centralized processing effort (e. g. Lunar and Mars Consortia) given the technologies available to the science community at the time. In the early 1990's one can hope that advances in computation and data management technologies, combined with an increased sophistication of the science community, will facilitate comparisons within a geographically distributed system. That hope will not become a reality without working on the beginning steps now.

With funding from the Pilot Planetary Data System (Information System Office, NASA) we are conducting technology experiments in distributed systems, including: (a) use of 9600 baud dial-up modems for synchronous data transfer, (b) use of common interfaces to relational data base software, (c) use of digital videodisks for high volume, low cost data transfer, (d) evaluation of work stations with significant local processing capabilities so as to offload processing from system central processors, (e) ways of searching Viking images by geographic coordinates, using spacecraft and scan platform state vectors. The distributed system involves Washington University; the U. S. G. S. , Flagstaff; University of Hawaii; and the Jet Propulsion Laboratory.

We are using comparisons of Viking and Earth-based observations of the surface of Mars as the science driver in conducting the technology experiments. In essence these data represent the kinds of data we will need to deal with during MGCO. The intent is to allow one group (Washington University) to maintain a subset of digital Viking images, another (U. S. G. S.) to maintain IRTM, another (JPL) to maintain radar, and finally, another (University of Hawaii) to maintain reflectance observations. We have received a set of Viking survey mission images on

tape from JPL. We are also implementing software to radiometrically and geometrically calibrate the data, including the use of ground control points to update camera pointing (C-matrix) information.
Scientifically, our efforts this year have centered on construction of an eight frame Viking digital image mosaic (341S03 to 10), with brightness values being proportional to bi-directional reflectance. Implementation of the software and generation of the mosaic have not been trivial tasks, since separate consultations with JPL, USGS Flagstaff, Cornell University, and Merton Davies, Rand Corp. were needed to move forward. The mosaic is complete and work is just now beginning on generation of a digital geologic map from the mosaic. The mosaic is located in the cratered terrain, covering the Baldet and Antoniadi basins. The intent is to use the mosaic and the map as a digital base for comparison with optical, thermal, and radar properties of the surface. We hope to be able to map bedrock and soil and test the hypothesis of isochemical weathering of soil from local bedrock. Goldstone 1982 radar data, which cover the area, are still being processed at JPL. Earth-based spectral reflectance data were acquired by the University of Hawaii over the test site in the spring of 1984 and those data are also still being processed. Finally, the IRTM data base query structure is presently being restructured at Flagstaff. IRTM data thus will not be available for several months. Thus, most of this year has been spent getting ready to do the science, and particularly for us, in implementing procedures for calibration and mosaicking of Viking images.

REFERENCES CITED

1. Bernstein, R., R. Arvidson, et al., 1982, Data Management Computation: Volume 1: Issues and Recommendations, CODMAC, National Academy Press, 167 p.

2. Arvidson, R., et al., 1984, Data Management and Computation: Volume 2: Guidelines for Planning, Implementing, and Operating Space Science Data Management Units, CODMAC, In Press.

PLANETARY SCIENCE EXPERIMENTS ABOARD SPACE STATION: WORKSHOP REPORT

R. GREELEY
Department of Geology, Arizona State University, Tempe, Arizona, 85287

A workshop was held to consider experiments that could be conducted in an earth orbital environment to shed light on various planetary processes. The 22 participants represented a cross section of university, institution, and NASA Center investigators and included aerospace industry and Headquarters representatives. Many planetary processes (e.g. impact cratering, particle formation and interaction, crystal settling and magma evolution) are currently being studied through laboratory experiments. Although gravity is a critical term in many of these experiments, there is no suitable means for physically modelling reduced gravity in experiments conducted on Earth. Because most planetary environments involve low gravity conditions, workshop participants concluded that such experiments could be profitably carried out on a Space Station to gain fundamental knowledge of a wide variety of planetary processes. A developmental program could include feasibility experiments involving both the KC-135 aircraft (which provides microgravity conditions up to ~40 seconds duration) and shuttle. Such experiments would provide critical design information for the space station experiments and may yield significant science results as well. In addition, it was suggested that a second workshop be held to consider the full range of planetary investigations that could be conducted on Space Station.

PLANETARY NOMENCLATURE

M. E. Strobell, Harold Masursky, and C. D. Nordquist; U.S. Geological Survey, Flagstaff, AZ

Almost 4,000 names have been applied to surface features on planetary bodies. The majority have been applied during the last 20 years in conjunction with the space exploration program. Breakdown of names by planetary body is as follows: Moon, 2016; Mars, 927; Mercury, 270; Venus, 79; satellites of Jupiter, 340; satellites of Saturn, 191; total, 3823. These names will be listed in a series of annual Gazetteers of which the first version is being open filed by the U.S. Geological Survey early in FY 1985. Names in the Gazetteer are sorted in three ways: by planetary body and feature type, by feature type only, and alphabetically. An illustrated version of the Gazetteer will be published by the National Aeronautics and Space Administration in FY 1986.

In FY 1984, 32 additional names were proposed for craters on Mercury, 11 for craters on the Moon, 24 for features on 48 maps of Mars, 26 for features on three maps of Ganymede, 14 for features on 2 maps of Europa, and 43 for features on 3 maps of Io. The new names on the Moon and Mercury, 24 of the new names on Io, and several of the names on Mars and Ganymede were chosen at the request of investigators writing papers on these planetary bodies. Two new names for feature types on Venus and three on Mars were selected and given provisional approval by I.A.U. committees. The nomenclature on the 1:15 million-scale maps of Mars was prepared for publication in FY 1985; these maps will display all names that appear on maps at 1:2 million-scale or smaller, and will constitute the first complete compendium of names in a single map series. A name bank has been established for surface features on known Uranian satellites and for possible new satellites of Uranus. Ten to twelve names of representative features shown on new equal-area maps of Earth, Moon, Mercury, Venus, Mars, and four Jovian satellites have been chosen. Names for features on maps of the Saturnian satellites included in this series will be chosen next fiscal year.

Small satellites and Saturnian rings have also been named in FY 1984. In naming new satellites, an alphanumeric designation is assigned. Later, when Commission 20 of the International Astronomical Union considers that the orbit of a new satellite has been accurately determined, a formal name is assigned by the discoverer, working with the Working Group for Planetary System Nomenclature.

In FY 1985 the Gazetteer of Planetary Nomenclature will be updated and corrected to prepare it for publication by NASA. New names for features of potential interest to scientific investigators will be chosen for Uranian ring features and features on three to five additional maps of Ganymede, four maps of Io, three to five additional revised 1:5 million-scale maps of Mars, and a presently undetermined but potentially large number of 1:500,000-scale Martian maps. A report summarizing all nomenclature activity since the August 1982 meeting at Patras, Greece, will be prepared for presentation to the General Assembly of the International Astronomical Union at its triennial meeting in New Delhi, India, in November 1985. A chapter describing planetary nomenclature will be written for inclusion as a chapter in a forthcoming book on planetary cartography.

Task Group chairmen who should be consulted for nomenclature requirements and information are as follows: Moon, V. V. Shevchenko, Sternberg State Astronomical Institute, Moscow, U.S.S.R.; Mars, B. A. Smith, University of Arizona, Tucson, AZ; Mercury, David Morrison, University of Hawaii, Honolulu,

Hawaii; Venus, M. Ya. Marov, U.S.S.R. Academy of Sciences, Moscow, U.S.S.R.; and Outer Planets, T. C. Owen, State University of New York, Stoney Brook, L.I., NY. A new Task Group is being formed to name surface features on asteroids and comets. Harold Masursky, U.S. Geological Survey, Flagstaff, AZ, is president of the Working Group that oversees the Task Groups.

SOLAR SYSTEM NOMENCLATURE

Tobias Owen (ESS, State University of New York, Stony Brook, N. Y. 11794)

The work supported by this grant involves the selection of names for surface features on planets and satellites, the approval of names of new satellites, and the designation of discrete features within systems of rings. This activity is carried out within the structure of the International Astronomical Union, by a Working Group and several Task Groups. The present grant supports the activities of four American scientists on these groups: M. Davies, H. Masursky, T. Owen, and B. A. Smith.

During the present tenure of the grant, the principal focus of our work was the organization and support of an international meeting at Mkhseta in the Georgian SSR, in April of 1984. At that meeting, the various task groups met and submitted their recommendations to the Working Group, which in turn will pass them along to the Executive Committee of the IAU. A subsequent session was held at the COSPAR meetings in Graz, Austria in June. Highlights of the agreements reached at these meetings are as follows:

Satellite Names - K. Aksnes reported that no new satellites have been added to the list of those with confirmed orbits. The eclipses of Pluto's satellite that would give final definition to its orbit (and prove its uniqueness) have not yet begun. The group approved the following names for the two F-ring shepherds in the Saturn system:

1980	S-26	Pandora	(outer shepherd)
1980	S-27	Prometheus	(inner shepherd)

These names were suggested by the discoverers, S. A. Collins and D. E. Carlson. The names cannot be used until final approval of the orbits is given by IAU Commission 20. A name for Dione B will be chosen by A. Brahic in consultation with T. Owen and with the discoverer, J. Lecacheaux.

Surface Features on Satellites - P. Millman pointed out that both W. C. Bond and G. P. Bond deserve credit for the discovery of Hyperion. Hence initials of both of these astronomers must be added to the name "Bond" designating a dorsum on Hyperion. G. Burba and A. T. Basilevsky submitted a list of corrections for names on Io, Europa, and Callisto.

Nomenclature for Satellites of Uranus - There was considerable discussion of possible schemes for naming features on the surfaces of the satellites of Uranus. The most popular modes at present are to use names from Shakespeare's plays or names of mythical spirits from the literature of many countries. The possibility of using names of optimistic heroines from world literature for features on Miranda has also been raised. No decision has yet been reached.

Features in Saturn's Rings - The high resolution observations of structures in the rings of Saturn has led to a need for additional names. The group decided to continue the existing tradition, using names of scientists who have made substantive contributions to the theory or observations of the rings. A list of such names was compiled for distribution to scientists working in the field. The Group will then review suggestions from these workers and submit approved names to the Working Group.

Atmospheric Features on Giant Planets - R. Beebe volunteered to form a subgroup consisting of herself, B. Smith, and V. Teifel' to develop a self-consistent system for designating long-lasting dynamical regimes on all of the giant planets.

Lunar Nomenclature - The Working Group approved three lists of names presented by the Lunar Task Group Chairman, V. V. Shevchenko.
Mercury Nomenclature - A request has been received from scientists working on Mercury topographic features for approximately 100 new names. An appropriate list is being developed by D. Morrison and M. Davies.
Venus Nomenclature - The success of the Venera 15 and 16 radar orbiters has led to a requirement for additional names and for new descriptive feature terms. The Working Group approved a list of mythological names presented by Venus Task Group Chairman, M. Marov. A proposal was made to include names of radio engineers and space scientists as a category to be used in naming Venus features. This proposal, as well as lists of additional names and new descriptive terms, will be reviewed by the Task Group during the next year, for presentation at the 1985 meetings.
Mars Task Group - The Working Group approved the new names suggested by Chairman B. A. Smith with some minor modifications. The term Labes was substituted for Lapsus in response to a request from D. Ya Martynov. This term designates landslides. The term Fluctus to designate flows, was approved.
Gazeteer - H. Masursky reviewed the progress in compiling a complete listing of all the nomenclature for all the planets and satellites. This project will require additional effort and review during the coming year's activity.

ADDITIONAL ABSTRACTS

Page intentionally left blank

CRATER LYOT AND THE DISSECTION OF THE NORTHERN HIGHLAND SCARP OF MARS

H. M. Ferguson and B.K. Lucchitta, U.S. Geological Survey, Flagstaff, Arizona 86001

Geologic mapping based on medium- to high-resolution Viking images in the Ismenius Lacus quadrangle of Mars has led to an assessment of the interaction between the emplacement of crater Lyot and the dissection of scarps and channels of the fretted terrain (Fig. 1). Crater Lyot (lat 50.5° N., long 330.5° W.), a peak-ring basin 220 km in diameter, has a conspicuous ejecta blanket and well-developed radial secondary-crater chains similar to those associated with craters on the Moon. The ejecta and secondary craters are asymmetric around Lyot. Toward the southeast, secondaries extend about 1,500 km from the rim, but on Lyot's southwest and south sides, ejecta at places extend to only 80 km from the crater and secondary craters are extraordinarily sparse. This excluded zone is in a region of abundant mesas and associated debris blankets of the fretted terrain. A primary purpose of this study was to investigate whether the excluded zone is due to the obliqueness of Lyot's impact or is the result of mantling by plateau material; our results indicate that oblique impact is the more likely cause. This study also led to observations concerning the relative time of emplacement of Lyot with respect to the dissection of the highland scarp and the development of debris blankets. We conclude that Lyot postdates the major dissection of the scarp, but that the emplacement of "active" as well as most "inactive" debris blankets postdates Lyot.

On Lyot's southwest side, within the excluded zone, mesas are composed of two layers, a lower dark layer and an upper light layer. The light layer is stripped back or completely eroded from numerous mesas, but in this area never occurs without the dark layer beneath it. This superposition relation suggests that both layers belong to the layered plateau sequence and were dissected together. The mesas on which only the dark layer remains extend northward where they have been buried by increasingly thick ejecta and by more secondary craters from Lyot, and perhaps by wind-blown materials. The burial of mesas indicates that Lyot was emplaced after the major dissection of this area took place. On the other hand, secondary craters from Lyot are nowhere found on top of debris lobes surrounding mesas; in fact, debris lobes appear to override secondaries, suggesting that the debris-wasting process continued into post-Lyot time. This observation agrees both with Squyres' (1978) assertion that different erosional regimes dissected mesas and formed debris blankets, and with Lucchitta's (1984) contention that dissection and debris-generation belong to the same process, but that the process may have been cyclic or very slow.

On Lyot's south side, also largely within the excluded zone, very few secondary craters from Lyot are seen on the floor between mesas and debris blankets, and secondaries are even scarcer on top of mesas, which are capped by the light layer and appear very smooth. Careful inspection suggests that secondaries and ejecta were indeed deposited on these mesas, but became smoothed either by a thin superposed blanket or by relaxation of the upper layer. The superposition of Lyot's secondary craters on the top

layer of mesas suggests that Lyot's excluded zone is caused by oblique impact from the southwest, and not by a burying layer.

On Lyot's southeast side, mesas are outliers from the adjacent plateau, which has abundant superposed secondaries from Lyot. The secondaries occur on top of the plateau as well as on the floors of troughs dissected into the plateau, indicating that dissection in this region predates Lyot.

Debris blankets in the area are conspicuous around mesas and on channel floors. We have classified the blankets as "active" and "inactive" according to several criteria. Around mesas, the "active" blankets are short (about 20 km long) and have profiles that are convex upward. The debris has fine striations or lineations perpendicular to the scarp whence it issued; a few blankets have low, backward-facing scarps or very narrow moats separating them from the originating mesa or plateau scarp. In channels, lineations on "active" blankets curve downslope to become parallel to the channel near its center. "Active" blankets have very few superposed craters and appear to have moved relatively recently. "Inactive" blankets on mesas have level tops and at many places moats separate them from adjacent scarps. In channels, "inactive" debris tends to have thick flutes or ridges and grooves parallel to the channel, and this central fill may have rugged edges bordering wide moats.

All of the debris blankets are light in color. Only "inactive" blankets surround the dark mesas. "Active" debris blankets are associated with the light upper layers on mesas containing both layers, or on mesas on which only the light layer is exposed. Apparently only the light layer forms debris blankets; the "inactive" remnants around dark mesas seem to stem from a time before the light upper layer was removed. The level profile of these "inactive" blankets, compared with the convex-upward profile of "active" blankets, suggests that ice or water was lost from the "active" blankets with time owing to sublimation into the air or percolation into the ground.

Debris-blanket activity along the northern highland scarp is not uniform in time or space. Some areas appear to have "active" debris blankets, others only residues. Kochel and Peake (1984) saw an age progression from older mesas in the northeast to younger mesas in the southwest. The types of debris blankets in channels support their observation: the western channels have more "active" debris than those in the east. However, on mesas, "active" blankets are more abundant in the north and northeast than in the northwest, but these occurrences may be due to the presence of the light layer in the north and northeast and its absence in the northwest.

References

Kochel, R. C., and Peake, R. T., 1984, Quantification of waste morphology in Martian fretted terrain: Proceedings, Lunar and Planetary Science Conference, 15th, in press.

Lucchitta, B. K., 1984, Ice and debris in the fretted terrain, Mars: Proceedings, Lunar and Planetary Science Conference, 14th, J. of Geophys. Res., v. 89, supplement, B409-418.

Squyres, S. W., 1978, Martian fretted terrain: flow of erosional debris: Icarus, 34, 600-613.

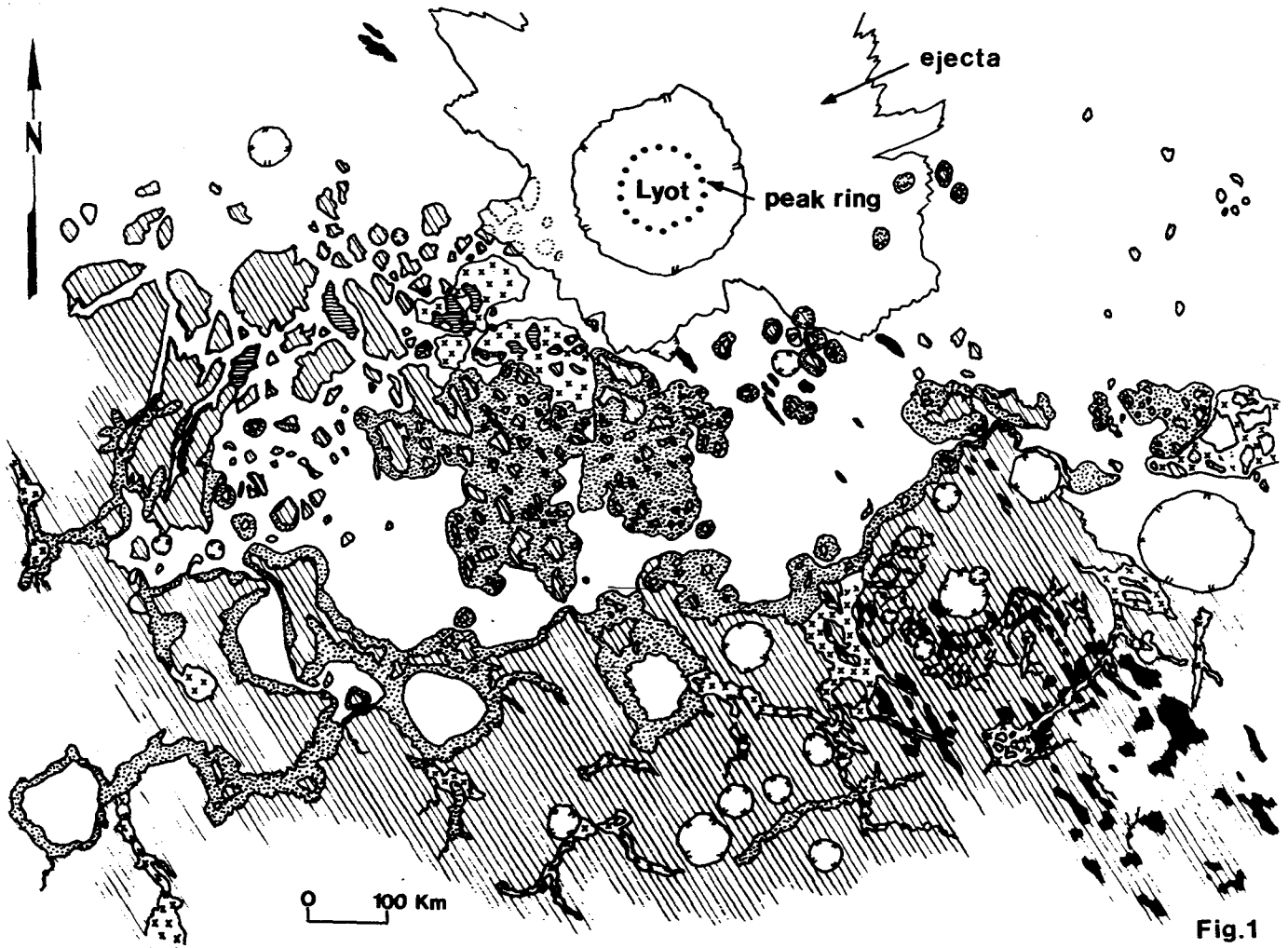

Fig.1

Mesa and plateau materials, undifferentiated

Dark-mesa materials

"Active" debris blankets and channel deposits

"Inactive" debris blankets and channel deposits

Other materials

Secondary craters

THEORETICAL INVESTIGATION OF THE EVOLUTION OF EOLIAN LANDFORMS

D. J. MacKinnon, USGS Flagstaff, AZ 86001, A. W. Ward, USGS Flagstaff, AZ 86001, R. Greeley, ASU Tempe, AZ 85281

The intent of this study is to develop a theoretically based numerical simulation of eolian processes in any planetary atmosphere. The effort involves: 1) utilization of existing fluid-flow computer codes to model wind flow; 2) employment of numerical, grid-generation techniques to account computationally for eolian landform shapes; 3) creation of empirical models of the erosional, transportational, and depositional response of sediment to the airflow; and 4) validation of the computer model by wind-tunnel simulation and by comparison with shape data obtained from terrestrial and Martian eolian landforms. The evolution of eolian landforms is simulated by successively employing the following steps: stating the landform shape, deriving the numerical grid, calculating the airflow, and changing the landform shape according to the erosional-response function. The model and validation procedures are being tested currently for two-dimensional forms (that are symmetric perpendicular to the airflow).

A general airflow computer program (supplied by Tom Pulliam, NASA-Ames) and a grid-generation program (provided by Reese Sorensen, NASA-Ames) have been tested for applicability to the landform modeling. For this study, the airflow program operates in a previously untested low-speed range and the grid program is applied to nonairfoil shapes with sharp corners.

Two experiments performed at the ASU wind tunnel facility generated a database to which the (grid/2-D) computer model has been compared. The first experiment measured the dynamic pressure over the surfaces of several plastic models. The models were built to span the entire width of the wind tunnel (perpendicular to the airflow) and differed only in cross-section parallel to the airflow. They ranged from half-cylinders to steep- and shallow-sloped, symmetric and asymmetric, triangular forms. The early computer model did not, however, reproduce the reverse eddy flow and dynamic pressure as measured behind all the wind tunnel models. After extensive computational tests at the Flagstaff USGS and NASA-Ames, a new version of the airflow program was compiled. The new program reproduces a reverse flow, but the dynamic pressure in the reverse flow region remains poorly modeled, in part because the established boundary layer in the wind tunnel is not duplicated fully in the computer models. Also, the calculated drag coefficients for simple cylinders are two to three times lower than those derived in experimental work (e.g. Fox and McDonald, 1973; Komar, 1983). The computer model does contain, however, a viscous dissipation model that can enhance the total drag. Even with these weaknesses, the airflow program reproduces with reasonable accuracy the airflow as observed over the cylindrical wind-tunnel models. The computed flow for the triangular models has not been generated, not only because of the previously mentioned program problems but also because of difficulty in modeling sharp points with the grid program.

In a second experiment at the ASU facility, the shape changes of simple erodible models were measured as a function of time. Two symmetric, triangular models, spanning the entire wind tunnel width, were formed of loose corn meal; two others were formed of sand. The ridge height of these models was 8 cm, and their bases ranged from 23 to 30 cm in width. In order to observe simple erosional processes, only one model was tested at a time and

the upstream airflow was free of sediment. The intent was to observe shape changes for a fixed wind speed, but the erosion ended after several minutes with only a slight downwind curving of the ridgeline. A speed increase up to a critical value caused the same minimal shape change. Beyond a critical value, rapid and extensive erosion began from a narrow, shallow depression in the ridgeline. The erosion occurred at the same location for each model tested, suggesting a possible cross-sectional flow asymmetry in the wind tunnel. As this depression widened and deepened the airflow became more channeled (Fig. 1). In less than 30 minutes the models eroded to a stable form whose cross-section taken at any location is that of the upper half of a two-dimensional airfoil (Fig. 2). The models showed the greatest erosion and smallest airfoil shapes at the location of the initial depression in the ridgetop; the erosion decreased on either side of this depression. Cross-sections were taken at several random locations across each model. All of the profiles, regardless of relative size, tended to fit closely a NACA airfoil with a thickness-to-length ratio of 0.25. This ratio also determines the minimum drag shape for this type of airfoil (Fox and McDonald, 1973). As Figures 3 and 4 show, the measured profiles do not attain a full airfoil shape; such was not expected because the granular material has gravitationally unstable slopes beyond the original model shape. The tendency for natural erosional forms to assume such a shape and ratio is common (e.g. Komar, 1983; Murty and El-Sabh, 1984; Ward and Greeley, 1984). These results, except for scale, support Komar's (1983) statement that the islands in Maja and Kasei Valles of Mars were sculptured by a turbulent fluid, but shape alone is insufficient to determine whether the primary agent was wind or water.

This research has not yet incorporated an erosional response model. It is important, however, to note the minimum drag forms suggested by the wind tunnel experiments. As an example, in an erosional response model, loose material might be removed at a point proportional to the local wind shearing stress above the threshold and deposited where the local wind stress is below threshold. With reference to the wind-tunnel forms, in this erosional response model, the front half of the form would be eroded and the back half filled in until a minimum wind drag shape was achieved. Furthermore, the size independence of the wind-tunnel forms suggests that some nondimensional airflow/erosion processes are operative. By varying specific planetary parameters, computer models of Martian and Venusian wind features may be developed.

References

Fox, R.W., and McDonald, A.T., 1973, Introduction of fluid mechanics: New York, Wiley, 630 p.

Komar, P.D., 1983, Shapes of streamlined islands on Earth and Mars: Experiments and analyses of the minimum-drag form: Geology, 11, 651-654.

Murty, T.S., and El-Sabh, M.I., 1984, Comments and reply on "Shapes of streamlined islands on Earth and Mars: Experiments and analyses of the minimum-drag form": Geology, 12, 569-572.

Ward, A.W., and Greeley, R., 1984, Evolution of the yardangs at Rogers Lake, California: Geological Society of America Bulletin, 95, 829-837.

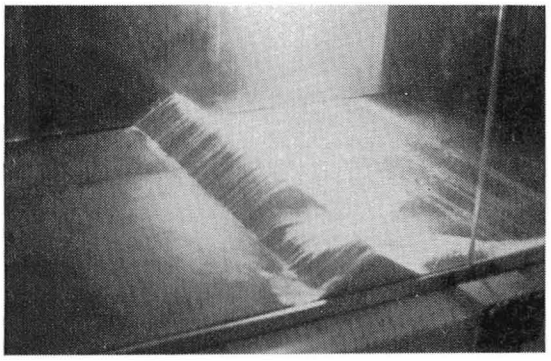

Fig.1 - Groove eroding in ridgeline of triangular model composed of sand.

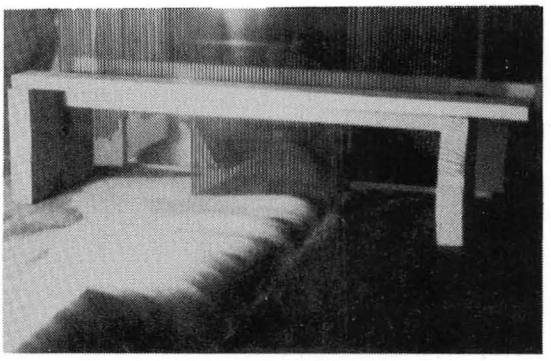

Fig.2 - Final shapes from sand model in Figure 1 taken with a profiler. Rod spacing one-quarter inch.

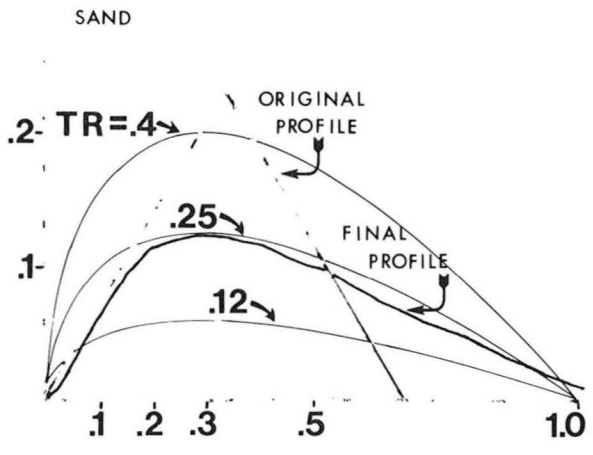

Fig.3 - Relative sizes of original and final profiles of sand model in Figure 1 compared to NACA airfoils of various thickness-to-length ratios (TR). Vertical scale exaggerated. In order to compare the final profiles to the NACA airfoil shapes, the horizontal position at which the maximum height on the final profile occurs was set equal to that same position (0.3) on the NACA airfoils. Numbers on the ordinate and abscissa are relative to the length of the NACA airfoils (1.0).

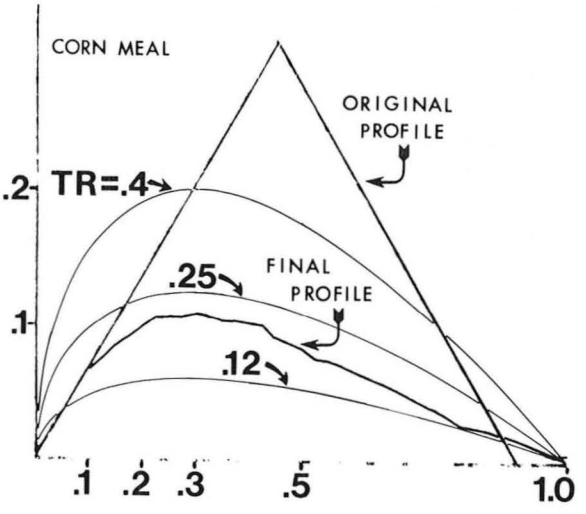

Fig.4 - Same as Figure 3 except material is corn meal.

STUDIES OF POTENTIAL MARS ROVER SAMPLE-RETURN SITES

Harold Masursky, D. H. Scott, and E. C. Morris, U.S. Geological Survey, Flagstaff, AZ

All of the Viking images, photomosaics, and geologic maps of Mars have been examined to select nine sites (Fig. 1) for detailed study, in view of a possible Mars Rover Sample-Return Mission. The sites were chosen on the basis of their location in areas where many varied geologic units are in close proximity. The sites will be targeted by the Mars Geoscience Climatology Orbiter to verify the presence of the inferred geologic units. If validated, the sites will become candidates for a rover mission with sample return in the mid-1990's. We are preparing photomosaic, topographic, and geologic maps of the selected areas that are more detailed than these previously compiled. The Memnonia site has been studied in detail by Scott and the Olympus Mons site by Morris; the Mangala Valles and Kasei Valles sites are under study by Masursky. These sites are located on the recently compiled geologic map of the western equatorial region of Mars [1]. The Memnonia region contains four geologic terranes of widely different ages formed in Amazonian, Hesperian, and Noachian time and of probably diverse chemical compositions. The Mangala site has similar units and, in addition, water-cut valleys that dissect the older units and are in turn overlain by younger deposits. Returned samples might therefore enable the radiometric dating of the fluvial episode in which the valleys formed. In the scarp surrounding Olympus Mons, four distinct basaltic flow units that constitute this great volcanic shield are available for sampling. Other sites are as follows: Candor Mensa, Elysium Montes, Nilosyrtis Mensae, Chasma Boreale, and Australe Planum. We have selected potential landing areas in half the sites. For site selection, we are assuming a 10-km diameter landing ellipse and a 50-km diameter roving capability with a total roving traverse of 100 km. In two of these sites all the inferred geologic units can be visited; in three others almost twice the roving capability is necessary to cover the primary objectives.

REFERENCE

[1] Scott, D. H., and Tanaka, K. L., 1984, U.S.G.S. Open-File Report 84-659-A, scale 1:15,000,000.

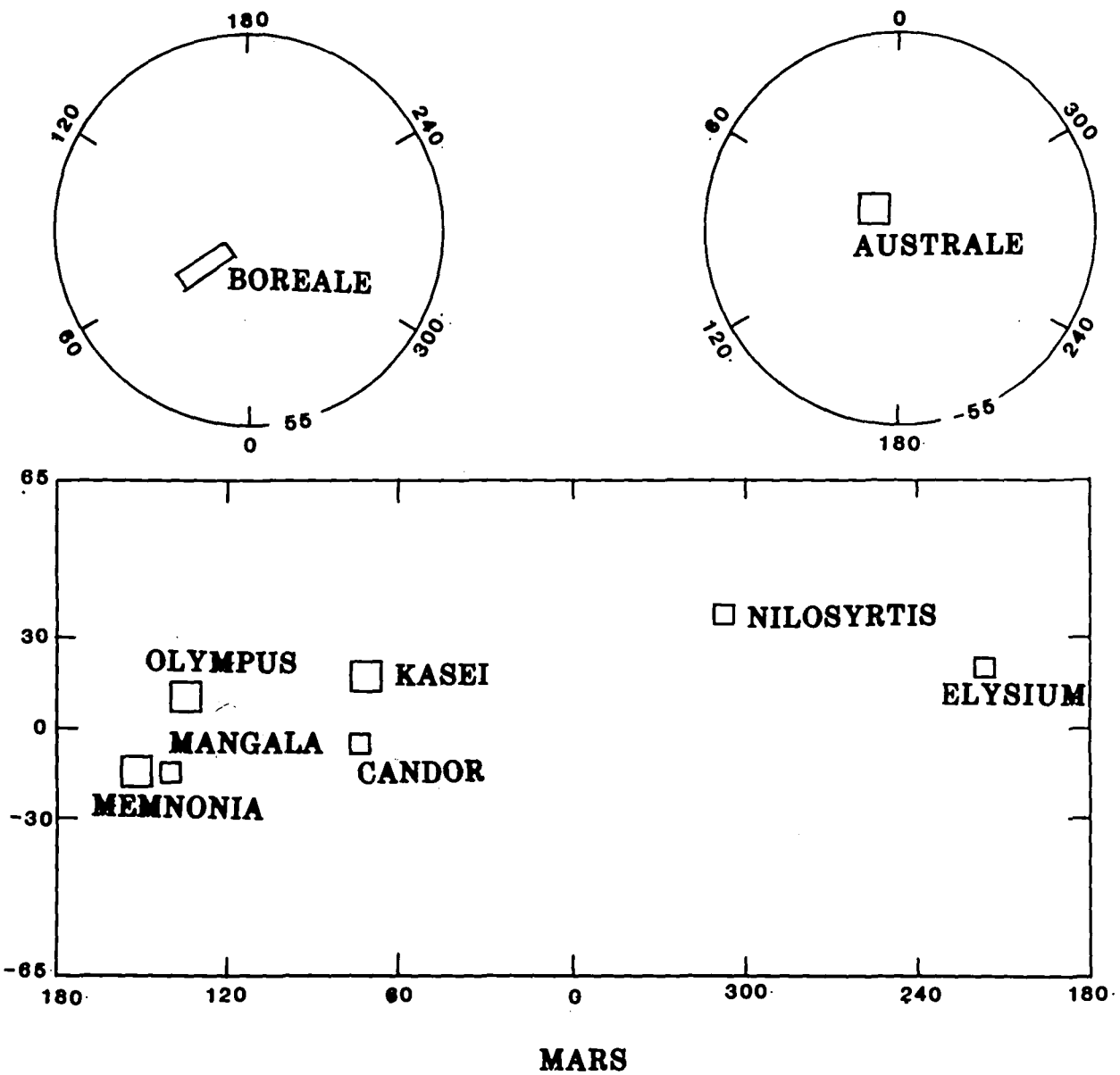

Figure 1. Location of the study sites on Mars that contain a variety of geologic units in close proximity.

THE GEOLOGY OF RHEA, J.B. Plescia, Astrogeology Branch, U.S. Geological Survey, Flagstaff, AZ 86001.

Rhea, with a radius of 765 km, is the largest of Saturn's icy, airless satellites. A first impression, that Rhea is a uniformly heavily cratered body that has undergone little or no geologic activity, is found to be misleading on further study. Geologic mapping indicates that several units and a variety of tectonic features are present. Although in many cases the differences between these units are subtle, they are nonetheless real.

Six geologic units have been identified in the sub-Saturnian hemisphere and north polar area: materials of the equatorial smooth plains, north polar plains, two cratered plains areas, dark plains, and bright highlands. In addition to these units are the bright, wispy materials on the trailing hemisphere.

The equatorial smooth plains material extends to lat 30^{o} N. and 45^{o} S. between long 0^{o} and 70^{o}. To the southwest and west, the unit extends beyond high-resolution coverage and its limits are unknown. Its boundary is irregular and sinuous but sharp. Texture of the underlying unit is highly subdued by mantling by the smooth plains material, which has almost completely obscured small craters and partly covered larger ones. The smooth plains material has been lightly impacted by small Population II craters (Smith et al., 1981, 1982).

Along its eastern margin, the mantling material thickens abruptly westward, as is reflected in the degree of crater burial. No flow structures were observed and, because all parts of the craters are covered to some extent by the mantle, it appears that the mantling material accumulated as an airfall deposit. Its source may have been clathrates that were explosively discharged along a fracture or series of fractures.

The north polar plains material is similar to the equatorial smooth plains material in that its surface is relatively featureless. Large craters are highly subdued but smaller, superposed Population II craters are fresh. The unit extends from lat 20^{o} N. to 80^{o} N. between long 20^{o} and 120^{o}.

The two cratered plains units occur on opposite sides of the equatorial smooth plains. Their surfaces appear pristine: fresh craters are separated by hummocky, rolling plains. Craters ~40 km in diameter are common but larger craters are absent.

A dark plains unit occurs within a narrow band centered near long 320^{o} that extends from the north pole to the south pole. The unit is characterized by an albedo that is low relative to those of the other units. Intercrater areas consist of smooth plains material. Craters ~20 km in diameter are rare. Larger craters are common and have been embayed to the extent that their flanks are buried. These observations suggest that regional flooding completely buried the small craters and covered only the flanks of the larger ones. Although no flow features were observed, the absence of cover on the upper parts of the large craters suggests that the material was emplaced as a liquid or semiliquid flow, rather than as an airfall deposit.

The bright highlands unit occurs east of about long 320^{o}. It extends eastward an unknown distance beyond the coverage of high-resolution images. This unit stands topographically higher than areas to the west and has a relatively high albedo. The unit is heavily cratered. Superimposed on it are the bright, wispy deposits.

The bright wispy deposits exhibit filamentary structure, particularly near their termini, and occur in bands 50-150 km wide. These bands occur east and west of what appears to be a large crater near lat 30° S., long 225°. Whether the central location of this crater is coincidental or not is uncertain. On Dione, two large craters are similarly associated with the bright, wispy markings (Plescia, 1983). On both bodies, these craters may have generated fractures that acted as conduits for the eruption of material forming the wisps. The bands on Rhea trend north-south, but those on Dione trend east-west (Plescia, 1983; Smith et al., 1981). On Rhea, bands east of the crater turn abruptly eastward at high latitudes, whereas those to the west continue straight into the high polar latitudes.

Craters of Populations I and II occur on Rhea, ranging in diameter from the limit of resolution (1.3 km/line pair) to 340 km. The distribution of the largest craters (~50 km in diameter) is highly irregular. In the north polar area they are common west of long 330° and absent to the east. Southward, they occur under the equatorial smooth plains and within the dark plains and bright uplands, but are absent from the cratered plains units. All of the observed craters have central peaks. No bowl-shaped craters nor craters with central pits were seen.

Structures and structural control of craters are common. Most craters have polygonal outlines, and linear crater walls are parallel to northeast- and northwest-trending lineaments of a global system. Lineaments have both positive and negative relief and are 2-3 km wide. In high-resolution images they are most noticable at the north pole.

Several other types of structures on Rhea are interpreted to be normal faults, monoclines or degraded normal faults, and arches. The normal faults occur over much of the planet, both separately and in pairs, forming grabens. Grabens are particularly common near the north pole. A series of bright lineaments 10-15 km wide that trend northeast to southeast are common in the equatorial and mid-northern latitudes. In stereographic viewing these lineaments appear to separate areas of different elevation. They are too wide to be simple faults, and are probably either normal faults whose shape has been deformed by viscous relaxation of the ice crust, or monoclines that reflect warping rather than faulting. In several high-resolution north polar images, a series of arches extends across the limb. The arches are 20-40 km wide and about 3 km high, as measured on the limb.

The presence of arches and normal faults indicates that both compressional and tensional stresses have operated on a global scale. However, relations between the geologic units and the tectonic features were not observed at sufficent resolution to determine the relative timing of these types of deformation.

Rhea has obviously experienced geologic evolution beyond its initial accretionary period. The satellite has undergone some type of resurfacing that has locally removed the large craters (~50 km). Additionally, many areas appear to have been repeatedly flooded or covered by airfall material of ice-clathrate composition. The presence of both tensional and compressional structures, which span the satellite, indicates that contrasting global stress systems have been active in the past.

Crater densities suggest that Rhea has been geologically active for a period that began during the heavy bombardment and extended past it. Geologic

activity appears to have taken place for at least 0.5 b.y. (Plescia and Boyce, 1984).

REFERENCES

Plescia, J.B., 1983, The geology of Dione, Icarus, 56, p. 255-277.

Plescia, J.B., and Boyce, J.M., 1984, Impact cratering history of the Saturnian satellites, J. Geophys. Res., in press.

Smith, B.A., et al., 1981, Encounter with Saturn: Voyager 1 imaging science results, Science, 212, p. 163-191.

Smith, B.A., et al., 1982, A new look at the Saturn system: The Voyager 2 images, Science, 215, p. 504-537.

Penetration and Subsurface Scattering of SIR-A Signals: Geologic Controls in the Mars-Like Eastern Sahara

Schaber, G. G., Breed, C. S., McCauley, J. F., and Grolier, M. J.;
U.S. Geological Survey, Flagstaff, AZ

Three field expeditions in 1982, 1983, and 1984 onto the Selima Sand Sheet in southern Egypt and northwestern Sudan have provided important new data on subsurface SIR-A signal responses as originally described by McCauley et al. (1982). This pioneering field research has provided corroborative data on the properties of materials that govern radar attenuation, signal refraction (penetration), volume scattering, and backscattering from subsurface dielectric interfaces of several distinct types within the hyperarid environment. Unexpectedly, volume scattering from disseminated rough caliche nodules, and increased radar reflectivity related to the presence of various sand-cementing calcium and sodium salts, were found to play a dominant role in moderating the SIR-A signal from within the upper meter or so of the surface.

Examination of more than 150 hand-dug pits (0.5 to 1.5 m deep) and backhoe trenches (2 to 4 m deep, 5 to 20 m long) established that bedrock, river sands, gravels, and discontinuous carbonate (caliche) horizons were all present locally in the shallow subsurface. In March 1984, a series of 20 backhoe trenches was excavated along a 3-km-long line, crossing an isolated, well-defined dark channel of the SIR-A image of the region south of Safsaf Oasis. The purpose of the excavation was to document the specific subsurface conditions responsible for the extremely sharp SIR-A delineation of this apparently fluvial feature (Figs. 1-3). The stratigraphy of the radar-dark channel was found to be totally different from that of the surrounding radar-bright, interchannel deposits; the latter are dominantly calichified sand deposits from an earlier fluvial event. Below the all-pervasive, thin (2-3 cm thick) eolian sand sheet, the channel itself was found to consist of poorly to moderately graded pea gravel and sand (size modes- 2.00 mm and 0.25 mm) whose paleosol color is indicative of a moderate degree of iron oxidation. The pea gravel is composed of 50% to 80% milky quartz and 20% to 50% quartzitic sandstone or sandstone conglomerate. No gravel of sufficient size exists to scatter the SIR-A signals, given the wavelength and incidence angle of the signals either at the surface (4 to 6 cm-size particles required), or within the substrate following signal propogation through the active sand sheet (2 to 3 cm-size particles required). Although small (0.5 to 1-cm size), stream-rolled caliche nodules were found in runnels (Fig. 2, black areas) on both shores of the channel, no caliche nodules were seen within the sand and gravel fill of the channel.

The upper few meters of the interfluve surfaces on either side of the SIR-A-dark channel (Figs. 1, 2), in striking contrast to the channel itself, consist of iron-free fluvial sands with abundant, irregularly shaped caliche nodules including calichified root casts (rhizoliths), representative of an advanced stage in the calichification process in arid environments (Giles et al., 1966) (Fig. 4). These fluvial sands have a unimodal size distribution with a mean size of 0.2 mm (excluding the caliche nodules and rhizoliths). A sufficient percentage of the nodules and rhizoliths characterizing the upper meter or so of the interfluve surface surpasses the minimum size (about 2 to 3 cm in diameter) to insure

diffuse scatter of the 24-cm SIR-A signals after refraction of the signals to higher incidence angles.

The strong SIR-A definition of the documented Safsaf channel is clearly related to signal absorption and direct specular reflection at the sand sheet-pea gravel interface, whereas the caliche nodules and associated high-dielectric salts together act to increase radar reflectivity and diffuse backscatter from the older fluvial sands in the interchannel areas. The braided channels south of the Safsaf Oasis have cut into a previously calichified fluvial sand deposit representing an earlier pluvial (wet) period, and are thus, by definition, younger than the calichification event. The upper limit on the age of the major calichification event has been determined to be 200,000 years B.P., based on the presence of Late Acheulean hand axes discovered by us buried in the calichified pea gravels to a depth of 1.7 m on the shore of a "radar river" in March 1984.

The Safsaf channel study documented the direct relation of material properties and climatic cycling to specific SIR-A responses. This relation may result in recognition of more sand-buried fluvial channels in the hyperarid Eastern Sahara, and perhaps in other hyperarid-to-arid desert regions, both terrestrial and extraterrestrial. The Eastern Sahara of southern Egypt and northwestern Sudan is a uniquely Mars-like environment; the present hyperarid conditions, the thin sand mantle, and the absence of radar-attenuating clay minerals are major factors contributing to ease of radar-signal penetration. Such radar-transparent, unconsolidated materials are found in very few localities on Earth. However, the electrical properties of the radar-transparent materials of the uppermost Selima Sand Sheet are nearly identical to the extensive homogeneous regoliths of the Moon, Mars and Mercury--each characterized by extremely low loss tangents of about 0.006.

References

McCauley, J.F., Schaber, G.G., Breed, C.S., Grolier, M.J., Haynes, C.V., Issawi, Bahay, Elachi, Charles, and Blom, Ron, 1982, Subsurface valleys and geoarchaeology of the Eastern Sahara revealed by shuttle radar, Science, 218, no. 4576, 1004-1020.

Giles, L.H., Peterson, F.F. and Grossman, R.B., 1966, Morphological and genetic sequences of carbonate accumulation in desert soils, Soil Sci., 101, no. 5, 347-360.

Figure 1. (a) SIR-A image of buried braided stream channels south of Safsaf Oasis, Egypt; arrow indicates part of radar-dark channel excavated March 1984. (b) Enhanced Band-7 Landsat MSS image of same area shown in (a) showing pervasive, flat sand sheet. Width of images 30 km.

Figure 2. Cross-section of dark channel shown in Fig. 1a. Trench locations shown by numbers. Dots indicate sand; small circles, pea gravel; small irregular outlines, caliche nodules; black areas, rolled caliche nodules; upper lined areas, capillary fringe of former water table; upper dashed line, upper limit of damp zone; lower dashed line, approximate position of present water table.

Figure 3. Ground photo showing backhoe trenches excavated in radar-dark channel material (pea gravels).

Figure 4. Ground photo of trench in SIR-A-bright interfluve surface showing caliche nodules below modern sand sheet. Width of photo 2 m.

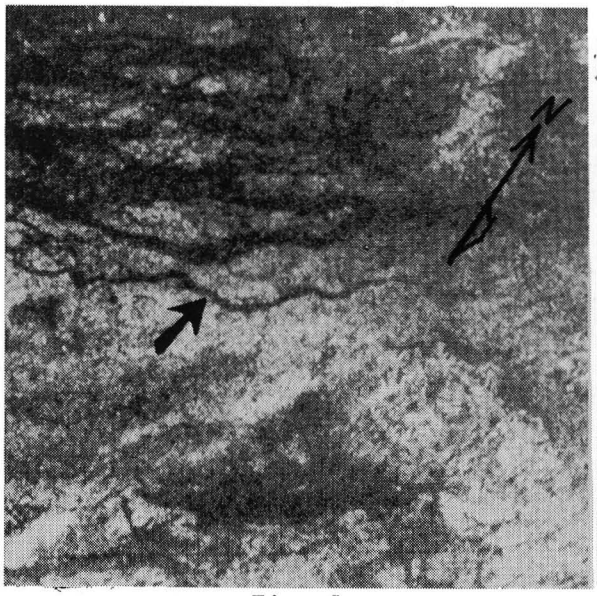

Fig. 1a

Fig. 1b

Fig. 2

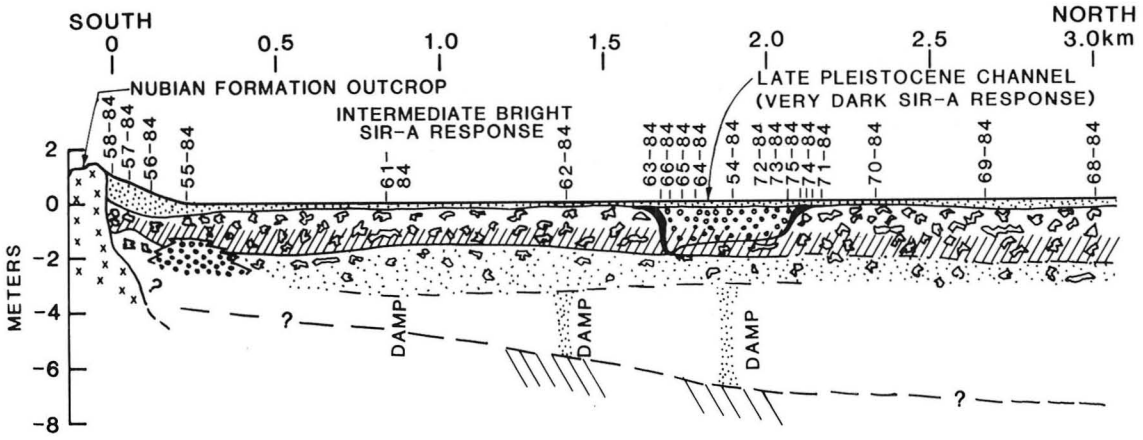

Fig. 3

Fig. 4

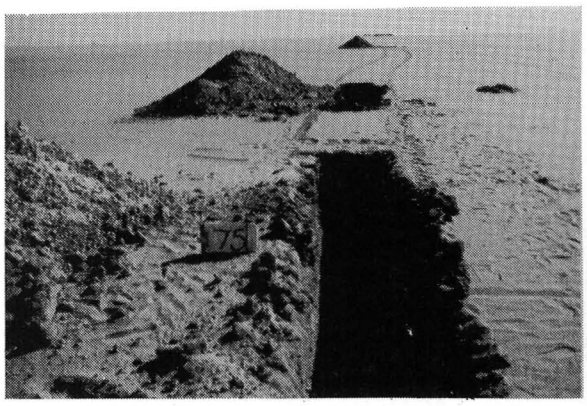

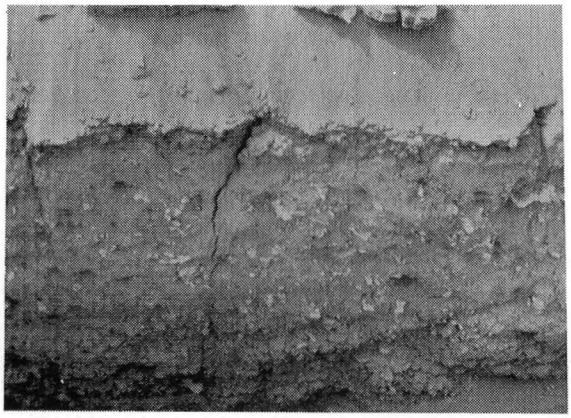

RECENT DISCOVERIES OF COMETS WITH THE PALOMAR 46-CM SCHMIDT CAMERA

Carolyn S. Shoemaker and Eugene M. Shoemaker, U.S. Geological Survey, Flagstaff, Arizona 86001

Among telescopes currently in use at observatories around the world, the 46-cm Schmidt camera at Palomar Observatory, California, is especially well suited for a survey or patrol of large areas of the sky. It was built and placed into operation in the 1930's and has enabled a long-term search for supernovae (Sargent, et al, 1974). More recently it has been used to conduct a survey for planet-crossing asteroids (Helin and Shoemaker, 1979). Two years ago we began a new survey with this instrument with the goal of discovering a sufficient number of the various planet-crossing asteroids and comets to (1) estimate the population of each class and (2) refine estimates of cratering rates on the terrestrial planets, the Moon, and the satellites of the giant planets.

Comets are important targets of our new survey, as collision of comets with the solid bodies in the Solar System has produced a large fraction of recent impact craters formed on those bodies. Planet-crossing asteroids are thought to have produced most of the recent impact craters on Mars, Earth, and Venus (Shoemaker et al., 1979; Shoemaker, 1981), whereas comets evidently have produced most of the recent impact craters on the Jovian and Saturnian satellites (Shoemaker and Wolfe, 1981 and 1982) and perhaps about half the recent craters on Mercury and the Moon (Shoemaker, 1981). Moreover, many asteroids that cross the orbits of Earth, Venus, and Mercury, as well as recently discovered asteroids that cross the orbit of Jupiter, very probably are extinct comets.

Coverage of a large area of sky is feasible with the 6-inch-diameter circular films for which the 46-cm Schmidt is designed. At a scale of 225 arcsec per mm, the effective field covered by each film is about 60 square degrees. We use Eastman Kodak's spectrographic emulsion IIa-D, and our standard exposure with this emulsion on the f/2 Schmidt is 4 minutes. On average, 3 minutes are needed to change film holders, set on a guide star, and begin a new exposure. Hence, about 80 films can be exposed during continuous acceptable observing conditions on a night of average length.

In order to detect and confirm planet-crossing objects, we take two exposures separated by about 30 minutes for each field. Each pair of films is examined with a stereomicroscope built specifically for use with the 46-cm Schmidt films. Stereoscopy was employed before the turn of the century by Max Wolf to detect asteroids on wide-field plates; since then, however, most observers have preferred to use blink machines. We have found the stereoscopic method to be fast and reliable, but effective use of the stereomicroscope requires training of the eyes and considerable experience. About 20 minutes are required to scan a pair of films for moving objects. Our stereomicroscope was designed to be portable, so that it can be taken to Palomar Mountain for use during each observing run.

Survey fields photographed during a given observing run generally span a range of about 5 hours in right ascension centered on opposition and a range of about 40° to 50° in declination. A standard set of guide stars has been chosen that minimizes overlap between fields without leaving significant gores or gaps in sky coverage. Average overlap is somewhat greater than the geometrical minimum of 34.6% required to avoid gores.

Our strategy has been to start an observing run with fields along the ecliptic and alternate (even-numbered) rows of fields above and sometimes below the ecliptic. Over the next several days, the films covering these

fields are scanned with the stereomicroscope for comets and for asteroids with unusual motion or position. Odd-numbered rows of fields are photographed on the second night. During the remainder of our 5-night run we try to obtain a second pair of films for fields that cannot be scanned during the time we are at Palomar and to extend the sky coverage as time and weather permit. By taking alternate rows of fields on successive nights, we obtain positions in the overlap areas on additional nights for about 30% of the objects discovered. All objects discovered during an observing run are followed for as many nights as remain in the run. Some exposures are allocated to provide followup astrometry of objects discovered in previous runs and to follow or recover other objects of interest. With good weather, as many as 94 fields have been photographed during a single run, but our average number of fields per run during the past year has been about 70. We observed during seven lunations in 1983, and six lunations in 1984. Our average annual coverage of the sky has been about 17,500 square degrees.

Under optimum conditions, the threshold for detection of a comet with the 46-cm Schmidt camera and the techniques we use is close to an apparent total B magnitude of about 16. With the small scale of the 46-cm Schmidt films and the camera driven at sidereal rate, the images of most comets are not noticeably trailed in the 4-minute exposures. Hence, it is generally not necessary to track a comet in order to reach the magnitude-16 detection threshold or to obtain images suitable for reliable astrometry. For images of nearly stellar appearance we can follow a comet to a limiting magnitude of about 17.5. A disadvantage of the small film scale is that fine details of the coma and tail are not resolved. Longer focal-length optics must be used to monitor many aspects of the activity of the relatively faint and commonly distant comets that we are likely to discover.

Shoemaker and Wolfe (1982) estimated that the number of long-period comets with absolute nuclear B magnitudes less than 18 that pass perihelion each year inside the orbit of Jupiter is somewhat less than 2000. At a total magnitude-detection threshold of 16, very roughly 100 of these comets should become bright enough at distances from the sun greater than 1 AU to be discovered. The steady number of observable comets at elongations greater than 90° should be of the order of one per 1000 square degrees. Not all observable comets represent potential new discoveries, of course, as many will already have been discovered, either by other observers or on prior observing runs.

It is of interest to compare these rough expectations with our actual observations of comets over the 2 years that our survey has been in progress. About two to three comets should be observed per observing run, under optimum conditions. In 1983 we observed an average of 1.3 comets per observing run; one of these, 1983p, was a new discovery. In 1984 we observed 2.3 comets per run. Among these, five (1984f, 1984q, 1984r, 1984s, and 1984u) were new discoveries. Two of the six new comets are periodic, which is about twice the proportion of periodic comets among all discovered comets. The increased frequency of our detection of comets in 1984 is due, at least in part, to better average observing conditions. In addition, a substantial random fluctuation in the number of observed comets should be expected, because of their small total number.

The distribution of perihelion distances of the long-period comets we have discovered so far (Table 1) suggests that we will find a substantially greater proportion of comets with large perihelion distance than has been found among all comets discovered to date. With a sufficient number of discoveries and appropriate analysis of the observational selection effects,

we hope to test whether the cumulative frequency of comets is a linear function of perihelion distance (beyond 0.5 AU), as predicted theoretically by Oort (1950), Weissman (1977), and Hills (1981), or whether the distribution follows some other function of perihelion distance, for example, that proposed by Kresák and Pittich (1978). From an earlier analysis of observational selection effects, Everhart (1967) found that the intrinsic frequency distribution of perihelion distances may be linear beyond 1.3 AU. The perihelion distances of all long-period comets discovered to date are so strongly weighted toward distances less than 1.3 AU, however, that the true underlying distribution beyond about 1.3 AU is uncertain. Our systematic survey is much less biased toward comets with small perihelion distance than were past circumstances of comet discovery, and a more certain result can be obtained from a much smaller set of discovered comets. Determination of the true underlying distribution is fundamental to the calculation of the impact-cratering rates on the satellites of the giant planets, to the estimation of the population of the Oort comet cloud, and to a full understanding of the capture of short-period comets from the long-period comet swarm.

References Cited

Everhart, E., 1967, Intrinsic distributions of cometary perihelia and magnitudes. Astron. J. 72, p. 1001-1011.

Helin, E. F., and Shoemaker, E. M., 1979, Palomar planet-crossing asteroid survey, 1973-1978. Icarus 40, p. 321-328.

Hills, J. G., 1981, Comet showers and the steady-state infall of comets from the Oort cloud. Astron. J. 86, p. 1730-1740.

Kresák, L., and Pittich, E. M., 1978, The intrinsic number density of active long-period comets in the inner solar system. Bull. Astron. Inst. Czechosl. 29, p. 299-309.

Oort, J. H., 1950, The structure of the cloud of comets surrounding the solar system, and a hypothesis concerning its origin. Bull. Astron. Inst. Netherlands 11, p. 91-100.

Sargent, W. L. W., Searle, L., and Kowal, C. T., 1974, The Palomar supernova search. In Supernovae and Supernova Remnants (C. B. Cosmovici Ed.), D. Riedel Publ. Co., Dordrecht-Holland, p. 33-49.

Shoemaker, E. M., 1981, The collision of solid bodies. In The New Solar System (J. M. Beatty, B. O'Leary, and A. Chaikin, Eds.), Sky Publishing Corp., Cambridge, Mass., p. 33-44.

Shoemaker, E. M., Williams, J. G., Helin, E. F., and Wolfe, R. F., 1979, Earth-crossing asteroids: Orbital classes, collision rates with Earth, and origin. In Asteroids (T. Gehrels, Ed.), Univ. Arizona Press, Tucson, p. 253-282.

Shoemaker, E. M., and Wolfe, R. F., 1981, Evolution of the Saturnian satellites: The role of impact (ext. abs.). Satellites of Saturn, Lunar and Planetary Science XII, Supplement A, p. 1-3.

Shoemaker, E. M., and Wolfe, R. F., 1982, Cratering time scales for the Galilean Satellites of Jupiter. In The Satellites of Jupiter (D. Morrison Ed.), Univ. Arizona Press, Tucson, p. 277-339.

Weissman, P. R., 1977, Initial energy and perihelion distributions of Oort-clould comets. In Comets, Asteroids, Meteorites (A. H. Delsemme, Ed.), Univ. Toledo, Toledo, Ohio, p. 87-91.

Table 1. Selected orbital elements for comets discovered in 1983 and 1984 with the Palomar 46-cm Schmidt

	q	e	ω	Ω	i	Reference
1983p	3.345	1.0004	176.0	164.0	137.6	MPC 8387
1984f	2.697	1.0006	235.5	49.0	116.7	MPC 9154
1984q	1.980	0.4738	18.2	339.4	26.4	IAUC 4000
1984r	5.492	1	183.2	237.9	179.2	IAUC 4011
1984s	1.214	0.9695	229.2	222.8	13.9	IAUC 4012
1984u	1.321	0.6874	317.1	54.8	22.0	IAUC 4015

A MERCURIAN CHRONOSTRATIGRAPHIC CLASSIFICATION

P.D. Spudis, U.S. Geological Survey, Flagstaff, AZ 86001 and Dept. of Geol., Ariz. State University, Tempe, AZ 85287

Introduction. In the earliest stages of planetary geologic mapping, the first steps usually taken are terrain reconnaissance and classification. Later, when the relations between photogeologically defined units become clearer, it is desirable to establish a formal chronostratigraphic (i.e., time-stratigraphic) classification system in order to correlate widely separated geologic units and provide a framework for interplanetary correlations of geologic time. In the now-classic paper of Shoemaker and Hackman [1], a chronostratigraphic classification was presented for the Moon. In this classification, chronostratigraphic systems were defined on the basis of superposition relations of observable rock-stratigraphic units [1, 2, 3]. This method, although modified by more detailed knowledge of lunar geology, is still in use today [3].

The geology of Mercury was initially mapped by physiographic/terrain units, although an attempt was made to indicate their lithology and relative stratigraphic order [4]. At present, a series of 1:5 M-scale maps of the Mercurian hemisphere imaged by Mariner 10 is nearing completion. This mapping relies on an informal rock-stratigraphic classification of crater, basin, and plains units arranged in order of relative age [5]. After mapping was begun, McCauley et al. [6] proposed a series of formal rock-stratigraphic units associated with the Caloris Basin as the first step in formulating a Mercurian stratigraphy. The present paper describes the use of the Caloris Group of [6] together with newly defined rock-stratigraphic units to develop a formal Mercurian chronostratigraphy (Table 1). This classification has been designed to facilitate global geologic mapping at a scale of 1:10 M [Spudis P., and Strom R., work in progress].

Mercurian chronostratigraphic systems. The two oldest Mercurian chronostratigraphic systems are divided by the impact that produced the Tolstoj Basin (lat -16°, long 164°). The informally named pre-Tolstojan System includes deposits formed prior to this impact. These units include vast intercrater plains [4], numerous large craters, and multi-ring basins.

The base of the formally named Tolstojan System is marked by the base of a distinctive lineated terrain unit composed of deposits related to the Tolstoj impact; the unit is here formally named the Goya Formation, after the unrelated, pre-Tolstojan crater Goya (-7°, 152°). The Goya consists of coarsely lineated to hummocky material that occurs as far as about one basin diameter from the rim of the Tolstoj Basin; its areal extent is about 7.8×10^5 km^2. Its type area extends from lat -8° to -11°, long 152° to 155°. The Goya includes basin ejecta, locally derived reworked debris, and Tolstoj secondaries. Its reference crater density ($D \geq 20$ km) is $8.5 \pm 1.4 \times 10^{-5}$/km^2. In addition to the Goya Formation, the Tolstojan System includes numerous smooth plains units and many crater and smaller basin deposits. The Tolstojan System ends at the moment of the Caloris impact.

The base of the formally defined rock-stratigraphic Caloris Group of [6] marks the beginning of the Calorian System. The Caloris Group comprises the Caloris Montes, Nervo, Odin and Van Eyck Formations [6]. These formations are interpreted as deposits resulting from the Caloris impact and include basin impact melt and ejecta, local material, and secondary crater material. Reference crater density ($D \geq 20$ km) for the Caloris Group is $6.1 \pm 1.4 \times 10^{-5}$/km^2.

The Calorian System encompasses all units between the base of the Caloris Group and the base of deposits of the crater Mansur (see below). This system embraces many widespread geologic units, including extensive smooth plains materials that fill and surround craters and basins. Much controversy has ensued over the origin of the Mercurian smooth plains [e.g. 8, 9]. Preliminary mapping suggests a distinct age difference between the Caloris Group and adjacent younger smooth plains [cf. 8, 10]; crater density ($D \geq 20$ km) is $3.9 \pm 1.2 \times 10^{-5}/km^2$ for the Caloris floor material, which a two-sided T test indicates is younger than the Caloris Group at the 95% confidence level. The relative youth of Caloris Basin floor material, as well as the pronounced tendency of the smooth plains to occupy depositional sites of ancient basins [7], suggests a volcanic origin for these units. Other units of the Calorian System include materials of craters and two-ring basins, and unusual hilly terrain antipodal to the Caloris Basin that probably resulted from concentration of antipodal seismic waves produced by the Caloris impact [11]. As is seen in Table 1, most geologic units on Mercury are of Calorian age or older.

The long period of time between the Calorian System and the present is divided into two intervals. The lower contact of deposits from the crater Mansur (48°, 163°) defines the base of the Mansurian System. This system, like the Eratosthenian on the Moon, includes materials of slightly degraded but still relatively fresh craters and minor plains materials, mostly crater-floor units that are probably impact melt sheets. The Mansurian System extends to the base of deposits of the crater Kuiper (-11°, 31.5°). The Kuiperian System includes all units emplaced after the Kuiper impact, up to the present day. This system is composed wholly of crater deposits, generally those of craters with preserved rays, and thus is analogous to the lunar Copernican System. No regional plains deposits of this age have been recognized.

Implications and comparisons with other planets. The Mercurian chronostratigraphic classification described here has thus far proven useful in delineating geologic events on a global basis. For example, it was proposed that the Tolstoj impact partly predated the last phases of emplacement of intercrater plains material [12]. However, definition and mapping of the Goya Formation demonstrate that it is everywhere younger than the intercrater plains material; its geometric asymmetry is probably the result of an oblique impact rather than the result of partial flooding by plains material. Such is the case for most lunar basins [3]. These relations suggest that the intercrater plains material is pre-Tolstojan in age.

The chronostratigraphic systems defined for Mercury are remarkably similar to the lunar systems [2]. On both bodies, almost all geologic activity occurred early in their history -- during pre-Tolstojan to early Calorian time on Mercury and pre-Nectarian to early Imbrian time on the Moon. A significant difference is the extended period of mare (smooth plains) deposition on the Moon, which may have extended into Copernican time [3, 13]. Such a wide age range is not evident for the Mercurian plains material, at least within the hemisphere imaged by Mariner 10.

In Table 1, the approximate ages of the systems are based on the assumption of a lunar-type flux history for Mercury; ages are keyed to absolute dates for the lunar time-scale. This assumption may be incorrect, and these ages are given solely as rough estimates. It is clear, however, that most of Mercury's surface was shaped within the systems of oldest relative age -- large areas of relatively uncratered units, such as are

widespread on Mars [14], do not occur on Mercury. It thus appears that in regard to geologic evolution, Mercury has more in common with the Moon than with Mars.

REFERENCES

[1] Shoemaker, E. and Hackman R., 1962, in The Moon: Int. Astron. Union Sym. 14, New York, Academic Press, 289-300.
[2] Wilhelms, D., 1970, U.S. Geol. Survey Prof. Paper 599-F, 47 p.
[3] Wilhelms, D., in press, Geologic History of the Moon: U.S. Geol. Survey Prof. Paper.
[4] Trask, N. and Guest, J., 1975, JGR 80, 2461-2477.
[5] Holt, H., 1978, Reports Planet. Geol. Prog. NASA TM 79729, 327.
[6] McCauley, J. et al., 1981, Icarus 47, 181-202.
[7] Spudis, P., 1984, Reports Planet. Geol. Prog.: NASA TM-86246, 87-89.
[8] Wilhelms, D., 1976, Icarus 28, 551-558.
[9] Strom, R. et al., 1975, JGR 80, 2478-2507.
[10] Basaltic Volcanism Study Project, 1981, Pergamon Press, Chap. 8, 1050-1127.
[11] Schultz, P. and Gault, D., 1975, Moon 12, 159-177.
[12] Schaber, G. and McCauley, J., 1980, USGS Map I-1199.
[13] Schultz, P. and Spudis, P., 1983, Nature 302, 233-236.
[14] Scott, D. and Carr, M., 1978, USGS Map I-1083.

Table 1. A Mercurian Chronostratigraphic System

System	Major units	Approx. age of base of system[1]	Lunar equivalent[2]
Kuiperian	crater material	1.0 AE	Copernican
Mansurian	crater material	3.0-3.5 AE	Eratosthenian
Calorian	Caloris Group; plains, crater, small-basin materials	3.9 AE	Imbrian
Tolstojan	Goya Fm.; crater, small-basin, plains materials	3.9-4.0 AE	Nectarian
pre-Tolstojan	Intercrater plains, multi-ring basin, crater materials	pre-4.0 AE	pre-Nectarian

1. See text.
2. Included for reference only; no implication of exact time correlation intended.

MARTIAN TECTONICS AS EVIDENCED BY LAVA FISSURES

A. W. Ward and Paul D. Spudis, U.S. Geological Survey, Flagstaff, AZ 86001

Major terrestrial fissure and dike provinces are related to "plate-scale" tectonics (the opening of new ocean basins and intracontinental rifting) (1). We have undertaken a study of Mars (2) to determine if its fissure systems are:

1) related to topographic features (such as impact basins and volcanoes) or if they reflect internal (mantle-lower crustal) stress fields.
2) due to local, regional, or global tectonic influences. If surface stresses dominate, lava fissures may be found only near edifices and impact basins. If internal stresses dominate, large eruptive centers may be caused by regional or global spreading planes.

Our purpose is to learn how Martian lavas, which presumably originated in the mantle, reached the surface. One possible route is along zones of weakness created or controlled by impact basins or large volcanic constructs (i.e., radial, concentric, and tangential fracture systems). Alternatively, fissure systems may be due to local to regional upwelling, or to regional or global spreading planes (similar to those forming terrestrial oceanic ridges).

So far we have found approximately four dozen probable single-fissure vents and vent swarms in the following areas (Examples are shown in figs. 1, 2; numbers below are keyed to fig. 3.)

(1) east and northeast of Olympus Mons, tangential to the edge of its shield scarp, trending ENE and NW
(2) at the far edge of the aureole north of Olympus Mons, striking NE
(3) throughout Memnonia Fossae and Sirenum Fossae, striking ENE
(4) west of Arsia Mons, striking NW; south of Arsia Mons, striking NE
(5) in Alba Fossae, striking NNW; in Tantalus Fossae and Ceraunius Fossae, striking NNE
(6) in Syria Planum (3), striking NW
(7) in Thaumasia Fossae, striking NE
(8) in Tempe Fossae, striking NE
(9) tangential to Nereidum Montes of Argyre Basin, striking NW; tangential to Hellespontus Montes at Hellas Basin, striking N
(10) radial to Hecates Tholus, striking NW and WNW
(11) between Elysium Mons and Hecates Tholus, striking NW
(12) in the cratered plains east of Hellas Basin, striking NE

Our data base is small and work is continuing. At present, however, we consider that the relatively young, smooth plains of the (Tharsis), Alba, Syria, and Elysium regions are resurfacing units (4) from both small, local fissures and large constructs (shields); most fissures are radial or tangential to the local shield. In older terrain, principally in the southern hemisphere, most fissures are radial, tangential, or concentric to visible or postulated (5, 6, 7) impact basins. Other fissures, however, trend NE-SW and NW-SE across vast areas and seem to be unrelated to impact basins.

We conclude that, in the southern hemisphere, lavas reached the surface principally along basin and basin-ring fracture systems; this type of control on the older volcanism is similar to that envisioned for lunar volcanic provinces (8). Many fractures, however, cannot be traced to known or postulated basins. Further work may indicate that these fractures were

controlled by basins not now recognized; however, the possibility of a tectonic "grid" (9) cannot yet be discounted. In the younger volcanic plains, which are mostly in the northern hemisphere, fissure patterns generally are related to topography; fissure patterns record or reflect the emplacement of magma in the upper crust that led to shield construction. As yet, we have found no evidence for precursor impact basins and their associated fracture patterns that created possible conduits for lava migration and shield construction for these younger flood lavas. Nor can we recognize any other type of crustal fracture pattern along which the magmas might have migrated. Schultz (5, 6), however, considered that all the Tharsis and Elysium volcanoes generally lie on the rings of old, buried basins. If such is the case, the radial, concentric, and tangential fissures that we recognize as related to these constructs may be concomitant with or even younger than the volcanoes and productive of relatively little lava. The source fissures and ring fractures that preceded the volcanoes, therefore, would be buried under the lava pile.

Finally, we consider that most Martian flood lavas initially reached the surface along planes or patterns of weakness created by great impacts, analogous to lunar mare emplacement. Shield emplacement has locally produced new fissure patterns on the younger plains, but the ancient pattern is faintly recognizable at places on these plains; perhaps some older fissures have been locally reactivated.

Mars could be more active internally than is generally believed. However, if such great patterns of weakness were created in the upper crust by perhaps a relatively few large impacts, it seems unlikely that internal activity would have created new spreading planes for lavas to reach the surface.

References:

(1) BVSP, Basaltic volcanism on the terrestrial planets; Pergamon Press, Inc., New York, 1286 p., 1981.
(2) Ward, A. W. and P. D. Spudis, LPS XV, 886-887, 1984.
(3) Mouginis-Mark, P. J., et al., Nature, 297, 5546-5550, 1982.
(4) DeHon, R. A., JGR, 87, 9821-9828, 1982.
(5) Schultz, P. H. et al. JGR, 87, 9803-9820, 1982.
(6) Schultz, P. H., LPS XV, 728-729, 1984.
(7) Pike, R. J. and P. D. Spudis, LPS XV, 647-648, 1984
(8) Schultz, P. H., Moon morphology, Univ. Texas Press, Austin, 626 p., 1976.
(9) Binder, A. B., Science, 152, 1053-1055, 1966.

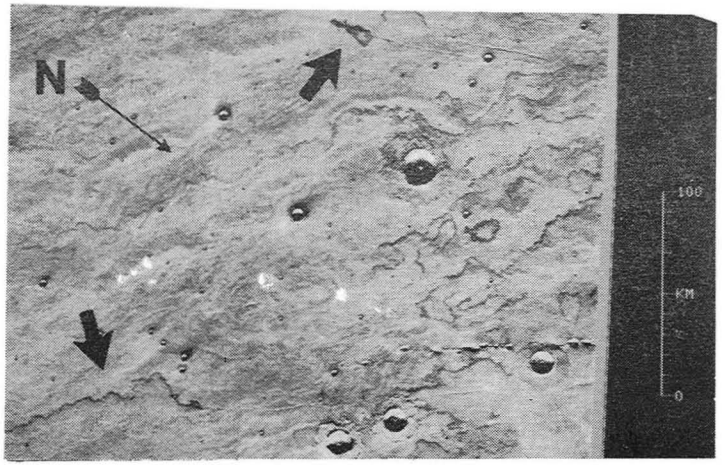

Figure 1. Viking image 643A63 showing fissure flows (two indicated by arrows) in Phoenicis Lacus.

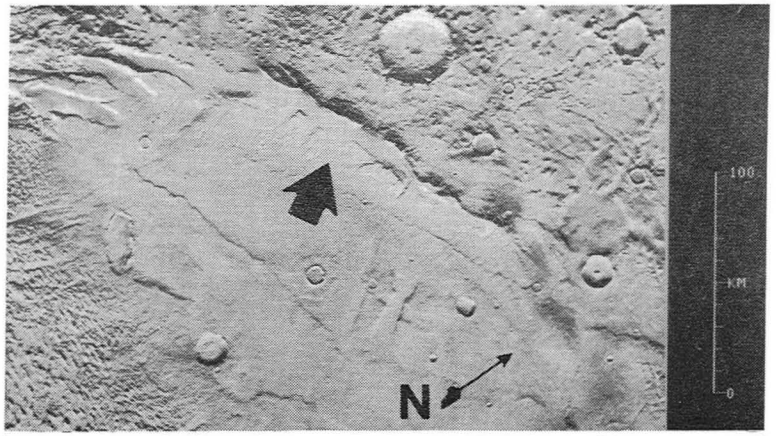

Figure 2. Viking image 851A32 showing fissure and residual lava (arrow) at edge of Olympus Mons Aureole, also shown at (2) in fig. 3.

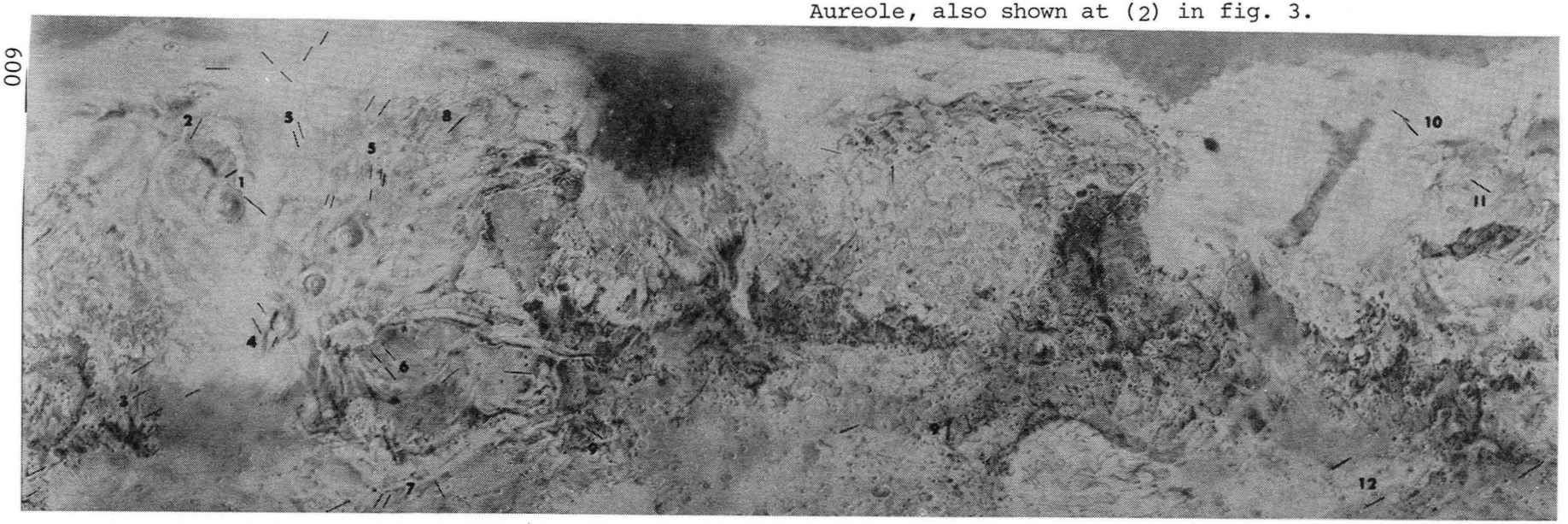

Albedo map of Mars showing fissures and fissure swarms (dark lines). Fissures in smooth plains of northern hemisphere seem related to volcanic shields; those in older cratered terrain (southern hemisphere) may be related to large impact basins. Base map courtesy Planetary Cartography Section, Branch of Astrogeology, USGS, Flagstaff.

HIGHLIGHTS IN VALLES MARINERIS MAPPING N.E. Witbeck and D.H. Scott U.S. Geological Survey, Flagstaff, AZ 86001.

Valles Marineris, the largest and one of the most complex structural features on Mars, is currently being mapped at 1:2 million scale. The map series will consist of four geologic quadrangle maps covering the area from Noctis Labyrinthus (long 100° W.) to the chaotic terrain of Margaritifer Chaos and Aureum Chaos (long 20° W.). The series will include all of MC17 NE, MC18 NW and NE, MC19 NW, and parts of MC18 SE and MC19 SW. Preliminary mapping has been done of all quadrangles except MC17 NE. This series is expected to be completed by the spring of 1985.

The major geologic units are those of the new preliminary 1:15 million-scale geologic map of the western equatorial region [1]; however, many additional units and features can be shown in detail at 1:2 million scale (Table 1), and can better illustrate the complex nature of Valles Marineris geology. For example, in the region along the canyon between long 22° W. and 90° W, 16 geologic units and 5 symbols were mapped at 1:15 million scale. The detailed mapping of the new series will include more than 35 units and 18 symbols.

One of the more striking physiographic transitions along the length of Valles Marineris occurs between the narrow trough of Coprates Chasma and the much wider Capri and Eos Chasmata to the east (Figure 1). The abrupt widening and change in orientation of the canyons may be caused by a combination of structure, stratigraphy, and topography. Major fault trends associated with the canyons also change direction here, from the dominant ESE trend of Coprates Chasma to ENE and NE trends to the east. Radar data show that the regional gradient slopes eastward but diminishes near this intersection. In terrestrial channels, widening commonly occurs where gradient decreases, and these Martian relations may be analogous. A major geologic boundary also occurs near the junction of Coprates and the eastern canyons (Figure 1). The boundary marks the eastern limit of the ridged plains material, a resistant unit thought to consist of lava flows. The dominant cap unit east of the boundary is the older, highly cratered and possibly more easily eroded cratered plateau sequence [1]. This difference in resistance is possibly the most important factor that influenced the abrupt physiographic change along the canyons.

Previous geomorphic mapping in Capri Chasma [2] indicates that the valley has been subject to multiple episodes of fluvial activity. Our mapping in Eos Chasma (Figure 2) supports this observation. Here, an old terrace whose channels and flowlines are oriented northeasterly is truncated on the south and east by the main channel of Eos Chasma that also flowed to the northeast. A younger channel, which appears to originate from a collapsed part of the terrace, flowed to the northwest.

REFERENCES

[1] Scott, D.H., and Tanaka, K.L., 1984, Preliminary geologic map of the western equatorial region of Mars: U.S. Geological Survey Open-File Report 84-69-A.

[2] Boothroyd, J.C., and Timson, B.S., 1981, Geomorphic mapping in Capri Chasma, In Reports of Planetary Geology Program-1981, NASA Tech. Memo. 84211, p. 302-304.

[3] Roth, L.E., Downs, G.S., and Saunders,R.S., 1980, Radar altimetry of south Tharsis, Mars: Icarus 42, p. 287-316.

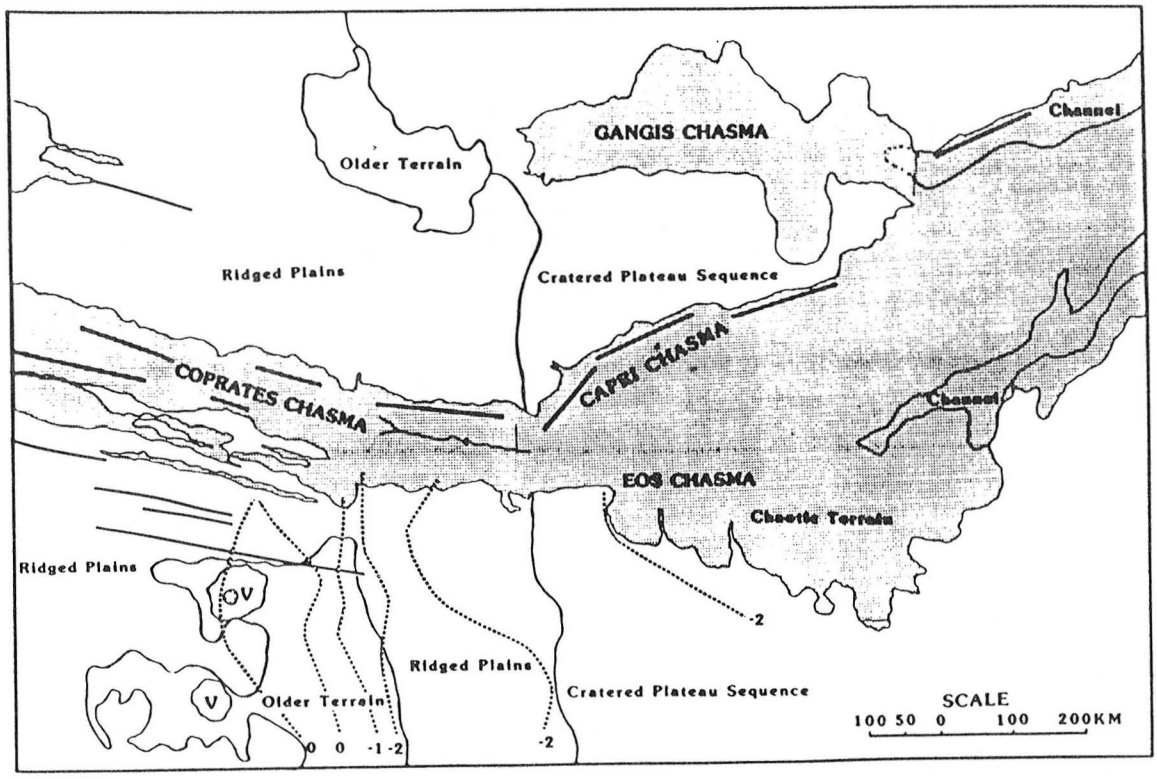

Figure 1. Junction of Coprates Chasma and the canyons to the east (Capri and Eos Chasmata). Structural orientations shown by heavy black lines; volcanic areas indicated by (V); major canyons are stippled; dotted lines are 1-km contours derived from radar data [3]; map area lat 5° S. to 22° S., long 38° to 65° W. map generalized from [1].

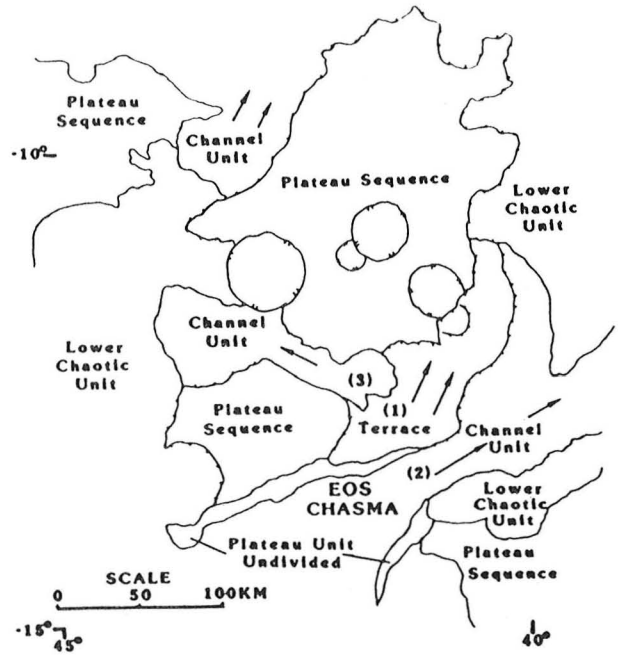

Figure 2. Shetch map of Eos Chasma region. Channels numbered from oldest to youngest (1-3); flowlines indicated by arrows.

TABLE 1. VALLES MARINERIS MAP UNITS

(Unit names on the 1:2 million-scale maps are working names only.)

Dissected Plateau and Channel Units				Surficial and Interior Valley Units			
1:15 million [1]		1:2 million (current mapping)		1:15 million [1]		1:2 (current mapping)	
Hch	Channel unit	Hch	Channel unit		No equivalent	Ae	Eolian unit
		Hchb	Channel bar unit		No equivalent	Ad	Dune unit
Hchp	Floodplain unit	Hchp	Floodplain unit	As	Slide material	AHhs	Hummocky unit
Hcht	Chaotic unit	$Hcht_2$	Upper chaotic unit			AHls	Landslide unit
		$Hcht_1$	Lower chaotic unit			AHsf	Smooth floor unit
HNcw	Canyon wall unit	HNcw	Canyon wall unit			AHI	Interior unit undivided
	No equivalent	Hpll	Lower plateau unit			AHiv	Volcanic unit
	No equivalent	Hdf	Degraded floor unit	AHps	Smooth plains unit	AHid	Interior dark unit
						Hff	Fractured floor unit
						Hrf	Rough floor unit
						Hhf	Hilly floor unit
						AHlm	Layered/mottled unit
						Hll	Interior layered unit
				AHvl	Layered unit	Hisu	Interior smooth upper unit
						Him	Interior massive unit
						Hif	Interior fluted unit
						Hisi	Interior intermediate smooth unit

Cratered plateau sequence not shown in table.

COMPARISON OF METHODS DEFINING PLANETARY TOPOGRAPHIC DATUMS

Sherman S. C. Wu, U. S. Geological Survey, Flagstaff, AZ 86001

In this paper, various planetary topographic datums are compared. Comparison is made between geometric figures (triaxial ellipsoid, biaxial oblate spheroid, and sphere) and the physical surfaces of Mars and the Moon (determined by gravity measurements).

For Mars topographic mapping, we have been using a topographic datum based on the Martian gravity field described in terms of fourth-degree, fourth-order spherical harmonics. In order to defend the use of this method and to seek the official adoption of it by the International Union of Geodesy and Geophysics, a comparison is made between the topographic datums calculated from geometric figures of Mars and the datum previously defined by a gravity field (Wu, 1981). Datums based both on geometric figures and on the gravity surface were calculated for 5° intervals in both latitude and longitude (Wu, 1984). The differences, derived by subtracting the geometric datums from the gravity datum, are listed in Table I. The oblate spheroid has been used for the Mars figure for the computation of map projections. Because the Mars triaxial ellipsoid figure in Table I is derived from, and used for the estimation of, the Mars gravity datum, differences are not too significant. However, if we compare a triaxial figure of Mars that was derived by using the Mars radio occultation data (A=3,399.3 km, B=3,394.0 km, C=3,376.4 km) (Standish, 1973), the result of the comparison with the gravity datum ranges from 0 m to 5,059 m. These elevation differences are too large for use in scientific studies.

A similar comparison was made for the Moon (Table II), in which the datum based on a sphere was also subtracted from the datum based on gravity (Wu, 1981). The triaxial ellipsoid figure derived from the gravity datum is also compared with it. Results correspond much more closely than do those for Mars.

Topographic datums can be defined arbitrarily. However, the concept of a height or elevation reference system must be carefully defined to accommodate the final goal of providing topographic information. In the case of Earth, mean sealevel surface has been used. Departures of sea level from an equipotential surface are better understood today than a few decades ago. Now that gravity data are available, the approximation using an oblate spheroid is no longer necessary, and a new elevation system can be defined based on the actual gravity field of Earth (Boal et al., 1984, Holdahl, 1984). As the purpose of planetary mapping is to provide topographic information for scientific studies and for the support of mission planning and operation, it is of vital importance that elevations be closely related to actual morphologies on the planetary surface such as those of lava flows and channel slopes and also inclinations. In the case of Mars, the proposed Geoscience and Climate Orbiter mission will provide an elevation precision of 10 m and 2-km resolution as it covers the entire Martian surface with radar altimetry. Therefore, for long-range planning and consistency, the gravity method is the most appropriate means to define a topographic datum of Mars, and probably of other planetary bodies as well.

References

Boal, J. D., Young, F. W., and Mazaachi, R., 1984, Geometric aspects of vertical datums: Technical Papers of the 44th Annual Meeting, American Congress on Surveying and Mapping, p. 589-600.

Holdahl, S. R., 1984, Aspect of a new height system for North America: Technical Papers of the 44th Annual Meeting, American Congress on Surveying and Mapping, p. 63-77.

Standish, E. M., Jr., 1973, The figure of Mars and its effect on radar-ranging: Astron. and Astrophys., v. 26, p. 463-466.

Wu, S. S. C., 1981, A method of defining topographic datums of planetary bodies: Annales de Géophysique, AGEPA 7, Tome 37, fasc. 1, p. 147-160.

Wu, S. S. C., 1984, Planetary elevation reference systems, gravity or tri-axiality: 15th Lunar and Planetary Science Conference, LPI/USRA, part 2, p. 943-944.

TABLE I: MARS TOPOGRAPHIC DATUMS: COMPARISON OF TWO GEOMETRIC DATUMS WITH THE DATUM DEFINED BY GRAVITY.

Differences were calculated by subtracting values of the geometric datums from values of the gravity datum. Radii of each datum were computed for 5° intervals in both latitude and longitude. Percentages were obtained from 2,522 data points.

DATUM	DIFFERENCES (METERS)						
	>1500	>1000	>500	>200	>100	RANGE	AVRG.
Biaxial Oblate Spheroid 1/							
A=3393.4 km	1.7%	4.5%	58.3%	83.6%	91.3%	+211	
B=3375.5 km						to	612
						-1799	
Triaxial Ellipsoid 2/							
A=3394.6 km						+435	
B=3393.3 km			0.7%	59.7%	89.5%	to	160
C=3376.3 km						-592	

1/ Geometric figure used for the computation of map projections.
2/ Geometric figure derived from gravity datum

TABLE II: TOPOGRAPHIC DATUMS OF THE MOON: COMPARISON OF TWO GEOMETRIC DATUMS WITH THE DATUM DEFINED BY GRAVITY.

Differences were calculated by subtracting values of the geometric datums from values of the gravity datum. Radii of each datum were computed for 5° intervals in both latitude and longitude. Percentages were obtained from 2,522 data points.

DATUM	DIFFERENCES (METERS)						
	>400	>300	>200	>100	>50	RANGE	AVRG.
SPHERE						+450	
R=1738 km	0.1%	17.3%	46.1%	76.1%	88.4%	to	193
						-300	
Triaxial Ellipsoid 1/							
A=1738.299 km						+331	
B=1738.182 km				5.6%	34.8%	to	85
C=1737.649 km						-212	

1/ Geometric figure derived from gravity datum.

MARS CONTROL-NETWORK EXTENSION

Sherman S. C. Wu, Francis J. Schafer, and Patricia A. Garcia, U. S. Geological Survey, Flagstaff, AZ 86001

Work has begun on an extension of the Mars control network to fill in areas of the Martian surface not covered by the recently completed planetwide control network (Wu and Schafer, 1984). Approximately 500 high-altitude pictures taken by Viking Orbiters 1 and 2 have been selected and computer processed for photogrammetry. These pictures cover the 30% of the Martian surface not covered by the existing net. Footprints of the photo coverage to be used are shown in Figures 1 and 2.

Criteria for photo selection include tilt angle and altitude. Table 1 lists these characteristics for the data set. The pictures were digitally processed to correct camera distortions according to camera calibration data, and to enhance image contrast.

This control-network extension will be accomplished by the same analytical aerotriangulation that was used for the existing net. The procedure involves selection and mensuration of pass points and adjustment using the U. S. Geological Survey GIANT program. The adjustment will be done to tie the new small blocks to the existing control system. Additional control points, including Earth-based radar observations (Downs et al., 1975), occultation points from both Mariner 9 and Viking missions (Kliore et al., 1973; Lindal, 1979), spacecraft positions determined by Earth-based tracking, and the planimetric control points derived by the Rand Corporation (Davies et al., 1978), will be used where they occur in the new areas.

References

Davies, M. E., Katayama, F. Y., and Roth, J. A., 1978, Control net of Mars: The Rand Corp., R-2039-NASA, 91 p.

Downs, G. S., Reichley, P. E., and Green, R. R., 1975, Radar measurements of Martian topography and surface properties: Icarus, v. 26, p. 273-312.

Kliore, A. J., Fjeldbo, G., Seidel, B. L., Sykes, M. J., and Woiceshyn, P. M., 1973, S-Band radio occultation measurements of the atmosphere and topography of Mars with Mariner 9: Jour. Geophys. Res., v. 78, p. 4331-4351.

Lindal, G. F., Hotz, H. B., Sweetnam, D. N., Shippony, Z., Brenkle, J. P., Hartsell, G. V., and Speer, R. T., 1979, Viking radio occultation measurements of the atmosphere and topography of Mars: Jour. Geophys. Res., v. 84, B14, p. 8443-8456.

Wu, S. S. C. and Schafer, F. J., 1984, Mars control network: Technical Papers of the 50th Annual Meeting, American Society of Photogrammetry and Remote Sensing, v. 2, p. 456-463.

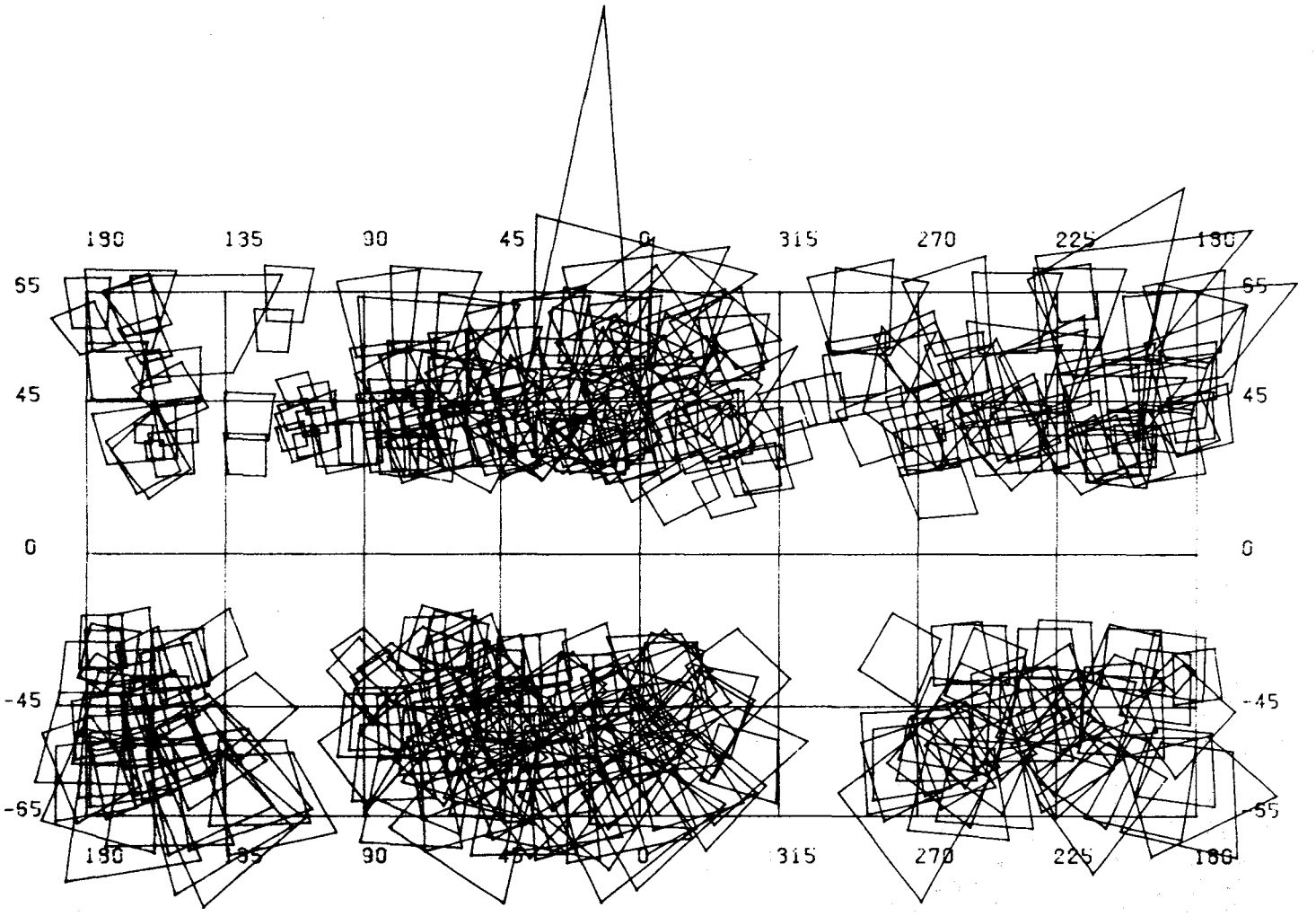

Figure 1 - Photo coverage of Mars control-network extension (equatorial belt)

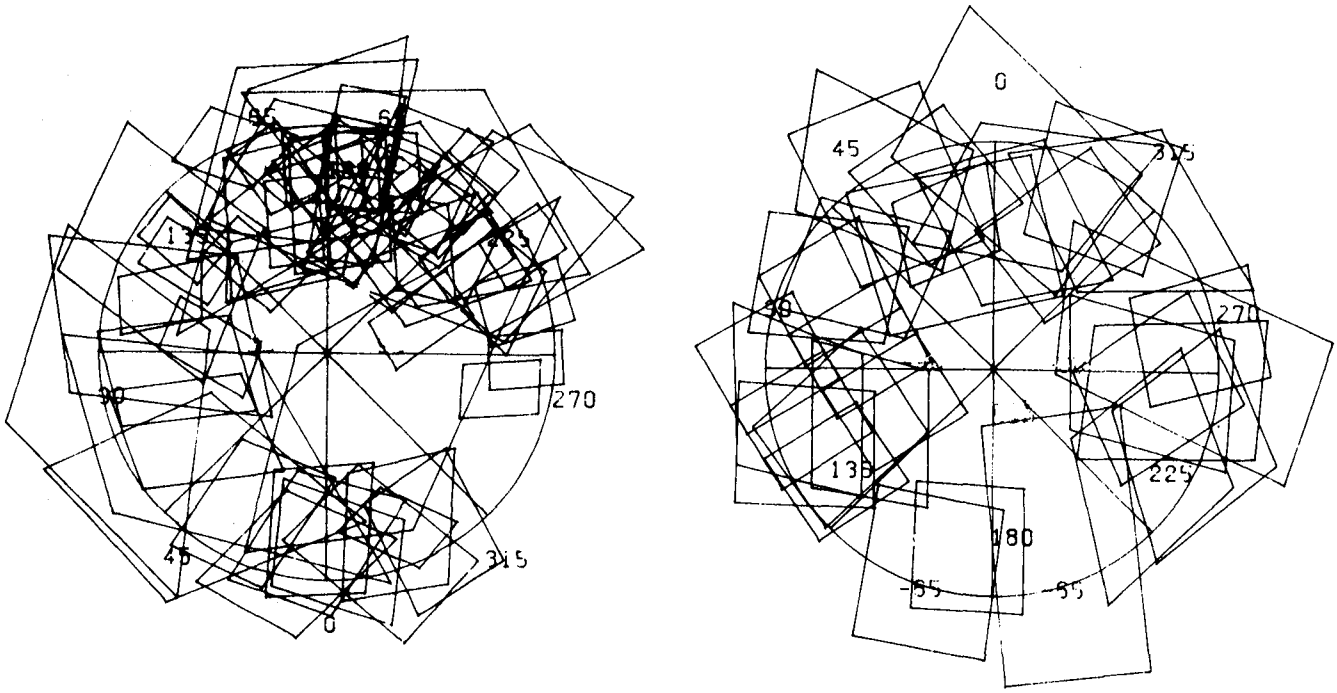

North Pole South Pole

Figure 2 - Photo coverage of Mars control-network extension (polar regions)

TABLE 1 - CATEGORIES OF VIKING ORBITAL PICTURES USED FOR THE MARS CONTROL-NETWORK EXTENSION

MISSION		Numbers of Pictures		
		VO-1	VO-2	TOTAL
RMAG 1/ (KM)	< 10,000	0	0	0
	10,000 to 24,000	54	1	55
	24,001 to 37,000	250	174	424
	37,000	1	19	20
TILT ANGLE (DEGREES)	1 to 25	98	88	186
	25 to 40	124	82	206
	40 +	83	24	107
TOTAL		305	194	499

1/ Range from Mars mass center

1:500,000-SCALE TOPOGRAPHIC MAPS OF MARS

Sherman S. C. Wu, Patricia A. Garcia, Raymond Jordan, and Francis J. Schafer, U. S. Geological Survey, Flagstaff, AZ 86001

We have begun experimental compilation of 1:500,000-scale topographic maps of Mars. This work involves the use of high-resolution Viking Orbiter pictures for generating secondary control points from block adjustment, using the GIANT computer program. We then use these data to compile contour lines on analytical stereoplotters. As an example, in the Tithonium quadrangle, covering the area between lat 2.5° S. and 7.5° S., long 80° W. and 85° W., we have 213 control points produced from 67 pictures. These control points are tied to the Mars planetwide control net (Wu and Schafer, 1984) and refer to the Mars topographic datum (Wu, 1981). The altitude of Viking Orbiter pictures used for the 1:500,000-scale mapping is limited to less than 10,000 km. The relative accuracy of elevation adjustment is about 60 m, enabling a contour interval of 200 m; the absolute horizontal accuracy is about 4 minutes, which is about 4 km on the ground in the equatorial region. For the Tithonium quadrangle, more than 30 stereomodels were established. Special compilation techniques previously developed (Wu et al., 1982) are employed in the large-scale topographic mapping. The map grid is a transverse Mercator projection.

For Mars geologic studies or for studies of possible Mars landing sites, compilation of these 1:500,000-scale topographic maps will be continued wherever high-resolution stereocoverage is available.

References

Wu, S. S. C., 1981, A method of defining topographic datums of planetary bodies: Annales de Géophysique, AGEPA 7, Tome 37, fasc. 1, p. 147-160.

Wu, S. S. C., Elassal, A. A., Jordan, Raymond, and Schafer, F. J., 1982, Photogrammetric application of Viking Orbiter photography: Planetary and Space Science, v. 30, no. 1, p. 45-55.

Wu, S. S. C., and Schafer, F. J., 1984, Mars control network: Technical Papers of the 50th Annual Meeting, American Society of Photogrammetry and Remote Sensing, v. 2, p. 456-463.

DEVELOPMENT OF NEW PHOTOGRAMMETRIC TECHNIQUE FOR PLANETARY TOPOGRAPHIC MAPPING

Sherman S. C. Wu and Annie-Elpis Howington, U. S. Geological Survey, Flagstff, AZ 86001

A new technique has been developed to accomplish on-line preparatory computations for stereophotogrammetric orientation of Viking Orbiter pictures. These pictures have such narrow fields of view that conventional off-line photogrammetric orientation techniques (Wu et al., 1982) are inadequate for setting up models on a stereoplotter. In the new process, the software stores all the adjusted camera parameters (positions and attitudes) and all the control points from the Mars control network in a moving-head disc of the stereoplotter computer. Thus rapid and efficient access is possible during the stereocompilation process (Wu, 1984). The operator needs only to enter the identification of the stereopair of pictures and to perform the interior orientation to activate the system, which then produces a properly oriented stereomodel.

The model-orientation parameters are computed by using the adjusted camera position and orientations in the control-net adjustment (Wu and Schafer, 1984). Stereomodels are produced that are often suitable for compilation without further modification. The orientation may be refined, however, by reference to the control points. In this process, the operator merely enters identification of control points in the area and moves the plotter's cursor to each of those points. The computer then locates the control points in the master file on the disc and refines the absolute orientation automatically. The current file contains coordinates of about 3,000 control points and parameters of all 715 Viking Orbiter pictures in the Mars planetwide control network.

Future development will include on-line geometric corrections for film shrinkage and lens distortions and real-time conversion of digital data for the production of orthophotographs.

References

Wu, S. S. C., 1984, Analytical systems for data reduction with images of extraterrestrial bodies: International Archives of Photogrammetry and Remote Sensing, v. XXV, p. 549-557.

Wu, S. S. C., Elassal, A. A., Jordan, Raymond, and Schafer, F. J., 1982, Photogrammetric application of Viking orbital photographs: Planetary and Space Science, v. 30, no. 1, p. 45-55.

Wu, S. S. C. and Schafer, F. J., 1984, Mars control network: Technical Papers of the 50th Annual Meeting, American Society of Photogrammetry and Remote Sensing, v. 2, p. 456-463.

COMPILATION OF MARS 1:2,000,000-SCALE TOPOGRAPHIC MAP SERIES

Sherman S. C. Wu, Raymond Jordan, and Francis J. Schafer, U. S. Geological Survey, Flagstaff, AZ 86001

Development of special photogrammetric techniques (Wu et al., 1982) and completion of the Mars planetwide control network (Wu and Schafer, 1984) have enabled compilation of a 1:2,000,000-scale series of topographic maps of Mars from Viking Orbiter pictures. Seventeen quadrangles of the series have been compiled: MC1-A, -B, MC8-NE, -SE, -SW, -NW, MC9-NE, -SE, -SW, -NW, MC16-NE, -NW, MC17-NE, -NW, MC18-NW, and MC30-A and -B. It is anticipated that all 140 quadrangles will be compiled eventually. Compilation of 7 to 15 stereomodels on analytical stereoplotters is required to make each map. Film positives of Viking Orbiter pictures that have been digitally corrected for geometry are used.

Contour lines are referred to the Mars topographic datum (Wu, 1981). The contour interval is 1 km. Digital elevation models will be made later either with data collected during map compilation or by digitizing the topographic maps. The scale is true only at latitudes of ± 27.476°. As an example, Figure 1 is the topographic map of the Phoenicis Lacus Northeast quadrangle (MC-17NE).

Factors that limit the accuracy of compilation include low resolution (800 to 1000 m/pixel) of high-altitude photography, the very narrow field of view of the Viking cameras, weak model geometry (i. e., small base-to-height ratios), and the presence of dust and haze in the Martian atmosphere.

The topographic maps already completed provide more detailed knowledge of vertical relief and have helped in the understanding of the geologic processes that have formed the Martian surface. The combination of the existing planetwide control network of Mars and the new control-network extension (Wu et al., this issue) will enable the topographic mapping of the entire Martian surface at a scale of 1:2,000,000.

References

Wu, S. S. C., 1981, A method of defining topographic datums of planetary bodies: Annales de Géophysique, AGEPA 7, Tome 37, fasc. 1, p. 147-160.

Wu, S. S. C., Elassal, A. A., Jordan, Raymond, and Schafer, F. J., 1982, Photogrammetric application of Viking Orbiter photography: Planetary and Space Science, v. 30, no. 1, p. 45-55.

Wu, S. S. C., and Schafer, F. J., 1984, Mars control network: Technical papers of the 50th Annual Meeting, American Society of Photogrammetry and Remote Sensing, v. 2, p. 456-463.

Wu, S. S. C., Schafer, F. J., and Garcia, P. A., 1985, Mars control-network extension: NASA Technical Memorandum, this issue.

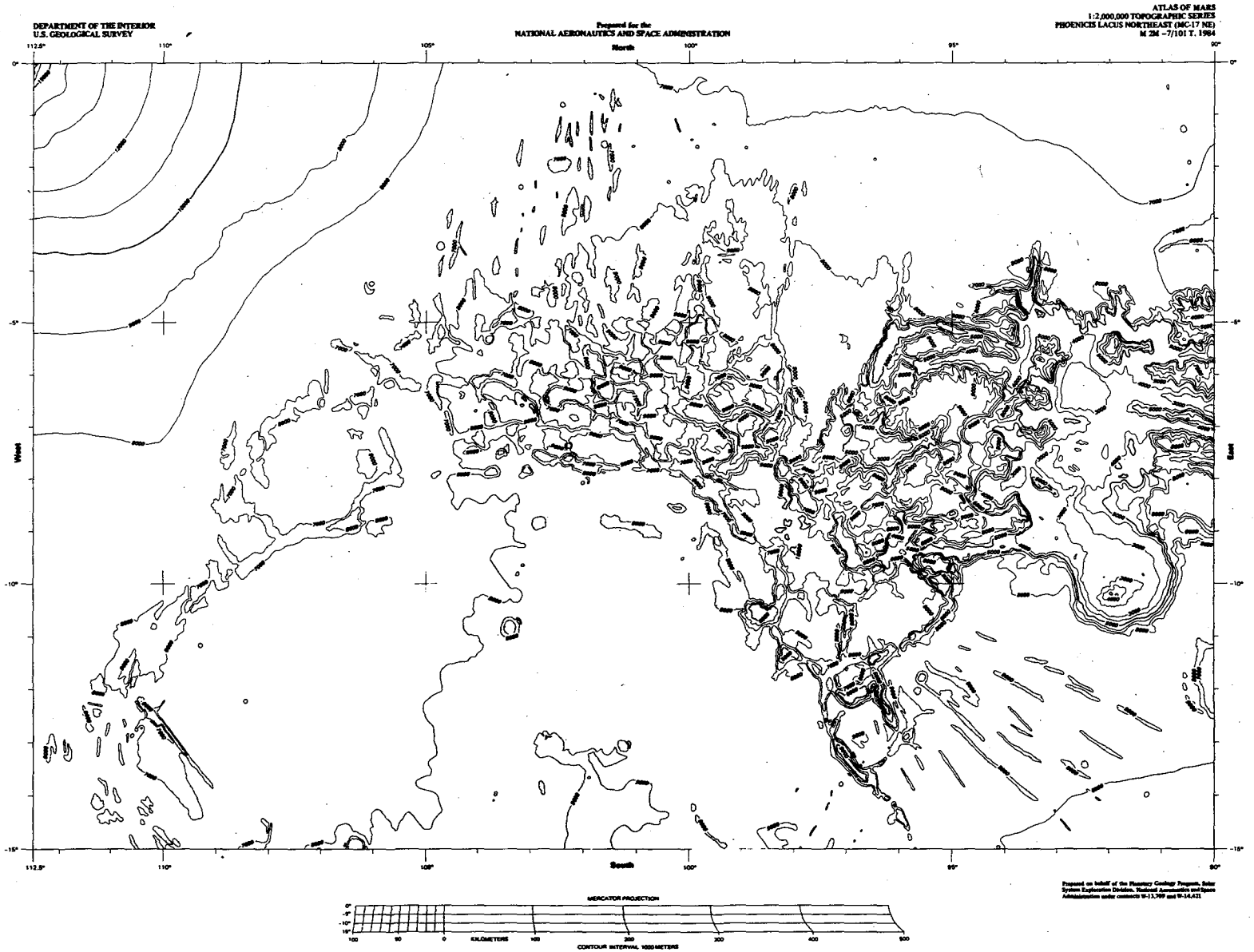

Figure 1 - Topographic map of Phoenicis Lacus Northeast quadrangle of Mars, MC-17NE, at reduced scale.

Page intentionally left blank

AUTHOR INDEX

1. Report No.	2. Government Accession No.	3. Recipient's Catalog No.
NASA TM-87563		

4. Title and Subtitle	5. Report Date
Reports of Planetary Geology and Geophysics Program - 1984	April 1985
	6. Performing Organization Code: EL
7. Author(s): Henry E. Holt and T. R. Watters, Compilers	8. Performing Organization Report No.
	10. Work Unit No.
9. Performing Organization Name and Address: Planetary Geology Program, Office of Space Science and Applications, Solar System Exploration Division, Washington, DC 20546	11. Contract or Grant No.
	13. Type of Report and Period Covered: Technical Memorandum
12. Sponsoring Agency Name and Address: National Aeronautics and Space Administration, Washington, DC 20546	14. Sponsoring Agency Code

15. Supplementary Notes

16. Abstract

This is a compilation of abstracts of reports from Principal Investigators of NASA's Planetary Geology and Geophysics Program, Office of Space Science and Applications.

The purpose is to provide a document which succinctly summarizes work conducted in this program. Each report reflects significant accomplishments within the area of the author's funded grant or contract.

No attempt has been made to introduce editorial or stylistic uniformity; on the contrary, the style of each report is that of the Principal Investigator and may best portray his research.

17. Key Words (Suggested by Author(s))	18. Distribution Statement
Planetary Geology Solar System Evolution Planetary Geologic Processes	Unclassified - Unlimited Subject Category 91

19. Security Classif. (of this report)	20. Security Classif. (of this page)	21. No. of Pages	22. Price
Unclassified	Unclassified	640	A99

N-305

For sale by the National Technical Information Service, Springfield, Virginia 22161

☆U.S. GOVERNMENT PRINTING OFFICE:1985 -537 -086/ 56· REGION NO. 4

National Aeronautics and
Space Administration

Washington, D.C.
20546

Official Business
Penalty for Private Use, $300

SPECIAL FOURTH CLASS MAIL
BOOK

Postage and Fees Paid
National Aeronautics and
Space Administration
NASA-451

NASA

POSTMASTER: If Undeliverable (Section 158
Postal Manual) Do Not Return